Techniques in deep imaging within biological tissue

UNIVERSITY OF STRATHCLYDE

A Thesis Submitted to

The Department of Physics

University of Strathclyde

For the Degree of

Doctor of Philosophy

By

Simon Poland

August 2006

Declaration of author's rights

To my family

"Every time I learn something new, it pushes some old stuff out of my brain. Remember when I took that home winemaking course and forgot how to drive?"

Homer Simpson

Acknowledgements

I wish to extend my gratitude to the following people for the completion of this thesis and the work contained within.

Firstly, many thanks must go to my supervisor Dr John Girkin for all his help, guidance and support during my studies and for giving me the opportunity to carry out research at the Institute of Photonics. I also want to thank Dr Amanda Wright for her incalculable contribution to this work as well as a special thanks to Dr. Walter Lubeigt, Dr. David Burns, Dr. Gareth Valentine, Dr. Andrew Hall and Dr. Chris Longbottom for all their help. Many thanks must go to all staff and students of the Institute of Photonics, in particular Scott, Nicolas Carol-Anne, Untzizu and Chris for making my time here a happy one. Without the unique mix of people at the Institute, the time during my PhD would not have been so educational and colourful. I also extend my thanks to Mrs. Lynda Mc Laughlin, Mr Paul Hynd and Ms. Lisa Reid.

Finally, on a personal level, I must thank Priscilla, my parents, family and friends for their continued love and support during my studies. I do not know how I would have got through my study without them.

To anyone I have not mentioned by name, I also extend my gratitude.

Simon Poland

August 2006

Abstract

This thesis is concerned with the development of low-cost and practical biological optical imaging and diagnosis systems that will allow the user to image and resolve structure deep into biological tissue without the need for physical dissection. Research within this thesis can be divided into two main sections, namely (a) the development of optically sectioning microscopy systems incorporating adaptive optics to compensate for system and specimen induced aberrations, and (b) as an example of biological tissue and disease, the development of dental imaging devices to detect and diagnose dental disease (caries).

Section (a)

The ability of confocal and multiphoton microscopy techniques to image optical sections deep within biological samples is a major advantage in biology. Unfortunately, as one images deeper within a sample, image degradation increases due to aberrations and scattering. In this investigation, operating a confocal microscope in reflection, a deformable membrane mirror (DMM) was used to counteract for sample aberrations within a closed feedback loop. By selecting various image properties (e.g. brightness, contrast or resolution), various optimisation algorithms were used to improve this property by altering the shape of the DMM and compensate for aberrations. Taking axial and lateral point spread functions (PSFs), the improvement of the system was monitored. The ability of the adaptive optic system to optimise to a particular axial PSF (PSF engineering) was also examined.

The use of various algorithms with an adaptive element in a confocal system has been demonstrated to show significant improvement in the axial resolution and signal intensity. While global optimisation algorithms such as the genetic algorithm are more likely to find the global maximum in solution space in comparison to hillclimbing, it usually takes longer to achieve an optimum solution. Particular fitness parameters have shown promise in increasing the effectiveness of the algorithmic search routines. Optimising certain axial PSF components appears to have a detrimental effect on the lateral PSF and resolution. In the situation where the

best axial and lateral resolution is required, optimising for intensity appears to show the best all round result.

By adapting the axial fitness parameter program, it has been shown that particular desired axial PSF shapes can be reproduced within an aberrated sample. This does appear to have some limitations due to the relative power of the mirror (stroke).

Section (b)

Using optical techniques, physiological changes associated with the onset of disease in biological tissue can be detected. Taking dental tissue as an example of a highly scattering biological media, a computer model based upon commercially available software was used to theoretically reproduce experimental results taken using a fibre optical confocal system on dental tissue. From simulations, it has been shown that such a system could microscopically measure the optical properties of a caries lesion within dental enamel non-invasively.

A system based on the use of structured light to penetrate and quantify early stage dental caries was presented as a possible aid to dentistry. Although the system was able to optically section the carious surface as well as detect inhomogeneities greater than 60μm deep into the tooth sample, more studies must be carried out to assess the limitations of the system.

On a macroscopic scale, a cost effective system known as near-infrared Lateral Illumination (L.I.) (which is based on transillumination techniques) was presented. In a preliminary study involving 15 ex-in vivo adult pre-molars and molars at various stages of dental decay, L.I. was shown to be the most effective occlusal caries diagnosis system when compared to some techniques currently available and in development.

Table of contents

Chapter 1: Biological cell and tissue structure and their interactions with light

1. Introduction

The onset of disease usually results in physiological changes, which can be detected as an alteration in the optical properties of the tissue. Therefore, the development of such systems requires a good understanding of the complex structure of biological tissue as well as optical interactions with matter. The term 'deep imaging' used throughout this thesis is relative in context to the application each imaging system is developed for. In the case of microscopy systems a·depth of ~2mm would be considered extremely deep while in macroscopic systems (such as those used when imaging a whole tooth), deep refers to a depth of several centimetres.

This chapter presents a short generalized historical background to optical imaging from its early beginnings to present day. A brief overview of the composition of biological cells and animal tissue structure provides an outline of the complexity of the problems faced when trying to image deep into biological samples. There is a description of the properties associated with light and a summary of the various ways in which light can interact with matter. This chapter includes a more detailed examination of the effects of absorption and optical scattering and a short introduction into optical aberrations and their effect when imaging. Finally, this chapter concludes with a brief preview of each of the subsequent chapters of this thesis.

2. Introduction to biological imaging

2.1 Historical background

Of the five senses, it can be argued that sight is considered the most important. Such a high importance was given to our vision that earlier cultures thought that the eyes provided windows into our souls. We rely on vision to gather information and navigate through the world around us. Our vision does have its limitations, in that it can only let us see certain wavelengths and sensitivities. This is due to both the optical components

that make up our eye (lens and pupil size), as well as the density of and sensitivity of the rods and cones (responsible for converting light into an electrical signal which can be interpreted by the brain) to certain wavelengths.

Our vision allows us to distinguish between objects that are 1arc minute apart from a 6 metre testing distance (Snellen visual acuity test [1], where the human subject has a visual acuity of 20/20) and detect light within a small portion of the electromagnetic spectrum (400nm – 700nm). Due to these restrictions associated with our vision, most of the interactions that occur in the physical world are not visible to the naked eye. This has led to the development of instruments that allow one to overcome these limitations.

Although the concept of a 'burning glass' was well known in ancient times, it was not until the 13th century that spectacles first appeared in Florence, Italy [2 & 3]. These early devices although considered quite crude by today's standard of glass making and design, allowed the user to magnify an object to a certain degree, as well as compensating for eye defects such as myopia (short-sightedness). It was not until the late 16th century that compound devices (comprising of two or more lenses) such as the telescope and the microscope were invented by Lippershey and Janssen respectively.

In the 17th century, several major advancements were made in optics, undoubtedly due in part to a major drive within the scientific community to understand how these new ground breaking devices functioned. Although previously observed by many scientists, it was not until 1621 that Snell explained the phenomenon of refraction in terms of an equation which later became known as Snell's law. This was the first comprehensive description of refraction and led the way for other developments in optics. In 1647, Cavalieri, through his lensmaker's formula, was able to link the focal length of a lens to the refractive index, and the curvatures of the lens' surfaces. In 1670, Newton derived the imaging equation, which related the distance between the object and image planes in terms of the focal length of the lens.

These developments in optics led to the production of more sophisticated devices. In the newly formed field of microscopy, several discoveries were being made that were redefining the way man perceived the world. One such discovery by Marco Malpighi, using a light microscope, proved theories earlier postulated by William Harvey on blood circulation. In Robert Hooke's publication in 1665 [4], illustrations were presented of several samples (including cork and fleas) which showed microscopic details never before seen.

In the 18th and 19th centuries, improvements in optical and mechanical design, which in turn allowed enhancements in resolution and magnification, helped to facilitate more biological discoveries. Improvements in glass design and the production of homogeneous glass materials aided in removing chromatic aberration from an image. Owing to previous experiments (e.g. Young's double slit) which suggested the wave nature of light, in 1865, electromagnetic wave theory of light was firmly established by James Maxwell [5]. In 1873, Abbe's interpretation of image formation led to the development of laws governing diffraction theory [6], which govern modern microscope design today.

2.2 Modern imaging

The discovery of the quantum nature of light at the start of the 20th century has led to numerous advancements associated with modern imaging systems today. In particular the invention of the computer and advancements in image processing techniques, in addition progress in new light detection techniques (such as charge coupled device), have led to a revolution in optical imaging. Today, the advancement of new materials and devices has allowed the development in imaging systems to exploit many kinds of light-matter interactions (i.e. scattering or polarisation effects) throughout all of the electromagnetic spectrum. Using new techniques, biological light imaging systems are being developed that can reach, and in some cases surpass, the theoretical limits imposed in conventional optics theory, which in turn helps to further our understanding of life processes and disease.

2.3 Cell and tissue structure

The cell can be described quite simply as the 'building block of life'. Taken from the Latin word *cella*, (meaning small room) the cell is the "structural and functional unit of all living organisms" [7]. All life on this planet ranges from single celled prokaryotic (such as bacteria and archaea) and eukaryotic organisms (i.e. protests), to large multicellular eukaryotic organisms (fungi, plants and animals) containing mainly billions of cells, all working together in a symbiotic relationship. It is estimated that humans are composed of ~ 10^{14} cells. Since this thesis concerns the development for biological imaging in human tissues, only animal cellular structure will be discussed.

A cell is responsible for a number of processes or activities, which may be defined by its degree/level of specialisation. However, regardless of how specific they are, all cells share a number of common capabilities, which are:

1. Reproduction – achieved by cell division.
2. Metabolism – each cell is responsible for metabolizing organic molecules to convert chemical energy to drive all cell processes.
3. Proteins synthesis – proteins are used to maintain cell functionality.
4. Response to stimuli – all cells are sensitive to some form of stimuli (such as pH, temperature etc.)

All animal cells are composed of a cell membrane, which surrounds the cell, protects and provides a barrier from the environment. These membranes also function to control the passage of compounds into and out of the cell. Within the cell, a complex array of microfilaments, known as the cytoskeleton, serves to maintain cell shape and structure. The cell contains a number of subcellular components, known as organelles, which are responsible for cell operation and function. Figure 1 shows the typical structure of an animal cell containing subcellular constituents.

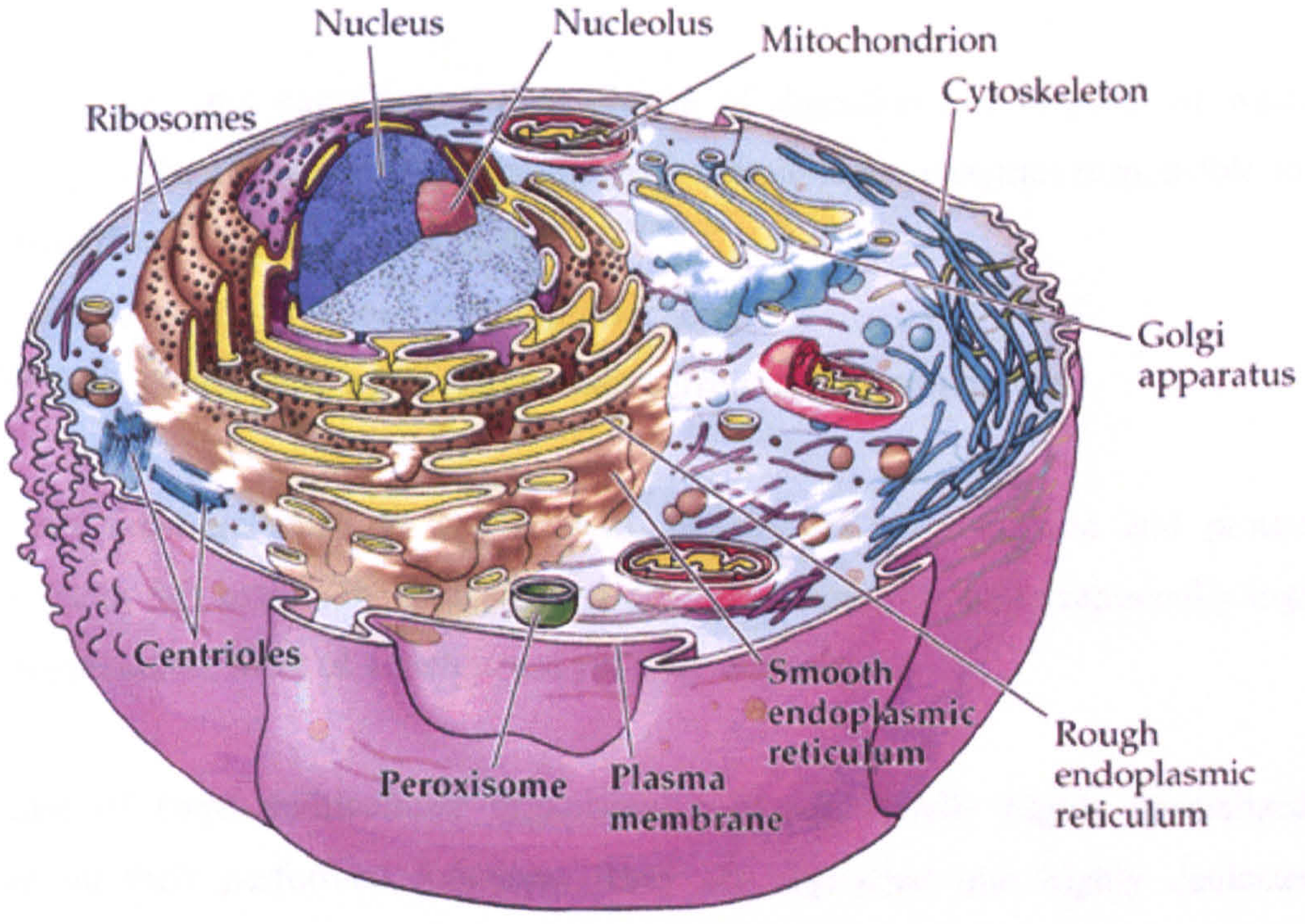

Figure 1: Showing the typical structure of an animal cell [8].

These organelles as shown in the diagram are responsible for a number of functions within the cell:

1. Nucleus – serves as the centre of the cell providing information and administration and houses the genetic material (DNA).
2. Ribosomes – are responsible for carrying out orders and producing proteins depending on the information provided by messenger genetic material (mRNA) from the nucleus.
3. Mitochondria – these organelles contain their own DNA and are responsible for all metabolism within the cell through complex chemical pathways. They serve as the powerhouses of the cell.
4. Endoplasmic reticulum – this is a network that controls and modifies chemical compounds which are to be used within or outside the cell.

5. Golgi apparatus – controls the delivery of chemical compounds into and outside the cell.
6. Lysosomes and peroxisomes – in charge of digestion and disposal of waste compounds. These membrane bound sacs contain many enzymes responsible for breakdown.
7. Centrioles – aid in mitosis (cell reproduction).
8. Vacuoles – food and water storage sacs surrounded by a membrane.

Normal cell functions such as cell growth, metabolism, reproduction and protein synthesis are in fact extremely sophisticated processes, requiring an exceptionally high level of organization, most of which is not yet fully understood.

In the case of large multicellular organisms, cells are usually highly specialized, dependant on their performed functions. They are organized into highly dedicated structures and bound together within an interstitial medium with numerous fibrous connections. This is known as biological tissue.

In terms of animal tissues, there are typically four basic types of tissues (figure 2) which make up all of the organs, structures and contents of the animal (including humans). These are:

1. Epithelium – these tissues provide protective linings for the animal and are also responsible for secretion and absorption, e.g. skin and digestive wall lining.
2. Muscle – these tissues through the use of contractile filaments which change cell sizes serve a number of functions. Three types of tissue are skeletal (movement), smooth (organ inner linings) and cardiac (heart) muscle.
3. Nerve – cells which include the brain, the spinal cord and nervous system.
4. Connective – this tissue is responsible for holding everything together, e.g bone and blood.

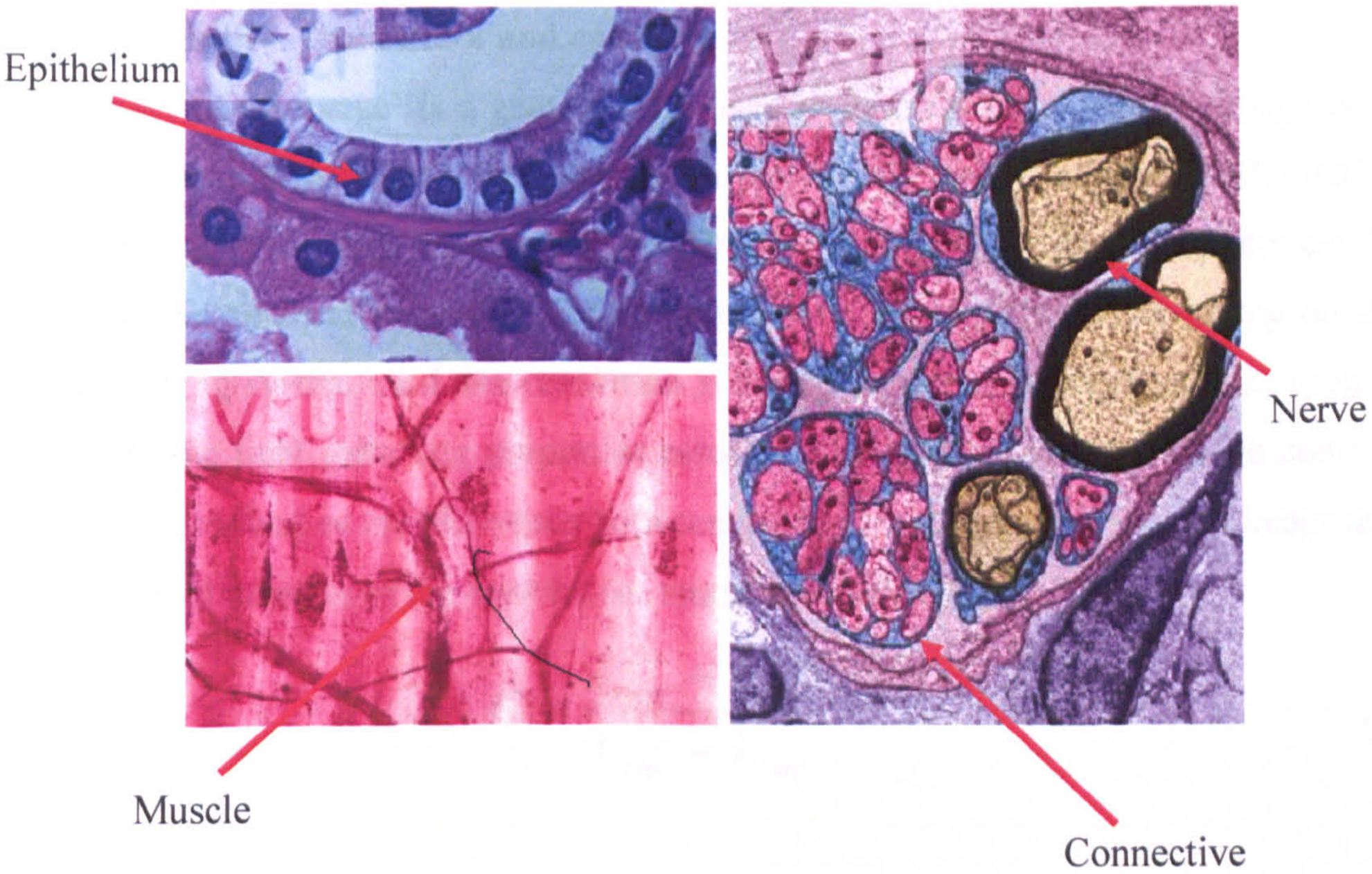

Figure 2: Examples of the four main types of tissues within an animal [9].

From these four basic types, further specialization occurs in order to perform all the specific functions required in a large multicellular organism (such as the human body). From this brief outline of cell and tissue composition, it has been shown that biological tissue is indeed quite complex in structure, and provides a turbid and dynamic media through which one must examine.

3. Requirements for biologists and clinicians

Ideally, the best imaging system would be one that is capable of producing crisp, clear, aberration free, high frame rate, real-time, three dimensional images of live biological cell and tissue structure with diffraction-limited resolution (or higher!), without perturbing or damaging the sample. At present, such a system does not exist and usually in order to achieve the theoretical limits for one factor, one must exchange with one or more several other factors.

3.1 Image quality – resolution and contrast

The 'quality of an image' is a generic term used to describe how good an image is. It takes into account resolution and contrast, as well as the degree of useful information that can be extracted from the image itself. The resolution of any imaging system can be defined as the smallest resolvable feature that can be distinguished. Depending on the optical imaging system used, the resolution is reliant on the wavelength of light used in addition to the light gathering properties associated with the technique. Image contrast [1] can be described as the difference between the dark and light points on an image and can be defined in terms of the contrast (or modulation) ratio C, as:

$$C = \frac{I_{\max} - I_{\min}}{I_{\max} + I_{\min}} \tag{1}$$

where C can have a value from 0 to 1.0.

In any imaging system, contrast is extremely important in distinguishing objects. For a system with the best achievable resolution, but with little or no contrast, the ability of the user to discriminate between resolvable features is quite low. In biological imaging systems, the loss in resolution and contrast (and hence image quality) are due to the effects of aberrations and scattering respectively, both of which will be discussed in much greater detail later in this chapter.

Depending on the application, biologists do not necessarily require an imaging system that gives both the best resolution and contrast. It can be simply described as finding the right tool for the job. In the case of examination and diagnosis, the best instruments are those that present the most useful information to the biologist or practitioner without damaging or perturbing the sample.

3.2 Properties of Light

As mentioned previously in this chapter the use of light is a particularly suitable tool for studying biological tissue and as an aid in the diagnosis of disease. Light can be seen as having both particle and wave characteristics. As a wave, light is composed of both electric and magnetic components, which travel together at right angles to each other. The distance between successive troughs or crests of the wave defines the wavelength λ of the light, which is associated to the energy E (contained within the wave), via Planck's Law [10]:

$$E = \frac{hc}{\lambda} \tag{2}$$

where h = Planck's constant =6.62×10^{-34} Js, and c = the speed of light in a vacuum.

Due to the inverse proportionality between wavelength and energy shown in equation 2, the smaller the wavelength of light, the greater the energy associated with it. This has implications in terms of absorption and the possible photo damage to biological tissue when using light at shorter wavelengths in the visible and UV range. The electromagnetic spectrum and the small region that visible light occupies within it, is shown in figure 3.

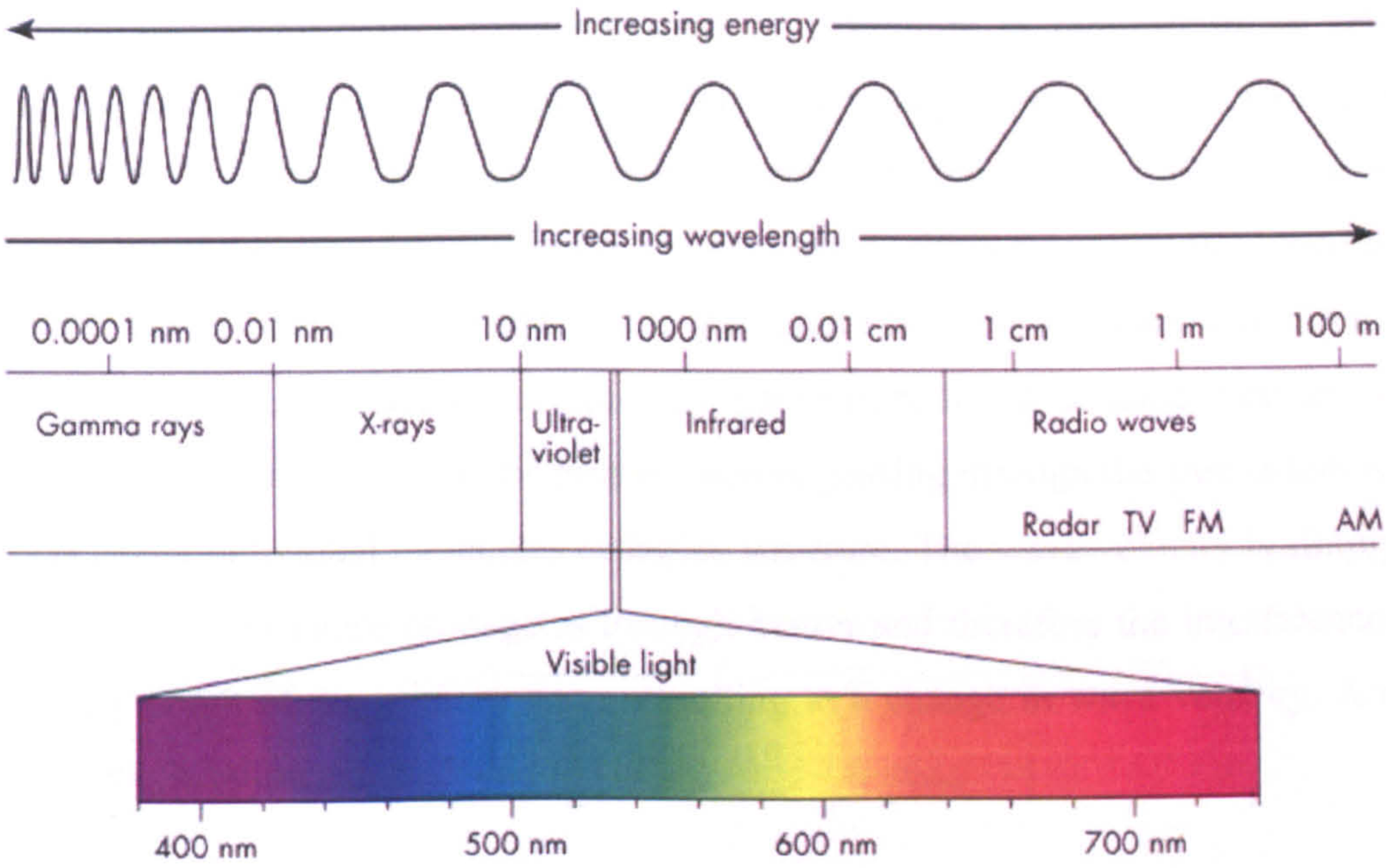

Figure 3: Showing the electromagnetic spectrum [11].

3.3 Light and its interactions with matter

The speed of light c, when traveling through a vacuum is constant at ~3 x $10^8 ms^{-1}$. When light travels through matter, its speed decreases which is related to the refractive properties of that material.

3.3.1 Refractive index

The refractive index of a material defines the factor by which the velocity of the light at a particular wavelength is slowed by that material, relative to the velocity of light in a vacuum. The refractive index, n is defined by the equation:

$$n = \frac{c}{v} \tag{3}$$

where v = the velocity of light within the medium and $n = 1$ when light travels in a vacuum.

The difference between the velocity of light in a vacuum as opposed to its velocity within matter is due to scattering effects, which can be explained in molecular and wave terms. Matter is composed of molecules interspersed in empty space. When light enters matter, some of the wave interacts with bound charges within the molecules, resulting in secondary waves, identical to those due to Rayleigh scattering in gases (explained later in this chapter). In the case of an optically transparent liquid or solid medium, these secondary waves interfere with the primary waves passing through the free space, which exists between individual molecules or lattice structure. The wave velocity is simply the rate at which equal phase propagates through matter and therefore the interference will modify the phase of the primary wave, resulting in a change in wave velocity. A more thorough explanation can be found in [12].

Light can interact with matter in a diverse number of ways as shown in figure 4. By developing techniques to measure these interactions, information on some of the processes that occur within the biological cells and tissues can be found.

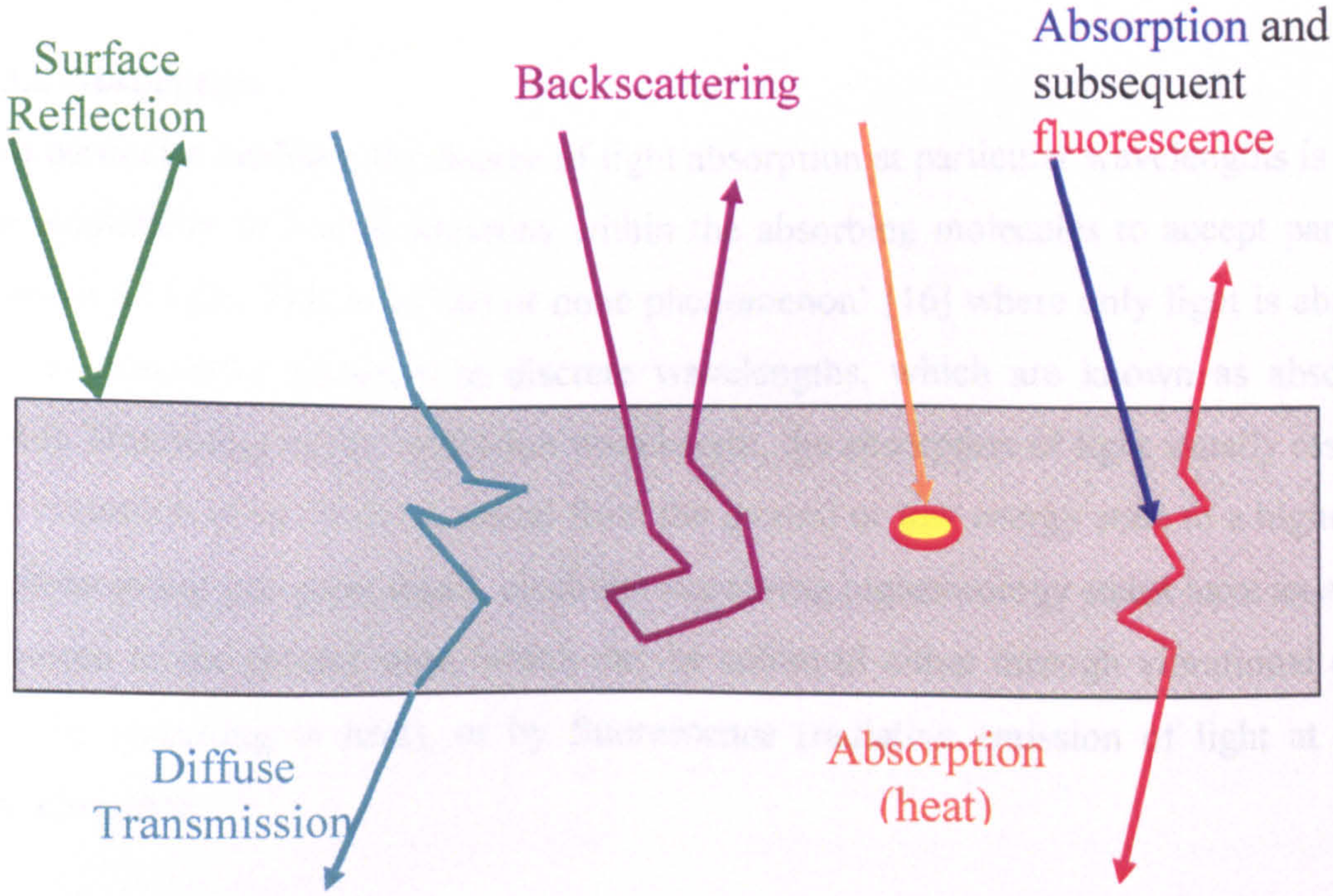

Figure 4: Showing light interactions with matter.

Light interactions are usually a combination of reflection, scattering, and absorption when traveling through with a medium. In the case of absorption, the energy associated with the light is either dissipated in the form of heat, or re-emitted in the form of fluorescence. Depending on the material, the degree at which each interaction occurs is normally affected by the wavelength of the light.

When developing techniques to optically diagnose biological tissue, it is essential that the links between optical and biological properties be understood. In biology, "disease can be defined as any abnormal condition of an organism that impairs function" [13]. Metabolic and physiological cell changes such as those associated with a disease usually result in modifications in the optical properties of tissues [14 & 15]. Development of diagnostic devices relies on measuring these (variations in) optical properties accurately and in a manner that can be understood. In the case of biological tissues, absorption and scattering are two of the main physical phenomena (both of which have some wavelength dependence), and these will be discussed in more detail.

3.3.2 Absorption

In a particular medium, the degree of light absorption at particular wavelengths is due to the availability of bound electrons within the absorbing molecules to accept particular photons of light. This is an 'all or none phenomenon' [16] where only light is absorbed by the absorbing molecule at discrete wavelengths, which are known as absorption bands. Depending on the excitation wavelength, the absorption of light usually results in the excitation of an electron orbital from the ground or low energy state to a higher one. Without going into great detail, electrons occupying higher energy states have an affinity to return to the ground state, which can be achieved either through vibrational energy transfer (resulting in heat), or by fluorescence (radiative emission of light at longer wavelengths).

Neglecting any scattering effects, for a specific homogeneous material, the absorption co-efficient μ_a (which is described in mm^{-1} units) for a particular wavelength of light is defined as:

$$\delta I = -u_a I \delta x \tag{4}$$

where δI is the differential change in intensity of a collimated light of intensity I, which passes through a homogeneous medium of small distance δx.

By integrating this equation over a distance x gives the Lambert-Beer law:

$$I = I_o \exp^{-\mu_a x} \tag{5}$$

where I_o is the starting intensity of the light before it enters the absorbing medium.

In the case of a biological medium, the degree of absorption is very important. Depending on the wavelength of illumination and light intensity used, absorption can lead to possible cell damage from heating and the production of free radicals associated with ionization of bound electron states.

The development of fluorescence detection has been used in microscopy to reveal features, which have been previously been undetectable for standard microscopes. Fluorescent dyes can bind to particular molecules and structures within biological tissue allowing labeling, and using suitable wavelength filters to isolate fluorescent light from illumination light offers a high degree of sensitivity. The use of fluorescence in microscopy will be discussed in much greater detail in Chapter 2.

3.3.3 Scattering

Another source of attenuation when imaging through biological tissue is due to scattering. When imaging at visible wavelengths, light scattering associated with biological media is wavelength dependant, decreasing as the wavelength approaches the near infrared. On a microscopic scale, scattering within biological tissues is due to

refractive index mismatches between extracellular media and cellular constituents such as cell membranes, cytoplasmic media and organelles (nuclei, mitochrondia, ribsomes etc).

There are two main theories to describe scattering within media. These are namely (a) Rayleigh scattering, and (b) Mie Scattering. Rayleigh scattering [12] (named after Lord Rayleigh who first proposed it) is associated with scattering due to particles which are generally much smaller than the wavelength used. Closely related to scattering associated with the refractive index of liquids and solids, and used to explain why the sky appears blue, Rayleigh scattering has a $1/\lambda^4$ dependency on wavelength. This type of scattering phenomena is restricted to situations where the scattering particles are smaller than a tenth of the wavelength used, and is generally used to describe gaseous scattering events.

Mie theory [17 - 19] is used to describe situations where the scattering particles are close to, or larger than, the wavelength of light used. It is a complex theory taking into account particle size, refractive index, shape, dielectric constant and absorptivity of the particles as well as the refractive index of the surrounding medium. Scattering associated with Mie theory can be seen in colloidal suspensions such as milk and clouds, where the scattering particles (fat globules and water droplets respectively) are larger than the visible wavelength band of light. These colloid examples appear white due to the scattering having a much weaker dependency on wavelength [19].

Within biological media, due to the relative sizes of the scattering particles (organelles range from 0.2 – 10μm in size [14]), when illuminating with visible or near infrared light, Mie scattering is generally much more prevalent. In a similar situation to absorption, of a collimated light source, the scattering co-efficient μ_s can be defined in the equation, [20]:

$$I = I_o \exp^{-\mu_s x} \tag{6}$$

where I is the non-scattered collimated light that has traveled through distance x of a non-absorbing medium. The units for μ_s are expressed in mm^{-1}.

The scattering co-efficient μ_s is related to the particle density ρ, by the equation:

$$\mu_s = \rho\sigma_s \tag{7}$$

where σ_s is the scattering cross section.

In an isotropic medium, light scattering events occur in all directions with equal intensity. For biological tissues, it has been shown they are generally optically anisotropic in nature, owing to the birefringence of the tissue [14 & 21]. Without going into great detail, birefringence of a material is the dependence of the refractive index of the medium on the direction of the optical axis. In the case of biological tissue, birefringence is mostly due to the anisotropic structure of extracellular fibrous configurations, which are cylindrical in shape [14].

This angular dependence of scattering can be characterized by the anisotropy factor, g, which is defined by the equation:

$$g = \int_{-1}^{1}(\cos\theta) f \cos\theta \tag{8}$$

where the anisotropy can be described in relation to the mean cosine of the scattering angle to the incident light.

In the situation where the scattering medium is completely isotropic in nature, g = 0. When g =1, the medium completely scatters the incident light wave in the forward direction. For an anisotropic medium, in order to describe and compare its scattering co-efficient to an isotropic medium, one must calculate the reduced scattering co-efficient u_s' from the equation, [20]:

$$\mu_s' = \mu_s(1-g) \tag{9}$$

where the average distance the collimated light beam must traverse before becoming isotropic traversed by the collimated light beam before it can be viewed as being isotropic being $1/\mu_s$'.

Taking into account both scattering and absorption effects, the total attenuation co-efficient u_t which incorporates both scattering and absorption co-efficients, can be written as:

$$\mu_t = \mu_a + \mu_s \tag{10}$$

where the mean free path before either an absorption or scattering event is defined as $1/\mu_t$.

3.4 Image formation and optical aberrations

In most optical imaging systems, such as the light microscope discussed later in Chapter 2, light (either reflected, scattered or emitted) from an object is collected by a single or multiple lens system, and projected as an image onto a screen or detector. In the case of an optically simple imaging system such as the human eye, the lens present within the eye focuses light from the object onto the retina, which acts as a detector. Variations in the shape and thus lens curvature (due to muscular changes), controls the convergence of the lens allowing objects from a range of distances to be imaged.

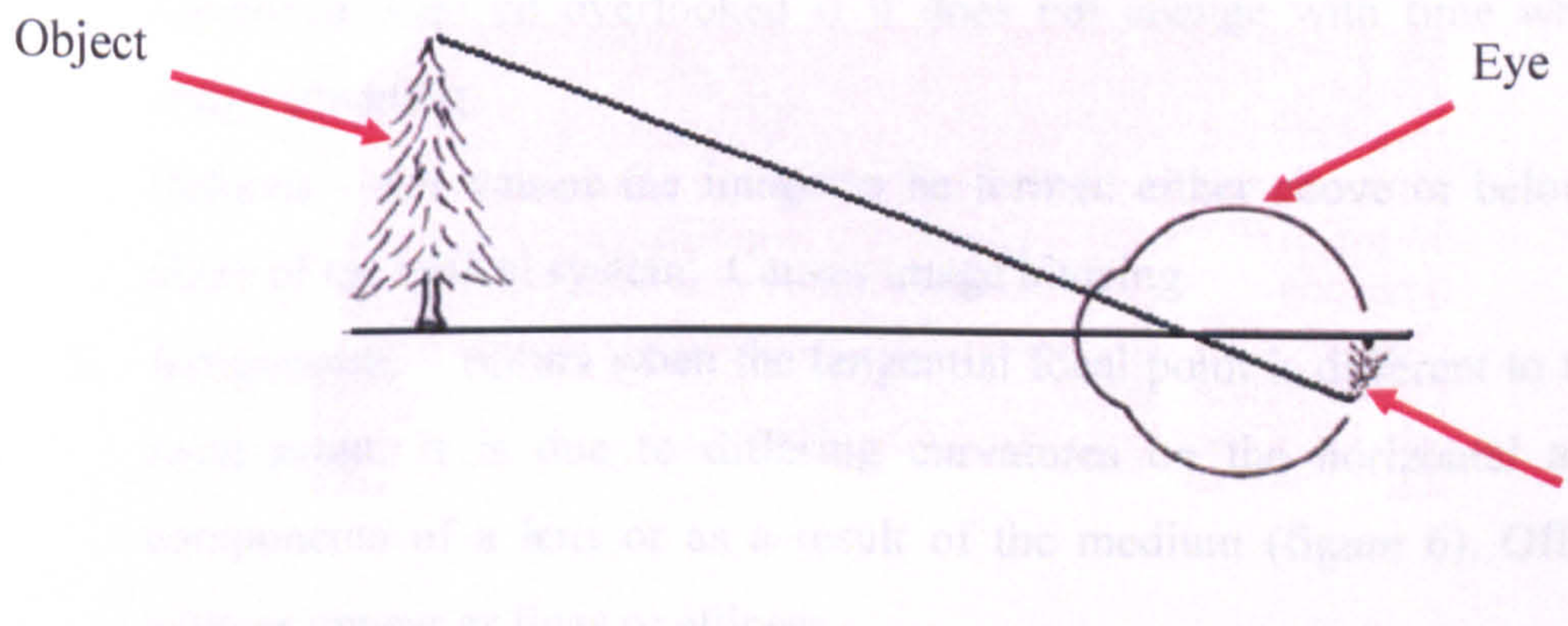

Figure 5: Showing the focal control of the human eye.

Unfortunately, due to imperfections in optical systems, the reproduced image of the object is not ideal. These imperfections are due to deficiencies in the optical system as well as refractive index mismatching within the sample being imaged. In the case of the eye, defects in the lens as well as differences in the refractive index between the cornea, aqueous humour fluid, lens and vitreous humour fluid, lead to distortions to the incoming wavefront. Without going into detail with regards to the optical microscope systems when imaging in biological cells and tissues, the refractive index variations as well as causing scattering effects are responsible for distorting the wavefront and introducing optical aberrations.

3.4.1 Optical Aberrations

When conditions are ideal, light focused from a point source should result in a diffraction limited spot. In the case of a conventional and confocal system, these are defined by equations quoted in Chapter 2. Deficiencies in optical systems, as well as refractive index mismatches associated with the medium (through which the object is being imaged), lead to deformations in the optical wavefront [22 & 23]. These deformations are caused by optical aberrations, the most important of which are described below:

1. Piston – this is a global shift in the wavefront and is due to either vibrations or a variation in the mean refractive index.
2. Tip/tilt – as the name suggests is a result of an overall tipping or tilting of the wavefront. Can be overlooked if it does not change with time which causes image smearing.
3. Defocus – this causes the image to be formed either above or below the focal plane of the optical system. Causes image blurring.
4. Astigmatism – occurs when the tangential focal point is different to the sagittial focal point. It is due to differing curvatures on the horizontal and vertical components of a lens or as a result of the medium (figure 6). Off axis point sources appear as lines or ellipses.

5. Coma – these aberrations are due to light traveling at different angles being focused at separate points. Causes point objects to appear as comet-like or coma shapes (figure 7).
6. Spherical – occurs when light passing through the edge of the lens gets focused at a separate position to light passing through the centre. This results in the blurring of focus (figure 8).

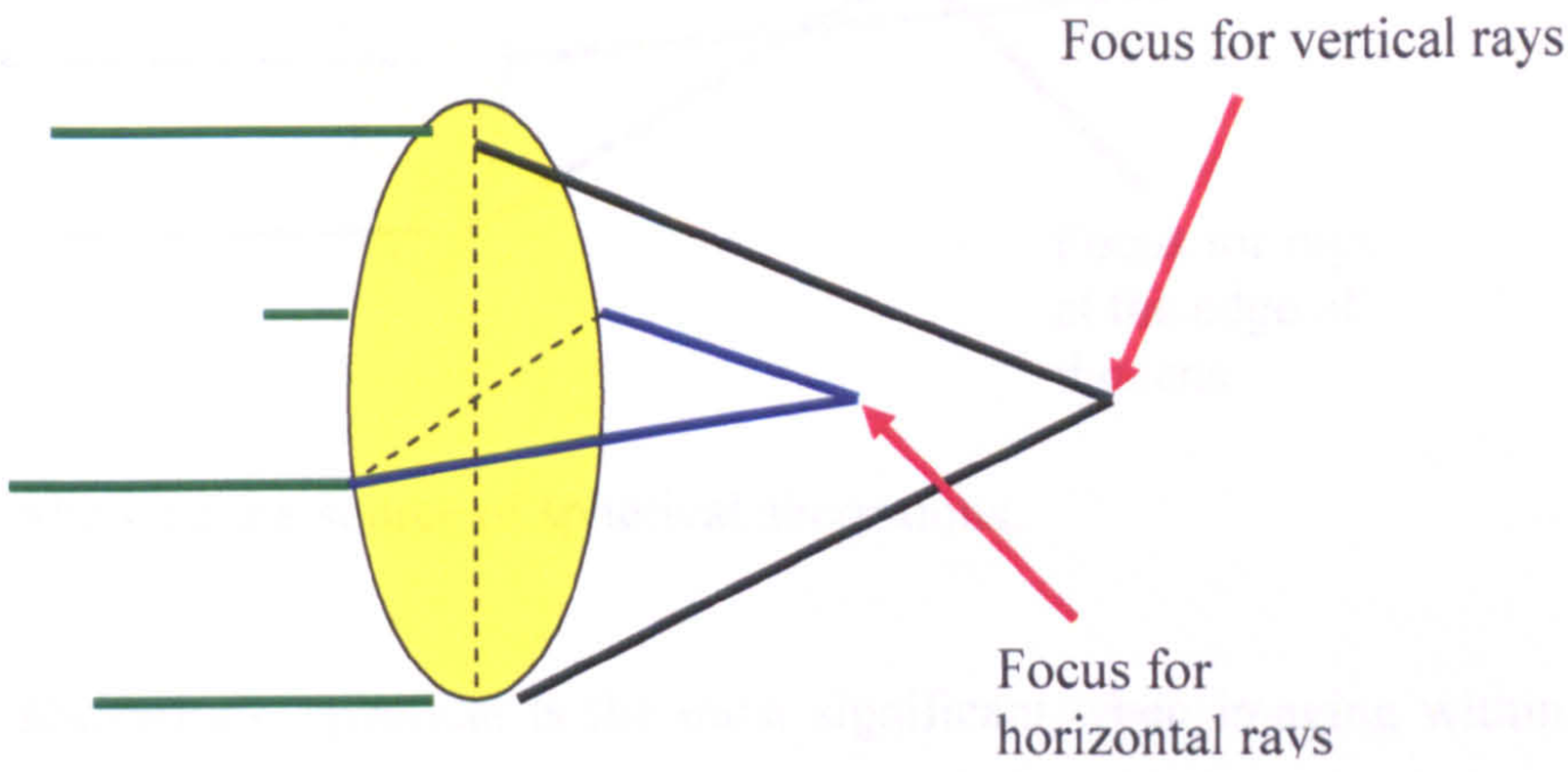

Figure 6: Showing the source of astigmatism aberrations.

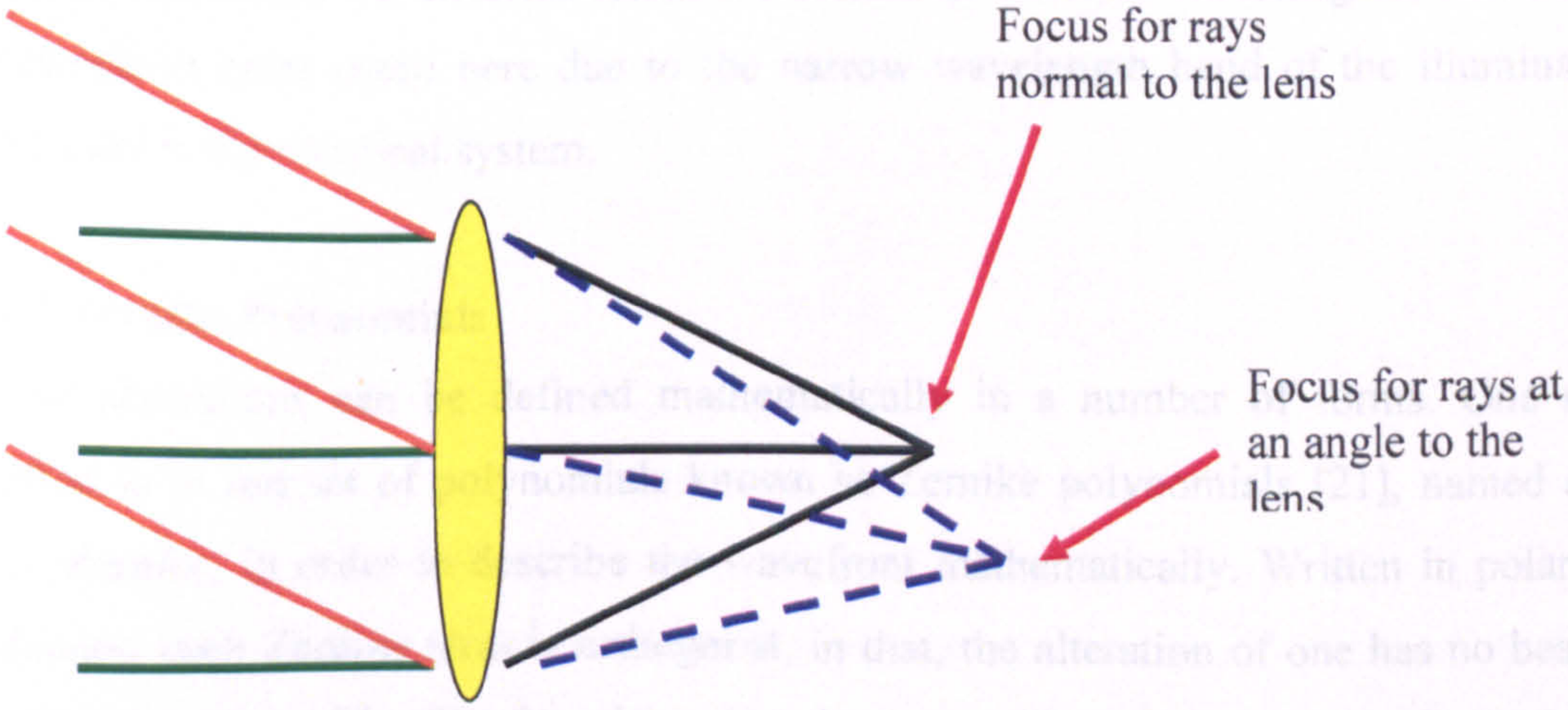

Figure 7: Showing the source of coma aberrations.

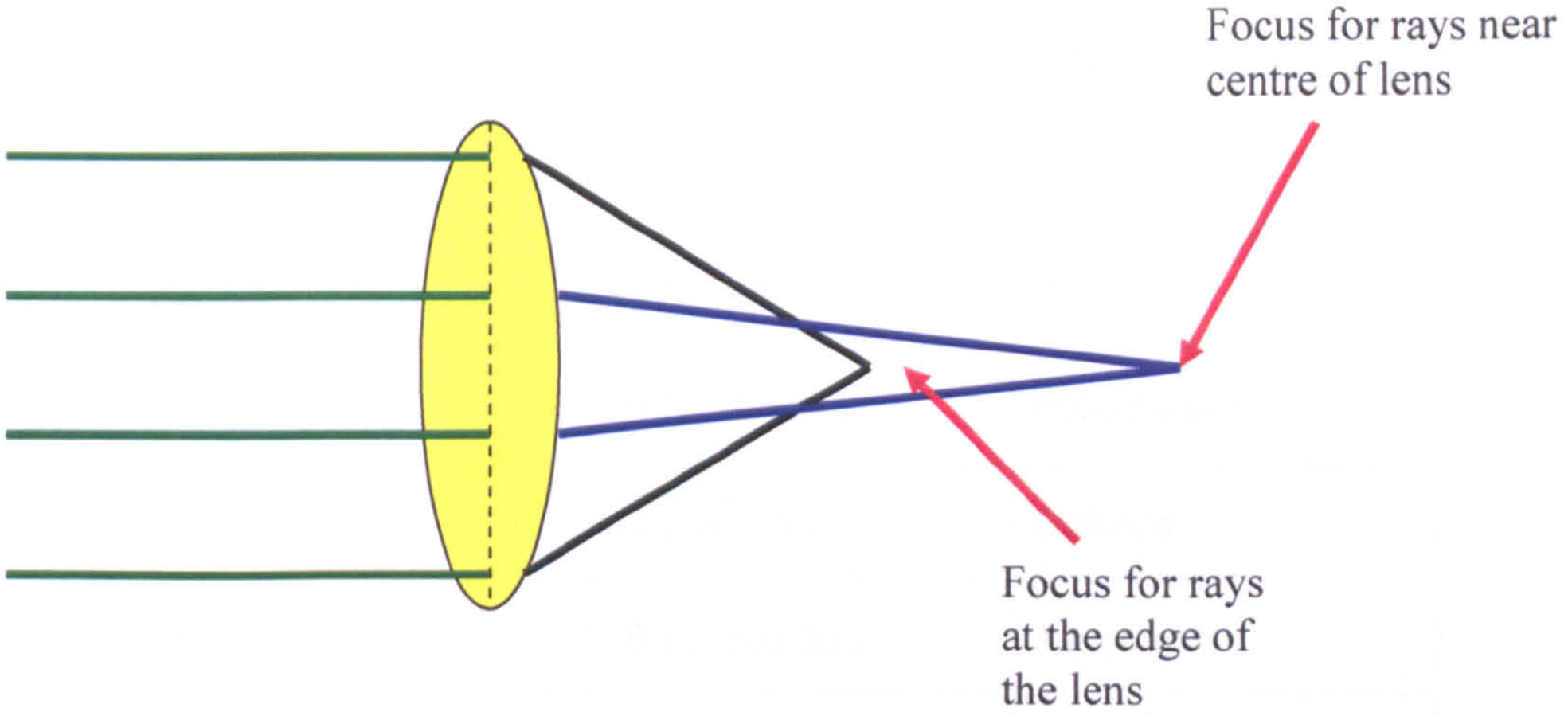

Figure 8: Showing the source of spherical aberrations.

Of these aberrations, spherical is the most significant when imaging within biological samples. As the depth at which one images increases, the effects associated with these aberrations increases also [24 & 25].

Before continuing it should be noted that chromatic aberration which due to optical materials experiencing different refractive indices at different wavelengths, will not be discussed in great detail here due to the narrow wavelength band of the illumination laser used in the confocal system.

3.4.2 Zernike Polynomials

These aberrations can be defined mathematically in a number of forms. One such method is to use set of polynomials known as Zernike polynomials [21], named after Frits Zernike, in order to describe the wavefront mathematically. Written in polar co-ordinates, each Zernike term is orthogonal, in that, the alteration of one has no bearing on the other terms. The first few aberrations in terms of Zernike modes are shown in the table below.

Zernike Mode	Radial Polynomial	Description
0	$\sqrt{1}$	Piston
1	$\sqrt{4}\ (\rho \sin\theta)$	Prism
2	$\sqrt{4}\ (\rho \cos\theta)$	Prism
3	$\sqrt{6}\ (\rho^2 \sin 2\theta)$	Astigmatism
4	$\sqrt{3}\ (2\rho^2 - 1)$	Defocus
5	$\sqrt{6}\ (\rho^2 \cos 2\theta)$	Astigmatism
6	$\sqrt{8}\ (\rho^3 \sin\theta)$	Trefoil
7	$\sqrt{8}\ (3\rho^3 - 2\rho \cos\theta)$	Coma
8	$\sqrt{8}\ (3\rho^3 - 2\rho \sin\theta)$	Coma
9	$\sqrt{8}\ (\rho^3 \cos\theta)$	Trefoil
10	$\sqrt{10}\ (\rho^4 \sin 4\theta)$	Secondary Astigmatism
11	$\sqrt{10}\ (4\rho^4 - 3\rho^2 \sin 2\theta)$	Quadrafoil
12	$\sqrt{5}\ (6\rho^4 - 6\rho^2 + 1)$	Spherical
13	$\sqrt{10}\ (4\rho^4 - 3\rho^2 \cos 2\theta)$	Quadrafoil
14	$\sqrt{10}\ (\rho^4 \cos 4\theta)$	Secondary Astigmatism

Table 1: Showing the first 15 Zernike terms.

In table 1 the first 15 terms of the Zernike expansion within a unit circle are shown – that is the radius ρ varies between 0 and 1. θ defines the azithmuthal angle (from 0 to 2π) within the unit circle (figure 9). It is important to note that terms 1 and 2, which are known as horizontal and vertical prism, move the position of the point spot in the image

and have no effect on the image quality of a monochromatic light source. Each Zernike term can be broken down into three parts, that is, (a) the normalisation factor, (b) how the mode affects the wavefront in terms of radial position, and (c) how the mode affects the wavefront in terms of angle.

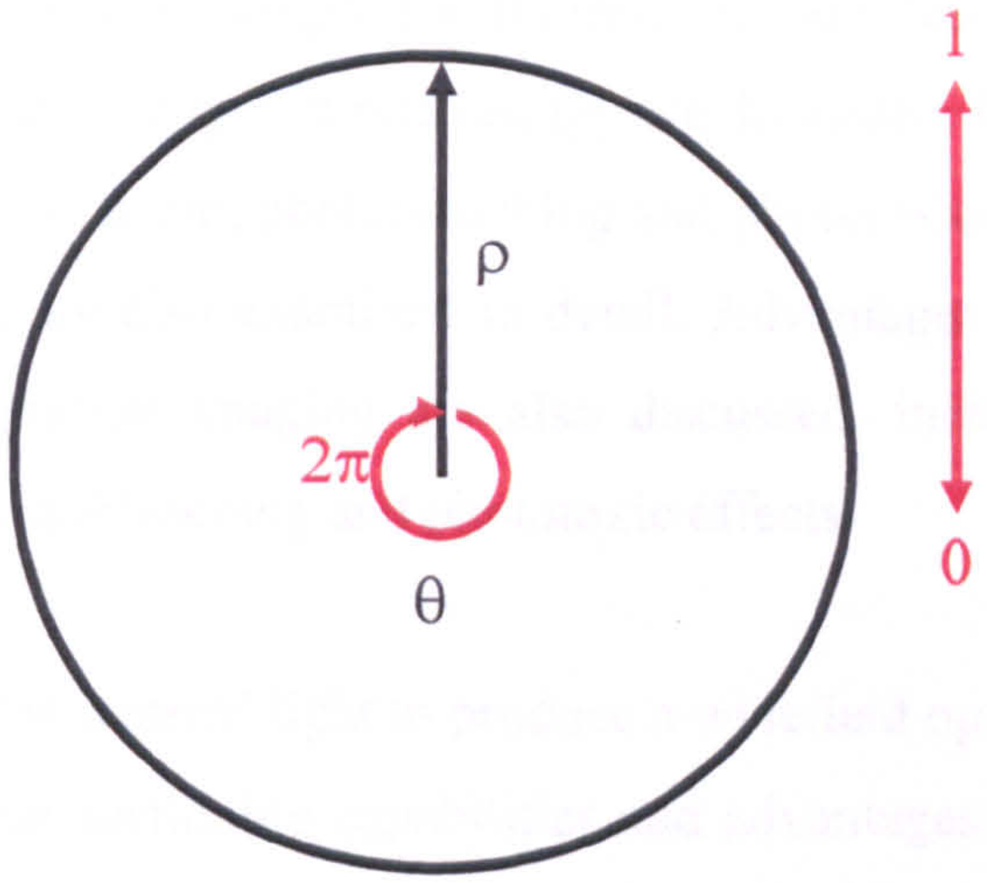

Figure 9: The descriptive diagram showing θ and ρ within a unit circle.

Zernike polynomials are not always the best polynomials for fitting wavefront data. In certain situations such as representing the wavefront error associated with air turbulence, Zernikes cannot be used accurately represent the aberrations present. This is due to the higher order aberrations introduced by the atmosphere not being represented effectively within the polynomials. In the case of biological imaging, Zernike modes can provide an accurate interpretation due to the low order aberrations being introduced.

4. Chapter summaries

This section sets out the summaries of the subsequent chapters.

4.1 Chapter 2

In chapter 2, three optically sectioning methods used in microscopy, namely (a) confocal, (b) multiphoton, and (c) structured light, (used in this investigation) are

examined. This chapter includes a brief historical background and detailed overview of the confocal system, including optical design and how it functions. Different types of confocal systems are discussed and the advantages and limitations of the system are examined.

The properties of single and multiphoton fluorescence are described in this section and their applications and advantages in microscopy are discussed. Problems associated with fluorescence such as ionisation, photobleaching and phototoxicity and their implications in biological imaging are also examined in detail. Advantages of multiphoton imaging compared to single photon imaging are also discussed, including optical sectioning capability, reduced photobleaching and phototoxic effects.

The theory and use of structured light to produce a widefield optically sectioned imaging is presented. Its optical sectioning capabilities and advantages over more conventional confocal and multiphoton systems are also examined.

4.2 Chapter 3

In this chapter, the structure of dental tissue and the nature of dental disease (caries) as an example of biological tissue are described. Currently, at the dentist's disposal there are a number of commercially available methods for caries detection, but presently none of these techniques have the ability of to measure early stage caries. Dentists require a system that can measure, or quantify, lesion growth and activity in order to determine the correct course of treatment, and at present there are a number of techniques in development which may aid in this goal. The theoretical background and operation of both commercially available systems and those currently in development are also outlined in this chapter.

Development of dental diagnosis techniques have been limited due to the complexity of the tooth structure as well as a limited understanding of the nature of optical and scattering variation associated with caries onset. A computer model simulation based on

non-sequential ray-tracing developed using commercially available software is presented in order to provide information on the structure and properties of dental tissue and hence its health. The development of the simulation model, (based on the fibre optical confocal microscope configuration) and a comparison with experimental data from ex-in vivo naturally occurring dental caries are presented.

4.3 Chapter 4

Using a technique based upon transillumination, which makes use of the increased scattering properties associated with carious tooth tissue (when compared with healthy tissue), a cost-effective system capable of detecting caries on the occlusal surface (biting surface) is presented in this chapter. The device uses near-infrared illumination source operating at 810nm to illuminate the tooth laterally with subsequent image measurement at the occlusal surface to detect early stage caries. In a preliminary study involving 15 ex-in vivo adult pre-molars and molars at various stages of dental decay, the infrared lateral illumination device is compared with other dental caries diagnosis techniques presently available and techniques currently in development.

4.4 Chapter 5

In this chapter, the historical background, theory, and the use of optics in counteracting aberrations are examined. In particular the exploitation of adaptive optics in astronomy is discussed and an overview of present systems presented. This consists of a detailed description of an adaptive optic system incorporating a feedback loop as well as the constituent parts associated with such a system. The use of a wavefront sensor (eg. fringe analysis/Shack-Hartmann) are explained as well as the type of adaptive optical element itself such as mirrors (bimorph, piston, and electrostatic) or spatial light modulators (ferromagnetic, twisted nematic) and advantages and limitations associated with each.

Comparisons between imaging through atmospheric and tissue optics and the problems associated with adapting such a system are also considered. The concept of solution

space and the ability of various types of algorithms to find an optimal solution are investigated. The development of an adaptive optic feedback system incorporating an optimisation algorithmic feedback loop for use in confocal and multiphoton microscopy is discussed in detail.

4.5 Chapter 6

In this chapter, the practical confocal microscope system set-up containing the adaptive optic element will be outlined. The equipment and control systems used to control both the confocal and adaptive optic system will be described in detail. This includes the adaptive optic mirror (15mm, 37 actuator Okotech mirror) as well as the laser scanning system, hardware control, objectives, piezo translational devices and custom written LabVIEW and LabWindows software interfaces used. The procedure used in characterizing the optical system (measurement of the axial and lateral resolution) will also be described in detail as well as the method used for optimisation using the adaptive optical element.

4.6 Chapter 7

The effectiveness of a number of algorithms in optimising for sample induced aberrations were examined. These are (a) modified hill climbing (MHC), (b) random search (RS), (c) adaptive random search (ARS), (d) genetic algorithm (GA), and (e) simulated annealing (SA). The viability and efficiency of a number of fitness parameters used in the optimisation routines is also considered. These include the image brightness, the axial resolution and the shape of the axial point spread function of the sample. The algorithms and fitness parameters are compared in terms of reliability and repeatability of the solutions, the time required to complete an optimisation and the final axial resolution of the system.

Using various axial fitness parameters which where optimised using the GA, the effect of optimisation has on the lateral resolution of the system is examined. Using a modified fitness parameter and the GA, the ability of the adaptive optic system to optimise to a

particular axial PSF is also examined. In this instance, Gaussian curves of various full-width half-maxima ranging from 2 μm to 30μm.

4.7 Chapter 8

The procedure used in examining structured light as a possible diagnosis tool in dentistry is outlined in this section. This includes optical set-up of the system as well as a description of the custom written software written in LabVIEW that is used to control the system and process the images.

Images showing the optical sectioning capabilities of the structured light system are presented. Optically sectioned images showing caries enamel close to the surface are shown. Present problems associated with the present procedure is also be examined (such as the loss of signal deeper within the sample due to scattering) and possible solutions discussed.

4.8 Chapter 9

In this chapter the conclusions will be discussed and some further developments will be outlined.

References

1. Jones, B. W., (2006). Visual Acuity, Webvision retrieved 10th of March 2006 from http://webvision.med.utah.edu/KallSpatial.html.
2. Bradbury, S. (1967). *The evolution of the microscope*. Peragamon Press, Oxford.
3. Mait, J. N. (2006). A History of Imaging : revisiting the past to chart the future. OPN Feburary 2006, OSA, retrieved 8th of April 2006 from www.osa-opn.org.
4. Hooke, R. (1665). *Micrographia*. Royal society, London.
5. Maxwell, J. C. (1865). A Dynamical Theory of the Electromagnetic Field. *Philosophical Transactions of the Royal Society of London* 155, 459-512.
6. Abbe, E. (1873). Beiträge zur Theorie des Mikroskops und der mikroskopschen Wahrnehmung. *Schultzes Arc. F. Mikr. Anat.*, 9, 413-468.
7. (2006) Cell (biology). wikipedia - the free encyclopedia, retrieved 10th of March 2006 from http://en.wikipedia.org/wiki/Cell_%28biology%29
8. Wagner, K. (2005). Animal Cell. Leibniz Institute for Age Research - Fritz Lipmann Institute (formerly Jena Centre for Bioinformatics), retrieved 10th of March 2006 from http://www.imb-jena.de/~rake/Bioinformatics_WEB/gifs/cell_animal.gif.
9. Microscopy images, Visual unlimited, retrieved 11th of March 2006 from http://www.visualsunlimited.com/.
10. Jenkins, F. A., White, H. E (1976). Chapter 33: The dual nature of light. *Fundamentals of optics*, 4th edition, McGraw-Hill, New York.
11. Arny, T. T. (2001). Explorations: An Introduction to Astronomy, retrieved 14th of March, 2005 from http://www.mhhe.com/physsci/astronomy/arny/indexnew.mhtml.
12. Jenkins, F. A., White, H. E (1976). Chapter 22: Absorption and scattering. *Fundamentals of optics*, 4th edition, McGraw-Hill, New York.
13. Disease. Wikipedia, the free encyclopedia, retrieved 20th of July 2006 from http://en.wikipedia.org/wiki/Disease.

14. Tuchin, V.V. (2005). Optical immersion tools for controlling the optical properties of tissues and blood. *Las. Phy.*, 15 (8), 1109-1136
15. Mourant, J. R. , Freyer, J. P., Hielscher, A. H., Eick, A. A., Shen, D.. Johnson, T. M. (1998). Mechanisms of light scattering from biological cells relevant to noninvasive optical tissue diagnostics. *Appl. Opt.*, 37 (16), 3586-3593.
16. Hernan, B. (1998). Chapter 1: fundamentals of fluorescence, *Fluorescence microscopy*, 2nd Edition, BIOS scientific publishers, Oxford.
17. Mie, G. (1908). Beitrage zur optik truber medien, speziell kolliodaler metallosungen. *Ann. d. Phys.*, 25, 377-445.
18. Born M, Wolf E (1983). Chapter 13.5: Diffraction by a conducting sphere, theory of Mie. *Principles of Optics*, 6th edition, Pergamon Press, Oxford.
19. Meyer-Arendt, J. R. (1995). Chapter 16: Light Scattering. *Introduction to classical and modern optics*, Prentice Hall, New Jersey.
20. Schmidt, F. E. W. (1999). Chapter 4: Fundamentals of tissue optics. *Development of a time-resolved optical tomography system for neonatal brain imaging.* PhD thesis submitted to University College London.
21. Khlebtsov, N. G., Maksimova, I. L., Tuchin, V. V., Wang (2002). *Handbook of optical biomedical diagnostics*, PM 107, SPIB press, Bellingham, WA.
22. Tyson, R. K. (1991). Chapter 1: History and background. *Principles of adaptive optics*, 2nd Edition, Academic Press, Boston.
23. Wyant, J. C., Creath, K. (1992). Chapter 1: Basic wavefront aberration theory for optical metrology. *Applied optics and optical engineering XI*, Academic Press, USA.
24. Wilson, T., Carlini, A. R. (1989). The effect of aberrations on the axial response of confocal imaging systems. *J. of Microscopy*, 154, 243-256.
25. Sheppard, C., Gu, M., Brain, K., Zhou, H. (1994). Influence of spherical aberration on axial imaging of confocal reflection microscopy. *App. Opt.*, 33, 616-624

Chapter 2: Methods to produce three dimensional optically sectioned images

1. Introduction

Since the development of laws governing diffraction theory and the theoretical foundation of modern light microscopy were finally established over a century ago by Ernst Abbe [1 & 2], there have been numerous advances in both the fundamental design and technology incorporated in microscopy. The advancement of new technologies such as laser illumination, computing, image detection and formation techniques have led to a revolution in microscopy devices. This in turn has led to the development of systems that allow for increased sensitivity and resolution required in biological measurements. Currently biologists require an imaging system that is capable of producing crisp, clear, aberration free, high frame rate, real-time, three dimensional images of live biological cell and tissue structure with diffraction-limited resolution (or higher!), without perturbing or damaging the sample. Of course this is no small order, and at present such a system is not available. Unfortunately for the biologist, in order to improve upon one factor within the system usually requires a substitution of one or more other factors.

There are a number of established techniques as well as those currently in development which have an optical sectioning capability without the need for physical dissection. In confocal microscopy, the use of a pinhole in front of the detector rejects out-focus light, and using either light scanning or sample scanning mechanisms, a two dimensional image can be built up.

Multiphoton excitation microscopy, which in some respects is similar to the confocal technique, functions by the non-linear excitation of fluorophores resulting in fluorescence within a small volume of the sample. Akin to confocal microscopy, a two dimensional image can be produced through laser or sample scanning but unlike confocal systems, a pinhole is not required to reject unfocused light since all fluorescent light collected originates from the focused spot.

In structured light illumination techniques, a single frequency grid pattern is projected onto a sample and the sample image is collected using a CCD device. When imaging the sample, the grid pattern (which is physically located at a conjugate point to the sample and sample image) will only be present on those parts of the image that are in-focus. By removing only those parts of the image where the grid pattern exists, the system produces optical sectioning capabilities similar to those that exist in the confocal and multiphoton cases.

Each technique described so far works upon the basis that by taking successive focused two dimensional images of optical sections at successive depths, a three-dimensional image can be constructed. In this chapter the theory and operation, as well as, the benefits and limitations associated with each of these three optically sectioning techniques is explained in greater detail. In a practical situation, each system presents a certain set of advantages and limitations and dependant on the application it is simply a case of "finding the right tool for the right job" [3].

2. Confocal Microscopy

2.1 Historical background

The idea for the confocal microscope was first proposed in 1957 by Marvin Minsky [4]. As a young post-doctoral fellow at Harvard University, whose main research field was in artifical intelligence, Minsky was interested in examining brain tissue structure at high resolution in three dimensions. At the time, no such technique existed which would allow optical sectioning to such a high resolution, so he invented and built his own. In Minsky's transmission design (figure 1), the condenser present in the conventional microscope configuration was replaced with another objective lens of equal attributes. With a pinhole in front of the illumination, light from this pinhole expanded to fill the entrance pupil of the first objective lens. The objective lens then focused the light to a small spot on the specimen. Light was then collected by the second objective lens where it is refocused onto the detector. With a pinhole present at the detector, the field of view was limited by this second pinhole placed confocally to the first pinhole and to the

illuminated specimen spot. Light was detected from the sample using a photomultiplier tube. In the epi-illumination design shown in figure 2, only one objective was used for both illumination and condensation.

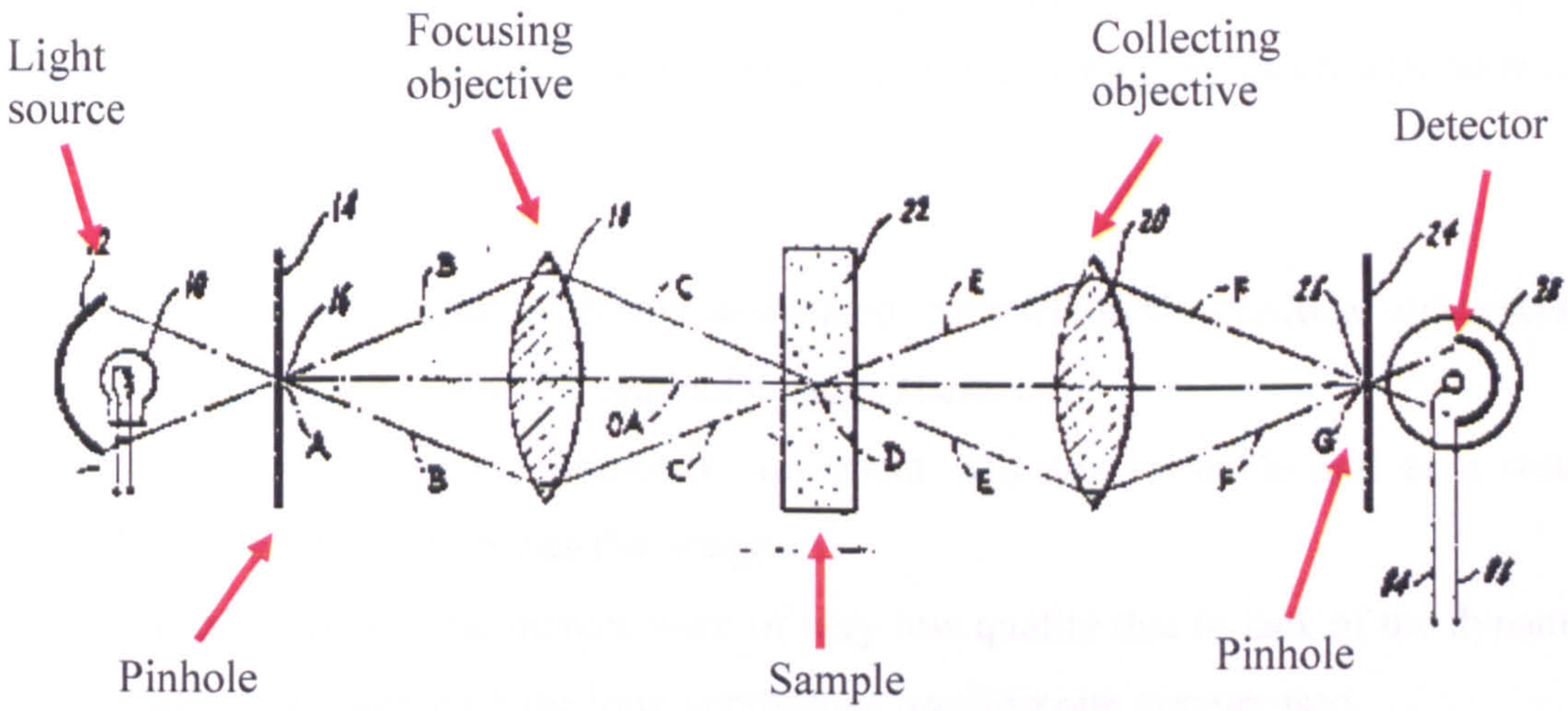

Figure 1: Minsky's original confocal microscope in transmission.

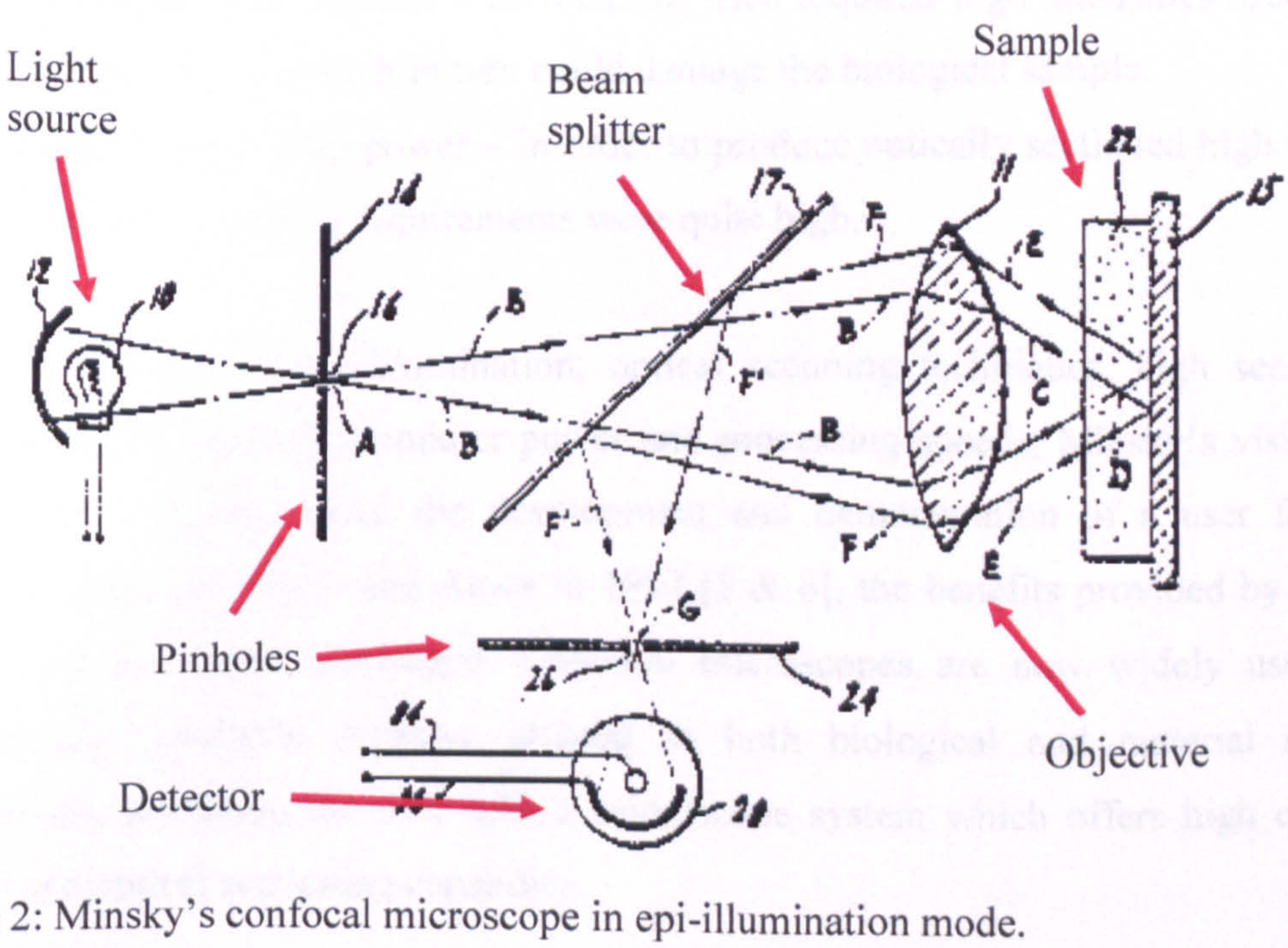

Figure 2: Minsky's confocal microscope in epi-illumination mode.

With the sample placed on a stage with two orthogonally positioned tuning forks vibrating at 60Hz and 60kHz respectively (which provided the x and y position movement), the sample moved in a raster scan across the stationary focused spot. From the signal output of the photomultiplier, the image was produced by synchronizing the tuning forks to the display screen which in this case was a long persistence cathode ray oscilloscope.

There were however some problems associated with Minsky's confocal microscope which were in no fault due to the original design. These were:

1. Sample stage – the vibrational movement was not so stable and as a result introduced distortion into the image.
2. Display screen – the images were of very low quality due to lack of the dynamic range associated with the long persistence oscilloscope system used.
3. Light source – the zirconium arc light source was not of sufficient brightness and required the invention of the laser.
4. Photomultiplier detector – the detector used required high intensities (due to its low sensitivity) which in turn could damage the biological sample.
5. Lack of computing power – in order to produce optically sectioned high quality images, computing requirements were quite high.

With the advent of laser illumination, optical scanning techniques, high sensitivity photodetectors, increased computer power and processing speeds, Minsky's vision has been slowly realized. Since the development and demonstration of a user friendly confocal system by White and Amos in 1987 [5 & 6], the benefits provided by such a system can be clearly envisaged. Confocal microscopes are now widely used and commercially available systems, utilised in both biological and material science applications, providing the user with a microscope system which offers high contrast images and optical sectioning capability.

2.2 Theory of confocal microscopy

Confocal microscopy is a technique for improving the contrast of an image [7]. Using a pinhole in front of the detector allows the confocal microscope to accept only light that is in focus. Unfortunately, due to the presence of the pinhole, the system can only image a point at any one time, unlike conventional microscopy which images the entire field.

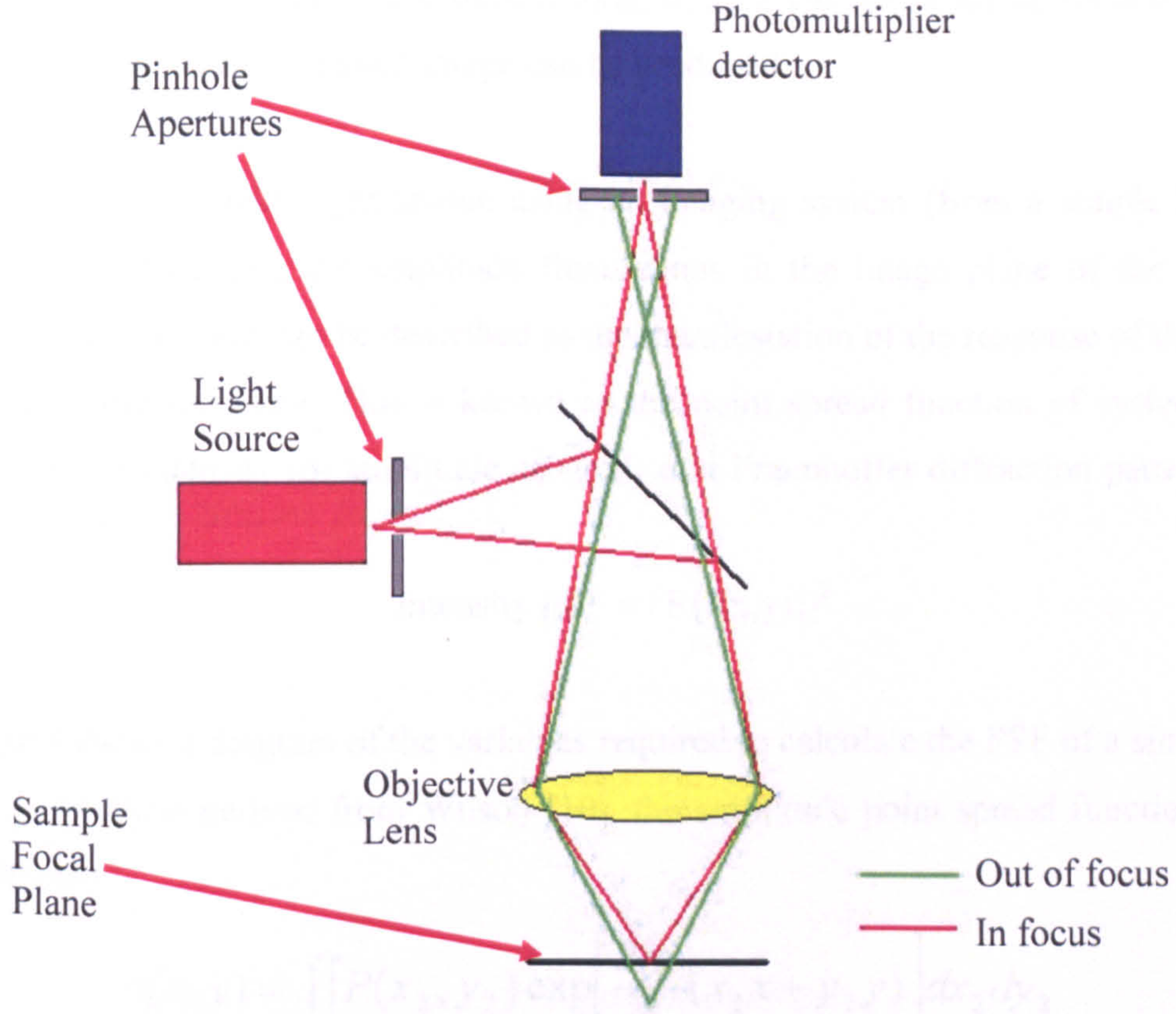

Figure 3: Showing the ability of the confocal system to reject out of focus light.

Light from the illumination source passes through a pinhole (which acts as a spatial filter), where it is then directed by the beam splitter onto the back aperture of the objective lens. Light is then focused by the objective into a spot (which is diffraction limited). The reflected or resultant fluorescent light from the sample then passes through the objective and beam splitter, where it is focused through a pinhole and collected by the light detection device (typically either a photomultiplier tube (PMT) or a photo-diode). As one can see from figure 3 above, light that has not originated from the

objective focal plane will be rejected by the pinhole and thus not detected by the photomultiplier. The intensity of the light collected by the detector is found to reduce rapidly with defocus [8] which will be explained in more detail later.

A two dimensional image can be produced by moving the sample or by scanning the laser beam to move the point of focus along the sample. By altering the position of the microscope objective along the optical axis, images can be taken at successive focal planes and a three dimensional image can be produced.

When imaging a point light source using an imaging system (from a simple lens to a complex microscope), the amplitude fluctuations in the image plane of the resultant electromagnetic field can be described as the manifestation of the response of the optical system to the specimen. This is known as the point spread function of system and is given by the intensity (or amplitude squared) of a Fraunhoffer diffraction pattern of the aperture [9]:

$$\text{Intensity PSF} = |\, F\{f(x,y)\}|^2 \tag{1}$$

Figure 4 shows a diagram of the variables required to calculate the PSF of a simple lens. Using equations derived from Wilson [10], the amplitude point spread function can be written as:

$$h(x,y) = \iint P(x_2, y_2) \exp\left[\frac{2\pi i}{\lambda}(x_2 x + y_2 y)\right] dx_2 dy_2 \tag{2}$$

where P is the pupil function and defines the physical parameters associated with the lens itself.

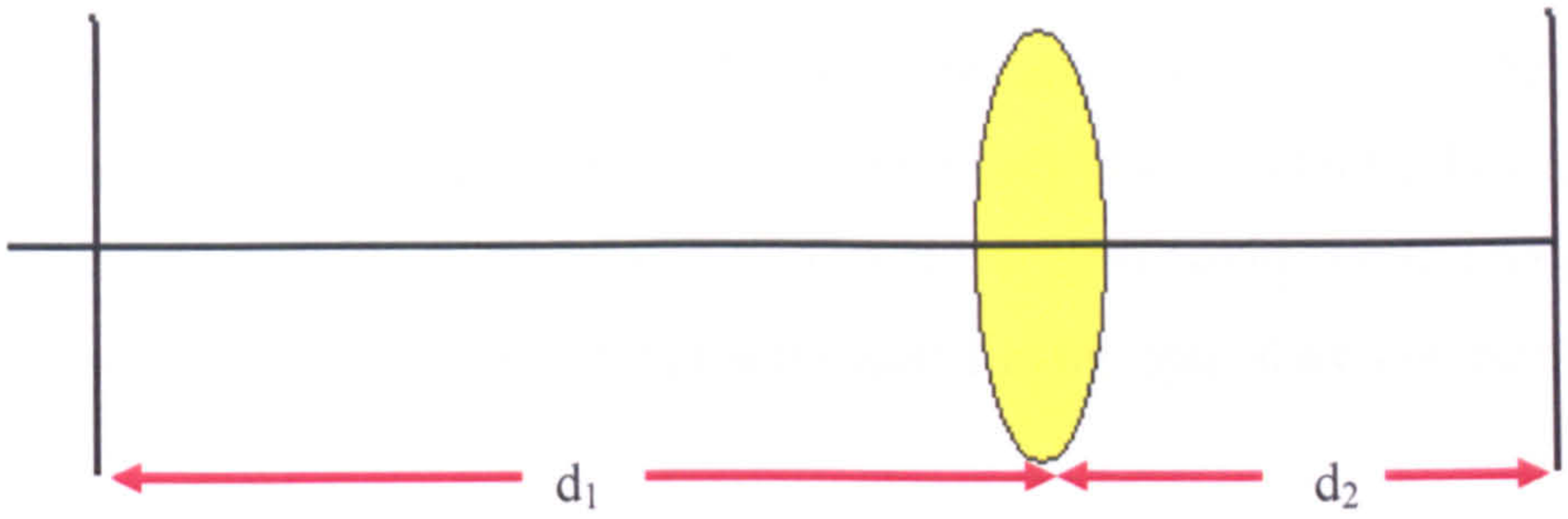

Figure 4: Geometry used in the formation of an image [10].

The intensity of the image can be then rewritten [10 - 12] as:

$$I(v) = \left| 2 \int_0^1 P(\rho) J_0(v\rho) \rho d\rho \right|^2 \tag{3}$$

where the pupil function $P(\rho)$ is related to the pupil radius a by the equation $\rho = r_2 / a$, J_0 is a zero order Bessel function, $r_2 = \sqrt{x_2^2 + y_2^2}$, and the normalized optical co-ordinate v, is related to the radial co-ordinate r_3 by the equation :

$$v = \frac{2\pi}{\lambda} r_3 \sin\theta \tag{4}$$

where $sin\theta$ is given by a/d_2, and $r_3 = \sqrt{x_3^2 + y_3^2}$. Therefore for the ideal situation, where the pupil is uniform and the system is without aberrations, the intensity of the image $I(v)$, can be written as:

$$I(v) = \left(\frac{2J_1(v)}{v} \right)^2 \tag{5}$$

where the $J_1(v)$ is the Bessel function of the first order and has the profile of the Airy function [11 & 13]. For a microscope objective lens that is well-corrected, this three dimensional PSF is sectioned in the focal plane and is observed as an Airy disk diffraction pattern.

2.2.1 Resolution of a confocal system

As described previously, the resolution of an imaging system can be defined as the smallest distance separating two resolvable points [14]. In confocal microscopy, this is divided into two, the lateral resolution of the system being the resolution in the focal plane, with the axial resolution being measured in the optical axis of the system.

2.2.2 Lateral resolution

According to the Rayleigh Criterion when there exists two equally bright spots of light separated by a small distance d, "the images are said to be resolved when d is larger or equal to the radius of the Airy disk" [15]. The Airy disk radius, R_{Airy}, is defined as the radius of the central maximum and is calculated by the equation:

$$R_{Airy} = \frac{0.61\lambda}{N.A.} \tag{6}$$

where λ is the wavelength of light used and $N.A.$ is the numerical aperture of the objective.

The lateral resolution is also limited by the field of view. As the pinhole size of the system decreases, the field of view itself decreases. It is important to note that in the case of the conventional microscope, the imaging associated with it is incoherent, thus the intensities add directly. In the confocal case however, the amplitudes are added together and subsequently squared to form an intensity image. This coherence simplifies the confocal system into a two lens arrangement where the PSF is effectively given by the product of both PSFs [8] to give the equation:

$$I(v) = \left(\frac{2J_1(v)}{v}\right)^4 \tag{7}$$

Figure 5 compares equation 5 and equation 7 showing v against I(v) to show the form of the Airy disk when imaging a single point for conventional and confocal system respectively. From the graph it can be clearly seen that the central crest of the confocal

response is in fact narrower than the conventional microscope response. Also the presence of sidelobes are less apparent in the confocal scan. Measurement of these theoretical lateral responses has been confirmed experimentally [8, 16].

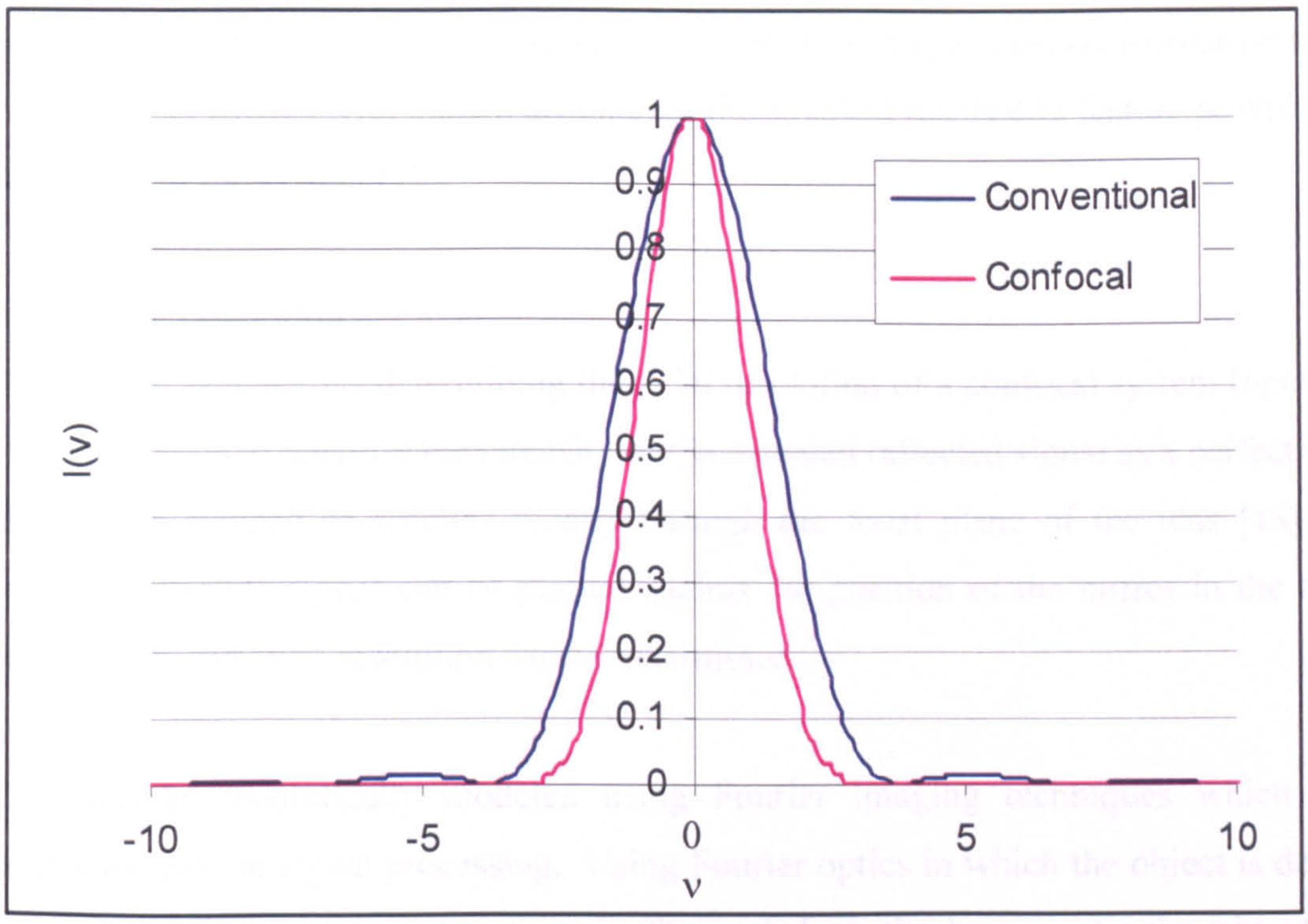

Figure 5: Showing the lateral intensity PSFs for a point object in conventional and confocal microscopes.

In lateral co-ordinates (ν), the full-width half-maxima (FWHMs) of the PSF (which is a measure of resolution) for conventional and confocal situation were found to be around 3.2ν and 2.3ν respectively, which shows that the confocal lateral resolution has in fact improved by a factor of ~1.4. Therefore in a system in which the pinhole size translates to a field of view that is infinitely small, the confocal lateral resolution is defined as:

$$resolution_{confocal} = \frac{r_{airy}}{\sqrt{2}} \cong \frac{1}{1.4} \cdot \frac{0.61\lambda}{N.A.} \qquad (8)$$

When diffraction limited points of illumination are not available, the normal practice for measuring the lateral resolution of the system is to use a resolution target by attempting to resolve structures (such as a high reflective/low reflective edge) which have dimensions smaller than the resolution of the system. Using a standard resolution target, with patterns written with known accuracies, the smallest resolvable feature provides the resolution of the system [17].

2.2.3 Axial resolution

The normal practice for determining the axial resolution of a confocal system (operating in reflection) is to measure the intensity of the detected reflected signal as a perfect plane reflector is stepped or scanned axially through the focal plane of the lens [18]. The resultant intensity signal can be plotted against the position of the mirror in the z-axis from which, the axial resolution can be determined.

This can be theoretically modeled using Fourier imaging techniques which were originally used in signal processing. Using Fourier optics in which the object is defined by $t(x,y)$ and its frequency spectrum is $T(m,n)$ (where the lens can be thought of as a spatial frequency filter), the Fourier transform pairs are:

$$T(m,n) = \iint t(x,y)\exp[2\pi i(mx+ny)]dxdy \tag{9}$$

and

$$t(x,y) = \iint T(m,n)\exp-[2\pi i(mx+ny)]dmdn \tag{10}$$

where m and n are the corresponding spatial frequencies to x and y.

When substituted into the equation which describes the confocal system:

$$I = \left|(h_1)^2 \otimes t\right|^2 \tag{11}$$

where h_I is the PSF of the objective for the case of a perfect reflector, where t(x, y) =1, can be shown to give [8, 19]:

$$I(u) = \left(\frac{\sin(u/2)}{(u/2)} \right)^2 \tag{12}$$

where u is axial co-ordinate:

$$u = \frac{8\pi}{\lambda} z \sin^2(\theta/2) \tag{13}$$

Equation 12 is then plotted in terms of I(u) against u to show the shape of the axial response (figure 6).

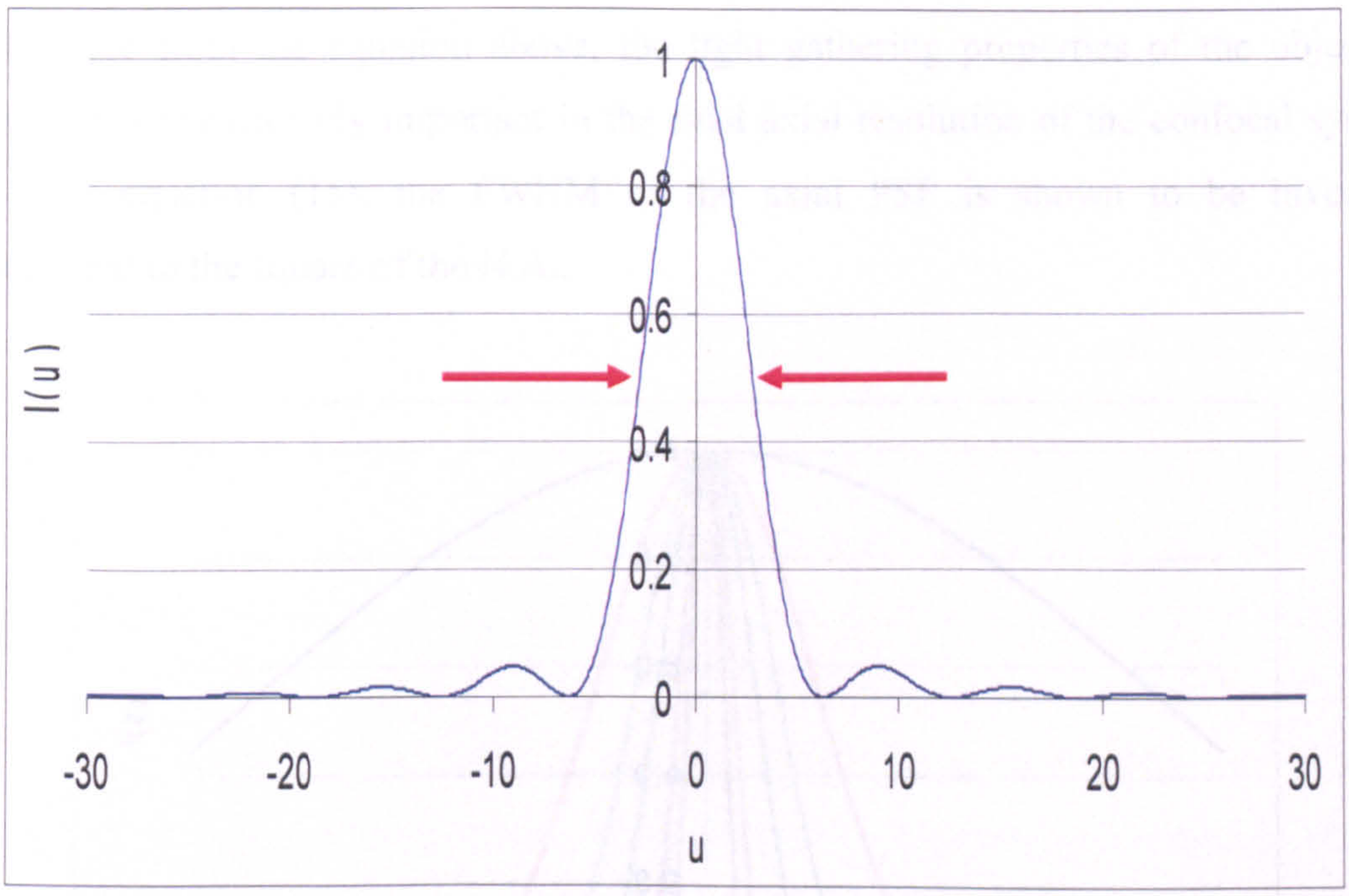

Figure 6: The theoretical axial response I(u) when viewing a plane reflection through a dry objective taken from equation (12).

From figure 6 the FWHM was calculated to be 5.6u. In order to convert this into units that are practically useful in microscope optics one must make a paraxial approximation,

in that for small angles $\theta \approx \sin\theta$. In the case of the axial co-ordinate this can be written as:

$$u = \frac{2\pi}{\lambda} nz \sin^2(\theta) \tag{14}$$

So for small angles, the *FWHM* can be approximated in terms of z to be:

$$FWHM = \frac{0.90n\lambda}{(N.A.)^2} \tag{15}$$

Figure 7 shows how the theoretical axial PSF changes with N.A. for dry objectives (n=1) using a helium-neon (HeNe) laser illumination light source operating at 632.8nm. As one can see from the equation above, the light gathering properties of the objective lenses used are extremely important in the final axial resolution of the confocal system and from equation (15), the FWHM of the axial PSF is shown to be inversely proportional to the square of the N.A..

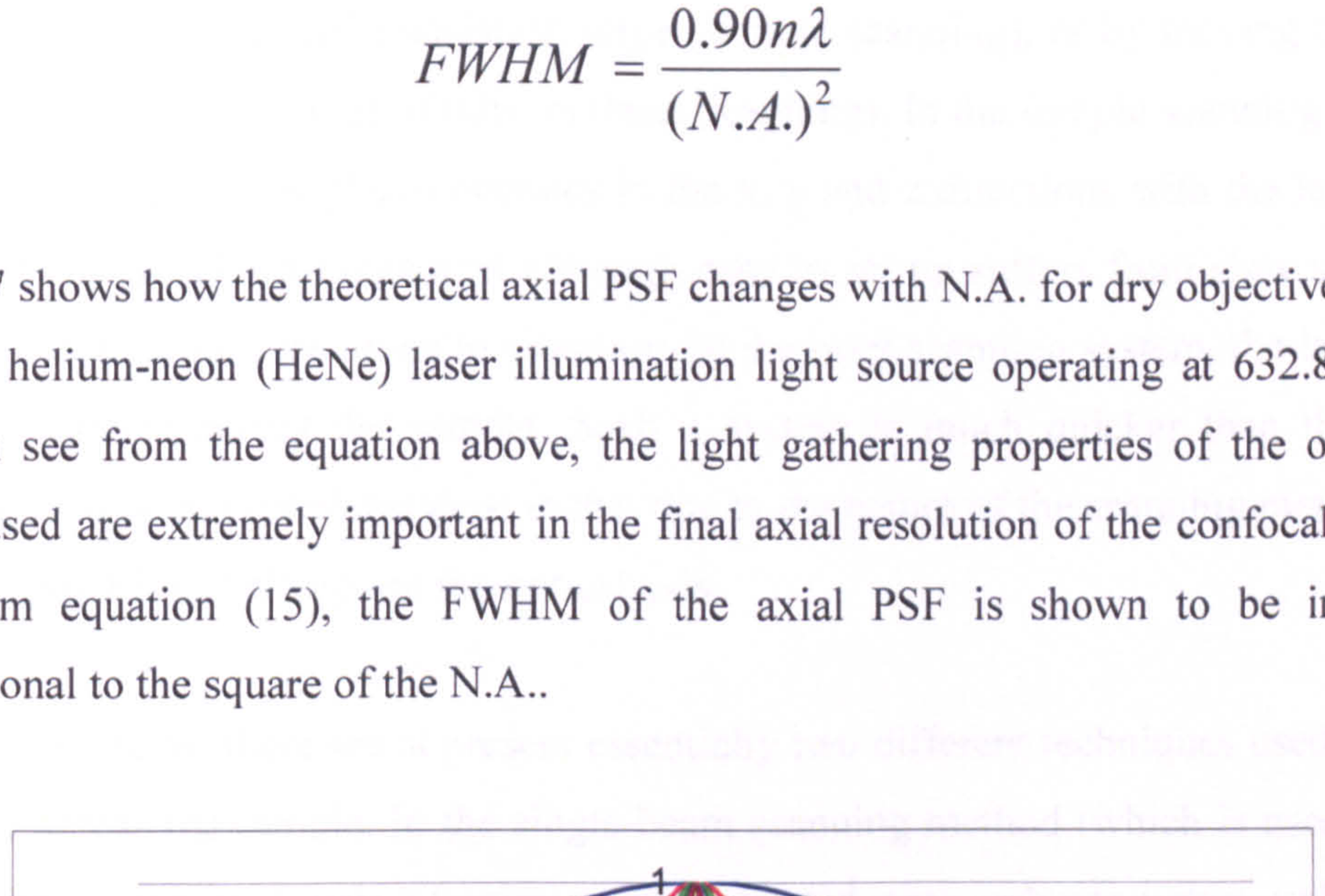

Figure 7: The theoretical axial response I(z) when viewing a plane reflection through dry objectives of different N.A..

2.4 Types of Confocal systems

As described previously, in order to produce a confocal image, the diffraction limited spot must be scanned across the sample. This can be achieved in a variety of ways which are usually purposely targeted for a particular function. The most successful method currently in use is the laser scanning method in which the diffraction limited spot is scanned across the specimen [20]. This can be achieved either by moving the sample on an electronically controlled translation stage (sample scanning), or by moving the laser across the sample using a set of mirrors (laser scanning). In the sample scanning system, the translation stage (e.g piezo) operates in the x, y and z directions with the laser spot fixed in position. This arrangement although easy to set up suffers from slow scanning times on stages which are prone to vibration. In the laser scanning system, the laser spot is raster scanned across the sample. Such a system is much quicker than the stage scanning method but problems exist in that due to the nature of the scanning method, the scanning point is not always on the optical axis.

In modern systems, there are at present essentially two different techniques used to scan the beam across the sample. In the single-beam scanning method (which is used in this investigation), where a pair of mirrors are mounted onto galvonometers (which are computer controlled) to control the x and y direction of the beam. By moving the mirrors at different rates, the beam can be raster scanned across the sample to produce a image at rates of up to several frames per second [21 & 22]. Video frame rates can be produced using either oscillating mirrors or acousto-optical beam deflection methods. In comparison, in multiscanning or tandem scanning [23 - 25] systems incorporate the use of a spinning Nipkow disk which is composed of an array of pinholes. Using this array of pinholes with the distance between pinholes at sufficient distance as to not interfere with each other many spots can be imaged at once. A complete image is produced by moving the pinholes (spinning the disk) so the space is filled between them.

When using this type of system in biological imaging, arc-discharge lamps are often used to limit any damage caused to the sample. The advantage of such a system is that

high frame rates can be achieved and images can be collected using CMOS or CCD technology with [24] present systems providing frame rates of 700/sec. Problems exist in that such a system is complex and difficult to align as well as issues involving the type of illumination used and problems due to cross-talk between scanning beams (figure 8).

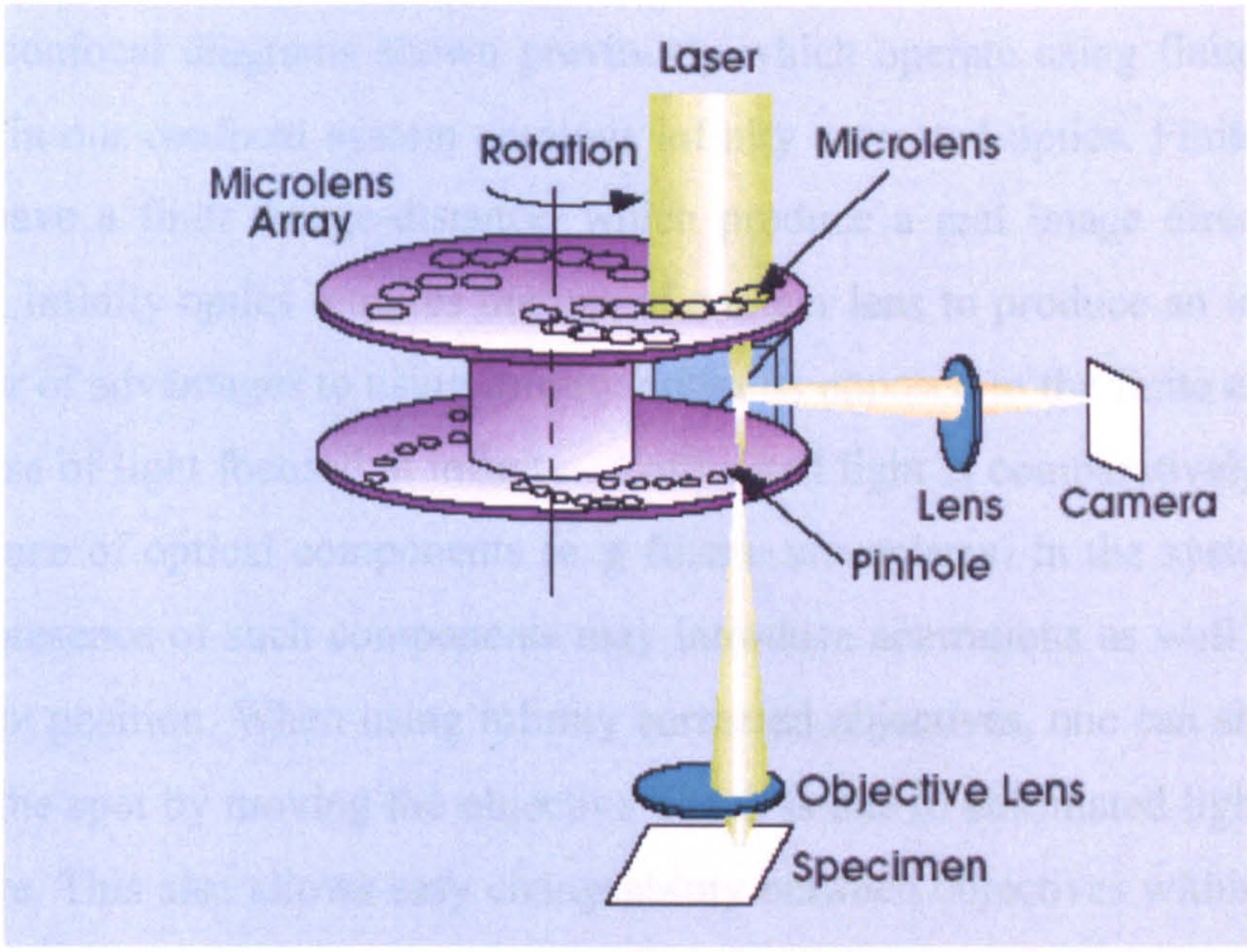

Figure 8: showing the Nipkow disk system which uses multiple pinholes to scan at high speeds [26].

.

2.5 Laser sources used in confocal microscopy:

Considering one of the main uses in confocal microscopy is in fluorescence in biological imaging, the characteristics of the laser illumination light source is of major importance. Fluorescence which will be described in more detail later in this chapter, requires a certain wavelength which is dependant on the fluorophores used within the biological structure being imaged. The wavelength used also has a determination on the lateral and axial resolution of the system as one can see from equations (8) and (15) respectively. The common characteristics of a laser which include a high degree of monochromaticity, a small divergence angle, high level of both spatial and temporal coherence as well as a

high degree of brightness and plane polarised emission, make them much more suitable for use in the confocal system as opposed to other types of illumination devices.

2.6 Finite Vs. Infinity optics

Unlike the confocal diagrams shown previously which operate using finite optics, the optics used in our confocal system employs infinity corrected optics. Finite optics and objectives have a finite image-distance, which produce a real image directly [27]. In comparison, infinity optics requires the use of another lens to produce an image. There are a number of advantages to using infinity optics as opposed to the finite case which is due to the use of light focused at infinity. Collimated light is comparatively insensitive to the presence of optical components (e..g filters, waveplates) in the system. In finite optics, the presence of such components may introduce aberrations as well as changing the focal spot position. When using infinity corrected objectives, one can shift the focal position of the spot by moving the objective which is due to collimated light hitting the back aperture. This also allows easy changeability between objectives within the system without having to alter any other optics. Figure 9 shows the confocal set-up using infinity optics.

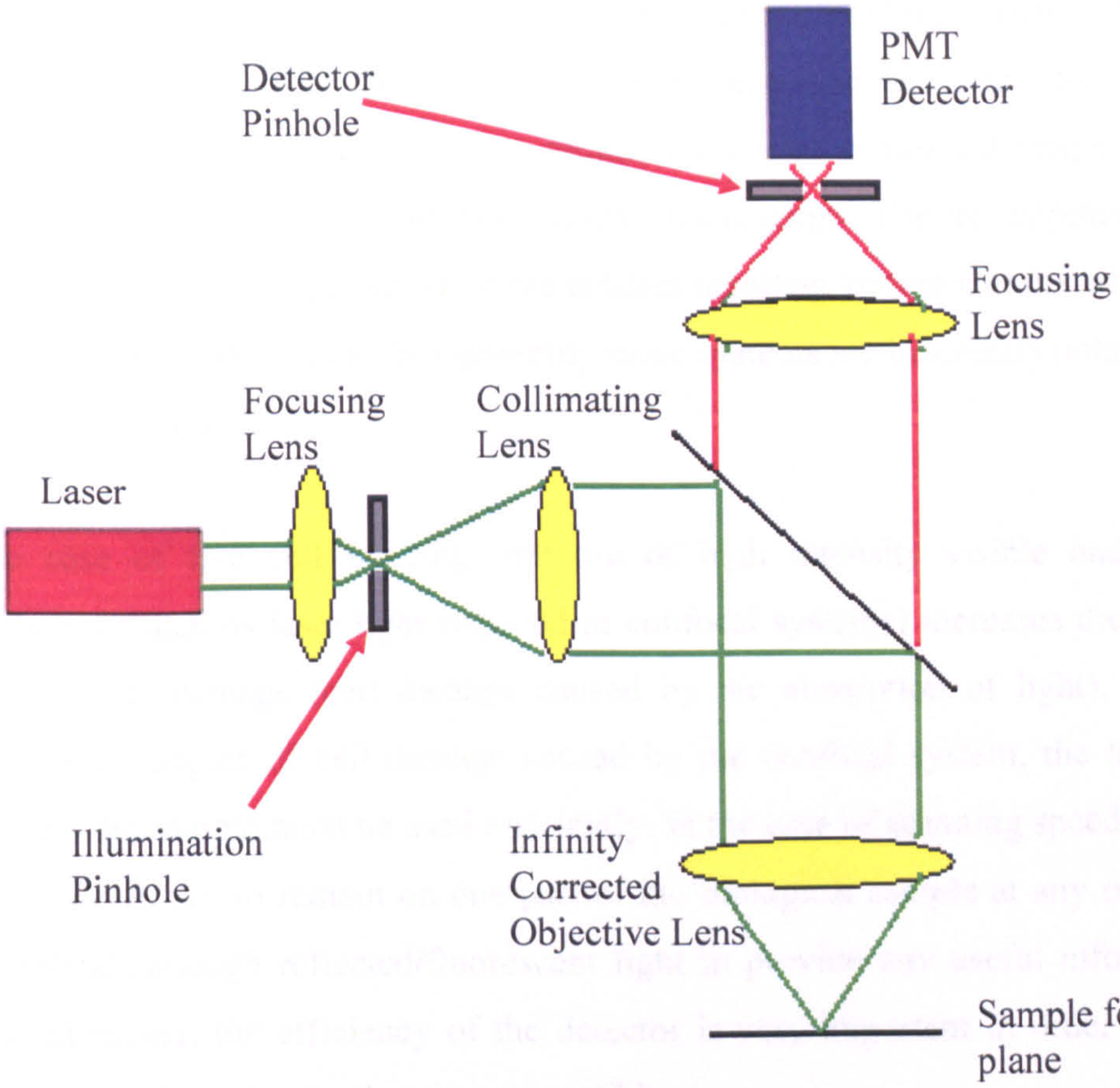

Figure 9: Showing the confocal set-up with infinity optics.

2.7 Advantages and limitations of confocal microscopy

As shown, the confocal system provides the user with the ability to produce optical sections without the need for physical dissection. By removing out-of-focus light from the image and increasing the signal to noise ratio, the system produces images that have greater contrast and resolution. Combining confocal microscopy with advanced computer processing and function built software packages currently available, three-dimensional volume renders can be produced from optical sections, which can provide valuable insight into the inner workings of cell design and function for the biologist. It can be easily modified for use in fluorescence imaging and provides the user with a powerful optical tool for live cell imaging.

There are, however, some limitations associated with confocal microscopy. Due to only one confocal point being imaged at any one time and the need for a scanning mechanism, the image acquisition time required to record a confocal image is generally much longer than for wide-field conventional microscopy. The development of multi-scanning confocal techniques such as the tandem scanning system mentioned previously, speed up the acquisition time, but generally these systems are inherently noisy and are of much lower contrast.

In the case of live cell imaging, the use of high intensity visible and ultraviolet illumination (such as laser light required in confocal systems) increases the probability of photo-toxic damage (cell damage caused by the absorption of light). In order to minimize the degree of cell damage caused by the confocal system, the light used to illuminate the sample must be used efficiently. In the case of scanning speeds, they must be fast enough not to remain on one part of the biological sample at any one time, yet must provide enough reflected/fluorescent light to provide any useful information. As explained earlier, the efficiency of the detector is very important in order to detect as many photons from the focal region as possible.

Another problem associated with confocal microscopy when imaging biological material, and is inherent of any in-depth optical imaging system, is the reduction of image quality due to aberrations and optical scattering. Neglecting aberrations introduced by the confocal system itself, problems are induced due to refractive index mismatching of biological tissue. As well as causing the highly scattering properties of the cellular media also leads to the introduction of aberrations which in turn results in a severe degradation to the optical sectioning capability. As the depth of imaging through biological tissue increases (hence the degree of induced aberrations increases), the result is a spreading of the PSF with more pronounced side lobes. This in turn lowers axial resolution and in order to image a focal plane at a greater depth, greater laser powers are required (increasing the possibility of cell damage). The most common of these

aberrations associated with biological imaging is spherical aberrations, the origin and characteristics of which were discussed in much greater detail in chapter 1.

3. Fluorescence theory

Fluorescence can be described as "the property of some atoms and molecules to absorb light of a particular wavelength and after a brief interval, termed the fluorescence lifetime, to re-emit light at longer wavelengths" [28]. The fluorescent molecule (known as a fluorophore) absorbs and then subsequently re-emits light at certain specific wavelength bands, which are dependant on the bound electron energy states of the molecule.

Figure 10 shows an example of a typical excitation and emission spectrum for a fluorophore. A single photon from the light source, if of sufficient energy, excites an electron within the molecule taking it from an unexcited "ground state" to an excited state. The electron in an excited state consequently returns to the ground state via a lowest excited singlet state, by emitting energy in the form of a photon of light, which has a longer wavelength than the excitation photon.

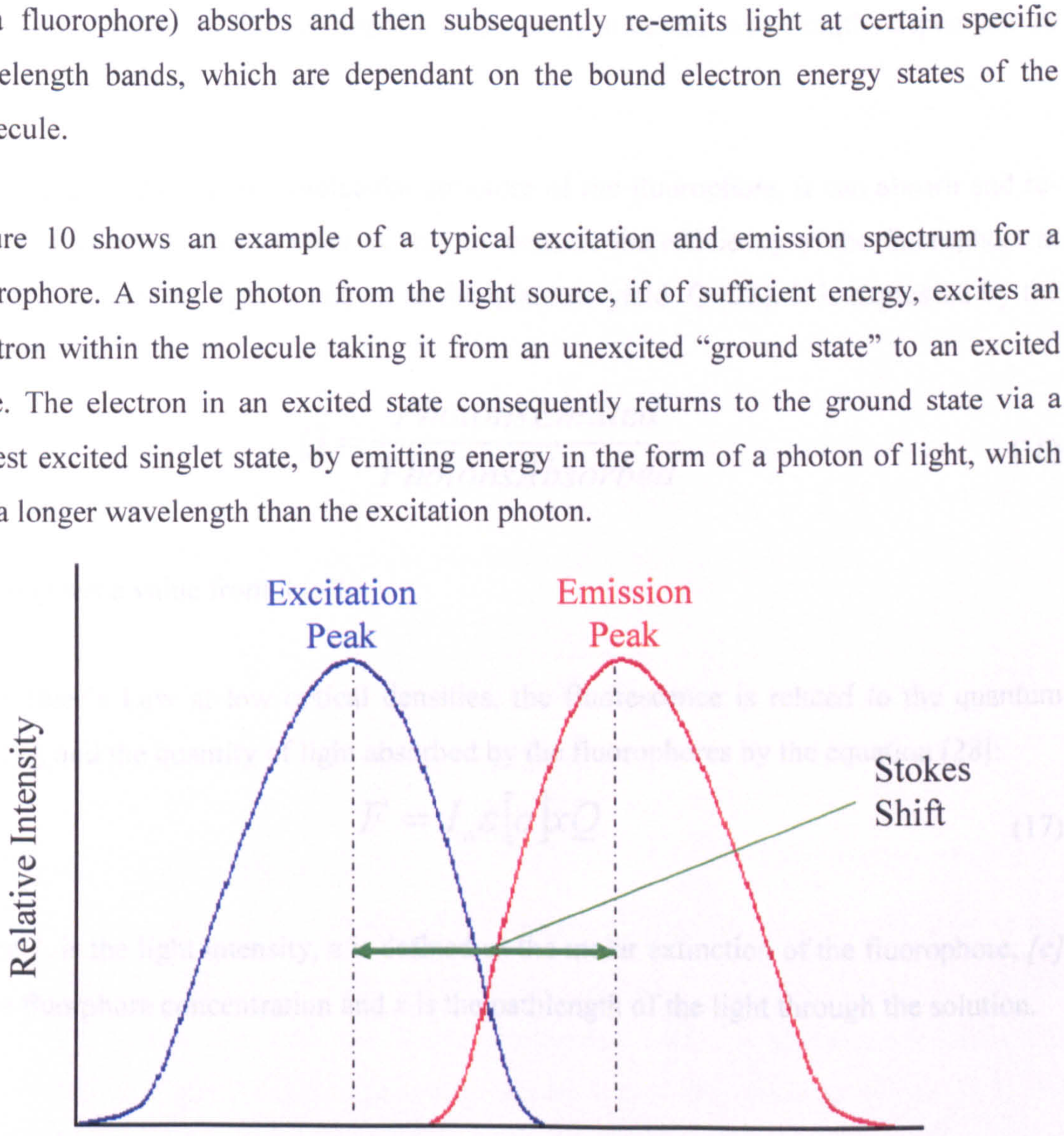

Figure 10: The excitation and emission spectrum of a typical fluorophore.

The extra energy is lost thermally from the transfer from the excited state to the lowest state. This shift from excitation to emission wavelength is known as Stokes shift [29]. Due to this Stokes shift, a low level of emission photons can be measured against the background of high number of excitation photons using spectral filtration. After the electron associated with fluorescence in the fluorophore has successfully returned to the ground state, it can be re-used many times again until it is bleached. The effect of bleaching is very important and will be discussing in much more detail later. It is important to note that light absorption only occurs at certain wavelengths dependant on the fluorophore used.

Depending on the internal molecular structure of the fluorophore, it can absorb and re-emit at photons at various rates. A way to measure the efficiency of the fluorophore at emitting fluorescent light is known as the quantum yield, Q [28]. It is expressed by the equation:

$$Q = \frac{PhotonsEmitted}{PhotonsAbsorbed} \tag{16}$$

where Q has a value from 0 to 1.

From Beer's Law at low optical densities, the fluorescence is related to the quantum yield Q, and the quantity of light absorbed by the fluorophores by the equation [28]:

$$F = I_o \varepsilon [c] x Q \tag{17}$$

where I_o is the light intensity, ε is defined as the molar extinction of the fluorophore, *[c]* is the fluorphore concentration and x is the pathlength of the light through the solution.

In the absence of non-radiative energy transfer mechanisms, the time taken for a fluorescent molecule to return to the ground state from an excited state is known as the fluorescence lifetime, τ, and is related to the fluorescent emitted light intensity *I(t)* at time *t*, by the equation:

$$I(t) = I_o \exp(-t/\tau) \tag{18}$$

where I_o is the initial light intensity at t=0.

As one can see from the equation above, the rate of fluorescent decrease with time follows an exponential pattern. From this equation, the fluorescent lifetime can be calculated to be when $I(t) = I_o / \exp(1)$ which equals 37% of I_o.

There are, however, a number of methods of energy transfer that can contribute to reducing the number of electrons in the excited state by non-radiative means. This includes molecule collisions which result in the transfer of energy from the fluorophore to another molecule. This process is known as quenching and serves to reduce the fluorescent lifetime of the system. The measured lifetime τ_F, [28] is related to the quantum yield *Q*, (described previously in equation 16) by the equation:

$$Q = \frac{PhotonsEmitted}{PhotonsAbsorbed} = \frac{\tau_F}{\tau_o} \tag{19}$$

where τ_o is now described as the intrinsic lifetime.

3.1 Fluorescence in microscopy

The use of fluorescence in microscopy is a technique first developed at the start of the 20th century to increase image contrast in biological images. Using a suitable illumination source and with the aid of appropriate filters (to separate excitation and emission wavelengths), the fluorescent molecules within the specimen are excited, and the fluorescence detected. Using an excitation source matched to a particular dye, fluorescent microscopy can reveal features which have been previously been

undetectable for standard microscopes. Fluorescence in biological imaging has many advantages over normal microscopy which operate by either absorbance or reflectance [28]. These are:

1. Specificity – each molecule displays its own specific excitation and emission spectra which is dependant on its constitution and shape. This can be used to act as a fingerprint.
2. Sensitivity – due to the presence of band pass filters in front of the detector, fluorescence can be detected at low levels.
3. Quantification – due to the relationship between the quantum yield Q, and the emitted fluorescence F (from equation 17), quantitative measurements can be taken.
4. Environmental sensitivity – this is related to the specificity. The immediate environment in which the fluorophores occupy can cause them to change shape which in turn causes their specific excitation and emission spectra to change. As a result, fluorphores can be used to sense changes in their environment such as pH and Ca^{2+} concentration levels.
5. High temporal resolution – using fluorescence chemical reactions can be detected at high speeds.
6. High spatial resolution – with only a small number of fluorophores, single molecules can be detected using fluorescent techniques.

Thus combining the optical sectioning capabilities and improvements in lateral and axial resolutions of the confocal microscope with the inherent advantages associated with fluorescent microscopy, provides the user with an extremely powerful tool in biological imaging. In the case of the confocal system, the use of fluorescence has been described as "probably the most important optical readout mode in biological confocal microscopy" [30]. Of course, the advantages associated with fluorescence microscopy are dependent on the properties and composition of the phorophore used. Applications in fluorescent confocal microscopy include live cell imaging and the monitoring of

intracellular ion concentration, both of which are extremely important in the understanding of cell processes.

3.2 Problems associated with fluorescence in biological imaging

There are, however, some problems associated with the use fluorescent microscopy in biological confocal imaging:

1. Photo-toxicity – as mentioned previously in this chapter, in the case of live cell imaging, the use of high intensity laser light required in confocal systems increases the probability of photodynamic damage. This problem is further exasperated due to the lower wavelengths (thus higher energy) of light required to excite the fluorophores. In the case of some fluorescent dyes that fluoresce in the visible, the need for an ultra violet excitation source is highly damaging to cell structure.
2. Photo-bleaching – each fluorophore is said to have a particular "photochemical lifetime" [31] in which it will emit a given number of photons after which they will be damaged and rendered non-fluorescent. In the case of a fluorescent dye, the loss or fading of fluorescent signal is known as photo-bleaching and the rate at which it occurs is dependant on the excitation energy and duration of exposure time.
3. Photodynamic damage – particularly important in live cell imaging, photodynamic damage is a process in which the cells themselves are damaged due to an interaction and modification of the fluorescent dye with the excitation light source used.

Although the use of confocal microscopy with fluorescence has shown to be quite useful, it still has many limitations due to photo-bleaching and photodynamic damage due to the fluorophore. As well as this, in the confocal case, even though only one focal spot is being imaged, the whole depth of field is being irradiated. This in effect restricts the intensity of illumination being used [32]. One such system which overcomes many of the limitations associated with confocal fluorescence microscopy is multiphoton

excitation microscopy, which has become the preferred method for 3 dimensional imaging of life cells and tissues amongst biologists.

3.3 Multiphoton fluorescent excitation microscopy

The theory of multiphoton excitation was first envisaged by Maria Goeppert–Mayer in 1931 [33]. She predicted that an atom or molecule can absorb two photons simultaneously (10^{-16}-10^{-17}s) leading to fluorescence emission. In comparison with normal fluorescence, (where a single photon is absorbed with subsequent fluorescent emission by the fluorophore) two photon excitation requires photon energies half that of single photon excitation (figure 11). This is due to excitation energies of each photon absorbed in a multiphoton absorption event, being combined in a single quantized event, to produce an excitation normally due to a single photon with a shorter wavelength.

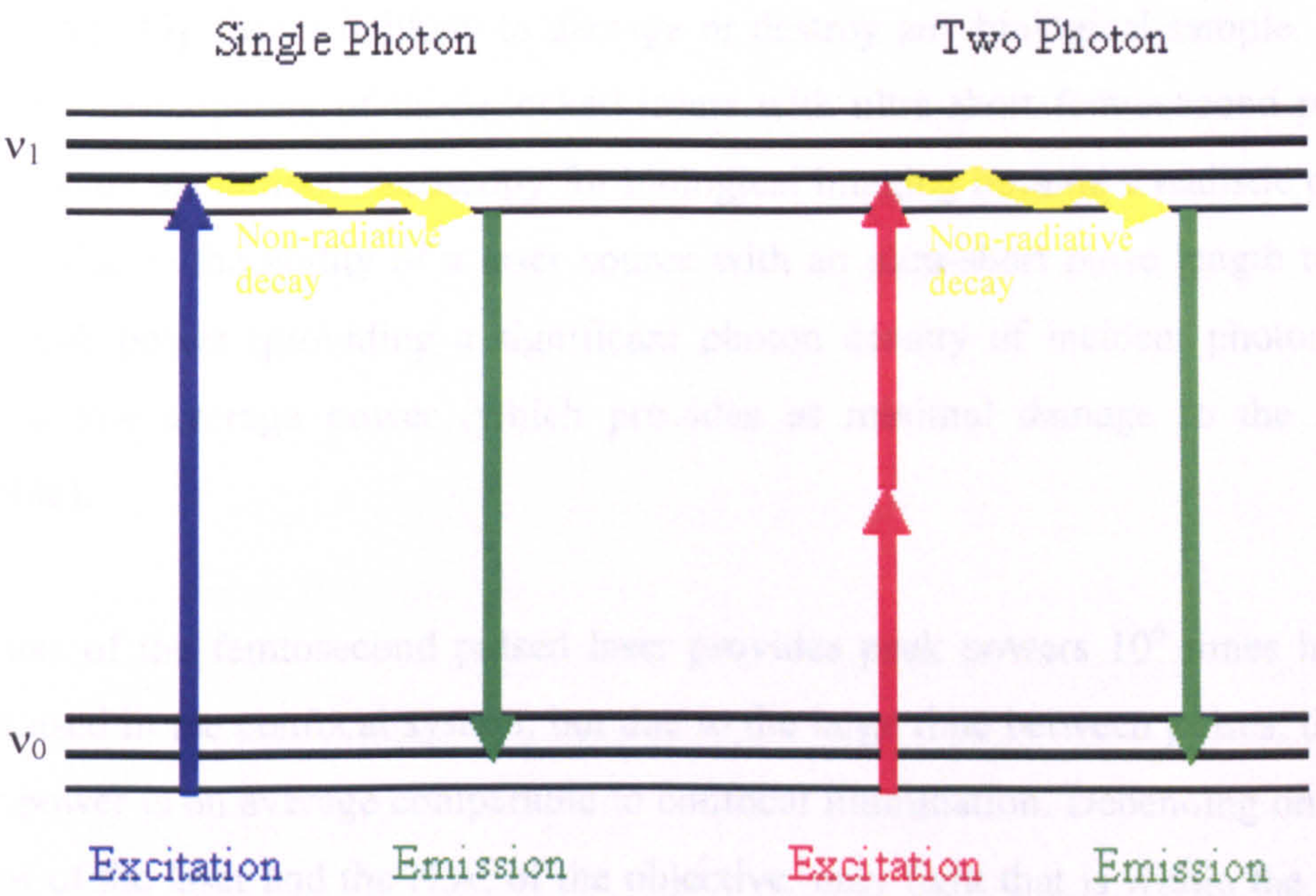

Figure 11: Showing the energy level diagram of a single photon against a two photon excitation and fluorescence process.

Due to the short time (10^{-17}s) required in which two photons must occupy the same space for two photon excitation and emission to occur, the technique requires a significant density of incident photons. This significant photon density was only available upon the invention of the laser in 1960 [34] and the development of high peak power laser sources required using ultrafast femtosecond pulse mode-locked lasers [35]. Using $CaF_2:Eu^{2+}$ as a fluorescent material, Kaiser and Garrett [36] were the first to show two-photon excitation and subsequent fluorescence. The potential of using a multiphoton system was first suggested in 1978 [37 & 38] but the successful application of such a technique was not realized until 1991 by Winfried Denk *et al.* [39].

For two photon absorption, the probability of absorption is proportional to the square of the photon intensity. Using a laser operating in continuous-wave (CW), two photon fluorescence is possible, but the power required to induce fluorescence is so high (500-1800mW) [40], that it is likely to damage or destroy any biological sample. It was not until the development of mode-locked lasers with ultra-short femtosecond pulses, that multiphoton excitation microscopy for biological imaging became a realistic possibility. This is due to the ability of a laser source with an ultra-short pulse length to generate high-peak power (providing a significant photon density of incident photons), but to have a low average power (which provides as minimal damage to the sample as possible).

The use of the femtosecond pulsed laser provides peak powers 10^6 times higher than those used in the confocal system, but due to the large time between pulses, the average peak power is on average comparable to confocal illumination. Depending on the power output of the laser and the N.A. of the objective, only light that is within the focus is of sufficient density to allow multiphoton excitation to occur. The multiphoton system in effect provides optical sectioning capability comparable to the confocal system and as in the confocal case by scanning this focused beam in the x, y and z axes, a three dimensional image can be produced.

The fluorescent signal, N, from the multiphoton system is shown to be related to the laser source [41], via the equation:

$$N = \left\{ \left((Power)^2 \times \delta \right) \Big/ PulseWidth x (\mathrm{Re}\, petitionRate)^2 \right\} \times \left\{ \left(\pi \times N.A.^2 \right) \Big/ hc\lambda \right\}^2 \qquad (20)$$

where the *power*, *pulse width* and *repetition rate* refer to the laser source used, *N.A.* is the numerical aperture of the objective lens, h, π, c are standard constants, λ is the laser wavelength, and δ is the two-photon absorption cross-section of the fluorescent molecule.

3.4 Advantages of multiphoton microscopy

The multiphoton system has a number of specific advantages over the single photon excitation confocal approach when imaging biological samples. Many of these result from the fact that two-photon events do not take place outside the focus of the objective. These are:

1. Reduced photo-bleaching – effects restricted to the focal region since fluorescence only occurs at the focal region, only fluorophores located at the focal spot can be bleached.
2. Reduced photo-damage – like photo-bleaching, this is restricted to the focal region where fluorescence occurs.
3. No confocal pinhole aperture – every photon is important, due to all the fluorescence originating from the focal spot. By removing the pinhole aperture, the collection efficiency of the system is increased.
4. No de-scanning required – the detector can be placed close to the specimen and simplifies the optical arrangement. As well as this the light collecting efficiency is increased due to the returned light passing through less optics.

In figure 12, the localized fluorescence associated with multiphoton excitation fluorescence is compared with single photon conventional fluorescence.

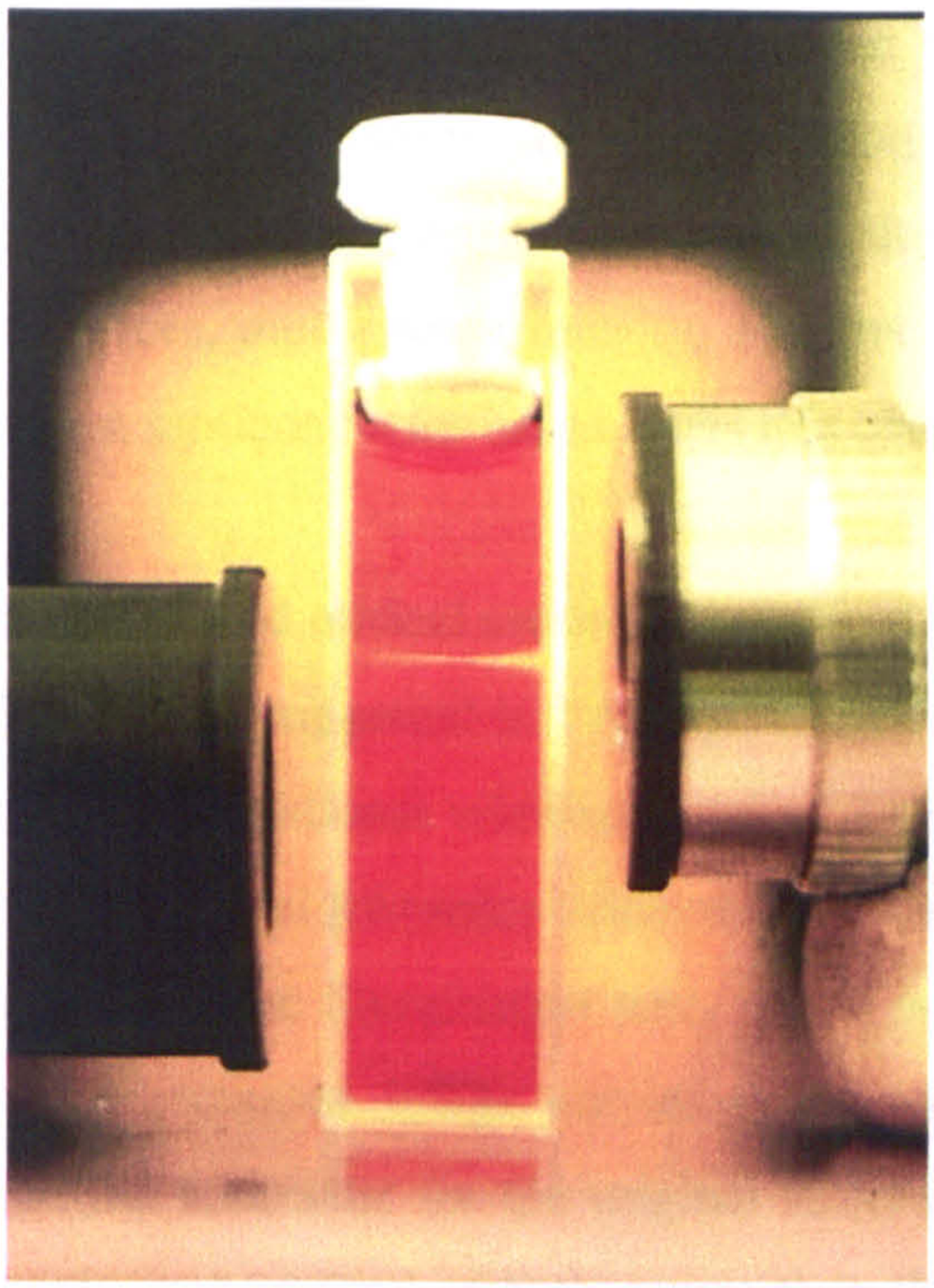

Figure 12: Multiphoton and single photon fluorescence [42].

Other advantages associated with the multiphoton system are due to the excitation energy of the light used. When collecting fluorescence in the visible, the use of longer wavelengths (near-infrared) required for multiphoton excitation allows deeper imaging within the sample than its single photon counterpart, which relies on UV or visible light for excitation. This is due to some of the scattering associated with tissue imaging being somewhat wavelength dependent. Another added advantage to using near-infrared light is that it is far less damaging to living samples, than visible or UV light due to it being less energetic.

Since the first practical realisation of the multiphoton system, there have been numerous advancements in ultrafast laser sources, laser scanning mechanisms, ultra fast and highly sensitive detection devices as well as improvements in computing power and software. This has led to the multiphoton excitation microscope increasingly establishing itself as the imaging method of choice for deep biological imaging [43]. Using tunable near-

infrared laser sources such as the Ti:Sapphire modelocked laser (which can operate in a wavelength range from 700nm to 1100nm) allows excitation of many fluorophores previously excited in the UV or visible spectrum. At present, due to the cost of suitable pulsed laser illumination sources, multiphoton imaging systems are quite expensive but with developments in low cost semiconductor based lasers this could change.

4. Structured light illumination and optical sectioning

The use of structured light was first suggested in 1997 by Neil *et al.* [44]. It was shown by Neil and colleagues that in a conventional widefield optical imaging system, all spatial frequencies aside from the zero spatial frequency attenuate with defocus. By introducing a single frequency grid pattern into the illumination path, which is subsequently projected onto a sample, an optically sectioned image similar to the confocal system can be extracted. Figure 13 shows the schematic for the original structured illumination system [44]. The grid pattern is only present (and of high contrast) in those parts of the sample image that are in focus. As one moves out of the focal plane, the contrast of the grid pattern attenuates until it completely disappears. By removing only those parts of the image where the grid pattern exists, the system produces optical sectioning capabilities similar to those that exist in the confocal and multiphoton cases.

By taking images corresponding to three spatial phases of the grid pattern (at 0, $2\pi/3$ and $4\pi/3$), images equivalent to the conventional widefield and optically sectioned image can be produced.

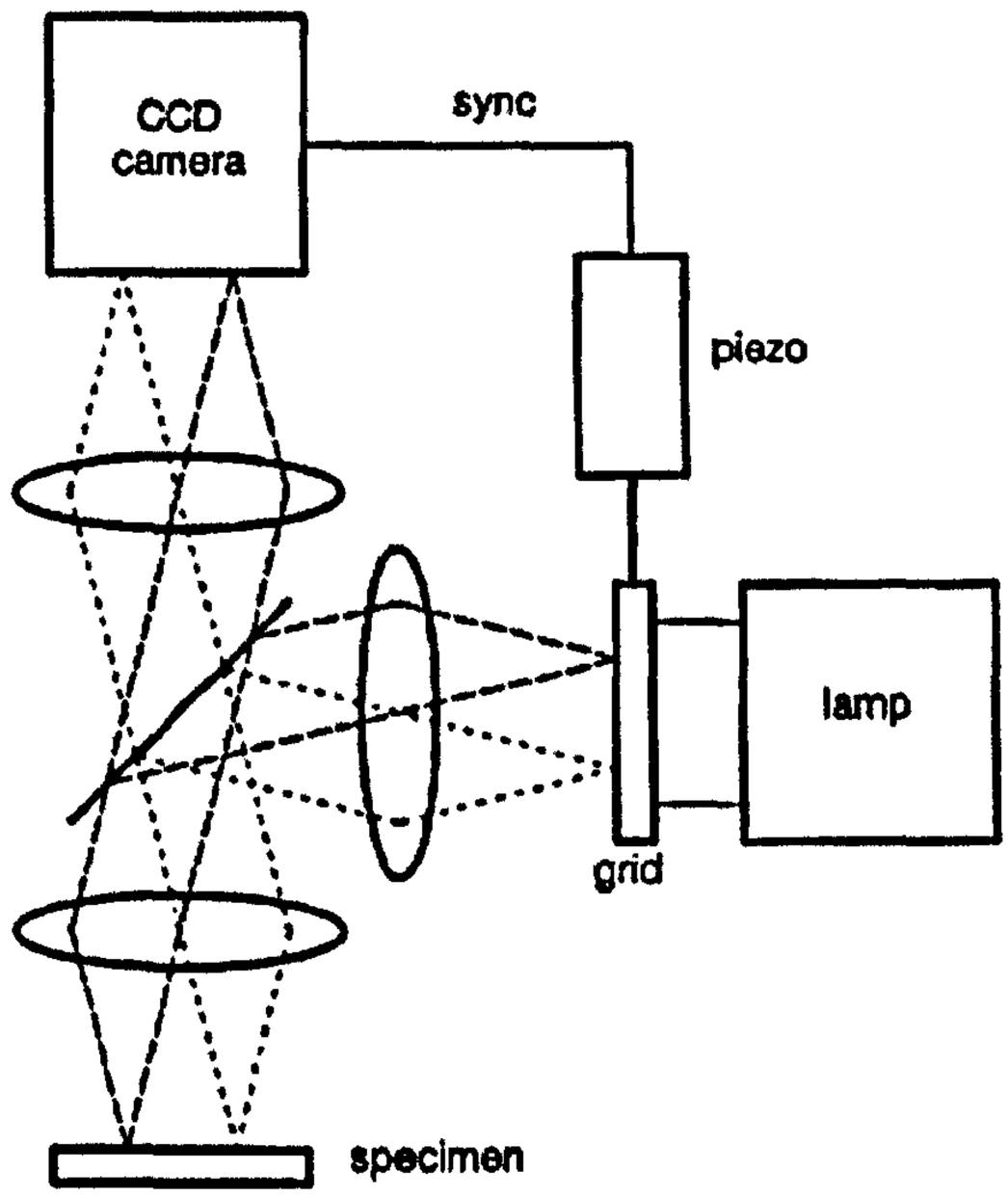

Figure 13: Showing original schematic of the structured illumination system [44].

4.1 Theory of structured light illumination

From [45], it is shown that the image produced *(I)* when a single frequency grid pattern is used to illuminate a conventional microscope is defined as:

$$I(t,w) = I_o + I_c \cos(\phi_o) + I_s \sin(\phi_o) \tag{21}$$

where the optical co-ordinates *(t, w)* are associated to (x, y) by the equation (t, w) = $(2\pi/\lambda)$(x, y) n sin α, I_o is the conventional widefield image, and I_p is calculated by the equation:

$$I_p = \sqrt{\left(I_c^2 + I_s^2\right)} \tag{22}$$

By taking three images at the corresponding spatial phases of 0 (I_1), $2\pi/3$ (I_2), and $4\pi/3$ (I_3) one can extract both the conventional widefield I_o and sectioned I_p images from the image calculations:

$$I_o = \tfrac{1}{3}\left(I_1 + I_2 + I_3\right) \tag{23}$$

and

$$I_p = \sqrt{\frac{2}{3}} \cdot \left[(I_1 - I_2)^2 + (I_1 - I_3)^2 + (I_2 - I_3)^2 \right]^{1/2} \tag{24}$$

From [45], it has been shown that the theoretical axial PSF of the structured light system from a plane reflector can be calculated using the equation:

$$I_p \approx \left| 2 \frac{J_1[2u\bar{\upsilon}(1 - \bar{\upsilon}/2)]}{[2u\bar{\upsilon}(1 - \bar{\upsilon}/2)]} \right| \tag{25}$$

where J_1 is the Bessel function of the first kind, first order, with the normalised spatial frequency, $\bar{\upsilon}$, being:

$$\bar{\upsilon} = \frac{\beta \lambda \upsilon}{N.A.} \tag{26}$$

and

$$u = 8\left(\frac{\pi}{\lambda}\right) z \sin^2(\alpha/2) \tag{27}$$

where β is the magnification between the specimen and the grid plane, λ is the wavelength of the illumination light used, υ is the actual spatial frequency of the grid pattern, *N.A.* is the numerical aperture, z is the axial distance, and α is the acceptance angle of the objective.

The normalised spatial frequency, $\bar{\upsilon}$, of the system determines the the optical sectioning capability of the structured illumination system, with a value of $\bar{\upsilon} = 1$ corresponding to the maximum sectioning strength, and $\bar{\upsilon} = 0$ equivalent to removing the grid pattern altogether.

Using equation 25, the optical sectioning properties of the structured light system are shown in figure 14 below.

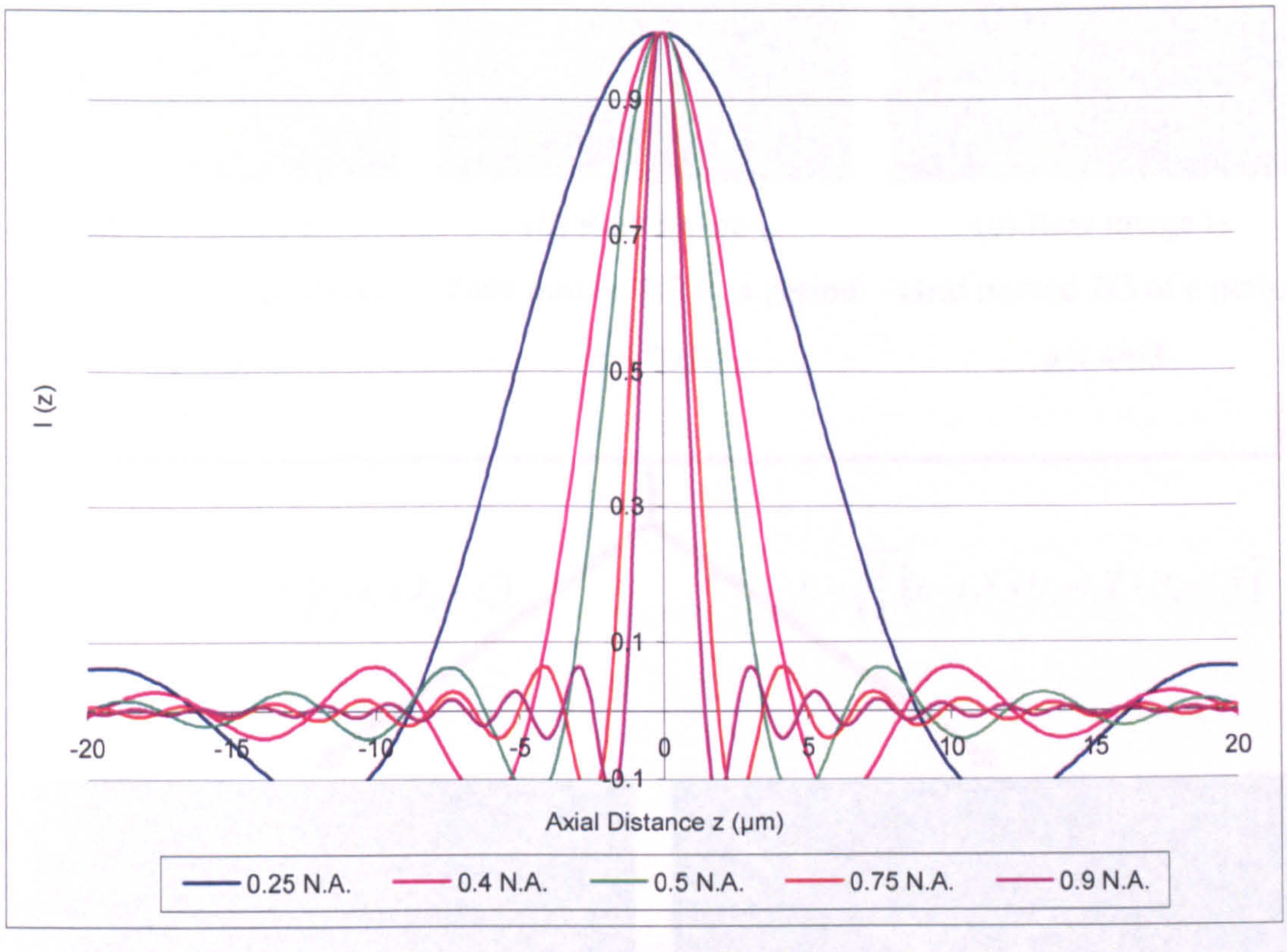

Figure 14: The theoretical axial response I(z) of the structured light system when viewing a plane reflection through dry objectives of different N.A. (wavelength λ = 800nm, magnification $\beta = 5$, and $\nu = 40$ lines/mm).

Figure 14 shows that as the N.A. of the objective lens is increased, the optical sectioning strength of the structured light system is also enhanced. Athough fundamentally different in nature to the confocal and multiphoton techniques, the main peak of the structured light axial PSF follows a similar normal distribution curve. Figure 15 is a schematic showing how the sectioned and conventional widefield images are produced form the raw images taken.

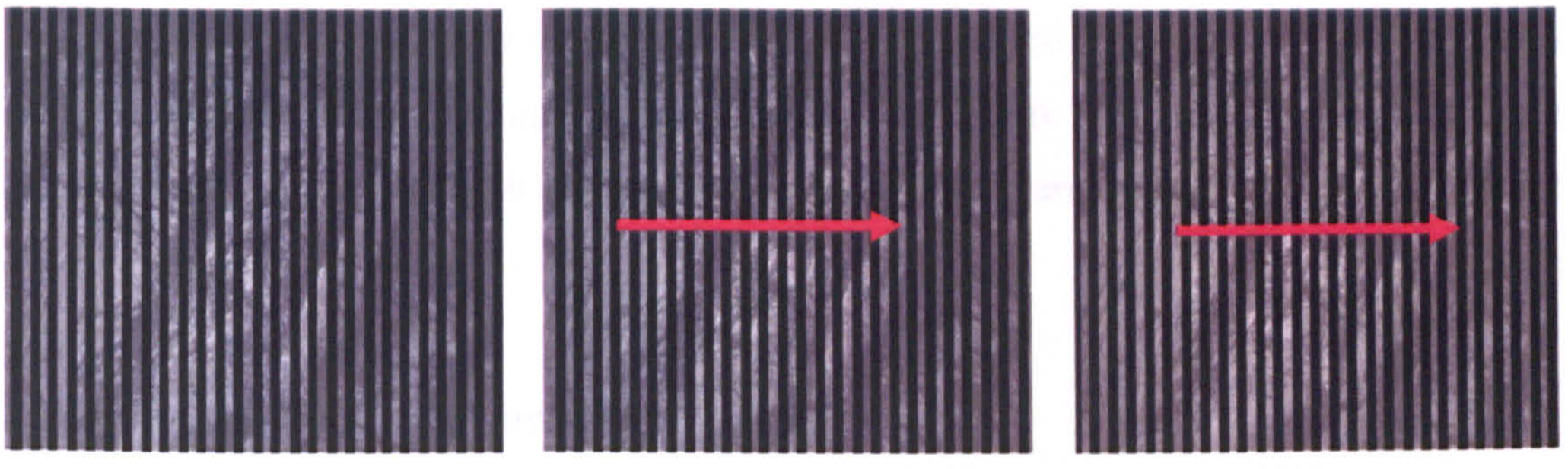

(d) Conventional widefield image I_o (e) Optically sectioned image I_p

Figure 15: Showing raw images of a sample (coin surface) with the grid pattern at 3 spatial phases (0, $2\pi/3$ and $4\pi/3$) and the constructed conventional widefield and optically sectioned images.

The grid pattern is projected onto the specimen and moved in steps corresponding to a 1/3 of a period. By performing image calculations (figure 15) on I_1, I_2, and I_3, using equations (23) and (24), both the conventional widefield and optically sectioned image can be produced.

4.2 Developments in structured light

Since its invention, structured light has already been developed for use in a number of specific applications. By replacing the microscope objective with a zoom lens system, the structured light system was shown to produce near real-time 3-dimensional imaging for macroscopic structures [45]. A structured light system using laser illumination has also been presented for use in fluorescent microscopy [46]. Using a laser provides a greater illumination intensity at specific wavelengths (in comparison to the use of a white light source with filters) to sufficiently excite the fluorophores present in biological samples, producing results comparable to conventional confocal fluorescence techniques.

It has also been shown by Karadaglic *et al.* [47] that the structured light illumination system could be used with endoscopy (with in-vivo applications in mind) to produce optically sectioned images. Using a rigid endoscope to guide the illumination path, a single frequency grid pattern was projected onto tissue to produce both optically sectioned and conventional wide-field fluorescent images.

At present there are two commercially available techniques based on this form of structured illumination. These are the Optigrid system developed by Thales Optem (also known as Qioptiq) [48], and the Apotome system produced by Carl Zeiss [49] (see figure 16). Both of these systems are modular and with only small modifications to a conventional widefield microscope, providing confocal-like optical sectioning at a fraction of the price.

(a) Optigrid (Thales Optem)

(b) Apotome (Carl Zeiss)

Figure 16: Showing the Optigrid and Apotome commercial S.L. systems.

4.3 Comparing structured light illumination with conventional confocal techniques

The structured light system has a number of advantages over a typical confocal or multiphoton system, namely:

1. Greater photon efficiency – in the confocal situation, only light that has passed through the pinhole is collected by the detector, making the system extremely inefficient at collecting light. In the structured light system, a CCD camera is used to collect light from the whole image so that virtually no light is lost in the capture process. This great photon collection efficiency can reduce the light exposure of a sample (extremely important in biological imaging to prevent photo-toxicity) as well as allowing the use of incoherent light sources.
2. Real-time imaging – as only 3 images (with the grid pattern at spatial phases of 0, $2\pi/3$ and $4\pi/3$) are required to produce an optical section, high speed CCD cameras can be incorporated to produce optical sectioning at video rates. Although these rates are comparable to multi-beam confocal scanning systems mentioned previously, it is still much faster than single beam scanning confocal systems currently available.

3. Widefield and sectioned images simultaneously – through the nature of the structured light system, in which both the conventional widefield and the optically sectioned image can be reconstructed from the same three raw images gives it another advantage over present confocal systems.
4. Cost – as mentioned previously, present day confocal microscopy systems are quite expensive (>$100K). In comparison structured light systems are generally much more affordable with the pre-mentioned Optigrid being quoted at ~$15-20K.

Of course the structured light system is not without its limitations. These include errors introduced into the system due to the grid pattern not being at the correct spatial phases well as problems associated with sample movement during image capture. This results in unwanted grid pattern artifacts in both the calculated sectioned and conventional images [50]. There is no doubt that present commercially available structured light systems employ extensive algorithmic routines to aid in the optically sectioning process (using some form of deconvolution) to remove artifacts from the final optically sectioned image.

5. Summary

In this chapter the theory and characteristics associated with confocal, multiphoton and structured light for use in microscopy were explained in great detail. A brief historical background and detailed overview of the confocal system was described, including the function and importance of the confocal pinhole in the optical design. Different types of confocal systems were discussed and the advantages and limitations of the system are examined.

The phenomena of single and multiphoton fluorescence and their application and advantages that they bring to microscopy were discussed. Problems associated with fluorescence such as ionisation, photo-bleaching and photo-toxicity and their implications in biological imaging were considered and the advantages associated with

multiphoton imaging were are also discussed. These would include optical sectioning capability, reduced photo-bleaching and photo-toxic effects.

The theory and use of structured light as an alternative to conventional confocal images was examined. Its optical sectioning capabilities and advantages as well as limitations when compared to confocal and multiphoton systems were explored.

Each of these three optically sectioning techniques that has been shown present a certain set of advantages and limitations. In a world were there are most certainly trade-offs when using one technique instead of another, it is simply a case of using the particular technique which is best suited for a specific imaging application.

References

1. Abbe E. (1873). Beiträge zur Theorie des Mikroskops und der mikroskopschen Wahrnehmung. *Schultzes Arc. F. Mikr. Anat.*, 9, 413-468.
2. Abbe E. (1884). Note on the proper definition of the amplifying power of a lens or lens-system. *J.of R. Microscopy Soc.*, 4, 348-351.
3. Girkin, J. (2005). *Private communication,* Institute of Photonics, University of Strathclyde.
4. Minsky M., (1957). Microscopy apparatus, U.S. Patent #03013467
5. White, J. G. and Amos, W. B. (1987). Confocal microscopy comes of age, *Nature* 328: 183-184.
6. White, J. G., Amos, W. B. and Fordham, M. (1987) An evaluation of confocal versus conventional imaging of biological structures by fluorescence microscopy. *J. Cell Biol.* 105:41-48.
7. Webb, R. H. (1996). Confocal optical microscopy, *Reg. Prog. Phys.* 427-471
8. Wilson, T. (1990). *Confocal Microscopy,* Academic Press, London.
9. Hecht, E. (1998). Chapter 11: Fourier Optics. *Optics*, 3rd Edition, Addison Wesley Longman Inc.
10. Wilson, T. (1990).Chapter 1: Confocal Microscopy, *Confocal Microscopy,* edited by Wilson, T. Academic Press.
11. Born, M., Wolf, E. (1983). *Principles of Optics*, 6th ed, Pergamon press, Oxford.
12. Wilson, T. & Sheppard, C. (1984). *Theory and Practice of Scanning Optical Microscopy*. Academic Press, London.
13. Kino G. S., Xiao G .Q. (1990). Real-time scanning optical microscopes. *Confocal microscopy*, Wilson, T. ed., Academic Press, London.
14. Abramowitz, M., Davidson, M. W. (2004). Atonomy of the microscope, Optical microscopy primer, molecular expressions, Retrieved the 9th of December 2005 from http://micro.magnet.fsu.edu/primer/anatomy/numaperture.html
15. Inoué, S. (1995). Chapter 1: Foundations of confocal scanned imaging in light microscopy., *Handbook of Biological Confocal Microscopy*, 2nd Edition, Pawley, J. ed, Plenum Press, New York, 1-17.

16. Brakenhoff, G.J., Binnerts, J.S., P. Barends. (1979). Confocal scanning light microscopy with high aperture immersion lenses. *J. Microscopy*, 132, 1-7.
17. Centonze, V., Pawley, J. (1995). Chapter 36: Tutorial on practical confocal microscopy and the use of the confocal test specimen. *Handbook of biological Confocal Microscopy*, 2nd Edition, Pawley, J. ed, Plenum Press, 549 – 569.
18. Cogswell, C. J., Larkin, K. G. (1995). Chapter 8: The specimen illumination path and its effect on image quality, *Handbook of biological Confocal Microscopy*, 2nd Edition, Pawley, J. ed, Plenum Press, New York, 127 – 137.
19. Amos, W. B. (1995). Appendix I: Axial units, *Handbook of biological Confocal Microscopy*, 2nd Edition, Pawley, J. ed, Plenum Press, New York, 579
20. Claxton, N. S., Fellers, T. J., Davidson M. W. Laser scanning confocal microscopy
21. Stelzer, E. H. (1995). Chapter 9: The intermediate Optical System of Laser-scanning confocal microscopes, *Handbook of biological Confocal Microscopy*, 2nd Edition, Pawley, J. ed, Plenum Press, 139 – 154.
22. Tsien, R. Y., Bacskai, B. Y. (1995). Chapter 29: Video-rate confocal microscopy. *Handbook of biological Confocal Microscopy*, 2nd Edition, Pawley, J. ed, Plenum Press, 459 – 478.
23. Kino, G. S. (1995). Chapter 10: Intermediate Optics in Nipkow Disk Microscopes, *Handbook of biological Confocal Microscopy*, 2nd Edition, Pawley, J. ed, Plenum Press, New York, 155-165.
24. Gratton E., vandeCen M. J. (1995). Laser Sources for Confocal Microscopy, *Handbook of biological Confocal Microscopy*, 2nd Edition, Pawley, J. ed, Plenum Press, New York, 69-97.
25. Kashima, S. (1995). Development of Laser Scanning Microscopy Using a Near Ultraviolet Laser, *Scanning*, 17, 66-69.
26. Zhao, F. (2005). Part 1: Principles of Confocal microscopy, *Confocal Microscopy tutorial*, Advanced Microscopy unit Department of Pathology Haartman Institute, University of Helsinki, retrieved the 9th of December 2005 from http://www.hi.helsinki.fi/amu/AMU%20Cf_tut/cf_tut_part1-9.htm

27. Keller, H. E. (1995). Chapter 7: Objective lenses for confocal microscopy, *Handbook of biological Confocal Microscopy*, 2nd Edition, Pawley, J. ed, Plenum Press, New York, 111-126.
28. Hernan, B. (1998). Chapter 1: fundamentals of fluorescence, *Fluorescence microscopy*, 2nd Edition, BIOS scientific publishers, Oxford.
29. Abramowitz, M., Davidson, M. W. (2004). Overview of Fluorescence Excitation and Emission Fundamentals, the physics of light and color, Olympus microscopy resource centre retrieved the 9th of December 2005 from http://www.olympusmicro.com/primer/lightandcolor/fluoroexcitation.html.
30. Tsien, R. Y., Waggoner, A. (1995). Fluorophores for confocal microscopy. *Handbook of biological Confocal Microscopy*, 2nd Edition, Pawley, J. ed, Plenum Press, New York, 267 – 279.
31. Hernan, B. (1998). Chapter 3: Practical fluorescence microscopy, *Fluorescence microscopy*, 2nd Edition, BIOS scientific publishers, Oxford.
32. Hernan, B. (1998). Chapter 7: Single and multiphoton microscopy, *Fluorescence microscopy*, 2nd Edition, BIOS scientific publishers, Oxford.
33. Goeppert-Mayer, M., (1931). Ueber Elemenarkte mit zwei Quantenspruengen, *Ann. Phys.*, 9, 273.
34. Maiman, T. (1960). Laser, U.S. Patent #3353115.
35. Fork, R. L., Greene, B. I., Shank, C. V. (1981). Generation of optical pulses shorter than 0.1ps by colliding pulse modelocking. *App. Phys. Lett.*, 38, 671-672
36. Kaiser, W., Garrett, C. G. B. (1961). Two-Photon Excitation in CaF_2: Eu^{2+}. Phys. Rev. Lett., 7, 229–23.
37. Shepherd, C. J. R., Kompfiner, R. (1978). Resonant scanning optical microscope *Appl. Opt.*, 17, 2879-2891.
38. Wilson, T., and Shepherd, C. J. R. (1984). Chapter 10: Non-linear microscopy, *Theory and Practice of Scanning Optical Microscopy*, Academic, Boston.
39. Denk, W., Strickler, J. H., Webb, W. W., (1990). Two-photon excitation in laser-scanning fluorescence microscopy, *Science*, 248, 73-76.

40. Hell, S. W., Booth, M., Wilms, S., Schnetter, C., Kirsch, A., Ardnt-Jovin, D., Jovin, T. (1996). Two photon near- and far-field fluorescence microscopy with continuous wave excitation. *Opt. Let.*, 23, 1238-1240.
41. Denk, W., Piston, D. W., Webb, W. W. (1995). Chapter x: Two-photon excitation in laser scanning microscopy *Handbook of Biological Confocal Microscopy* 2nd Edition, Pawley, J. ed, Plenum Press, New York, 445-458.
42. Image showing multiphoton and single photon fluorescence, photo courtesy of Brad Amos, MRC Cambridge.
43. Girkin, J. M. (2003). Optical physics enables advances in multiphoton imaging. *J. Phys. D: Appl. Phys.*, 36, R250-R258.
44. Neil, M. A. A., Juskaitis, R., Wilson, T. (1997). Method of obtaining optical sectioning by using structured light in a conventional microscope. *Opt. Lett.*, 22, 1905-1907.
45. Wilson, T., Neil, M. A. A., Juskaitis, R. (1998). Real-time three-dimensional imaging of macroscopic structures. *J. of Microscopy*, 191, 116 – 118.
46. Neil, M. A. A., Squire, A., Juskaitis, R., Bastiaens, P. I. H., Wilson, T. (2000) Wide-field optically sectioning fluorescence microscopy with laser illumination. *J. of Microscopy*, 197, 1 – 4.
47. Karadaglic, D., Juskaitis, R.,Wilson, T. (2002). Confocal endoscopy via structured illumination. *Scanning*, 24, 301 – 304.
48. Optigrid structured light system, Qioptiq imaging solutions, Rochester NY, USA, http://www.qioptiqimaging.com/Products/
49. Apotome structured illumination system, Carl Zeiss microimaging GmbH, Germany, http://www.zeiss.com/
50. Karadaglic, D., (2004). *Wide-field optical sectioning microscopy using structured illumination.* University of Oxford, Department of engineering science, PhD Thesis.

Chapter 3: Dental tissue as an example for examining tissue structure and disease

1. Introduction

In this chapter, the structure of dental tissue and the nature of dental disease (caries) as an example of biological tissue is illustrated. Dental tissue was chosen as suitable example due to the ease with which it can be stored and preserved as well as it providing a highly scattering media through which one must image (which is illustrative of biological tissue usually.) Caries is a disease driven by bacterial invasion, which when detected at its earliest stages can be arrested and reversed. It can be described as a mineral change of the tooth structure [1], caused by minute changes in the pH, which are a result of the metabolism of sugars by bacteria. This demineralisation process results in an alteration of the optical and scattering properties of the tissue and are representative of tissue disease in general. The nature and onset of caries disease is discussed in greater detail later in this chapter.

Currently, at the dentists' disposal there are a number of commercially available methods for caries detection, but presently none of these techniques have the ability to measure early stage caries. Dentists require a system that can measure or quantify lesion growth and activity in order to determine the correct course of treatment, and at present there are a number of techniques in development which may aid in this goal. The theoretical background and operation of both commercially available systems and those currently in development are outlined in the following chapter.

Development of dental diagnosis techniques have been limited due to the complexity of the tooth structure as well as a limited understanding of the nature of optical and scattering variation associated with caries onset. In order to gain a greater understanding of the change the optical and scattering properties associated with tooth decay, a computer model simulation based on non-sequential ray-tracing was developed using

commercially available software. The model is based on the fibre optical confocal microscope configuration [2 & 3], which with previous experimental results, could be used to provide information on the structure and properties of dental tissue and hence its health. The development of the simulation and a comparison with experimental data from ex-in vivo naturally occurring dental caries is presented in this chapter.

2. Dental structure

A diagram showing the structure of the tooth can be seen in figure 1. The tooth is composed of two main regions, which are the known as the crown and the root. The crown is the part of the tooth that is almost completely exposed above the gum line with the root being the section of the tooth which is embedded into the jawbone. The tooth is composed of three main components. These are:

(a) Enamel – a protective hard white translucent substance covering the crown of the tooth.

(b) Dentine – this is composed of a yellow bone like structure which makes up the majority of the tooth.

(c) Pulp - this is the living portion of the tooth composed of blood vessels nerves and connective tissue which provides sustenance to the tooth.

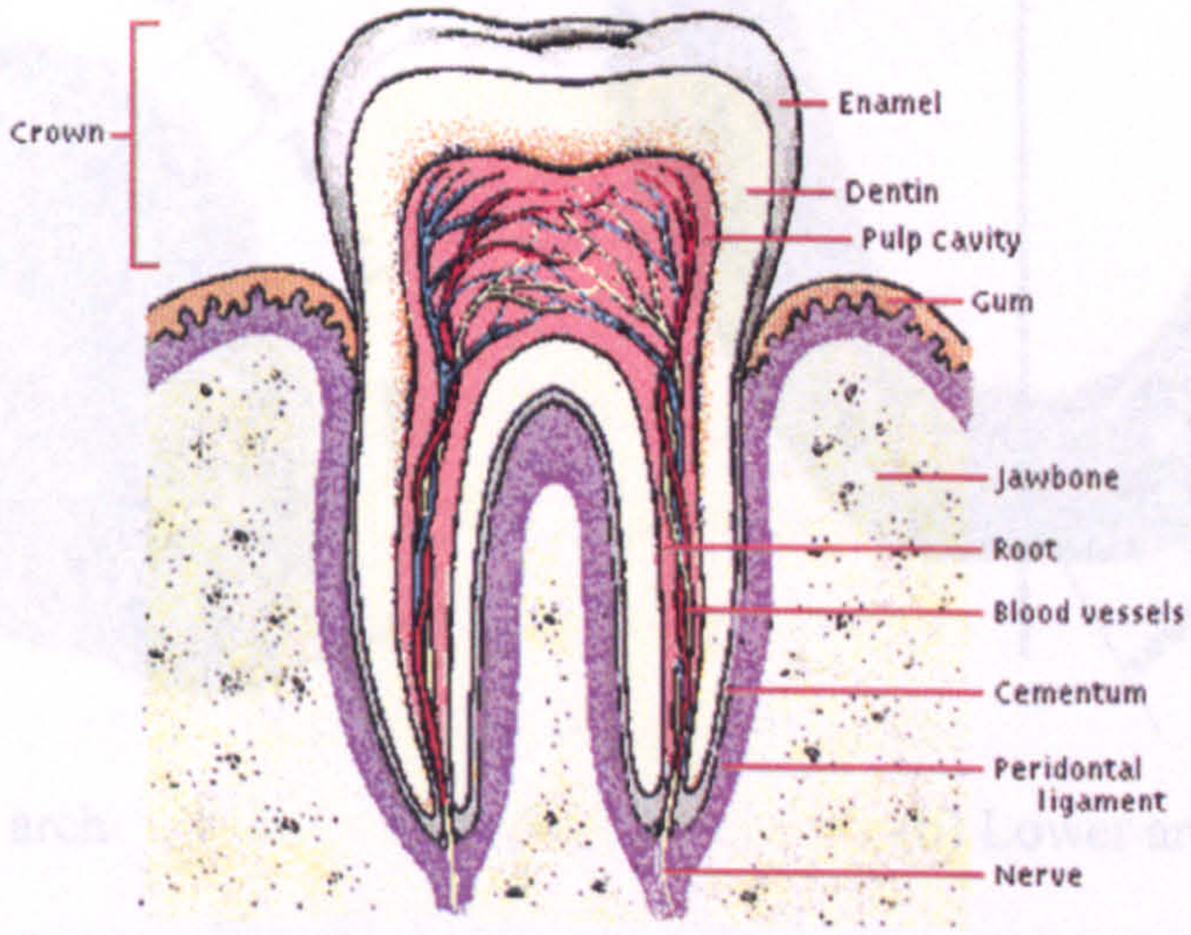

Figure 1: The structure of the tooth and its surrounding tissues [4].

The root itself is covered with a soft bone like tissue known as cementum, the function of which is to provide both a protective layer to the root dentine, as well as a connection layer to the periodontal ligament. The periodontal ligament is composed of a fibrous tissue which acts as a connective tissue to the alveolar bone (which contains the spaces provided for the tooth roots) and to the gingiva (which is the region of gums surrounding the tooth). These tissues which hold and support the teeth in place are together known as the periodontium. Other regions not discussed previously are the apex which is the region at the tip of the root and the *apical foramen*, which is the hole at the root which allows nerve and blood vessels to enter the tooth.

Depending on its position within the mouth, each tooth is specialised in order to optimise on its particular function. As well as this, each region on a particular tooth is known by a specialised nomenclature, depending on its position within the mouth. Figure 2 shows the position and nomenclature within the oral cavity. Incisors and canine teeth are together called anteriors with pre-molars and molars known as posterior teeth. Tooth surfaces which are next to cheeks and lips are known as the buccal surfaces with surfaces next to the tongue being described as lingual.

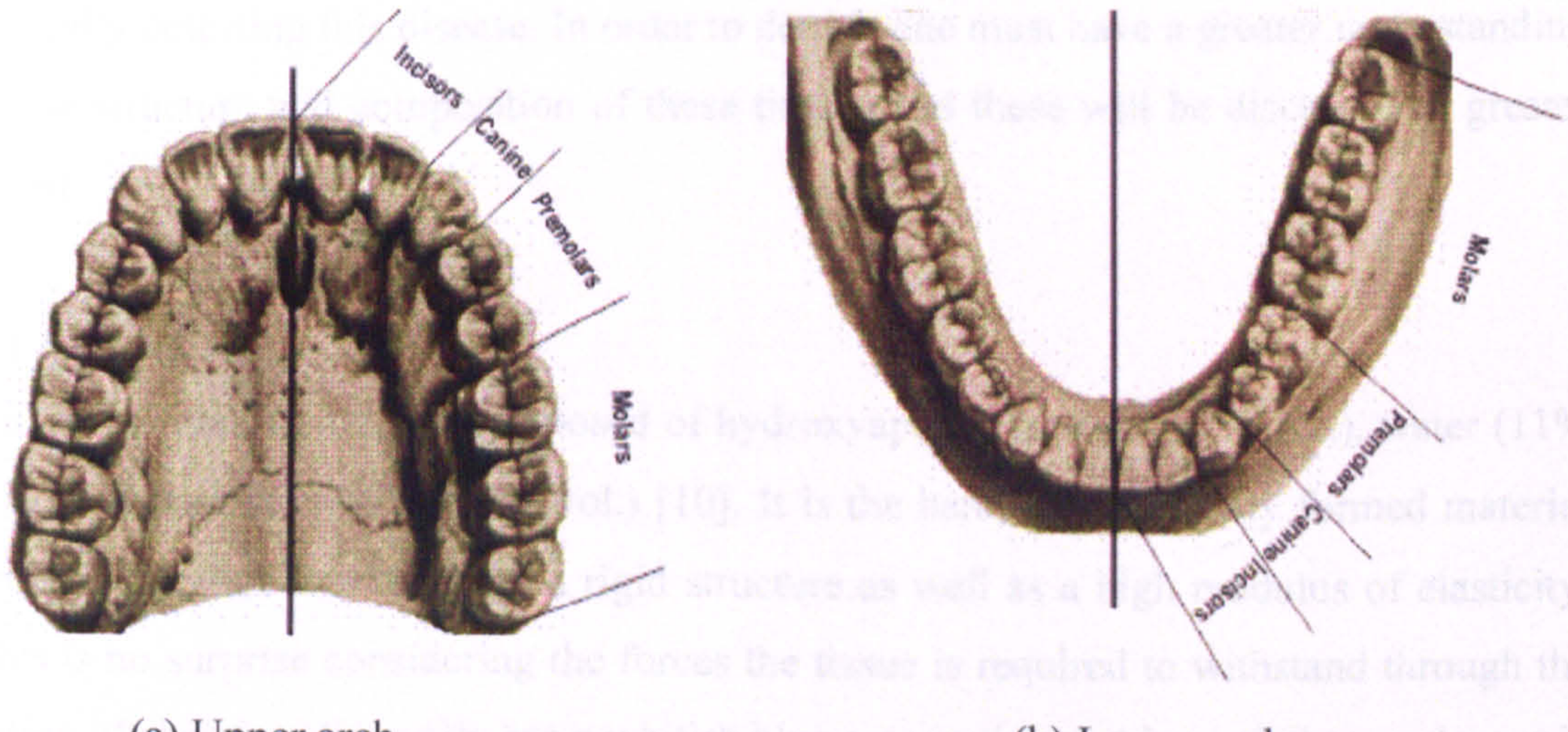

(a) Upper arch (b) Lower arch

Figure 2: Locations and types of teeth present within the mouth [5].

As one can see from figure 2, an imaginary line is present between the central incisors, which is used to distinguish between the surfaces at which two teeth touch. Tooth surfaces facing this imaginary line are called mesial surfaces and surfaces pointing away from this midline called distal surfaces. Together, distal and mesial surfaces are known as proximal surfaces with the sections in between entitled interproximal regions. The biting surfaces are called incisal (anterior) and occlusal (posterior) depending on the tooth.

There are a numerous range of diseases that can afflict the tooth as well as the surrounding tissues within the oral cavity. These include gingivitis [6] (otherwise known as gum disease) which is the recession of the gum line resulting in the exposure of cementum and root dentine to bacterial attack. Another disease, known as periodontitis [7], is the body's response to bacterial infection in the jawbone (related to gingivitis), which results in the re-absorption of alveolar bone and subsequent tooth loss. Other diseases such as xerostomia (dry mouth syndrome) [8] and tooth abscesses [9] (which are a result of an infection within the pulp tissue) are also important in tooth care. However in this chapter and the subsequent chapter, the main concern is the process of dental caries which affects the enamel and dentine structure and the methodology for optically detecting this disease. In order to do this one must have a greater understanding of the structure and composition of these tissues and these will be discussed in greater detail.

2.1 Enamel

Human dentinal enamel is composed of hydroxyapatite crystals (87% vol.), water (11% vol.) and organic material (2% vol.) [10]. It is the hardest biologically formed material present in nature and has both a rigid structure as well as a high modulus of elasticity. This is no surprise considering the forces the tissue is required to withstand through the action of chewing. It usually has a whitish blue colouration and is partially translucent in visible light with a refractive index of 1.62 [11].

The chemical structure of hydroxyapatite is written as $Ca_{10}(PO_4)_6(OH)_2$. Due to the structure and arrangement of hydroxyapatite crystals into a prismatic or rod like arrangement, enamel is birefringent in nature. These prisms are roughly 4 to 6μm wide [12] and are known to carry on from the dentine-enamel junction to the surface of the enamel. These prisms are closely packed in such a way that the tail of one prism lies between the heads of two other prisms [13]. In the area between prisms, known as the interprismatic region, the association between crystals is random in nature [12]. This randomisation results in a lower amount of mineral, and an increased amount of space, which constitute a porous region. In vivo, these pores are usually filled with water or organic material and previous research have shown that they make up 3-5% of the volume of healthy dental enamel [14].

2.2 Dentine

Dentine is a yellow bone like structure which lies underneath the enamel and surrounds the pulp of the tooth. It is largely responsible for the colouration for the tooth due to the translucent nature of enamel at visible wavelengths. Composed of calcium hydroxyapatite mineral (48% vol.), organic material (28% vol.) and water (24% vol.) [15], it makes up the majority of the tooth structure. Similar in composition to bone though much harder, dentine is highly elastic and has a high tensile strength due to the presence of collagen. Dentine crystals are composed into an overlapping plate like structure.

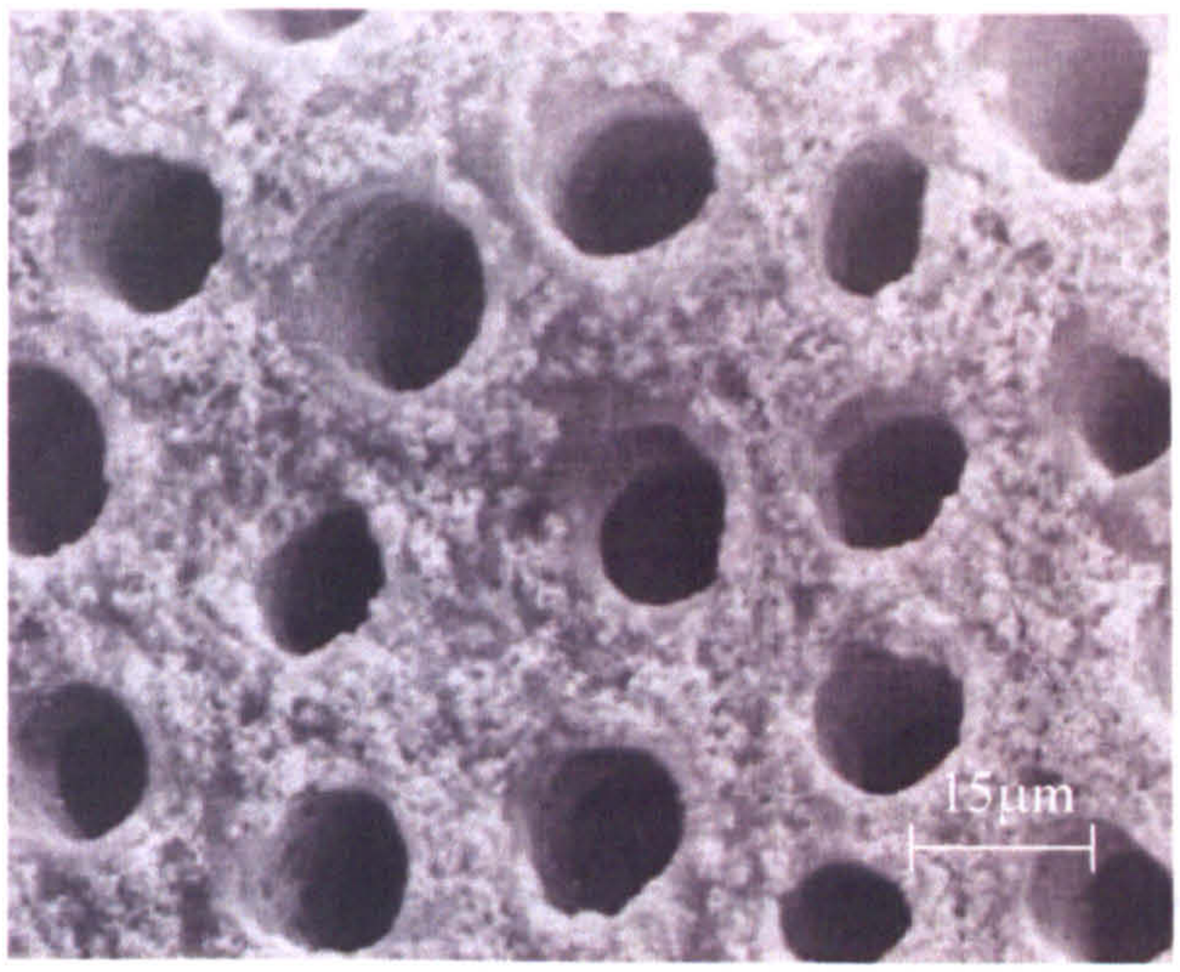

Figure 3: Showing tubular like structures present in dentine [16].

Dentine contains a system of tunnel like structures known as dentine tubules (See figure 3). These tubules begin at the inner region of nerve space with a diameter of 2 to 5µm and end at the outer surface of the dentine with a diameter of 1µm [14]. The tubules themselves contain projections of cells known as odontoblasts that line the inside of nerve space, which are subsequently connected to nerve axons. These odontoblasts can detect movement from the surface of the tooth which is then sensed by the connected nerve cells. This allows nerves sensitivity to detect any dentine that has been exposed.

3. Dental disease (caries)

3.1 The process of dental caries

Dental caries can be defined as a localised, progressively destructive disease of the teeth that starts at the external surface. It is a slowly progressing disease, driven by bacterial attack which causes demineralisation of the tooth. In Figure 4, the process of dental decay is shown.

1. The process of dental caries begins after the process of eating or drinking with the formation of dental plaque on the surface. Dental plaque is composed of a biofilm of bacterial biomass (which are naturally present within the tooth cavity)

embedded within a matrix of food and bacterial waste metabolites.

2. Sugars within the plague biofilm are metabolised by the bacteria to produce acid, which causes some enamel surface erosion to occur. Some mineral loss also occurs deeper within the tooth structure.
3. After further erosion, a surface region forms which increases porosity and acts as a semi-permeable barrier, allowing the further transfer of minerals deeper within the tooth. It should be noted that at this point the demineralization process being dynamic and is in fact reversible due to the presence and absorption of remineralisation of calcium and phosphates present in saliva which is also in contact with the tooth surface.
4. If further acid production occurs, the intact enamel surface degrades and disintegrates (cavitation) allowing rampant decay of the region. The only option available to the dentist is removal of the diseased portion of the tooth and the addition of a protective amalgam to prevent further decay.

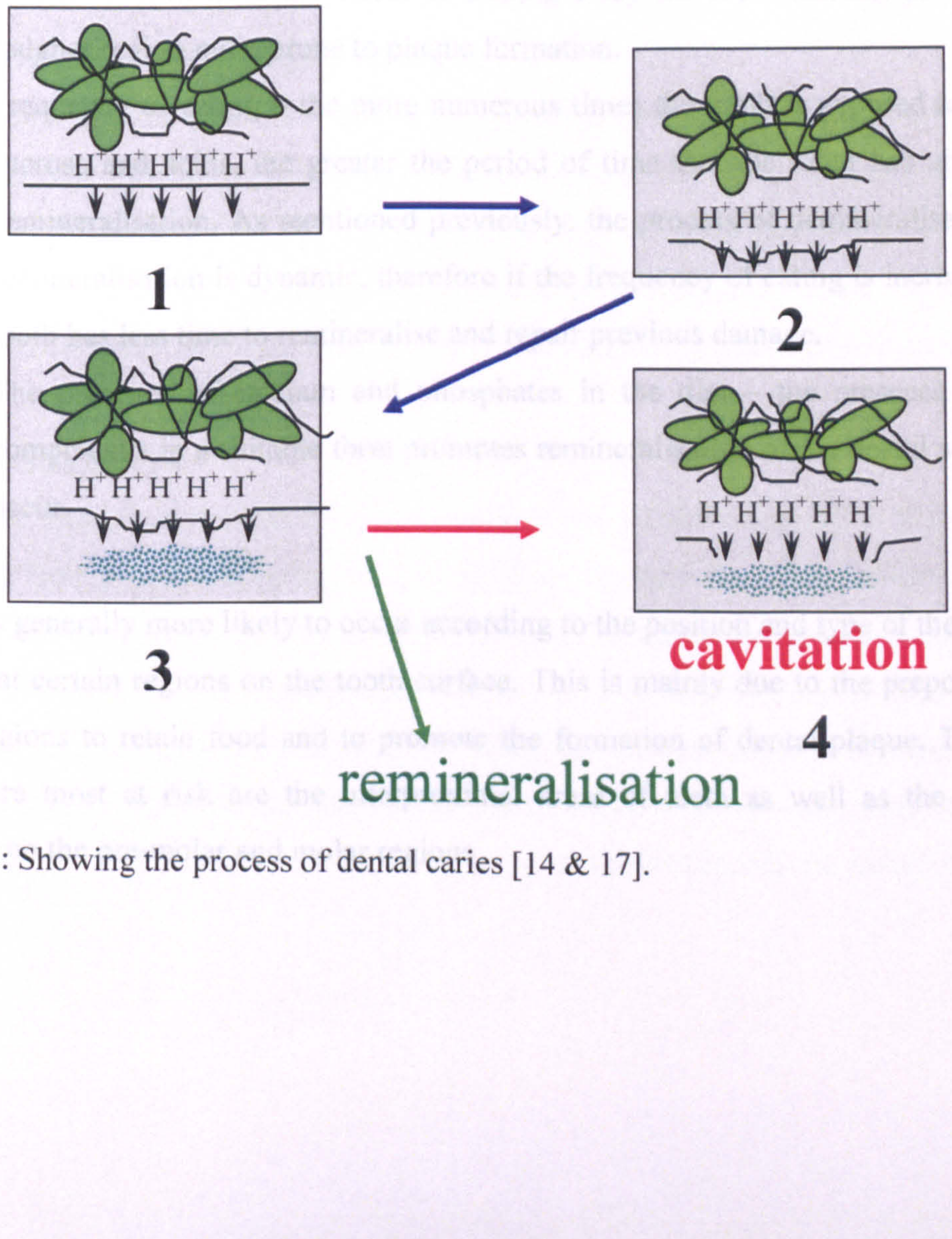

Figure 4: Showing the process of dental caries [14 & 17].

3.2 Factors affecting dental disease

From the present understanding of the disease, there are a number of major factors [18 & 19] which affect the existence of, and rate of development of dental caries. These include diet (which includes the quantity and type of nutrition), the type and position of the tooth, oral hygiene, and exposure to fluoride as well as saliva production.

Diet is extremely important in the development of caries. In particular there are a number of factors that participate in this:

1. The presence of sugar in diet – caries relies on sucrose and in particular its sub-components glucose and fructose for bacterial metabolism and subsequent conversion to acid. Acid formation results in the breakdown of the enamel and dentine structure.
2. Acids in diet – acids such as carbonic acid and phosphoric acid (present in soft drinks) as well as citric acid and ascorbic acid (otherwise known as vitamin C) present in fruit have the effect of etching away the tooth surface, producing a rougher region more prone to plaque formation.
3. Frequency of eating – the more numerous times the tooth is exposed to dietary sucrose and acids, the greater the period of time that the tooth has undergone demineralisation. As mentioned previously, the process of demineralisation and remineralisation is dynamic, therefore if the frequency of eating is increased, the tooth has less time to remineralise and repair previous damage.
4. The presence of calcium and phosphates in the diet – the presence of such components in a suitable form promotes remineralisation of the dental surface to occur.

Caries is generally more likely to occur according to the position and type of the tooth as well as at certain regions on the tooth surface. This is mainly due to the preposition of some regions to retain food and to promote the formation of dental plaque. The areas which are most at risk are the interproximal areas of teeth as well as the occlusal surfaces on the pre-molar and molar regions.

Oral hygiene is also extremely important in preventing the formation of dental caries. The use of a tooth brush and dental floss to remove food and dental plaque from the tooth surface and gum line helps to prevent bacterial attack. Present dental products also contain fluoride components which are extremely important. In the process of demineralisation and remineralisation in an environment rich in fluoride, fluoride replaces the carbonate component of the apatite crystal. The result is a stronger and much less soluble apatite crystal less prone to bacterial attack. The presence of fluoride also has an added advantage in that it inhibits acid formation by bacteria.

Saliva within the oral cavity acts as a natural buffer to acid either present in food or as a by-product of sugar metabolism by bacteria. It raises the pH in the mouth, and acts as a transportation system for the components required in the remineralisation of apatite crystals. High saliva flow rate has been shown to resist demineralisation and the onset of dental caries.

4. Techniques for dental disease detection

The demineralisation process involved in bacterial attack causes a breakdown of the regular enamel structure resulting in a change in the optical and scattering properties. Due to the differing optical and scattering properties of sound and carious sections of tooth (which is the case for healthy and diseased tissues in general), the use of optical techniques has been used with some success in characterising lesion growth and activity.

4.1 Visual inspection

At present there are a number of optical methods at a dentist's disposal to detect caries, each with their own particular advantages and disadvantages. The most common of these is known as visual detection. As an aid to visual detection, an air syringe is used to dry the tooth surface for subsequent examination. Due to a change in refractive index between sound and carious sections of the tooth, early caries can then be seen as a dull white spot on the tooth surface. Drying the tooth surface removes water from the porous carious lesion, thus changing the refractive index of the intercrystalline spaces from 1.33

(H_20) to 1.0 (sound tooth enamel has a refractive index of 1.62), which increases the boundary reflectivity and scattering properties, thus enhancing the contrast between sound and carious tissue further. Of course, even with this enhanced contrast, it is still quite difficult for a dental practioner to distinguish between healthy and diseased sections of tooth. In fact, it has been shown that the use visual inspection has a low sensitivity in detecting caries [20] (lower than 30%) and other examinations [21 & 22] indicate that the use of a probe to measure discontinuities in the surface actually damages the surface integrity. This highlights the need for other diagnosis techniques for the dentist to correctly identify tooth decay.

4.2 X-ray detection

Another tool at the dentists' disposal is the use of X-rays to detect and quantify disease present within the tooth. Carious sections of tooth attenuate less X-rays than normal dental tissue, so when projected onto an X-ray sensitive photographic film, caries appears more transparent than healthy tissue on a dental silhouette. From this the dentist can make some assessment to the degree of tooth damage. An X-ray image also gives information on the position of the enamel, dentine, pulp, and root canal due to the varying attenuation of X-rays through these structures (see figure 5).

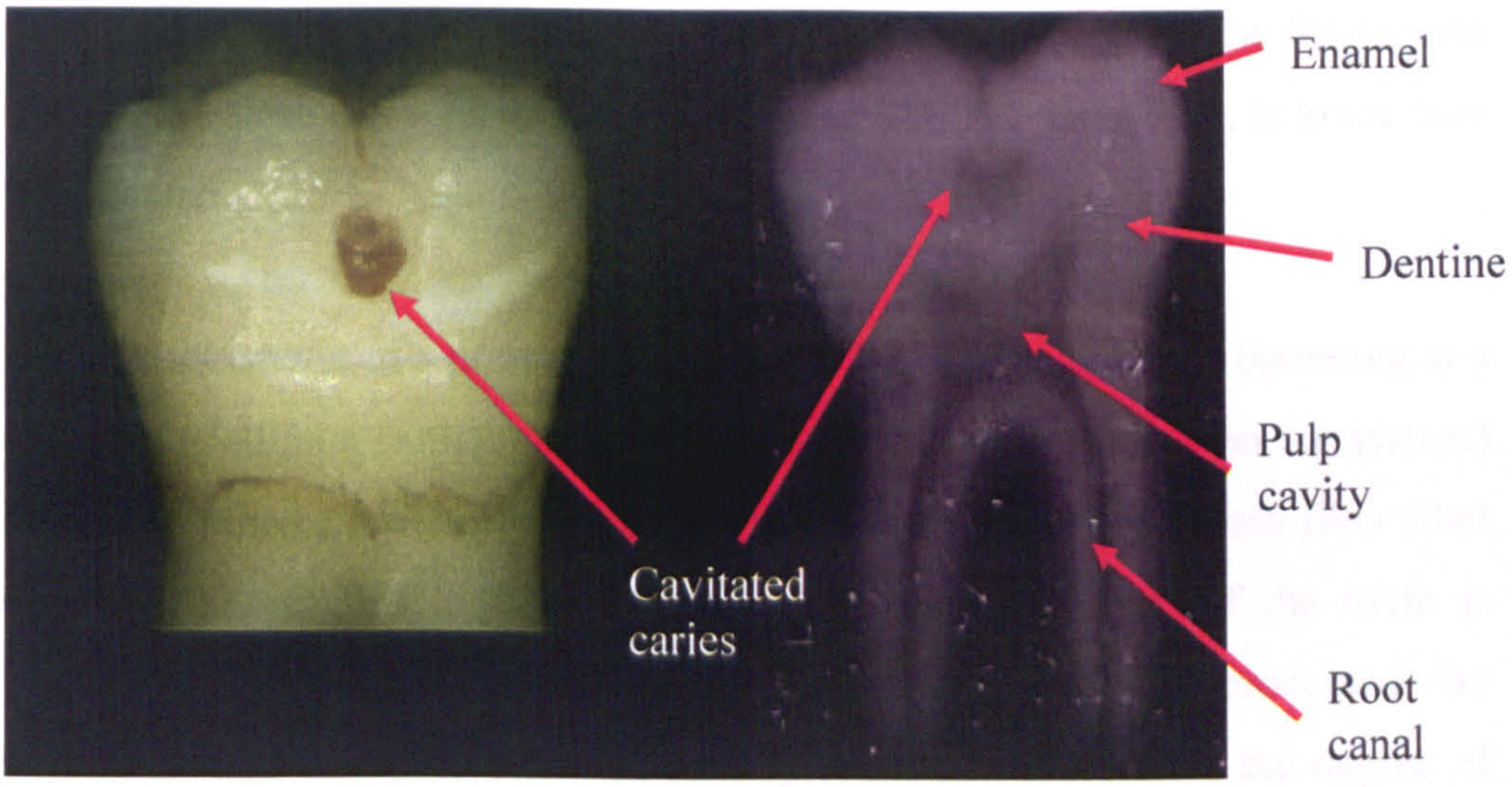

(a) (b)

Figure 5: Comparison of (a) a visual image and (b) an X-ray image of the same cavitated molar tooth.

There are however some problems associated with the use of X-rays. These include difficulties in diagnosing caries at an early stage, due mainly to the sensitivity of the system as well as the superposition of lingual and buccal enamel [23] onto the X-ray image. There are other concerns that with continued X-ray use, its radiative ionising properties (albeit at low levels) potentially could cause possible tissue damage.

4.3 Fluorescent techniques

4.3.1 Quantitative light induced fluorescence

The fluorescent properties of dental tissues have also been examined for possible use in caries detection. Fluorescence can be described as the ability of a material to absorb light at one wavelength, and to remit light at a less energetic wavelength. One method known as quantitative light-induced fluorescence (QLF) [24] is based upon the variation in detected auto-fluorescence between healthy and carious regions on dental tissue. The basis for modern QLF can be found in techniques first proposed in 1982 [25 & 26]. It was shown that in areas of demineralisation, scattering of the light induced fluorescence (when excited at 488nm) is greater than for areas of sound enamel, with the degree of

scattering being related to the amount of demineralisation. This relates to the fluorescent radiance of the caries lesion, which when viewed using the QLF technique, is lower than that of sound enamel.

Figure 6 shows a schematic of a present QLF system. Light from the laser operating at a lower wavelength of 405nm (although this wavelength varies depending on the system) is directed via an optical fibre onto a tooth surface. Using a high band pass filter (that only allows light greater than 540nm to pass), a fluorescent image of the tooth is captured on a CCD camera and stored onto the computer where it can be processed. By determining the change of fluorescence in healthy and carious sections, the degree of demineralisation can be quantified [27 & 28]. Unfortunately such a method provides no information on mineral change with depth from the tooth surface. Furthermore it has been shown (see chapter 4) that QLF is not well suited to occlusal or interproximal caries as the tooth morphology and arrangement make these areas difficult to image.

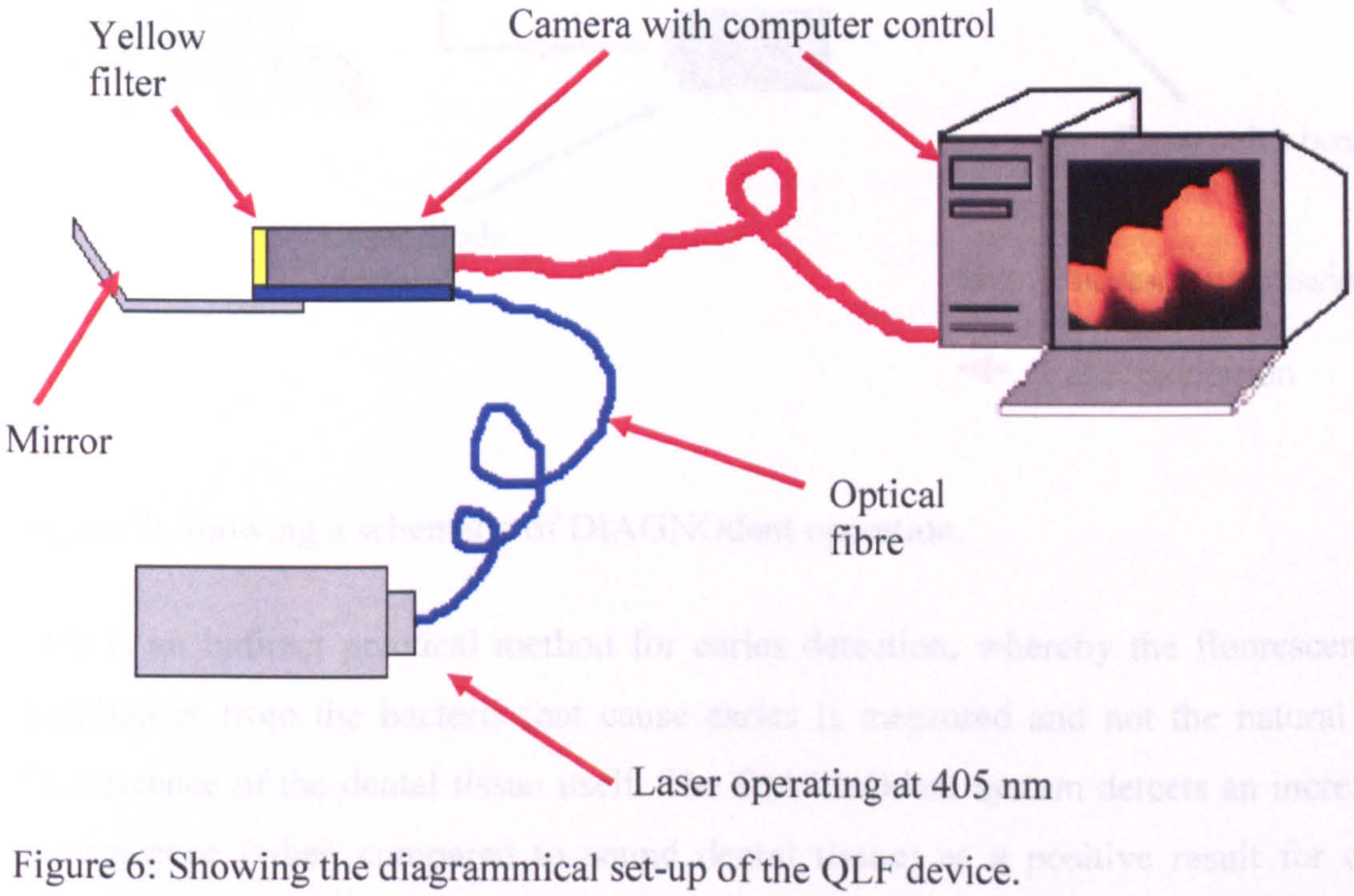

Figure 6: Showing the diagrammical set-up of the QLF device.

4.3.2 DIAGNOdent

Another fluorescent technique DIAGNOdent [KaVo GmbH] [29], first evaluated by Lussi in 1999 [30] is based upon the measurement of infrared fluorescence (when excited at 655nm) of bacterial metabolites from the bacteria that cause caries. From figure 7 which shows DIAGNOdent operation, light is delivered via a fibre from a 1 mW laser diode operating at 655nm, to the handheld probe which then illuminates the tooth surface. Subsequent fluorescent light is collected from a fibre bundle (also present on the probe) through a high band pass filter (> 720nm) where it is directed back to the control box and the light intensity is measured.

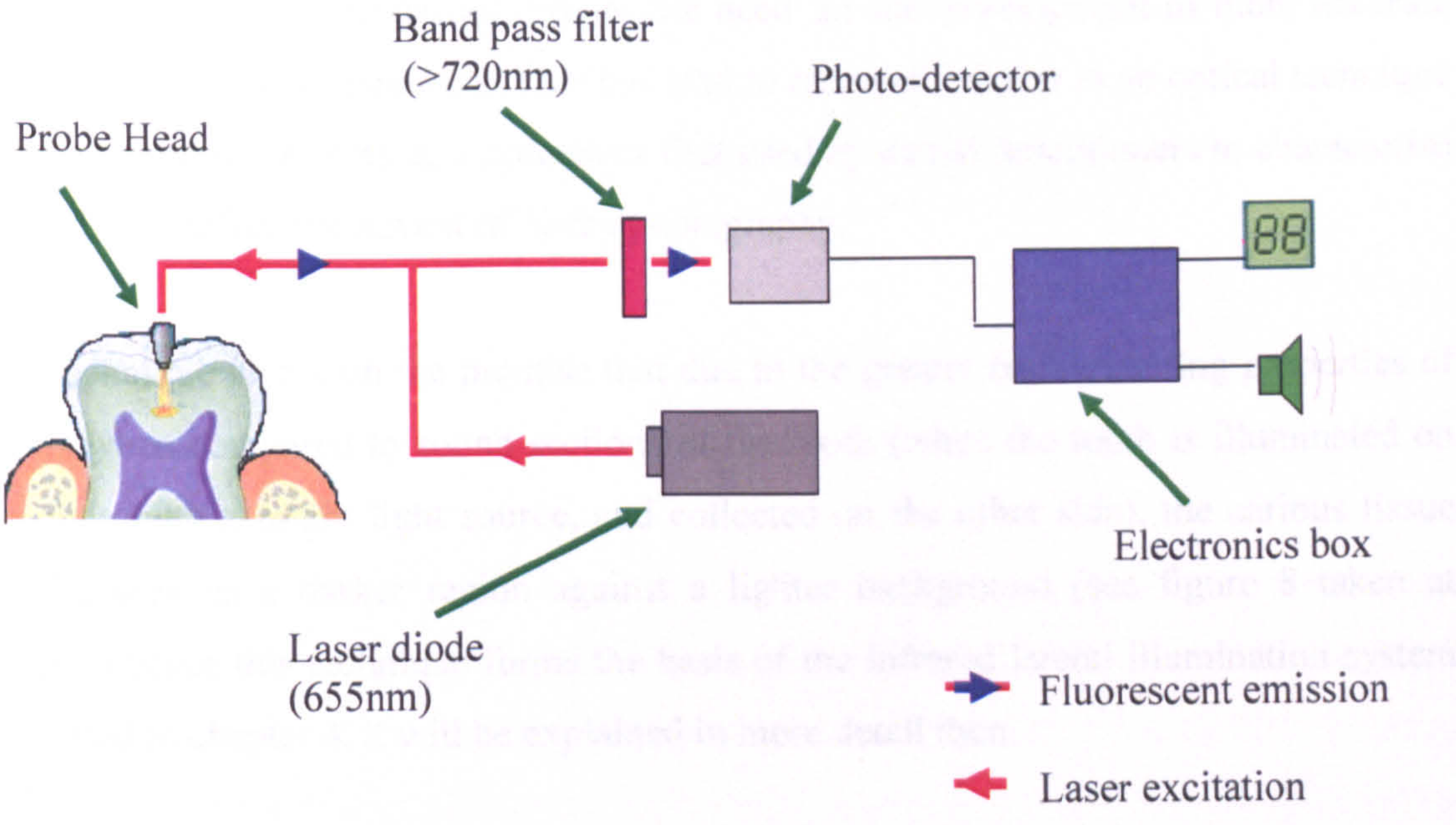

Figure 7: Showing a schematic of DIAGNOdent operation.

This is an indirect practical method for caries detection, whereby the fluorescence of metabolites from the bacteria that cause caries is measured and not the natural auto-fluorescence of the dental tissue itself. The DIAGNOdent system detects an increase in fluorescence (when compared to sound dental tissue) as a positive result for caries. There are however a number of difficulties associated with such a system. This includes its sensitivity to stains, calculus and other deposits, which also naturally fluoresce when

excited at 655nm [31], resulting in false positives (i.e. gives a positive measurement of disease when the tooth is in fact is healthy.)

Unlike QLF, the DIAGNOdent tool only gives an indication that disease is present and does not provide any information on the amount of mineral loss of the tooth. Both these dental fluorescent techniques have been developed for commercial use.

4.4 Transillumination

Although these fluorescent detection systems provide some indication to the presence of dental disease, their limitations require the need for the development of more accurate techniques for dental diagnosis. This has lead to renewed interest in an optical technique known as transillumination, a procedure first used by dental practitioners to characterise tooth decay before the advent of X-ray photography.

The technique works on the premise that due to the greater backscattering properties of caries when compared to sound sections of the tooth (when the tooth is illuminated on one side with a bright light source, and collected on the other side), the carious tissue can be seen as a darker region against a lighter background (see figure 8 taken at 810nm.) Since this technique forms the basis of the infrared lateral illumination system discussed in chapter 4, it will be explained in more detail then.

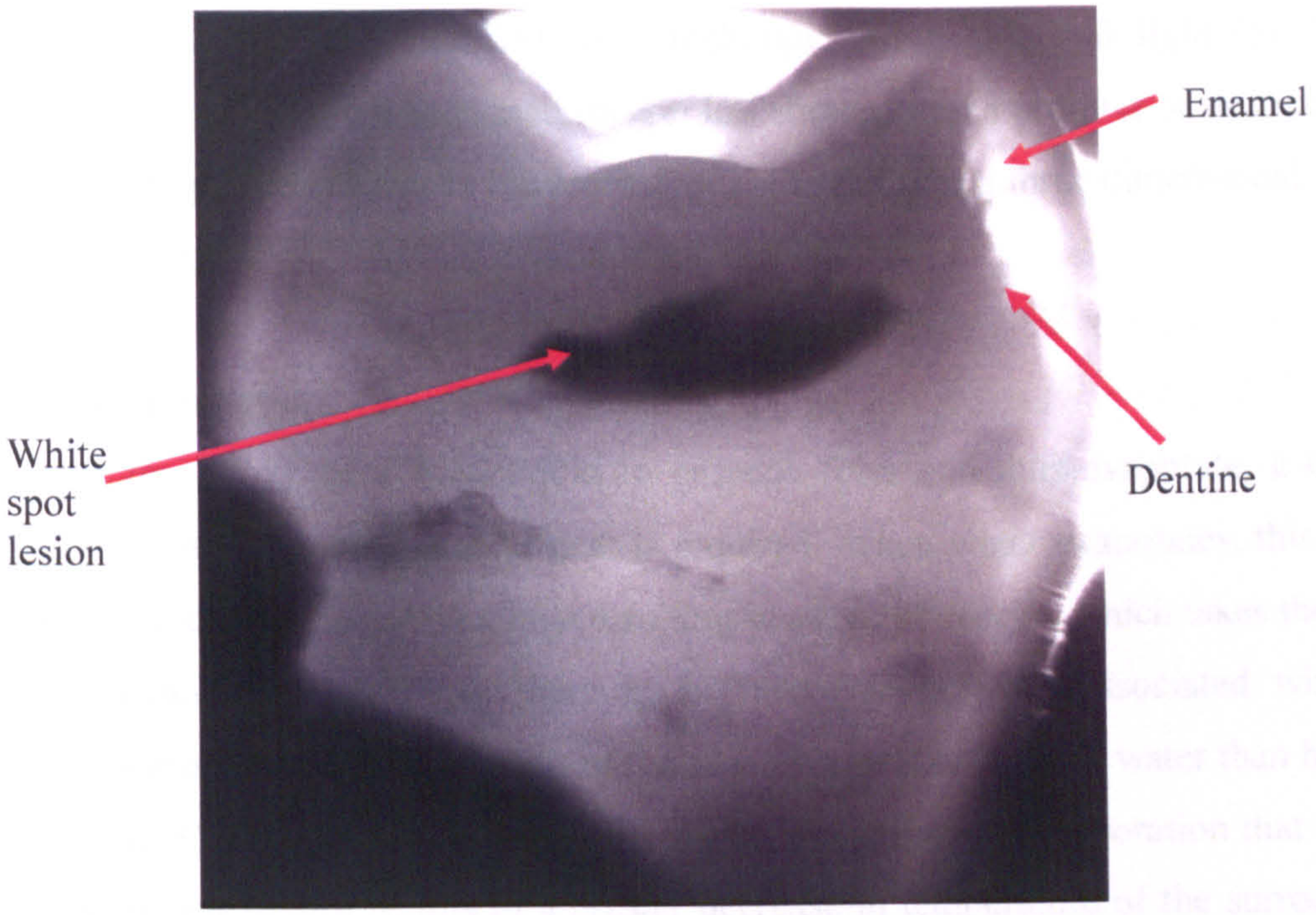

Figure 8: Showing the transillumination of a white spot lesion at 810nm.

4.5 Optical coherence tomography (OCT)

Optical coherence tomography is a method based upon auto-correlation in which interference is measured from a super luminescent diode which has been split using a beam splitter into a reference beam and a probe beam. The probe beam is directed to the sample whereas the reference beam is directed onto a mirror, which has been mounted on a piezo translational stage. The return light from the sample that has been backscattered is re-combined with the reference beam where it is then detected by the photodiode. An interferometric signal is detected when the distance of the sample path length and the reference path length is matched with the intensity of interference due to the degree of scattering. The axial resolution of the OCT is determined by the coherence length of the illumination source used and by varying the distance of the reference mirror (using the piezo-translational stage), a depth scan (also known as an A-scan) can be taken. By combining laterally successive A-scans, a cross-sectional tomograph (B-scan) can be constructed.

At present, the use of a modified OCT technique using polarised light (to further improve the contrast of the sectioned image) has showed much promise in dentistry [32 & 33], though problems exist in the amount of time taken for a three dimensional image to be produced.

4.6 Thermal imaging

For water to change state from liquid to gaseous form and thus evaporate, a certain quantity of energy known as latent heat is required. When water evaporates, this latent heat is removed from its surroundings resulting in a loss of energy, which takes the form of a temperature decrease. As there is an increased porosity associated with the demineralisation process, demineralised tissue is able to absorb more water than healthy dental tissue. Due to the presence of more water, the amount of evaporation that occurs is greater, which in turn results in a greater decrease in temperature of the surrounding dental tissue. This is the basis behind thermal imaging in dentistry [34] where using an infrared camera to measure surface temperature changes, caries can be seen as a colder area on a warmer background. This system sounds promising at first glance and has been shown to work quite effectively in-vitro, but major problems exist in trying to measure these small variations in temperature in-vivo within the oral cavity.

4.7 Electro-conductance and resistance measurements

It has been shown for resistance [35 & 36], and for conductance [37 & 38], that as the tooth undergoes the process of demineralisation, and the onset of caries, its electrical conductivity (conductivity = 1/ resistivity) increases. This is due to the carious process itself which as a result of sugar metabolism, subsequent acid production and its interaction with apatite crystals, resulting in increased porosity of the tooth structure. As saliva fills these pores, the number of conductive pathways are increased which increase the conductivity of the sample. The system shows some promise in laboratory conditions with high sensitivity and specificity values for the detection of caries and its size, but problems exist trying to take readings in vivo in a predominantly wet environment such as the oral cavity.

4.8 Ultrasound

The use of sound at ultra-high frequencies (>20kHz inaudible to the human ear), known as ultrasound, and its interaction with biological tissues is already being used to great effect in medicine to provide information on tissue shape and structure and foetal monitoring. Sound is a longitudinal wave that relies on a medium to allow it to travel. Its capability to travel through different media relies on the mechanical properties which include density and elasticity. Sound waves have the same properties associated with all waves which include reflection, refraction, absorption as well as scattering effects with different wavelengths interacting differently with the same medium. As a result of the demineralisation process associated with caries, the density and elastic properties of the tooth change, which in turn alter its interaction with sound waves.

Using a coupling agent connected to both the tooth surface and the probe to minimise boundary reflections, ultrasound originating from a piezo-electric crystal enters the tooth sample. As the ultrasonic wave reaches the boundary between two media, some of the energy is reflected back to the probe that also acts as a detector. From this information about lesion depth could be measured through the time taken for the reflection to reach the probe. Ultrasound can also give information on the degree of demineralisation that has occurred as the reflection intensity is related to the acoustic impedance, Z, of each medium which itself depends on the elasticity, density and the speed of sound within the medium.

Some studies have shown [39 – 41] that ultrasound may be effective in detecting carious regions on proximal surfaces (using water as a coupling agent) as well as the enamel/dentine junction and dentine/pulp interface (using a metal rod as a coupler) [42] but these findings are restricted to the type of coupling agents used. Extra investigation is necessary to provide a more useful instrument in dentistry.

5. Fibre optical confocal microscopy (FOCOM) as an aid in dentistry and the development of a computer simulated optical model

One more recent non-invasive method which may provide early disease detection and diagnosis is the use of confocal microscopy (explained previously in chapter 2) [43] which provides a technique for taking optical sections through translucent samples.

5.1 FOCOM operation

It has been shown previously that by using a single mode fibre, a depth profile of the tooth from the surface could be measured [2 & 3]. In this system (see fig. 9) a single mode fibre was used to direct light to the target area, which in this case was the caries lesion. Light returned to the fibre, due to reflection or back-scattering, was subsequently collected by the fibre and directed to the detector.

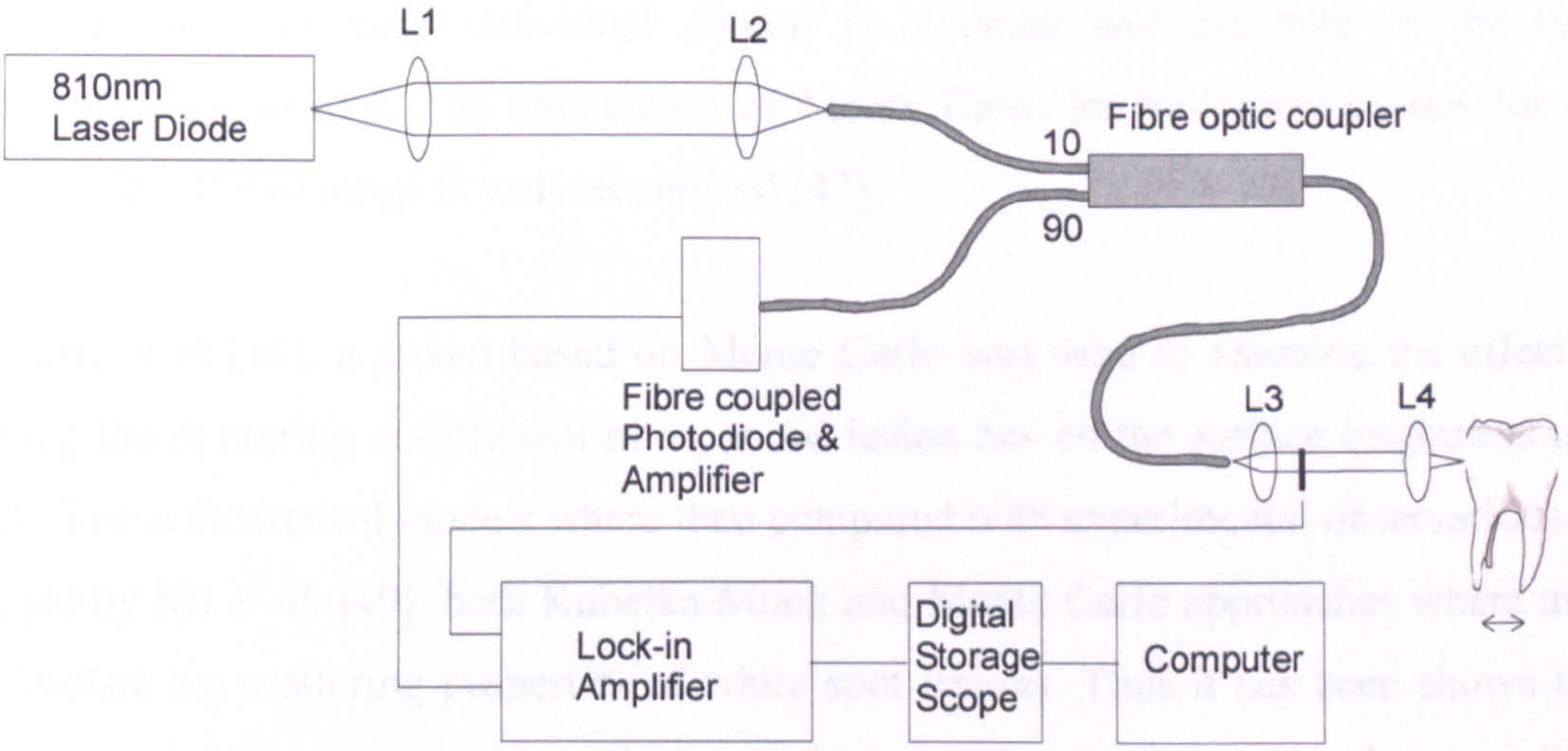

Figure 9: Showing the Fibre optical confocal set-up.

This therefore means the fibre acts as both a light delivery system and a very specific collection system. Light only re-enters the fibre if it originates from the focus point of the optics, hence, a confocal imaging system is created with the single mode fibre acting as an aperture in front of the detector. By developing a computer model based on the

fibre optic confocal configuration, previous experimental results could be used to provide information on the structure and properties of dental enamel, and thus its health. At present, the production of a definitive computer model of a tooth has been met with limited success. This has mainly been due to the complexity of tooth structure as well as the variation in the optical properties of teeth from sample to sample due to their biological nature. There are, however, are a number of methods available that allow theoretical modeling of light propagation within biological samples.

Two examples of such models are based on the (i) Kubelka-Munk (deterministic model) [44 & 45], and (ii) the Monte Carlo (stochastic model) [46] simulations. In the Kubelka-Munk approach, two-flux theory is used in which the radiation is assumed to be composed of two oppositely directed radiation fluxes through a continuous medium. Monte Carlo methods allow the simulation of radiative transfer through a medium where the propagation of each individual photon is modeled and the path of the light determined statistically. The application of Monte Carlo for biological tissues for the visible and infrared range is well recognized [47].

In Wang et al [48], a model based on Monte Carlo was used to examine the effect of varying the scattering co-efficient of a carious lesion has on the surface brightness of a tooth. These theoretical models where then compared with experimental observations. In a paper by Ko *et al.* [49], both Kubelka-Munk and Monte Carlo approaches where used to simulate the scattering properties of white spot lesions. Thus it has been shown that computer modeling techniques could be used to examine the interaction between light and dental structure with each model having its own set of advantages and drawbacks. Monte-Carlo requires the use of more estimated parameters for lesion modeling, increasing the inaccuracy of the result; whereas Kubelka-Munk is more simplified and generalized view of the structure of tooth. Other reviews of two-flux methods and their limitations can be found in Cheong *et al.* [50], Patterson *et al.* (1991) [51] and van Gemert and Star [52].

Another major factor for the inability to match theoretical models to experimental results is due in part to the inaccuracies in the determining the refractive indices, absorption co-efficients, scattering co-efficients and anisotropy of sound and carious dental tissue for any given wavelength. At present the only methods available to experimentally measure these co-efficients require physical dissection of enamel sections from the tooth [12]. These values will differ due to the orientation of the dissection cut due to the prism like structure and birefringent properties of enamel.

5.2 Computer Modeling

In this investigation, an optical model was constructed using commercial available software (OptiCAD) [53] to simulate the use of a single mode fibre optical confocal microscope in obtaining an optical section through tooth structure [2 & 3]. OptiCAD is a non-sequential ray tracing optical analysis program, with the capability to perform ray-tracing taking into account reflection, refraction, and scattering properties. As well as control of the dimensions, position, surface reflectivity and refractive index, n, of materials, the package allows the user to control its scattering properties (degree of scattering by the scattering co-efficient 's', and the probability of scattering at any angle by the anisotropy value 'g'). It should be noted that OptiCAD is not based on rigorous diffraction theory therefore does not take into account diffraction effects.

The exact ray path within a scattering material is determined using a Monte Carlo simulation. This is governed by the equation:

$$p(s) = \mu_s e^{-\mu_s x} \tag{1}$$

where μ_s = the scattering co-efficient and x = the random distance between scatterers. The scattering distribution function which defines the probability of a change in direction with respect to the z-axis is:

$$p(\theta) = \frac{1 - g^2}{4\pi(1 + g^2 - (2g\cos\theta))^{3/2}} \tag{2}$$

where g = anisotropy and θ = the angle with respect to the z-axis [54].

The *OptiCAD* model is illustrated in figure 10. The pinhole aperture of the confocal system was set to 1μm, giving an axial resolution of 5μm. The objective used in this simulation imitated an infinity corrected lens. By altering the position of the sample, or objective along the optical axis, reflected or backscattered light was recorded on the simulated detector (film in the software terminology) from successive focal planes.

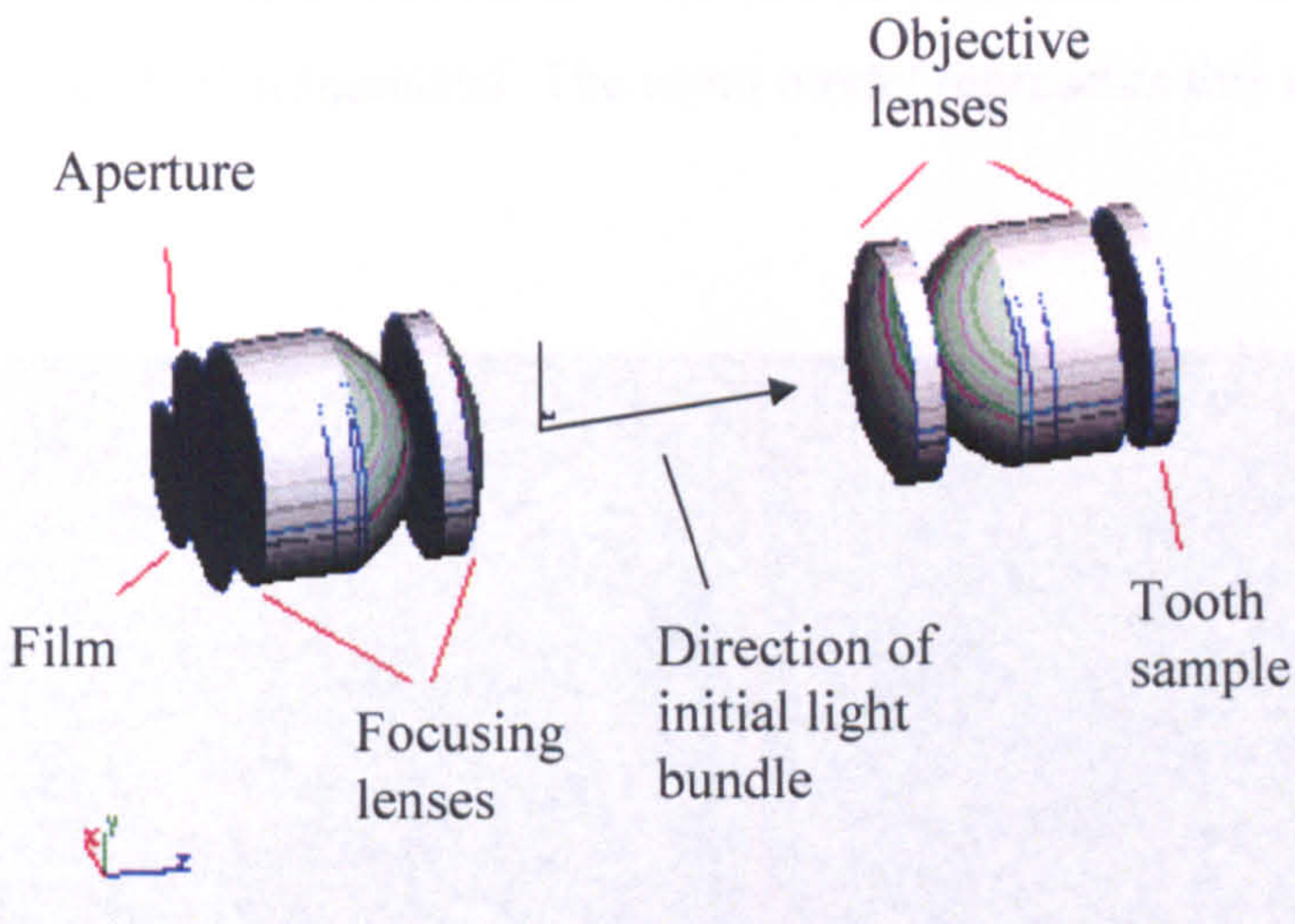

Figure 10: Showing the computer generated optical model containing the confocal system.

Collimated light rays were initiated between the two sets of lenses, where they were directed along the z-axis towards the objective. The collimated light was composed of a 30 x 30 array of rays in a circular formation of diameter 2mm, which provided a sufficient number of rays for analysis. The light was focused by the objective onto the sample with the objective position determining the focusing depth. The light reflected or backscattered from the sample was re-collimated through the objective and subsequently refocused by the focusing lenses through the pinhole aperture onto the film (detector). The pinhole aperture thus rejecting light not originating from the focal point of the objective lens in an identical manner to the optical fibre in the practical system [3]

(experimental resolution ~ 5μm). The number of rays that were recorded on the film was taken as a direct measurement of the reflected light intensity from any given focal plane.

In order to simulate caries within the tooth structure, the tooth sample was composed of a carious layer sandwiched between upper and lower sound enamel regions. This is representative of the carious process at an early stage with the surface tooth remaining intact while demineralization occurs deeper within the tooth enamel. Figure 11 shows a histological section of the dental enamel. As can be seen from the image, three distinct regions can be clearly distinguished. The tooth model represents this arrangement and is shown in figure 12.

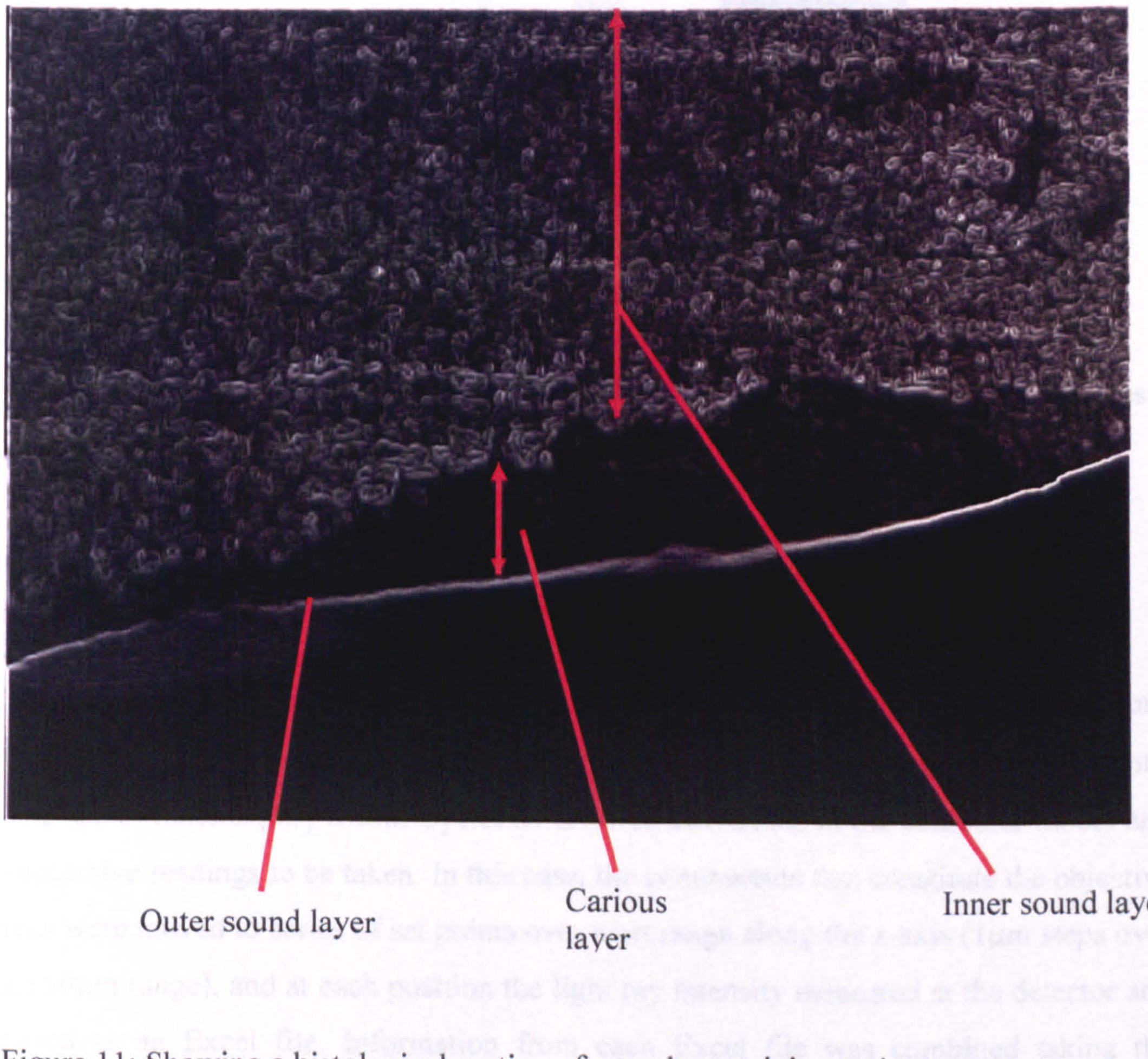

Figure 11: Showing a histological section of a tooth containing caries.

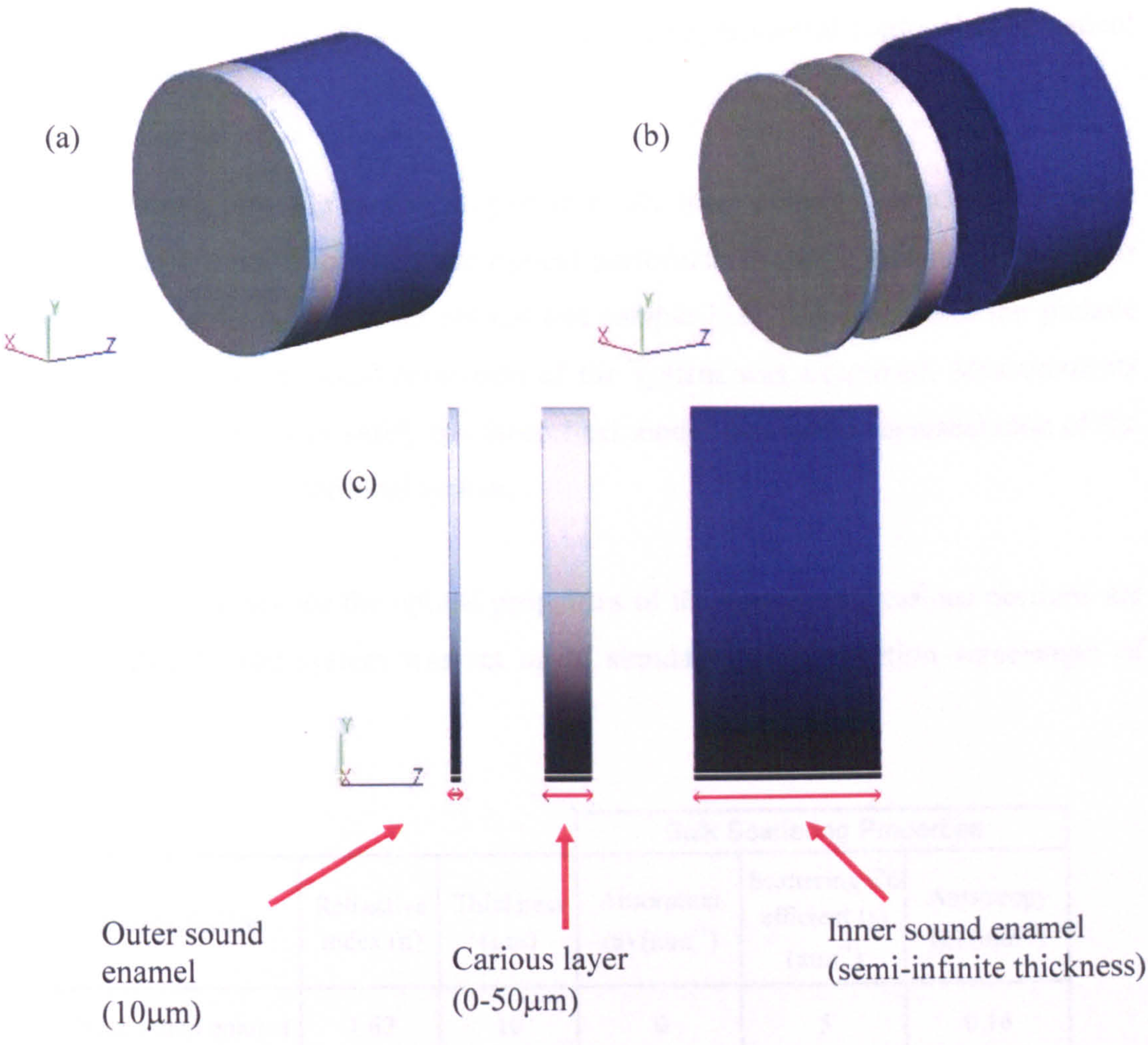

Figure 12: The constituent parts of the optical modeled tooth sample.

The outer sound enamel region was set at a thickness of 10μm. Sound and carious regions differed in refractive indices as well as anisotropies and scattering co-efficients. The use of macros [55] within OptiCAD allowed alterations in the computer model and successive readings to be taken. In this case, the components that constitute the objective lens were moved to series of set points over a set range along the z-axis (1μm steps over a 150μm range), and at each position the light ray intensity measured at the detector and saved as an Excel file. Information from each Excel file was combined taking the

intensity reading for each position to produce 'axial scan' through the sample. This is comparative to axial measurements taken using the experimental confocal fibre optical set-up [3].

Before examining how the optical properties of the tooth affected the axial scan, tests where first carried out to confirm the optical performance, in particular confocality of the system. Using a mirror as an optical test sample [56], the effect that the pinhole aperture size had on the axial resolution of the system was examined. Measurements were also taken in order to verify the theoretical model was a true representation of the experimental fibre optic confocal system.

The preliminary values for the optical properties of the sounds and carious portions are shown in table 1. The system was set up to simulate an illumination wavelength of 810nm.

			Bulk Scattering Properties		
Sample Section	Refractive Index (n)	Thickness (μm)	Absorption (a) (mm^{-1})	Scattering Co-efficient (s) (mm^{-1})	Anisotropy (g) (mm^{-1})
Outer sound enamel	1.62	10	0	5	0.16
Carious layer	1.2	50	0	15	0.46
Inner sound enamel	1.62	5000	0	5	0.16

Table 1: Showing the default optical properties when other sample variables are altered.

To the author's knowledge, the scattering co-efficients and anisotropies of sound and carious enamel are not known for this wavelength and these values are based upon trends from values quoted for other wavelengths [15]. Absorption properties of both sound and carious tooth sections were neglected due to the small distances of sample involved. With the number of source collimated rays set to 30 x 30 (which provides

ample illumination) over a 2mm diameter circular formation, the axial profile was measured.

Setting all other variables to their default values (table 1), the axial profile of the sample was calculated as the scattering co-efficient for the carious section was varied over a range of 0 – 25mm^{-1}. This was repeated, recording the axial profile as the anisotropy g, the refractive index, and the thickness of the carious section were varied. The effect of changing the bulk scattering properties of sound enamel on the profile was also examined and all results were normalized (taking the maximum intensity as 1) and presented graphically.

5.3. Results and Discussion

5.3.1 Confocality and comparison with experimental system

In figure 13, the effect of the pinhole size on the confocality of the system is shown. As one can see from figure 13, by increasing the pinhole size, the optical section of the system increased. The pinhole discriminates between focused and out of focus light. By increasing this size, more out of focus light is measured on the detector. The full-width half-maximum values being in line with the previous practical work i.e. the results for the 1 μm pinhole set-up closely matching that of the single mode optical fibre, figure 14.

It should be noted that the system has a certain "sensitivity" which is related to the number of rays used in the simulation. By increasing the number of rays emerging from the light source, the overall sensitivity of the system to reflective surfaces is enhanced and the effect of "noise" is decreased. The down side is that the simulation time is increased. Noise effects are apparent in the axial scans in figure 13.

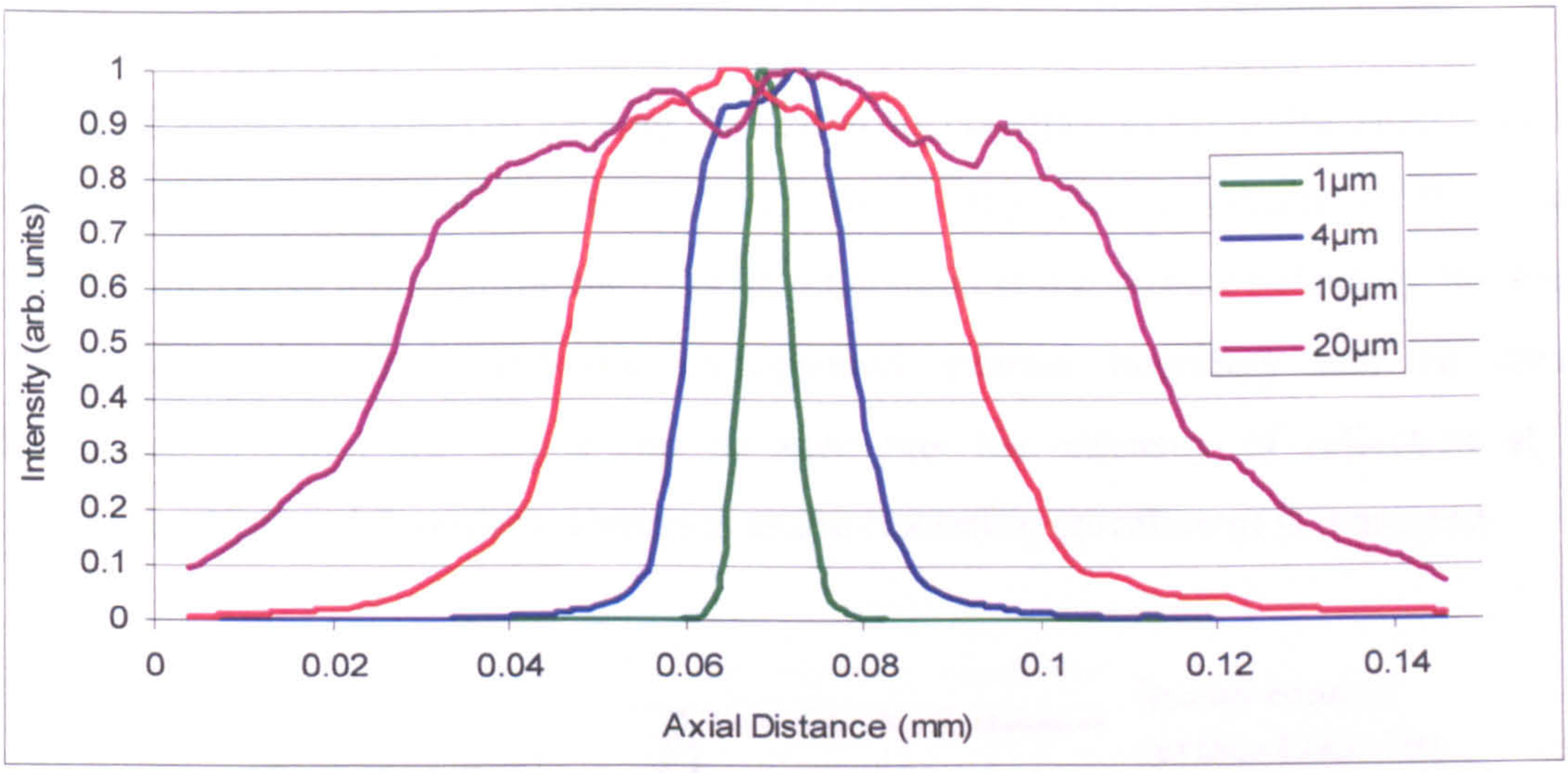

Figure 13: A normalised graph showing how pinhole size affects confocality of the simulated system by taking an axial scan through surface of low reflectivity.

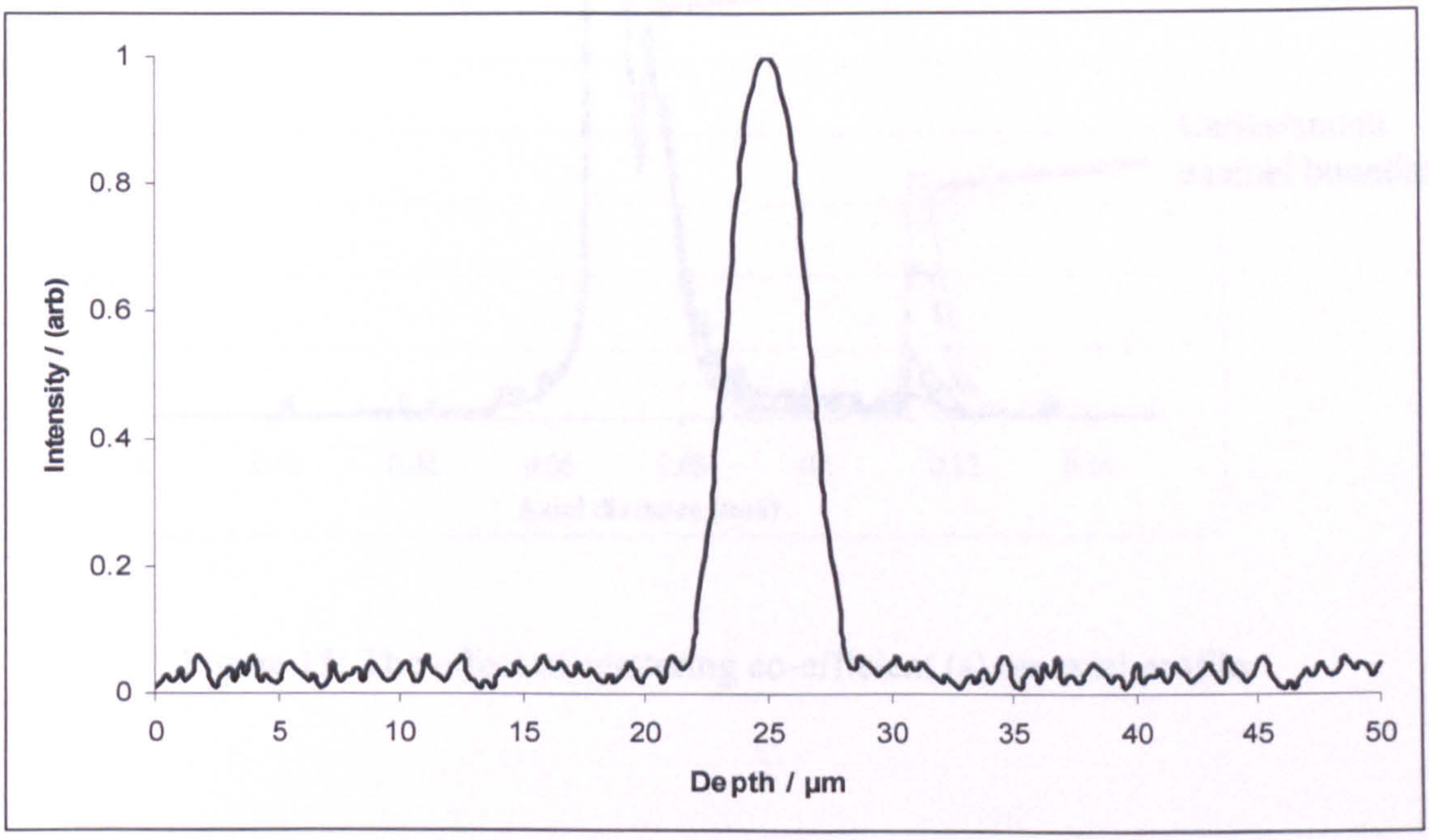

Figure 14: Normalised graph of the axial resolution of the experimental fibre optic system.

5.3.2 Scattering co-efficient

Figure 15 shows the effect of varying the scattering co-efficient (s) of the carious section has on the axial profile of the sample. Due to the high axial resolution of the system (~5μm), the peaks representing the Fresnel reflections at the surface boundary, the sound enamel/caries boundary and the caries/sound enamel boundary can be clearly distinguished. From fig. 15, it can be seen that the intensity of reflection at the caries/sound enamel boundary decreases as the scattering co-efficient is increased.

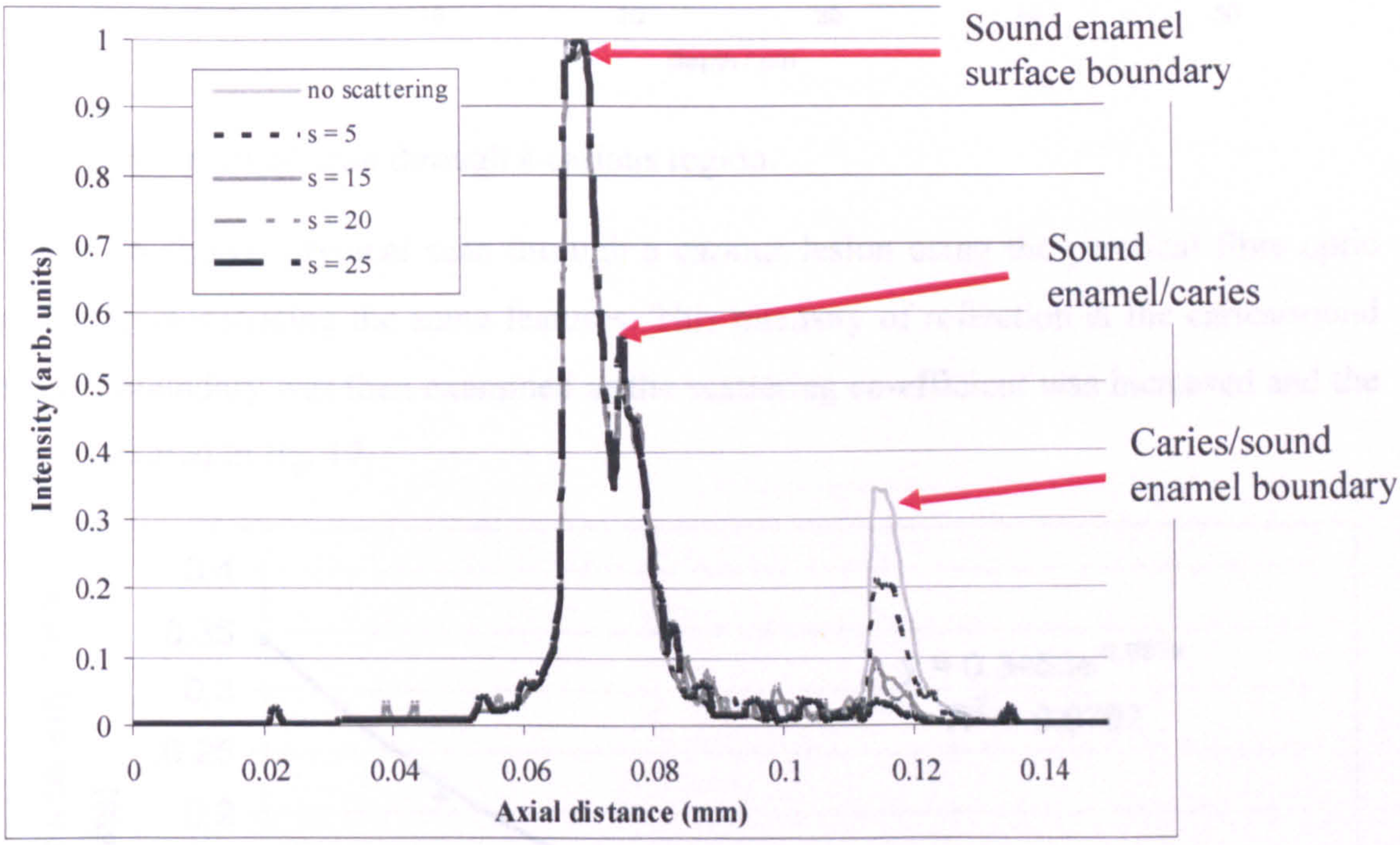

Figure 15: The effect of scattering co-efficient (s) on axial profile.

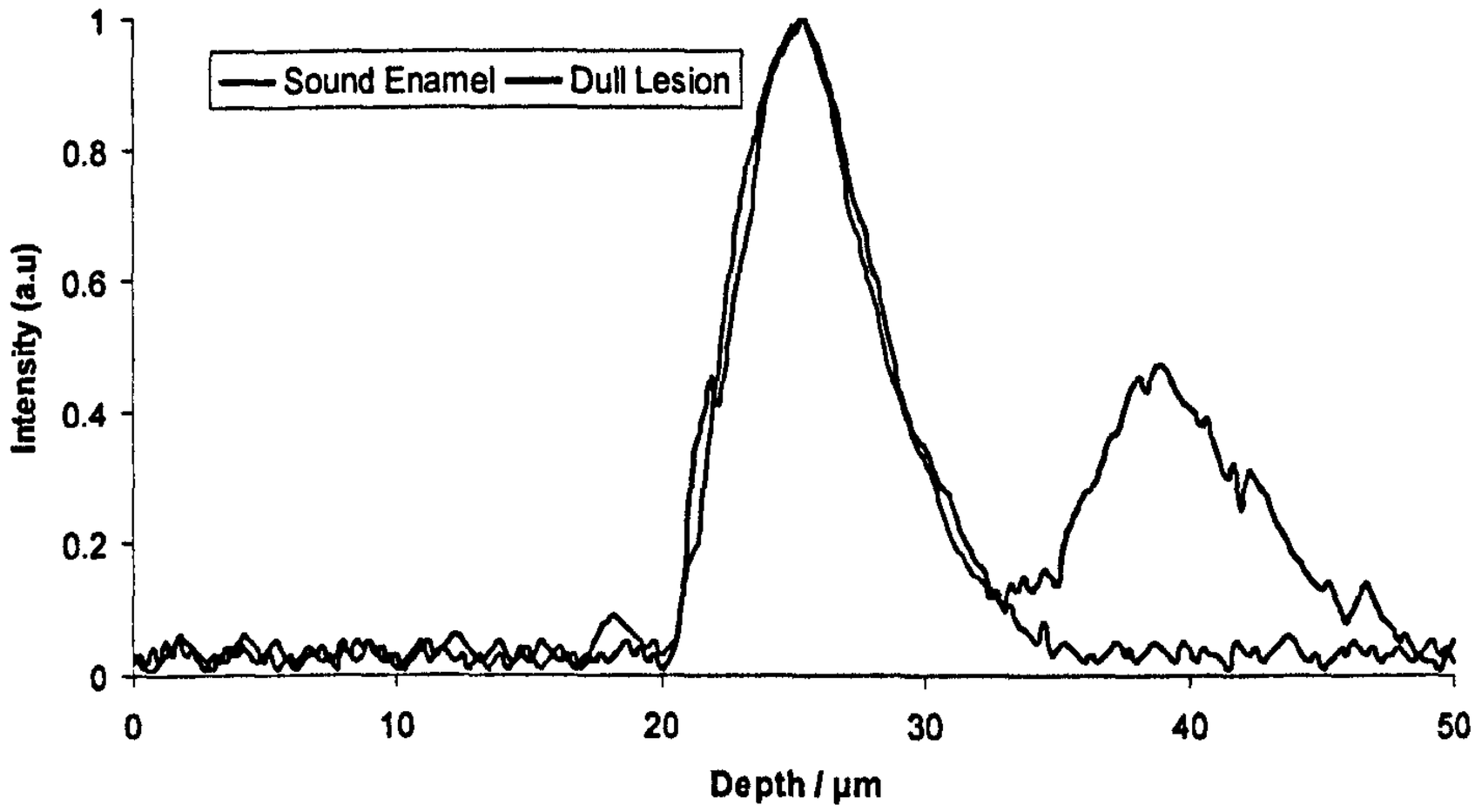

Figure 16: Practical scan through a carious region.

Figure 16 shows a typical scan through a carious lesion using the practical fibre optic system demonstrating the same features. This intensity of reflection at the caries/sound enamel boundary was then examined as the scattering co-efficient was increased and the results plotted in fig. 17.

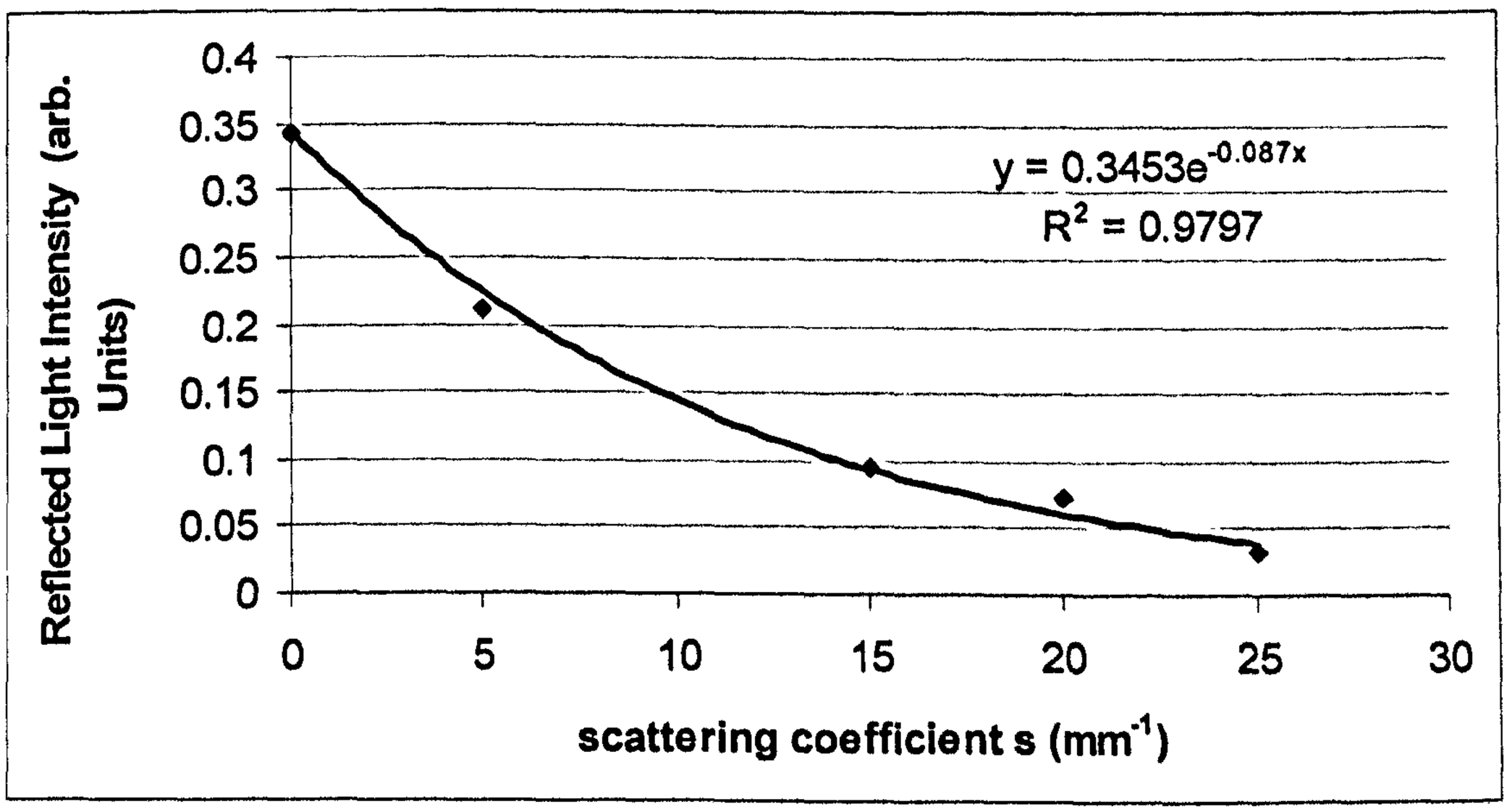

Figure 17: The effect of the scattering co-efficient on the reflected intensity at the caries/sound enamel boundary.

From figure 17, it can be seen that the reflected light intensity at the caries/sound enamel boundary is in fact exponentially dependent on the scattering co-efficient. This is due to the laws governing the computer model simulation itself (see equation 1) in which the probability of scattering events occurring have an exponential dependence on the scattering co-efficient. This can be used to determine the effectiveness and sensitivity of the confocal system at measuring the degree of demineralisation that can be detected for particular depths.

5.3.3 Refractive index

The refractive index of the carious section was varied from 1.3 to 1.0 and its effect on the axial profile of the sample examined. This refractive index range was chosen simply because of the dental disease process itself which results in the loss of mineral. Water or air (which have refractive indices of 1.3 and 1.0 respectively) usually occupies large parts of these demineralised regions. Therefore it is sensible to assume that the refractive index for carious enamel lies somewhere within this region. Note that the upper sound enamel region has a refractive index of 1.62. The results are shown in figure 16. The variation in refractive index of two media at their discrete interface is responsible for Fresnel reflection. At normal incidences, this is governed by the equation:

$$R = \frac{(n_1 - n_2)^2}{(n_1 + n_2)^2} \tag{3}$$

where n_1 = 1.62 and n_2 = 1.0 for a air/healthy enamel boundary.

At normal incidence, for boundaries that contain greatest variations in refractive indices, the reflectivity is greatest. It should be noted that the thickness of the carious layer was kept constant at 50μm.

From figure 18, it can be seen that as the refractive index of the carious layer was increased from 1.0 to 1.3, the apparent depth of the carious layer (taken from the

measurement of the distance between the sound/caries and caries/sound boundaries) decreased.

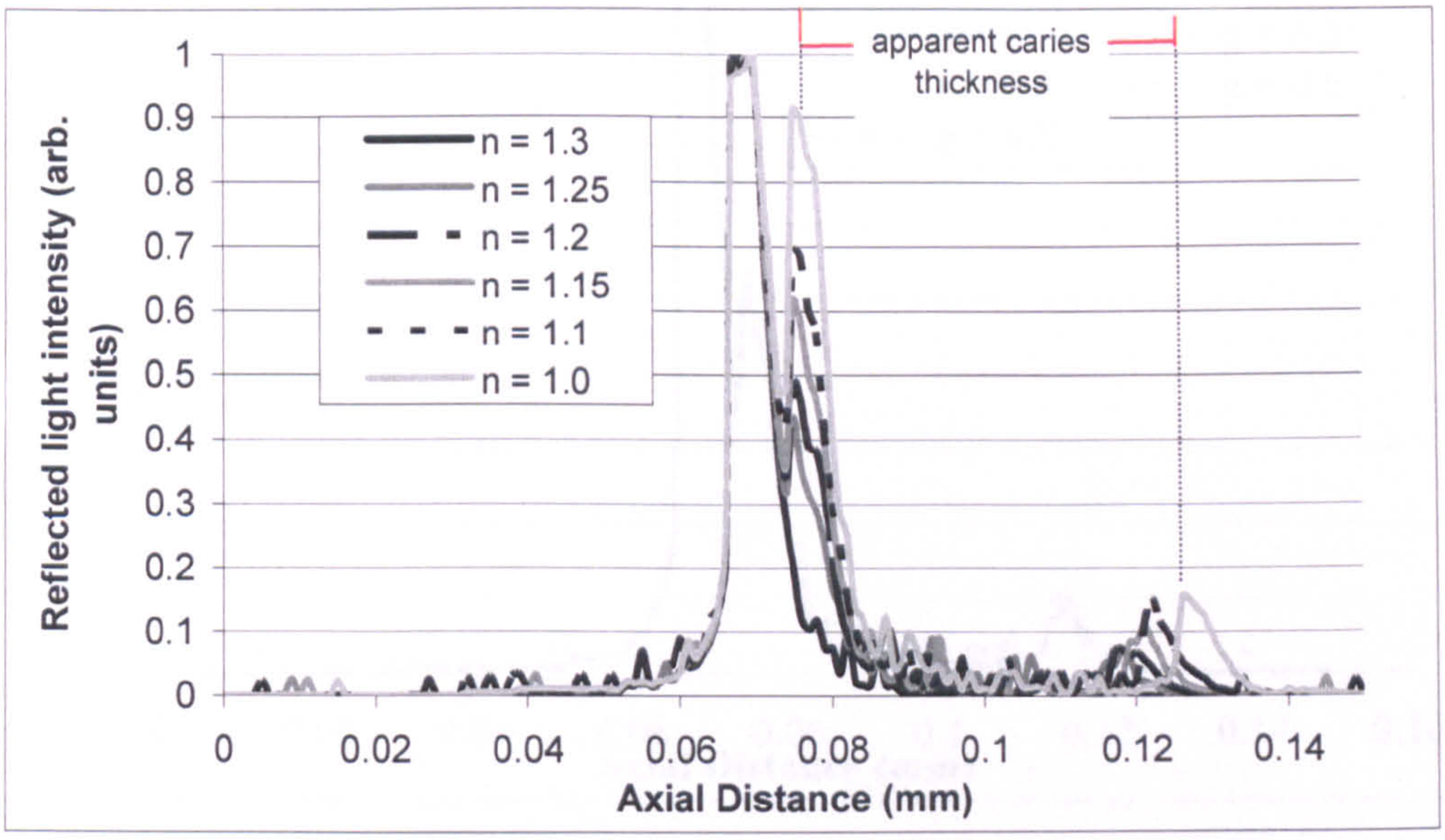

Figure 18: The effect of caries' refractive index on axial scan.

This is due to a focal shift when focusing through media of differing refractive indices, full details can be found in [57]. When moving an objective lens, over a distance Δz, axially through a specimen of refractive index greater than 1, the focus moves a distance $\Delta z'$. This distance $\Delta z'$ increases as the refractive index of the sample increases. Therefore objects would appear thinner than they actually were. This focal shift is also explained in more detail in Chapter 7.

5.3.4 Anisotropy

In figure 19, the effect of varying the anisotropy in the bulk scattering properties of the carious region is examined. From fig. 19 it appears as though anisotropy has little or no effect on the axial scan of the system when the scattering co-efficient remains constant.

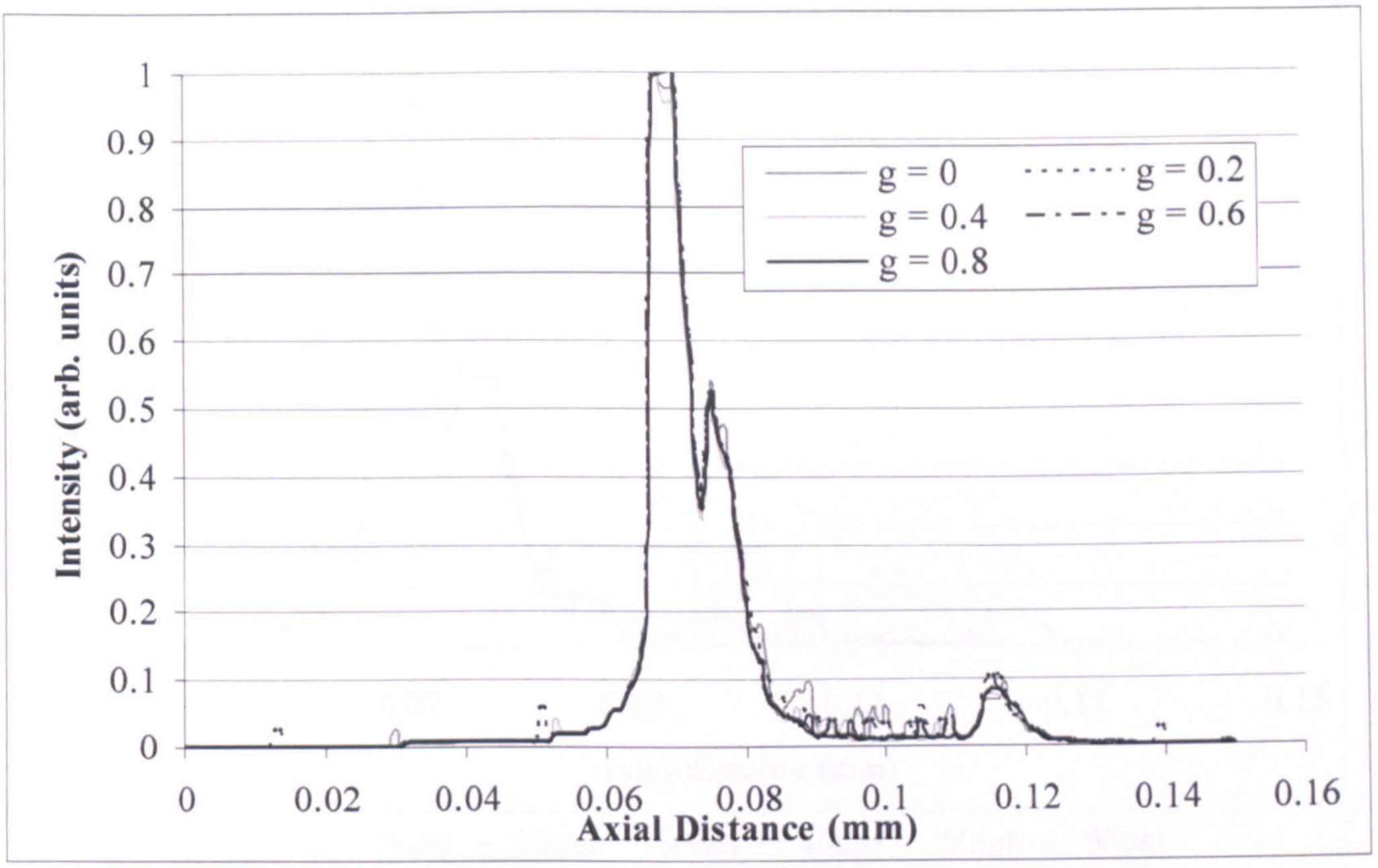

Figure 19: The effect of anisotropy (g) on the axial scan.

This is due to the fact that light is only being collected at close to normal incidence to the optical axis with the N.A. of the collimating lens limiting the collection angle. If the angle of collection was varied significantly from normal incidence, the change in anisotropy would be seen to have an effect.

5.3.5 Caries thickness

The thickness of the caries region was varied from 10 to 60μm and for each caries section thickness, an axial scan was taken. The results are shown in fig. 20. It can be seen that as the caries thickness is increased, the relative intensity of the Fresnel reflection at the caries/sound enamel boundary decreases. This is due to the scattering properties of the caries medium, which have a greater effect as the thickness of the medium is increased. This in turn results in increasing loss of light as one focuses more deeply within the sample.

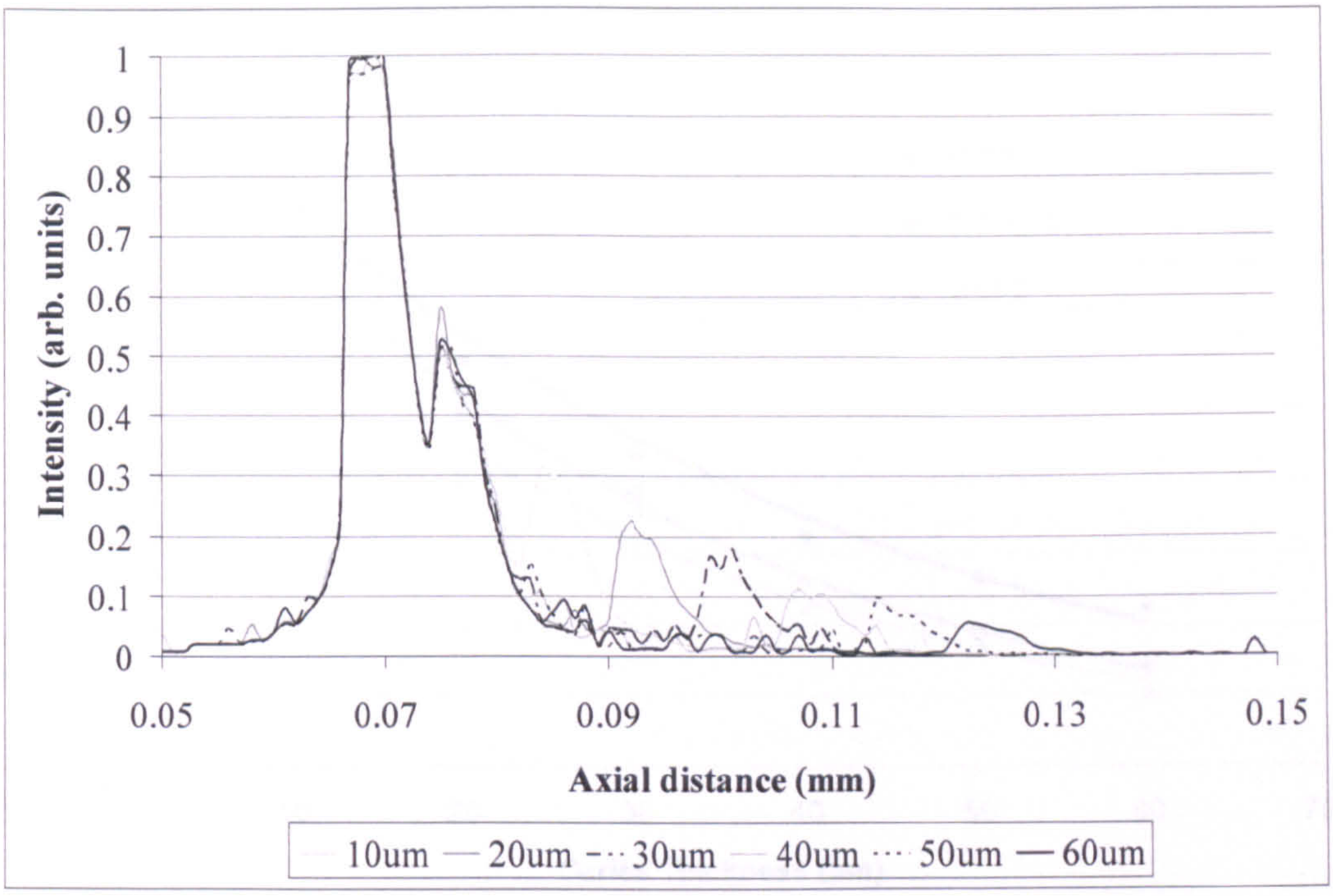

Figure 20: The effect of caries thickness on the axial scan.

The reflected light intensity at the caries/sound boundary was then measured at various lesion depths and it was shown (figure 20) to be exponentially proportional to the lesion thickness. This exponential dependence of boundary reflection on lesion depth was then examined for different values of caries refractive index, and from figure 21 it can be seen that each refractive index follows a different exponential curve.

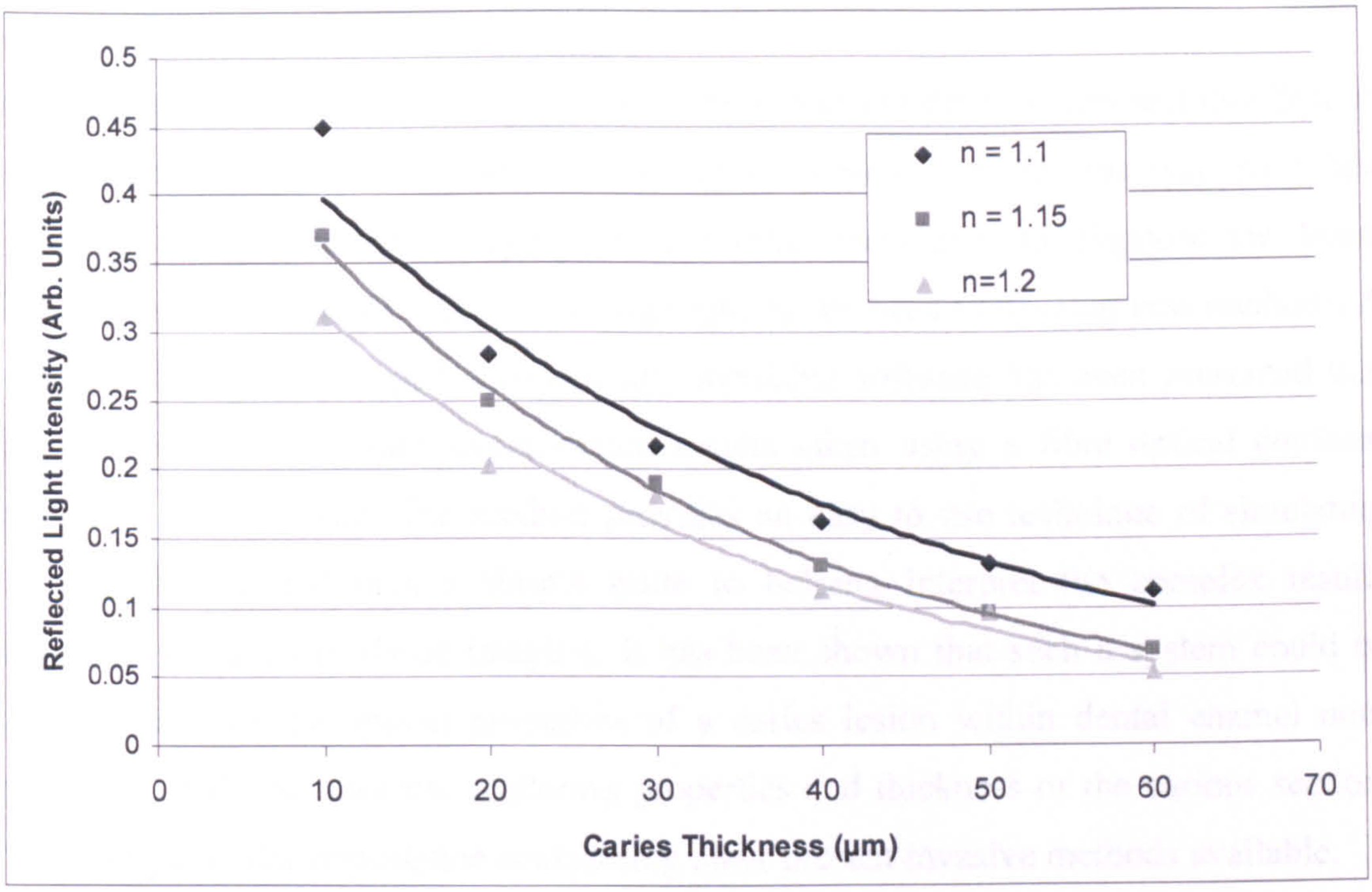

Figure 21: Effect of Refractive index on the intensity reflection at the caries/sound enamel boundary at different depths.

This has far reaching implications in that if caries/sound boundary reflection measurements could be taken of a lesion at different depths, this could be matched to the computer model giving a measurement of the degree of mineral loss. From these comparisons the refractive index of the diseased portion of the tooth could be determined and the degree of demineralization established. Natural lesions are in fact wedge or conically shaped [58], therefore by taking axial scans of a lesion at different lateral positions should be possible (see figure 11). An assumption that the scattering properties within the particular lesion are constant must be made to produce an accurate determination.

6. Summary

In this chapter the structure of dental tissue, the process of dental caries and its effect on dental tissue has been examined. A number of present methods (as well as a few currently in development) using optical and other techniques to diagnose for dental decay have been considered as well as highlighting the need to develop new methods. A computer model based upon commercially available software has been presented that can theoretically reproduce experimental results taken using a fibre optical confocal system on dental tissue. The method provides an easy to use technique of simulating tissue scattering and thus a simple route to helping interpret the complex results frequently obtained in tissue imaging. It has been shown that such a system could be used to measure the optical properties of a caries lesion within dental enamel non-invasively. This includes the scattering properties and thickness of the carious section. This is of particular importance considering other present invasive methods available.

It was found that the reflected light intensity at the caries/sound enamel boundary was shown to exponentially decay as the scattering co-efficient and the lesion thickness were increased in line with both practical and complex theoretical calculations. This sets upper limits for both the depth of axial scan and the sample scattering co-efficient to which such a system can distinguish a boundary reflection signal from background noise.

The program does, however, have some limitations. The carious lesion is defined as being homogenous with definite boundaries, which may not be the case in a biological sample. Our present simulation also does not take into account any surface roughness and surface scattering effects which may influence the axial scan of the sample. In future this can be added to the computer model to further increase its accuracy.

Although this computer simulation focuses on the onset of disease in dental tissue, it should be noted that alterations in the optical and scattering properties of tissue are representative of disease in general. This model can be easily modified for the

examination of optical and scattering properties in other biological situations and is thereby not restricted to dentistry. The method has been demonstrated in a confocal imaging system but the OptiCAD software allows the images to be made and hence optical transmission can also be modeled.

References

1. Featherstone, J. D. B. (1987). The mechanism of dental decay. *Nutrition today*, May/June, 10-16.
2. Rousseau, C., Girkin, J. M., Hall, A. F., Strang, R., Vaidya, S. (2002). Application of a novel confocal imaging technique for the early detection of dental decay. *Proceedings of SPIE*, 3064, 212-218.
3. Rousseau, C., Poland, S., Girkin, J. M., Hall, A. F., Whitters, J. (2006). Development of fibre-optic confocal microscopy for detection and diagnosis of dental caries. Accepted by *Car. Res.*
4. DeYoung, E. (2004). Dental amalgam and mercury. *Dep. of Chemistry, University of Georgia.* Posted 2004. Retrieved 23rd of November 2005, from http://www.arches.uga.edu/~edeyo/Alternatives.htm.
5. Iyyer, B. S. Arrangement of teeth. *32 teeth online*. Retrieved 23rd of November 2005, from http://32teethonline.com/intropage3.htm.
6. Page, R. C. (1986). Gingivitis. *J. of Clin. Periodontol*, 13 (5), 345-359
7. Listgarten, M. A. (1986). Pathogenesis of periodontitis. *J. of Clin. Periodontol*, 13(5), 418-430.
8. Fox, P. C., Van der Ven, P. F., Sonies, B. C., Weiffenbach, J. M., Baum, B. J. (1985). Xerostomia: evaluation of a symptom with increasing significance. *J. of Am. Dent. Assoc.*, 110(4), 519-525.
9. Jacobs, J. Tooth Abcess. Medline Plus, U.S. National Library of Medicine. Retrieved 25th of November, 2005, from http://www.nlm.nih.gov/medlineplus/ency/article/001060.htm.
10. Jenkins, G. N. (1978). The physiology and biochemistry of the mouth. Blackwell Scientific, Oxford (pp. 54-112).
11. Ten Bosch, J. J., Spitzer, D. (1974). The absorption and scattering of light in bovine and human dental enamel. *Calcificated Tissue Research*, 17, 129-137.
12. Zijp, J. R., Ten Bosch, J. J., Groenhuis, R. A. J. (1995). HeNe-laser light scattering by human dental enamel. *J. of Dent. Research*, 74, 1981-1898.

13. Griebstein, W. J., (1965) *Discussion of fourth session. In Tooth enamel.* John Wright and Sons ltd. Bristol, pp. 191.
14. Rousseau, C. (2003) *Development and Application of Novel Optical Techniques for the Early Detection of Dental Decay.* PhD. Thesis, Chapter 2, University of Strathclyde.
15. Zijp, J. R. (2001). *Optical properties of dental hard tissues.* PhD. Thesis, Chapter 1, Rijksuniversiteit.
16. Spiller, M. S. (2000). Tooth anatomy. *Doctorspiller.* Posted 2000. Retrieved 28th of November 2005, from http://www.doctorspiller.com/tooth_anatomy.htm.
17. Reiss, S. M. (2001) Help arrest dental decay. *Biophotonics International.* 38-41.
18. Dental Disease. *Studyworld.* Retrieved 28th of November 2005, from http://www.studyworld.com/newsite/ReportEssay/Science/Physical%5CDental_Disease-382966.htm.
19. Mount, G., Hume, R. Dental caries. Dental department, UCLA. Retrieved 28th of November 2005 from http://www.dent.ucla.edu/ce/caries/.
20. Lussi, A. (1993). Comparison of different methods for the diagnosis of fissure caries without cavitation. *Caries Research*, 27(5), 409-416.
21. van Dorp, C. S., Exterkate, R. A., ten Cate ,J. M. (1988). The effect of dental probing on subsequent enamel demineralization. ASDC J. of Dent. Child., 55(5), 343-347.
22. Ekstrand, K., Qvist, V., Thylstrup, A. (1992). Light microscope study of the effect of probing on occlusal surfaces. *Caries Research,* 26(2), 89-93.
23. Kidd, E. A. , Ricketts, D. N., Pitts, N.B. (1993). Occlusal caries diagnosis: a changing challenge for clinicians and epidemiologists. *J. of Dent.* 21(6), 323-331.
24. van der Veen, M. H., de Josselin de Jong, E. (2000). Application of Quantitative light-induced fluorescence for assessing early caries lesions. *Assessment of Oral Health*, 17, 144-162.

25. Bjelkhagen, H., Sundtröm, F. (1981). A clinically applicable laser luminescence method for the early detection of dental caries. *J. of Quantum electronics*, 80, 110-122.
26. Bjelkhagen, H., Sundtröm, F., Angmar-Månsson, B., Rydén, H. (1982). Early detection of enamel caries by the luminescence excited by visible light. *Swed. Dent J.*, 6, 1-7.
27. Enami, Z., de Josselin de Jong, E., Sundtröm, F., Angmar-Månsson, B., (1993). Quantification of mineral loss on initial caries on natural enamel surfaces with laser fluorescence and longitudinal microradiography. (abstract 36). *Caries Research*, 27, 217.
28. Ando, M., Hall, A. F., Eckert, G. J., Schemehorn, B. R., Analoui, M., Stookey, G. K. (1997). Relative ability of laser fluorescence techniques to quantitate early mineral loss in vitro. *Caries Research*, 31, 125-131.
29. Diagnodent. KaVo USA. Retrieved 1st of December 2005, from www.kavousa.com/products/handpieces_accessories/special_instruments/diagnodent.
30. Lussi, A., Imwinkelreid, S., Pitts, N. B., Longbottom, C., Reich, E. (1999). Performance and reproducibility of a laser fluorescence system for detection of occlusal caries in vitro. *Caries Research*, 33(4), 261-66.
31. Shi, X. Q., Welander, U., Angmar-Mansson, B. (2000). Occlusal caries detection with KaVo DIAGNOdent and radiography: an in vitro comparison. *Caries Research*, 34(2), 151-158.
32. Baumgartner, A. Dichtl, S., Hitzenberger, C. K., Sattmann, H., Robl, B., Moritz, A., Fercher, A. F, Sperr, W. (2000). Polarisation-sensitive optical coherence tomography of dental structures. *Caries Research*, 34, 59-69
33. Fried, D., Xie, J., Shafi, S., Featherstone, J. D., Breunig, T. M., Le, C. (2002). Imaging caries lesions and lesion progression with polarisation sensitive optical coherence tomography. *J. of Biomed. Opt.*, 7, 618-627.

34. Kaneko, K., Matsuyama, K., Nakashima, S. (2000). Quantification of early carious enamel lesions by using an infrared camera in vitro. *Early detection of dental caries II, Proceedings of the 4th annual Indiana conference*, pp. 83-99.
35. Ricketts, D. N. J., Kidd, E. A. M., Wilson, R. F. (1995). A re-evaluation of electrical resistance measurements for the diagnosis of occlusal caries. *British Dental J.* 178, 11-17.
36. Lussi, A., Firestone, A., Schoenburg, V., Hotz, P., Stich, H. (1995). In vivo diagnosis of fissure caries using a new electrical resistance monitor. *Caries Research* 29, 81-87.
37. Ashley, P. F., Ellwood, R. P., Worthington, H. V. , Davies, R. M. (2000). Predicting occlusal caries using the electronic caries monitor, *Caries Research*, 34(2), 201-203.
38. Pine, C. M., ten Bosch, J. J. (1996). Dynamics of and diagnostic methods for detecting small carious lesions. *Caries Research*, 30(6), 381-383.
39. Yanikoğlu, F. C., Öztürk, F., Hayran, O., Analoui, M., Stookey, G. K. (2000) Detection of natural white spot caries lesions by an ultrasonic system. *Caries Research*, 34, 225-232.
40. Bab, I. A., Fuerstein, O., Gazit, D. (1997). Ultrasonic detector of proximal caries. *Caries Research*, 31, 322.
41. Ziv, V., Gazit, D., Beris, D., Fuerstein, O., Aharonov, L., Bab, I. A. (1998). Correlative ultrasonic histologic and roentgenographic assessment of approximal caries. *Caries Research*, 322, 294.
42. Barber, F. E., Lees, S., Lobene, R. R. (1969). Ultrasonic pulse-echo measurements in teeth. *Arch.Oral.Biol.*, 14, 745-760.
43. Pawley, J. B. (1995). Handbook of Biological Confocal Microscopy 2nd Edition Plenum Press, New York.
44. Kubelka, P. (1948). New contributions to the optics of intensely light scattering materials, Part I. *J. of Opt. Soc. Am.*, 38, 448
45. Kortum G (1969). Reflexionspektroskopie, Grundhagen, Methodik, Anwendungen, Heidelberg:Springer.

46. Cashwell, E. D., Everett, C. J. (1959). A practical manual on the monte carlo method for random walk problems. Pergamon Press, New York.
47. Marbach, R.,.Heise, H..M. (1995). Optical diffuse reflectance accessory for measurements of skin tissue by near infrared spectroscopy. *Appl. Opt.*, 34, 610-621.
48. Wang, T., Ko, C-C., Cao, Y., DeLong, R, Huang, C-C., Douglas, W. H. (1998). Optical simulation of irradiated carious tooth by Monte Carlo method *ASME BED*
49. Ko, C-C., Tantbirojn, D., Wang, T., Douglas, W. H. (1998). Optical scattering power of a carious lesion:1-D approach comparing Kubelka-Munk method to Monte Carlo simulation *ASME*
50. Cheong, W., Prahl, S. A., Welsh, A. J. (1990). A review of the optical properties of biological tissue. *J. of Quantum Electron.*, 26, 2166-2185.
51. Patterson, M. S., Wilson, B. C., Wyman D. R. (1991). The propagation of optical radiation in tissue I. Models of radiation transport and their application. *Lasers in Med. Sci.*, 6, 155-168.
52. van Gemert, M. J. C., Star, W. M. (1987). Relations between the Kubelka-Munk and the transport equation models for anisotropic scattering"; *Lasers in Life Sci.*, 1, 287-298.
53. Wang, L., Jacques, S. L., (1992) Monte Carlo modeling of light transport in multi-layered tissues in standard C. University of Texas M.D. Anderson Cancer Center.
54. Heney, L. G., Greenstein, J. L. (1941). Diffuse radiation in the Galaxy. *Astrophys. J.*, 93, 70-83.
55. OptiCAD users manual 7.0 (chapter 3).
56. Zucker, R. L. (2004). Confocal Microscopy System Performance: Axial Resolution. *Microscopy today*, 12:1.
57. Dirchx., J. J. J., Kuypers, L.C., Decraemer, W. F. (2005). Refractive index of tissue measured with confocal microscopy. J. of Biomed. Opt., 10(4), 1-8.

58. Kidd, E. A. M., Fejerskov, O. (2004). What constitutes dental caries? Histopathology of carious enamel and dentin related to the action of cariogenic biofilms. *J. Dental research* special issue C, proceedings, 35-38.

Chapter 4: The use of Infrared lateral illumination to detect occlusal caries

1. Introduction

Dental diagnosis systems currently available have great difficulty in detecting occlusal caries (due to its uneven surface) and can usually only detect disease when it is at an advanced stage. Using a technique based upon transillumination, which makes use of the increased scattering properties associated with carious tooth tissue (when compared with healthy tissue), a cost-effective system capable of detecting caries is presented. The device uses near-infrared illumination source operating at 810nm to illuminate the tooth either on the proximal (buccal or distal), buccal or lingual surfaces, with subsequent image measurement at the occlusal surface to detect early stage caries. In a preliminary study involving 15 ex-in vivo adult pre-molars and molars at various stages of dental decay, the infrared lateral illumination device is compared with other dental caries diagnosis techniques presently available and techniques currently in development.

2. The origin and need for lateral illumination (L.I.)

2.1 Transillumination

As mentioned previously in chapter 3, when demineralisation and the onset of caries occurs within dental tissue, the regular crystalline structure associated with hydroxyapatite crystals within tooth structure breaks down. This results in an alteration in the optical and scattering properties associated with dental tissue. The reduction in mineral content, as well as disrupting the regular crystalline structure, also increases the porosity of the tissue, resulting in further refractive index mismatches (between healthy and diseased sections) within the tissue and increased scattering properties. This also marks a decrease in the overall refractive index of the tissue, which includes both the mineral crystals (hydroxyapatite) and surrounding media (i.e. water, lipids, proteins).

Although through the measurement of various properties such as reflection (e.g visual inspection), fluorescence (e.g. QLF) and absorption (e.g X-ray), it has been shown that optical methods have been somewhat useful in detecting these changes associated with caries, their limitations require the need for the development of more accurate methods for dental diagnosis. This has led to renewed interest in an optical technique known as transillumination, a procedure first used by dental practitioners to characterise tooth decay before the advent of X-ray photography. The transillumination technique works on the premise that due to the greater backscattering properties of carious when compared to sound sections of the tooth, when the tooth is illuminated on one side with a bright light source, and the light is collected on the other side (using a camera), carious tissue can be seen as a darker region against a lighter background (see figure 1).

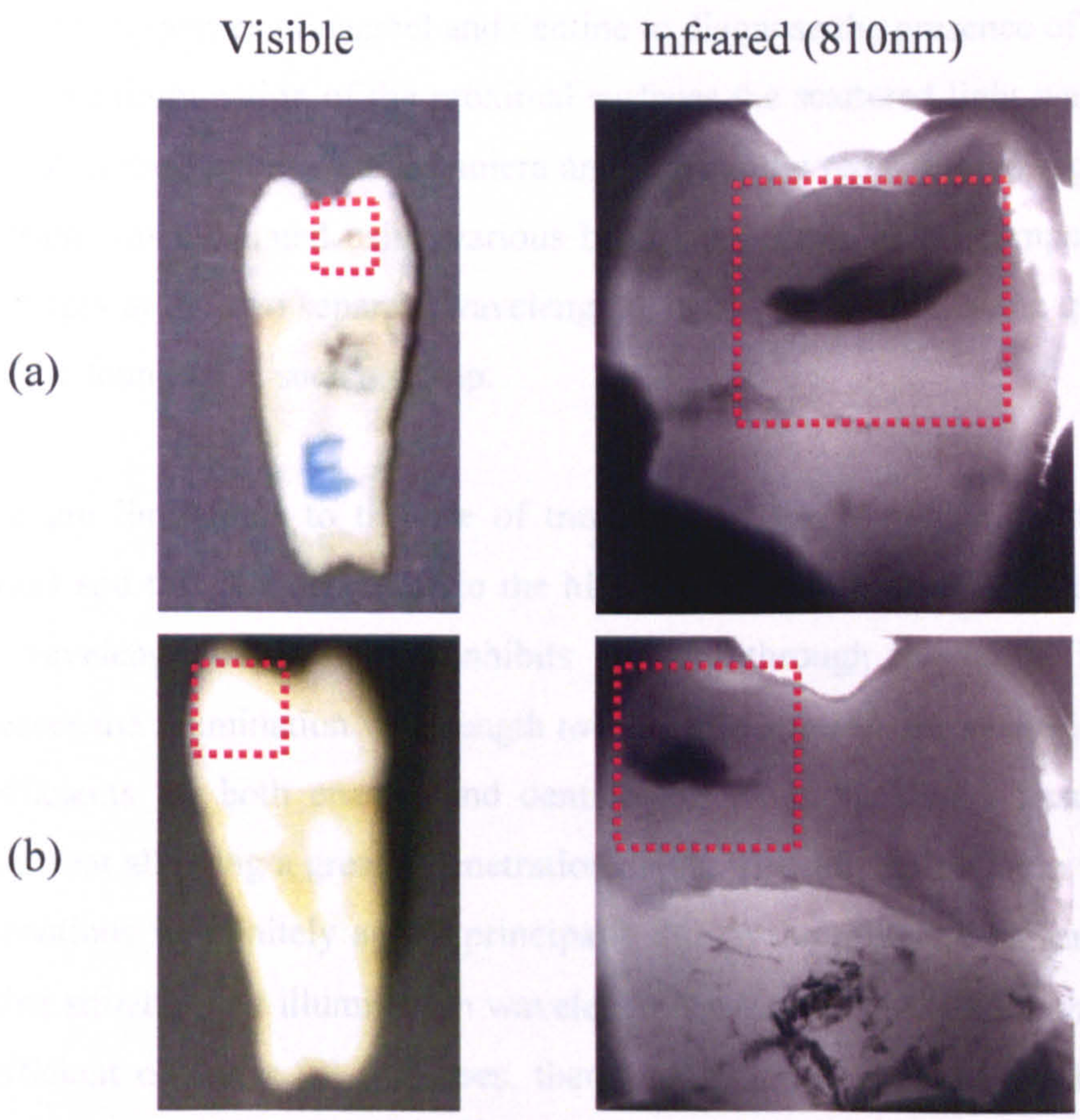

Figure 1: Showing carious regions of the proximal surfaces of a pre-molar tooth viewed in visible and using infrared transillumination techniques for (a) a brown spot lesion and (b) a white spot lesion.

Over the last 30 years the application of transillumination using white light has been shown to be partially successful in detecting interproximal lesions [1-3]. However, there are a number of methods which vary the original technique, in order to increase the sensitivity of the system. Verdonschot *et al.* [4] demonstrated that by illuminating the occlusal surface and using a photocell, scattered light could be detected at the proximal region and variations in intensity measured. In another study by Scheiderman *et al.* [5], dedicated algorithms were used to analyse images and detect to a certain degree, the presence of proximal caries quantitatively in a similar manner to those employed in the QLF.

Vaarkamp *et al.* [6] examined the viability of utilizing wavelength-dependent light scattering properties of enamel and dentine to diagnose the presence of proximal lesions. Following illumination of the proximal surfaces the scattered light was measured at the occlusal surface using a CCD camera and light in the red and blue region of the visible spectrum was evaluated using various band pass filters. After comparative analysis of the images at the two separate wavelengths, it was shown that some quantitative results could be found from such a set-up.

There are limitations to the use of transillumination at visible wavelengths (400nm-700nm) and this is mainly due to the highly scattering properties of dental structure in this wavelength range which inhibits imaging through the tooth. However, as one increases the illumination wavelength towards the infrared, the scattering and absorption co-efficients for both enamel and dentine fall [7 & 8]. Dental tissues become more transparent allowing a greater penetration depth. This improvement in transparency does not continue indefinitely and is principally due to the presence of water in enamel and dentine structure. At illumination wavelengths greater than 1400nm, the light absorption co-efficient of water [9] increases, therefore in order to penetrate the same depth of tissue, greater illumination intensities are required (see figure 2). This introduces problems of its own in that increasing illumination power at increased absorption rates could potentially lead to tissue damage.

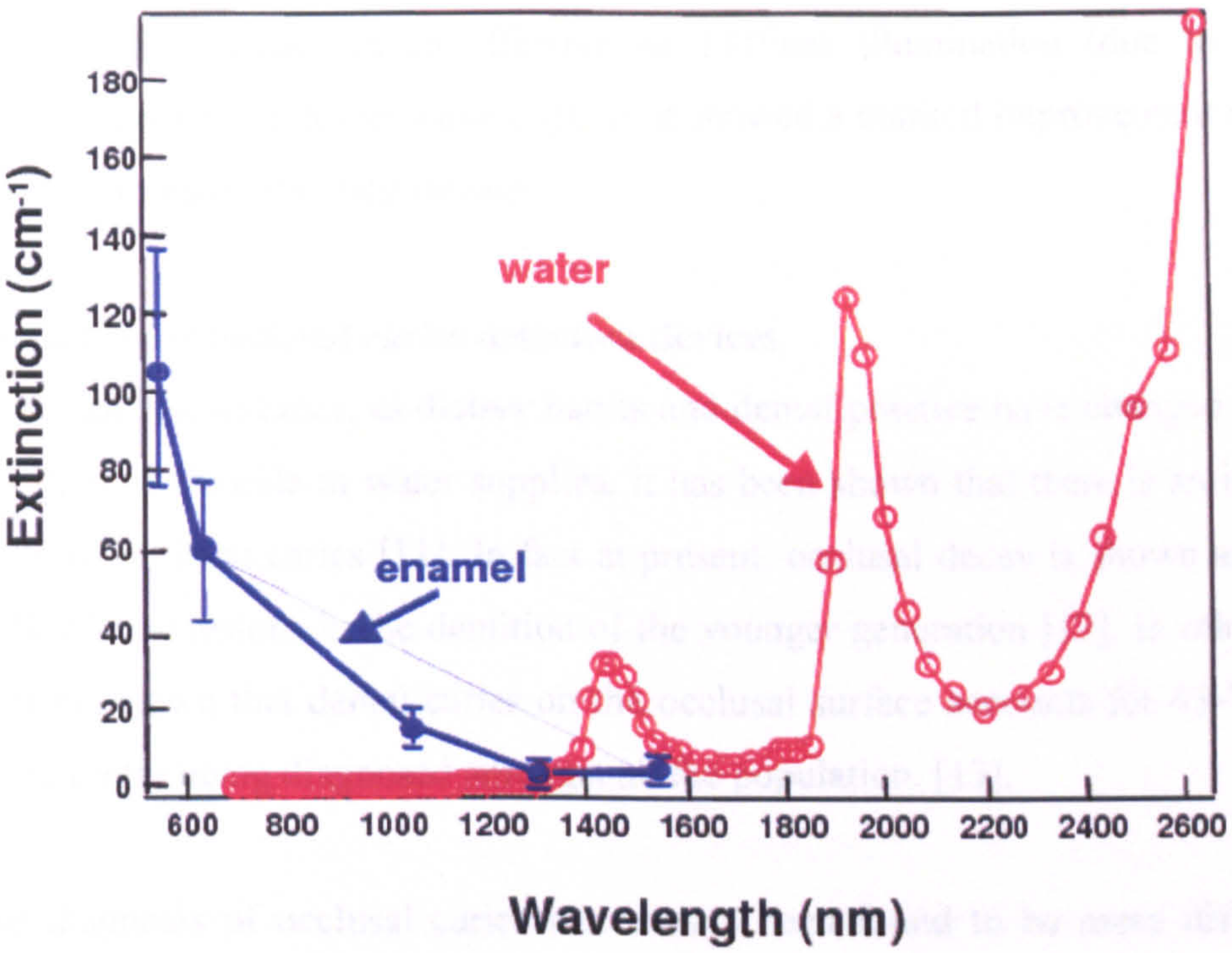

Figure 2: Showing the co-efficient of attenuation of dental enamel [9].

In Jones *et al.* [9] this window of transparency was used to transilluminate teeth at 1310nm using a super-luminescent diode light source in order to detect simulated carious lesions. Due to the insensitivity of silicon based CCD detectors at this wavelength, the transilluminated image was detected using an InGaAs focal plane array. By illuminating at a wavelength of greater transparency, this technique showed promise in detecting interproximal lesions, but the use of 1310nm illumination and detection required the need for specialised and expensive InGaAs imaging equipment.

In another study [10] it was shown that an effective transillumination system could still be produced that could capitalise on the increasing transparency of dental tissue at near-infrared wavelengths, while maintaining a relatively low cost. Using an 830nm light source to transilluminate the sample, light could be detected using a relatively low cost silicon based CCD camera. In this instance interproximal lesions were simulated by

drilling a hole into the interproximal region and filling it with a hydroxyapatite paste. It was shown that while not as effective as 1310nm illumination (due to increased scattering properties at lower wavelengths), it showed a marked improvement over other visible light transillumination devices.

2.2 The need for occlusal caries detection devices

Over the last few decades, as dietary habits and dental practice have changed as well as the addition of fluoride in water supplies, it has been shown that there is an increase in the level of occlusal caries [11]. In fact at present, occlusal decay is shown account for the bulk of new lesions in the dentition of the younger generation [12]. In other studies, it has been shown that dental caries on the occlusal surface accounts for 43-75% of all caries currently being diagnosed amongst all the population. [13].

Precise diagnosis of occlusal caries has always been found to be more difficult than other forms of caries. This is mainly due to the uneven nature of the occlusal surface which hinders diagnosis. More recently, there has been the suggestion of the presence "occult" or hidden caries formation [14] underneath sound enamel in some cases, which may be due to the effect of the presence of increased fluoride levels in ones diet. This is quite worrying in that for all the caries detection methods described previously in chapter 3, DIAGNOdent is the only commercially available system that has been purposely designed for detecting occlusal caries. Thus this highlights the need for more procedures that can accurately detect occlusal decay.

In this chapter a cost effective infrared imaging system capable of detecting natural occlusal caries at an early stage from ex-in vivo teeth samples is presented. The aims were to accurately detect early caries and facilitate the monitoring and assessment of lesion behaviour at the occlusal surface. In this study a selection of healthy teeth as well as some teeth containing natural occlusal carious lesions (as perceived by visual inspection), were examined using the infrared imaging technique. The teeth were also

examined using some other commercial techniques currently available and the sensitivities and specificities were compared.

3. Procedure

The lateral illumination configuration is shown in figure 3. The infrared radiation was provided by a collimated 50mW 810nm laser diode module [Laser 2000]. Using a variable neutral density filter located between the laser source and the tooth, the illumination intensity was controlled. The tooth was illuminated at the proximal surface at the junction between the crown and the root of the tooth. Using a Pulnix 9701-TM CCD camera and frame grabber (PCI-1422) [National Instruments], images of the occlusal surface were taken and stored on computer. A narrow band infrared filter (810+/-10nm) [Comar Ltd] was placed in front of the detector camera to allow only light which originated from the laser and to block out room light. Due to the sensitivity of silicon to near infrared wavelengths, the use of an illumination wavelength at 810nm allows the use of a CCD device without the need of more expensive imaging equipment. The tooth was mounted onto an Aerotech U500 rotary stage with 360° rotation and PC based control, which allowed easy manipulation of the postion of illumination on the tooth.

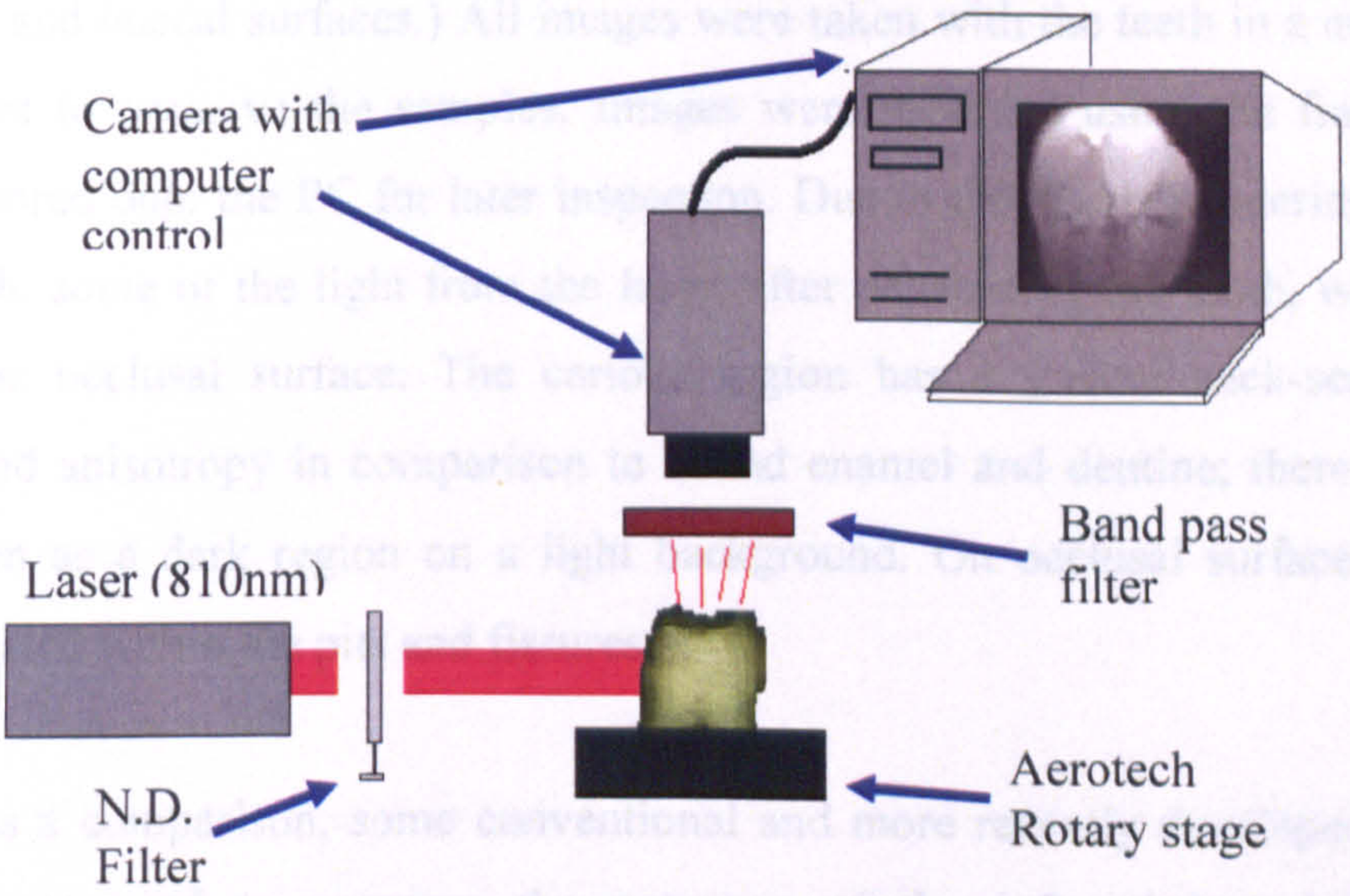

Figure 3: Set-up for the lateral illumination system to image the whole occlusal surface.

For this study, 15 extracted posterior teeth (molars and pre-molars) were examined categorised as perceived by visual examination by two experienced dental practitioners [Andrew Hall and Christopher Longbottom known henceforth as AH & CL respectively] into the following categories:

1. Sound Unstained – healthy teeth with no staining.
2. Early Caries – caries can be seen at an early stage as a white region on a white background and is located in the pits and fissures where the build-up of plaque is most likely.
3. Carious/Cavitated – caries is at an advanced stage. Caries can be seen as a dark region on the tooth surface. Some cavitation (where the outer tooth structure has disintegrated) may have also occurred.
4. Sound Stained – these teeth appear healthy with just some staining present.

3.1 Lateral illumination

For lateral illumination, images of the occlusal surface were taken at various laser intensities (using the N.D. filter to control the dynamic range of the camera) and using the rotary stage, at various rotations of the tooth with respect to the laser illumination (in that the tooth was illuminated through each of the proximal (mesial and distal) as well as the lingual and buccal surfaces.) All images were taken with the teeth in a moist thymol environment to preserve the samples. Images were recorded using the frame grabber card and stored onto the PC for later inspection. Due to the highly scattering properties of the tooth, some of the light from the laser, after penetrating the tooth, was scattered towards the occlusal surface. The carious region has a greater back-scattering co-efficient and anisotropy in comparison to sound enamel and dentine; therefore lesions can be seen as a dark region on a light background. On occlusal surfaces, these are usually located within the pits and fissures.

To serve as a comparison, some conventional and more recently developed diagnostic methods were used to compare the accuracy of the infrared lateral illumination technique. These were: (i) visual inspection, (ii) bitewing X-Ray photography, (iii)

DIAGNOdent, (iv) quantitative light-induced fluorescence (QLF) and (v) Tooth dissection by hemi-section with visual inspection (which serves as the gold standard for which all other techniques were compared against).

3.2 Visual Inspection

Before visual examination, each sample was first cleaned and then dried using a water and air syringe respectively. Using white light to illuminate the sample, the proximal and occlusal surfaces of each tooth were examined for signs of caries and cavitation. Due to the increased reflectivity (associated with Fresnel reflections for boundaries of differing refractive indices) as well as increased backscattering properties associated with carious tissue, early caries appears as a brighter white spot on a duller white background. Cavitation occurs when caries is in an advanced state, whereby the surface integrity of the tooth has been compromised. Each tooth was examined at both the occlusal and proximal surfaces for signs of demineralisation. The results were recorded and then compared with the other methods of diagnosis.

3.3 Bitewing X-Ray photography

Using an Oralix dental X-Radiation machine [Philips] (with a non-collimated X-ray output of 60kV), X-Rays were directed first through some bluetac (to simulate the attenuation effects of cheek tissue and then onto the buccal surface of the tooth (as done in vivo). The X-rays where collected onto a specialised photographic film at the lingual surface of the tooth. These photographs where subsequently processed and this was repeated for each tooth sample. In the processed photograph, caries can be seen as a darker region on a lighter background. The photographs were interpreted for signs of occlusal caries.

3.4 DIAGNOdent

Before evaluation using the system, the teeth were dried using an air syringe. For each tooth, each occlusal surface was measured under standardised conditions by DIAGNOdent using the conical shaped probe specified from the manufacturer's

recommendations. Before each measurement, the standard value for each individual tooth was calibrated by measuring the fluorescence of a sound region of the tooth. For each occlusal surface, a number of measurements were taken, specifically at regions at which caries is most likely to occur i.e. the pits and fissures. A positive result for caries was accepted when the DIAGNOdent system gave a value greater than 20.

3.5 QLF

The QLF device used was a Clin-QLF machine [Inspektor Research BV], with a Xenon arc lamp light source filtered to produce light with a mean wavelength of 470nm. Before examining the occlusal surface using the QLF device, the tooth was first dried using an air syringe. Using the QLF hand-piece (which contains both the camera and the laser illumination), the device was aimed at occlusal surface and illuminated at a mean wavelength of 470nm. With a band-pass filter in front of the camera (which filtered out all reflected and backscattered light), auto-fluorescence from the dental tissue was measured and recorded onto computer. Due to the greater scattering properties of carious tissue when compared to sound dental tissue, fluorescent light from the sound enamel is more likely to be remitted than fluorescent light from carious enamel. Therefore lesions can be seen as darker regions in a lighter background. Using software provided with the QLF device, each occlusal image was analysed, whereby the loss in detected fluorescence between carious and sound enamel was calculated to determine the amount of mineral loss (and hence the presence of caries.)

3.6 Tooth dissection and visual inspection

After examination using all the methods, the teeth were dissected using a specialised cutting tool and polished along the dissection line, before being examined for disease. For each tooth, a dissection line was chosen which would have the greatest probability of detecting caries. As this was considered the gold standard for the experiment, only caries regions that occurred along the dissection line could be correlated with other methods. Early caries can be seen as an increased whiteness originating from a pit or fissure (where caries is most likely to occur.) Advanced caries should be clearly evident

as a brownish discolouration where tooth structure has clearly broken down. Each method of caries recognition was then analysed for each tooth sample and were then compared with tooth histology to calculate their sensitivities and specificities.

4. Results

Figure 4 below shows images of the *sound 1* tooth using each of the different techniques described earlier. From visual inspection after dissection, the tooth was assessed to be healthy with no sign of demineralisation.

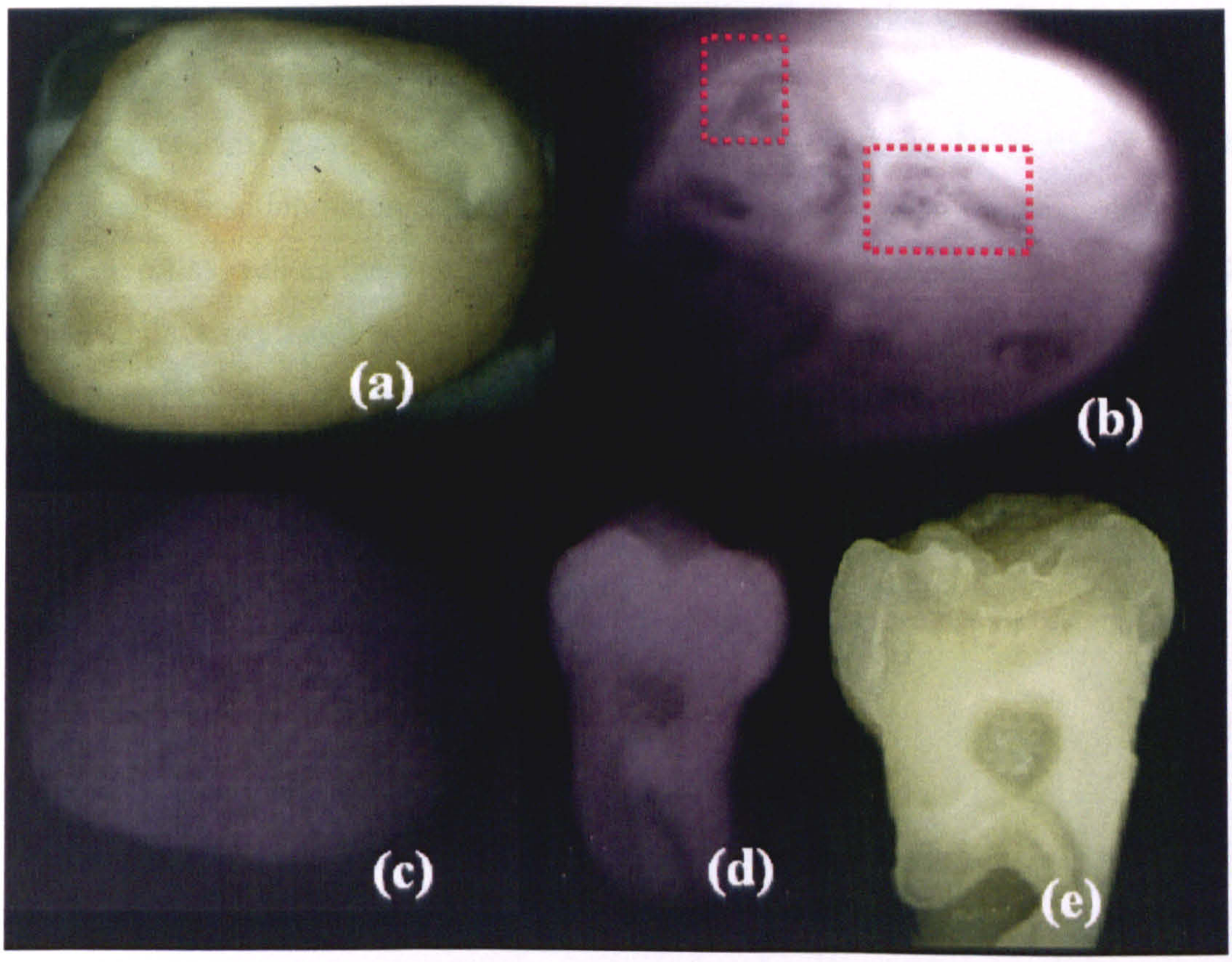

Figure 4: Showing *Sound 1* which contains hypomineralisation (a) Visual Inspection, (b) Lateral Illumination, (c) QLF, (d) Bitewing X-ray photography, (e) Visual Inspection after dissection.

From the lateral illumination image in figure 4 (b), a number of darker regions are evident (two of which are highlighted with red boxes). These regions are in fact located on the cusps of the occlusal surface which are areas where caries is least likely to occur. From closer examination of the tooth after dissection, these regions were diagnosed as areas of hypomineralisation, which were caused during dental tissue formation. Hypomineralisation is a structural modification of dental tissue due to either low amounts of calcium, or the presence of high amounts of fluoride (fluorosis) [15] in ones diet which results in hypocalcified, porous and brittle enamel structure. 5 readings were taken using the DIAGNOdent device, of those, only one was taken in a region of hypomineralisation which gave a value of 2, indicating that caries was not detected.

Figure 5 shows images of each of the different techniques using the *cavitated 1* tooth. From visual inspection before dissection, it is clearly evident from the discolouration at the central pit as well as the fissures that the tooth is at an advanced state of decay. The tooth is in fact cavitated both in the central pit of the occlusal surface and on the proximal surface. This assessment of caries at the central pit of the occlusal surface was verified using each of the diagnosis techniques.

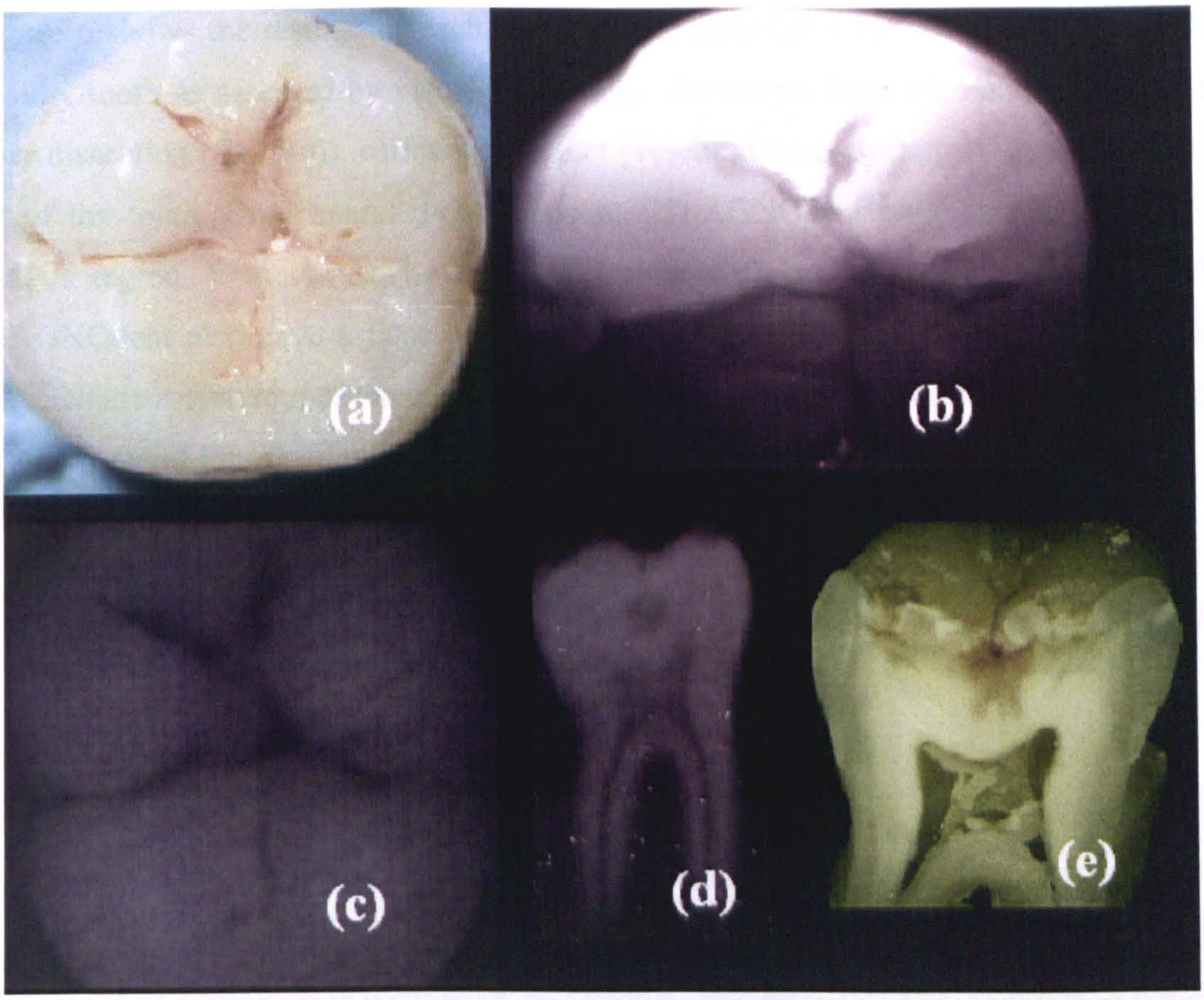

Figure 5: Showing *cavitated 1* decay using all techniques (a) Visual Inspection, (b) Lateral Illumination, (c) QLF, (d) Bitewing X-ray photography, (e) Visual Inspection after dissection.

All techniques used give a positive result for caries in the central pit of the tooth. On examination of the tooth after dissection, the presence of tooth decay in the central pit was confirmed. It was shown to be at quite an advanced stage, where the degree of decay from the central pit has progressed almost all the way through the dentine into the pulp cavity. Only the lateral illumination and the DIAGNOdent techniques (which gave an average reading of 55 +/- 25 for 10 readings taken at central pit and fissures) are sensitive enough to detect caries within all the fissures, which are verified after dissection and inspection.

Figure 6 shows the results for each of the dental techniques for *sound 2*, a supposedly healthy tooth as assessed by visual inspection. As shown from the image of the tooth after dissection (fig. 6(e)), caries was in fact present at an early stage within the central pit of the tooth. Only lateral illumination and DIAGNOdent were able to detect this carious region. It must also be noted that on a different region on the same tooth, DIAGNOdent also gave a false negative reading (i.e. caries was in fact present when DIAGNOdent system measured a healthy region of <20). The carious area is highlighted in 2(b) (Lateral illumination) & (e) (visual inspection after dissection) by the white box.

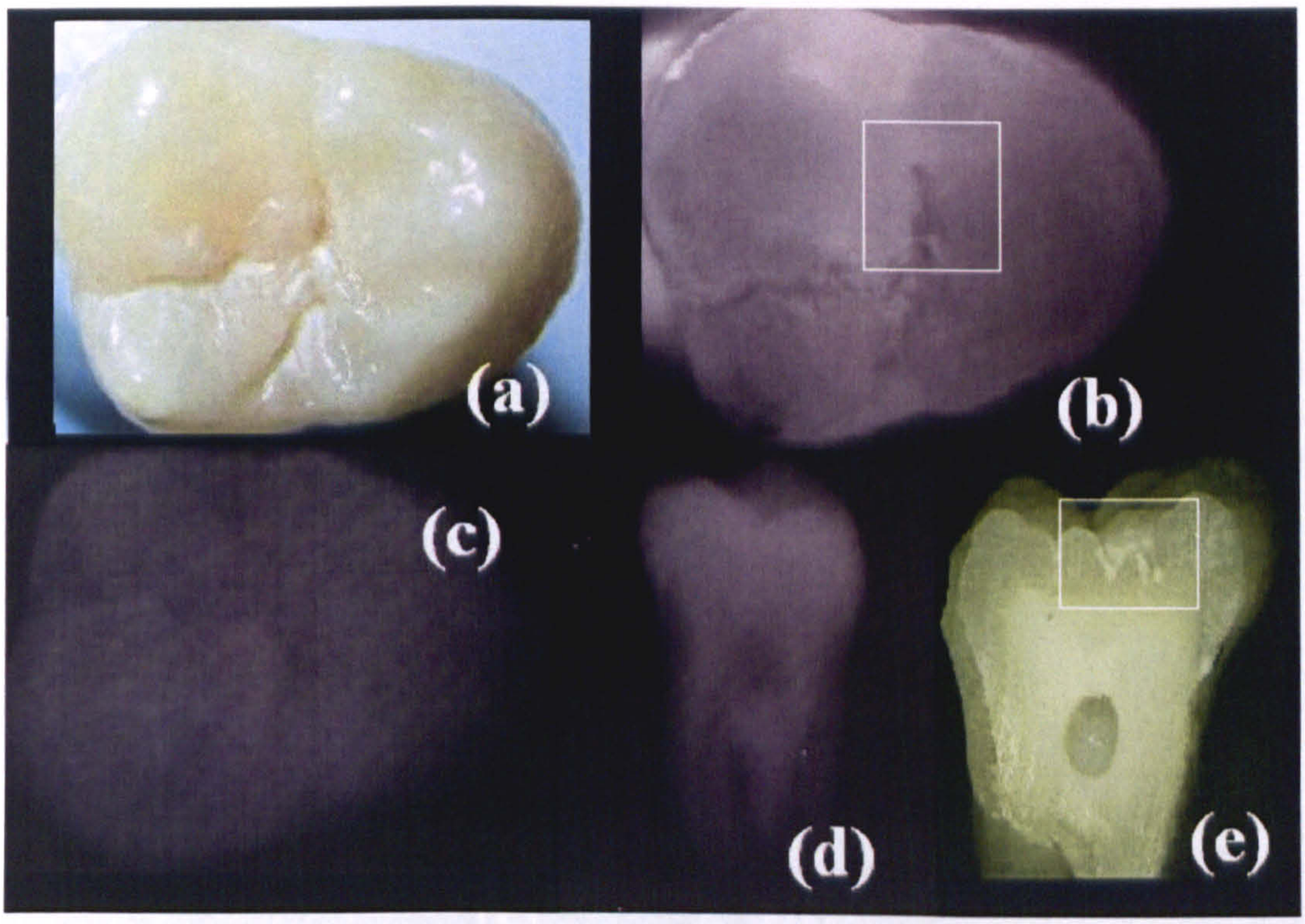

Figure 6 : Showing images of a supposedly sound tooth (*sound 2*) using the various techniques: (a) Visual Inspection, (b) Lateral Illumination, (c) QLF, (d) Bitewing X-ray photography, (e) Visual Inspection after dissection.

In Figure 7 below, results from each of the techniques on *sound stained 2* are shown. From visual inspection, this tooth was assessed to be sound with some staining present.

On examination after dissection, early caries was found to occur in one instance in an extremely small region highlighted by the red box in figure 7 (a). This does not show up on any of the other diagnosis methods except DIAGNOdent. This shows some limitations in terms of how apparent a certain size of carious tissue can be seen through a certain depth of healthy tissue using the lateral illumination system. Figure 7 (b) shows how staining is seen using the lateral illumination method. Although dark on a light background (similar to caries), it is somewhat speckly in appearance and can be easily distinguished.

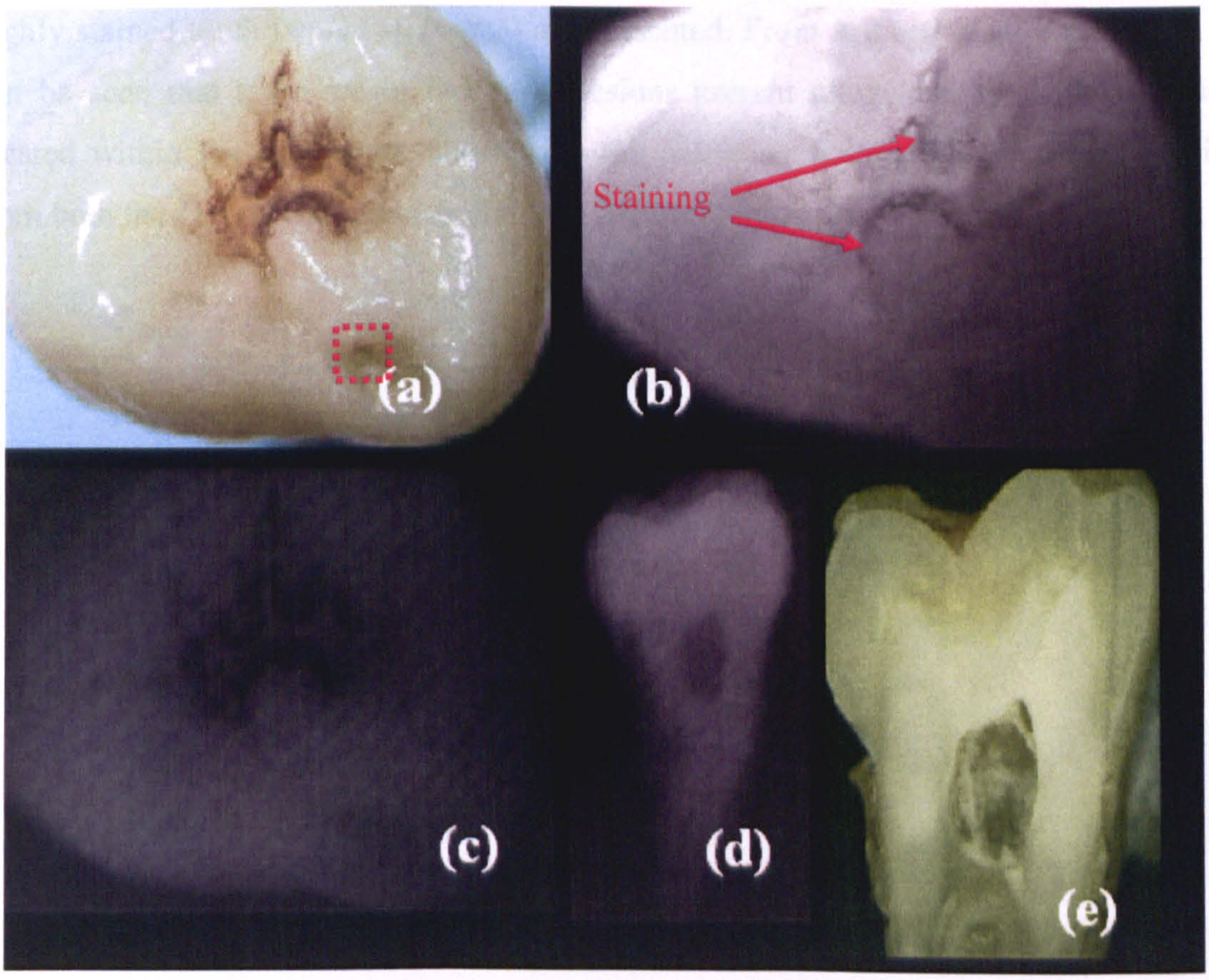

Figure 7 : Showing *sound stained 2* and in particular how staining is observed under infrared illumination (a) Visual Inspection, (b) Lateral Illumination, (c) QLF, (d) Bitewing X-ray photography, (e) Visual Inspection after dissection.

This example clearly shows one of the main limitations associated with the DIAGNOdent system. Although it was the only system tested which was capable in detecting the only carious region on the occlusal surface of the tooth (this could have been incidental to the presence of staining on the same position), due to the presence of staining, it measured a positive result for caries in healthy dental tissue. In fact of the 6 readings taken using the DIAGNOdent device, values were found to range from 11 to 62 with an average of 32 +/- 22.

In figure 8, results from each of the diagnosis techniques of a supposedly sound but highly stained tooth (*sound stained 3*) are presented. From inspection after dissection it can be seen that there are in fact three lesions present altogether, two of which are located within the central pit, and one in the adjoining fissure. This confirms results from both the Lateral illumination and DIAGNOdent systems.

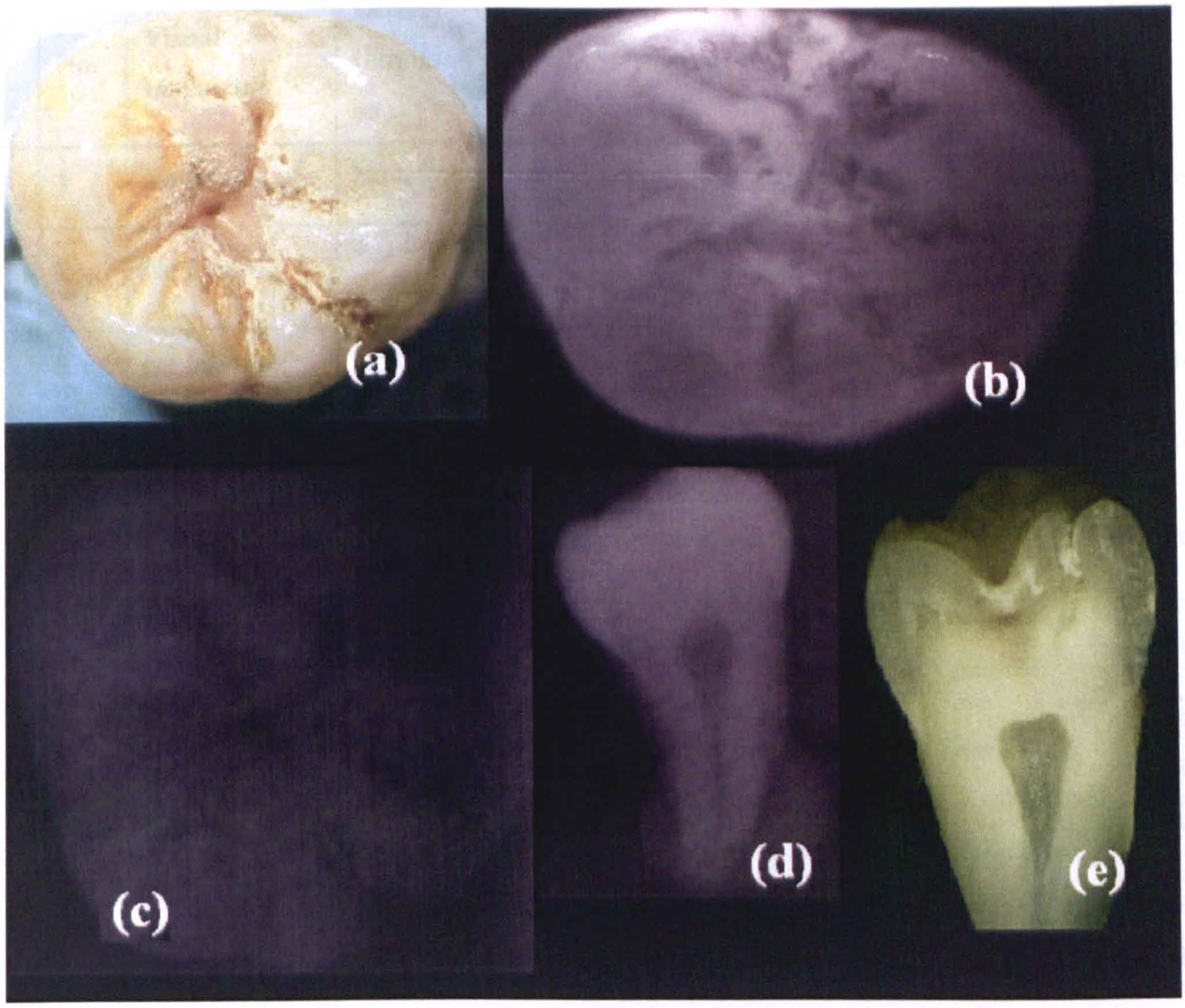

Figure 8 showing *sound stained 3* highlighting the difference between stained and carious sections of the tooth (a) Visual Inspection, (b) Lateral Illumination, (c) QLF, (d) Bitewing X-ray photography, (e) Visual Inspection after dissection.

Lesions can be distinguished from staining in the lateral illumination method due to the greater homogeneity in the darker region of the image.

In table 1, the number of lesions detected for each technique for each tooth is shown and compared with the gold standard for this investigation. In tables 2(a)-(d), positive and negative results for each technique were compared with the the gold standard of visual inspection after dissection.

		Dental decay Technique					
Type of Tooth	**No.**	**Visual Inspection**	**Lateral Illumination**	**DIAGNOdent**	**Bitewing X-ray**	**QLF**	**Inspection after Dissection**
Sound Unstained	**1**	No lesions	No lesions	No lesions	No lesions	No lesions	No lesions
	2	No lesions	2 lesions detected	2 lesions found (only 1 matched)	No lesions	No lesions	2 lesions
	3	No lesions	No lesions	No lesions	No lesions	No lesions	No lesions
	4	No lesions	No lesions	1 lesion detected	No lesions	No lesions	No lesions
Early Caries	**1**	Possible lesions	4 lesions detected	1 lesion detected	No lesions	4 lesions detected	4 lesions
	2	Caries in pits & fissures	4 lesions detected	2 lesions detected	2 lesions detected	4 lesions detected	6 lesions
	3	Possible lesion in pit	No lesions	No lesions	No lesions	No lesions	1 lesion in central pit
	4	Possible fissure lesions	No lesions	No lesions	No lesions	No lesions	1 proximal lesion
Caries Cavitated	**1**	Cavitated pit and fissures	5 lesions detected	3 lesions detected for 3 readings	1 lesion detected	2 possible lesions	5 lesions
	2	Carious and etched surface	1 detected 2 possible	1 lesion detected	No lesions	No lesions	3 lesions
	3	Carious pit, surface chip	2 detected 1 on chip	1 detected	No lesions	1 lesion detected	1 lesion
	4	Pits & fissures contain caries	3 lesions detected	2 lesions detected for 2 readings	No lesions	3 lesions detected	3 lesions
Sound Stained	**1**	Highly stained but sound	1 lesion detected	2 lesions detected, only 1 match	No lesions	2 lesions, 1 matches	2 lesions
	2	Stained but sound tooth	staining, no lesions	3 lesions detected, 1 match	No lesions	2 lesions, no match	1 small lesion
	3	Staining, tooth sound	3 lesions detected	3 lesions detected	No lesions	1 lesion detected	3 lesions

Table 1: Showing a short description of the number of lesions detected for each technique that were verified by visual inspection after dissection.

		(a) Lateral illumination	
		negative	positive
caries (visual inspection after dissection)	absent	5	1
	present	8	24

(a)

		(b) DIAGNOdent	
		negative	positive
caries (visual inspection after dissection)	absent	12	8
	present	14	16

(b)

		(c) QLF	
		negative	positive
caries (visual inspection after dissection)	absent	3	5
	present	15	16

(c)

		(d) Bitewing X-ray	
		negative	positive
caries (visual inspection after dissection)	absent	3	0
	present	29	3

(d)

Tables 2(a)-2(d): Showing correlation between each occlusal detection technique and visual inspection after dissection

Where the true and false positives and negatives are shown in table 3 below:

		Tested technique	
		Negative	**Positive**
Gold standard	**Absent**	True negative	False negative
	Present	False negative	True positive

Table 3: The origin of true and false negatives and positives.

Using the correlated results from tables 2(a) – 2(d), the sensitivities and specificities for each technique were calculated. Sensitivity and specificity are statistical processes used to determine the accuracy of certain techniques in detecting disease [16]. *Sensitivity* is a measure of the accuracy of a technique in detecting disease when the disease is actually present and is determined by the equation:

$$Sensitivity = \frac{(TruePositive)}{(TruePositive) + (FalsePositive)} \quad (1)$$

Specificity is a measure of the accuracy of the technique in detecting healthy tissue when the tissue is in fact healthy and is determined by the equation:

$$Specificity = \frac{(TrueNegative)}{(TrueNegative) + (FalseNegative)} \quad (2)$$

The sensitivities and specificities for each technique for all 15 tooth samples are shown in table 3 below. As one can see, the sensitivities and specificities for lateral illumination at detecting occlusal caries are greater than all other methods including DIAGNOdent, which has been specifically designed for this purpose.

Technique	Sensitivity	Specificity
Lateral Illumination	0.75	0.83
DIAGNOdent	0.53	0.6
QLF	0.52	0.375
Bitewing X-Ray	0.094	1

Table 4: showing sensitivity and specificity values for each technique.

The X-ray specificity has been found to be 1 and is due to X-ray bitewings only being able to detect caries at an advanced stage. Therefore if the tooth is healthy, the X-ray will agree with this, but with a corresponding low sensitivity.

4. Summary

From the sensitivity and specificity values, lateral illumination has been shown to be the most effective technique at distinguishing between healthy and carious dental tissue on the occlusal surface. As with all techniques, there are a few problems associated with the correct diagnosis of disease using lateral illumination. These include the presence of staining on the tooth surface which also produces a darker region on the image. Generally though, due to its 'speckly' appearance, staining can be easily dissociated from carious sections. Hypomineralisation of the tooth surface can also be seen as a darker region on a lighter background, but is also easily distinguishable from diseased sections due to its location on the occlusal surface.

The presence of any staining on the tooth surface was found to adversely affect any measurements taken using the DIAGNOdent procedure, as found in previous work [17]. This was due to staining materials (i.e. tea) fluorescing at the same wavelength as the bacterial metabolites which in turn give a false positive for caries. This would account for its low sensitivity and specificity values. For QLF the specificity and sensitivity values were low, which shows that clearly not suitable for early occlusal caries diagnosis.

For any occlusal caries detected using X-ray bitewing radiography, disease was already at an advanced stage of development. At this stage, any clinical management of the disease could only have been possible with operative intervention.

As with all techniques currently available, lateral illumination requires the use of an experienced dentist to assess the results it produces. With the need for more precise diagnostic techniques for occlusal surfaces required, the development of lateral

illumination would vastly improve the monitoring and assessment of lesion behaviour and activity. Through the use of both low cost near-infrared laser diodes and CMOS detection technology, a cost effective infrared lateral illumination system can be developed.

References

1. Peltola, J., Wolf, J. (1981). Fiber optics transillumination in caries diagnosis. *Proc. Finn. Soc.*, 77, 240-244.
2. Barenie J., Leske G., Ripa, L.W. (1973). The use of fiber optic transillumination for the detection of proximal caries. *Oral surg.*, 36, 891-897.
3. Pine, C.M. (1996). Fiber-optic transillumination (FOTI) in caries diagnosis. *Early detection of caries*, G.S. Stookey, ed., Indiana Press, Indianapolis.
4. Verdonschot, E. H., van de Rijke, J. W., Brouwer, W., ten Bosch, J. J., Truin, G. J. (1991). Optical quantitation and radiographic diagnosis of incipent approximal caries lesions. *Caries Research*, 25(5), 359-364.
5. Schneiderman, A., Elbaum, M., Shultz, T., Keem, S., Greenbaum, M., Driller, J. (1997). Assessment of dental caries with Digital Imaging Fiber-Optic Transillumination (DIFOTI): in vitro study. *Caries Research*, 31(2), 103-110.
6. Vaarkamp, J., Ten Bosch, J. J., Verdonschot, E. H., Tranaeus, S. (1997). Quantitative diagnosis of small approximal caries lesion utilizing wavelength-dependent fiber-optic transillumination. *J. Dent Res.*, 76(4), 875-882.
7. Fried, D., Featherstone, J. D., Glena, R. E., Seka, W. (1995). The nature of light scattering in dental enamel and dentin at visible and near-IR wavelengths. *Appl. Optics*, 34, 1278-1285.
8. Hale, G. M., Querry, M. R. (1973). Optical constants of water in the 200nm to 200μm wavelength region. *Appl. Optics*, 12, 555-563.
9. Jones, R. S., Huynh, G. D., Jones, G. C., Fried, D. (2003). Near-infrared transillumination at 1310nm for imaging of early dental decay. *Optics Express*, 11(18), 2259-2265.
10. Jones, G. C., Jones, R. S., Fried, D. (2004). Transillumination of interproximal cares lesions with 830-nm light. Proceedings of SPIE, Lasers in dentistry X, may 2004, 17-22.
11. Mc Comb, D., Tam, L. E. (2001). Diagnosis of Occlusal Caries: Part I. Conventional Methods. *Clinical Practice*, 67 (8), 454-457.

12. Kaste, L. .M., Selwitz, R. .H., Oldakowski, R. .J., Brunelle, J. A., Winn, D. .M., Brown, L. J. (1996). Coronal caries in the primary and permanent dentition of children and adolescents 1-17 years of age: United States, 1988-1991. *J. of Dent Research*, 75, 631-641.
13. Dental Disease. *Studyworld.* Retrieved 28th of November 2005, from http://www.studyworld.com/newsite/ReportEssay/Science/Physical%5CDental_Disease-382966.htm.
14. Ricketts, D., Kidd, E., Weerheijm, K. L., de Soet H. (1997). Hidden caries: what is it? Does it exist? Does it matter? *Int. Dent. J.*, 47 (5), 259-265.
15. Ahuja B. A novel approach for treating fluorosis stains. *Healthmantra.* Retrieved 9th of December 2005, from http://www.healthmantra.com/ypb/apr01/fluorosis.htm.
16. Feinstein, A. R. (1977). Chapter 15: On the sensitivity, specificity, and discrimination of diagnostic tests. Clinical Biostatistics, C.V. Mosby Company, St.Louis.
17. Bashir A, Al-Mullahi A, Welsh G, Hannah, A, Hall A, Foye R. (2000). Effect of staining on artificial lesions measured with the DIAGNOdent. *J Dent Res*, 79, 1174.

Chapter 5: Origins of adaptive optics and use in confocal microscopy

1. Introduction

The ability of confocal and multiphoton techniques to image optical sections deep within biological samples is a major advantage in biology. Unfortunately, as one images deeper within a sample, image degradation increases due to aberrations and scattering. These aberrations are mostly due to refractive index mismatches within the sample which causes a significant reduction in image resolution as well as signal intensity [1 & 2]. The width of the image point spread function increases, and as a result a higher laser power is required to reproduce an image of the same brightness deeper within the sample, with potentially damaging consequences.

There have been many suggestions on how to compensate for these sample induced aberrations. One such method is based on astronomical adaptive optics technology [3] which uses a deformable optical element to counteract for atmospheric aberrations. In astronomical adaptive optics systems, a high powered laser beam excites a sodium layer approximately 100 km up in the atmosphere, which produces an artificial guide star. Using a wavefront sensor, these atmospheric distortions in the guide star's wavefront are measured and the appropriate compensation required by the adaptive element determined. In microscopy, such a 'guide star' cannot be produced to provide information about the aberrating media without possibly damaging or destroying the sample, therefore different methods for determining the adaptive optic shape are needed.

One approach adopted in microscopy is to measure the wavefront error created by the sample, expressing the aberrations present in terms of Zernike polynomials [4]. Unfortunately there are problems with implementing such a technique in a biological sample when imaging at depth. This is due to deterioration of the signal as well as the complexity of the aberrations present. An alternative technique used in confocal and multiphoton microscopy is to optimise the system using an optimisation algorithm routine [5 – 8]. The output of a conventional confocal scan head is directed onto an

actively controlled membrane mirror, before being focused by the microscope objective. By selecting various image properties (e.g. brightness, contrast or resolution), an optimisation algorithm is then used to maximise this value, and compensate for aberrations. It should be noted that the adaptive element could also be placed before the scanning head system.

In this chapter, the historical background, theory, and the use of adaptive optics in counteracting aberrations are examined. In particular the exploitation of adaptive optics in astronomy is discussed and an overview of existing systems presented. This consists of a detailed description of an adaptive optic system incorporating a feedback loop as well as the constituent parts associated with such a system. The use of wavefront sensors (eg. fringe analysis/Shack-Hartmann) are explained as well as the type of adaptive optical element itself such as deformable mirrors (bimorph, piston, and electrostatic) or spatial light modulators (ferromagnetic, twisted nematic).The advantages and limitations associated with each are discussed in detail.

Comparisons between imaging through atmospheric and tissue optics and the problems associated with adapting such a system are also considered. The concept of solution space and the ability of various types of algorithms to find an optimal solution are investigated. The development of an adaptive optic feedback system incorporating an optimisation algorithmic feedback loop for use in confocal and multiphoton microscopy is discussed in detail.

2. Aberrations in microscopy and the need for adaptive optics

2.1 Effect of Aberrations in microscopy

In a paper by Wilson *et al.* [9], the effect of sample aberrations on the confocal axial resolution was theoretically and experimentally tested. It was found that while coma had no effect on the axial response, for an asymmetrical PSF to occur, both spherical and astigmatism had to present in the system. It should be noted that this was for low N.A. objectives (typically less than 0.5N.A). In Sheppard *et al.* [10], the effect of spherical

aberrations were theoretically examined for both small and large refractive index mismatches. A theoretical model relating the first, fifth and higher order spherical aberrations, to the immersion depth, and refractive index mismatch was made. It was also shown experimentally that by changing the effective tube length of the objective, spherical aberrations could be compensated for.

2.2 The need for adaptive optics (AO) in confocal microscopy

As one can see from the literature, spherical aberration, in particular, is the most significant error and is due to mismatches in the refractive indices between the sample and objective. The effect of these aberrations includes the lowering of the resolution and signal intensity of the sample image. There have been many suggestions on how to compensate for this effect. These have included the use of immersion medium objectives that matched the sample's refractive index [11]. In other studies by Meglinski *et al.* [12] (confocal) and Yeh *et al.* [13] (multiphoton) involved the use of glycerol to dehydrate the sample. The removal of water (and replacement of glycerol which has a refractive index of 1.47) resulted in refractive index matching in the tissue structure, thus reducing the level of spherical aberrations present. Other methods tried involved the use of lenses [14], or varying coverslip thicknesses [15], placed into the system that counteract for the spherical aberrations introduced.

All these methods mentioned so far provide either a fixed solution to imaging at a certain depth within the sample or an alteration of the chemical composition of the sample. In order to find a dynamic solution without perturbing the sample, that removes aberrations along a range of optical sections, one must look to the use of adaptive optics (AO) which until recently has only been available for use in astronomy and military applications.

3 Origins and theory of adaptive optics

3.1 Historical background

One of the greatest problems associated with astronomical imaging is astronomical seeing [16] which restricts the resolution due to the distortions introduced by the atmosphere. These distortions originate from turbulence within the atmosphere, which in turn are caused by small temperature variations, leading to micro-variations in both its density and refractive index. These small changes in refractive index (10^{-6}) [17] over large distances (atmosphere depth ≈ 100km) can build up causing large refractive index variations. This results in a significant reduction in image resolution and signal intensity when imaging any celestial object from ground-based telescopes. Before the development of adaptive optic systems, telescopes were placed on top of mountains (e.g. Hawaii, La Palma) to reduce the degree of atmospheric turbulence, or into space (i.e. the Hubble space telescope) to remove atmospheric disturbance altogether. Of course, it seems that space based telescopes would provide the best solution, but difficulties exist in that development and launch of such a system is extremely expensive, as well as the uncertainties involved with space travel at present. Therefore any solution which could overcome astronomical seeing due to the atmosphere as well as improving the detected signal (without increasing telescope mirror sizes) would be of enormous benefit.

The use of adaptive optics was first suggested in 1953 by H. W. Babcock [17 & 18] whereby, with the aid of a wavefront sensor and adaptive element, atmospheric distortions could be detected and compensated. In his original system, Babcock suggested using a revolving knife edge above an orthicon to act as a wavefront sensor, where the electric signal output controlled the electron beam intensity of an electron gun. By aiming the spatially varying electron beam at a mirror coated with a thin layer of oil, it was proposed that the resultant phase introduced by the change in thickness of the film would compensate for aberrations. Although the principle was sound, the technology required to compensate for the turbidity of the atmosphere required several thousand changes per second, which was unachievable at the time. It was not until recent developments in electronics and computing as well as wavefront sensing and

deformable mirrors, that the use of dynamic aberration correction devices has become a practical solution.

3.2 Adaptive optical systems

Most present adaptive optical systems are composed of three main components [19], these are:

1. Wavefront sensor – measures the wavefront of the light to be corrected. This can be either done directly or by calculating the error between the desired and actual wavefront. The signal is then sent to the control system.
2. Control system – translates the signal sent from the wavefront sensor into a signal that can control the adaptive element and thus compensate for aberrations.
3. Wavefront modulator – this is the adaptive element that modulates the wavefront to correct for aberrations.

Any subsequent change to the wavefront modulator is detected by the wavefront sensor via the closed loop (figure 1) which incorporates computer control.

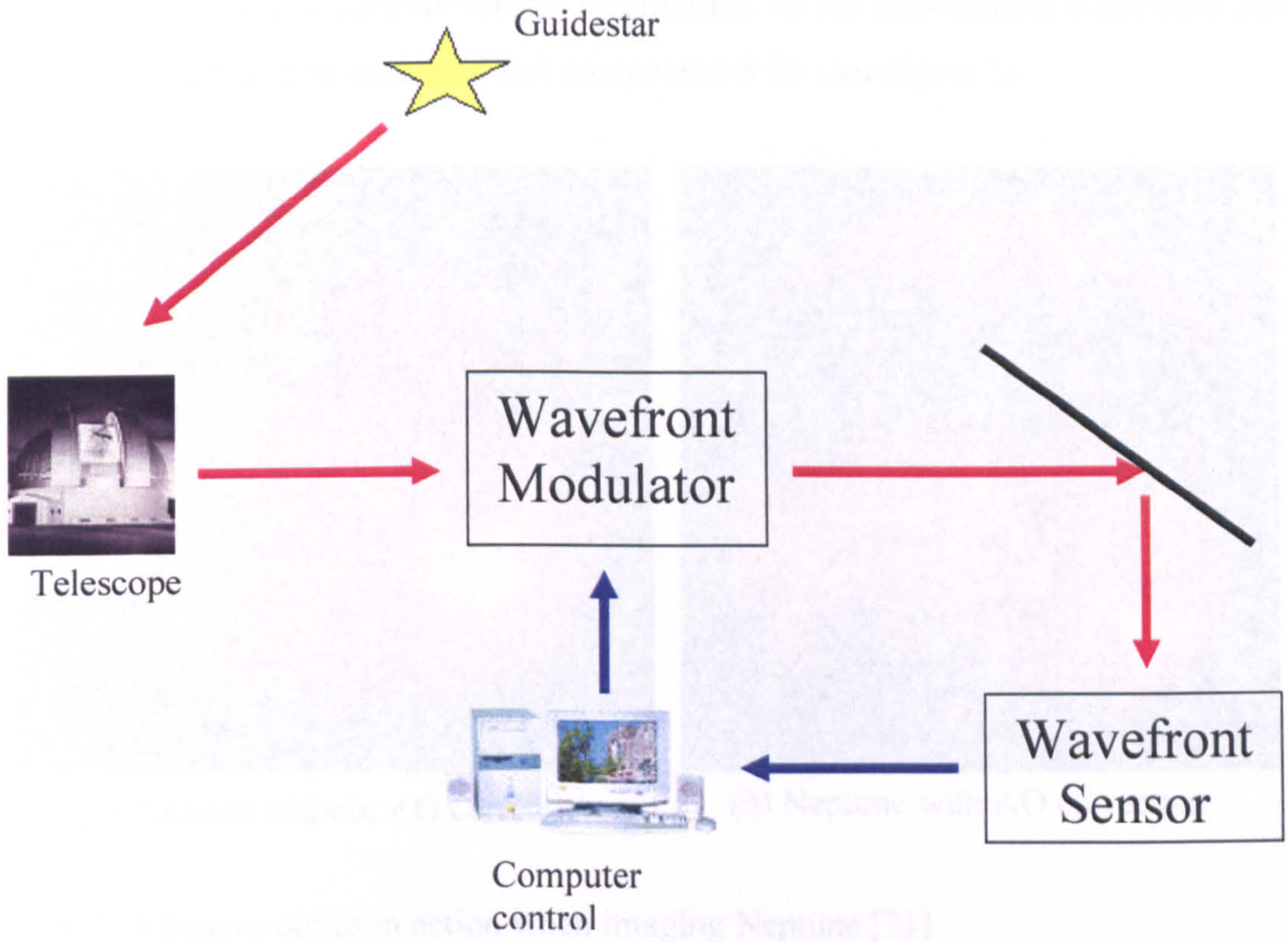

Figure 1: A schematical representation of an astronomical adaptive optical system.

In astronomy, the use of adaptive optics can only function if the wavefront sensor can receive enough light to detect the shape of the wavefront. In the case where light from a galaxy or star is of insufficient intensity, the incoming wavefront from a bright star (known as a guide star), which occupies the same vicinity of the night sky can be measured. Since light from the bright source and the dim source travel through the same region of atmosphere, it is assumed that they are affected by the same atmospherical distortions. Problems exist in that there are not enough guide stars present to provide wavefront information for the whole sky.

One possible solution, first suggested by Linnik [20], was to detect the wavefront shape of a probe or beacon high in the atmosphere, and calculate the degree of wavefront correction required. Presently such a beacon can be produced by focusing a high power pulsed laser beam to excite sodium atoms located high in the atmosphere. By detecting

the emission using a wavefront sensor, information on the atmospheric distortions from the region of sky can be measured and compensated for (see figure 2).

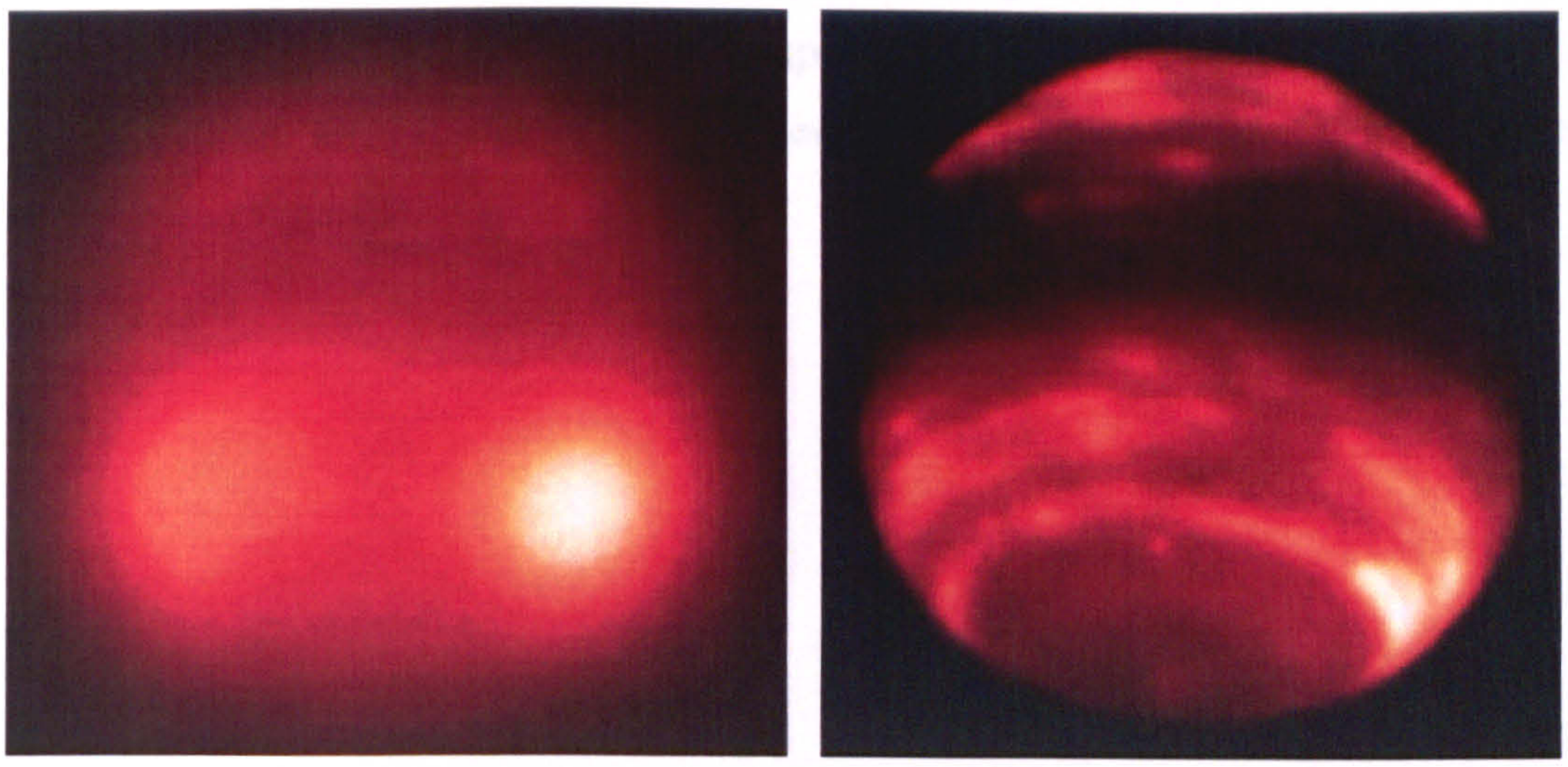

(a) Neptune without AO correction (b) Neptune with AO correction

Figure 2: Adaptive optics in action when imaging Neptune [21].

4. Types of wavefront sensors and adaptive optic elements

4.1. Wavefront sensing techniques

In order to determine the correction required to compensate for aberrations in the system, the wavefront must be first measured. This can be either achieved by measuring the surface profile of the wavefront directly or by calculating the error between the desired and actual wavefront. At present there are a number of different techniques for measuring the wavefront [22], which work on the basis of:

1. Geometrical – in which optical ray path variations are measured which are dependent on propagating wavefront phase profile.
2. Interferometric – determines the wavefront through the coherent mixing of a reference wavefront with the incoming wavefront to produce an interferogram.
3. Phase retrieval – this method of wavefront measurement is based on intensity distributions either side of the focal plane being related to the phase profile.

4.1.1 Geometrical

There are a number of different geometrical methods that can be used to measure the incoming wavefront with the most commonly used being the Shack-Hartmann technique [23 & 24]. The Shack-Hartmann sensor employs the use of a two-dimensional lenslet array and detector array (usually a CCD camera) to measure the local tilt in the incoming wavefront (see figure 3).

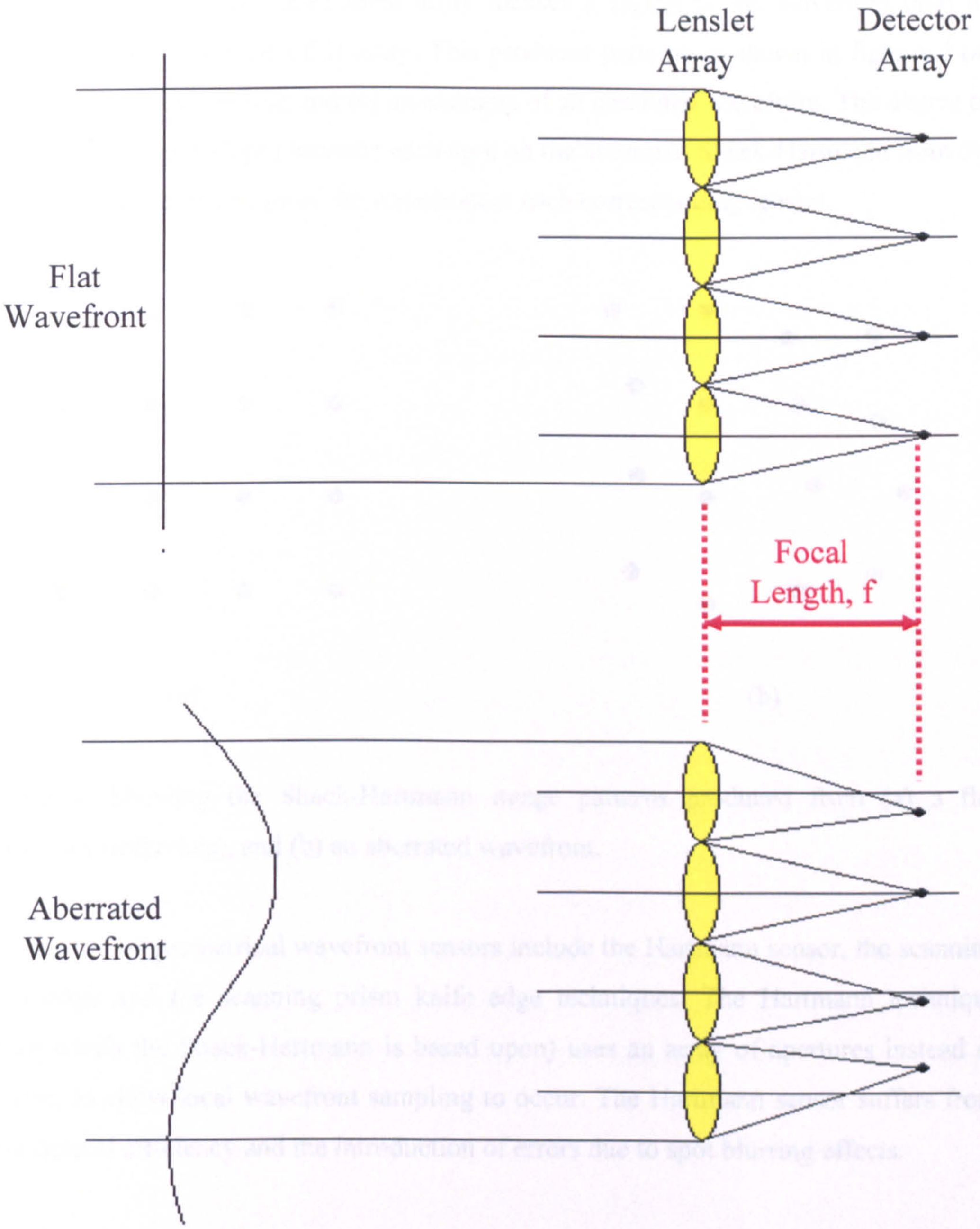

Figure 3: The schematical set-up of a Shack-Hartmann sensor for a plane and aberrated wavefront.

Each lenset in the two dimensional array focuses a region of the wavefront onto its corresponding cell on the CCD array. This produces patterns as shown in figures 4 (a) and (b) for a flat wavefront and (b) an example of an aberrated wavefront. The degree of spatial variation (or slope) between each spot on the aberrated Shack-Hartmann from the centroid indicates the slope of the wavefront at each corresponding lenslet.

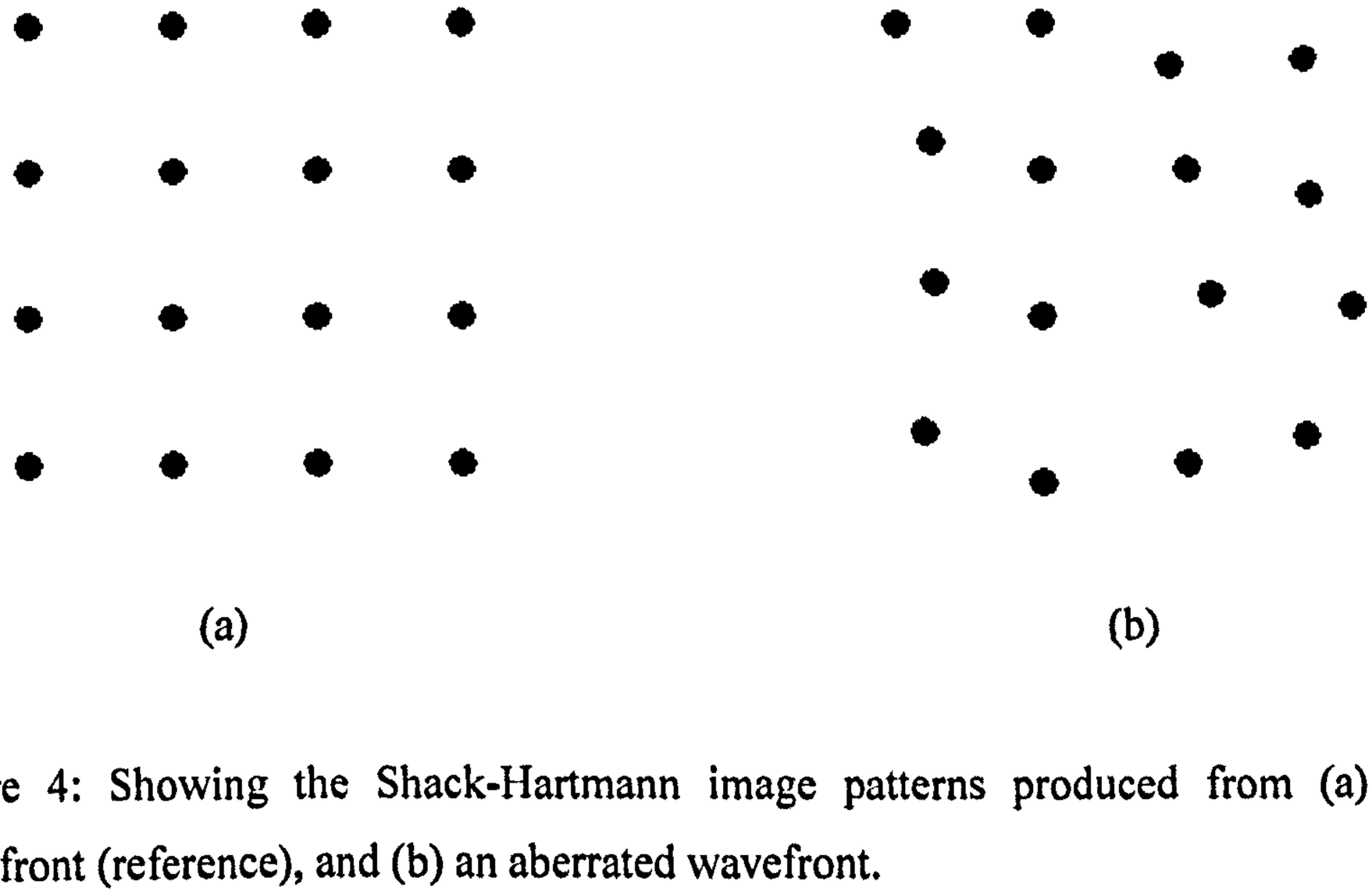

(a) (b)

Figure 4: Showing the Shack-Hartmann image patterns produced from (a) a flat wavefront (reference), and (b) an aberrated wavefront.

Other types of geometrical wavefront sensors include the Hartmann sensor, the scanning knife-edge and the scanning prism knife edge techniques. The Hartmann technique (from which the Shack-Hartmann is based upon) uses an array of apertures instead of lenslets to allow local wavefront sampling to occur. The Hartmann sensor suffers from poor optical efficiency and the introduction of errors due to spot blurring effects.

The scanning knife-edge technique (developed from the Foucault knife-edge test) uses two orthogonally placed knife edges which perform a two-dimensional scan over the focal plane of the optical system. From this, the shape of the wavefront can be determined. However due to the inherent slowness of the scan, the system cannot be used in highly dynamic systems. The scanning prism system is a variation of the

previously mentioned technique, with the knife-edges being replaced with thin obtuse triangular prisms.

4.1.2 Interferometric

In interferometic techniques, the incoming wavefront is coherently mixed with a reference wavefront to produce an interferogram. The most useful of these (for wavefront measurement) is the shearing interferometer, in which, with the use of a shearing device, two copies of the wavefront are produced at the pupil plane. These two wavefronts are shifted with respect to each other, which when subsequently mixed onto a detector produce an interferogram from which phase information can be obtained. The use of shearing allows an interferogram to be produced without the need for a plane wave reference (self-referencing) [25].

Although there are many types of shearing interferometers currently available, depending on how the shear is introduced [22 & 26], a generalised shearing interferometer will be discussed (see figure 5). The incoming wavefront is separated into two constituents each shifted from the other by a shear distance defined by the shearing device used. The interference condition associated for each pixel on the detection array, for a small shear separation s, is dependant on the phase difference between each of the sheared wavefronts. From these phase difference measurements, the slope of the wavefront can be deduced, provided that it has been normalised with the shear distance. To produce a complete wavefront, two interferograms must be produced where the shear distance is orthogonal.

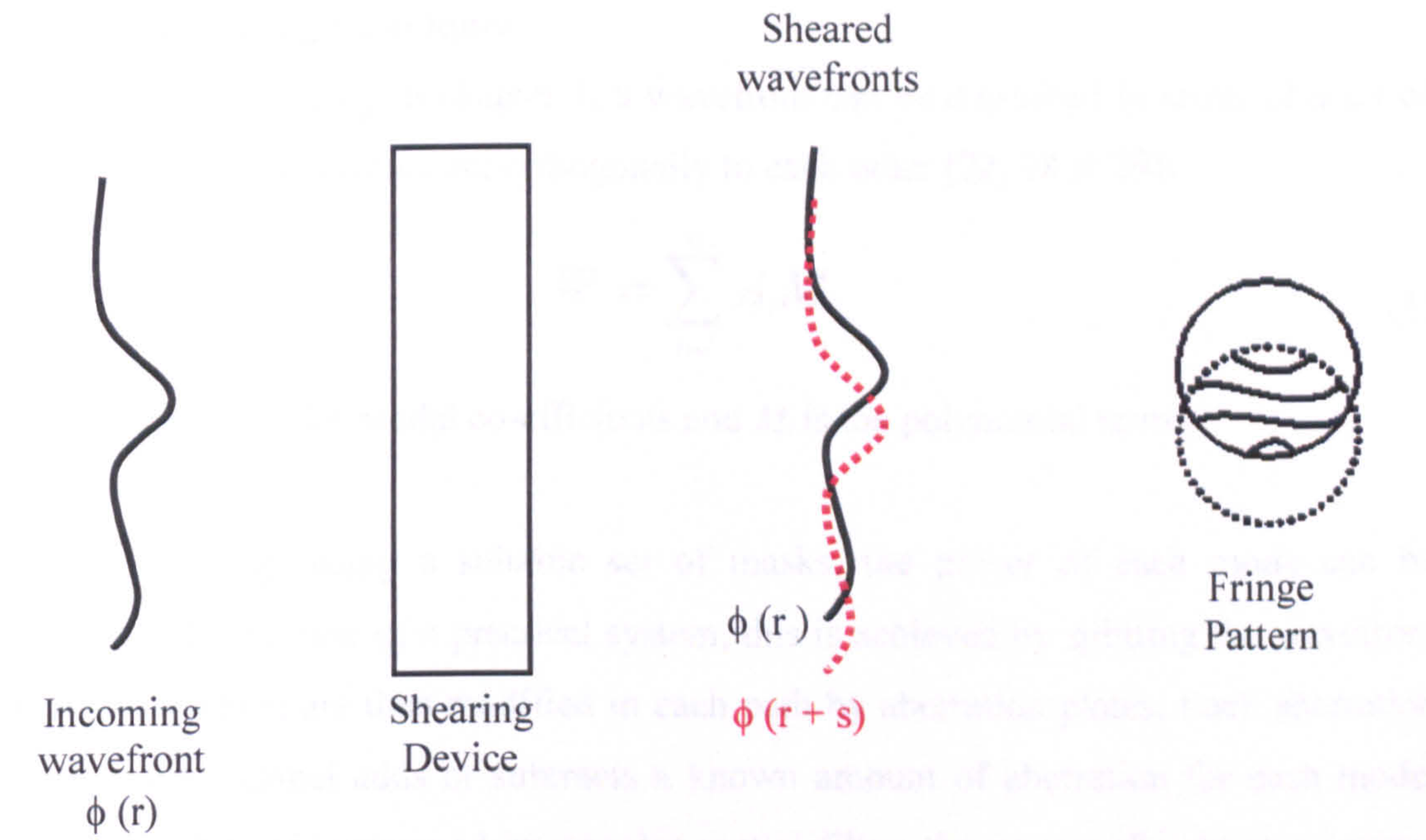

Figure 5: Showing shearing interferometry.

4.1.3 Phase retrieval

Phase retrieval operates on the principle that by measuring intensity distributions at either side of the focal plane, the phase profile can be estimated. There are a wide range of techniques currently available to perform this operation [27]. The two techniques that will be discussed are (a) the phase diversity and (b) the wavefront curvature sensing techniques. In the phase diversity technique, two intensity distributions are measured, with one of them having undergone an identified quantity of optical aberration. Using iterative algorithms, the wavefront phase can be estimated from these two intensity distributions. In the wavefront curvature sensing technique, the curvature of local wavefront is calculated by measuring the difference between two intensity distributions place symmetrically about the pupil or image plane of the system. Using the wavefront curvature intensity transverse equation, the wavefront phase can be determined.

4.1.4 Modal sensing techniques

As explained previously in chapter 1, a wavefront can be described in terms of a set of modes (i.e. Zernikes) which act orthogonally to each other [22, 28 & 29]:

$$W = \sum_{i=l}^{n} A_i M_i \tag{1}$$

where A_l are the scalar modal co-efficients and M_l is the polynomial terms.

In modal sensing, using a suitable set of masks, the power of each mode can be determined. In the case of a practical system, this is achieved by splitting the wavefront into n-paths which are then modified in each path by aberration plates. Each aberration plate in each channel adds or subtracts a known amount of aberration for each mode. Using a number of lenses and an annular spatial filter, the power of light at a narrow band-pass of spatial frequencies is measured (in terms of voltage V) for the positive and negative aberration to give:

$$A = \frac{V_i^+ - V_i^-}{V_o} \tag{2}$$

where V_o is the power of the light when no negative or positive aberrations have been applied.

4.2 Wavefront modulators

In any adaptive optical system, wavefront modulators are used to spatially generate a phase change onto the wavefront. This can be achieved in a wide range of different ways using various types of mirror and liquid crystal display technologies. Figure 6 shows a schematic of the different type of wavefront modulation techniques currently available.

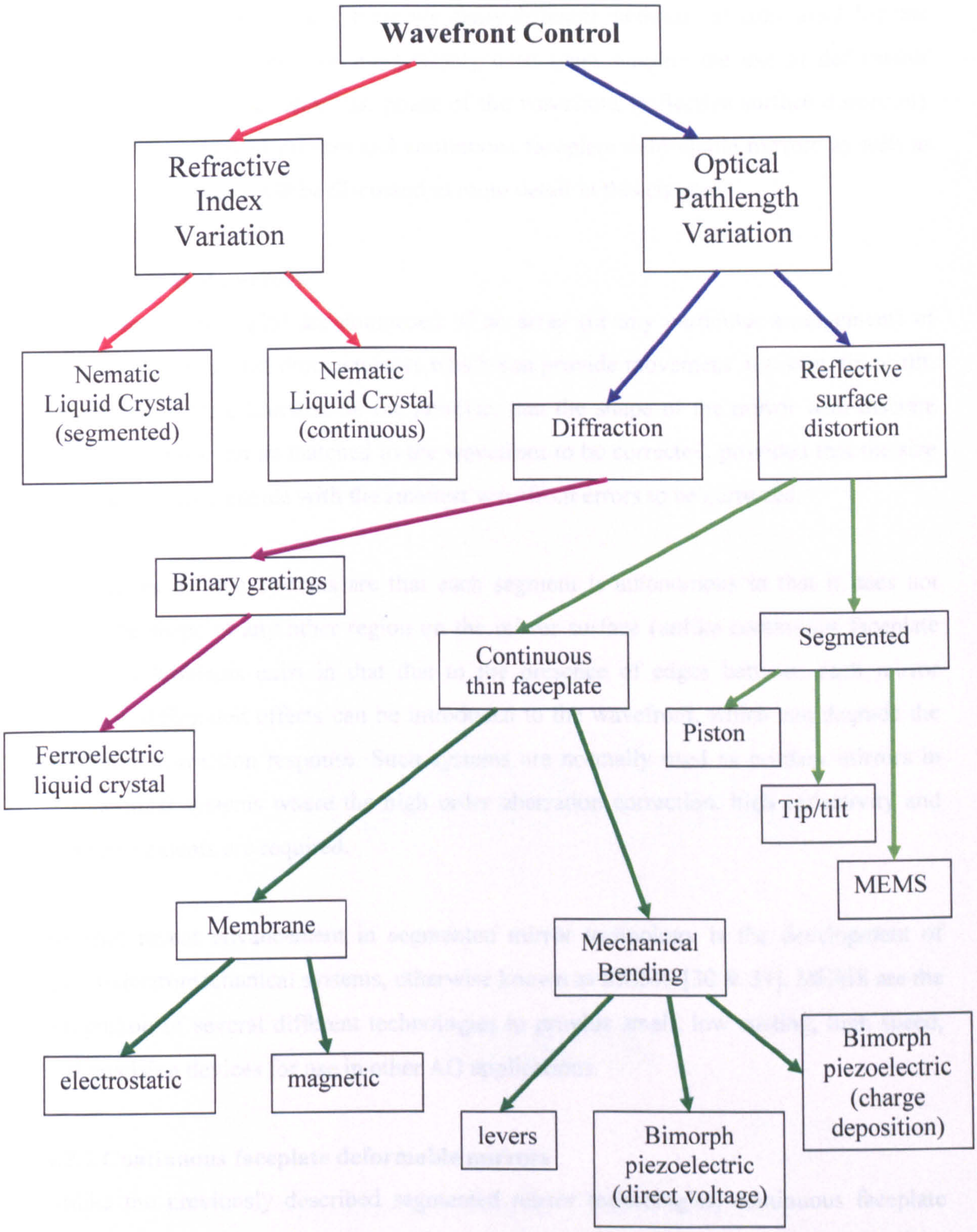

Figure 6: A schematic showing of the origin of several wavefront modulators [30].

As one can see from figure 6, there are many different methods currently available that can alter the wavefront. The most widely used types employ the use of deformable mirrors to control and adjust the phase of the wavefront (reflective surface distortion). The use of segmented mirrors and continuous faceplate deformable mirrors as well as light crystal displays will be discussed in more detail in this chapter.

4.2.1 Segmented mirrors

Segmented mirrors [30] are composed of an array (or any particular arrangement) of small mirrors mounted onto actuators which can provide movement in piston, tip or tilt. Segmented mirrors function on the premise, that the shape of the mirror with discrete mirror segments can be matched to the wavefront to be corrected, provided that the size of the segments coincide with the smallest wavefront errors to be corrected.

Advantages in such systems are that each segment is autonomous in that it does not affect the shape at any other region on the mirror surface (unlike continuous faceplate systems.) Problems exist in that due to the presence of edges between each mirror segment, diffraction effects can be introduced to the wavefront, which can degrade the wavefront correction response. Such systems are normally used as primary mirrors in astronomical systems where the high order aberration correction, high reflectivity and large movements are required.

Another recent advancement in segmented mirror technology is the development of micro-electromechanical systems, otherwise known as MEMS [30 & 31]. MEMS are the integration of several different technologies to provide small, low costing, high speed, and precision devices for use in other AO applications.

4.2.2 Continuous faceplate deformable mirrors

Unlike the previously described segmented mirror technologies, continuous faceplate mirrors (as the name suggests) provide a continuous deformation over the whole of the mirror. This is known as a modal correction and continuous mirrors are generally more

appropriate for situations where corrections in low-order aberrations are required. In this section, the design and use of two of the most common types of continuous deformable mirrors, namely (a) bimorph and (b) membrane, will be discussed in detail.

4.2.2.1Bimorph (piezoelectric) mirrors

A bimorph mirror operates on the principle, that by applying a voltage through a piezo-electric plate, this in turn causes the plate to change thickness. When bonded to a passive faceplate substrate (which has the reflective surface), the change in thickness of the piezoelectric plate results in a bending moment. Figure 7 shows the operation of a biomorph mirror. Since the use of piezo-electric technology in adaptive optics in a simplified layered design was first suggested close to 30 years ago [32 & 33] there have been numerous advancements in the development of such technology. Today biomorph mirror designs are composed of many layers, usually containing more than one piezoelectric plate, which allows deformations to occur in both directions and offers many microns of movement.

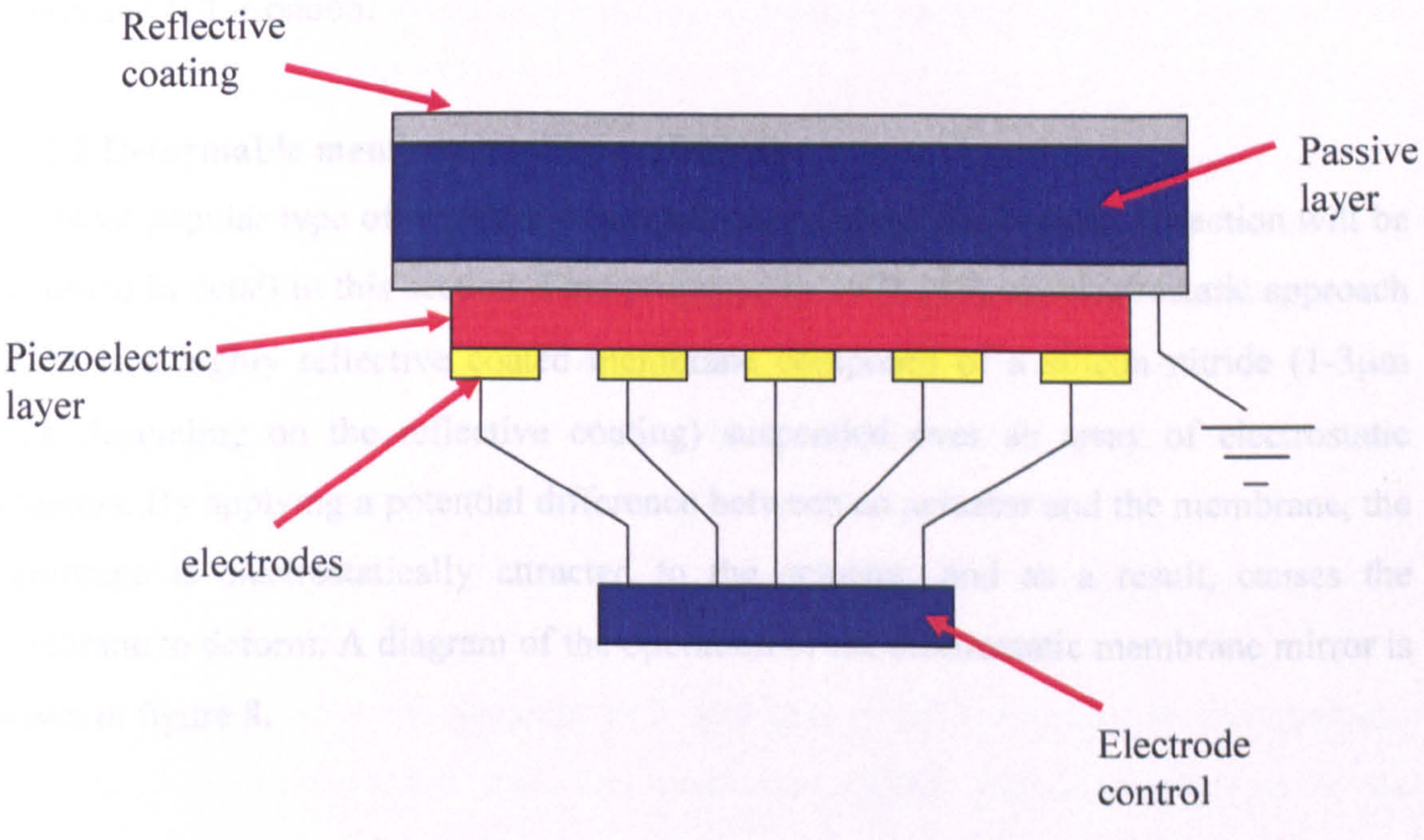

Figure 7: Showing the diagrammatical representation of a bimorph mirror.

Bimorph mirrors offer several advantages over other mirrors currently available. These include their sturdiness and high damage threshold (which can be enhanced with water cooling techniques [34]) which makes them suitable for use in high laser powered applications [35–37]. Other advantages include their relatively large stroke (tens of microns) as well as their ability to manipulate the reflective surface in both the inward and outward direction.

Of course, such a mirror is not without its problems, which include its relatively high cost (in comparison with membrane devices) as well as hysteresis (~10%), which is inherent of all piezo-electrical systems. It should be noted that at present, with the more continued development of this technology, including mapping techniques into hysteresis [38], these limitations are being addressed. Bimorph mirrors have been described as the BMW 7 series of adaptive optic modulation techniques [39].

At present several commercially available bimorph mirrors can be bought from IPLIT in Russia and ICL London.

4.2.2.2 Deformable membrane mirrors (DMM)

The most popular type of membrane mirror incorporating electrostatic attraction will be discussed in detail in this section. First proposed in 1977 [40], an electrostatic approach DMM is a highly reflective coated membrane composed of a silicon nitride (1-3μm thick depending on the reflective coating) suspended over an array of electrostatic actuators. By applying a potential difference between an actuator and the membrane, the membrane is electrostatically attracted to the actuator, and as a result, causes the membrane to deform. A diagram of the operation of the electrostatic membrane mirror is shown in figure 8.

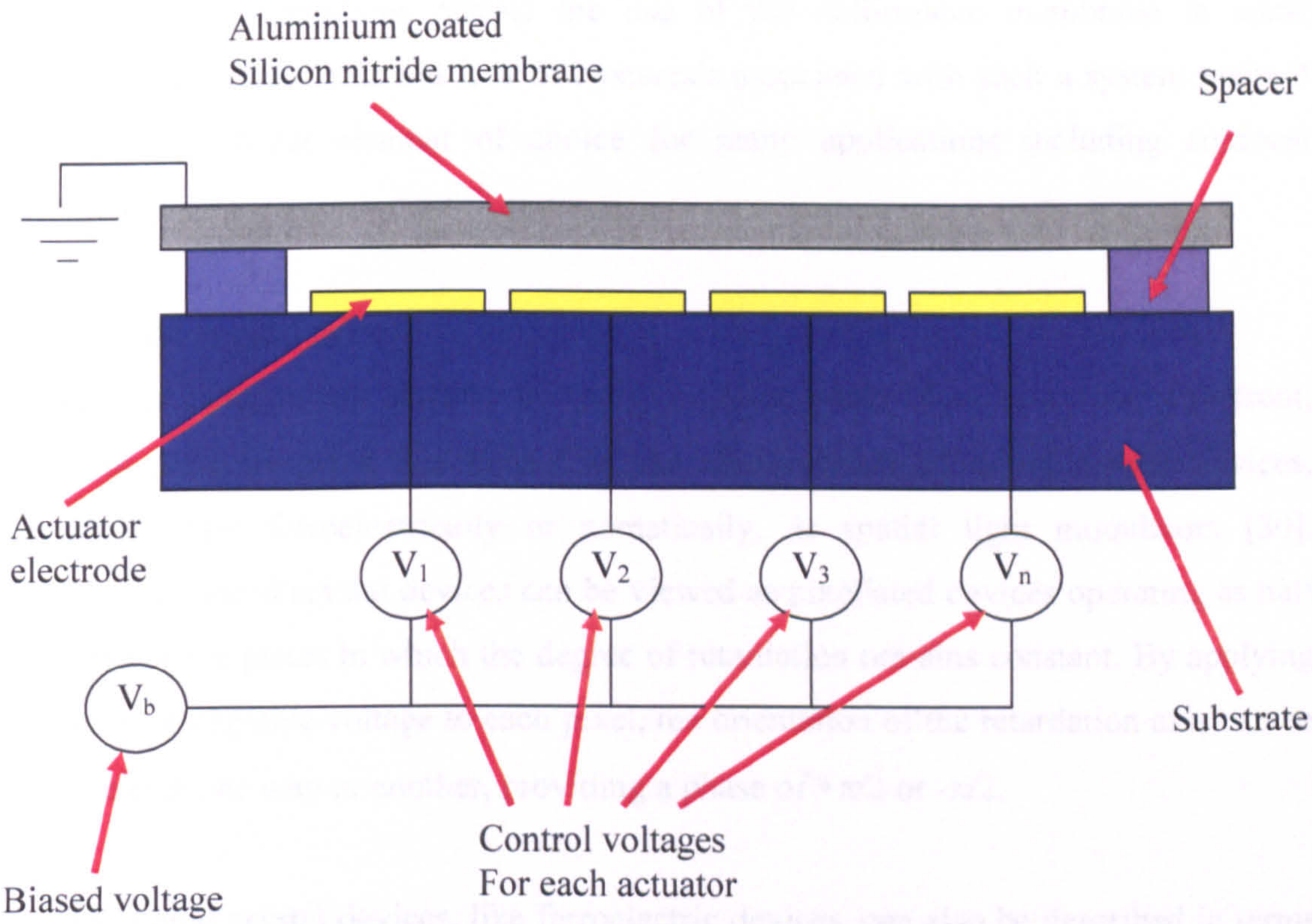

Figure 8: A diagram of the operation of the electrostatic membrane mirror (design taken from Okotech) [41 & 42].

Current developments of electrostatic membrane mirrors from companies such as Okotech have revolutionised the use of adaptive optics in a wide range of new applications. This is due to their low cost in fabrication when compared to other available wavefront modulation techniques. Although there are of course some problems associated with the technique which includes the use of electrostatic attraction only allowing the mirror membrane to be pulled. This can be addressed by the utilization of pre-biasing, (where the wavefront is altered before making contact with the adaptive element), which allows the apparent push and pull of the membrane to be simulated. Other limitations associated with the membrane mirror include restrictions in the maximum deformation that it can achieve in comparison with its bimorph counterpart, as well as possible thermal deformation issues (which are particularly important in medium and high power laser use) [30, 43 & 44].

Although these limitations restrict the use of the deformable membrane in some applications, the low cost and lack of hysteresis associated with such a system make it the adaptive optical element of choice for many applications including confocal microscopy.

4.2.3 Liquid crystal devices

As well as using mirror devices to apply localised phase changes to the wavefront, presently much research has gone into the development of liquid crystal devices, operating either ferroelectrically or nematically, as spatial light modulators [30]. Ferroelectric liquid crystal devices can be viewed as pixellated devices operating as half or quarter wave plates in which the degree of retardation remains constant. By applying a positive or negative voltage to each pixel, the orientation of the retardation axis can be shifted either one way or another, providing a phase of $+\pi/2$ or $-\pi/2$.

Nematic liquid crystal devices, like ferroelectric devices, can also be described in terms of linear waveplates. In the nematic case, the retardation orientation axis is fixed, but the degree of retardation or birefringence is dependant on the voltage applied to the pixel. In comparison with mirror devices, nematic liquid crystal devices are somewhat analogous to piston only segmented mirrors, in which the phase at each pixel can be altered to compensate for the wavefront. Although the phase change possible in any individual nematic pixel is limited to 2π, using phase wrapping, the global phase change that can be applied to a wavefront can be much greater than 2π and is only limited by the resolution of the nematic liquid crystal SLM itself. Present problems with such systems exist due to the slow response rate (15Hz) as well as the low optical efficiency (typically ~30%).

At present several companies are in the process of developing SLMs that can hopefully compete with the fast-switching times associated with mirror system. Companies such as Hamamatsu, Holoeye, and Boulder presently produce commercially available spatial light modulators systems.

5. Present uses for adaptive optics

Today the use of adaptive optics in astronomy can be seen as a mature and established technology. Due to the development of inexpensive systems, adaptive optical systems are being exploited in a wide range of applications in medicine and industry. A number of these applications will be discussed in more detail.

5.1 Ophthalmology

Presently, there is great interest in AO to assess and monitor patient vision using wavefront sensing and modulation techniques [30, 45 – 49]. When the technology is fully developed it should greatly decrease the time required to determine the degree of the patient's vision, as well as allowing vision measurement in cases where patient feedback is not available (i.e. new born babies). In the future, such technology will allow for the development of contact lenses which could compensate for higher order aberrations such as spherical. Contact lenses and glasses currently available only compensate for defocus and astigmatism.

These aberration compensation techniques are also being used in order to improve the resolution when imaging the retina of the eye. Improvements in retinal imaging (figure 9 Rochester on AO in operation) [49] can increase the rate of diagnosis of many diseases such as glaucoma and diabetes, which when detected at an early stage can be treated much more easily. Adaptive optics is also being used to examine and assess the cornea and to detect the presence of cataracts.

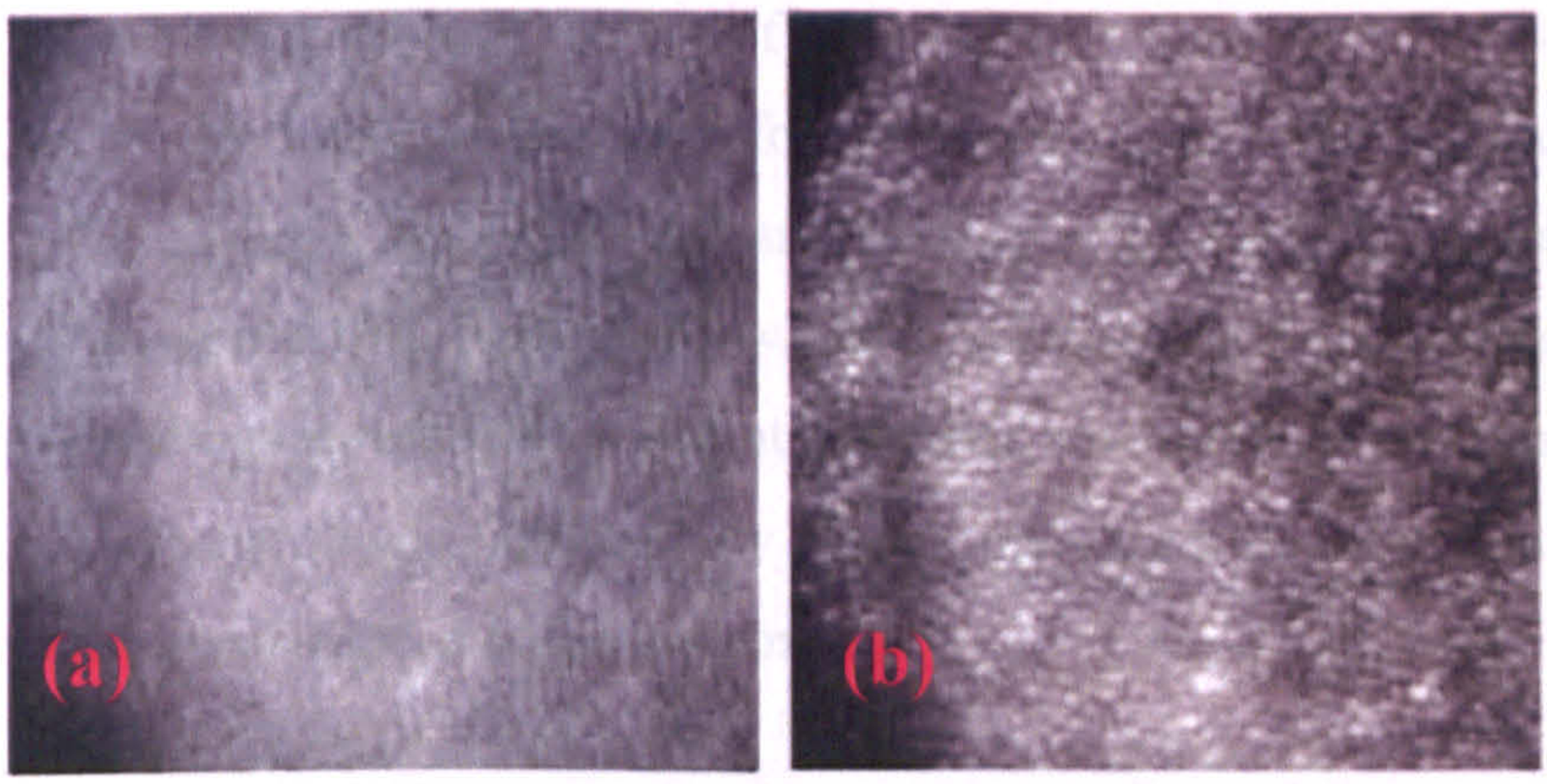

Figure 9: Images of the same retinal location (a) without correction of higher order aberrations and (b) with correction of higher order aberration using the adaptive optics system developed at the center for visual science [49].

5.2 Lasers (Intra-cavity)

At Present, laser systems are being developed which incorporate AO within the laser cavity to control the output transverse mode. Due to problems involved with placing a wavefront sensor intra-cavity, the wavefront modulator is controlled via an iterative approach (similar to the approach used in our AO system) that optimises for a particular parameter (i.e. beam profile or output power). These systems allow the user to compensate for effects caused by thermal lensing within the gain medium [43, 44, 50 & 51] and can be used to control the TEM output mode in cases where modes other than TEM_{00} are required.

5.3 Lasers (Extra-cavity)

There is currently a great deal of research into using adaptive optics to control characteristics of the laser after the laser beam has exited the laser cavity. These include beam quality control for material processing and lithography techniques, as well as pulse shaping where the energy distribution and length of a laser pulse can be manipulated [52].

Advancements are being made in the use of adaptive optic systems in free-space optics for wireless high speed data transfer of information from one building to another (see figure 10). In the case of a highly built-up area such as a city where communication via fibre-optics is inappropriate, high-speed wireless communication using near-infrared light between buildings is restricted due to atmospheric conditions. When completed, the free space AO system should substantially reduce the extent of information loss and increase the transmission speed of the system.

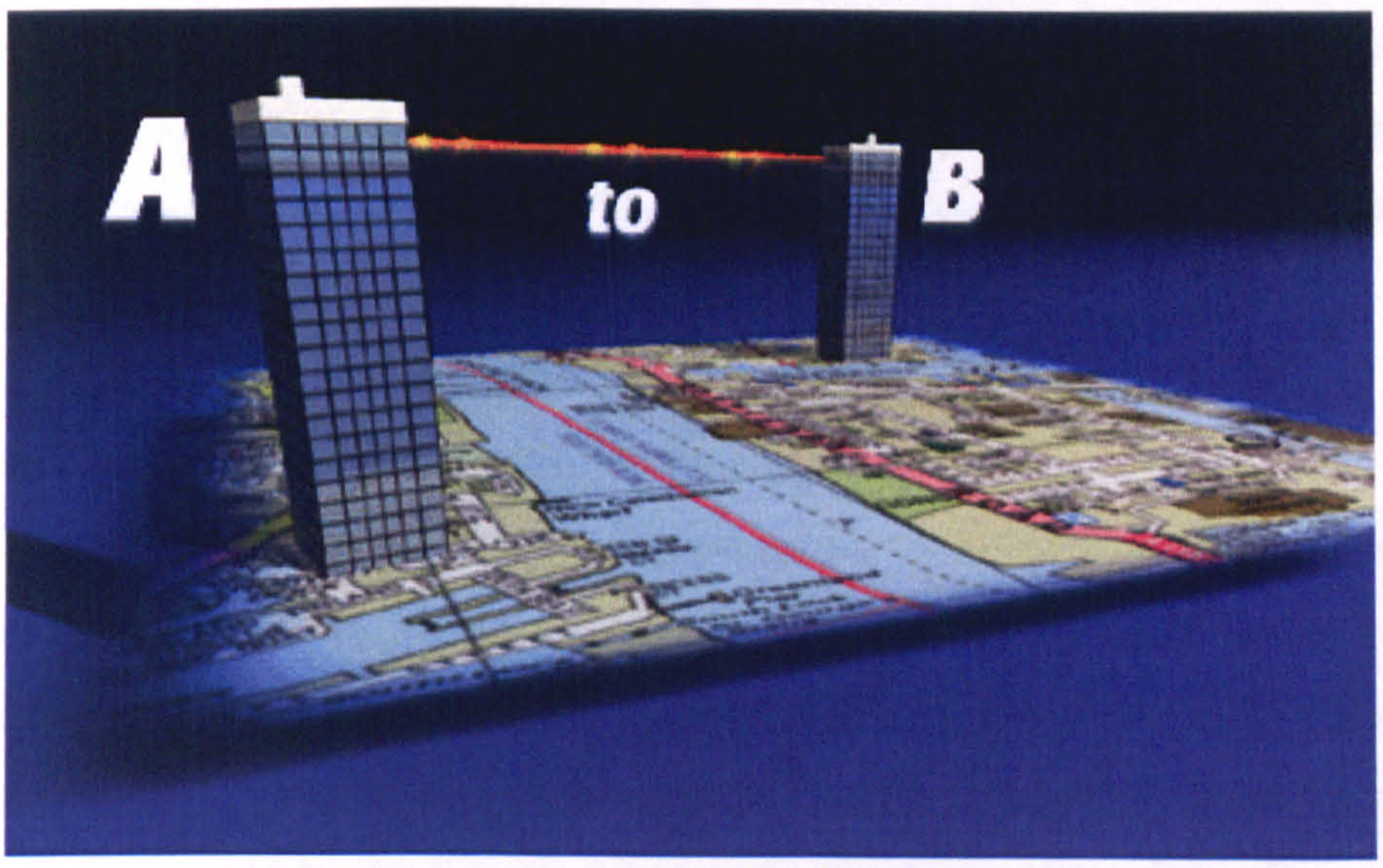

Figure 10: Showing an illustration of a free space optical system [53].

Adaptive optical systems are also being developed for use in high powered lasers in laser fusion experiments (National Ignition Facility, USA) and other high powered laser applications (HELEN in the UK, and LULI in France) [54]. In these experiments, AO is being used to compensate for thermal distortions and improve the overall laser efficiency.

5.4 Defence

Many present defence applications include the research into enhanced imaging systems for surveillance, as well as improving beam delivery which is used in missile targeting and tracking devices [54].

5.5 Three dimensional imaging

Current research using AO in three-dimensional imaging include confocal microscopy for biological imaging (discussed in much more detail later in this chapter) as well as new optical data storage techniques [55]. These emerging new optical storage techniques rely on multiple layers at various depths within a material to provide high storage space. AO is used to maintain the size of the focal spot at different depths through material for the writing and reading of information.

6. The use of adaptive optics in confocal systems

In one of the original papers to theorise the use of AO in a confocal system, Booth *et al.* [56] proposed the use of an "adaptive element". This would have the ability to distort the scanning laser beam before the sample in order to correct for aberrations in the sample. In Neil *et al.* [57], it was shown experimentally that aberration correction using an adaptive element could be used in microscopy. In this case a wavefront sensor was used to measure aberrations of a light beam, with a spatial light modulator as the adaptive system providing correction. In other papers, wavefront sensing devices were used to characterise the aberrations present in biological samples, which could be translated into Zernike terms for aberration correction [58 – 60].

There are of course problems associated with implementing wavefront sensing and modulating techniques when imaging in-depth into a biological sample. This is due to deterioration of the signal as well as the complexity of the aberrations present. As mentioned previously, wavefront sensing techniques require enough light to detect the shape of the wavefront. In confocal systems particularly when used in fluorescence, the collected light may not be of sufficient intensity to make an accurate determination of

the wavefront shape. Particularly in biological samples, the use of a 'guide star' cannot be produced to provide information about the aberrating media. Any attempt to produce one similar to that used in astronomy would no doubt damage or destroy the sample. Therefore other methods of wavefront correction, such as trial and error optimisations on certain aspects of the image quality, can be used.

6.1 Optimisation routines

An alternative technique used in confocal and multiphoton microscopy is to optimise the system using an optimisation algorithm routine. The output of a conventional confocal scan head is directed onto an actively controlled membrane mirror, before being focused by the microscope objective. By selecting various image properties (e.g. brightness, contrast or resolution), an optimisation algorithm can be used to maximise this value, and compensate for aberrations. It is important to note, this type of adaptive optic system can be regarded as a blind system in that no aberration information is required to complete optimisation.

6.2 Concept of solution space

If one considers a one dimensional problem where there are 20 possible outcomes for a single variable, x, the best solution can be easily found by checking each outcome and making a determination. When there are two variables (2 dimensions), named x and y, if there are 20 possible outcomes for each variable, there are 400 possible solutions. As the number of variables or dimensions increase, the possible number of solutions is defined by the multiplication of the possible number of solutions for each variable, such that the total number of solutions equals x^n, where x is the number of possible outcomes for each variable and n is the number of variables (dimensions).

The adaptive optic modulator used in this investigation is the 15mm diameter, 1μm thick silicon nitride membrane Okotech mirror (mounted on 37 individual electro-static actuators), where each actuator can be individually controlled at voltages of 0 – 200V in increments of 1V. This presents a situation where there are in effect 200^{37} (~1.4×10^{85})

possible solutions. By putting this value in some sort of context (the entire earth is composed of 10^{50} atoms), one can realize just how gigantic this number actually is. In order to search this solution space, for the best solution, an optimisation routine is required. Optimisation routines can be divided into three classes as shown in figure 11.

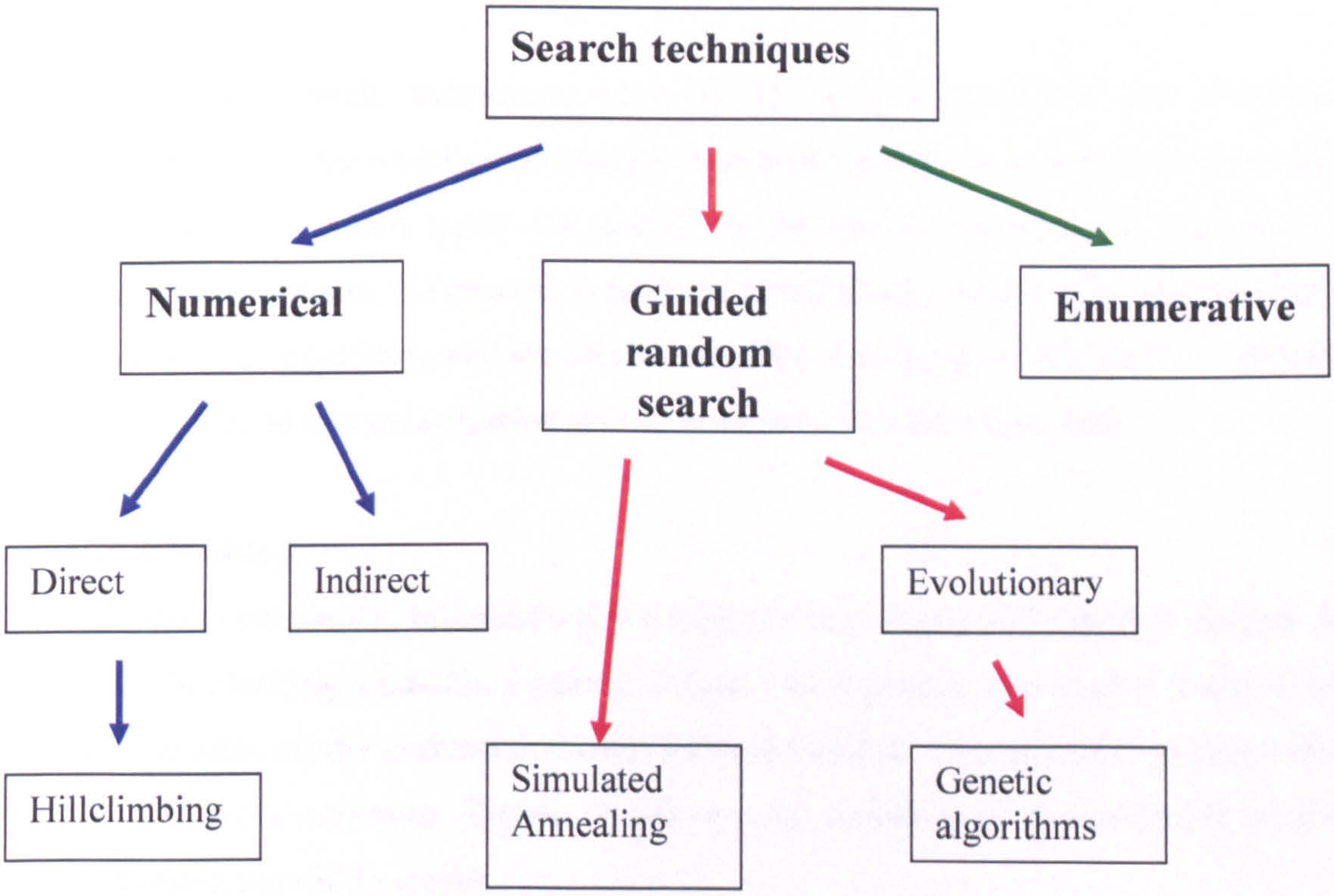

Figure 11: Showing various search routines [60].

In enumerative techniques, every position in solution space (or every possible solution) is checked in turn. As mentioned previously, this is not a practical solution in the adaptive optic case due to the shear size of the solution space itself. Even neglecting time restraints due to the time taken to physically change the adaptive optical element and to record the optimisation factor, at present computing speeds, enumerative methods would require ~1 x 10^{69} years to complete. (This is based on a computer with 4 GHz processing speed where a new solution is checked every 10 cycles.)

Numerical methods, which can be divided into either direct or indirect approaches, function by examining solution space for the best solution. In the indirect situation, the search operates by searching for maxima (i.e. peaks of the slope). In the direct method, the search follows the gradient until it reaches a peak. In the numerical situation, a solution is found when the solution itself satisfies a certain set of criteria.

Guided random search techniques, such as the genetic algorithm and simulated annealing methods, are based on previously mentioned enumerative methods but contain certain parameters which guide the search to the optimal solution. In the case of evolutionary algorithms, the process is guided in evolutionary terms. The process of hill climbing, genetic algorithm, and simulated annealing search algorithms used to optimise the mirror shape in this investigation will be discussed in much more detail.

6.2.1 Hillclimbing

As mentioned previously, hillclimbing is a type of direct numerical search technique. In a simple hill climbing situation, a path is chosen which gives an increase in value of (or positive gradient of) the parameter chosen for optimisation. The optimisation ends when the path reaches a maximum. Figure 12 shows a one dimensional representation of how a hill climbing algorithm works.

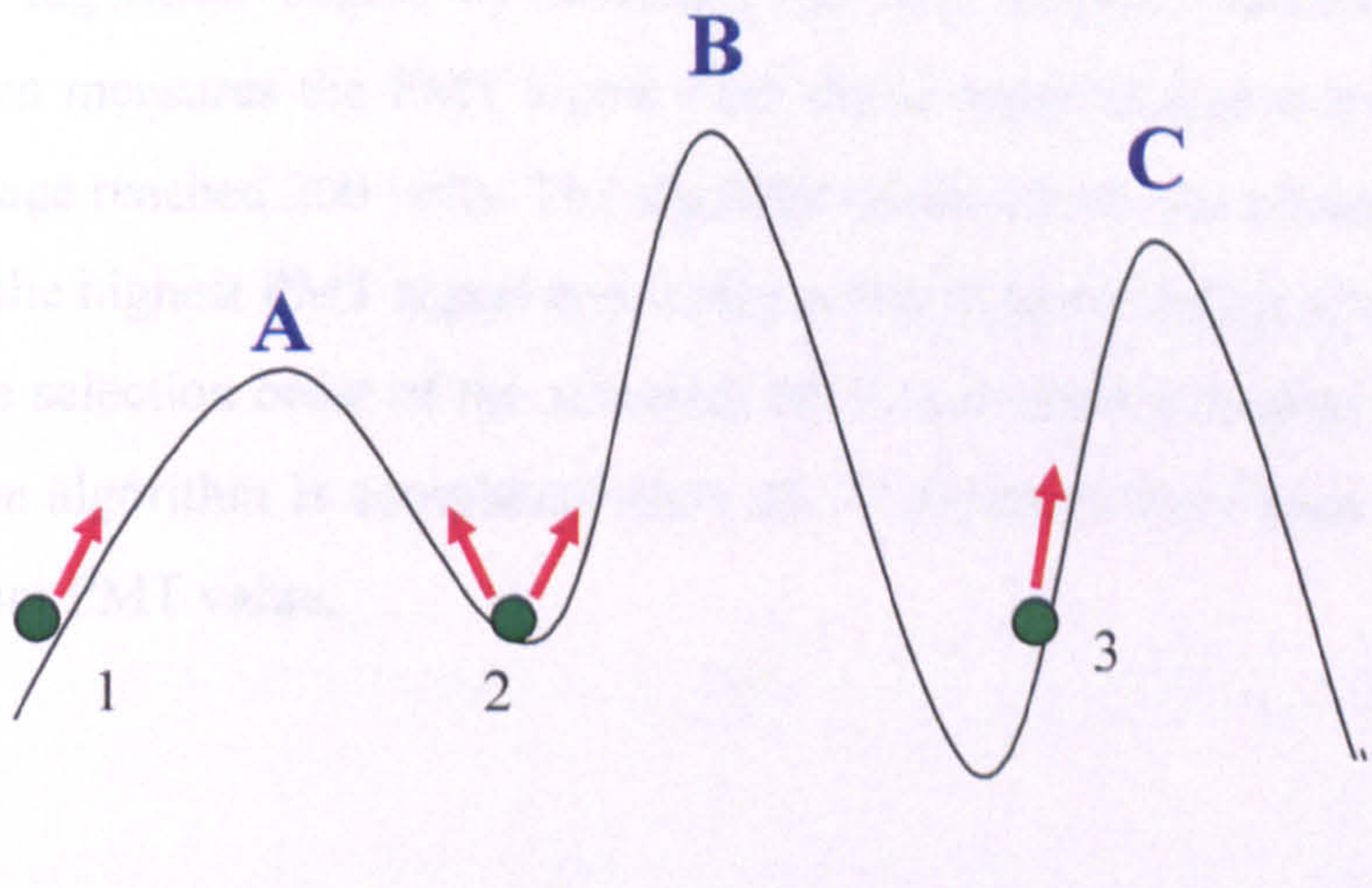

Figure 12: the hillclimbing algorithm operating in a 1-D representation of solution space.

In the one dimensional representation of solution space shown in figure 12, three peaks are highlighted as A, B and C respectively. In the three arbitrary starting conditions shown, only (2) has any chance of finding the global maximum in this example, and even this is dependant on the starting direction due to its position at the base of a trough. When beginning the algorithm at positions (1) or (3), local maxima of A and C are found respectively. Therefore in the case of a hillclimbing algorithm, only local maxima are generally found, which is dependent on the starting position of the optimisation and the shape of solution space being optimised; i.e. in the case where there is only one peak, with solution space being generally smooth, the maximum found would in fact be a global maximum.

The hillclimbing algorithm used in this investigation is in fact a version that was modified for coding simplicity and speed in mind. The modified hillclimbing function optimised the signal output of the photomultiplier tube by finding the maximum for each actuator (or dimension) in turn. This is in contrast with normal hillclimbing algorithms that would have instead followed the gradient of the local region of solution space. A schematical representation of the modified hillclimbing algorithm is shown in figure 13.

Starting with a flat DMM mirror shape (where all actuators are set at 0 volts), the Hillclimbing algorithm begins by selecting the first actuator (central actuator). The algorithm then measures the PMT signal with the actuator at incremental voltage steps until the voltage reached 200 volts. The algorithm then adjusts the actuator to the voltage which gives the highest PMT signal and with another actuator being selected the cycle is repeated. The selection order of the actuators follows an outward spiral pattern from the centre and the algorithm is completed when all 37 actuators have been adjusted to give their maximum PMT value.

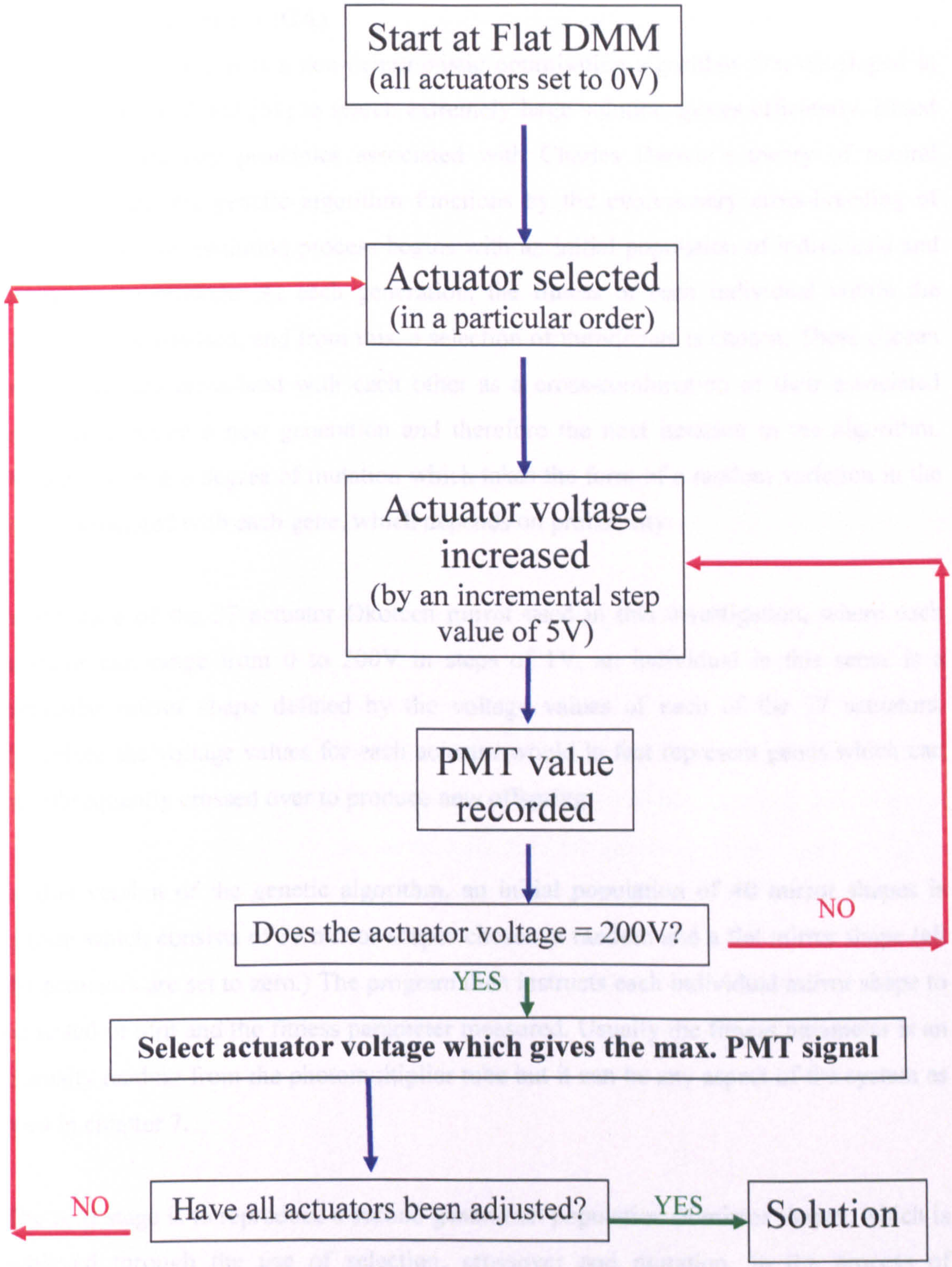

Figure 13: Showing the operation of the modified hillclimbing algorithm.

6.2.2 Genetic algorithm (GA)

The genetic algorithm is a non-deterministic optimisation algorithm first developed in 1975 by John Holland [61] to search extremely large solution spaces efficiently. Based on the evolutionary principles associated with Charles Darwin's theory of natural selection [62], the genetic algorithm functions by the evolutionary cross-breeding of populations. The evolution process begins with an initial population of individuals and occurs in generations. At each generation, the fitness of each individual within the population is assessed, and from this, a selection of individuals is chosen. These chosen individuals are cross-bred with each other as a cross-combination of their associated genes to produce a new generation and therefore the next iteration in the algorithm. Added to this is a degree of mutation which takes the form of a random variation in the value associated with each gene, which depends on probability.

In the case of the 37 actuator Okotech mirror used in this investigation, where each actuator can range from 0 to 200V in steps of 1V, an individual in this sense is a particular mirror shape defined by the voltage values of each of the 37 actuators. Therefore the voltage values for each actuator would in fact represent genes which can be subsequently crossed over to produce new offspring.

In this version of the genetic algorithm, an initial population of 40 mirror shapes is chosen which consists of 39 mirror shapes chosen at random and a flat mirror shape (all the actuators are set to zero.) The program then instructs each individual mirror shape to be tested in turn and the fitness parameter measured. Usually the fitness parameter is an intensity reading from the photomultiplier tube but it can be any aspect of the system as seen in chapter 7.

The next stage is to reproduce a second generation population of mirror shapes, which is achieved through the use of selection, crossover and mutation. In the process of selection, those mirror shapes that give the best fitness from the population are chosen to become the 'parents' of the new generation of mirror shapes. Following selection,

crossover (also known as recombination) is carried out on the parents. That is, the parents are paired off and the genetic material is swapped between each parent to produce two offspring. The probability that two parents will generate new offspring is determined probabilistically, which in the case of this system it is set to 85%. After selection, mutation is performed on the offspring which involves introducing a randomisation to a selection of their actuators (genes). Like crossover, the likelihood of mutation occurring is determined probabilistically and is set to typically 5%. It is important to note, that in the case of the genetic algorithm, mutation is extremely important and ensures that all of solution space is checked.

A new population of mirror shapes are produced and along with the best mirror shape from the generation before (which remains unmodified), undergo the same process of selection, crossover and mutation. This process continues until a stopping parameter is reached. In the case of the adapative optic system this occurs when the fitness has not increased by 2% in the last 50 generations.

The genetic algorithm (unlike the modified hillclimbing algorithm described previously) ensures that the global maximum is found by the optimisation, although problems do exist in that the time taken for the genetic algorithm is generally much longer. In figure 14, a schematic showing the genetic algorithm in operation for DMM optimisation is presented.

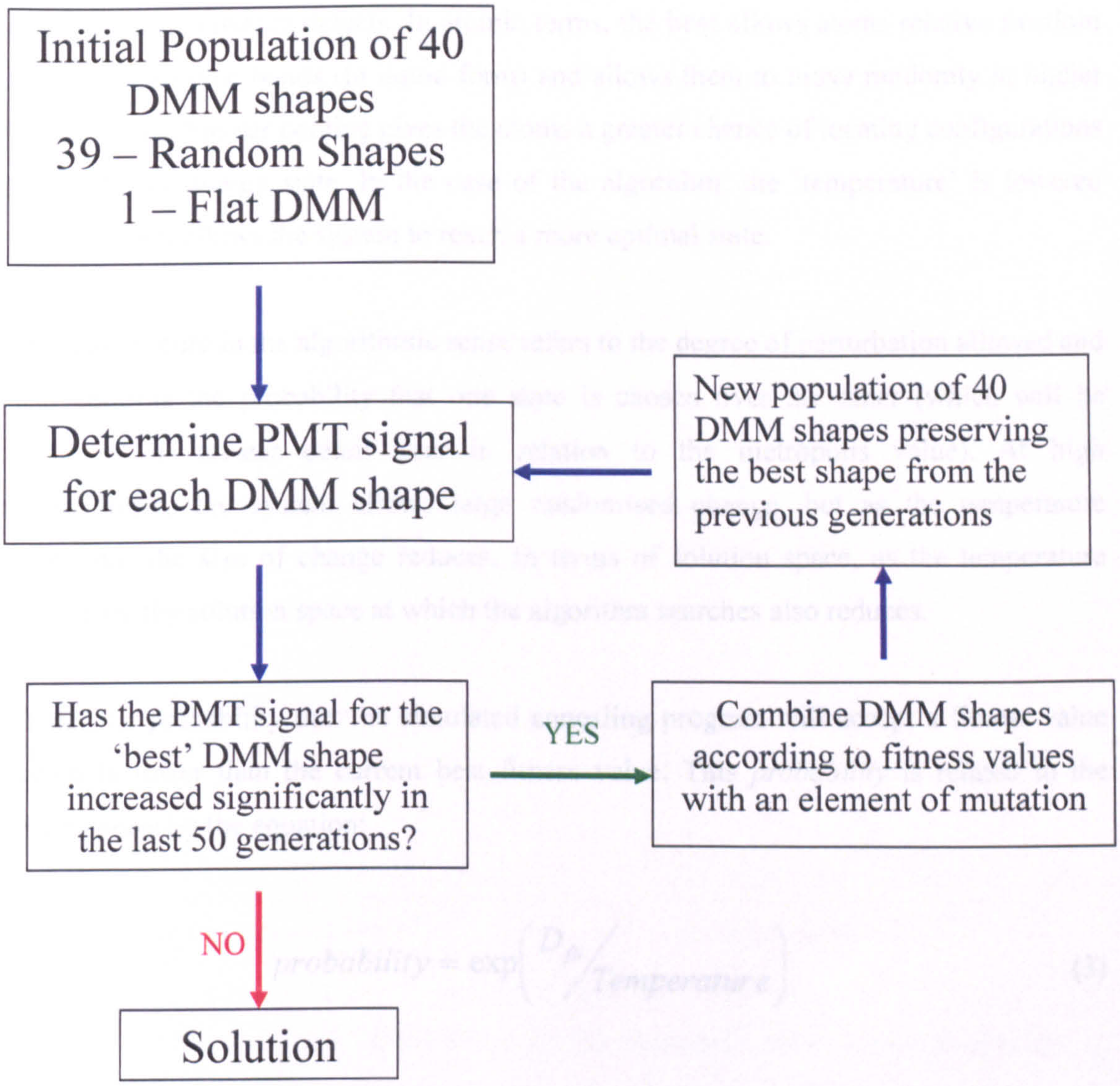

Figure 14: A schematic showing the genetic algorithm in operation for DMM optimisation.

6.2.3 Simulated annealing (SA)

One such algorithm that could possibly achieve a global optimisation whilst enhancing the speed of the process, is known as the simulated annealing algorithm. First developed by Kirkpatrick *et al.* in 1983 [63], the algorithm, as the name suggests, simulates the annealing process associated with crystalline solids. Physically, annealing is a technique which concerns the heating and subsequent controlled cooling, in order to increase the

crystal size and reduce defects. In atomic terms, the heat allows atoms relative freedom from their original bonds (in liquid form) and allows them to move randomly in higher energy states. Slower cooling gives the atoms a greater chance of locating configurations with a lower energy state. In the case of the algorithm, the 'temperature' is lowered slowly which allows the system to reach a more optimal state.

The temperature in the algorithmic sense refers to the degree of perturbation allowed and also controls the probability that one state is chosen over the other (which will be discussed in greater detail later in relation to the metropolis value). At high temperatures, the system allows large randomised change, but as the temperature decreases, the size of change reduces. In terms of solution space, as the temperature decreases, the solution space at which the algorithm searches also reduces.

There is a probability that the simulated annealing program will accept a fitness value which is lower than the current best fitness value. This *probability* is related to the *temperature* by the equation:

$$probability = \exp\left(D_{fit} \Big/ Temperature\right) \tag{3}$$

where $$D_{fit} = (Metropolis) x (1x10^{8}) x \left(\frac{NewFitness - OldFitness}{NewFitness}\right) \tag{4}$$

where the *metropolis* value is defined at the start of the algorithm.

The ability of the simulating annealing algorithm to accept a lower fitness value is controlled by the metropolis value, which ensures that in the course of the optimisation it is not trapped at a local maximum. Of course, for each particular solution, a certain degree of calibration may be required in relation to the starting temperature, the rate of temperature decrease, and the metropolis value, to make certain that the simulated

annealing algorithm returns the optimal solution. Figures 15 (a) – (d) shows the effects of the metropolis value on the probability of acceptance for 1% - 20% reduction in the fitness value from arbitary temperatures of 100 – 0.

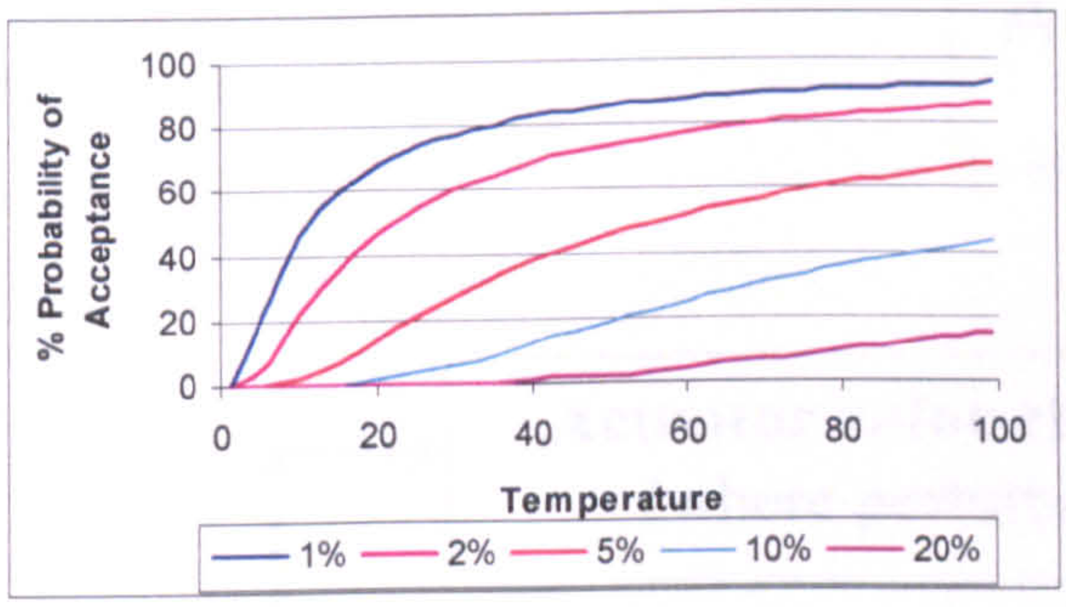

(a) Metropolis = 8×10^{-6}

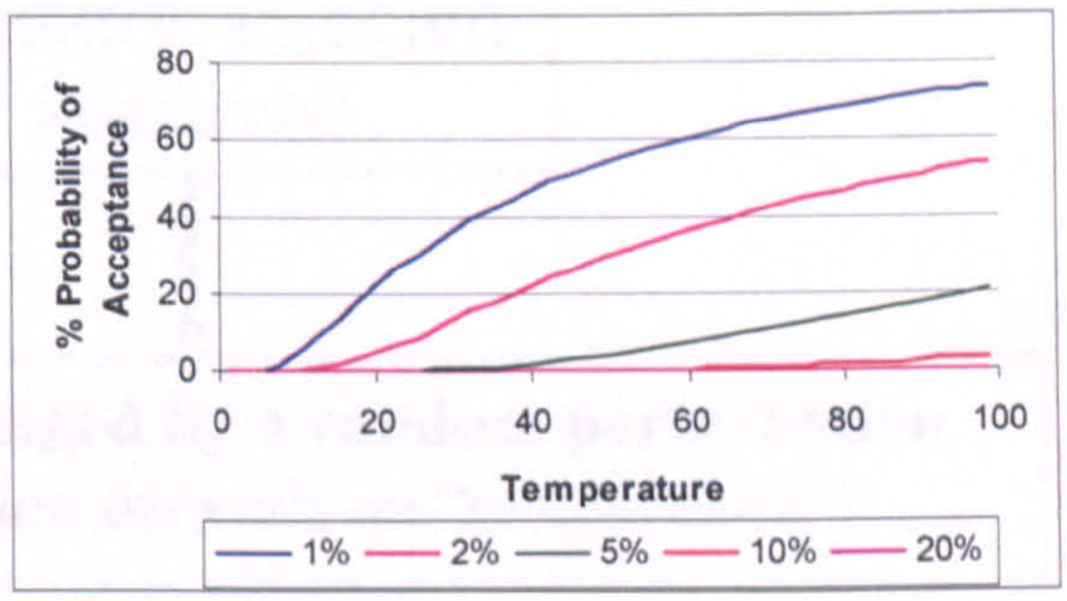

(b) Metropolis = 3×10^{-5}

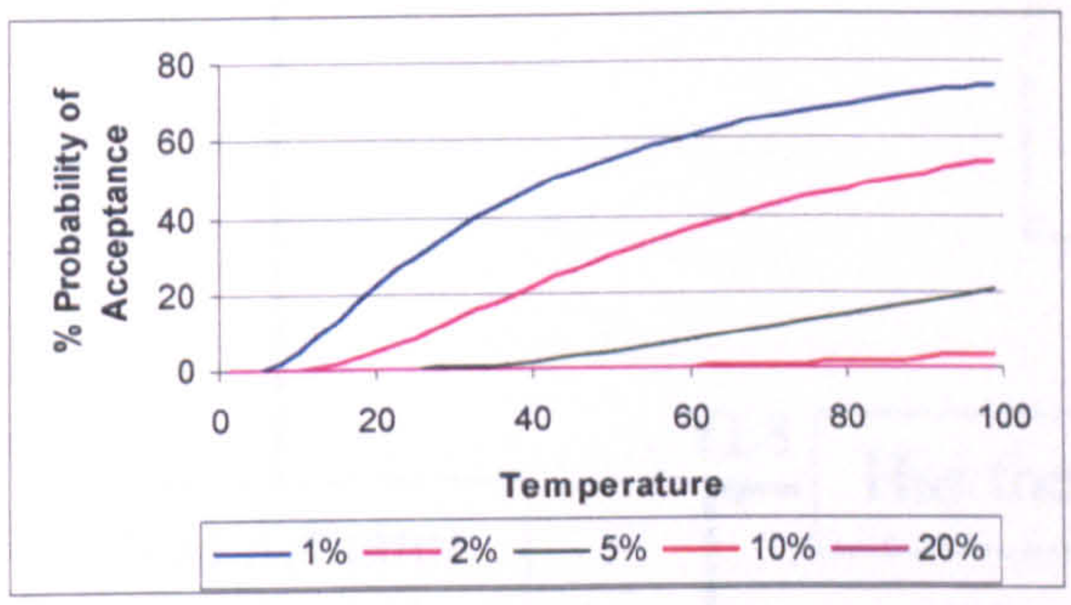

(c) Metropolis = 8×10^{-5}

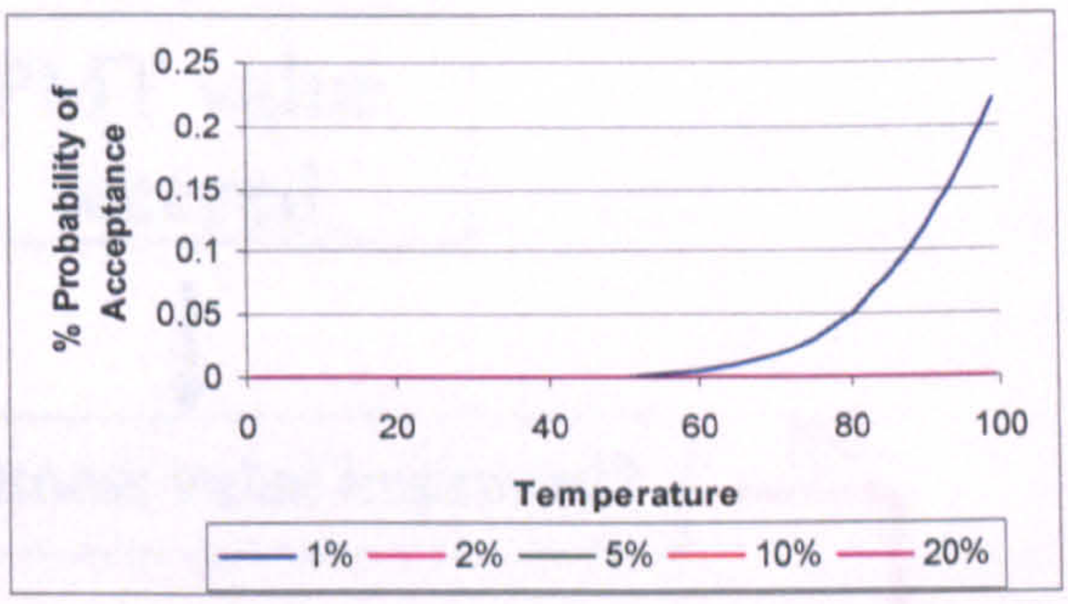

(d) Metropolis = 6×10^{-4}

Figures 15 (a) – (d) showing the effect of the metropolis value on the probability of acceptance for 1% - 20% reduction in the fitness value.

A flowchart explaining the simulated annealing algorithm in more detail is shown in figure 16.

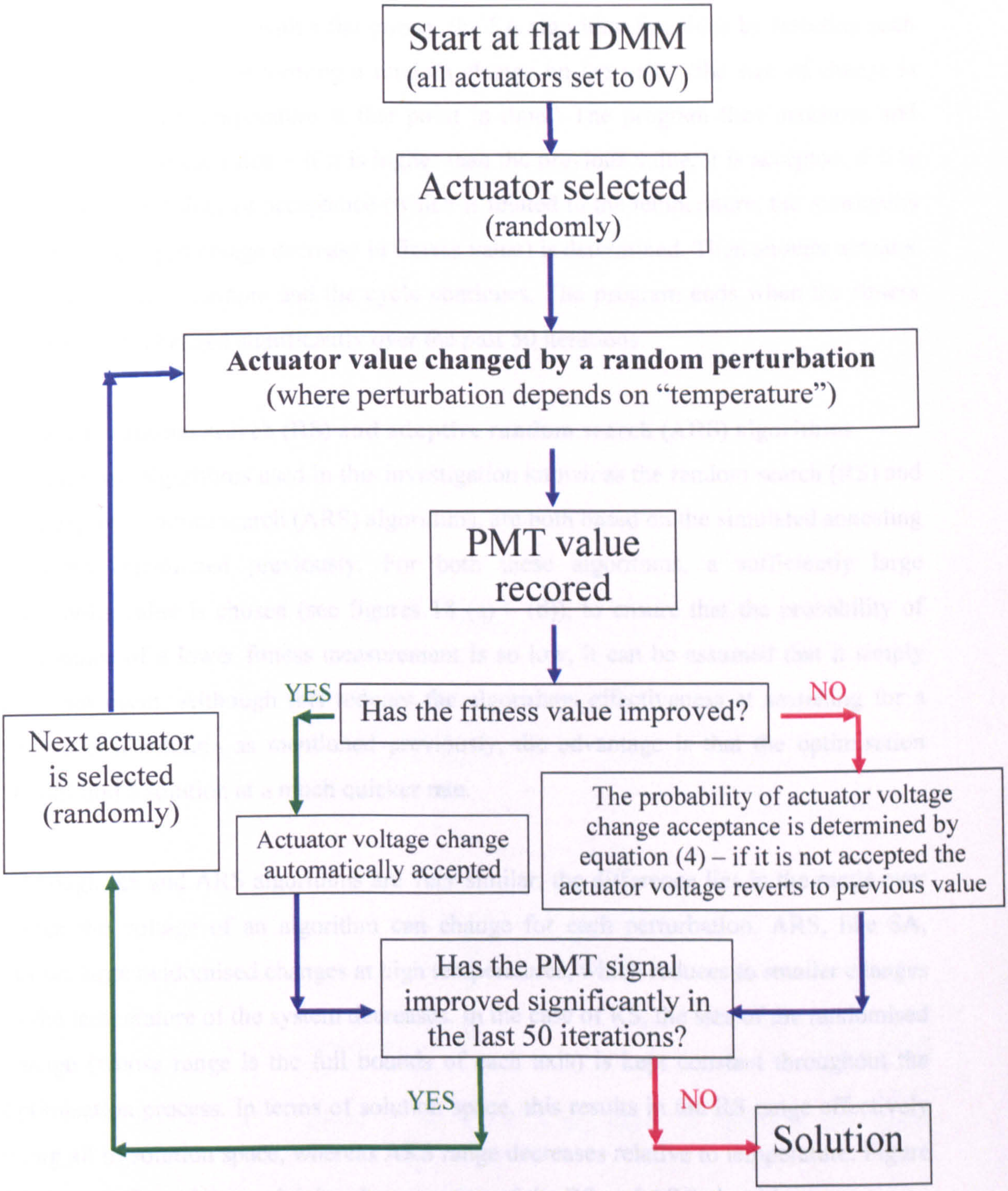

Figure 16: A schematic of the simulated annealing algorithm in operation for DMM optimisation.

From figure 16, starting with a flat mirror, the SA algorithm functions by selecting each actuator in turn, and performing a random change on the value (the size of change is dependant on the temperature at that point in time.) The program then measures and evaluates the fitness value – if it is higher than the previous value, it is accepted; if it is lower, the probability of acceptance (which is related to the temperature, the metropolis value, and the percentage decrease in fitness value) is determined. Then another actuator is then chosen at random and the cycle continues. The program ends when the fitness value has not changed significantly over the past 50 iterations.

6.2.4 The random search (RS) and adaptive random search (ARS) algorithms

Another two algorithms used in this investigation known as the random search (RS) and the adaptive random search (ARS) algorithms, are both based on the simulated annealing algorithm mentioned previously. For both these algorithms, a sufficiently large metropolis value is chosen (see figures 18 (a) – (d)), to ensure that the probability of acceptance of a lower fitness measurement is so low, it can be assumed that it simply does not occur. Although this reduces the algorithms effectiveness at searching for a truly global solution as mentioned previously, the advantage is that the optimisation should find a solution at a much quicker rate.

Although RS and ARS algorithms are very similar, the difference lies in the range over which the voltage of an algorithm can change for each perturbation. ARS, like SA, allows large randomised changes at high temperatures, which reduces to smaller changes as the temperature of the system decreases. In the case of RS, the size of the randomised change (whose range is the full bounds of each axis) is kept constant throughout the optimisation process. In terms of solution space, this results in the RS range effectively being all of solution space, whereas ARS range decreases relative to temperature. Figure 17 shows a flow chart explaining the operation of the RS and ARS algorithms.

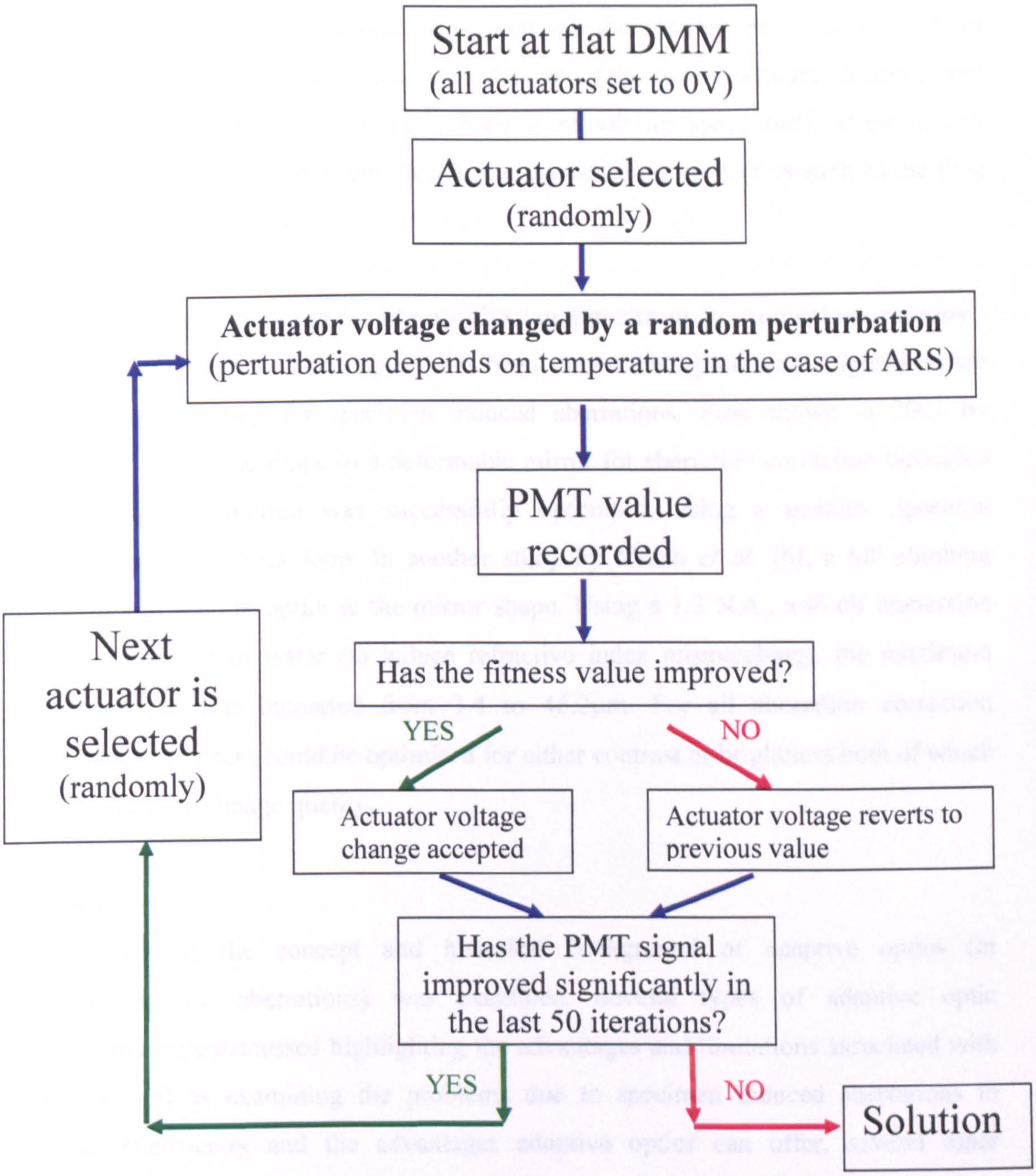

Figure 17: Showing a schematic of the RS/ARS algorithm in operation for DMM optimisation.

In all the optimisation methods described previously, only GA and SA algorithm can be

described as global optimisations, dependant on the starting parameters (such as population size and degree of mutation for GA, rate of temperature decrease and metropolis value for SA) as well as the shape of the solution space itself. In the case of confocal microscopy, the best optimisation to use relies on the factors such as the time taken for the best solution.

6.3 Previous research in the use of optimisation algorithms in confocal microscopy

In the case of confocal microscopy, it has been shown that optimisation algorithms are effective in correcting for specimen induced aberrations. First shown in 2001 by Sherman *et al.* [5], the shape of a deformable mirror for aberration correction through a Courmarin-water solution was successfully optimised, using a genetic algorithm incorporating a feedback loop. In another study by Marsh *et al.* [6], a hill-climbing algorithm was used to optimise the mirror shape. Using a 1.3 N.A., x40 oil immersion objective, imaging in water (to induce refractive index mismatching), the maximum scanning depth was increased from 3.4 to 46.2μm. For all aberration correction algorithms, the system could be optimised for either contrast or brightness both of which result in improved image quality.

7. Summary

In this chapter, the concept and historical background of adaptive optics (in compensating for aberrations) was examined. Several types of adaptive optic mechanisms were discussed highlighting the advantages and limitations associated with each. As well as examining the problems due to specimen induced aberrations in confocal microscopy and the advantages adaptive optics can offer, several other applications including laser physics and ophthalmology were considered.

In the case of confocal microscopy due to the deterioration of the signal as well as the complexity of the aberrations present when imaging biological samples, that conventional adaptive optical feed back loops (incorporating a conventional wavefront sensor) is not always the best route to take. One alternative is with the aid of

optimisation algorithms, particular features such as brightness or contrast associated with the detected image could be optimised. In the case of the mirror used in this investigation, the number of possible solutions is found to be extremely high (~1.4 x 10^{85}), and requires the use of an algorithm that can locate a solution much quicker than the enumerate method. The functions of each search algorithm used in this investigation were discussed in terms of solution space as well as in their operation in the confocal system scenario.

References

1. Wilson, T., Carlini, A. R. (1989). The effect of aberrations on the axial response of confocal imaging systems. *J. of Microscopy*, 154, 243-256
2. Wan, D., Rajadhyasksha, M., Webb, R. H. (2000). Analysis of spherical aberration of a water immersion objective: application to specimens with refractive indices 1.33-1.40. *J. of Microscopy*, 197, 274-284
3. Tyson, R. K. (1998). *Principles of Adaptive optics*, Academic Press
4. Booth, M. J., Neil, M. A. A., Juskaitis, R., Wilson T. (2002). Adaptive aberration correction in a confocal microscope. *PNAS*, 99, 5788-5792
5. Sherman, L., Ye, J.Y., Albert, O., Norris, T.B., (2002). Adaptive correction of depth-induced aberrations in muliphoton scanning microscopy using a deformable mirror. *J. of Microscopy*, 206, 65-71.
6. Marsh, P. N., Burns, D., Girkin, J. M. (2003). Practical implementation of adaptive optics in multiphoton microscopy. *Optics Express*, 11, 1123-1130.
7. Wright, A. J., Burns, D., Patterson, B. A., Poland, S. P., Valentine, G., Girkin, J. M. (2005). Active aberration correction in confocal and multiphoton microscopy. *Microscopy research and technique*, 67, 36 – 44.
8. Poland, S. P., Burns, D., Lubeigt, W., Patterson, B. A., Valentine, G., Wright A. J., Girkin, J. M. (2005). Use of optimisation algorithmic techniques with active optics for aberration correction in optical sectioning microscopy. *Proc. SPIE*, 6018, 60181H.
9. Wilson, T., Carlini, A.R, (1989). The effect of aberrations on the axial response of confocal imaging systems. *J. of Microscopy*, 154, 243-256.
10. Sheppard, C., Gu, M., Brain, K., Zhou, H. (1994). Influence of spherical aberration on axial imaging of confocal reflection microscopy. *App. Opt.*, 33, 616-624.
11. Wan, D., Rajadhyaksha, M., Webb, R. H. (2000). Analysis of spherical aberration of a water immersion objective: application to specimens with refractive indices 1.33-1.40, *J. of Microscopy*, 197, 274-284.

12. Meglinski, I.V., Bashkatov, A.N., Genina, E.A., Churmakov, D.Y., Tuchin, V.V. (2003). The enhancement of confocal images of tissues at bulk optical immersion. *Laser Physics*, 13, 65-69.
13. Yeh, A., Choi, B., Nelson, J., Tromberg, B. (2003). Reversible dissociation of collagen in Tissues. *J. of Investigative Dermatology*, 121, 1332-1335
14. Sheppard, C., Gu., M. (1991). Aberration compensation in confocal microscopy, *App. Opt.*, 30, 3563-3568.
15. Hellmuth, T. Seidel, R., Seigal, A. (1988). Spherical aberration in confocal microscopy. *Proc. SPIE*, 1028, 28-32.
16. Coulman, C. E. (1985). Fundamental and Applied Aspects of Astronomical "Seeing" Annual Review of Astronomy and Astrophysics, 23, 19-57.
17. Tyson R. K. (1998). Chapter 2: Sources of aberrations. *Principles of Adaptive optics*, Academic Press, Boston.
18. Babcock, H. W. (1953). The possibility of compensating astronomical seeing. *Publ. Astron. Soc. Pac.* 65, 229-236.
19. Greenaway, A., Burnett, J. (2003). Chapter 3: AO system design. *Industrial and Medical Applications of Adaptive Optics*, Technology Tracking, London.
20. Linnik, V. P. (1957). On the possibility of reducing the influence of atmospheric seeing on the image quality of stars. *Opt. Spectrosc.* 3, 401
21. Image of Neptune taken with the Keck II Telescope adaptive optics system in infra-red, 1999, Photo courtesy Keck Observatory, Adaptive Optics group
22. Greenaway, A., Burnett, J. (2003). Chapter 8: Wavefront sensing technologies. *Industrial and Medical Applications of Adaptive Optics*, Technology Tracking, London, 2003.
23. Platt, B., Shack, R. V. (1971). Lenticular Hartmann-screen. *Optical Sciences Center Newsletter*. University of Arizona, 5(1), 15-16.
24. Shack, R. V., Platt, B. (1971). Production and use of a lenticular Hartmann screen. *J. of Opt. Soc. Am.*, 61, 656.
25. Tyson R. K. (1998). Chapter 5: Wavefront sensing. *Principles of Adaptive optics*, Academic Press, Boston.

26. Horwitz, B. A. (1990). Multiplex techniques for real-time shearing interferometry. *Optical Engineering* 29(10), 1223-1232.
27. Fienup, J. R. (1982). Phase retrieval algorithms: a comparison. *Appl. Opt.* 21(15), 2758-2769.
28. Tyson R. K. (1998). Chapter 1: History and Background. *Principles of Adaptive optics*, Academic Press, Boston.
29. Wyant, J. C., Creath, K. (1992). Chapter 1: Basic wavefront aberration theory for optical metrology. Applied optics and optical engineering XI, Academic Press, USA.
30. Greenaway, A., Burnett, J. (2003). Chapter 7: WFM technologies. *Industrial and Medical Applications of Adaptive Optics*, Technology Tracking, London, 2003.
31. Gaughan, R. (2005). Miniature deformable mirrors bring adaptive optics within reach. *Photonics Spectra*, February 2005, 82 – 90.
32. Steinhaus, E., Lipson, S. G. (1978). Bimorph piezoelectric flexible mirror. *J. Opt. Soc. Am.* 69, 478-481
33. Kokorowski, S. A. (1979). Analysis of adaptive optical elements made from piezoelectric bimorphs. *J. Opt. Soc. Am.* 69, 181-187
34. Laboratory of the Adaptive Optics for Industrial and Medical Applications, Institute on Laser and Information Technologies, Russian Academy of Sciences - ILIT RAS, Svyatoozerskaya Str. 1, Shatura Moscow Region, 140700, Russia, http://www.laser.ru/adopt/.
35. Cherezova, A. Y., Kaptsov, L. N., Kudryashov, A. V. (1996). CW Industrial rod YAG:Nd3+ laser with intracavity active bimorph mirror. *Appl. Opt.* 35(15), 2554-2561.
36. Kudryashov, A. V., Samarkin, V.V. (1995). Control of high power CO_2 laser beam by adaptive optical elements. *Opt. Commun.* 118 (3), 317-322.
37. Marx, B. (2004). Bimorph mirror focuses to record intensities. *Laser Focus World*, 40(7), 41-46.

38. Dubra, A., Massa, J. S., Paterson, C. (2005). Hysteresis compensation in PZT bimorph mirrors: Preisach's classical and non-linear models. *Proc. SPIE*, 6018, 60181E.
39. Kudryashov, A. (2005). *Private communication*, Beijing, China.
40. Grosso, R. P., Yellin, M. (1977). The membrane mirror as an adaptive optical element. J. opt. Soc. Am. 67, 399 – 406.
41. Vdovin, G., Sarro, P. M. (1995). Flexible mirror micromachined in silicon. Applied optics, 34 (16), 2968 – 2972.
42. Flexible Optical B.V., PO Box 581, 2600 AN, Delft, the Netherlands, www.okotech.com.
43. Vdovin, G., Kiyko, V. (2001). Intracavity control of a 200-W continuous-wave Nd:YAG laser by a micromachined deformable mirror. *Opt. Lett.* 26(11), 798-800.
44. Lubeigt, W. (2005). Intra-Cavity Adaptive Optics Control of Solid-State Lasers, PhD thesis submitted to the Department of Physics, University of Strathclyde.
45. Liang, J., Williams, D. R., Miller, D. T. (1997). Supernormal vision and high-resolution retinal imaging through adaptive optics. J. of Opt. Am. A., 14, 2884 – 2892.
46. Fernandez, E., Iglesias, I., Artal, P. (2001). Closed-loop adaptive optics in the human eye. Opt. Lett. 26, 746 – 748.
47. Williams, D. (2005). Wavefront sensing and the eye's optical quality, Dave William's Lab @ the center for visual science, University of Rochester, Retrieved 5th of May 2006 from http://www.cvs.rochester.edu/williamslab/
48. Williams, D. (2005). Customized correction of the eye's aberrations with contact lenses and laser refractive surgery, Dave William's Lab @ the center for visual science, University of Rochester, Retrieved 5th of May 2006 from http://www.cvs.rochester.edu/williamslab/
49. Hofer, H., Chen, L., Yoon, G. Y., Singer, B., Yamauchi, Y., Williams D. R. (2001).Improvement in retinal image quality with dynamic correction of the eye's aberrations. *Optics Express, 8*, 631-643.

50. Lubeigt, W., Valentine, G., Girkin, J., Bente, E., Burns, D. (2002). Active transverse mode control and optimisation of all-solid-state laser using an intracavity adaptive-optic mirror. Opt. Express, 10, 550 – 555.
51. Lubeigt, W. Valentine, G. J., Burns, D. (2005). Brightness enhancement of a solid-state laser using an intra-cavity deformable mirror. *Proc. of SPIE*, 6018, 60180I.
52. Garduño-Mejía, J., Greenaway, A. H., Reid, D. T. (2004). Programmable spectral phase control of femtosecond pulses by use of adaptive optics and real-time pulse measurement, *J. Opt. Soc. Am. B* 21(4), 833-843.
53. Daniel Harman, D. (2003). Cable Free Solutions, Retrieved 5th of May 2006 from www.cablefree.co.uk.
54. Greenaway, A., Burnett, J. (2003). Chapter 4: Applications. *Industrial and Medical Applications of Adaptive Optics*, Technology Tracking, London, 2003.
55. Booth, M. J., Schwertner, M., Wilson, T. Nakano, M., Kawata, Y., Nakabayashi, M., Miyata, S. (2006). Predictive aberration correction for multilayer optical data storage. *Appl. Phys. Letters*, 88, 031109.
56. Booth, M.J., Neil, M.A.A., Wilson, T. (1998). Aberration correction for confocal imaging in refractive-index-mismatched-media. *J. of Microscopy*, 192:90-98
57. Neil, M.A.A., Juskaitis, R., Booth, M.J., Wilson, T., Tanaka, T. and Kawata, S. (2000). Adaptive aberration correction in a two photon microscope, *J. of Microscopy*, 200, 105-108.
58. Schwertner, M., Booth, M. J., Wilson, T. (2004). Characterizing specimen induced aberrations for high NA adaptive optical microscopy. *Optics Express*, 12(26) 6540 – 6552.
59. Schwertner, M., Booth, M. J., Neil, M. A. A., Wilson, T. (2004). Measurement of specimen induced aberrations of biological samples using phase stepping interferometry. *J. of Microscopy*, 213, 11 – 19.
60. Booth, M. J., Schwertner, M., Wilson, T. (2005). Specimen-induced aberrations and adaptive optics for microscopy. *Proc. of SPIE*, 5894, 589403.

61. Holland, J. H. (1975). *Adaptation in natural and artificial systems*. University of Michigan Press, Ann Arbor.
62. Darwin C. (1859). *On the origin of species by means of natural selection*. J. Murray, London.
63. Kirkpatrick S., Gelatt C. D., Vecchi M. P. (1983). Optimisation by simulated annealing. *Science*, 220(4798), 671-680.

Chapter 6: Confocal microcope system incorporating AO

1. Introduction

A major problem when imaging in depth within a biological sample in confocal microscopy is the introduction of sample induced aberrations. Sample induced aberrations are mostly due to refractive index mismatches within the sample which cause a significant reduction in image resolution and contrast as well as signal intensity [1 & 2]. There have been many suggestions on how to compensate for these sample induced aberrations. One technique used in confocal and multiphoton microscopy (which will be described in detail in this chapter) is to optimise the system using an optimisation algorithm routine [3 & 4]. The output of a conventional confocal scan head is directed onto an actively controlled membrane mirror, before being focused by the microscope objective. By selecting various image properties (e.g. brightness, contrast or resolution), an optimisation algorithm is used to maximise this value, and compensate for aberrations.

In this section, the confocal system set-up containing the adaptive optic element is outlined. The equipment and control systems used to control both the confocal and adaptive optic system are described in detail. This includes the adaptive optic mirror (15mm, 37 actuator Okotech mirror) as well as the laser scanning system, hardware control, objectives, piezo translational devices and the custom written LabVIEW and LabWindows software interfaces used. The procedure used in characterising the optical system (measurement of the axial and lateral resolutions) is described comprehensively as well as the method used for optimisation using the adaptive optical element.

2. Confocal set-up

The experimental set-up of the confocal microscope is shown in figure 1. Using either a 633 nm 2 mW Helium Neon laser or a frequency doubled Nd:YAG (power output 10mW) laser operating at 532nm, as an illuminating light source, light enters the MRC-600 BioRad scan head. The scan head consists of a fast and slow axes mirrors mounted

onto galvanometers to provide x and y scanning. Light then comes out through a beam expanding lens doublet, onto a polarising beam splitter cube, where one polarisation was rejected and the other incident onto a quarter wave plate and the deformable membrane mirror (DMM). The light reflected off the DMM passes through the quarter wave plate and is then focused using an objective onto the test sample.

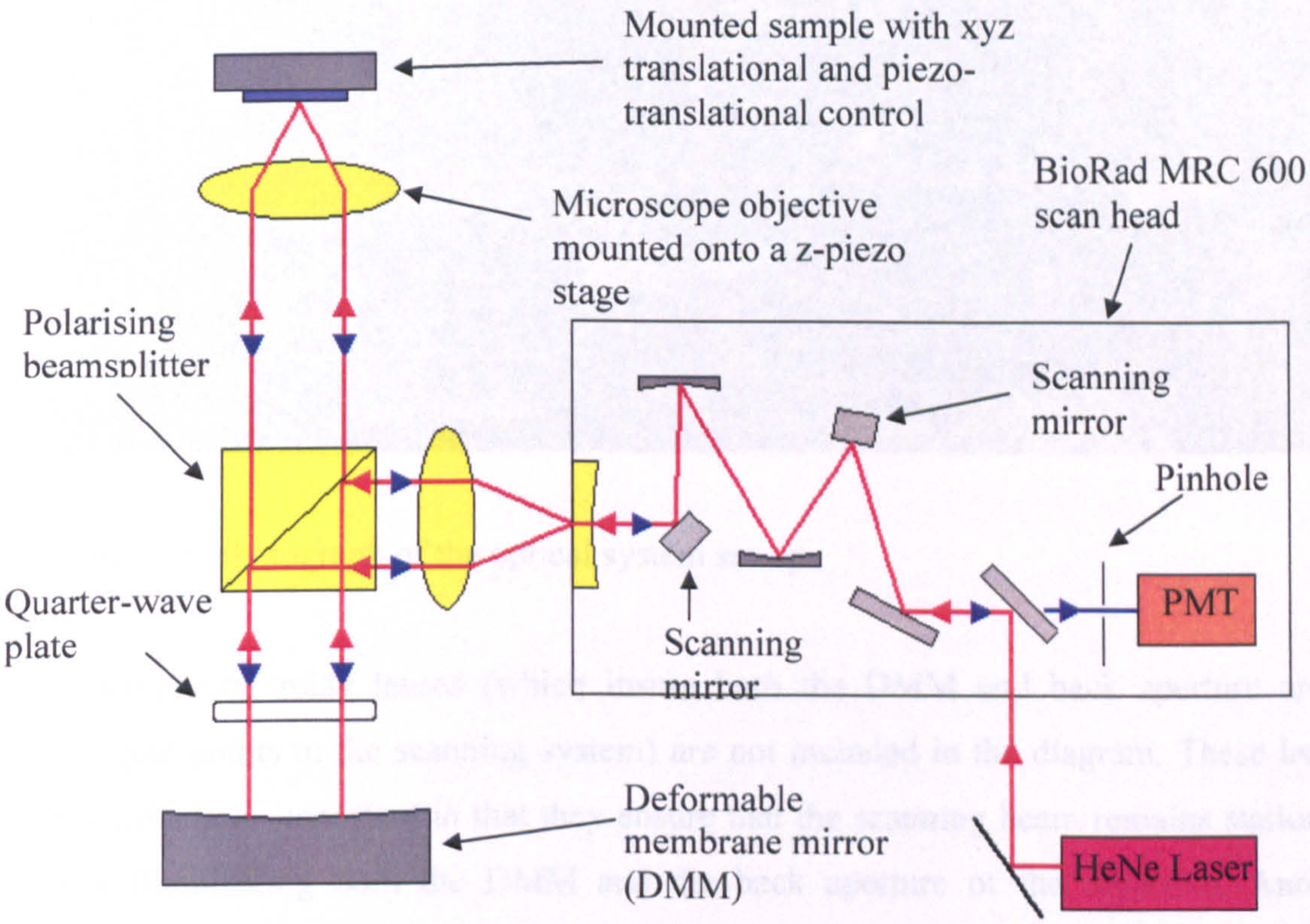

Figure 1: Showing the confocal adaptive optical set-up.

The default objective used is a 0.5 N.A. 20x (coverslip corrected, working distance 2.1mm) air microscope objective (Nikon) and is often used for deep multiphoton imaging due to it having a long working distance with reasonable numerical aperture (N.A.). Reflected light from the sample is then reflected off the DMM (second pass) back through the scan head onto a photomultiplier tube (PMT) which was covered by a pinhole aperture. This provided the confocality of the microscope system. A photograph of the optical system is shown in figure 2.

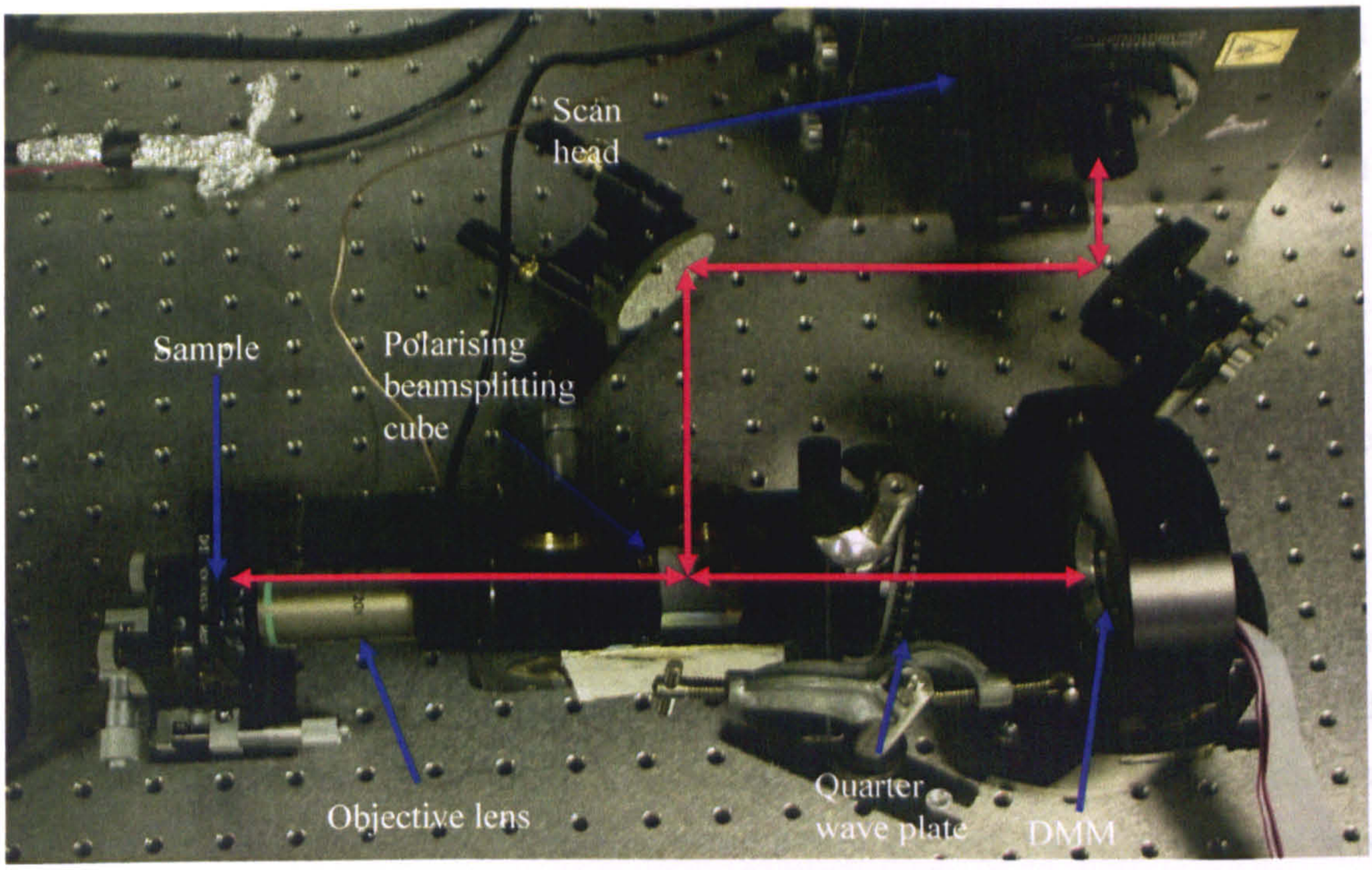

Figure 2: A photograph of the optical system set-up.

For simplicity, relay lenses (which insure both the DMM and back aperture are at conjugate points to the scanning system) are not included in the diagram. These lenses are particularly important in that they ensure that the scanning beam remains stationary when illuminating both the DMM and the back aperture of the objective. Another advantage to this stationary position is that any wavefront correction provided by the adaptive element is constant over the whole scanning range. It should be noted that the test sample is mounted onto a manually controlled xyz translational stage, which provides coarse control over the position of the sample.

2.1 Deformable membrane mirror

As mentioned previously, the adaptive optical element used was a deformable membrane mirror, manufactured by Okotech [5] using micromachining procedures. To begin with, the mirror was comprised of a micro-machined silicon wafer chip mounted onto a PCB container. The wafer chip was then coated with a thin layer of silicon nitride

(~0.5μm) over the top of the chip. Using etching techniques, a circular mask was cut through the wafer with the etch stopping at the silicon nitride layer. This results in the formation of a thin membrane which is characterised by the profile of the masked region. To produce the reflective surface, an aluminium coating was applied to the silicon nitride membrane using vacuum deposition techniques. A multilayered dielectric coating was then applied on top of the aluminium to optimise the reflectivity of the mirror in the visible. By applying a voltage to control electrodes, the shape of the membrane mirror could be changed electrostatically.

Photographs showing the DMM and the arrangement of the actuators responsible for electrostatically controlling the shape of the membrane are shown in figures 3(a) and 3(b). The 37 actuators are arranged in a hexagonal pattern with the whole structure having a total diameter of 12mm (the centre-to-centre distance between actuators was measured at ~1.25mm.). The membrane is positioned around 200μm above the actuators with a diameter of 15mm which overlaps the actuators due to its greater diameter. With the membrane earthed, each of the 37 electrostatic actuators can be individually controlled at voltages of 0-200V with a response rate of 1kHz due to the presence of individual connectors for each actuator. The control system used to control each actuator and hence, the mirror shape will be explained in more detail later.

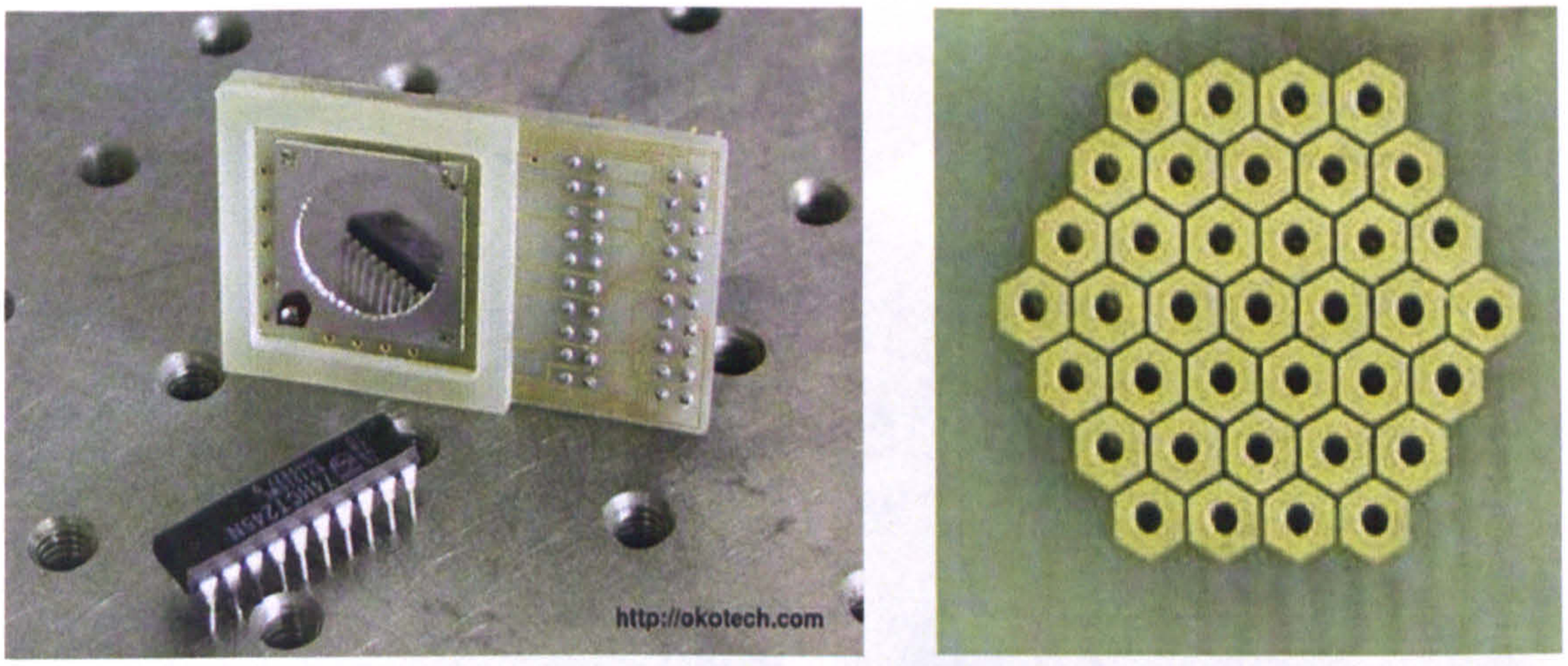

(a) (b)

Figure 3: Showing (a) the mirror and PCB mount and (b) the 37 actuator arrangement.

The maximum mirror deflection was quoted at 6μm by the manufacturer, but it was found that this could vary from 3–7μm depending on the thickness and type of reflective coating used [6]. Due to the sensitivity and fragility of the deformable membrane, it cannot be cleaned. Therefore a number of protective mounts were constructed, containing anti-reflection coated front windows (suitable for visible wavelengths) in order to guard against dust and drafts (e.g. caused by variations in air conditioning currents) which could damage and distort the mirror shape. Figures 4(a) and 4(b) show an original mount design and a more up-to-date version respectively.

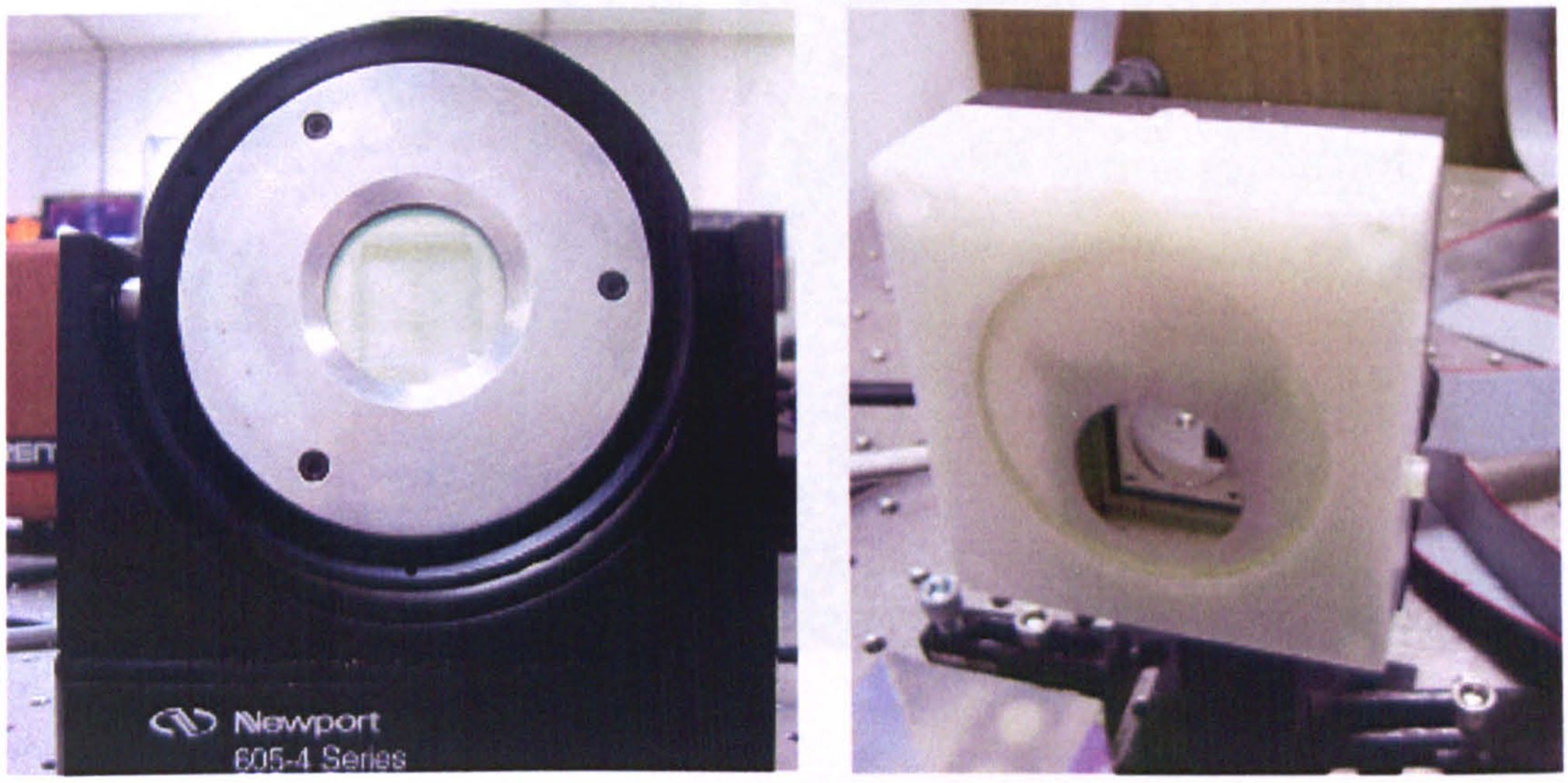

(a) (b)

Figure 4 (a) and (b) showing original and present protective mounts for the DMM.

2.2 Piezo translational stages

The piezo used to control the z-position of the microscope objective lens was a P721.17 High-Speed Nanofocusing/Scanning z-drive produced by Physik Instruments [7] which allowed fine control 100μm range with 10nm resolution) over the depth of the focal point. Figures 5(a) and (b) show the piezo stage and control box. The piezo was controlled using the E-662 LVPZT control box calibrated to the piezo stage which allowed, via an RS-232 connection, direct computer control using an interface.

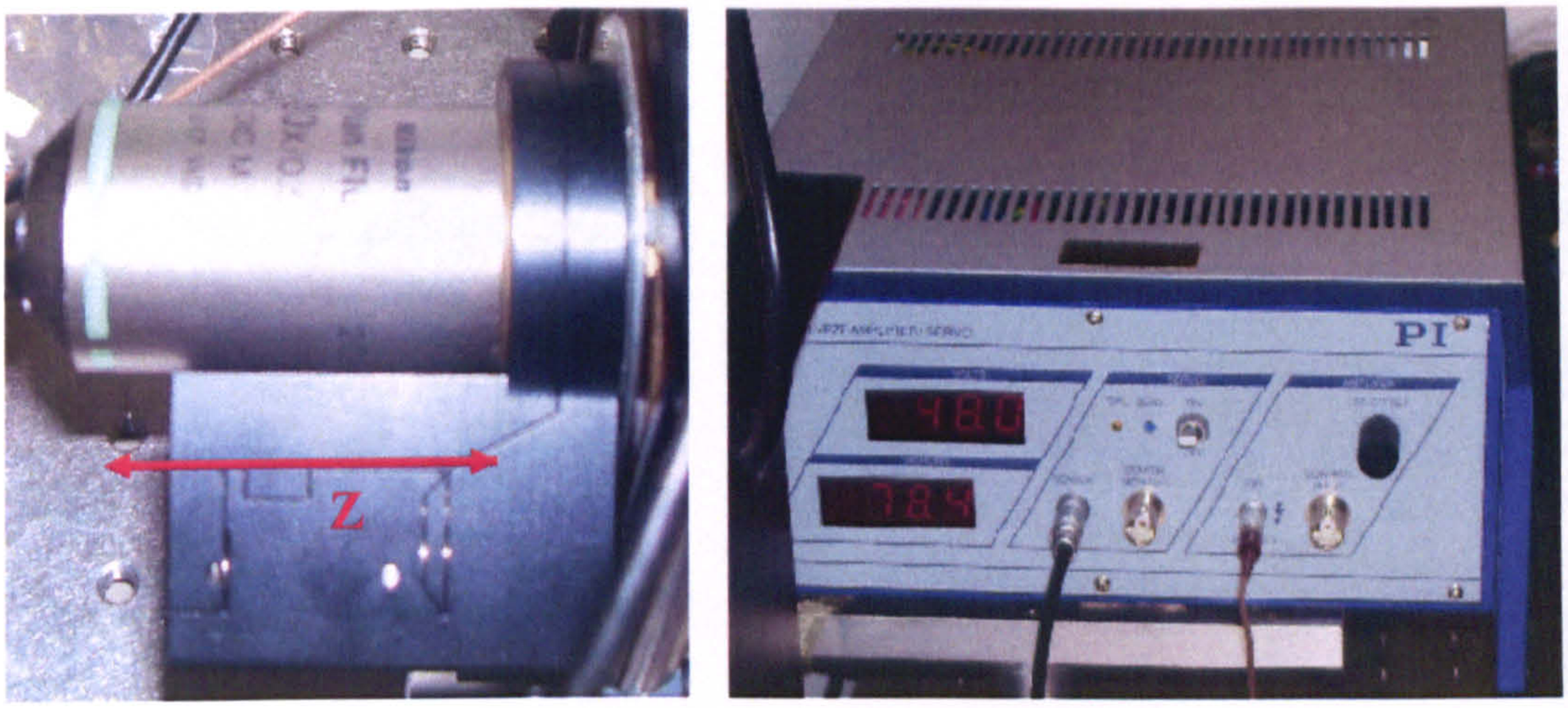

(a) (b)

Figure 5: Showing (a) the z-piezo P721 translational stage with objective and (b) control system.

Originally, only the z-piezo stage suitable for microscope objectives was used in order to give an axial intensity scan of the confocal system. To give lateral intensity scans (which were required to measure the lateral resolution of the system), the sample stage was placed on a xyz piezo P611.3SF (Nanocube) translation stage also produced by PI which allowed 100 μm control in the x, y and z directions with 10nm resolution in each axis. This should not be confused with the xyz manual translational stage which is mounted underneath the piezo. The piezo was controlled using an E-515 control box which allowed both manual and direct computer control using an interface via an RS-232 port connection.

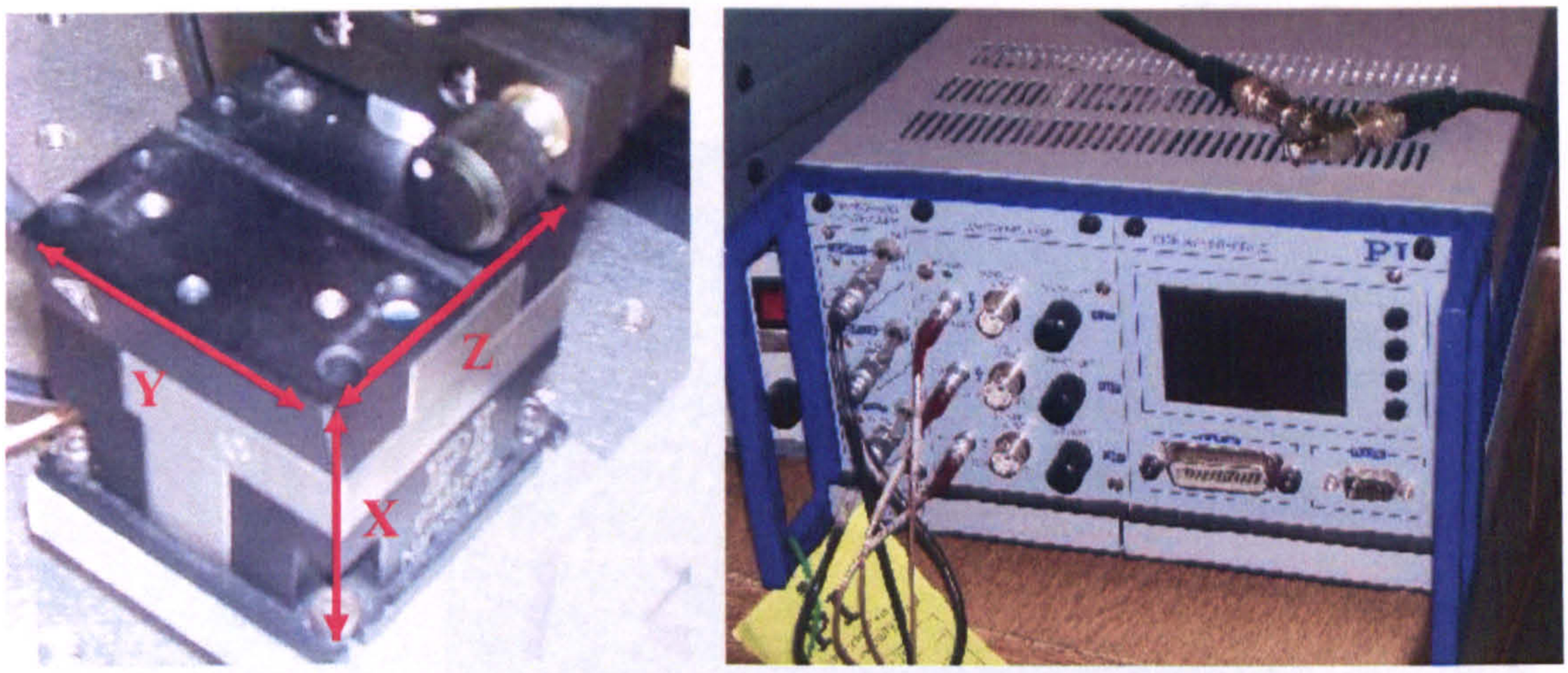

(a) (b)

Figure 6: Showing (a) the xyz-piezo P611 nanocube and (b) control system.

3. Control of the confocal system and deformable membrane mirror

The confocal scan head system, piezo translational stages and deformable mirror were computer controlled using separate discrete computer command systems which will be explained in this section.

3.1 Control of the MRC-600 scan head system

The BioRad MRC-600 scan head system is controlled using a pre-packaged electronics box with software that runs using the Microsoft Dos operating system. Figure 7 shows a picture of the control screen.

Figure 7: Showing the BioRad MRC-600 control interface.

From this computer interface, the parameters of the fast and slow galvonometers (galvos) (responsible for the laser scanning that produces an image in the confocal microscope) could be controlled. This includes the range over which the galvos move (which defines the scanning area), the speed of scan, as well as being able to park the galvos into a particular position. It should be noted that the fast (x-axis) and slow galvos (y-axis) can be positioned to 766 and 510 distinct individual positions respectively. Taking a PMT measurement at each unique galvo position, the BioRad program produces a confocal image of the scanned focused area which can be then subsequently saved. When taking an axial or lateral PSF measurement scan or performing an optimisation, the galvos are parked at their scan midpoints which are 383 and 255 respectively for the fast and slow scans. This is achieved by typing “park 383 255” at the BioRad computer interface command line.

3.2 Controlling the piezo z-stage and producing an axial scan

The piezo translational stages were controlled using a commercial graphical programming language called LabVIEW [National Instruments] that uses graphical interfaces or icons instead of lines of text to create applications.

3.2.1 LabVIEW control

LabVIEW is distinguished from text-based programming languages, in that it uses dataflow programming, where the flow of data determines execution rather than instructions determine program execution. In LabVIEW, using a collection of objects and tools, one can construct a user interface which is known as a front panel. Then using functions which are denoted by graphical symbols, the front panel objects are controlled [8].

The block diagram contains LabVIEW programs known as virtual instruments, or VIs, due to their appearance and operation, which emulate physical instruments in the real world (i.e. multimeters and oscilloscopes). Every VI uses functions that manipulate input from the user interface or other sources and display that information or move it to other files or other computers. A VI contains the following three components:

1. Front panel – which acts as the user interface.
2. Block diagram – this contains the source code in graphical form which characterises the functionality of the VI.
3. Icon and connector panel – identifies the VI so that it can be used within in another VI. A VI within another VI is called a subVI. A subVI corresponds to a subroutine in text based programming languages.

Figure 8 shows an example of a front panel with block diagram for a simple statistical program. As one can see from the diagrams, the front panel displays results and each sub-VI.

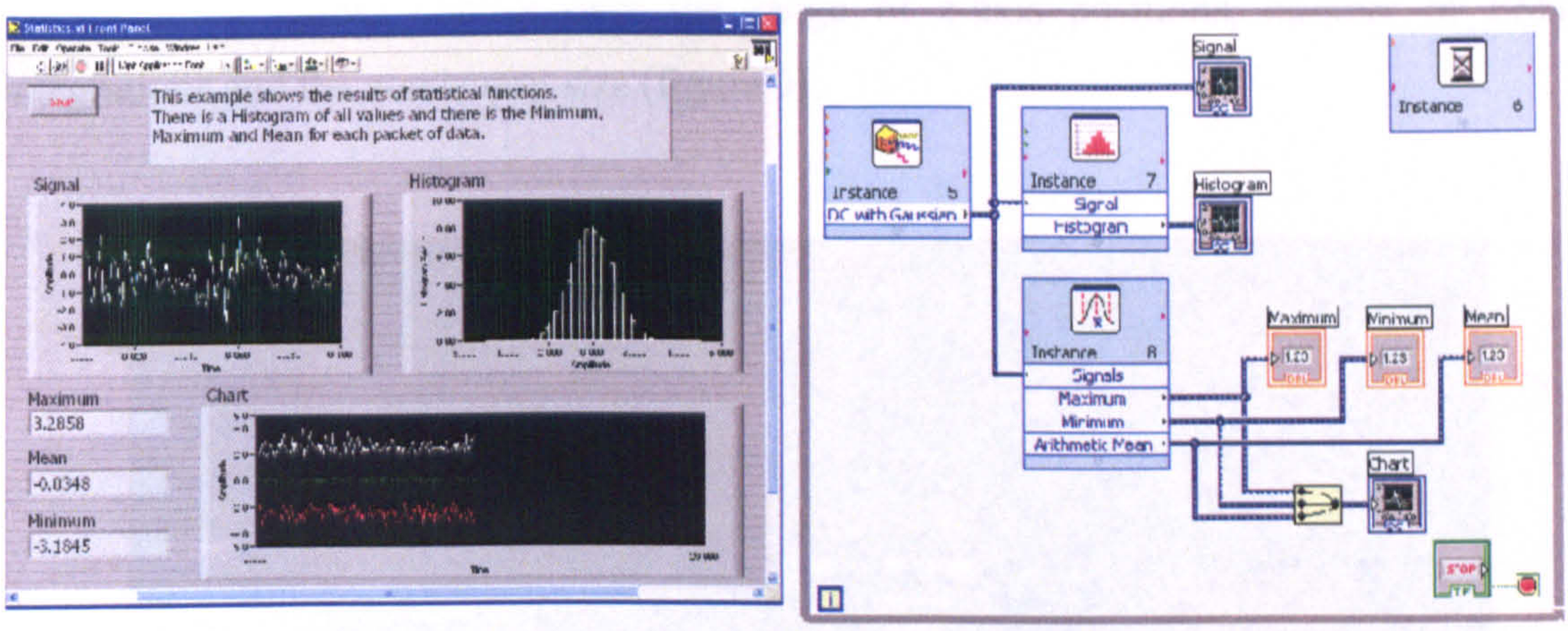

(a) (b)

Figure 8: An example of the (a) front panel with (b) block diagram for a simple statistical program.

As one can see from the diagrams above, the front panel (a) controls and displays information and (b) the block diagram, contains the set of functions, connected via a series of wires, which graphically represents the flow of information from one function to the other.

3.2.2 Axial PSF and Gaussian fitting program

Provided with the piezo translational stages were VI programs that could be used within the LabVIEW environment which via the RS-232 connection to the control box, allowed the piezo stages to be computer controlled. These VIs allowed the user complete control of the piezo stage with various commands such as read voltage, read position, set voltage, set position, and set channel.

In order to take an axial intensity scan of the confocal system and hence the axial point spread function of the system (as described previously in chapter 2), a program was constructed to record the PMT count, control the position of the piezo z-stage and calculate the axial resolution of the system using a Gaussian curve fitting sub-routine.

The program allows control over the range of z-axis positions, number of PMT integrations and the z-axis step size (figure 9).

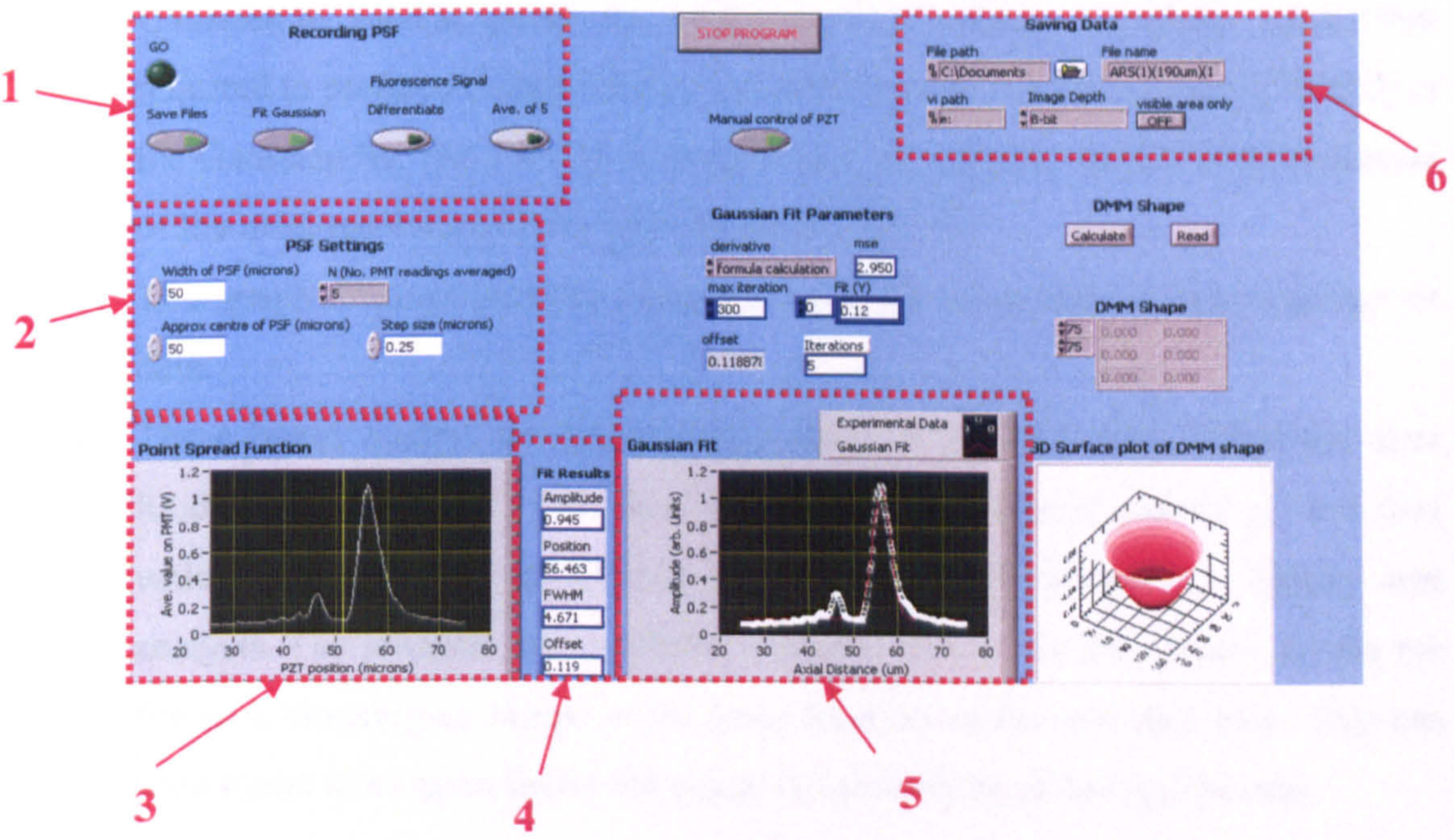

Figure 9: Front panel control for the axial PSF and Gaussian fit program written in LabVIEW.

Some of the main functions of the PSF program highlighted in the 6 boxes are explained in more detail:

1. Runs the program and toggles the Gaussian fit and save function. Also toggles an intensity differentiation and moving average function which is required when measuring a fluorescent signal from a fluorescent sea.
2. Controls the parameters of the axial scan such as width, approximate centre and step size of the scan (all in μm) as well as the number of integrations of the PMT per position. The integration function is particularly useful when taking an axial PSF by cancelling out noise from the system (ie. when the reflected light intensity is low).

3. This graph displays the measured intensity plots against axial position in real time (as the data is being measured).
4. Using the Gaussian fitting program, this table displays the parameters of the best Gaussian fit, such as amplitude, axial position of intensity maximum, noise offset required to produce a Gaussian fit, and the full-width half-maximum (FWHM) of the Gaussian fit. The FWHM is of particular importance, since it is an indication of the axial resolution of the system (see chapter 2).
5. This graph displays both the measured axial PSF data and the best Gaussian fit data.
6. These boxes control the location and name of the data files. When the save function is set to 'on', PSF data and Gaussian fit data are saved as text files which can be easily transferred into an Excel spreadsheet for display and analysis. The program also performs a screen grab of the front panel, saving the file as a bitmap/jpeg image in the same location as the raw data files. This has been found to be quite useful for quick visual analysis of data by the user.

Figure 10 shows a flow chart diagram explaining the functionality of the LabVIEW PSF Gaussian fitting VI program. In this flow chart the main features of the VI are described.

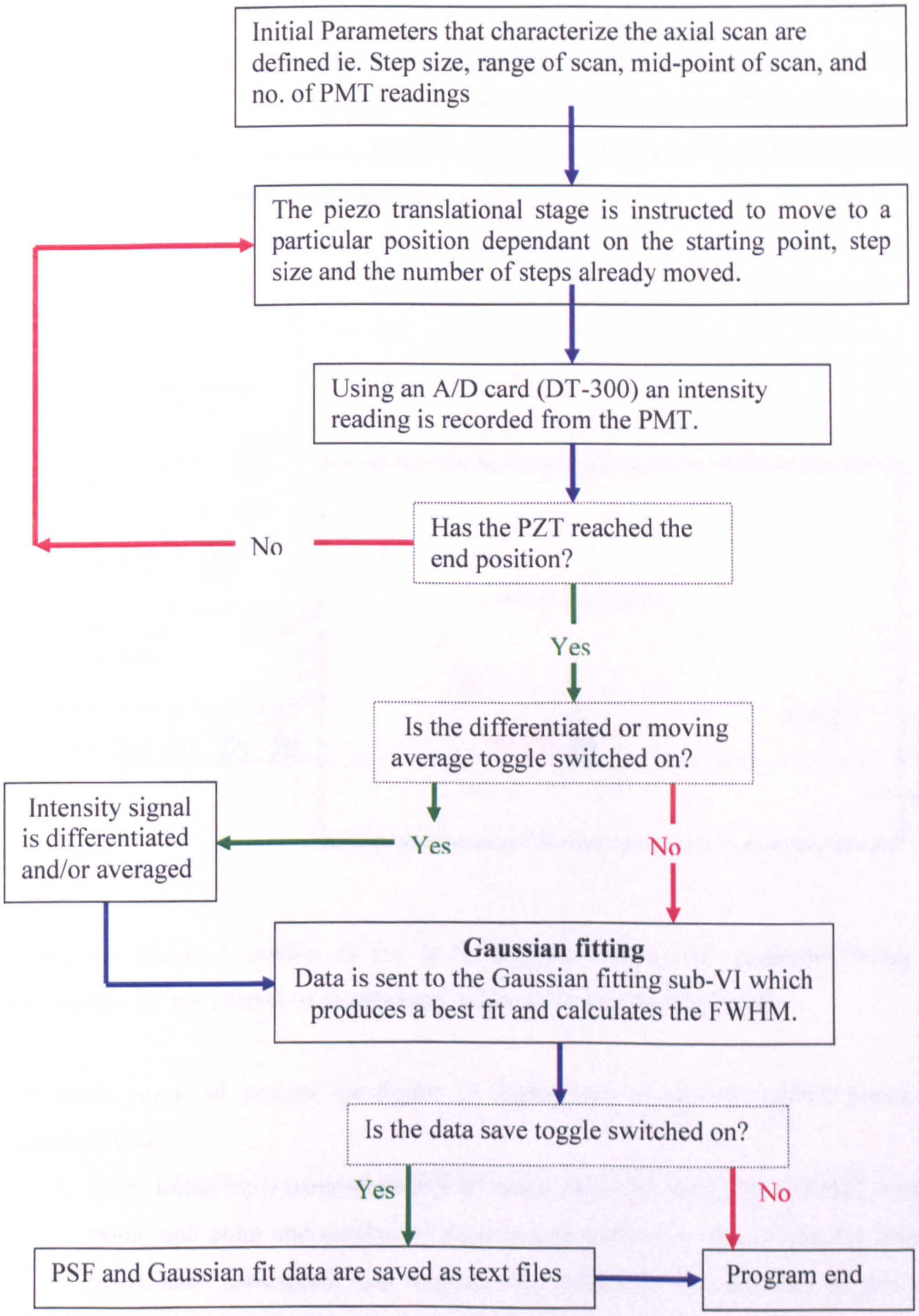

Figure 10: A flow chart explaining the function of the PSF program.

In the interests of completeness, the main features of the LabVIEW source code for the PSF Gaussian fitting VI are shown and explained in detail in figures 11 – 18 (with its corresponding text). For readers not interested in understanding the complete functionality of the constructed LabVIEW program, this section can be passed over. The next relevant section begins on page 196 (section 3.3).

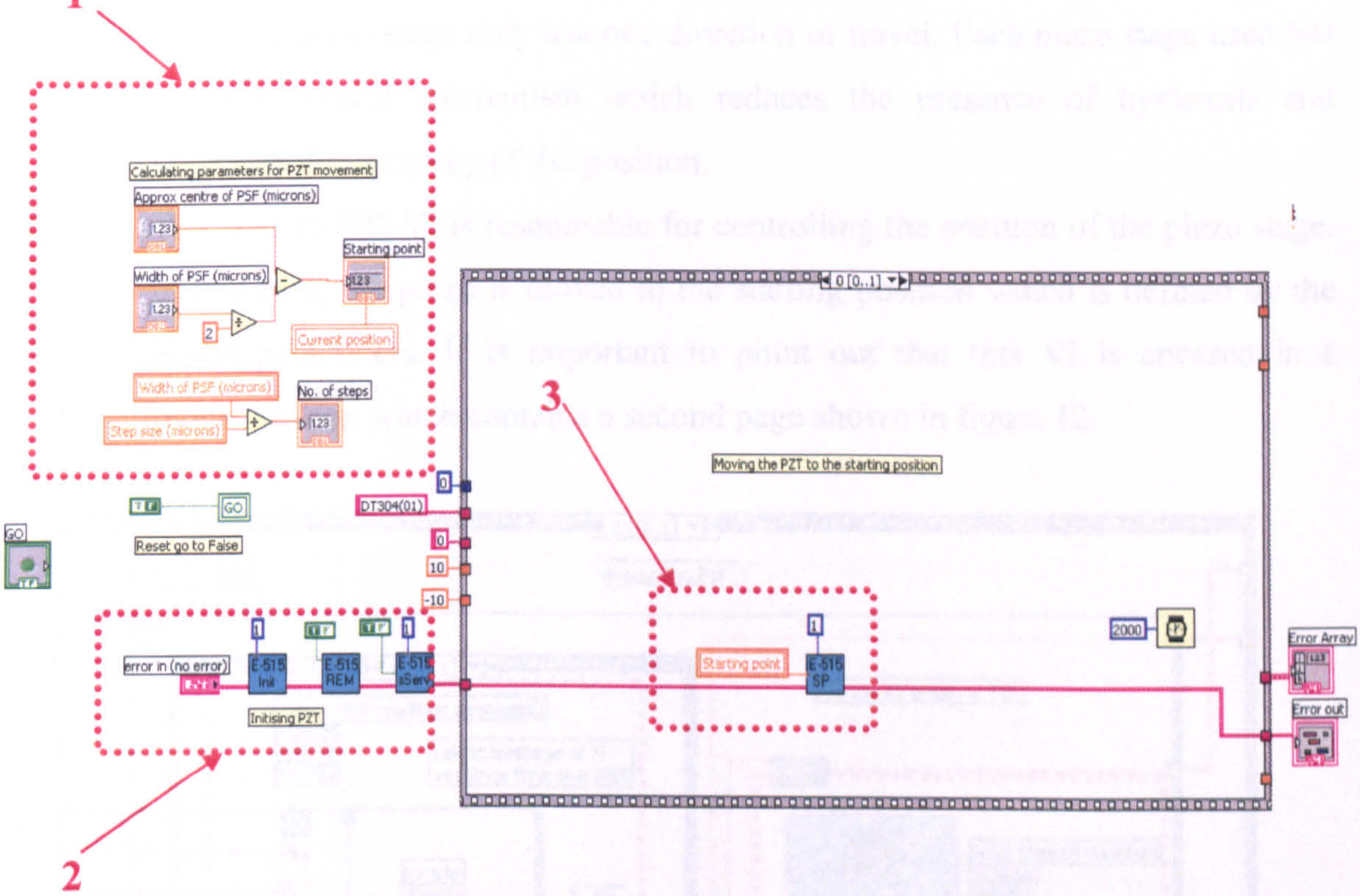

Figure 11: Shows a portion of the block diagram of the PSF Gaussian Fitting VI responsible for the control of the position of the piezo translational stage.

The main points of interest for figure 11 highlighted in the red dashed boxes are explained below:

1. From initial input parameters of PSF range, step size, and centre of PSF, starting point, end point and number of steps required are calculated. From the starting point, each subsequent step requires the addition of the step size in μm. The program ends when the position has reached the end point.

2. These VIs are responsible for setting up the E-515 piezo control box to accept commands from the computer. "E-515 init" initiates the control box to accept commands through a designated RS-232 port (in this case port 1). "E-515 REM" sets the local mode (manual control) or the remote mode (computer control) of the E-515 control box. "E-515 sServ" sets the servo mode for a particular channel using a true/false case command– in this case there is only one channel since the piezo stage only has one direction of travel. Each piezo stage used has a servo control mechanism which reduces the presence of hysteresis and improves the accuracy of the position.
3. The "E-515 SP" VI is responsible for controlling the position of the piezo stage. In this case, the piezo is moved to the starting position which is defined by the initial parameters. It is important to point out that this VI is encased in a sequence loop which contains a second page shown in figure 12.

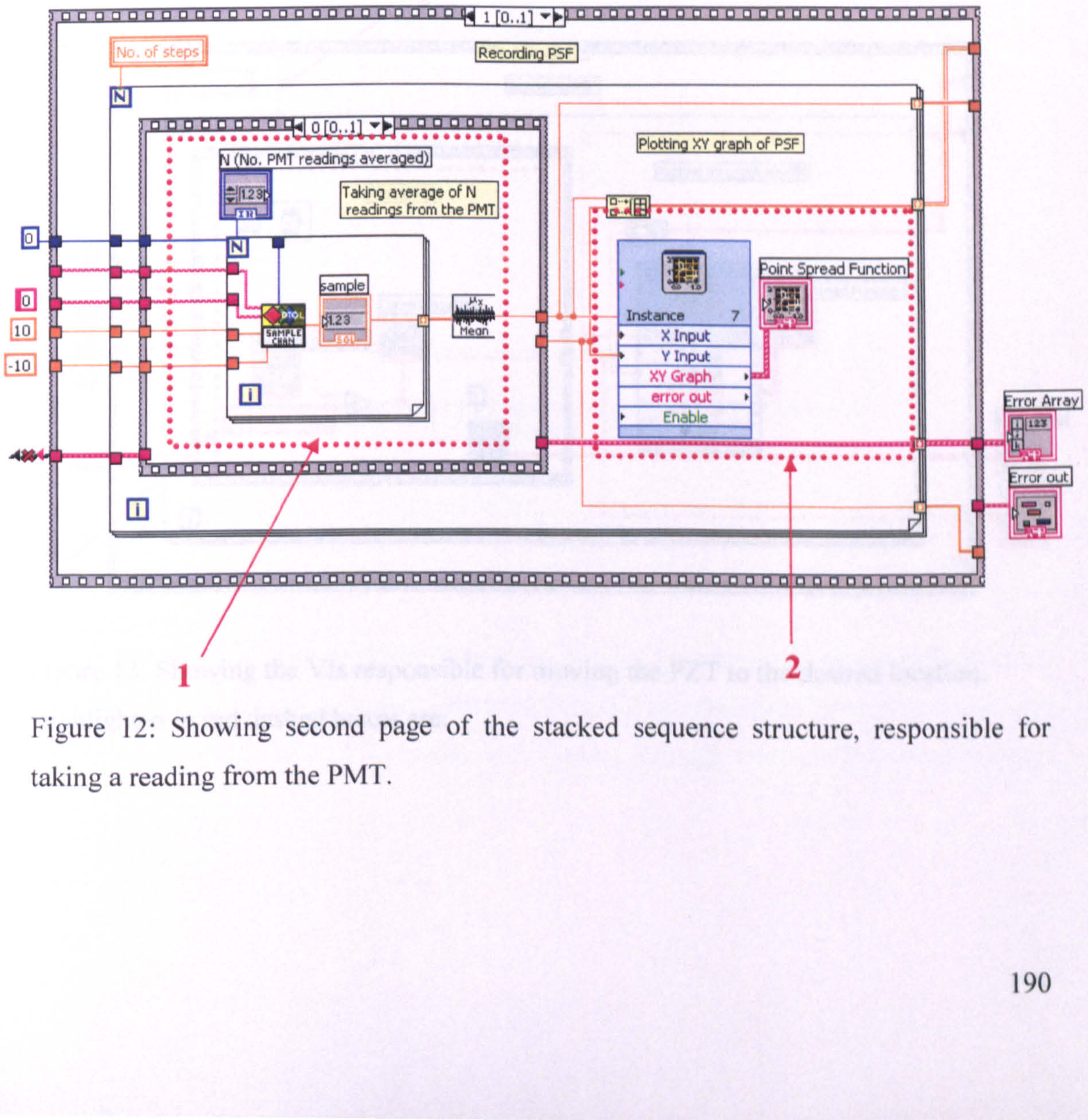

Figure 12: Showing second page of the stacked sequence structure, responsible for taking a reading from the PMT.

The highlighted boxes show the main points of interest in this section of the program:

1. This section contains the "DT AI Sample Scan" VI responsible for instructing the DT-300 A/D card [Data Translation] to record a reading from the PMT located within the MRC-600 scan head. The sample scan VI is incased in a 'for loop' which allows averaging of readings if the system is noisy.
2. As each measurement is taken, it is recorded and displayed on the real time plot using this X-Y graph plotting VI. The piezo position is on the x-axis and the intensity (measured from the PMT) is on the y-axis.

The next diagram (figure 13) shows the second part of the smaller stacked sequence located within the larger stacked sequence.

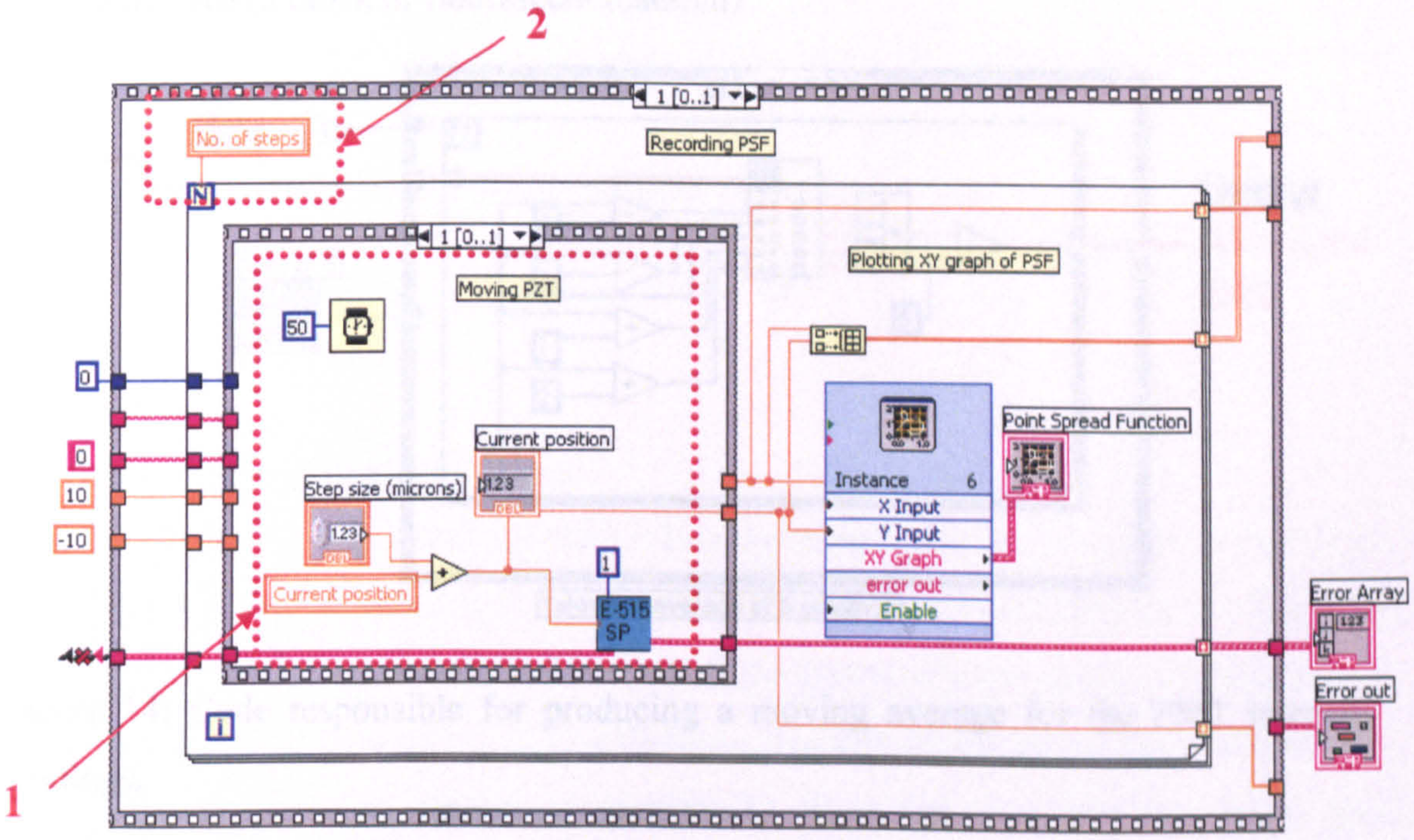

Figure 13: Showing the VIs responsible for moving the PZT to the desired location.

Highlighted in red dashed boxes are:

1. This second part of the stacked sequence is responsible for moving the PZT to its new position. Relatively simple, at the current position, the program adds a step size to it and instructs the PZT to move there.
2. This box highlights the constant (in this case the number of position steps) in control of the iteration size of the *for loop* in operation, which repeats the movement of the piezo and subsequent PMT measurement in the axial scan. The *for loop* reaches completion when the number of steps has been reached hence the end position in the axial intensity scan.

3.2.2.1 Moving average and signal differentiation (fluorescence)

Figures 14 and 15 shows the graphical code responsible for producing a moving average and performing a differentiation over the data respectively. Both of these techniques are particularly useful when measuring calculating the PSF from an axial intensity scan of a fluorescent sea (a block of fluorescent material)

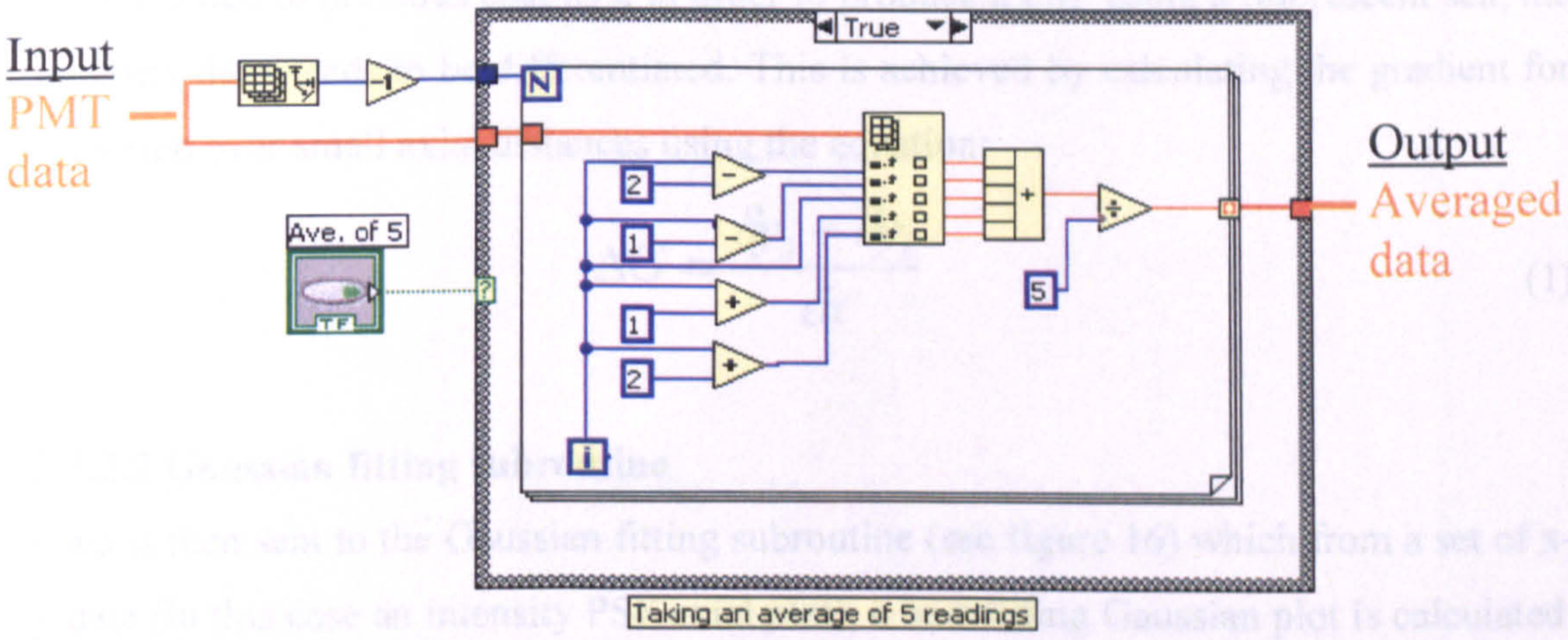

Figure 14: Code responsible for producing a moving average for the PMT intensity readings.

Input from the PMT is in the form of an array of data. Using a *for loop*, for each position on the array, an average is taken of its intensity and the immediate intensities of the two positions either side of it. This results in a moving average which helps to smooth any

noise spikes present within the PMT data. This function is incased in a case structure, which allows it to be switched on or off.

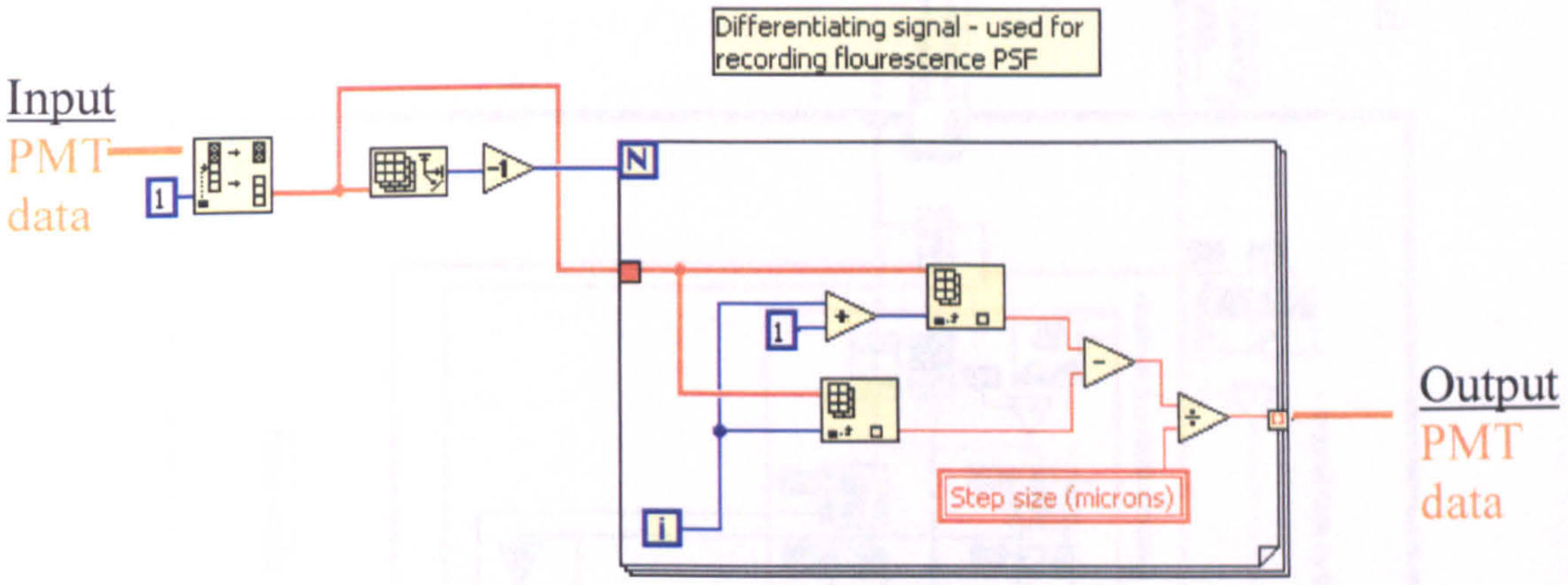

Figure 15: Showing the graphical code used to differentiate the PMT signal.

As explained in previous chapters, in order to produce a PSF using a fluorescent sea, the intensity data needs to be differentiated. This is achieved by calculating the gradient for each step over small axial distances using the equation:

$$\Delta G = \frac{\delta y_2 - \delta y_1}{\delta x} \tag{1}$$

3.2.2.2 Gaussian fitting subroutine

Data is then sent to the Gaussian fitting subroutine (see figure 16) which from a set of x-y data (in this case an intensity PSF axial plot), a best fitting Gaussian plot is calculated. The graphical code uses a modified version of the Levenberg-Marquadt algorithm [9] to determine the least squares set of co-efficients that best fit the set of input data points. The function has been altered to specifically fit a Gaussian function for a two dimensional data set and return the FWHM, the axial position of maximum, amplitude of maximum and the offset required.

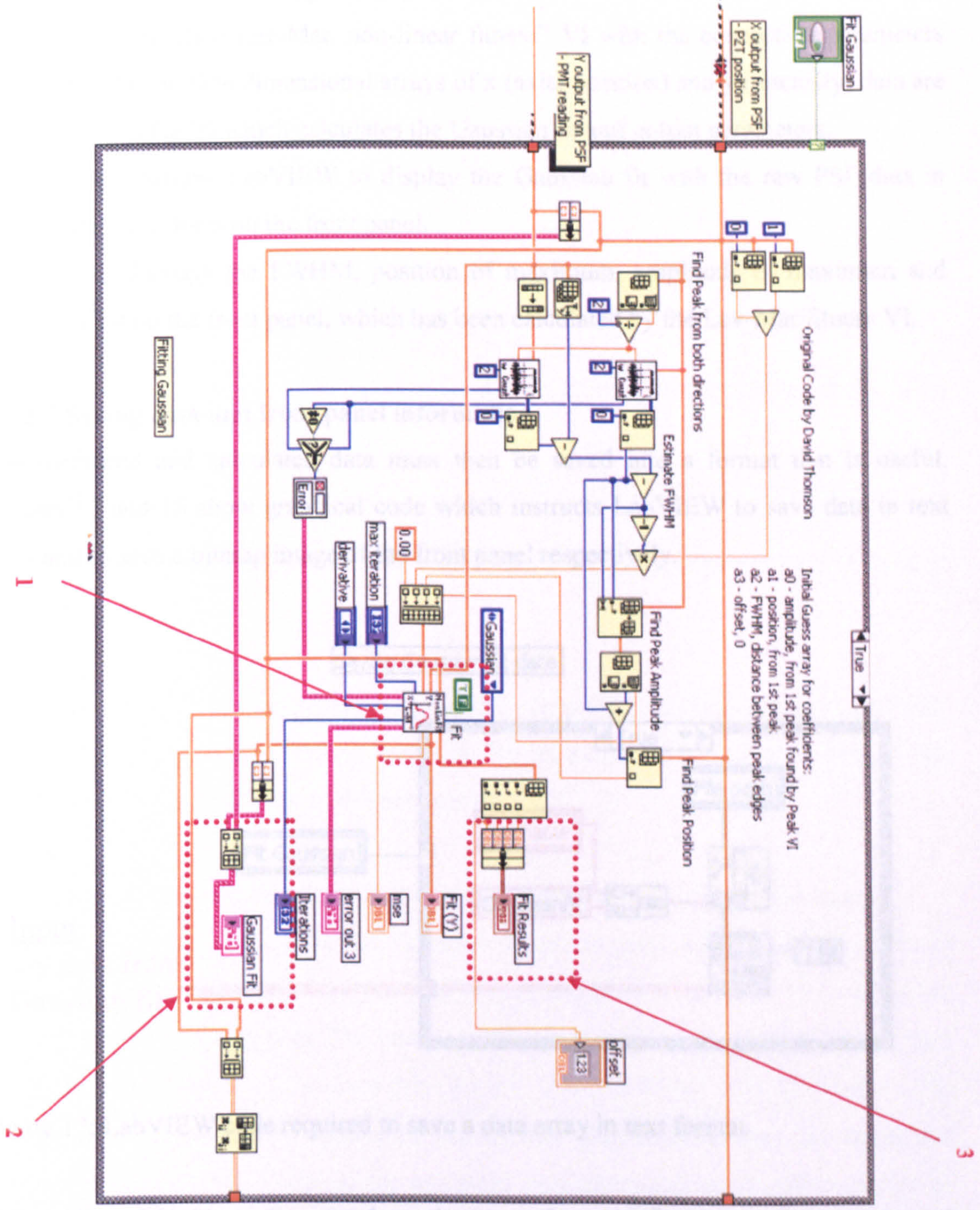

Figure 16: Showing the graphical code used to calculate a best Gaussian fit [9].

In figure 16, there are a number of highlighted boxes which show the main points of interest for the Gaussian fitting subroutine:

1. The "modified Lev-Mar. non-linear fitness" VI with the connection parameters are shown. One dimensional arrays of x (axial position) and y (intensity) data are send to the VI which calculates the Gaussian fit and output parameters.
2. This instructs LabVIEW to display the Gaussian fit with the raw PSF data in graphical form on the front panel.
3. This displays the FWHM, position of maximum, amplitude of maximum and offset on the front panel, which has been calculated by the Lev-Mar fitness VI.

3.2.2.3 Saving data and front panel information

The measured and calculated data must then be saved into a format that is useful. Figures 17 and 18 show graphical code which instructs LabVIEW to save data in text form and to save a bitmap image of the front panel respectively.

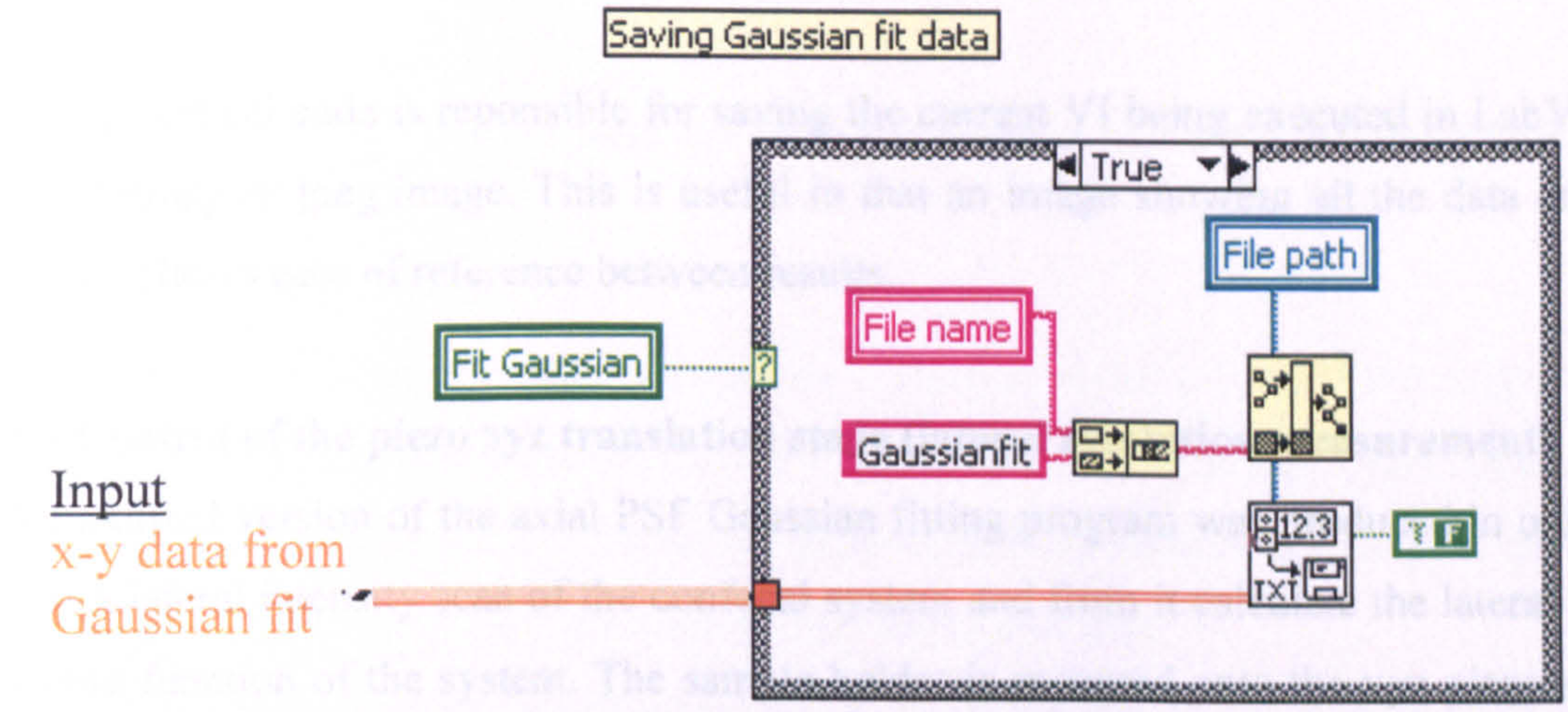

Figure 17: LabVIEW code required to save a data array in text format.

The section of the block diagram shows how x-y Gaussian fit data is transferred by a 2 dimensional array and converted into text format and saved under a certain filename. The file path defines which path i.e. d:\graphicaldata\ the text data is saved. These files

can be easily opened and manipulated for analysis using Excel. The code is encased in a case function in order to toggle the save function.

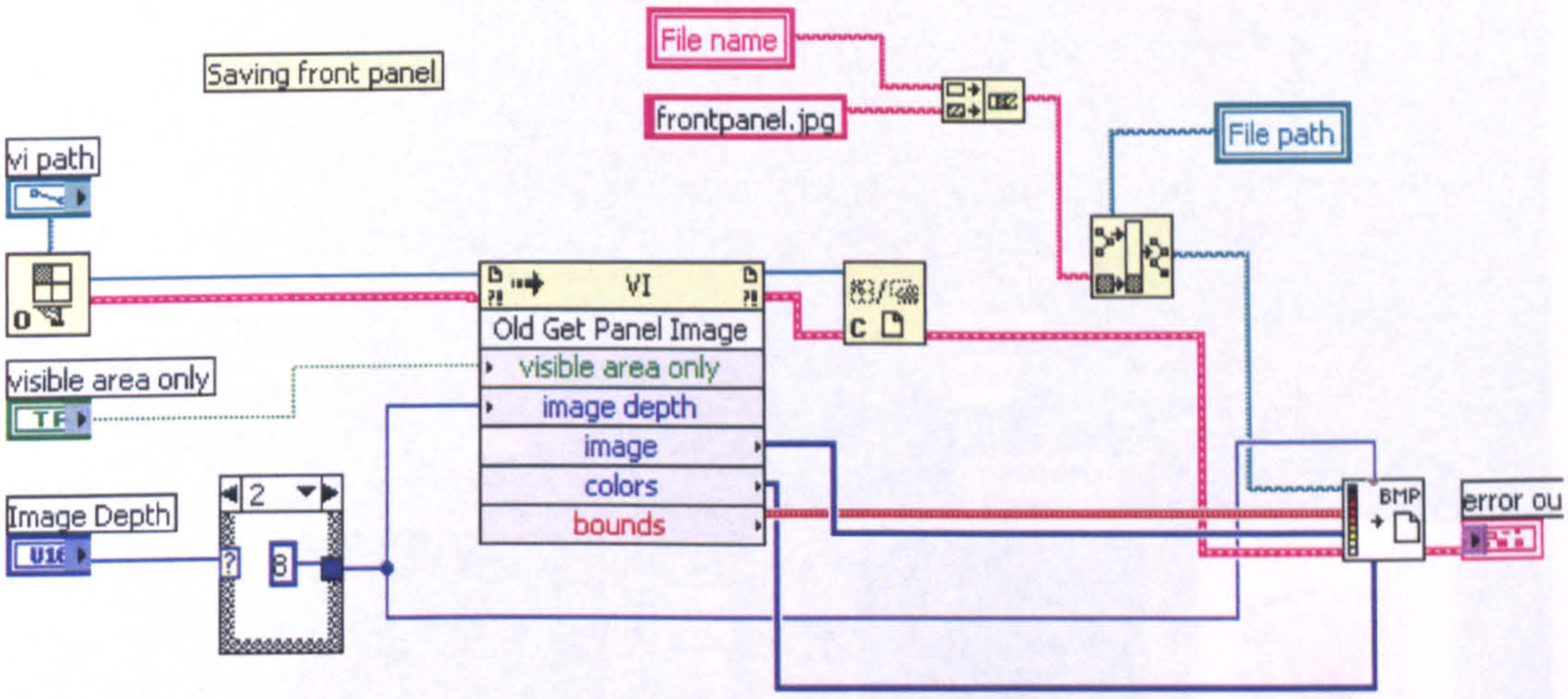

Figure 18: Showing the graphical code used to copy the front panel and save in .bmp or .jpg format.

This graphical code is reponsible for saving the current VI being executed in LabVIEW as a bitmap or jpeg image. This is useful in that an image showing all the data on one screen allows ease of reference between results.

3.3 Control of the piezo xyz translation stage (lateral resolution measurement)

A modified version of the axial PSF Gaussian fitting program was produced in order to take a lateral intensity scan of the confocal system and from it calculate the lateral point spread function of the system. The sample holder is mounted onto the xyz piezo stage. Using the same LabVIEW VIs used ("E-515 init" ,"E-515 REM" , "E-515 sServ" , "E-515 SP") when previously controlling the z-piezo translational stage, the status and position of each channel (axis) of the xyz stage was controlled by computer via the E-515 control box. Figure 19 shows the front panel of the lateral PSF and Gaussian fitting program.

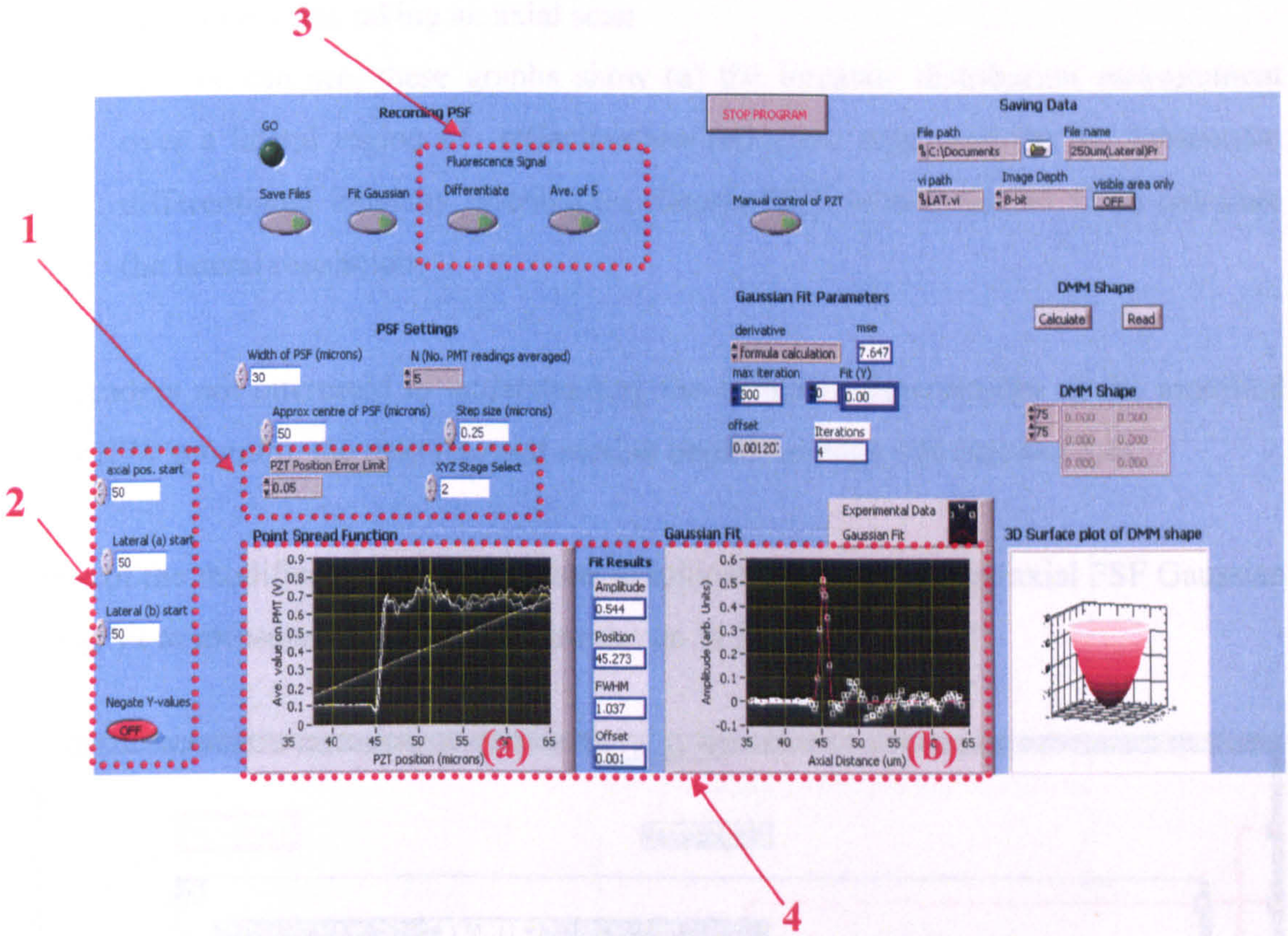

Figure 19: Showing the front panel control for the lateral PSF and Gaussian fit program written in LabVIEW.

The highlighted boxes show the main points of interest in this section of the program:

1. These numerical control boxes are responsible for selecting which axis of the xyz-piezo stage will perform the scan as well as controlling the position error limit (in μm) for each position moved within that axis.
2. These numerical controls define the starting position in μm of each of the axes. For the axes that are not chosen to perform the intensity scan, these values define their positions during the scan.
3. These buttons toggle the intensity differentiation and moving average functions. The differential function is required when measuring the lateral resolution from an lateral intensity distribution of a reflective edge. (See chapter 2 on lateral

resolution measurements.) The moving average function is used to smooth out any noise when taking an axial scan.

4. As one can see, these graphs show (a) the intensity distribution measurement over a lateral region of reflective/non-reflective edge, and (b) the subsequent differentiated intensity distribution (lateral PSF) with Gaussian fit to calculate the lateral resolution.

For readers not interested in understanding the complete functionality of the modified LabVIEW program, the next relevant section begins on page 199 (section 3.4).

Some of the modifications to the original graphical code to adapt the axial PSF Gaussian fitting VI to measure the lateral PSF are shown in figures 20 and 21.

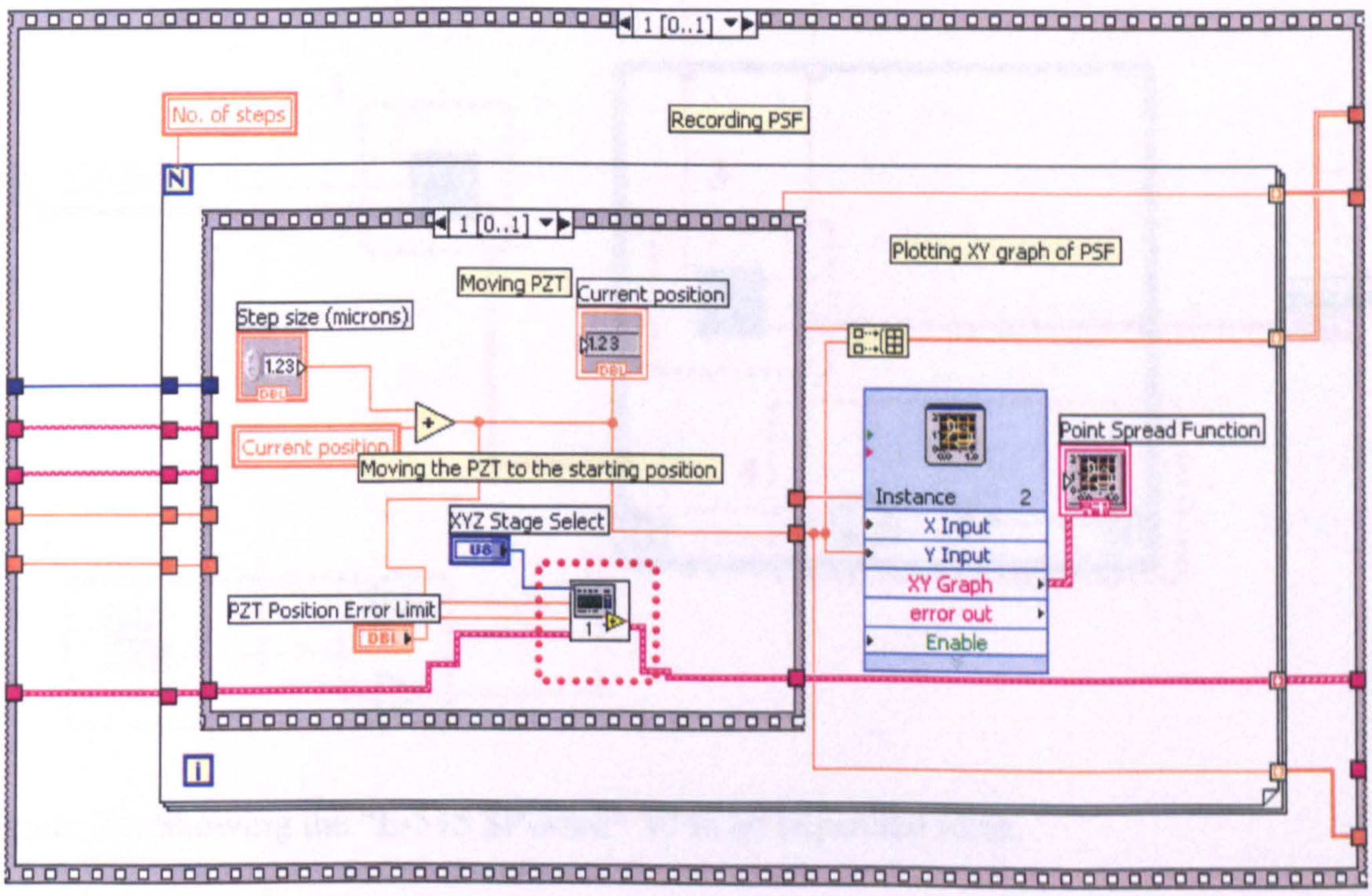

Figure 20: Showing the VIs responsible for moving the piezo stage to the desired location.

This is very similar to the section of graphical code present in the axial PSF Gaussian fitting VI (shown in figure 13) except that "E-515 SP" VI, responsible for controlling the position of the piezo stage, is now replaced with another VI known as "E-515 SP-Mod" VI which is shown in an expanded form in figure 21. Another important thing to note is that as well as the new VI having a position input, there are also two other inputs not present in "E-515 SP" VI. These allow the user (a) to select the required axis for the lateral intensity scan (inputs for each axis are X=1, Z=2, Y=0), and to (b) control the position error limit (in μm) for each position moved within that axis before the program will proceed further.

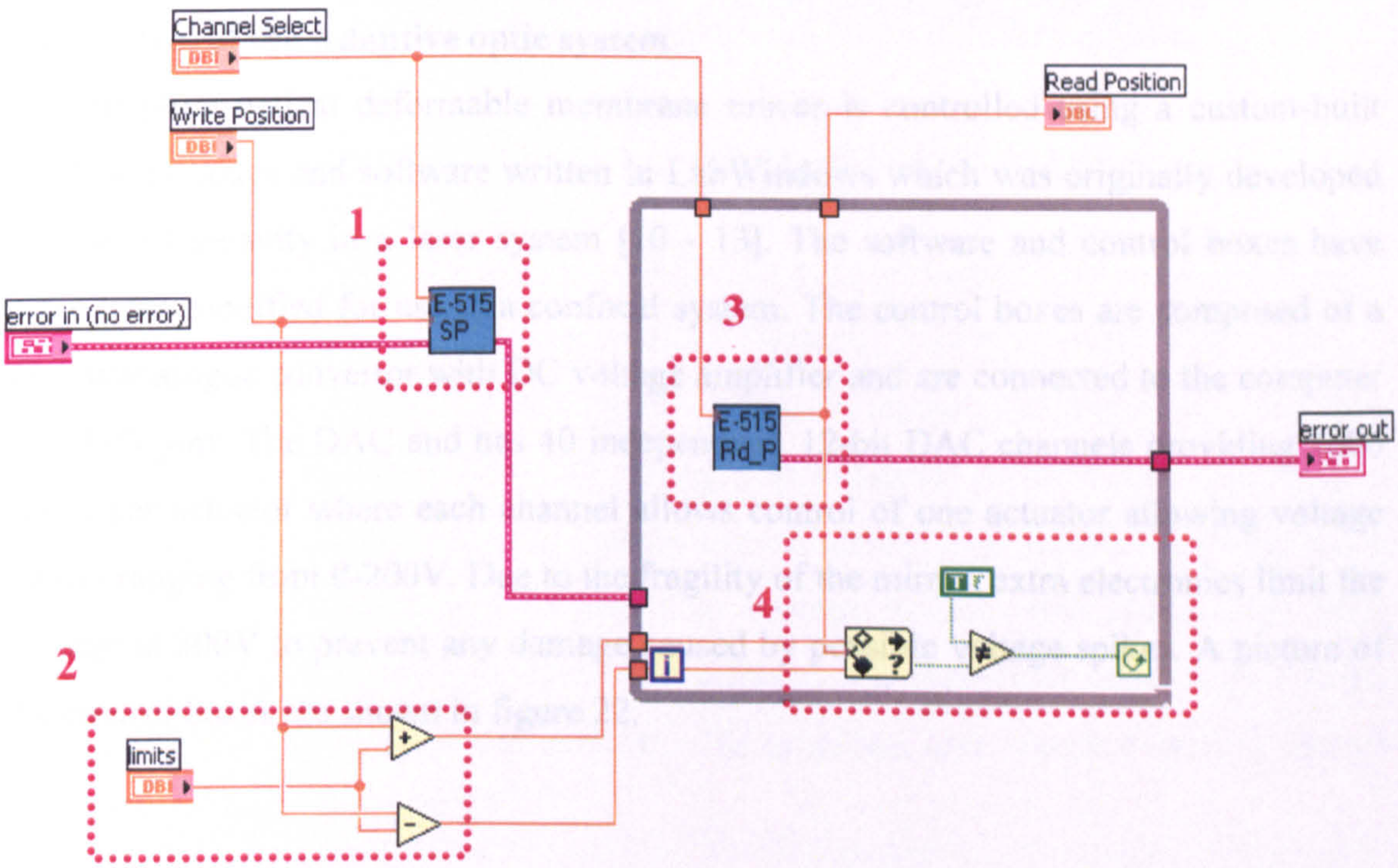

Figure 21: Showing the "E-515 SP-Mod" VI in an expanded form.

The purpose of this VI is to insure that the piezo translational stage has reached its destination within a set of pre-defined limits, before a reading from the PMT is taken. The main points of the VI are explained:

1. Using the "E-515 SP" VI, a command is sent to the E-515 control box to move an axis (defined by channel select) of the xyz piezo translation stage to a particular position.
2. From the limits input, the maximum and minimum allowed values are calculated.
3. Using the "E-515 Rd_P" (which commands the control box to send the current position of the chosen axis), a reading is taken of the piezo position.
4. The read position value is compared with the upper and lower range set by the position limit. If the read position is within these values, the program is completed. If not, the while loop instructs the program to re-read the position and compare with the upper and lower limits.

3.4 Control of the Adaptive optic system

The adaptive optical deformable membrane mirror is controlled using a custom-built electronics boxes and software written in LabWindows which was originally developed for use intra-cavity in a laser system [10 - 13]. The software and control boxes have since been modified for use in a confocal system. The control boxes are composed of a digital/analogue convertor with DC voltage amplifier and are connected to the computer via USB port. The DAC and has 40 independent, 12-bit DAC channels providing 4000 states per actuator where each channel allows control of one actuator allowing voltage output ranging from 0-200V. Due to the fragility of the mirror, extra electronics limit the voltage at 200V to prevent any damage caused by possible voltage spikes. A picture of the control boxes are shown in figure 22.

Figure 22: Showing the electronic boxes used in controlling the AO mirror.

As mentioned previously, the software control program was written in-house in ANSI C-code using LabWindows/CVI (National Instruments). LabWindows/CVI provides a programming environment for developing instrument control, automated test, and data acquisition applications in ANSI C. Using LabWindows provides the user with a graphical user interface editor, code builder wizard, control over Active X servers, and a development environment with windows to manage projects and source code with complete editing and debugging. Since the software was pre-written only modifications to the program will be described in detail. The graphical user interface used to control the mirror is shown in figure 23.

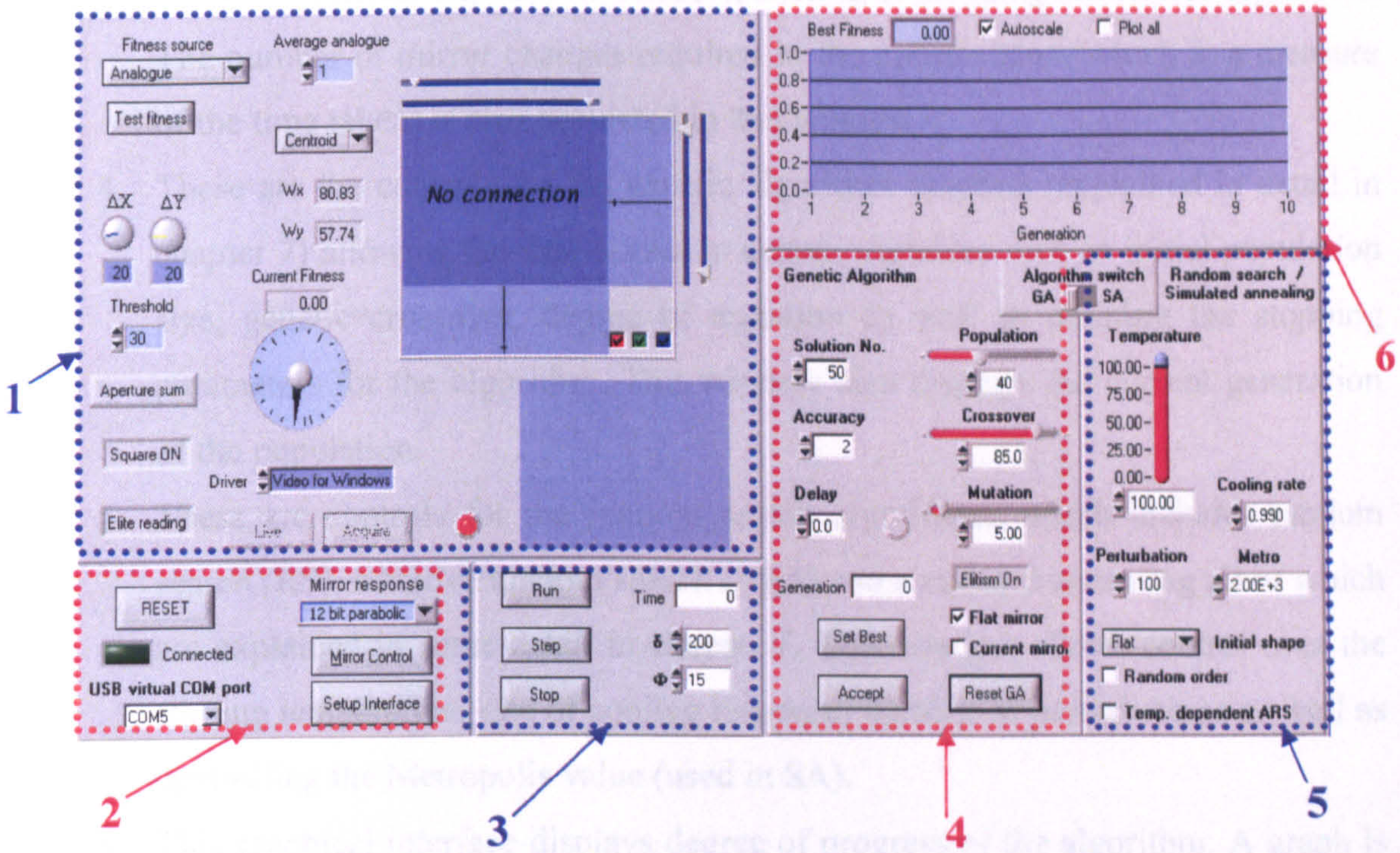

Figure 23: Showing the user interface of the LabWindows program responsible for controlling the DMM.

This program allowed mirror control through an interface or through various optimisation routines which optimise on a choice of fitness parameters. Some of the main functions of the program highlighted in the 6 boxes are explained in more detail:

1. This section allowed the user to control the fitness parameter being optimised as well as displaying the fitness value.
2. These are the interface controls of the system, two of which ("mirror control" and "set-up interface") provided access to sub-menus (see figures 24 and 25). The "USB virtual COM port" function selected defines which USB port is used to relay information to the electronic control box. The "mirror response" toggle controls an embedded square root function within the electronic control unit. This allows the mirror response to be controlled in a linear or a parabolic manner.

3. These are general algorithmic controls, starting or stopping the chosen algorithm. The number of mirror changes required in the optimisation (which is a measure of the time taken) is also presented in this window.
4. These are the controls for the genetic algorithm function (explained in detail in chapter 7) allowing the user access to certain variables such as initial population size, genetic crossover, degree of mutation as well as defining the stopping parameters for the algorithm. This window also displays the current generation of the population.
5. These are controls for the random search algorithms, which includes random search (RS), adaptive random search (ARS) and simulated annealing all of which are explained in some detail in chapter 7. This window allows control over the starting temperature, rate of cooling response, number of perturbations as well as controlling the Metropolis value (used in SA).
6. This graphical interface displays degree of progress of the algorithm. A graph is plotted showing the intensity of the fitness parameter against number of mirror changes.

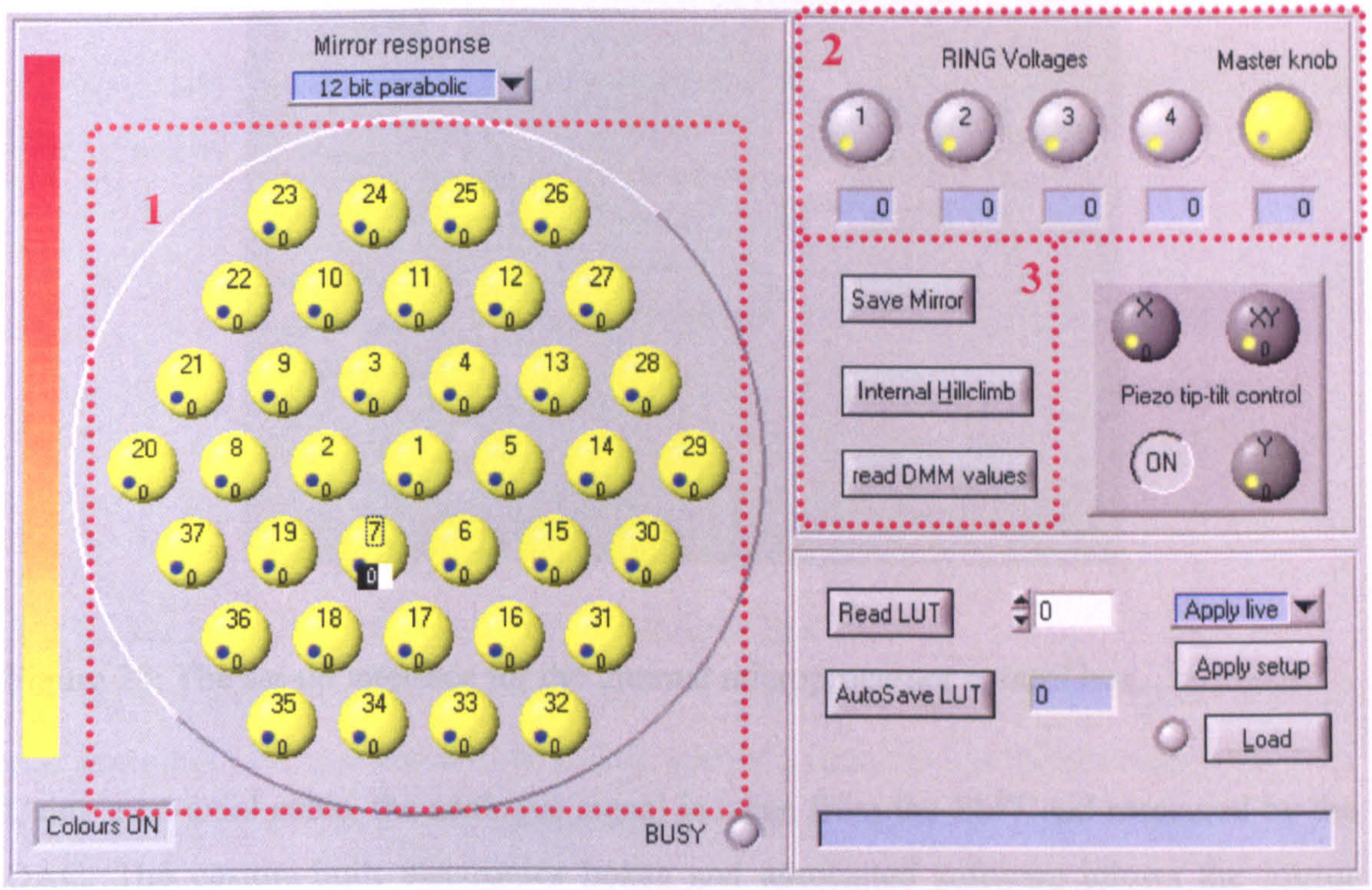

Figure 24: Showing the sub menu which allows manual mirror control.

The mirror response sub-menu, accessible using the "mirror response" button on the main menu, allows complete manual control of the deformable membrane mirror. The main points of interest for figure 24 are highlighted in the red dashed boxes:

1. This interface allows the user to individually control each of the 37 actuators.
2. This controls the actuators in the four main rings.
3. This allows the mirror shape to be saved in terms of actuator voltages. The internal hillclimb function, embedded within the microprocessor control box, can be switched on here.

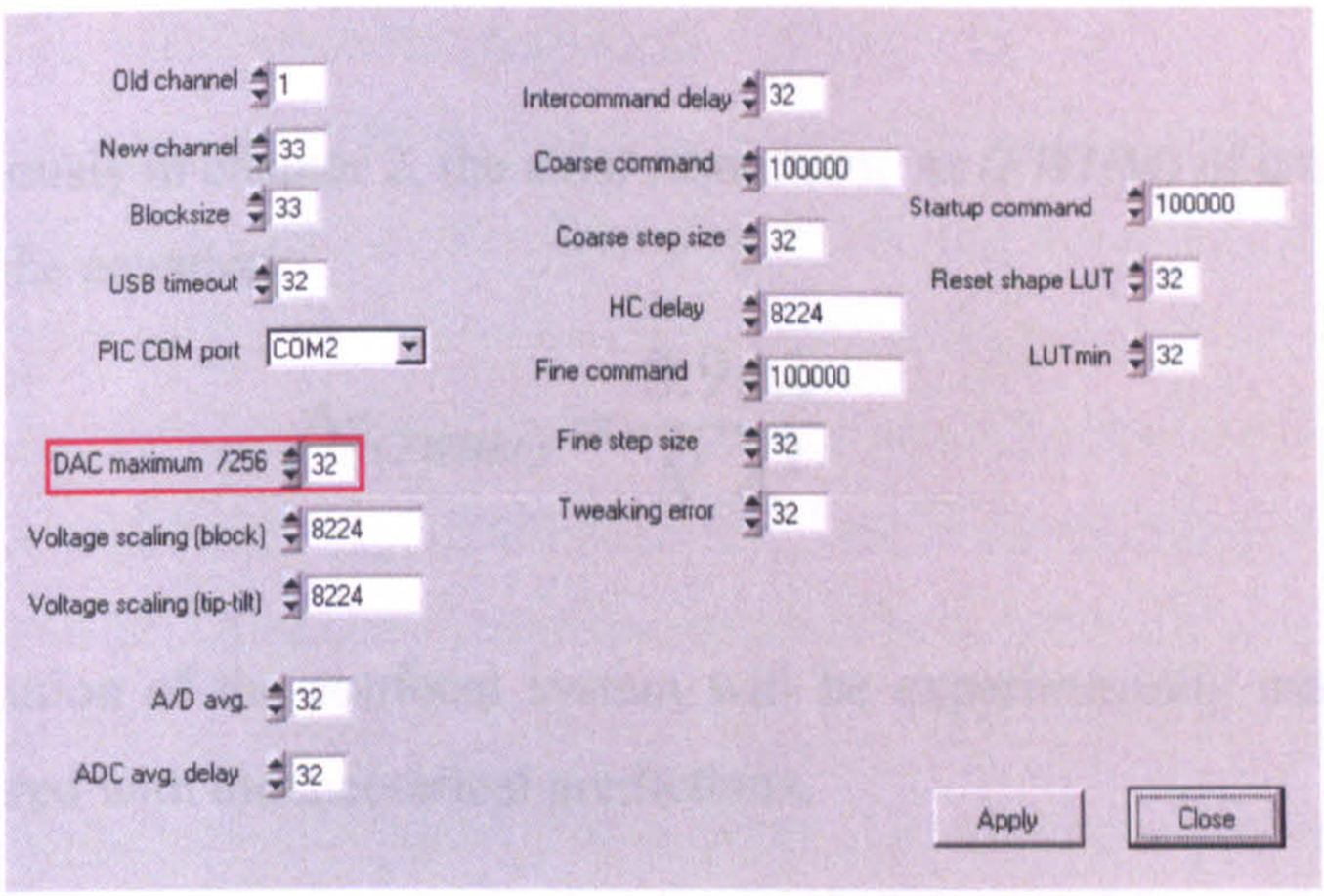

Figure 25: The set-up interface for the internal microprocessor control box.

Using a co-axial cable, the analogue signal is taken from the PMT and measured by the DAC. The custom-built electronics boxes and associated software allows the mirror shape to be altered via computer interface or through optimisation routines which where are either present in the software (GA, RS, ARS and SA) or embedded within a microprocessor within the electronics box (MHC). The signal output from the PMT, which measures the reflection intensity in the confocal system, is used as a fitness value and therefore can be optimised.

4. Confocal system characterisation

Before examining the use of an adaptive element in the confocal system, the properties associated with the confocal system itself were examined and evaluated. These include the optical sectioning capabilities and the effect of induced aberrations on the axial PSF and resolution. In particular the effect of varying:

1. the numerical aperture (N.A.) using various types of microscope objectives
2. The pinhole size in front of the detector which is responsible for rejecting out-of-focus light
3. The type of immersion media used (n)
4. Wavelength of the laser used (λ)

As shown previously in chapter 2, the axial resolution, Δz *(FWHM)* of a confocal system is governed by the equation:

$$\Delta z_{(FWHM)} = \frac{0.9n\lambda}{N.A.^2} \tag{2}$$

The axial resolution of the confocal system will be experimentally measured in each case and compared with the theoretical predictions.

4.1 Taking an axial PSF scan using the mirror test

For these confocal system characterisation experiments, the adaptive optical element was replaced with a plane mirror. Using computer control, the galvos responsible for scanning the laser across the sample were parked at the centre of the x and y ranges. Using a single coated aluminium mirror [Newfocus or Comar] placed into a sample position, the position of the central intensity peak was coarsely matched the midpoint of the z-piezo stage (50μm) using both the sample mounted xyz-translation stage and the z-piezo using the manual control located on the control box. Before performing an axial scan, care was taken to ensure that the PMT output response at the central intensity peak had not saturated (using the gain control).

Using the axial PSF and gaussian fitting program LabVIEW program previously described, an axial PSF (which is a measure of the light intensity through the z-axis) was taken from a depth scan of the mirror. Due to the main peak of the axial PSF closely following a normal distribution, a gaussian curve was fitted to the PSF and the FWHM measured. As mentioned in chapter 2, the measurement of the intensity distribution with depth (z-axis) using a single metallic coated mirror is considered the "gold standard" of axial resolution in measurement in confocal microscopy [14].

4.2 Objective N.A. effect on axial resolution

Axial PSFs were taken using three objectives with different N.A. using the HeNe laser illumination. Normalising all the data peaks to 1, the results are plotted and compared in figure 26. All objective lenses used were infinity corrected and manufactured by Nikon. These were an air immersion x10 achromat flatfield objective lens with 0.25 NA and a working distance of 6.1mm, an air immersion x20 plan fluor objective with 0.5 N.A and a working distance of 2.1mm, and an oil immersion x100 plan chromat 1.25 N.A. lens with a 0.18mm working distance. Care was taken to insure that the light completely filled the back aperture of the each objective lenses. The oil immersion medium used for the 1.25N.A. lens has a refractive index of 1.51.

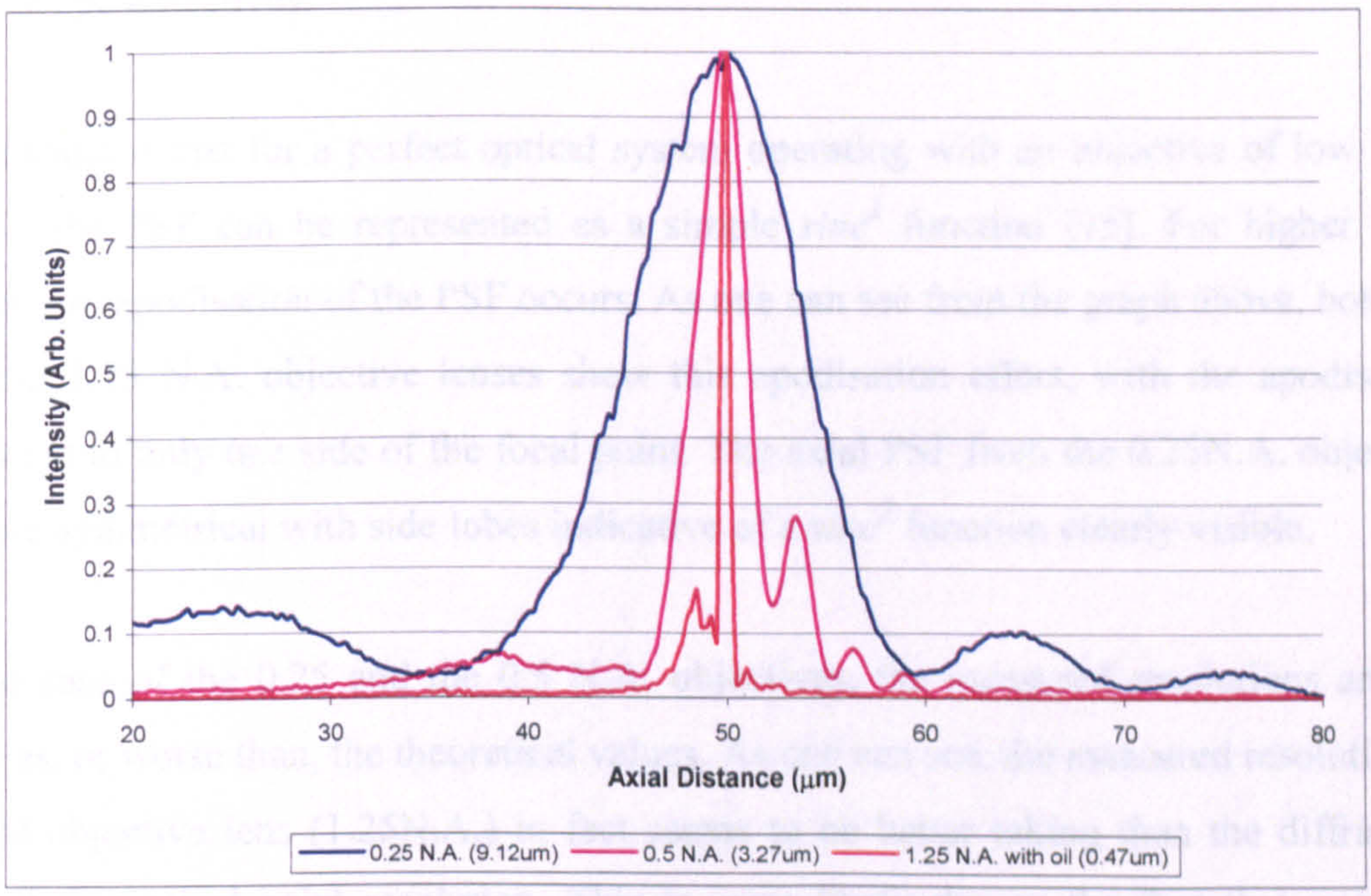

Figure 26: Axial PSFs using various microscope objectives.

The FWHMs for the 0.25N.A., 0.5N.A. and 1.25N.A. objectives were measured and compared with the theoretical calculations using equation 2. Results are shown in table 1.

Objective N.A.	immersion medium R.I., n	Experimental FWHM (μm)	Theoretical FWHM (μm)
0.25	1	9.1+/-0.5	9.1
0.5	1	3.3+/-0.5	2.3
1.25	1.51	0.47+/-0.05	0.55

Table 1: Comparing experimental and axial resolutions using various types of microscope objectives.

It is expected that for a perfect optical system operating with an objective of low N.A. (<0.5), the PSF can be represented as a simple $sinc^2$ function [15]. For higher N.A. objectives, apodisation of the PSF occurs. As one can see from the graph above, both the 0.5 and 1.25 N.A. objective lenses show this apodisation effect, with the apodisation restricted to only one side of the focal point. The axial PSF from the 0.25N.A. objective is more symmetrical with side lobes indicative of a $sinc^2$ function clearly visible.

In the case of the 0.25 and the 0.5 N.A. objectives, the measured resolutions are the same as, or worse than, the theoretical values. As one can see, the measured resolution in the oil objective lens (1.25N.A.) in fact seems to be better taking than the diffraction limited theoretical axial resolution. This is most likely due to the fact that errors in calculating the FWHM from the apodised PSF when using the Gaussian fitting program.

4.3 The effect on pinhole size on the PSF

The effect of the pinhole size on the capability of the confocal system to optically section was examined. The system used in this work employed a beam expander with an

iris as an effective confocal arrangement. The size of the iris was changed to give various 'pinhole' sizes and hence various degrees of confocality. In this case the iris was changed to four various positions with position 1, being the smallest size and position 4 being the largest. Figures 27-29 show the PSFs of the objectives with four effective pinhole sizes. From Wilson [16], it was shown that the strength of sectioning is dependent on the pinhole size, down to a certain limit, known as the optimal pinhole size, d_o. The optimal pinhole size required was found to be related to the total magnification of the system, M, the $N.A.$ of the objective, and the wavelength of the laser source λ, and can be calculated using the equation:

$$\frac{M}{N.A.} \geq \frac{\pi d_o}{2.5\lambda} \tag{3}$$

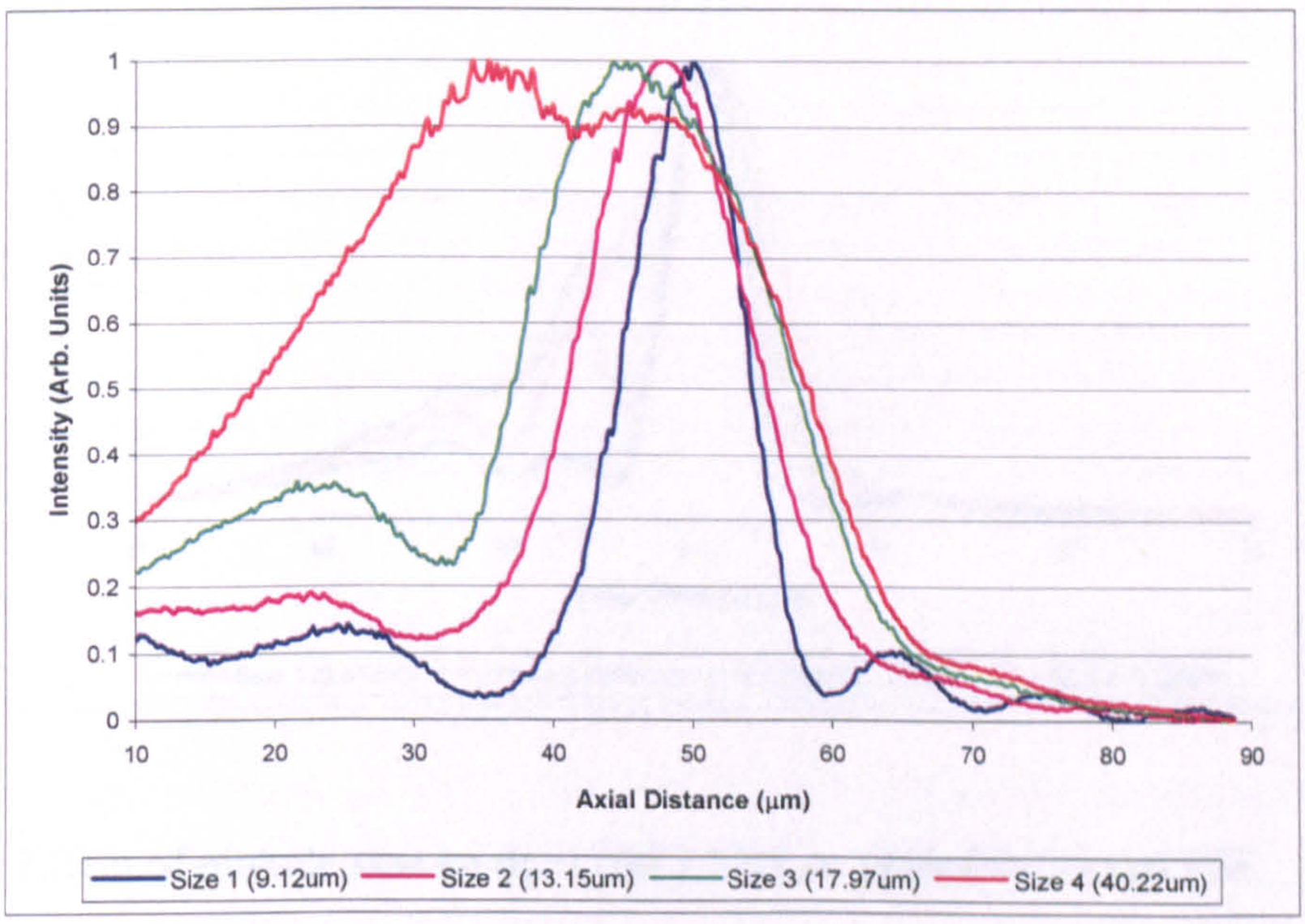

Figure 27: Effect of pinhole size on the x10 0.25N.A. objective's axial PSF.

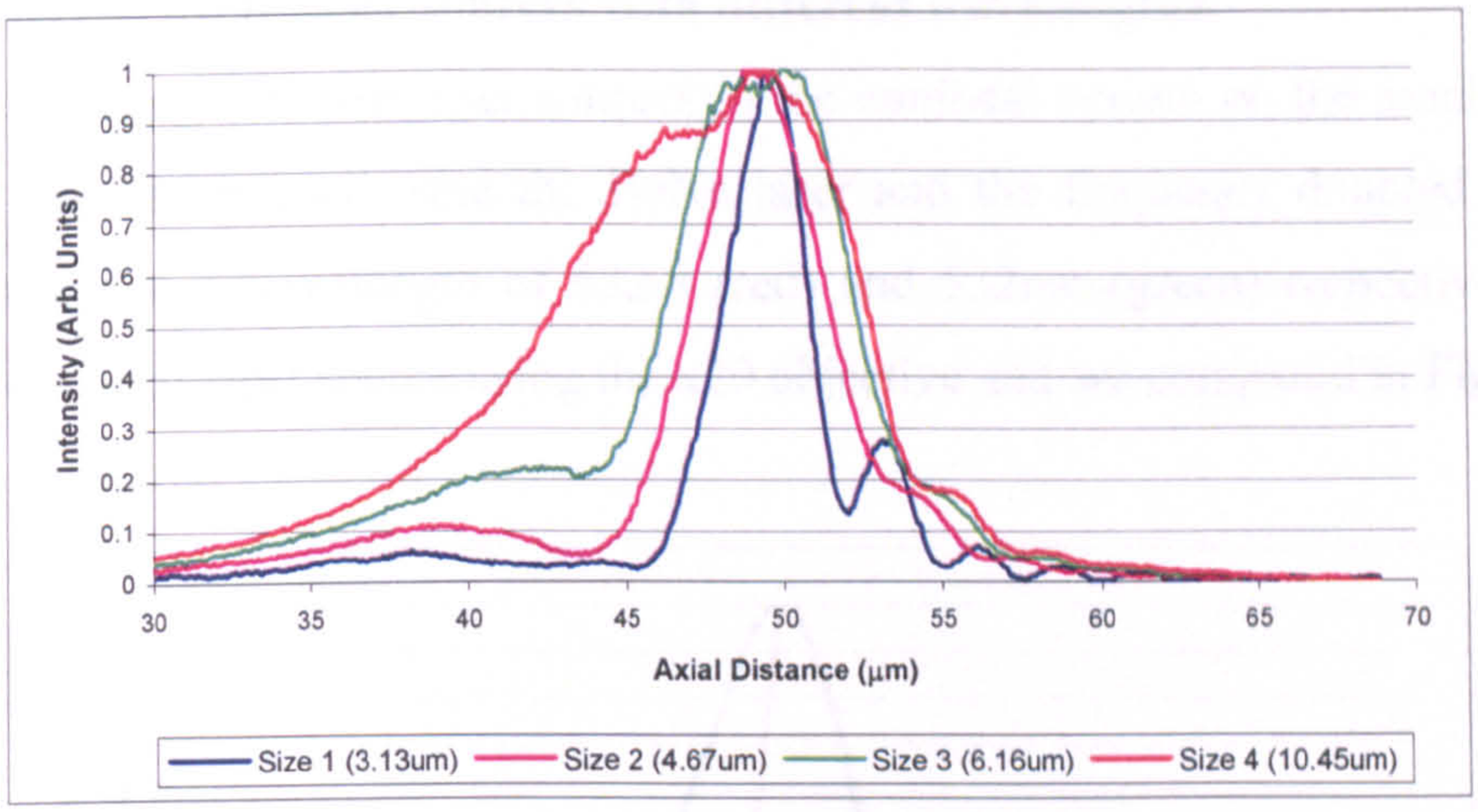

Figure 28: Effect of pinhole size on the x20 0.5N.A. objective's axial PSF.

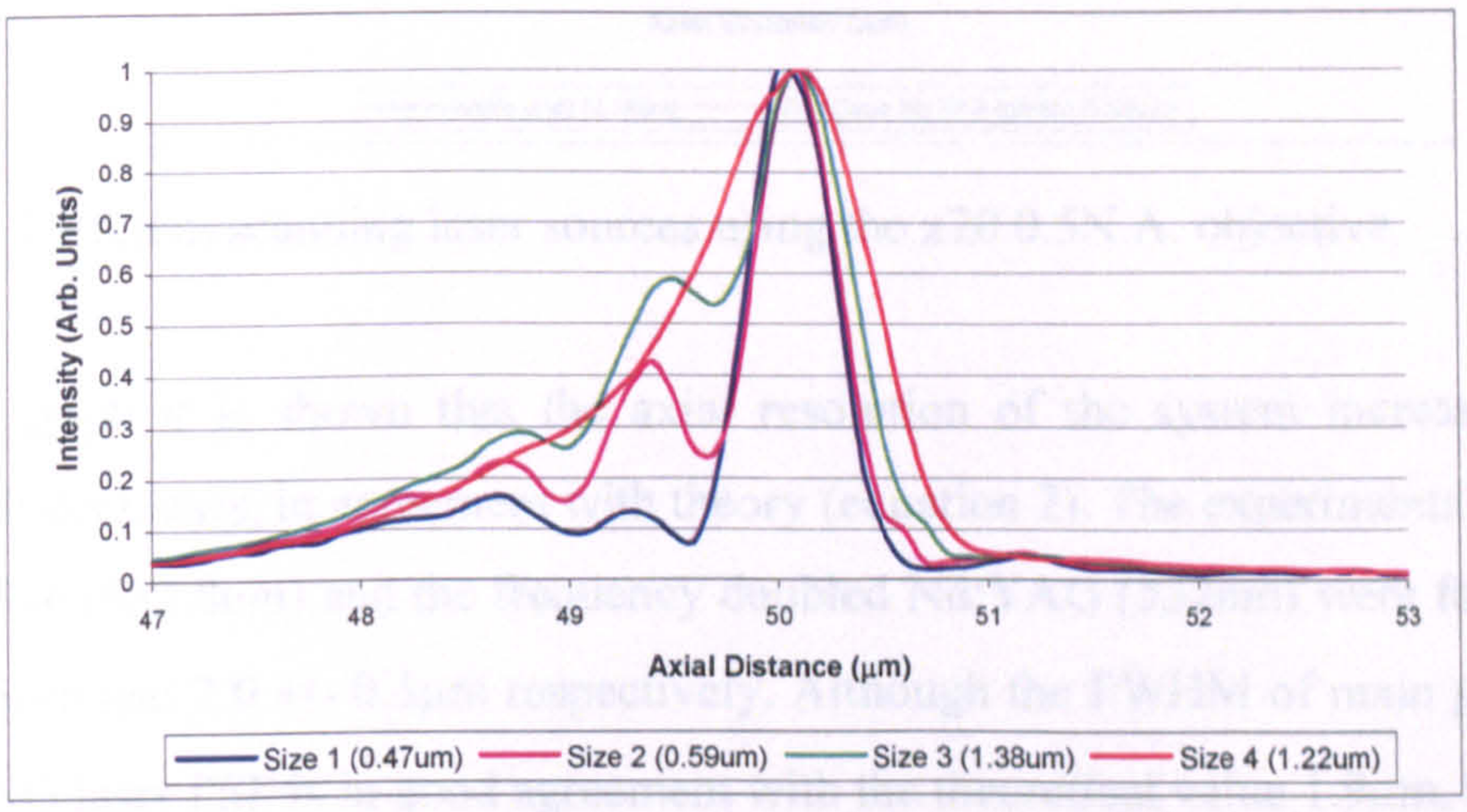

Figure 29: Effect of pinhole size on the x100 1.25N.A. objective's axial PSF.

From the Figures 27-29, it can be seen that as the pinhole size increased the PSF, as well as increasing in size, the profile becomes more asymmetrical, with one side of the peak falling off much more rapidly than the other. It was also noted that for all objectives the optimum pinhole size is lower than position 2.

4.4 The effect of using laser sources with different wavelengths:

The effect of using different laser sources in the confocal system on the axial PSF was measured. The lasers used were the HeNe laser and the frequency doubled Nd:YAG laser operating at a wavelength of 632.8 (red) and 532nm (green) respectively. PSFs were taken of each laser source using the x20 objective and are compared in Figure 30.

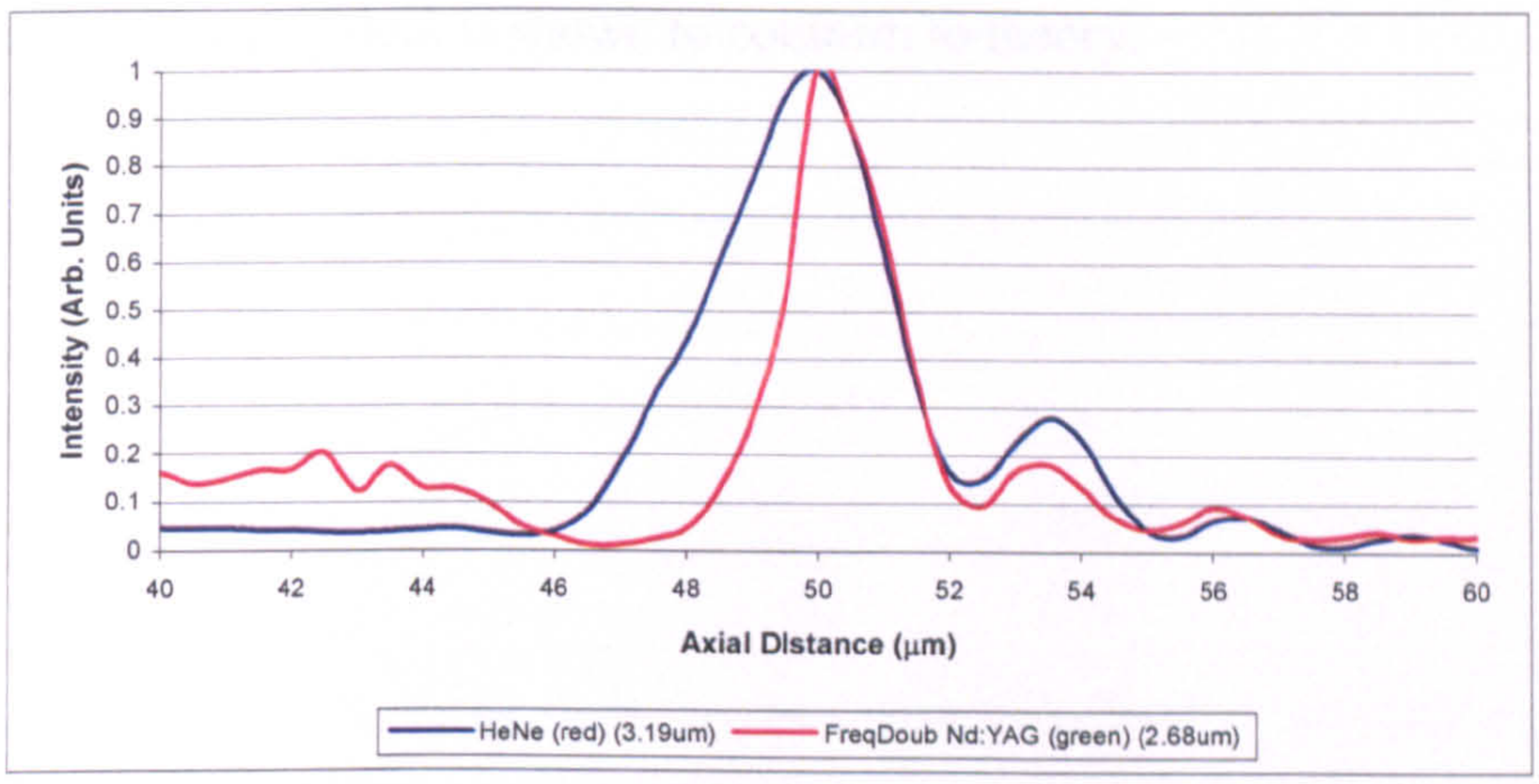

Figure 30: Different scanning laser sources using the x20 0.5N.A. objective.

From the graph it is shown that the axial resolution of the system increases as the wavelength decreases, in agreement with theory (equation 2). The experimental FWHMs for the HeNe (632.8nm) and the frequency doubled Nd:YAG (532nm) were found to be 3.2 +/- 0.5μm and 2.0 +/- 0.5μm respectively. Although the FWHM of main peak using the Nd:YAG laser PSF is in good agreement with the theoretical value 1.9μm, the PSF is highly asymmetrical in nature. The FWHM for the HeNe laser is found to be higher than expected (theoretical FWHM = 2.3μm). Like the asymmetry associated with the green laser PSF, this is most likely due to aberrations introduced by mis-alignments in the optical configuration of the system.

5. Summary

In this chapter, the optical design of the confocal system incorporating the adaptive optical element has been described in detail. Control of the main components which

includes the laser scanning system, piezo translational stages (responsible for sample movement and axial depth) as well as the deformable membrane mirror, have been illustrated. The computer programs (written in LabVIEW) and methods used to measure the axial and lateral PSFs and resolutions have been explained. By examining the effects of varying objective N.A., pinhole size and illumination wavelength on the axial PSF and resolution, the confocal system has been characterised. From the results, the experimental confocal system is shown to conform to theory.

References

1. Wilson, T., Carlini, A. R. (1989). The effect of aberrations on the axial response of confocal imaging systems. *J. of Microscopy*, 154, 243-256
2. Wan, D., Rajadhyasksha, M., Webb, R. H. (2000). Analysis of spherical aberration of a water immersion objective:application to specimens with refractive indices 1.33-1.40. J. of Microscopy, 197, 274-284
3. Marsh, P. N., Burns, D., Girkin, J. M. (2003). Practical implementation of adaptive optics in multiphoton microscopy. *Optics Express*, 11, 1123-1130.
4. Wright, A. J., Burns, D., Patterson, B. A., Poland, S. P. Valentine, G., Girkin, J. M. (2005). Active aberration correction in confocal and multiphoton microscopy. *Microscopy research and technique*, 67, 36 – 44.
5. Okotech (flexible optical B.V.), PO box 581, 2600 AN, Delft, the Netherlands, www.okotech.com.
6. Poland, S. P., Burns, D., Lubeigt, W., Patterson, B. A., Valentine, G., Wright A. J., Girkin, J. M. (2005). Use of optimisation algorithmic techniques with active optics for aberration correction in optical sectioning microscopy. *Proc. SPIE*, 6018, 60181H.
7. Physik Instrumente (PI), GmbH & Co. KG, Auf der Römerstr. 1, D-76228 Karlsruhe/Palmbach, Germany, www.pi.ws.
8. LabVIEW 7.1 full development software user manual, Chapter 1: Introduction.
9. Thomson, D. Gaussian fitting LabVIEW code. LabVIEW utility programs, Original Code Consulting, retrieved 2nd of May 2004 from www.originalcode.com.
10. Lubeigt, W., Valentine, G., Girkin, J., Bente, E., Burns, D. (2002). Active transverse mode control and optimisation of all-solid-state laser using an intracavity adaptive-optic mirror. Opt. Express, 10, 550 – 555.
11. Lubeigt, W., Van Grol, P., Valentine, G., Burns, D. (2004). Use of intra-cavity adaptive optics in solid-state lasers operating at 1μm. Proc. of EMRS DTC Conf. 2004, B6.

12. Lubeigt, W. Valentine, G. J., Burns, D. (2005). Brightness enhancement of a solid-state laser using an intra-cavity deformable mirror. *Proc. of SPIE*, 6018, 60180I.
13. Lubeigt, W. (2005). Intra-Cavity Adaptive Optics Control of Solid-State Lasers, PhD thesis submitted to the Department of Physics, University of Strathclyde.
14. Zucker, R.M. (2004) Confocal Microscopy System Performance. Axial Resolution. *Microscopy Today*, 12(1). Jan Feb 2004.
15. Cogswell, C. J., Larkin, K. G. (1995). Chapter 8: The specimen illumination path and its effect on image quality, *Handbook of biological Confocal Microscopy*, 2nd Edition, Pawley, J. ed, Plenum Press, New York, 127 – 137.
16. Wilson, T., (1995). The role of the pinhole in confocal imaging system. *Handbook of biological Confocal Microscopy*, 2nd Edition, Pawley, J. ed, Plenum Press, New York, 167 – 182.

Chapter 7: Adaptive optical methods for optimisation in confocal microscopy

1. Introduction

In this investigation, the effectiveness of a number of algorithms in optimising for sample induced aberrations are examined. These are (a) modified hill climbing (MHC), (b) random search (RS), (c) adaptive random search (ARS), (d) genetic algorithm (GA), and (e) simulated annealing (SA). The viability and efficiency of a number of fitness parameters used in the optimisation routines are also considered. These include the image brightness, the axial resolution and the shape of the axial point spread function of the sample. The algorithms and fitness parameters are compared in terms of reliability and repeatability of the solutions, the time required to complete an optimisation and the final axial resolution of the system.

Various axial fitness parameters associated with an axial PSF, optimised using the GA, are tested and compared with an intensity optimisation in terms of the number of mirror changes to reach optimisation and final FWHM value. The effects of these optimisation parameters on the lateral resolution of the system are also examined.

Using a modified fitness parameter and the GA, the ability of the adaptive optic system to optimise to a particular axial PSF is also examined. Although PSF engineering by altering the properties of pupil plane filters has been shown previously [1 - 4], in our set-up, the deformable mirror and GA optimisation algorithm are used to optimise for a specific set of PSF properties. In this instance, the system was tested to reproduce Gaussian curves having various full-width half-maxima ranging from 2 μm to 30μm.

2. Considerations associated with the axial resolution measurements

2. 1 Effects of specimen induced aberrations on the axial resolution

Using test samples instead of biological samples, it is possible to accurately control sample aberrations. These test samples were composed of various depths of water sandwiched between a coverslip (no. 1.5) and an aluminium mirror. Using shim splints of various known thicknesses placed between the mirror and the coverslip allowed control over the thickness of the sample (see figure 1). With a pipette, water was added by capillary action and the sample was sealed using nail varnish, which acts as both a glue and sealant.

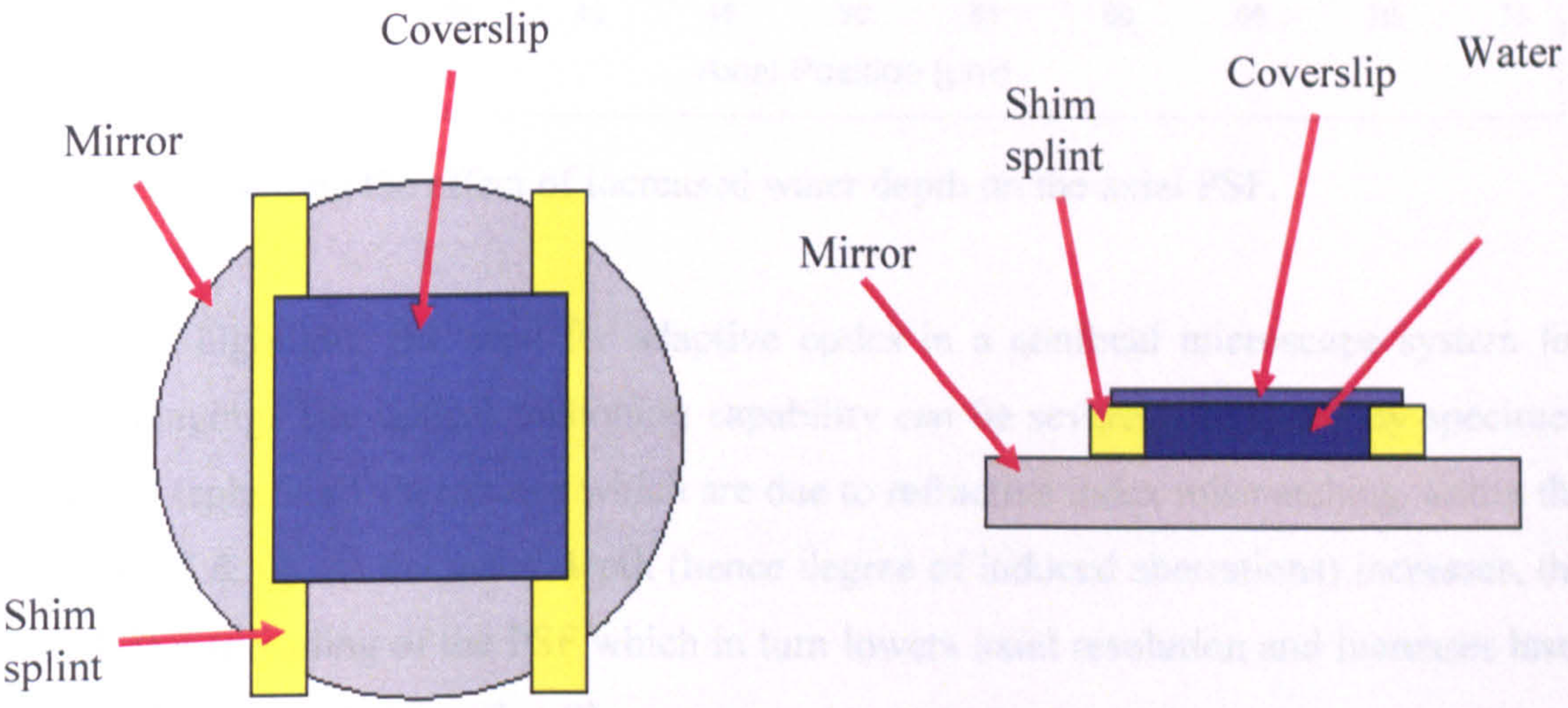

Figure 1: Showing test sample preparation.

Using the red HeNe laser and the x20 0.5 N.A. Nikon objective in the confocal set-up, axial PSFs were taken for test samples composed of various depths of water (see figure 2). It shown be noted that the results in figure 2 are not normalised to peak intensity.

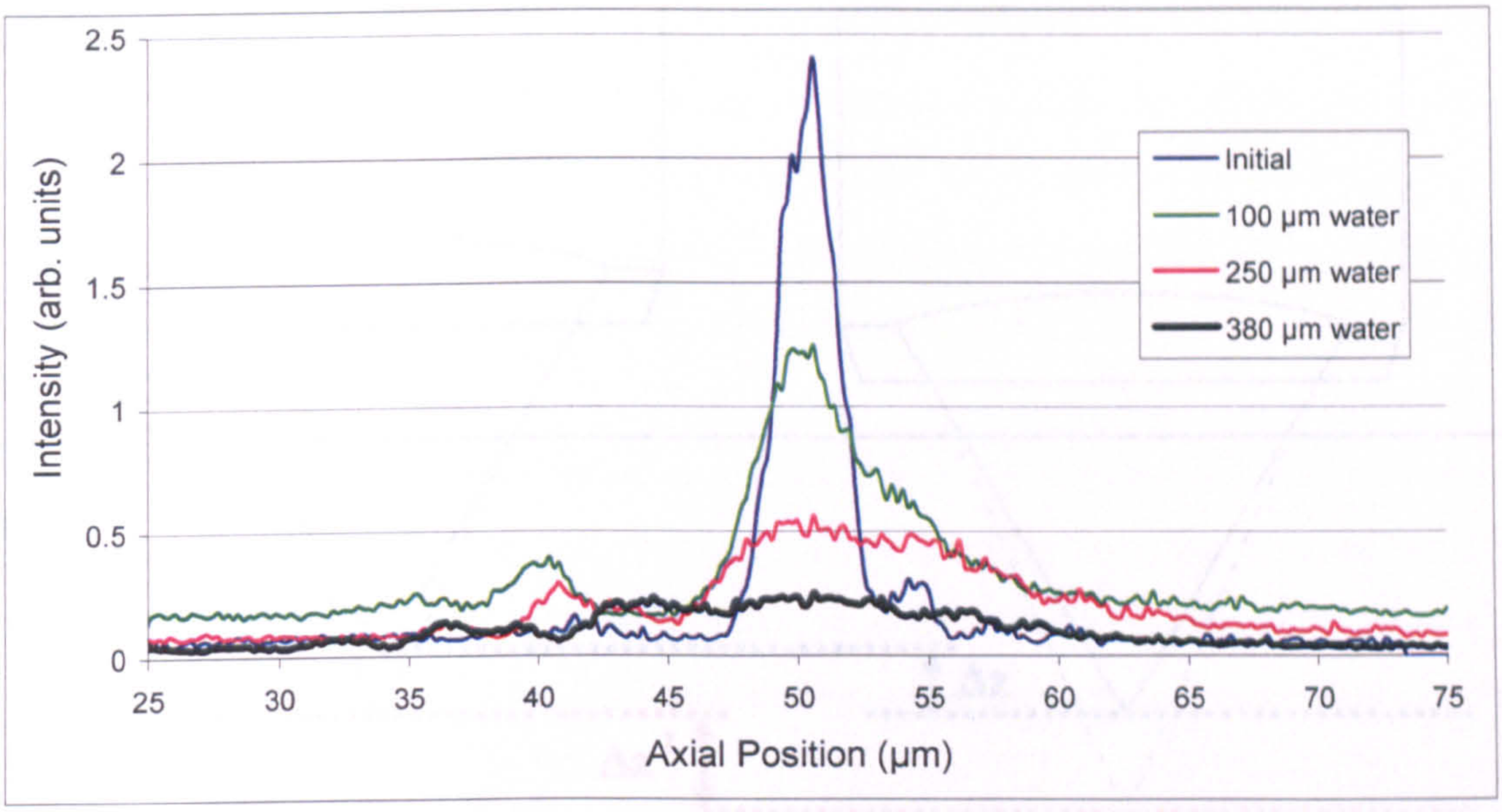

Figure 2: Showing the effect of increased water depth on the axial PSF.

Figure 2 highlights the need for adaptive optics in a confocal microscope system for deep imaging. The optical sectioning capability can be severely degraded by specimen induced (spherical) aberrations which are due to refractive index mismatching within the sample [5 & 6]. As the water depth (hence degree of induced aberrations) increases, the result is a spreading of the PSF which in turn lowers axial resolution and increases laser power for same intensity [7 – 9].

2.2 The focal shift

When taking axial scans through a multilayered media composed of different refractive indices, the axial distance traveled by the objective (controlled by the piezo stage) can be different to the axial distance traveled by the focal spot. This is known as a focal shift [10] and this causes the focus to move a greater distance than that moved by the piezo stage. This causes objects to appear thinner than they actually are, and is related to the refractive index change between the objective and the sample (see figure 3). For simplicity in this investigation, all axial and lateral measurements taken will be directly quoted from the piezo translational stage for ease of comparison.

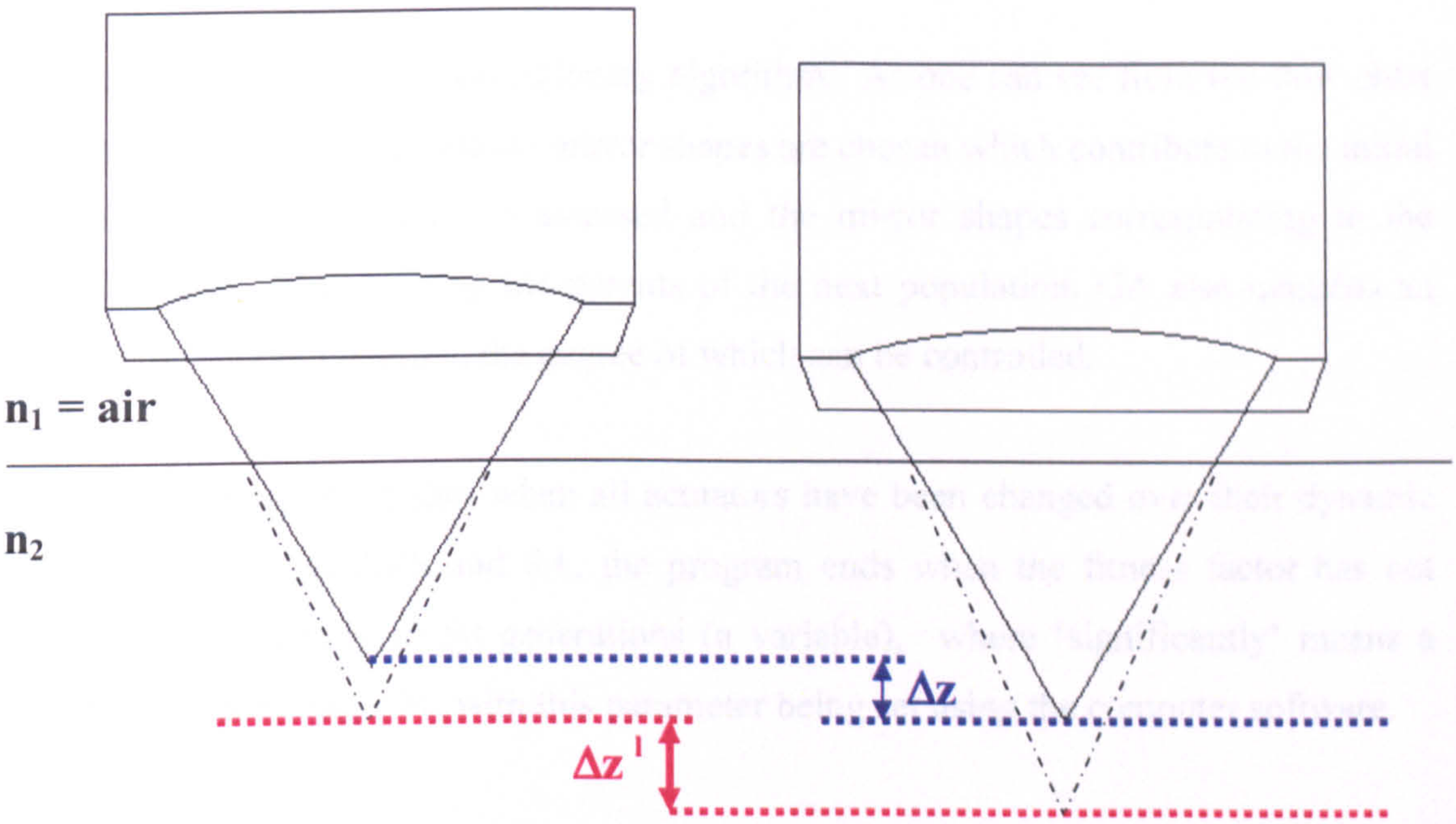

Figure 3: The focal shift when taking an axial scan.

As one can see from figure 3, when traveling an axial distance Δz into a sample with a refractive index n_2 which is greater than air ($n_1 = 1$), the focal spot travels an axial distance of Δz^1.

3. The use of algorithmic routines for optimisation of intensity

As described in chapter 5, when using MHC, RS, ARS and SA algorithms, each actuator is chosen in turn and the voltage value varied. For MHC, the algorithm finishes when all actuators have been changed over their dynamic range. ARS differs from RS in that the voltage change at each step is not constant but is in fact related to the 'temperature' of the system at the time, with the cooling rate and starting temperature all contributory factors to this. SA differs from RS in that there is a possibility that it accepts lower fitness values. The temperature of the system also contributes to a random acceptance of a lower fitness parameter.

GA can be described as an evolutionary algorithm. As one can see from the flow chart (chapter 5, figure 17), 40 random mirror shapes are chosen which contribute to the initial population. This population is assessed and the mirror shapes corresponding to the highest fitness value forming the parents of the next population. GA also contains an element of random mutation, the degree of which can be controlled.

The MHC algorithm finishes when all actuators have been changed over their dynamic range. For GA, RS, ARS and SA, the program ends when the fitness factor has not improved significantly in 50 generations (a variable), where 'significantly' means a change of greater than 1 %, with this parameter being set using the computer software.

Parking the scanning galvos at their midpoint positions, the light intensity of a point (the analogue output signal taken from the PMT) was taken as the fitness parameter. Before running the optimisation routine, an axial PSF was taken and the PZT was set to the axial position that gives the maximum signal. This should correspond to the axial focal point of the system that gives the maximum intensity output or the main peak. Problems exist in some cases where a highly aberrated PSF could contain more than one peak of equal amplitude. In this case, preliminary optimisations must be carried out to find the correct peak i.e. the one that corresponds to the greatest intensity increase during the optimisation process. In order to ensure that the PMT signal does not go over 1V, and therefore act non-linearly during the optimisation process, the pre-optimised gain of the PMT is initially set to ~0.3V.

Using each algorithm, the intensity was optimised for various test samples. Each algorithm was assessed according to its signal intensity improvement factor (final fitness value/starting fitness value), axial resolution improvement factor (initial FWHM/final FWHM) as well as the number of mirror shapes (a measure of the time taken) required to complete the optimisation.

3.1 Local optimisations versus global optimisations [8].

The pre-optimised axial PSF was taken with the membrane flat (when actuators are at 0V). Using a sample with a 250μm depth of water, the axial resolution of the system pre-optimisation was found to be 15.6 +/- 0.2μm. This is due to aberrations produced by the water which causing a widening of the PSF and a lowering of signal intensity. The other PSFs are taken after an optimisation routine had been performed and the DMM solution shape set. The results are plotted in figure 4.

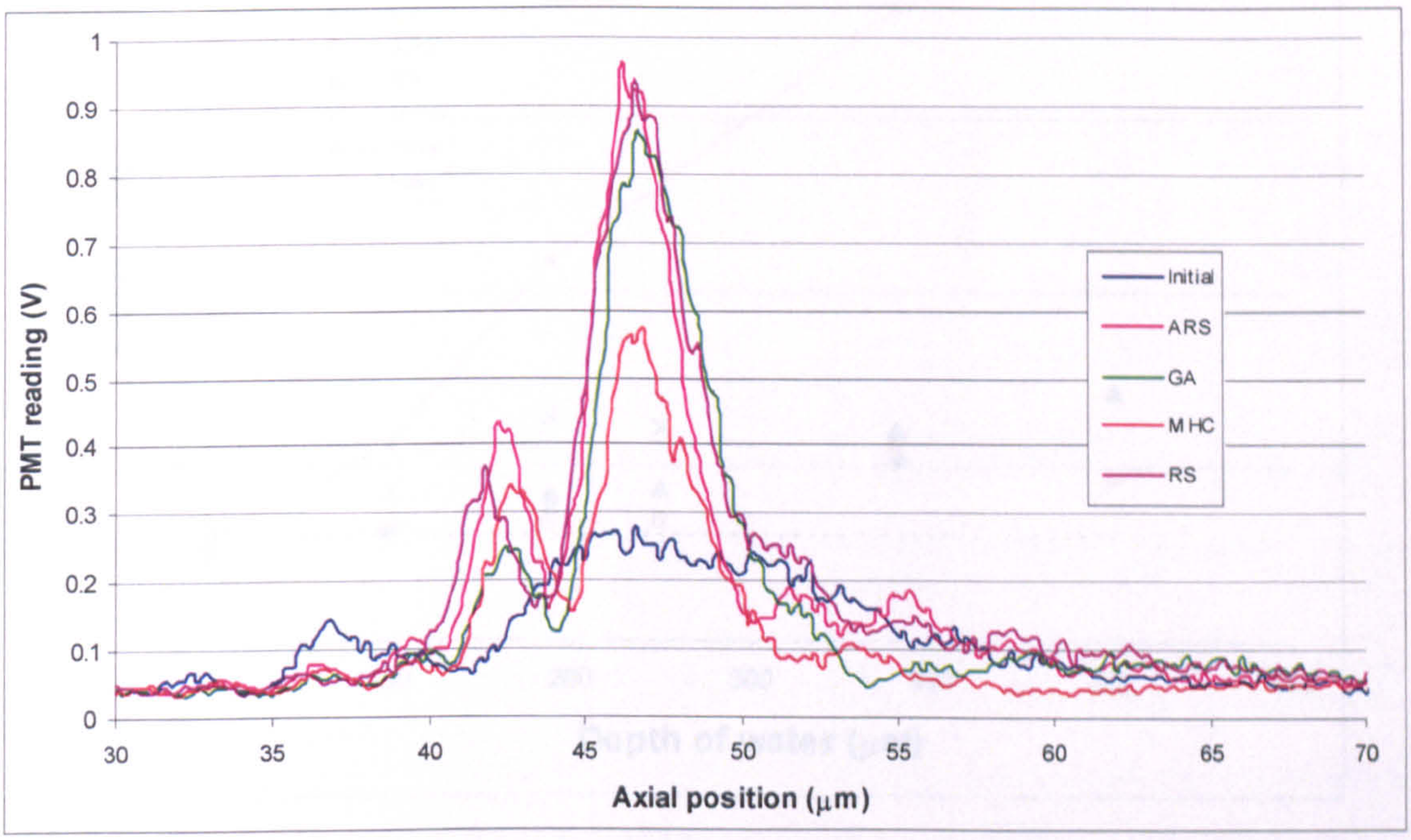

Figure 4: Comparing PSFs for each algorithm in using a test sample with a 250μm depth of water.

It can be seen from figure 4, each optimisation technique considerably enhanced the peak intensity of the PSF and, as a result, improved the axial resolution of the system. Comparing local to more global solutions, it can also be seen that ARS, RS, and GA showed greater improvement than the MHC at optimising for aberrations at this depth.

Using test samples containing water at different depths, each optimisation technique was evaluated. Figure 5 shows the relationship between the FWHM to the water depth of the test sample used in the optimisation. A comparison was also made with the initial pre-optimised FWHM at various water depths, as well as the FWHM with no induced aberrations (a plane mirror and coverslip containing no water).

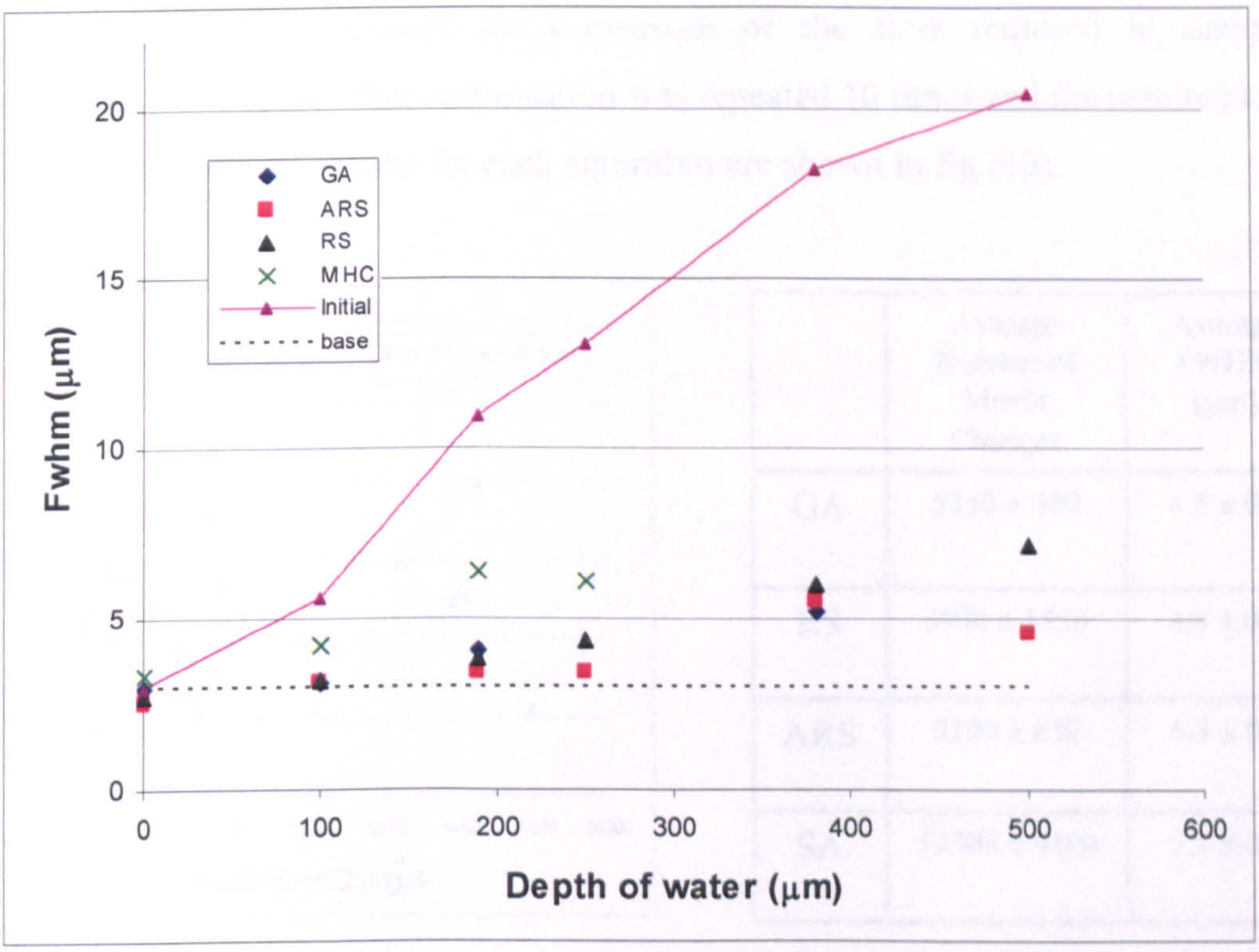

Figure 5: Showing FWHM against depth of water for each algorithm used.

Increasing water depth was found to increase the level of aberrations in the system, as seen from the pre-optimised data. From the graph, it can be seen that ARS, RS and GA showed significant improvement when compared to the MHC and to the pre-optimised sample. This is due to the MHC having located a local solution maximum rather than a global solution maximum.

3.2 Global optimisations [9]

Using a test sample with a 190μm depth of water, a comparision was then made between SA and all the other global algorithms i.e. GA, RS and ARS. The pre-optimisation axial FWHM was measured at 25μm. For each optimisation, the final axial FWHM and the number of mirror changes required to complete optimisation were measured. Since the time required for each mirror change being constant for each algorithm, the number of mirror changes were regarded as a measure of the time required to complete optimisation. Each algorithm optimisation was repeated 10 times and the results plotted in fig 6(a). The average results for each algorithm are shown in fig 6(b).

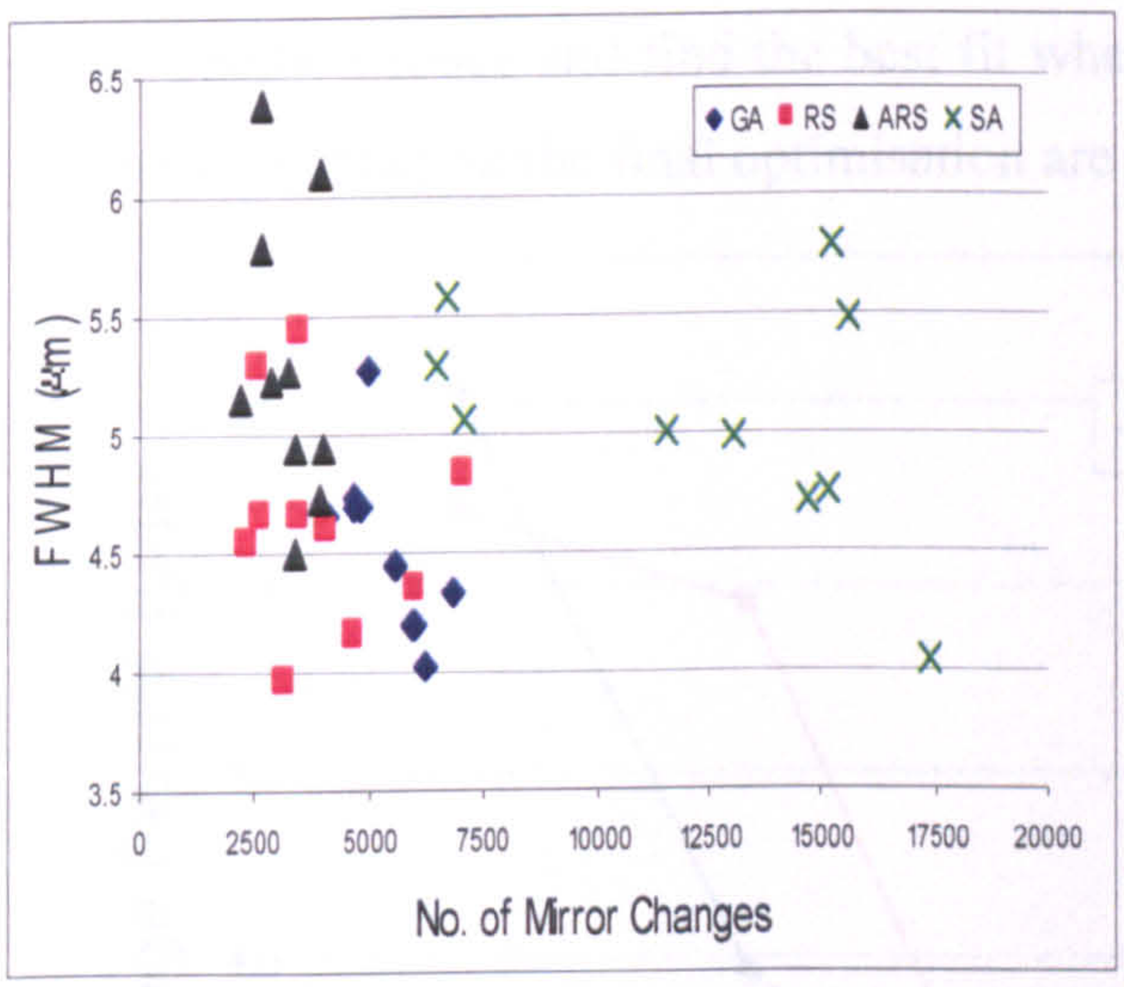

Fig. 6(a) Showing the number of mirror changes to reach optimisation against final FWHM for 190μm water test sample using GA, RS, ARS and SA

	Average Number of Mirror Changes	Average FWHM (μm)
GA	5350 ± 880	4.5 ± 0.4
RS	3930 ± 1550	4.6 ± 0.5
ARS	3190 ± 630	5.3 ± 0.6
SA	12300 ± 4100	5.1 ± 0.5

Fig. 6(b) Table showing average mirror changes against FWHM for 190μm water sample (pre-optimised FWHM = 25μm)

GA and RS were shown to give similar results, with GA generally taking longer but achieving the best optimisation on average. Due to the nature of ARS (the voltage change decreases after each iteration which is based on temperature), it can be assumed that it tended to locate local maximum solution when compared with to GA and RS. As one can see, ARS achieved the lowest axial resolution improvement. SA took on average

the greatest amount of time to reach optimisation with an improvement factor on average less than that achieved by the GA and RS algorithm.

3.3 The effect of changing the SA Metro value on final fitness value

As described in some detail in previous chapters, the main difference between SA and RS algorithms is the ability of the SA algorithm to accept a lower fitness value to the current best fit, as the new fitness value. This ability is dependent on a number of factors which include the 'temperature' at that point, the weighting of the probability function embedded within the algorithm, and the metropolis value which is pre-defined before an optimisation. This ability of the SA to accept a lower fitness value allows it to sample more solution space and find the best fit when RS does not. The results of varying the metropolis value on the final optimisation are presented in figures 7 and 8.

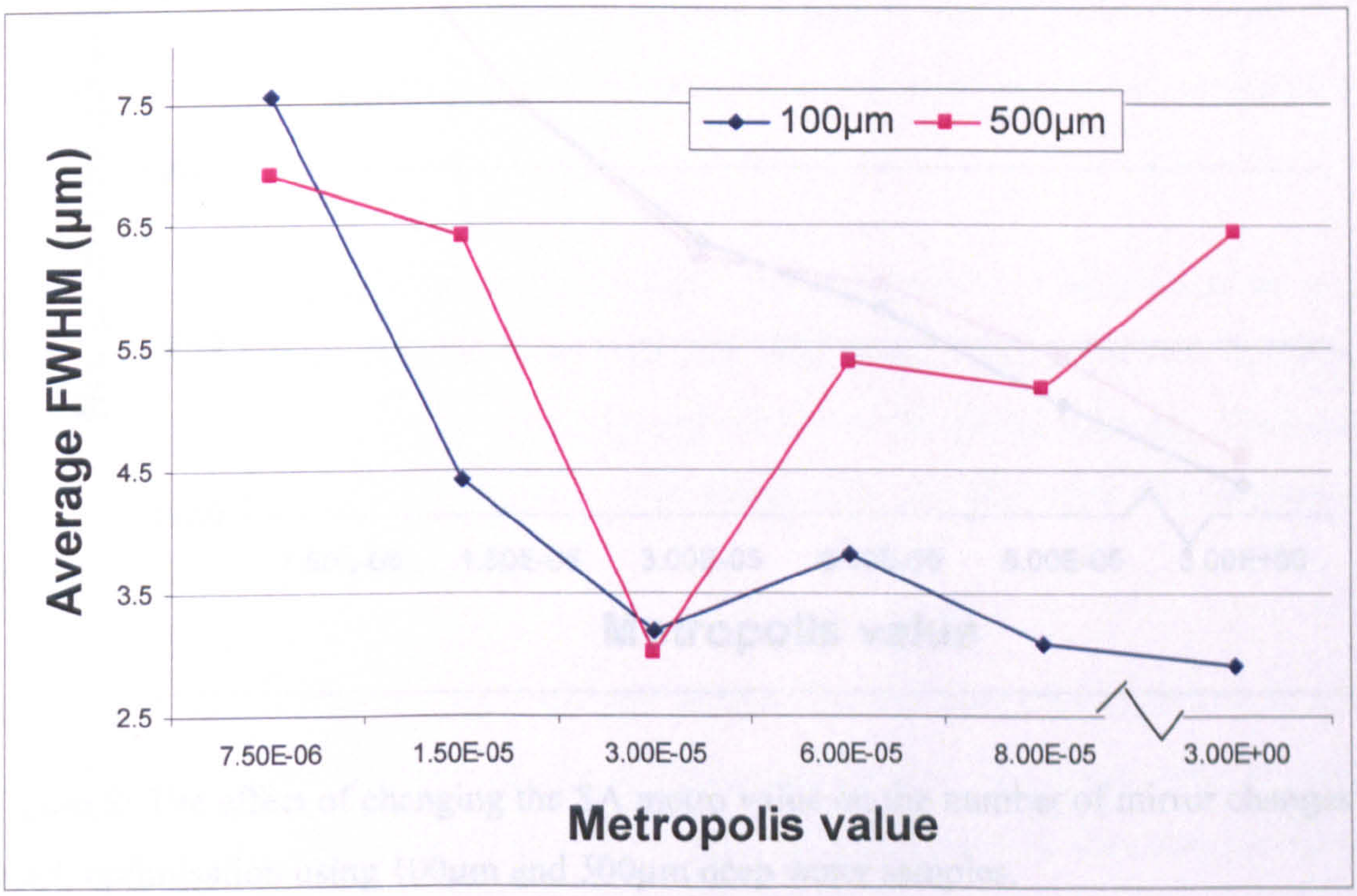

Figure 7: The effect of changing the SA metro value on the average final FWHM using 100µm and 500µm deep water samples to simulate aberrations.

As one can see in figure 7, for the 500μm water test sample, a metropolis value of $3x10^{-5}$ attained on average the best FWHM of 3.0+/-1.4μm. This is most likely due to the metropolis value closely suiting the situation in comparison to the other tested metropolis values. For the 100μm water test sample, the best results achieved using a metropolis value of 3 with an average FWHM of 2.91+/-0.29μm although the average FWHM appears to follow a curve which levels off around Metro = $3x10^{-5}$. From these results, it can be suggested that for particular conditions there could be a particular metropolis value which will allow the algorithm to reach the best possible solution.

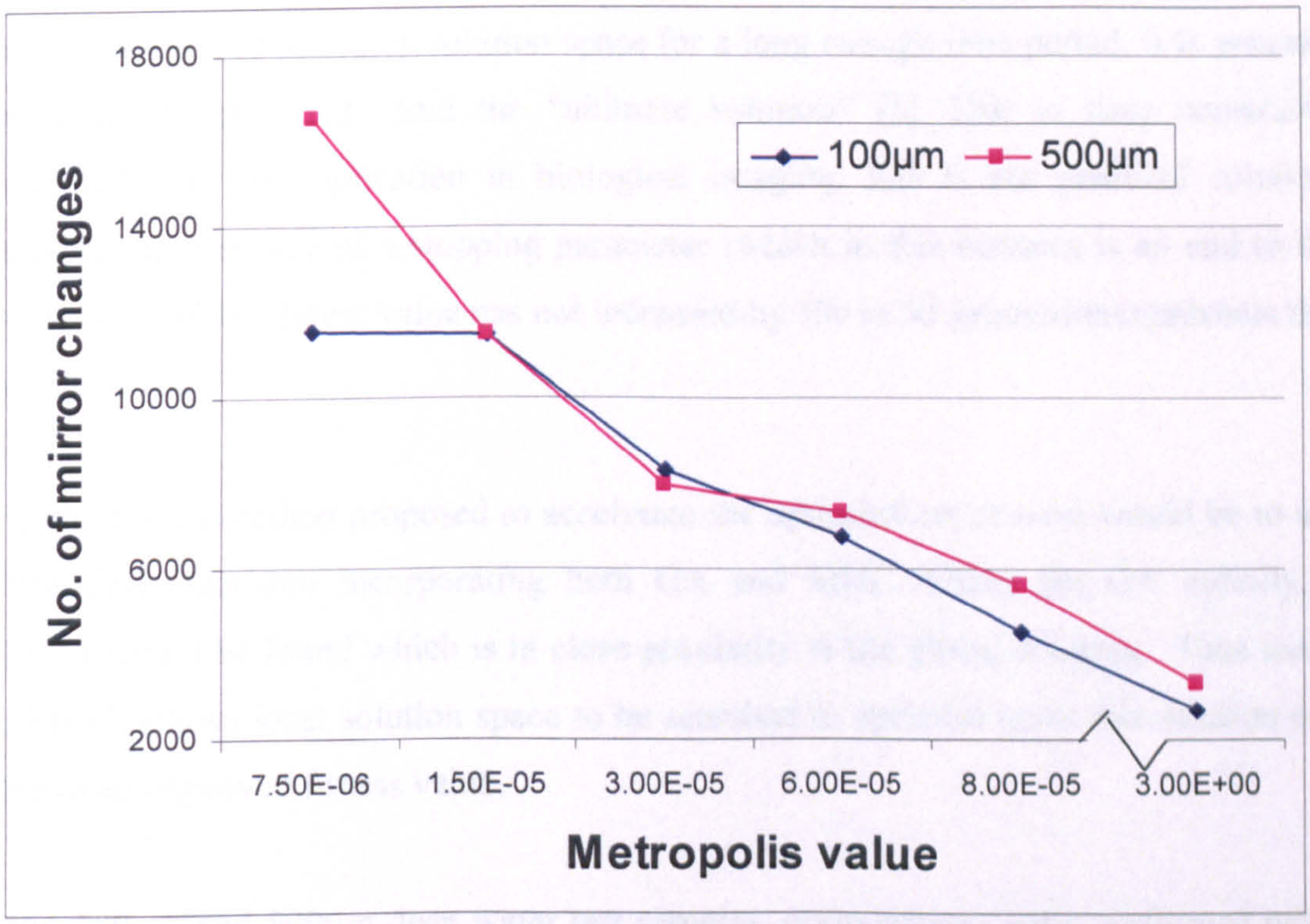

Figure 8: The effect of changing the SA metro value on the number of mirror changes to reach optimisation using 100μm and 500μm deep water samples.

From the graph, it can be seen that as the metropolis value of the SA algorithm decreased, the number of mirror changes required to complete the optimisation increased. This is understandable for if the metropolis value is too low, the algorithm

will generally accept lower fitness values for a much longer rate (see chapter 5, figures 18 (a)-(d)). The result is that for SA optimisations with a lower metropolis value, more of solution space is sampled.

Using the GA achieved an average optimisation FWHM of 2.11+/- 0.02 with an average of 3600 +/- 1500 mirror changes for 100μm and an average FWHM of 2.48+/-0.19 and an average of 5900+/-3800 mirror changes.

3.4 Using a modified algorithm search routine incorporating both GA and MHC

If GA was allowed to search solution space for a long enough time period, it is assumed that it would eventually find the "ultimate solution" [5]. Due to time constraints associated with its application in biological imaging, this is not practical solution; therefore the presence of a stopping parameter (which in this instance is an end to the optimisation if the fitness value has not increased by 1% in 50 generations) prevents this from occurring.

One alternative method proposed to accelerate the optimisation process would be to use a modified algorithm incorporating both GA and MHC. Using the GA initially, a solution would be found which is in close proximity to the global solution. Then using the MHC, allows local solution space to be searched to optimise upon this solution and achieve an improved fitness value.

Using 100μm and 500μm deep water test samples, optimisations were performed using the MHC, GA and a modified version incorporating the two. The results were plotted in figures 9 and 10. The modified GA+MHC algorithm functions by first running the GA algorithm and after the stopping parameter had been reached, the MHC algorithm is executed, taking its starting point as the best fit found using GA.

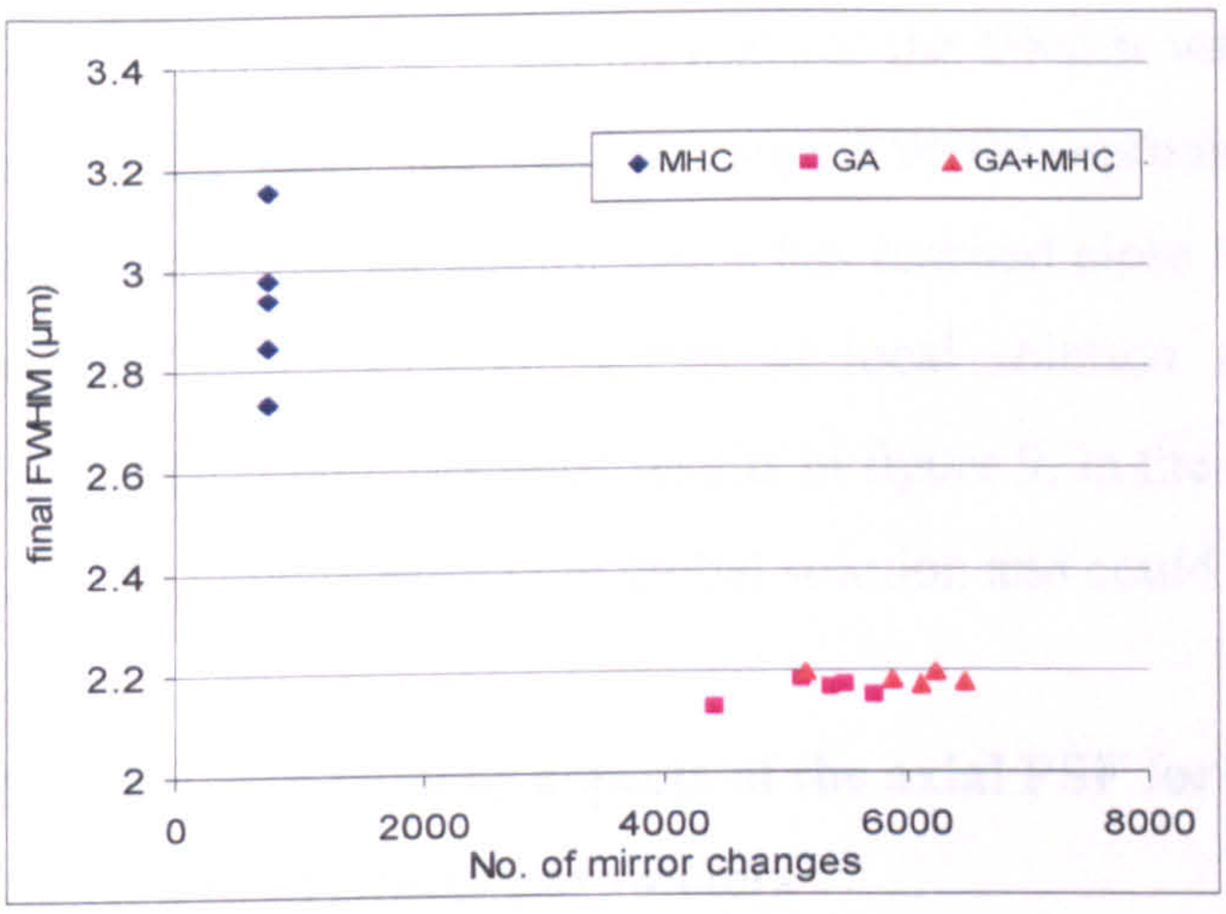

Algorithm type	Average number of mirror changes	Average FWHM (µm)
MHC	740.00	2.93±0.16
GA	5256±505	2.16±0.02
GA+MHC	5996±505	2.18±0.01

Figure 9(a): Showing the number of mirror changes against final FWHM for a 100µm water test sample using MHC, GA and GA+MHC combination.

Figure 9(b): Showing the average number of mirror changes against final FWHM for a 100µm water test sample using MHC, GA and GA+MHC combination.

From these results in figure 9, it was found that on average the GA provided the best fit. By running the MHC after the GA showed no improvement in the axial resolution of the system. In fact in most cases it showed a deterioration in the axial resolution, which can be attributed to mechanical and noise in the system.

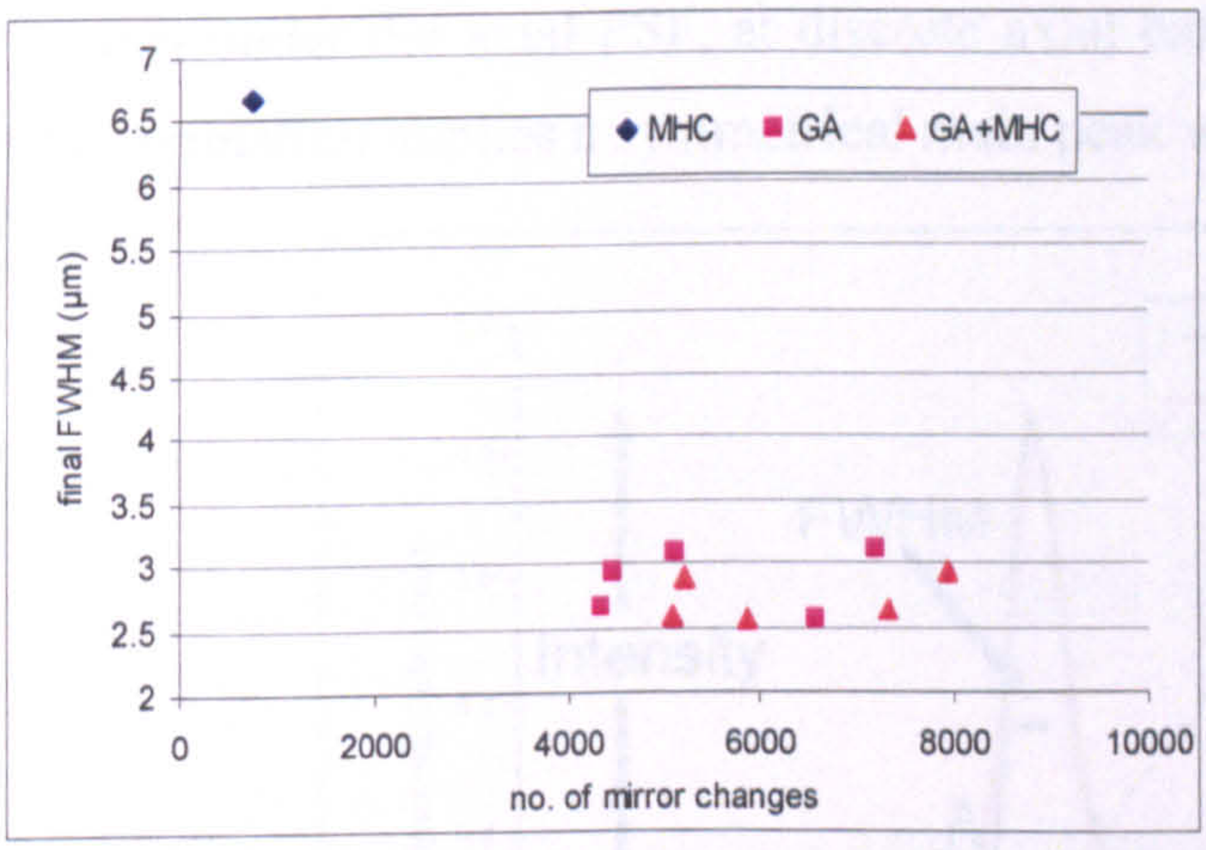

Algorithm type	Average number of mirror changes	Average FWHM (µm)
MHC	740	6.66
GA	5540±1270	2.86±0.24
GA+MHC	6284±1270	2.72±0.17

Figure 10(a): Showing the number of mirror changes against final FWHM for a 500µm water test sample using MHC, GA and GA+MHC combination.

Figure 10(b): Showing average number of mirror changes against final FWHM for a 500µm water test sample using MHC, GA and GA+MHC

From figure 10, it is shown that for the 500μm water sample, the modified GA+MHC algorithm gave the best average FWHM optimisation result. Using the GA, it is postulated that the mirror shape has reached close to the global solution where with the aid of MHC, a small search of local solution space has given a better result. In comparison with previous results in figure 9, in the case of the 100μm water sample, the GA has already found the global solution and could not be improved upon.

4. The use of various aspects of the axial PSF for optimisation

4.1 Origin of fitness parameters

In this part of the experiment, the GA algorithm was used to optimise for different fitness parameters shown in figure 11, which were namely (a) intensity brightness, (b) axial resolution (c) the area correlation with Gaussian fit, for a mirror test sample containing 100μm depth of water. The intensity refers to the intensity value at the peak and is analogous to the output signal taken from the PMT. The full-width half-maximum (FWHM) (as mentioned previously) is a measure of axial resolution and is found by fitting the main peak to a Gaussian curve. It was assumed that the main peak followed a normal distribution. Area correlation compares the area under the Gaussian fit curve to the area under the axial PSF, at discrete axial bands, for the whole axial scan. A high area correlation implies a symmetrical main peak with smaller side lobes.

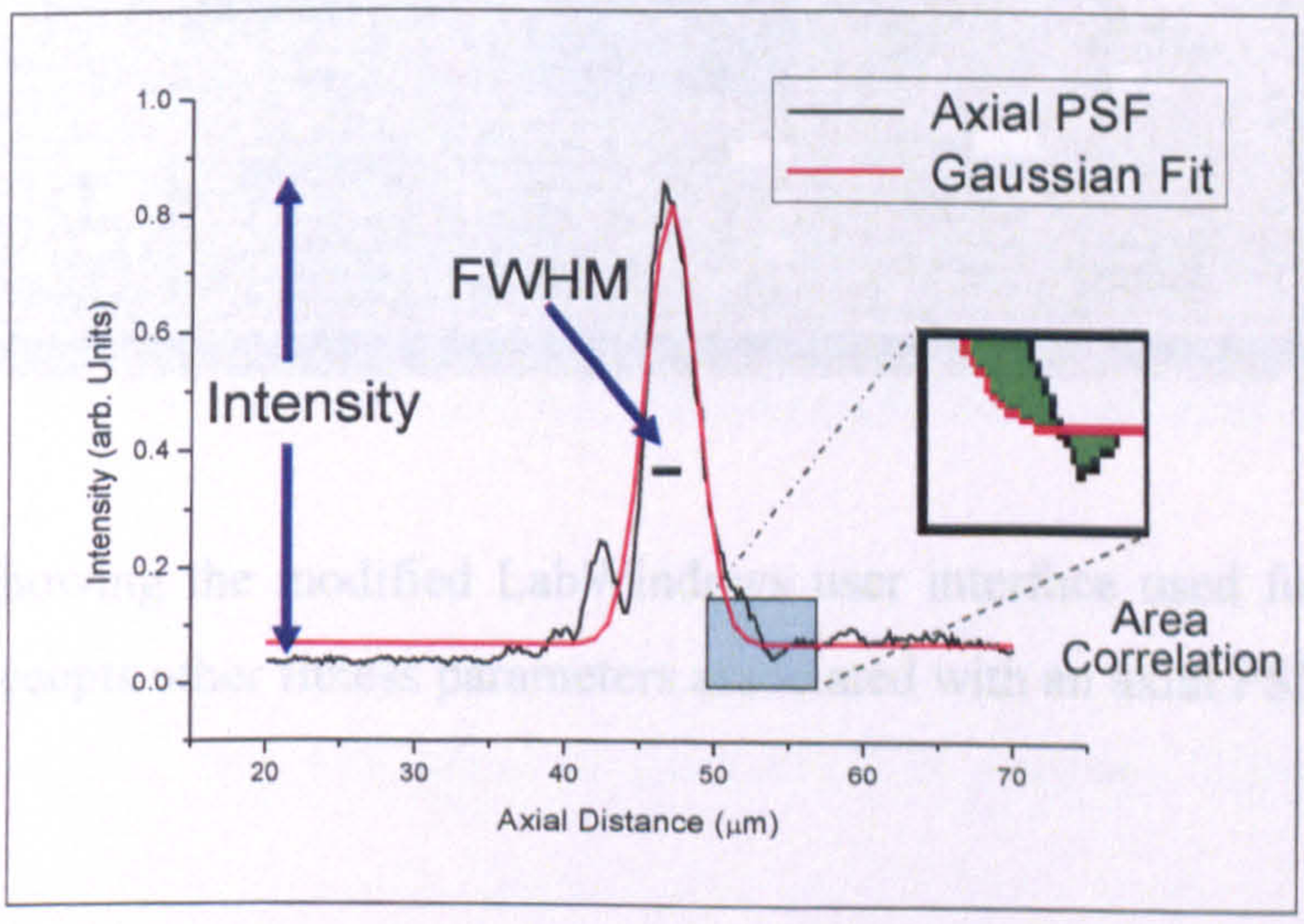

Figure 11: The origin of each fitness parameter in an axial resolution measurement.

4.2 Modifications to the LabWindows and LabVIEW code

The original LabWindows program used to control the mirror and algorithms (see chapter 6) was modified in order to accept a fitness parameter other than intensity. When the mirror change occurred during an optimisation, Active X was used to provide a link between the LabWindows and LabVIEW [11] interfaces. The LabWindows program instructed a LabVIEW program (called 'fitness parameter.vi') to measure the axial PSF, and retrieve fitness value (depending on the settings used). Minor modifications to the LabVIEW code also allowed the examination of hybrid fitness parameters such as area correlation/FWHM and intensity/FWHM. Each fitness parameter was evaluated in terms of increase in intensity and axial resolution. It should be noted that this LabWindows interface is a modified version of that described previously in chapter 6 (figure 24) and all other functions remain the same.

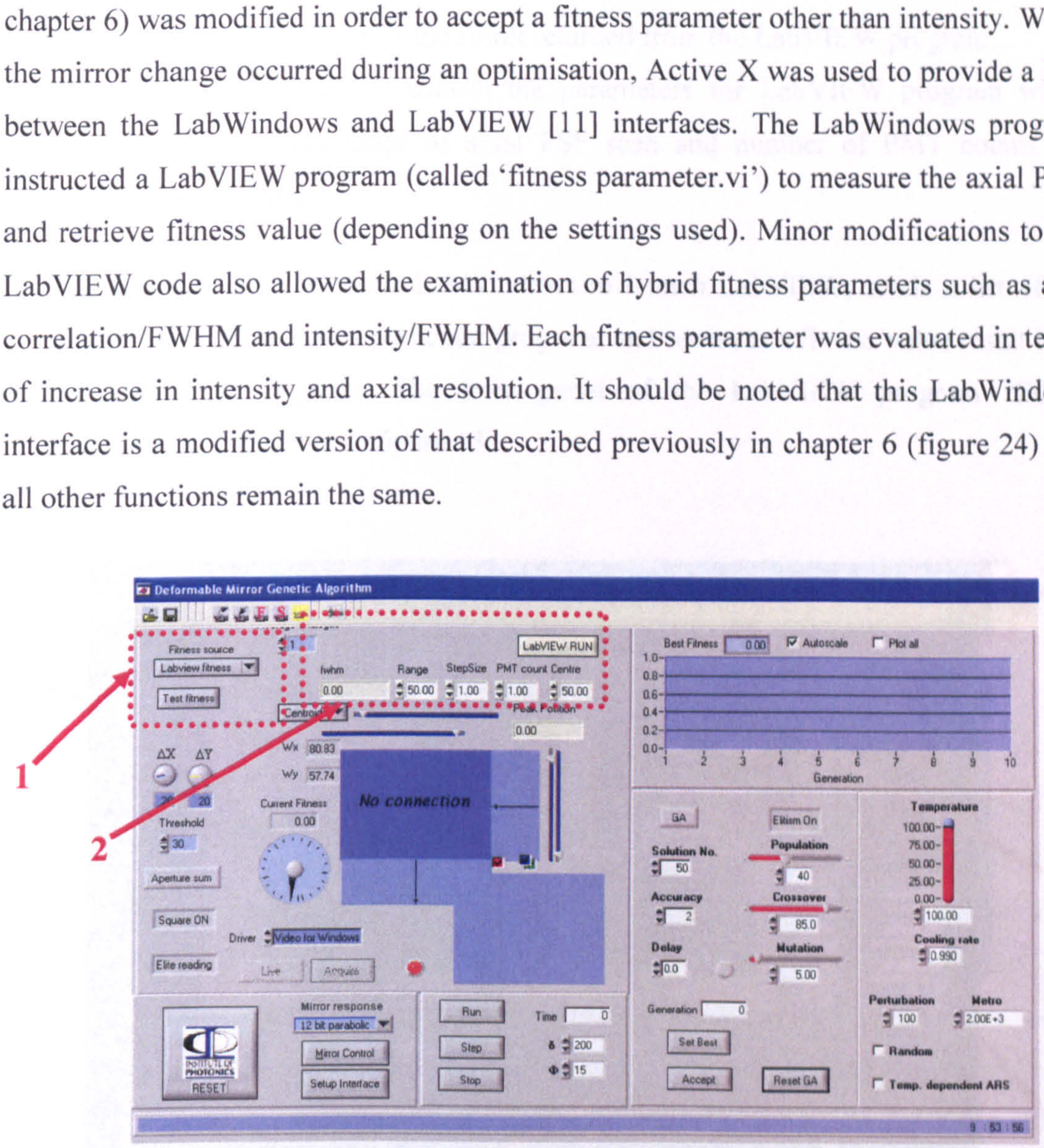

Figure 12: Showing the modified LabWindows user interface used for controlling the DMM, that accepts other fitness parameters associated with an axial PSF measurement.

Highlighted in the red boxes in figure 12 are:

1. Allows control over which fitness parameter used i.e. either intensity or the parameter determined by the result returned from the LabVIEW program.
2. Control boxes used to control the parameters for LabVIEW program which include step size, range of axial PSF scan and number of PMT counts per position reading.

The actual C-code instructs LabWindows to launch LabVIEW, sends a list of pre determined variables to a particular program, and retrieves a fitness value result from the LabVIEW program. The front panel of the LabVIEW program "fitness parameter.vi" is shown in figure 13.

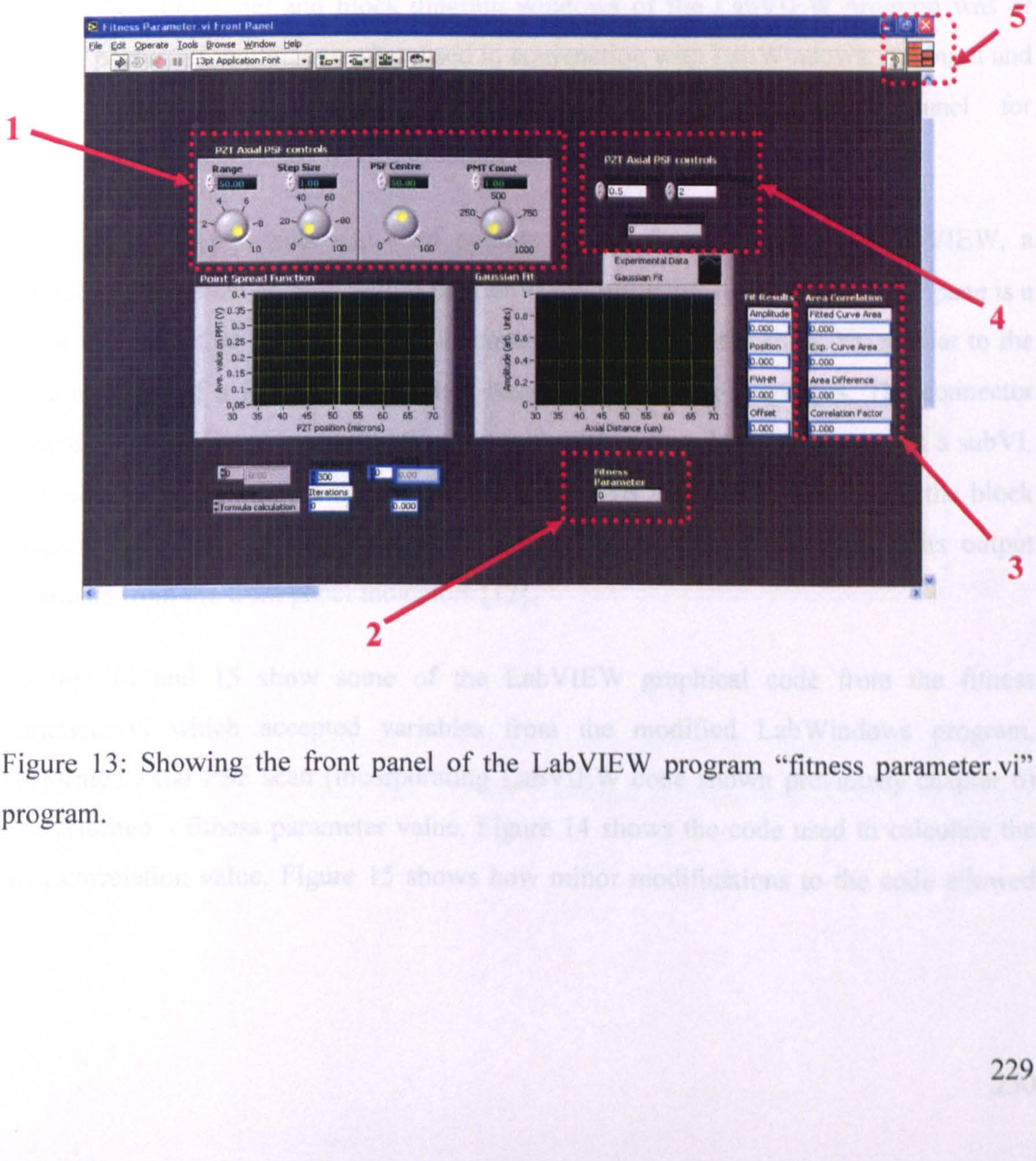

Figure 13: Showing the front panel of the LabVIEW program "fitness parameter.vi" program.

In figure 13 there are several highlighted red boxes shown:

1. These are the axial scan control variables such as width, approximate centre and step size of the scan (all in μm) as well as the number of PMT integrations taken the per position. These variables are controlled from the LabWindows interface (figure 12) when initiated by LabWindows.
2. This is the output fitness parameter value sent back to the LabWindows program.
3. The area correlation results between the PSF data and the best Gaussian fit are presented in these boxes.
4. Controls the Gaussian PSF shaping factors which will be explained later in this chapter.
5. The Icon and connector pane are located in the top right hand side corner of both the front panel and block diagram windows of the LabVIEW program was of particular importance when used in conjunction with LabWindows. All input and output variables must be declared using this connector panel for LabWindows/LabVIEW interfacing to occur.

In order to accept inputs and send outputs to and from LabWindows/LabVIEW, a connector pane must be built within the LabVIEW environment. The connector pane is a set of terminals that corresponds to the controls and indicators of that VI, similar to the parameter list of a function call in text-based programming languages. The connector pane defines the inputs and outputs wired to the VI so that they can be used as a subVI. A connector pane receives data at its input terminals and passes the data to the block diagram code through the front panel controls, or receives the results at its output terminals from the front panel indicators [12].

Figures 14 and 15 show some of the LabVIEW graphical code from the fitness parameter.vi which accepted variables from the modified LabWindows program, performed axial PSF scan (incorporating LabVIEW code shown previously chapter 6) and returned a fitness parameter value. Figure 14 shows the code used to calculate the area correlation value. Figure 15 shows how minor modifications to the code allowed

various fitness parameters to be constructed i.e. intensity/FWHM and (1/FWHM) x (area correlation).

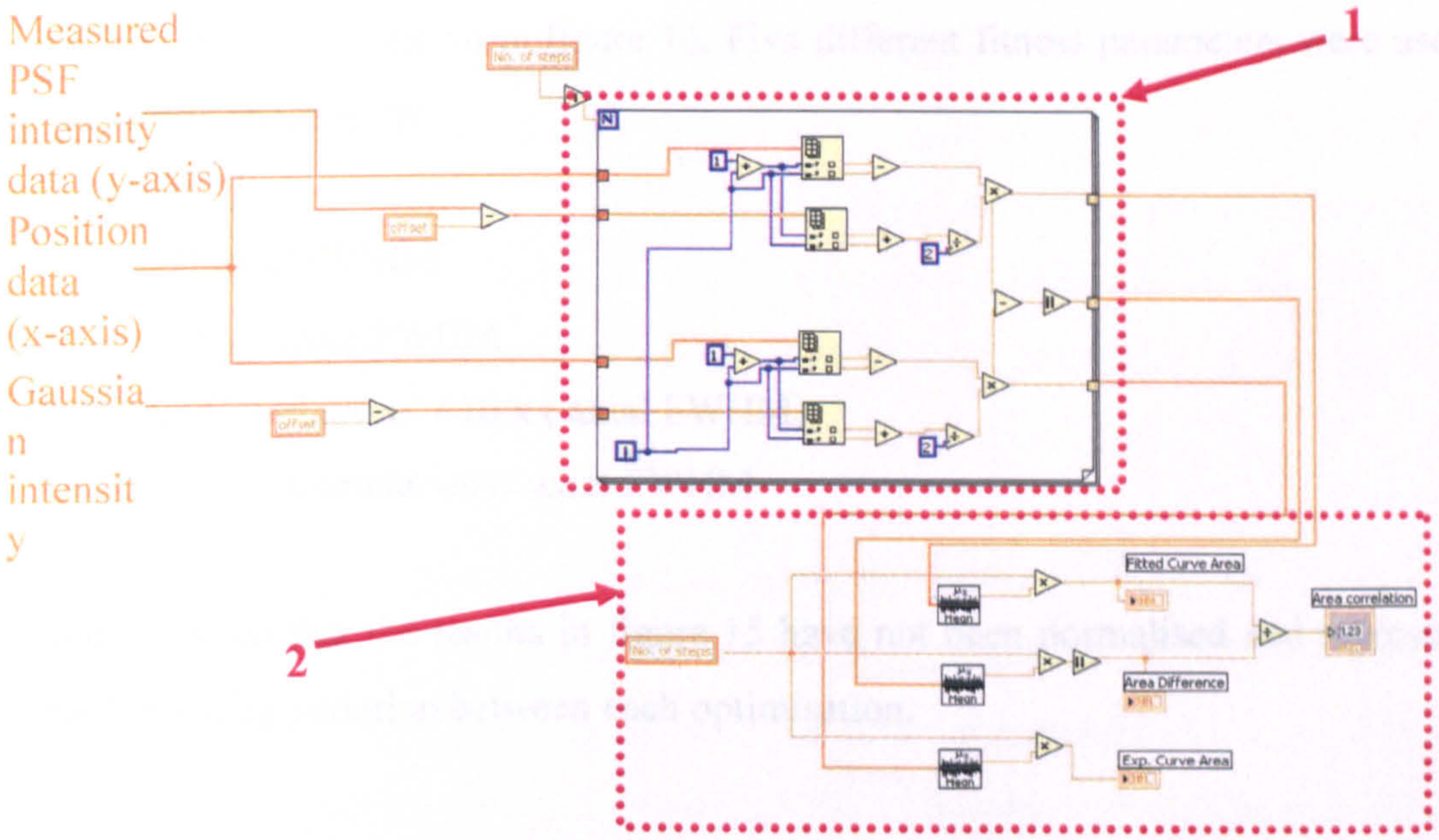

Figure 14: Showing the graphical code located within "fitness parameter.vi" used to calculate an area correlation between the experimental PSF data and the Gaussian fit.

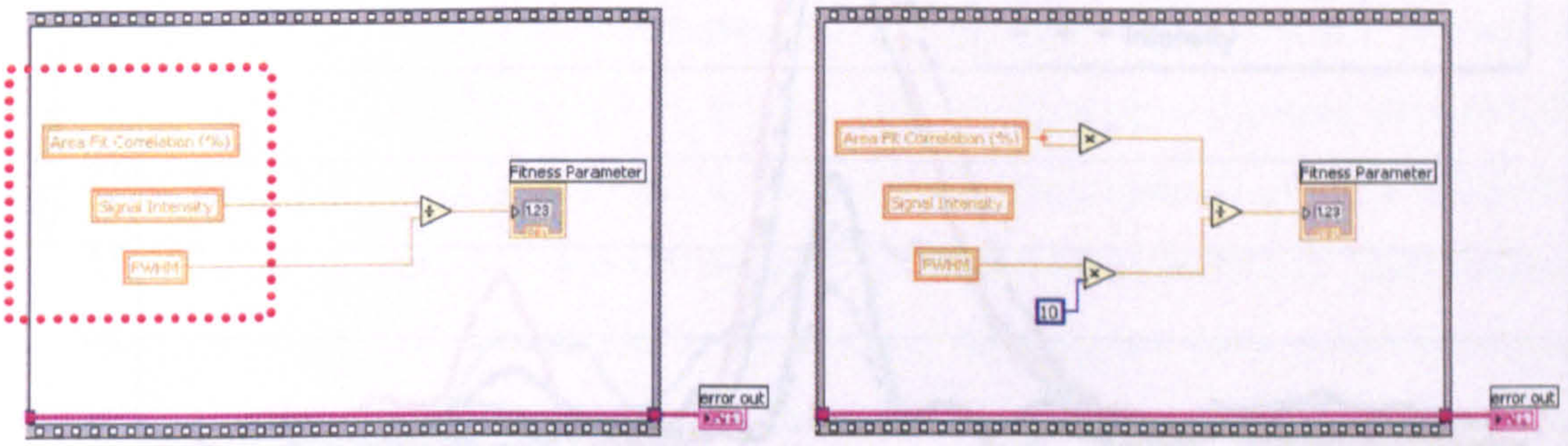

(a) (b)

Figure 15: (a) and (b) showing how the three fitness parameters (highlighted by the red box) associated with an axial PSF can be modified to produce a customized fitness parameter.

4.3 GA optimisation using different Fitness Parameters [6]

Taking a pre-optimised axial PSF scan for the 100μm of water provided an initial axial FHWM of 11μm. A number of various fitness parameters were then used to optimise the PSF and the results are shown in figure 16. Five different fitness parameters were used and compared. These were:

1. Intensity
2. 1000 / axial FWHM
3. Intensity / axial FWHM
4. (Area Correlation)^2 / 10 x (axial FWHM)
5. 10 x (Area Correlation) / axial FWHM

It should be noted that the results in figure 15 have not been normalised and represent the actual intensity variation between each optimisation.

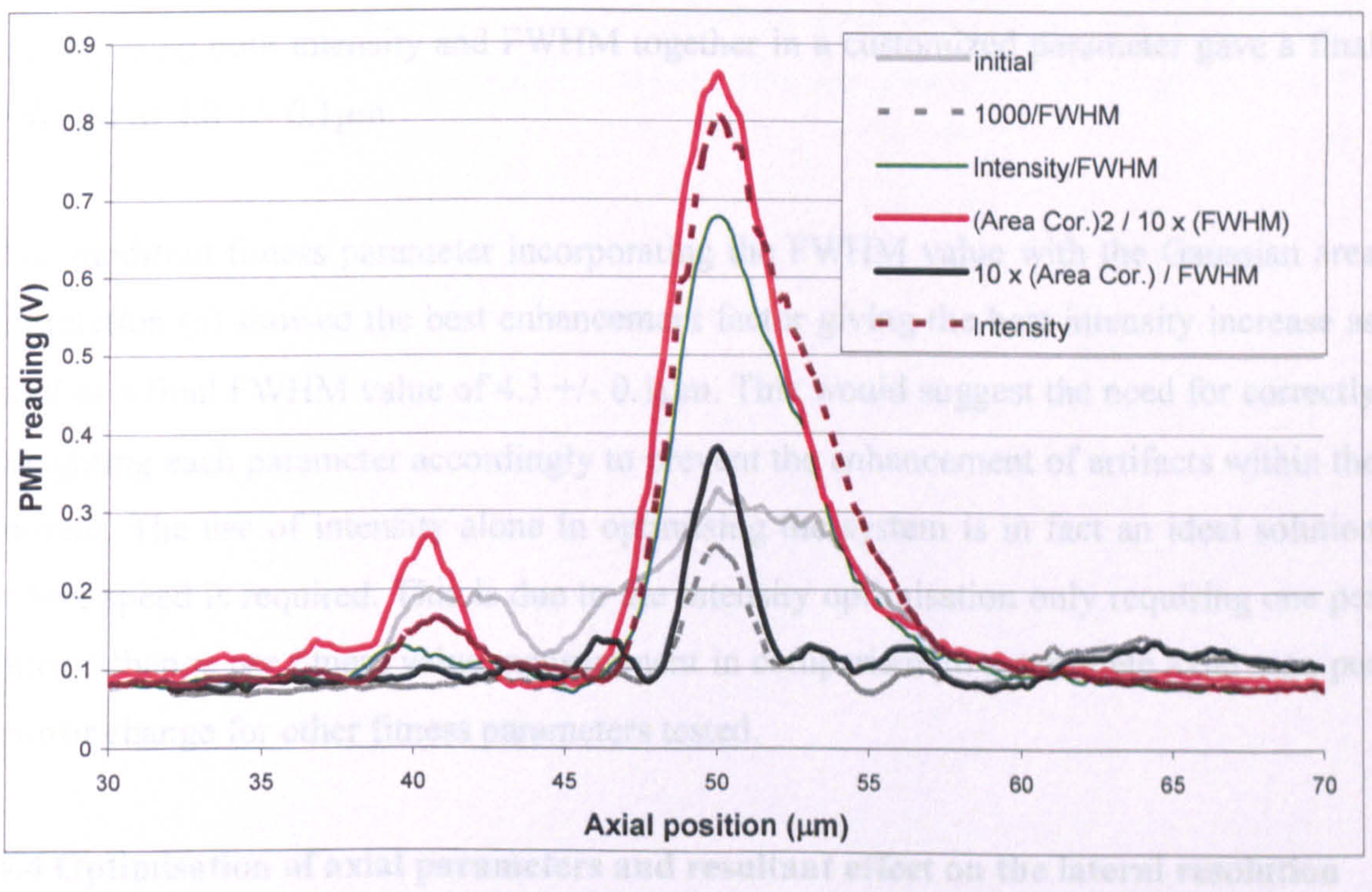

Figure 16: Optimised PSFs of a sample containing 100μm water using various fitness parameters in GA.

Using intensity as a fitness parameter, the axial PSF scan was shown to give a FWHM of of 5.1 +/- 0.1μm. It was found that when using the 1000/FWHM as a fitness parameter alone, a post-optimised axial FWHM of 2.0 +/- 0.1μm was measured, with little increase in peak light intensity from the pre-optimised measurement. When the focal shift (due to increased refractive index of water in relation to air) is taken into account this translates to an actual focal spot movement of 2.6μm, which does not breach the theoretical diffraction limit of 2.12μm for this system. Due to the intensity of the PSF not increasing it was assumed that by using the 1000/FWHM parameter, it has possibly optimised on an artifact.

A number of modified fitness parameters were then tested incorporating different aspects of the axial PSF. It was discovered that a combined area correlation with FWHM fitness parameter (b), although producing a similar final axial resolution (2.1 +/- 0.1μm) to using the FWHM parameter alone, increased the symmetry with a reduction of side lobes. Using both intensity and FWHM together in a customized parameter gave a final FWHM of 4.8 +/- 0.1μm.

The modified fitness parameter incorporating the FWHM value with the Gaussian area correlation (a) showed the best enhancement factor giving the best intensity increase as well as a final FWHM value of 4.3 +/- 0.1μm. This would suggest the need for correctly weighting each parameter accordingly to prevent the enhancement of artifacts within the system. The use of intensity alone in optimising the system is in fact an ideal solution where speed is required. This is due to the intensity optimisation only requiring one per mirror change per fitness value measurement in comparison to a complete axial scan per mirror change for other fitness parameters tested.

4.4 Optimisation of axial parameters and resultant effect on the lateral resolution

The use of various axial fitness parameters in a GA optimisation were then compared for 250μm depth of water, sandwiched between a coverslip and a Newfocus 5103 aluminum

coated mirror (which contains a non-reflective section at the mirror edge.) The effect optimising using axial parameters had on both the axial and the lateral PSF resolution were examined. Fitness parameters used were:

1. Intensity
2. 1000 / (axial FWHM) (for ease of use it is now known as FWHM (1))
3. (Area Correlation)^2 / 10 x (axial FWHM) (known as FWHM (2))
4. 10 x (Area Correlation) / (axial FWHM) (known as FWHM (3))

Using LabVIEW to control the x-y piezo sample stage, the differential intensity variation between the reflective and non-reflective surface was measured, and the lateral resolution determined. Due to the presence of noise, a moving average was used when taking a lateral scan. Axial and lateral measurements were taken with a 250μm deep water test sample pre-optimised with DM mirror flat, and after optimisation. Figures 17-20 show examples of post-optimised axial and lateral PSFs using each of the fitness parameters with the genetic algorithm optimisation. Each example is compared with pre-optimised measurements. All results in this section are normalised for peak intensity for ease of comparison.

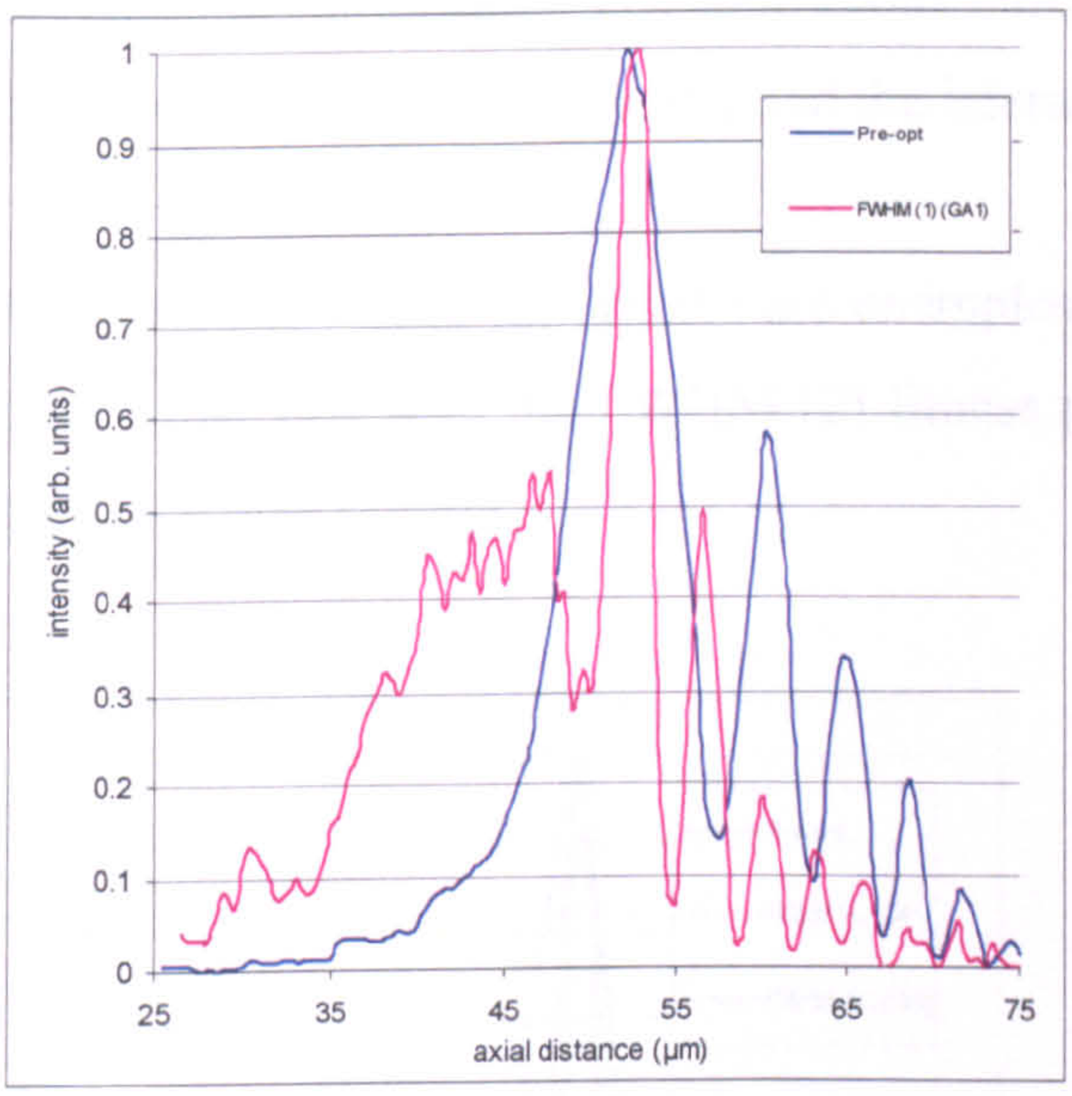

Figure 17(a): Comparing an example of the final axial PSF using FWHM (1) optimisation with the initial pre-optimised axial PSF.

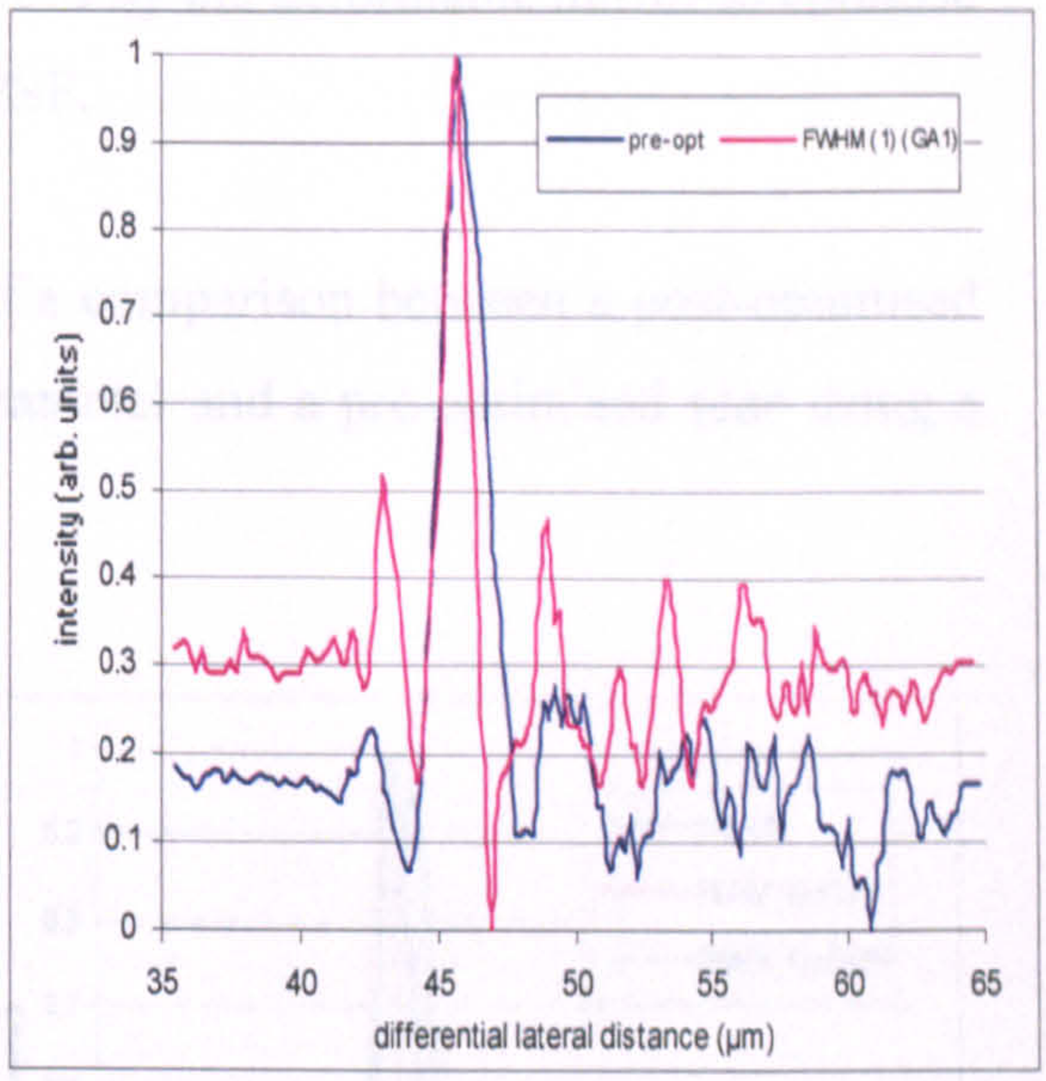

Figure 17(b): Comparing an example of the final lateral PSF using FWHM (1) optimisation with the initial pre-optimised lateral PSF.

Shown in figure 17 (a) and (b) is a comparison between a pre-optimised and post-optimised scans using GA with the FWHM (1) fitness parameter for a 250µm deep water sample. The pre-optimised axial and lateral resolutions were found to be 7.0 +/- 0.1µm and 1.48 +/- 0.05µm respectively.

As one can see from figure 17 (a), the post-optimised axial scan in fact appears to be highly aberrated with a multipeaked, asymmetrical PSF. This highlights the problems associated with using just the FWHM as a fitness parameter, and is most likely due to the way the Gaussian fitting program functions at fitting a Gaussian curve to multipeaked scans. For a multipeaked scan such as this, if the peaks are at a far enough apart, the fitting program fits to the peak with the highest intensity giving a FWHM of 1.85µm instead of including the several side-lobes present in the scan. In this case the peak has an extremely low FWHM value, which the optimisation program sees as the best fit due to the fitness parameter = 1000/FWHM. The post-optimised lateral resolution was found to be 1.33µm but the PSF appears to be highly aberrated due to the

presence of multipeaks. The aberrations introduced by the deformable mirror to optimise for an axial parameter also affected the lateral PSF.

Shown in figure 18 (a) and (b) are examples of a comparison between a post-optimised scan using GA with the FWHM (2) fitness parameter and a pre-optimised scan using a 250μm water sample.

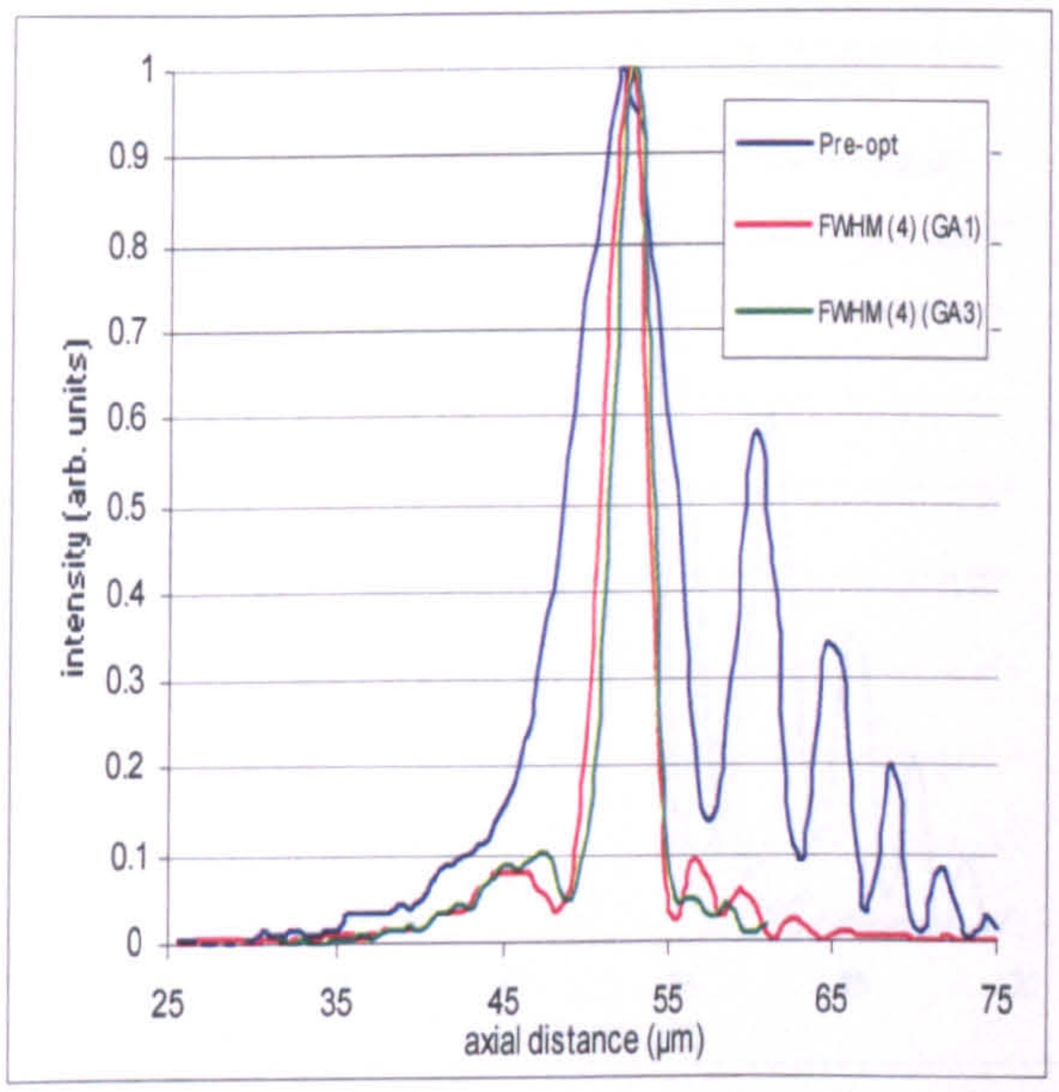

Figure 18(a): Comparing examples of the final axial PSF using FWHM (2) optimisation with the initial pre-optimised axial PSF.

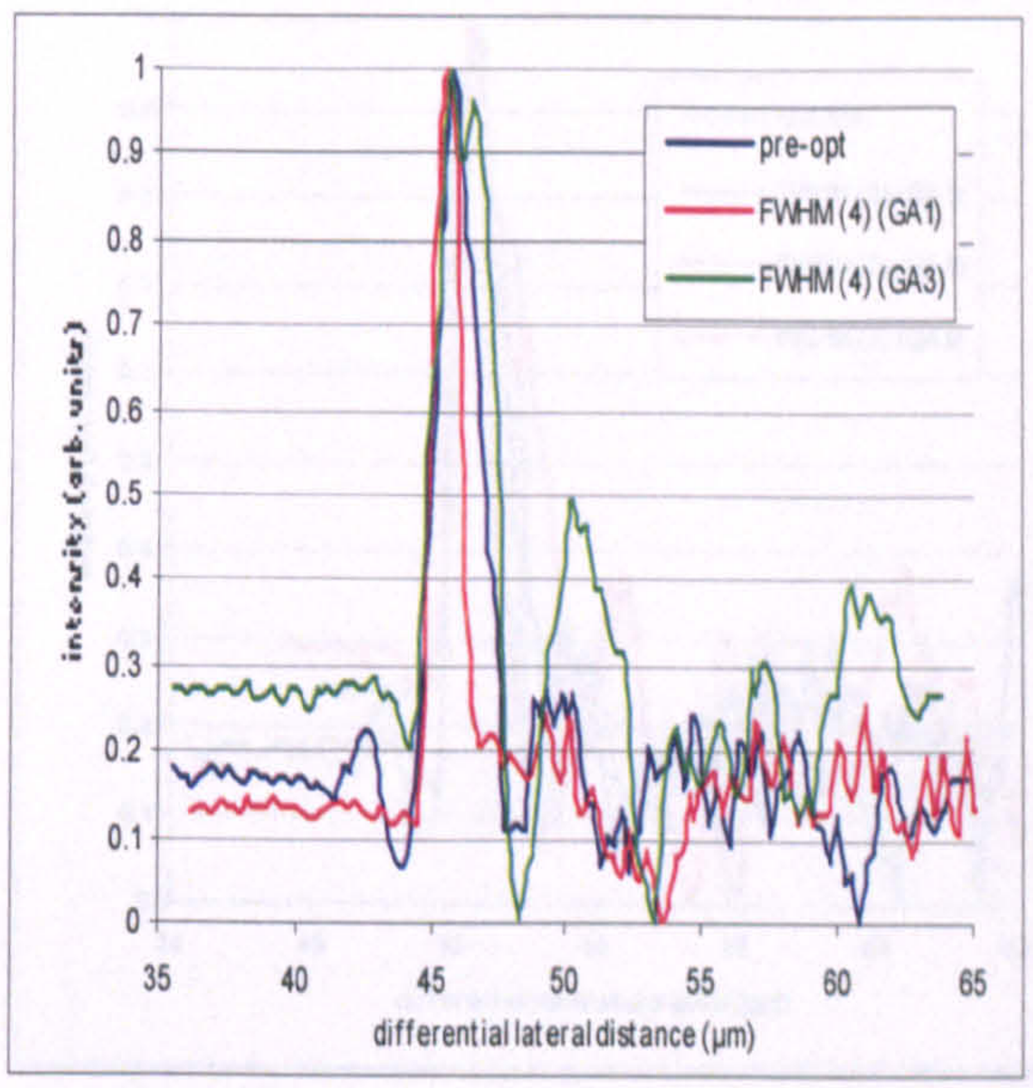

Figure 18(b): Comparing examples of the final lateral PSF using FWHM (2) optimisation with the initial pre-optimised lateral PSF.

The FWHM (2) fitness calculation as described before incorporates both area correlation and FWHM in order to produce a best fit. As one can see from the axial scan, the optimisation works extremely well giving post-optimised axial FWHMs of 3.0 +/- 0.1μm and 2.6 +/- 0.1μm for the FWHM (2) (GA1) and FWHM (2) (GA3) examples shown respectively. In incorporating the area-correlation, a more symmetrical PSF is produced with less prominent side-lobes. In optimising for the axial PSF, the lateral PSF has been affected giving post-optimised lateral FWHMs of 1.15 +/- 0.05μm and 1.94 +/- 0.05μm for the FWHM (2) (GA1) and FWHM (2) (GA3). In achieving a better axial

resolution, the FWHM (2) (GA3) example has adversely affected the lateral resolution of the system giving a worse resolution than that measured pre-optimisation.

In figure 19 (a) and (b) examples are shown comparing examples of post-optimised scan using GA with the FWHM (3) fitness parameter with a pre-optimised scan using a 250μm water sample.

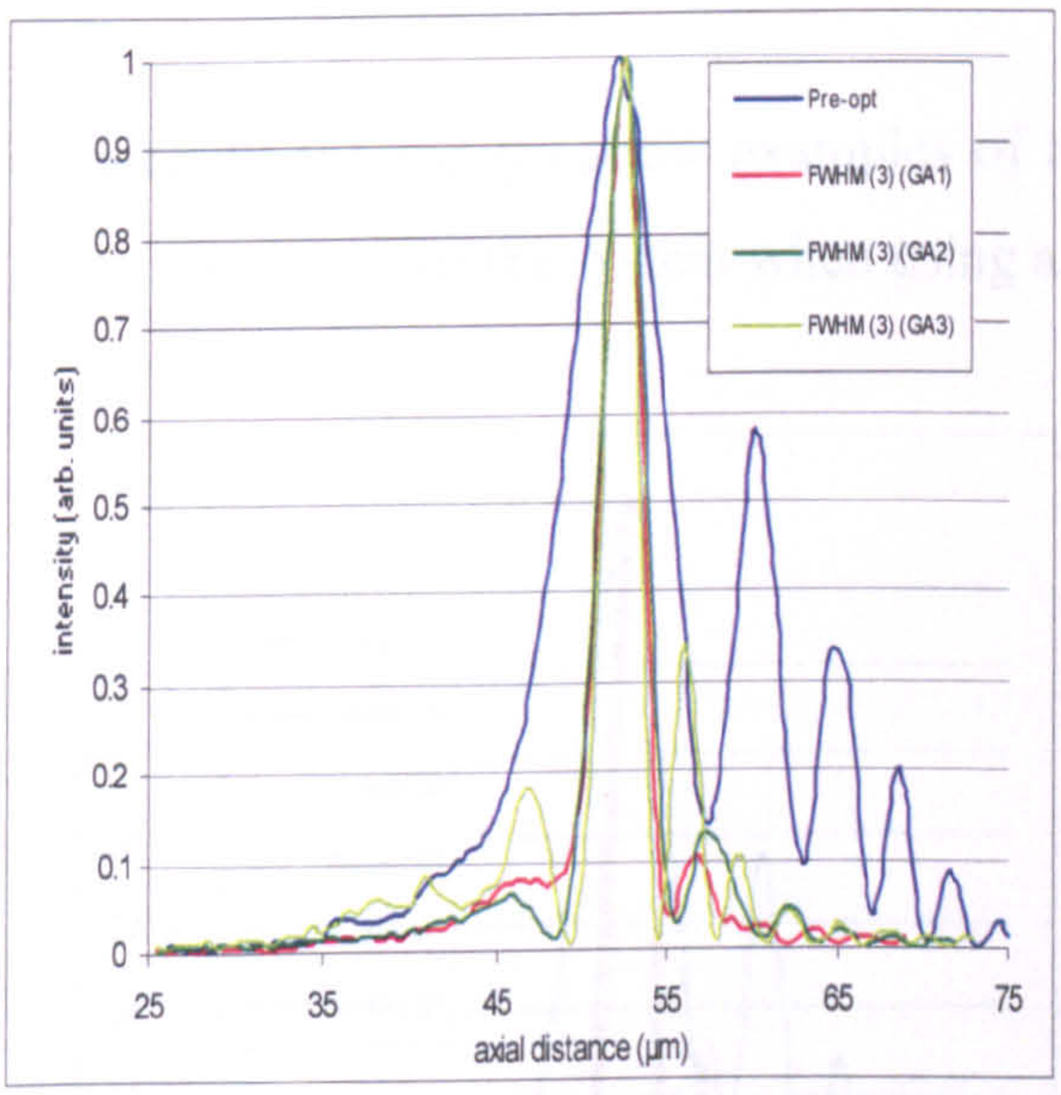

Figure 19(a): Comparing examples of the final axial PSF using FWHM (3) optimisation with the initial pre-optimised axial PSF

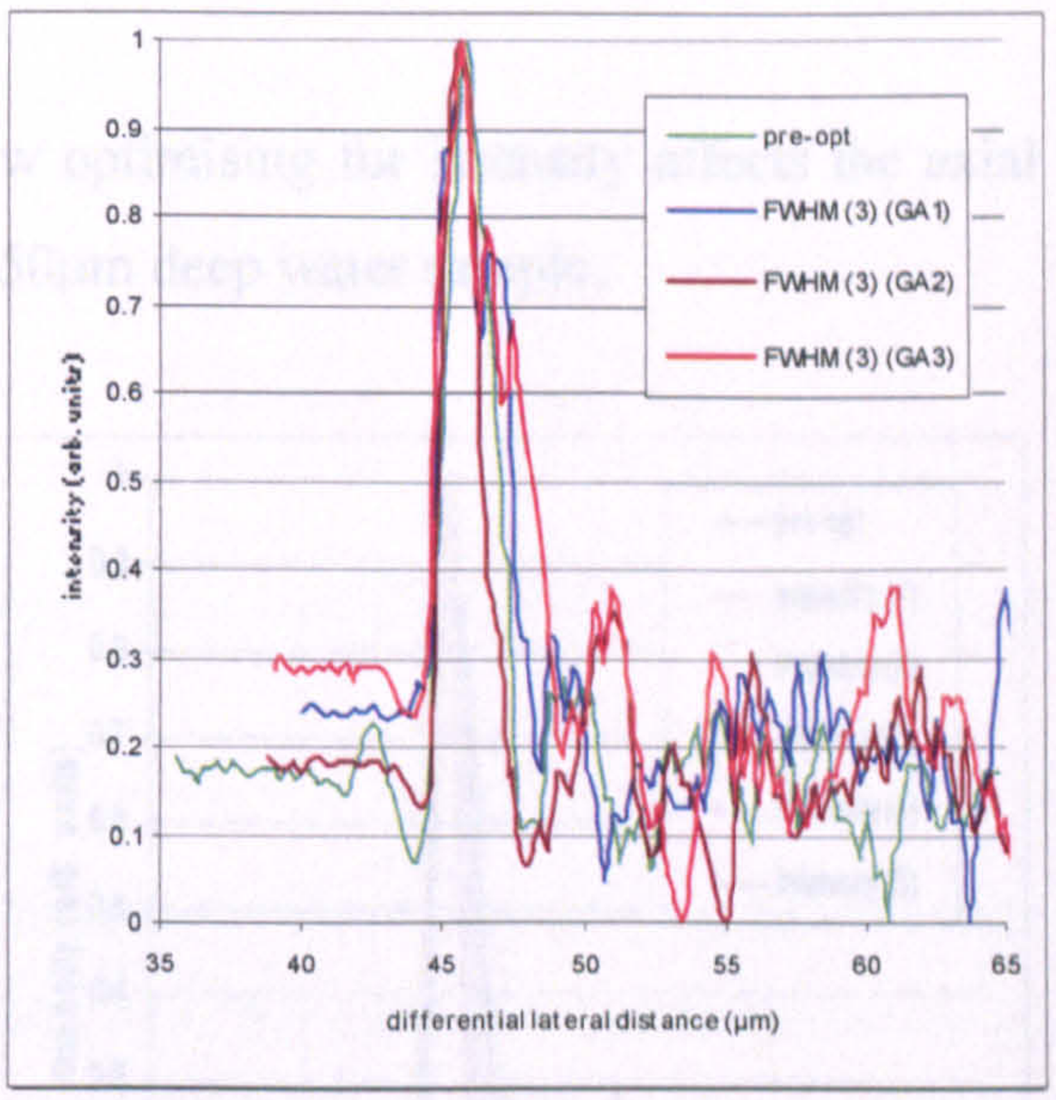

Figure 19(b): Comparing examples of the final lateral PSF using FWHM (3) optimisation with the initial pre-optimised lateral PSF

FWHM (3) fitness parameter function is similar to FWHM (2) in that it incorporates both area correlation and FWHM measurements into a modified fitness parameter function. Unlike FWHM (2) in which the area correlation has a quadratic influence, the FWHM (3) fitness parameter is linearly dependant on the area correlation. Therefore a different weighting factor is given to area correlation and FWHM with the greater emphasis given to FWHM factor. For the examples shown, the post-optimised axial FWHMs were 2.7 +/- 0.1μm, 2.9 +/- 0.1μm and 2.1 +/- 0.1μm for FWHM (3) (GA1), FWHM (3) (GA2), and FWHM (3) (GA3) respectively. In comparison with previous PSFs for the FWHM (2) the post-optimised PSFs contain more prominent side-lobes and

these are due to the lesser emphasis of area-correlation in the final fitness parameter. As seen in previous optimisations, in optimising for the axial PSF, the lateral PSF has been affected giving post-optimised lateral FWHMs of 2.51μm, 1.29μm and 3.02μm for the FWHM (3) (GA1), FWHM (3) (GA2), and FWHM (3) (GA3) respectively. As previously, in achieving a better axial resolution, it has adversely affected the lateral resolution of the system. In optimising for axial PSF factors, there appears to be a trade-off with the lateral PSF.

Figure 20 (a) and (b) show examples of how optimising for intensity affects the axial and lateral PSF of the system when using a 250μm deep water sample.

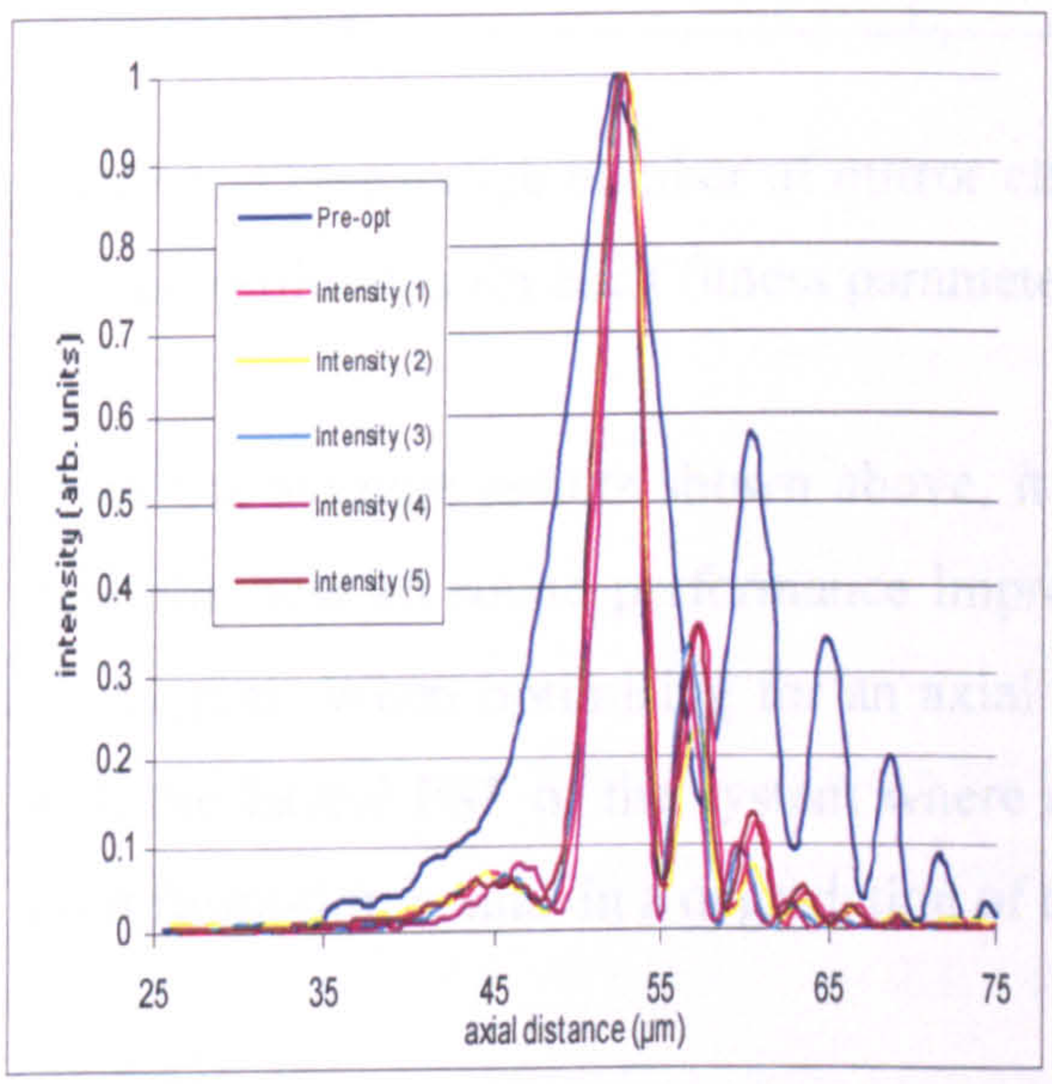

Figure 20(a): Comparing examples of the final axial PSF using intensity in the optimisation with the initial pre-optimised axial PSF.

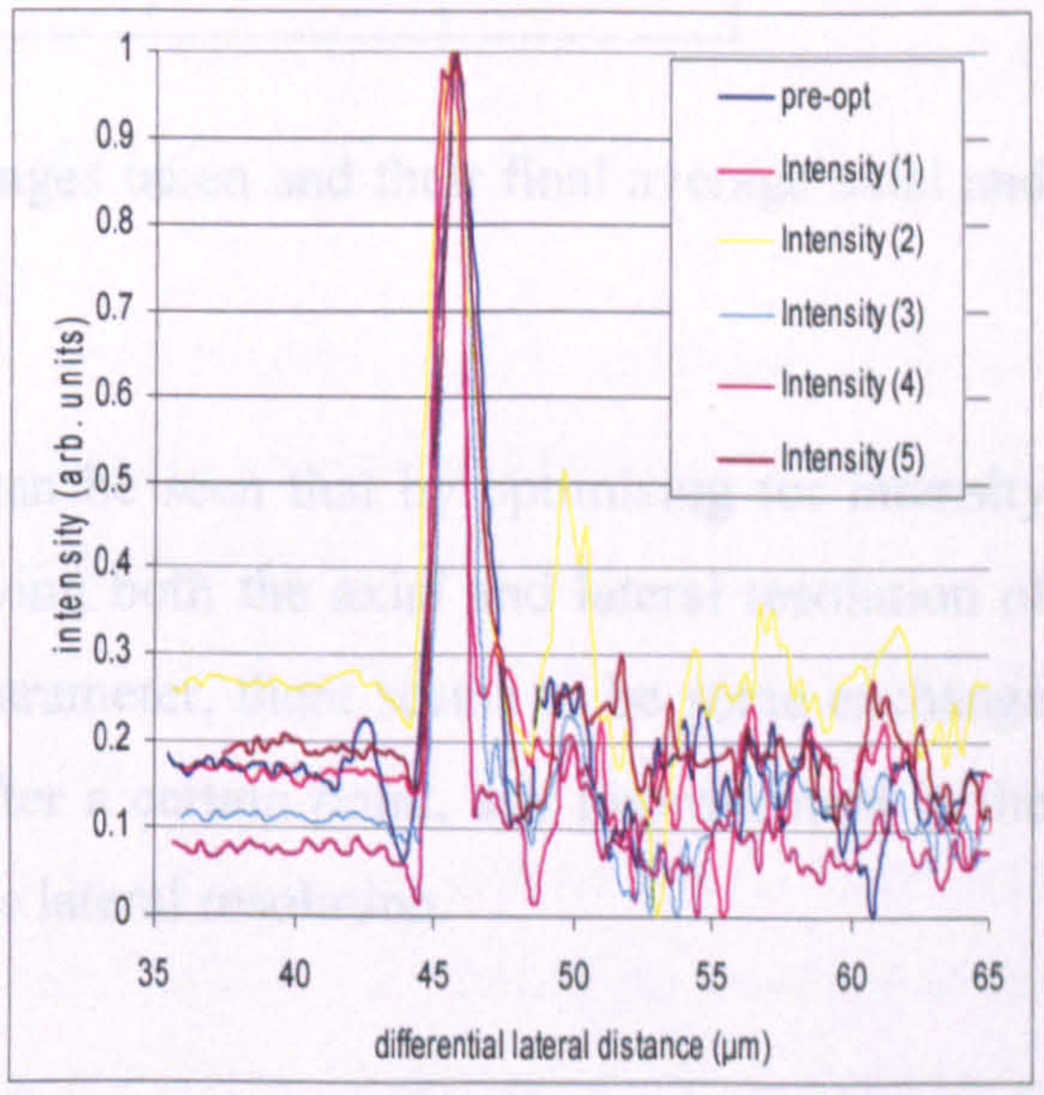

Figure 20(b): Comparing examples of the final lateral PSF using intensity in the optimisation with the initial pre-optimised lateral PSF.

From figure 20(a) and figure 20(b), in all the post-optimisation examples shown cases, it can be seen that by optimising for intensity using GA results in an improvement in the lateral as well as the axial resolution of the system. This is understandable considering that when optimising for intensity, the axial and lateral PSFs are not being distinguished.

Table 1 shows the average of three measurements taken for each of the optimisations showing the final axial and lateral resolutions as well as the number of mirror changes required to achieve optimisation.

		FWHM (μm)	
	No. of mirrors	Lateral	Axial
Pre-optimisation	-	1.51±0.18	6.83±0.25
Intensity	6500±3100	1.31±0.14	2.65±0.56
1000/FWHM	3560±600	1.11±0.21	7.6±10.1
$(AREA)^2$/10xFWHM	2760±330	1.43±0.43	2.89±0.27
AREAx10/FWHM	3710±870	2.28±0.89	2.55±0.40

Table 1: The average number of mirror changes taken and their final average axial and lateral resolutions for each fitness parameter.

From the average results shown above, it can be seen that by optimising for intensity gave the best all round performance improving both the axial and lateral resolution of the system. When optimising for an axial parameter, there seems to be some exchange with the lateral PSF of the system where after a certain point, any improvement in the axial resolution results in a degradation of the lateral resolution.

5. PSF shaping

One problem associated with the use of high N.A. optics in confocal biological imaging is the limited depth of field. This restricts the depth of axial section that can be imaged at any one time and to produce images throughout the biological sample requires many optical sections. In this case of live imaging using single-photon confocal fluorescence microscopy, the long acquisition time to produce an optical stack increases the risk of cell damage and photobleaching [13]. One technique currently in development is the use of point spread engineering to extend the depth of focus of these systems. Using a

modified fitness parameter and the GA, the ability of the adaptive optic system to optimise to a particular desired axial PSF is tested.

It is thought that given a deformable mirror with enough stroke and actuators, any wavefront of incident light that interacts with the mirror can be sufficiently altered to produce any PSF required. In the case of a blind system, where the mirror shape required is not known, the use of a fitness parameter and a search algorithm can be used to produce a particular PSF shape. The fitness parameter.vi compares the experimental axial PSF to the desired axial PSF, and their proximity is determined (which is defined by a fitness value). Using the GA and optimising for this fitness value, it is believed that solution space will be searched and an optimal solution will be found. In this part of the investigation, Gaussian shapes of various FWHMs were chosen to demonstrate the curve fitting capability and hence the PSF engineering capability of the system.

Previous versions of the fitness parameter used in this system incorporated just a measurement of the area correlation between the experimental and the desired axial PSF. Although it was shown that such a system was somewhat effective in producing the desired result, due to time constraints, problems associated with the system could not be sufficiently addressed. In the current incarnation for this part of the investigation, the fitness parameter incorporates area correlation as well as a measurement as to how close the measured FWHM value is to the desired FWHM. It should be noted that the measurement of how close the experimental FWHM is to the desired FWHM is determined using an algorithm that utilizes a normal distribution (such that a value of unity occurs when the experimental FWHM = desired FWHM, which falls off rapidly depending on the degree of variance set on the algorithm.)

For this investigation a sample was used containing a 250μm depth of water, sandwiched between a coverslip and a newfocus 5103 aluminum mirror, with a pre-optimised axial FWHM of 8.8+/-0.7μm. Using the genetic algorithm with the Gaussian shaping parameter, the axial PSF was optimised for desired axial PSFs with FWHMs of

2, 3, 5, 10, 15, 20 and 30 μm. The effect of the optimisation routine on the lateral PSFs were also examined and the results are plotted in figures 21 to 28.

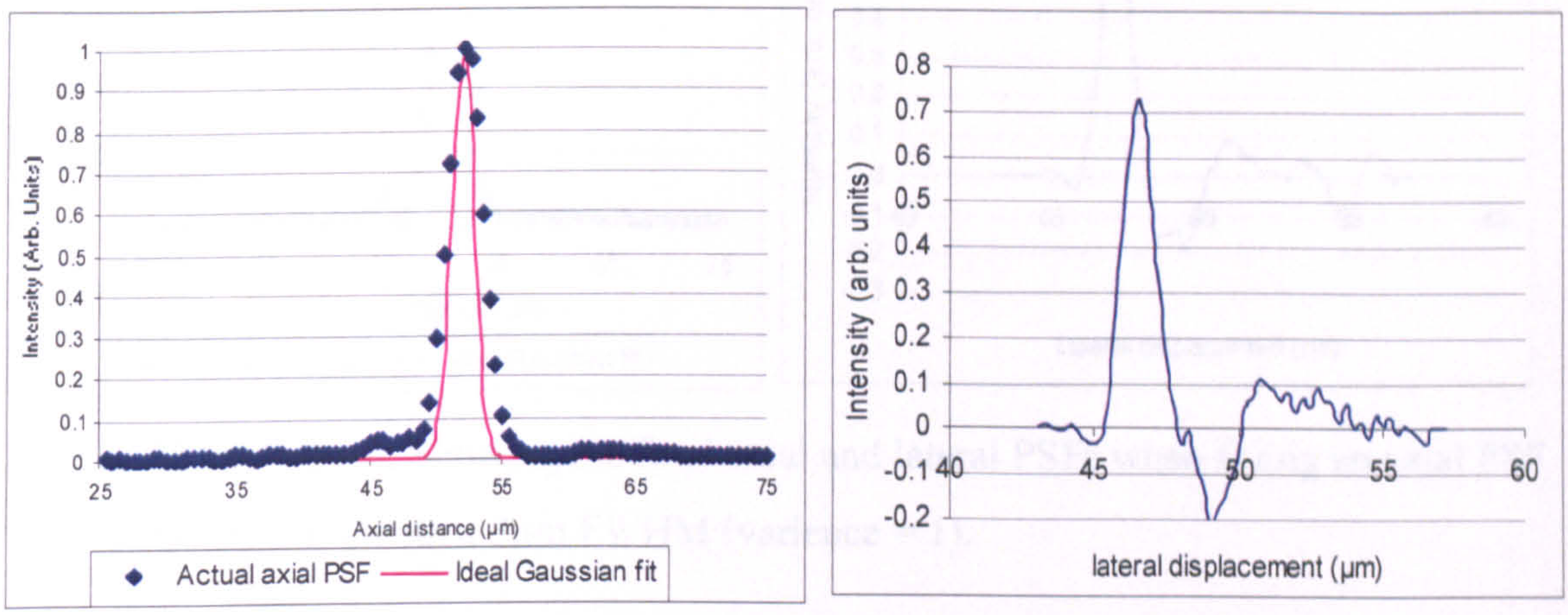

Figure 21 (a) and (b): Showing the final axial and lateral PSFs when fitting an axial PSF to a Gaussian curve with a 2μm FWHM. (Varience = 0.5)

The Gaussian Shaping capabilities of AO element (2μm FWHM) gives a final axial FWHM = 3.18 +/- 0.02μm and a lateral differentiated axial FWHM of 1.22 +/- 0.08μm. As one can see from the axial scan, the mirror seems to have a bit of trouble getting to the optimised axial PSF. This could be due to a number of factors such as an inefficient weighting of the fitness parameters of the lack of effective stroke on the deformable mirror.

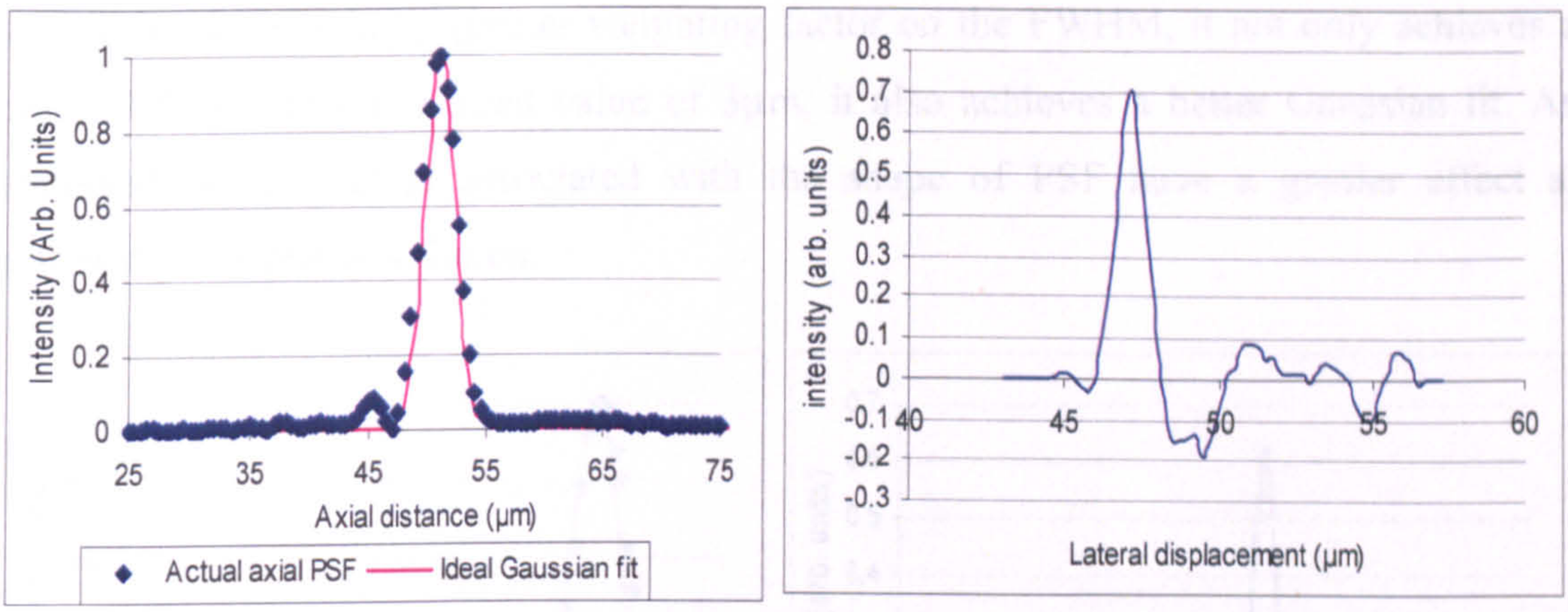

Figure 22 (a) and (b): Showing the final axial and lateral PSFs when fitting an axial PSF to a Gaussian curve with a 3μm FWHM (varience = 1).

In this instance a lesser weighting was placed on the FWHM by placing the varience to 1. This gave a final axial FWHM of 3.50μm and a differentiated lateral axial FWHM of 1.06μm.

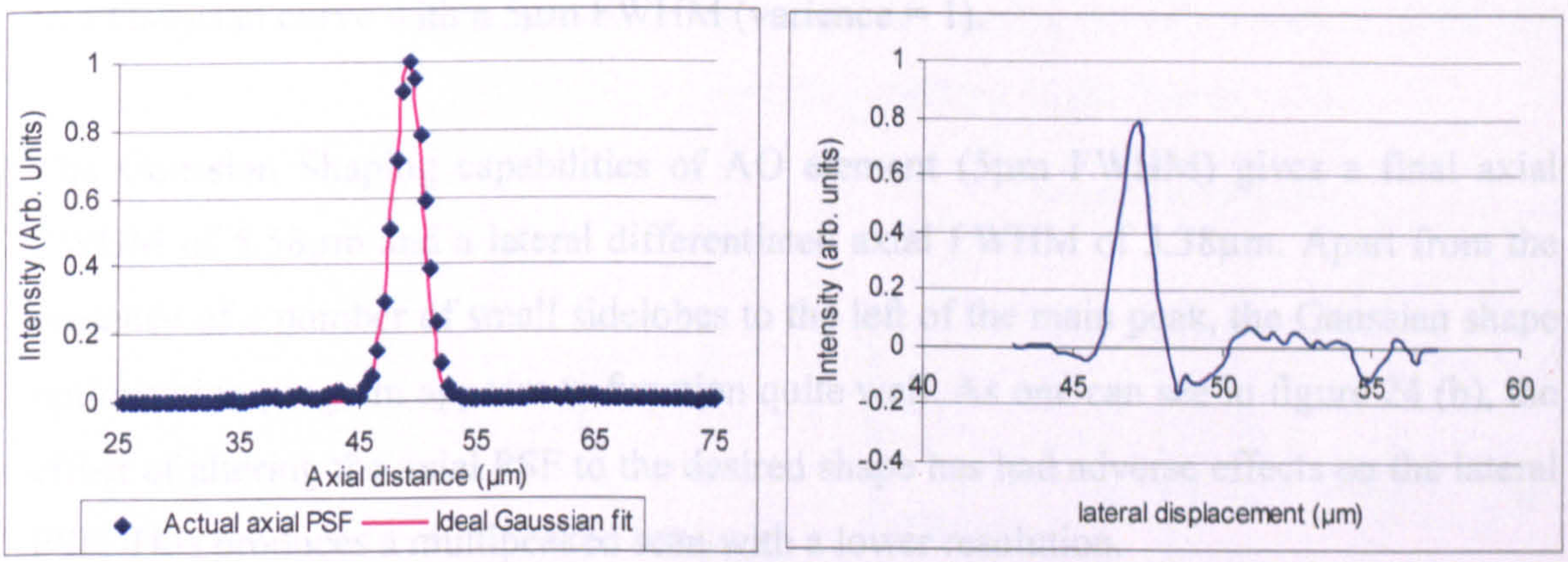

Figure 23 (a) and (b): Showing the final axial and lateral PSFs when fitting an axial PSF to a Gaussian curve with a 3μm FWHM (varience = 0.5).

In the results in figure 23, a greater weighting was placed on the FWHM within the fitness parameter by putting the varience to 0.5. This gives an axial FWHM of 3.22μm and a differentiated lateral FWHM of 1.16μm. In comparison with results in figure 22, it

seems that by placing a greater weighting factor on the FWHM, it not only achieves a closer FWHM to the desired value of 3μm, it also achieves a better Gaussian fit. As expected, some factors associated with the shape of PSF have a greater effect at achieving an optimal solution.

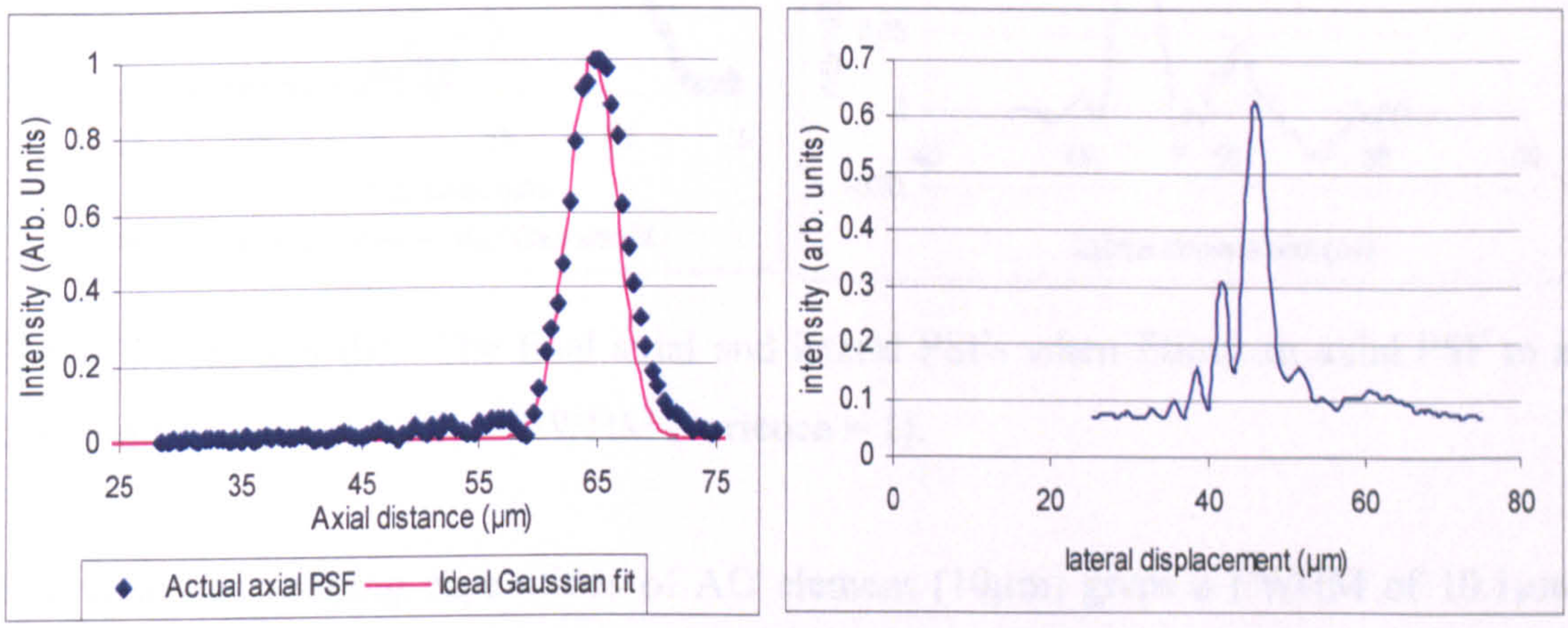

Figure 24 (a) and (b): Showing the final axial and lateral PSFs when fitting an axial PSF to a Gaussian curve with a 5μm FWHM (varience = 1).

The Gaussian Shaping capabilities of AO element (5μm FWHM) gives a final axial FWHM of 5.58μm and a lateral differentiated axial FWHM of 3.38μm. Apart from the presence of a number of small sidelobes to the left of the main peak, the Gaussian shape optimisation program appears to function quite well. As one can see in figure 24 (b), the effect of altering the axial PSF to the desired shape has had adverse effects on the lateral PSF. This produces a multipeaked scan with a lower resolution.

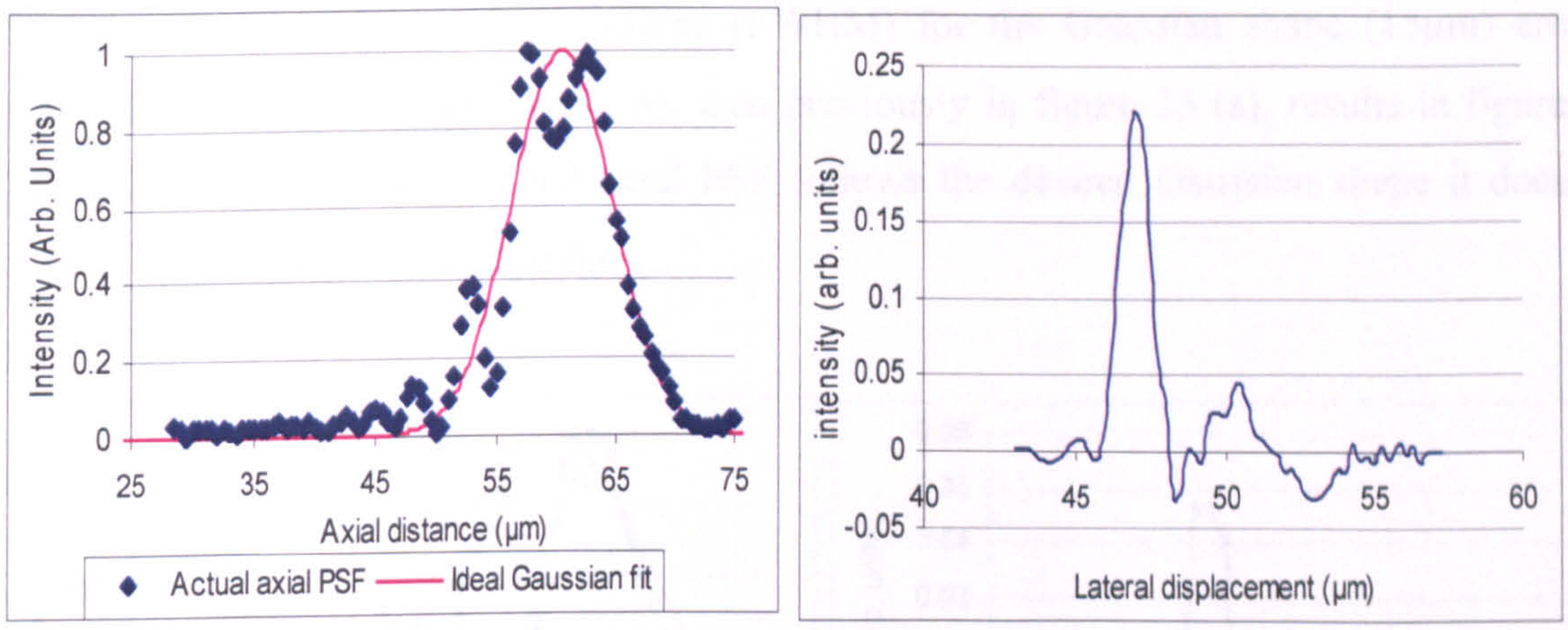

Figure 25 (a) and (b): The final axial and lateral PSFs when fitting an axial PSF to a Gaussian curve with a 10µm FWHM (varience = 1).

The Gaussian shaping capabilities of AO element (10µm) gives a FWHM of 10.1µm and a differentiated lateral axial FWHM 1.12µm. As one can see from figure 25 (a), the final axial PSF although following the desired Gaussian shape does contain a number of smaller peaks. This could be due to the mirror not having enough stroke to fulfill this PSF shaper or possibly a result of an incorrect weighting of the fitness value.

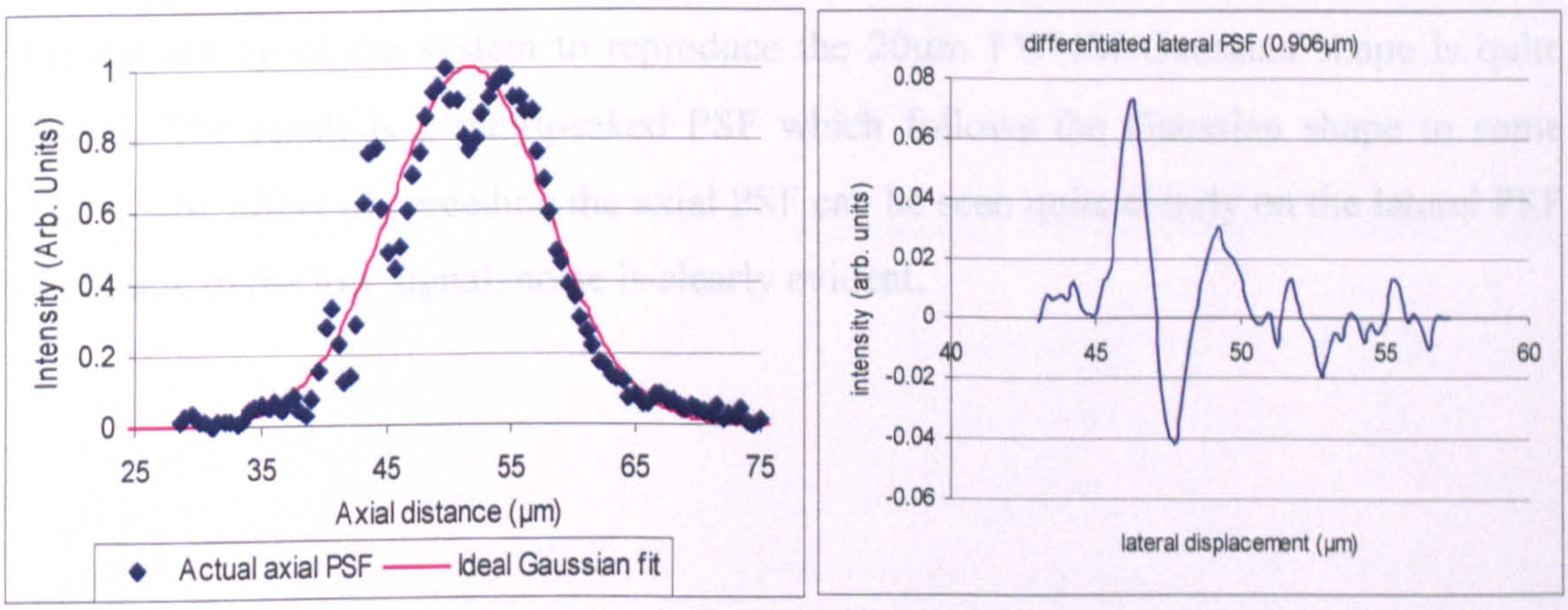

Figure 26 (a) and (b): The final axial and lateral PSFs when fitting an axial PSF to a Gaussian curve with a 15µm FWHM (varience = 1).

The final axial and lateral resolutions (FWHM) for the Gaussian shape (15μm) are 15.0μm and 0.93μm respectively. As seen previously in figure 25 (a), results in figure 26 (a) show that although final axial PSF follows the desired Gaussian shape it does contain a number of smaller peaks.

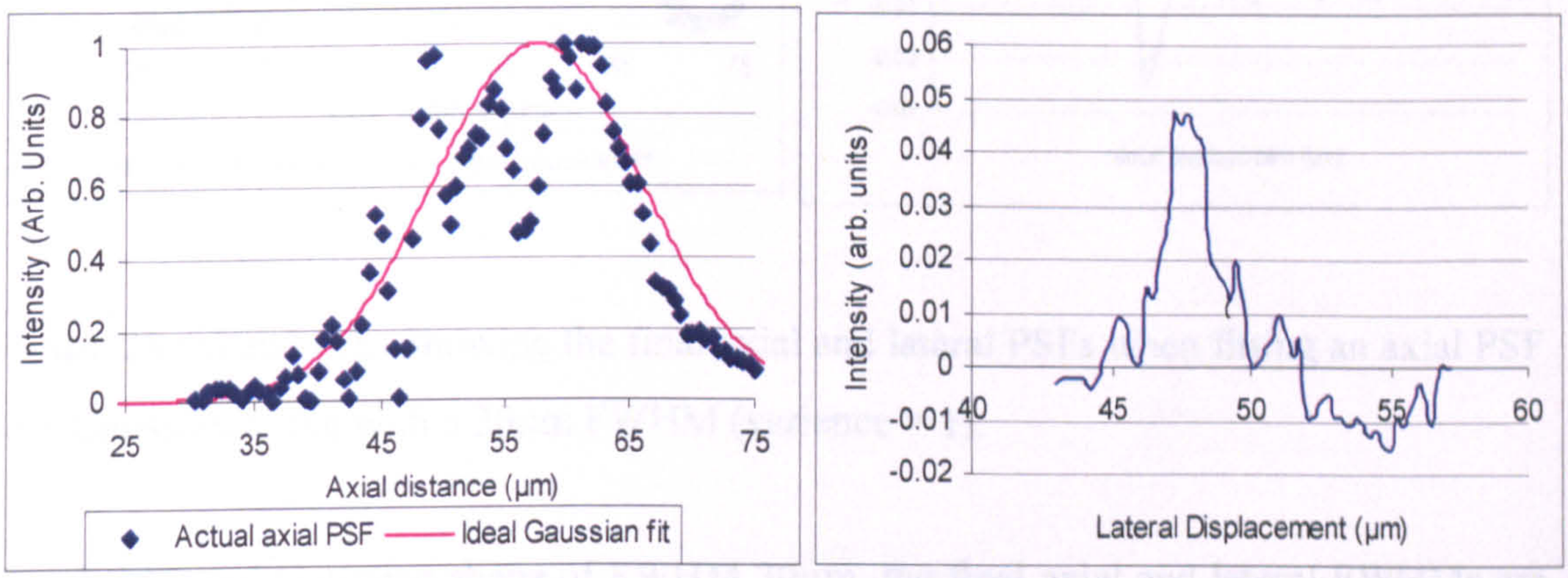

Figure 27 (a) and (b): Final axial and lateral PSFs for 20μm FWHM Gaussian curve.

The Gaussian shaping capabilities of AO element (20μm) gives a final FWHM of 21.5μm and a differentiated lateral axial FWHM 2.79μm. It can be seen from figure 27, that the ability of the system to reproduce the 20μm FWHM Gaussian shape is quite limited. The result is a multipeaked PSF which follows the Gaussian shape to some degree. The effect of spreading the axial PSF can be seen quite clearly on the lateral PSF where due to the low signal, noise is clearly evident.

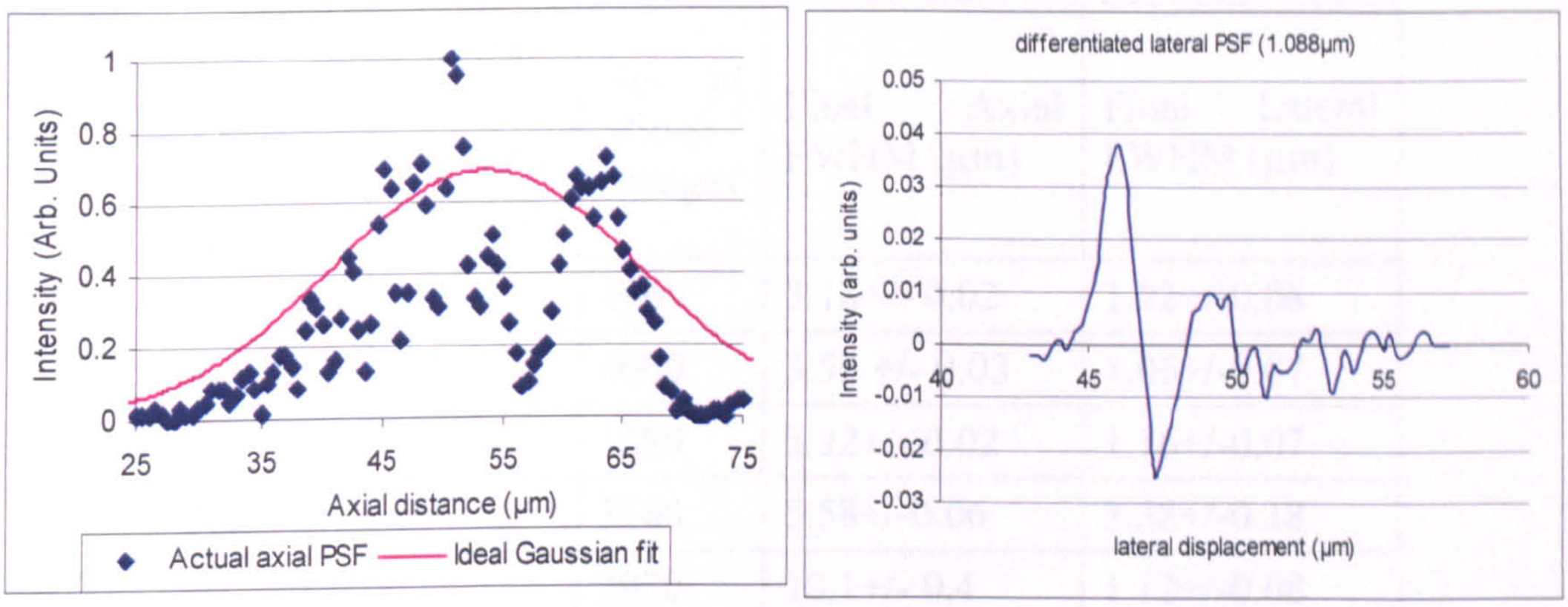

Figure 28 (a) and (b): Showing the final axial and lateral PSFs when fitting an axial PSF to a Gaussian curve with a 30μm FWHM (varience = 1).

For the desired Gaussian shape of FWHM 30μm, the final axial and lateral FWHMs are calculated to be 28.6μm and 1.08μm respectively. As one can see from figure 28 (a), the optimisation routine has a great deal of trouble in fitting the experimental axial PSF to the desired PSF. This is most likely due to limitations associated with the deformable mirror in that the degree of deformation is not enough to produce the wavefront required.

In table 2, all the results associated with the Gaussian curve fitting optimisations are shown.

Desired Gaussian Axial FWHM (μm)	FWHM fitness algorithm varience	No. of Mirror changes	Final Axial FWHM (μm)	Final Lateral FWHM (μm)
2	0.5	4960	3.18+/- 0.02	1.22+/-0.08
3	0.5	4000	3.50 +/- 0.03	1.06+/-0.07
3	1	1680	3.22+/- 0.02	1.16+/-0.07
5	1	3160	5.58+/-0.06	3.38+/-0.18
10	1	2920	10.1+/- 0.4	1.12+/-0.08
15	1	2560	15.0+/- 0.5	0.93+/-0.14
20	1	4560	21.5+/-2.3	2.79+/-0.22
30	1	2200	28.6+/- 4.0	1.08+/-0.14

Table 2: Showing axial PSF Gaussian fitting results.

6. Summary

The use of various algorithms with an adaptive element in a confocal system has been demonstrated and shows significant improvement in the axial resolution and signal intensity. While optimisation algorithms such as GA are more likely to find the global maximum in solution space in comparison to MHC, it usually takes longer to achieve an optimum solution.

Particular fitness parameters have shown promise in increasing the effectiveness of GA best mirror solution for various samples. In some biological applications, where speed may be required, compromises must be made with resolution. In some cases, the effect of optimising for particular axial PSF components has a detrimental effect on the lateral PSF and resolution. In the situation where the best axial and lateral resolution is required, optimising for intensity appears to show the best all round result.

By adapting the axial fitness parameter program, it has been shown that particular desired axial PSF shapes can be reproduced within an aberrated sample using the

optimisation procedure. This does appear to have some limitations due to the relative power of the mirror (stroke) and need for some possible weighting functions dependant on the shape required. It is expected that this would negate a particular problem presently found in when imaging biological samples, whereby allowing the operator to increase the FWHM, which in turn would help to locate the focal point of the system more easily.

References

1. Neil M. A. A., Juskaitis R., Wilson T., Laczik Z. J. (2000). Optimised pupil-plane filters for confocal point-spread function engineering. *Optics Letters*, 25(4), 245-247.
2. Martinez-Corral, M., Munoz-Escriva, L. Kowalcyk, M., Cichocki, T. (2001). One-dimensional iterative algorithm for three-dimensional point-spread function engineering. *Optics Letters*, 26(23) 1861 – 1863.
3. Martinez-Corral, M. (2003). Point spread function engineering in confocal scanning microscopy. *Proc. of SPIE*, 5182, 112 – 122.
4. Wilson, T., Juskaitis, R., Botcherby, E. (2005). Extended depth of focus microscopy. Focus on microscopy 2005, 28.
5. Wilson, T., Carlini, A. R. (1989). The effect of aberrations on the axial response of confocal imaging systems. *J. of Microscopy*, 154, 243-256.
6. Wan, D., Rajadhyasksha, M., Webb, R. H. (2000). Analysis of spherical aberration of a water immersion objective: application to specimens with refractive indices 1.33-1.40. *J. of Microscopy*, 197, 274-284.
7. Marsh, P. N., Burns, D., Girkin, J. M. (2003). Practical implementation of adaptive optics in multiphoton microscopy. *Optics Express*, 11, 1123-1130.
8. Wright, A. J., Burns, D., Patterson, B. A., Poland, S. P., Valentine, G., Girkin, J. M. (2005). Active aberration correction in confocal and multiphoton microscopy. *Microscopy research and technique*, 67, 36 – 44.
9. Poland, S. P., Burns, D., Lubeigt, W., Patterson, B. A., Valentine, G., Wright A. J., Girkin, J. M. (2005). Use of optimisation algorithmic techniques with active optics for aberration correction in optical sectioning microscopy. *Proc. SPIE*, 6018, 60181H.
10. Dirckx JJ, Kuypers LC, Decraemer WF. (2005). Refractive index of tissue measured with confocal microscopy.J Biomed Opt., 10(4):44014.
11. LabWindows/CVI Controlling LabVIEW, NI Developer Zone, National Instruments, retrieved 12th of January, 2005 from

http://sine.ni.com/apps/we/niepd_web_display.display_epd4?p_guid=B45EACE3D9E156A4E034080020E74861&p_node=DZ52051&p_source=external.

12. LabVIEW 7.1 Icon and connector pane overview. LabVIEW Help manual.
13. Cogswell, C., Chumachenko, V., Farrow, D. Coming into focus. OE Magazine, SPIE, November 2003, 21 – 23.

Chapter 8: Using structured light with infrared illumination to quantify dental caries

1. Introduction

As previously mentioned in some detail in chapters 3 and 4, if dental caries can be diagnosed at an early stage, it can be treated easily without resorting to more drastic measures such as amalgam restoration or tooth extraction. Currently, at the dentist's disposal there are a number of commercially available methods for caries detection, but none of these techniques have the ability to detect and quantify early stage caries.

New diagnostic systems currently in development such as fibre optical confocal microscopy (FOCOM) technique (modelled in chapter 3) provide a depth profile of the tooth from the surface as well as information on the degree of mineral loss. Although these new techniques are quite promising, in the case of FOCOM, only optical information in one dimension (depth) is returned. What the dental practitioner would ideally want is a fast and effective method to image the healthy and carious portions of the tooth in three dimensions, presenting a high level of both quantitative and qualitative information.

In this chapter an optical sectioning technique incorporating structured light illumination [1] is examined as a possible diagnosis tool in dentistry. The optical set-up of the system as well as a description of the system control with a custom software interface (written in LabVIEW) is presented. Also in this section the optical sectioning capabilities of the structured light system are characterised and in a preliminary study, optically sectioned images showing carious enamel close to the surface are shown. Present problems associated with the structured light illumination procedure are also examined (such as limitations on depth of imaging) and possible solutions discussed.

2. Using structured light illumination

As described earlier in chapter 2, structured light illumination functions by projecting a single frequency grid pattern onto a sample and collecting the image using a CCD device. Due to the object grid pattern and object sample being at conjugate points (i.e the image plane), the grid pattern will be present on those parts of the object image that are in-focus. By extracting only those parts of the image where the grid pattern is present (in-focus), the system exhibits optical sectioning capabilities similar to both the confocal and multiphoton systems. By taking successive images with the grid at three spatial phases (corresponding 0, $2\pi/3$ and $4\pi/3$), both the optically sectioned image and the conventional image can be reconstructed.

2.1 Structured light optical set-up

The experimental set-up of the structured light system is shown in figure 1 below. Using a super high power OD-50L GaAlAs IR LED [Opto. Diode Corp.], operating at 50 mW, at a peak wavelength of 880nm, a 40 lines/mm grid pattern [Comar] is illuminated, and the light collimated, using a set of relay lenses. The collimated light that then passes through a 50/50 beam splitter, hits the back aperture of the objective where it is focused onto the sample.

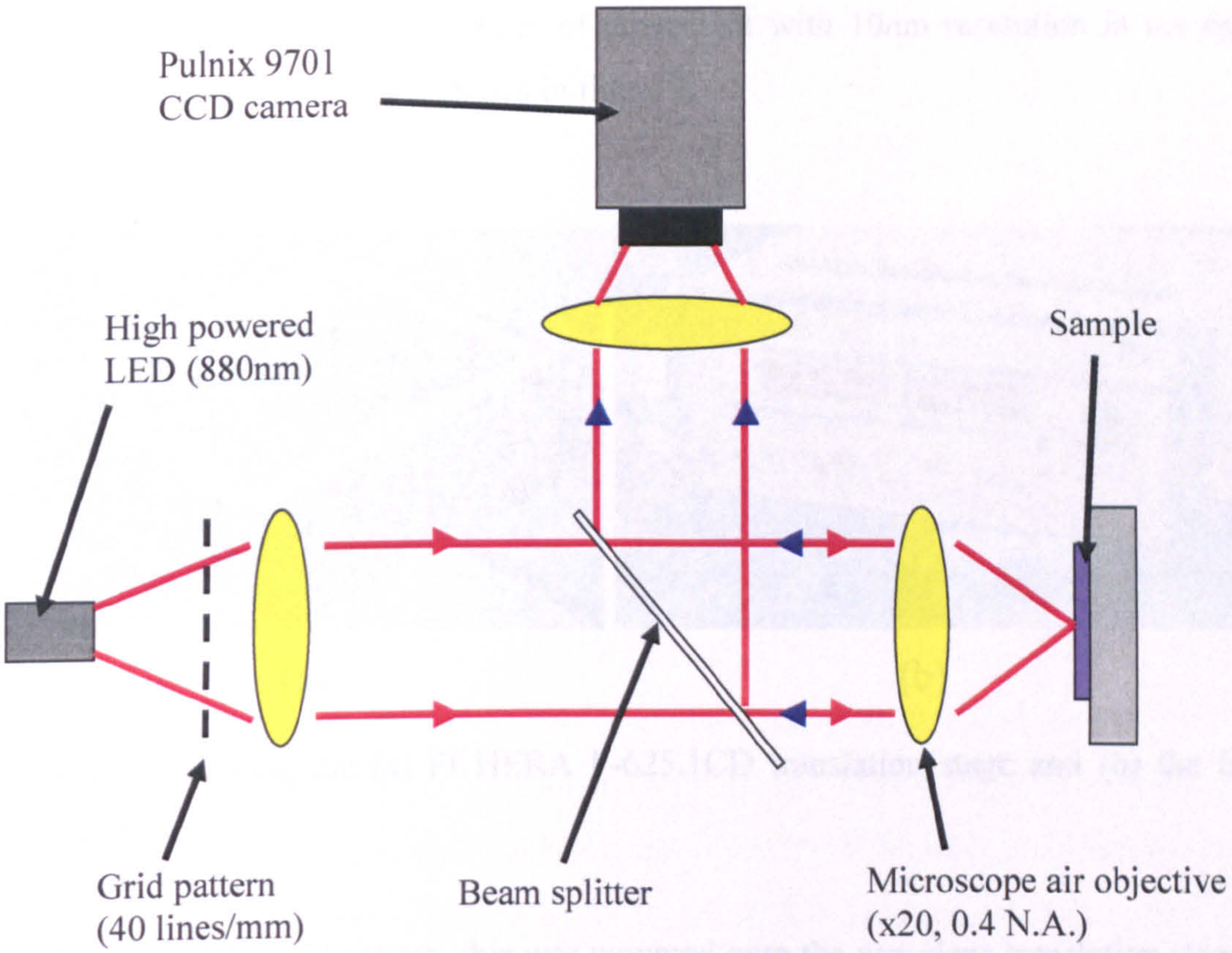

Figure 1: Showing a schematic of the structured light system set up.

Light reflected from the focus spot passes back through the objective is reflected off the beam splitter, passing through a set of relay lenses that re-image the sample onto the Pulnix TM-9701 CCD camera chip. For simplicity, relay lenses (which ensure that the grid pattern and sample focus spot are at conjugate points to the image focused on the CCD chip) are not included in the diagram. It should be noted that both the test sample and the grid pattern are mounted onto a manually controlled xyz translational stages, which allow coarse control of their positions. These are useful when calibrating the system (i.e. matching the grid pattern focus position with the sample image focus).

Both the objective and the grid pattern were mounted onto piezo translational stages both made by Physik Instruments (PI). Using a specialized fitting (built in-house), the objective was mounted onto a PI-625.1CD HERA stage which was controlled using an

E-665 control and provided 500μm of movement with 10nm resolution in the optical axis (axial direction). This is shown in figure 2.

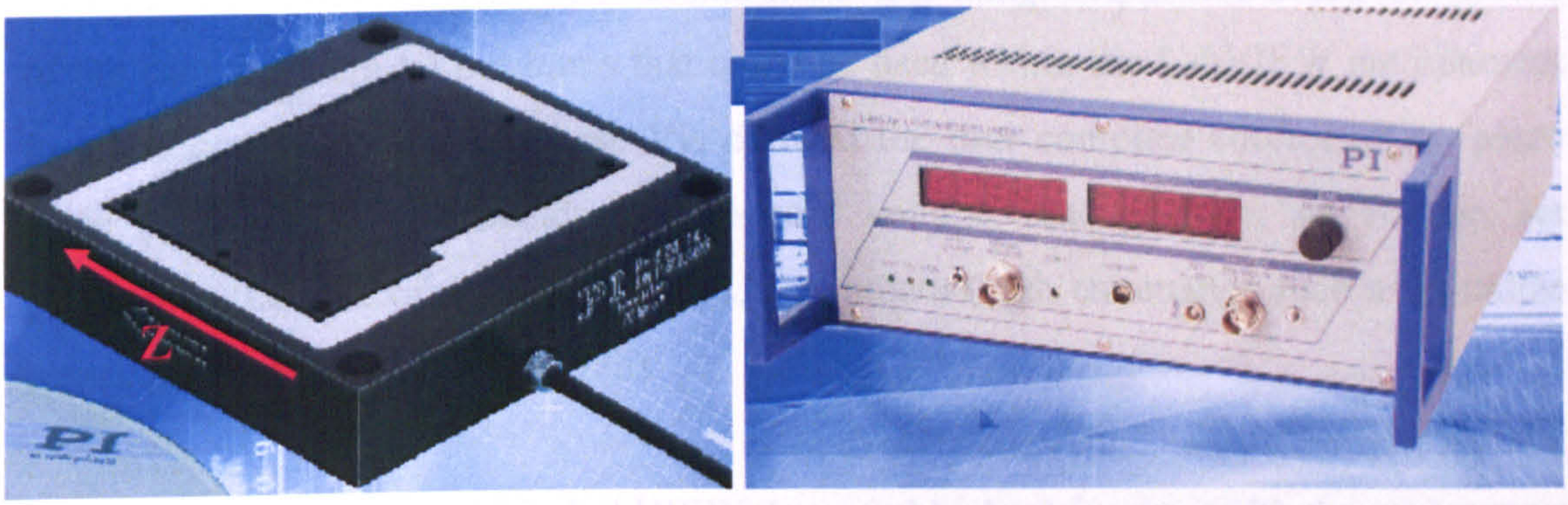

(a) (b)

Figure 2: Showing the (a) PI HERA P-625.1CD translation stage and (b) the E-665 control box.

In the case of the grid pattern, this was mounted onto the xyz piezo translation stage and controlled using an E-662 control box, which was described previously in chapter 6. Both piezo control boxes allowed either manual or direct computer control using a LabVIEW interface via an RS-232 port connection.

The Pulnix CCD camera was controlled by computer via an IMAQ-1422 image acquisition board [National Instruments] which was compatible with LabVIEW software. The Pulnix TM-9701 is a monochrome CCD camera with a resolution of 768 x 484 pixels and an internal shutter speed control from 1/60 to 1/16000 sec. The CCD chip size measures 8.9mm (H) x 6.6mm (V) and each pixel has an active area of 11.6μm x 13.6μm.

2.2 Structured light LabVIEW computer control

The piezo translational stages and camera were controlled using a commercial graphical programming language called LabVIEW developed by National Instruments (explained

in more detail in chapter 6), that uses graphical interfaces or icons instead of lines of text to create applications.

Provided with both the piezo translational stages and image acquisition board (connected to the camera) were VI programs that could be used within the LabVIEW environment to allow computer control. These VIs allowed the user complete control of the piezo stage (with various commands such as read voltage, read position, set voltage, set position in the case of the piezos) and CCD camera (with commands such as initialize board, image snap, and image grab).

A program was constructed in LabVIEW that would take 3 images (with the grid pattern at three spatial phases of 0, $2\pi/3$ and $4\pi/3$) for each axial position (controlled by the objective axial distance (HERA stage) and from image processing produce conventional widefield and sectioned images. The program also plotted the axial point spread function (PSF) and calculated the axial resolution of the system (using a Gaussian curve fitting sub-routine).

The program allows control over the range of z-axis positions, the z-axis step size, piezo accuracy limits as well as number of image integrations. Figure 3 shows the front panel of the structured light system.

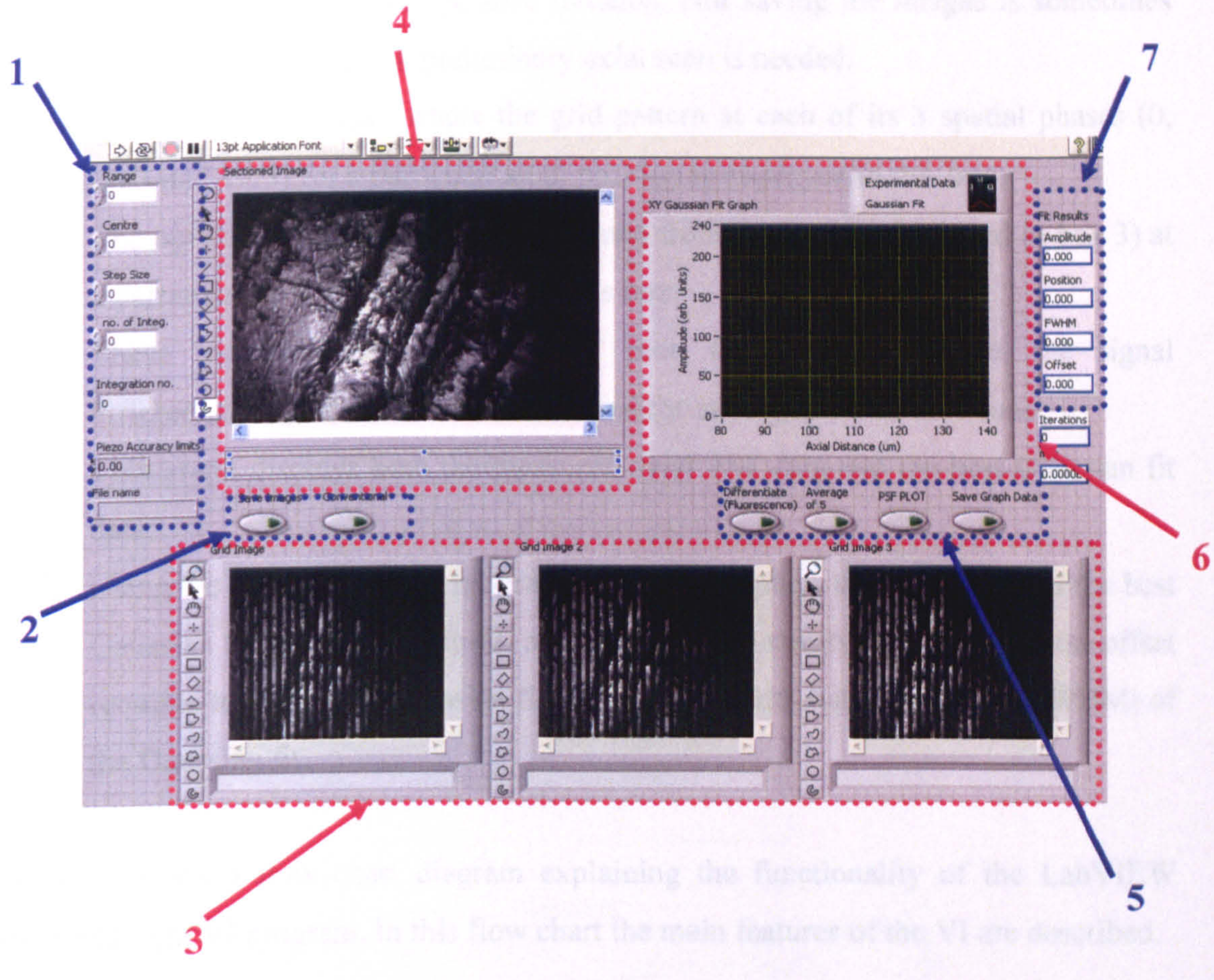

Figure 3: Showing structured light system front panel control written in LabVIEW.

Some of the main functions of the front panel of the structured light program highlighted in the 7 boxes are explained in more detail:

1. Controls the parameters of the axial scan such as range, approximate centre and step size of the scan (all in μm) as well as the number of image integrations per axial position. The integration function is particularly useful when taking an optical section cancelling out noise from the system (ie. when the reflected light intensity is low). The axial piezo accuracy and name of the saved files are also controlled here.
2. One toggle is responsible for controlling whether or not to calculate the conventional image as well as the sectioned image. The other toggle titled "save

images" controls the image save function. Not saving the images is sometimes quite useful when quick preliminary axial scan is needed.

3. The three raw images where the grid pattern at each of its 3 spatial phases (0, $2\pi/3$ and $4\pi/3$) for a particular axial position is displayed in this box.
4. The optically sectioned image (calculated from the images displayed in box 3) at a particular position is displayed in this box.
5. These toggles control of the PSF plot, the moving average, the signal differentation (used in fluorescence), and the save graph data functions.
6. This graph displays both the measured axial PSF data and the best Gaussian fit data.
7. Using the Gaussian fitting program, this table displays the parameters of the best Gaussian fit, such as amplitude, axial position of intensity maximum, noise offset required to produce a Gaussian fit, and the full-width half-maximum (FWHM) of the Gaussian fit.

Figure 4 shows a flow chart diagram explaining the functionality of the LabVIEW structured light VI program. In this flow chart the main features of the VI are described.

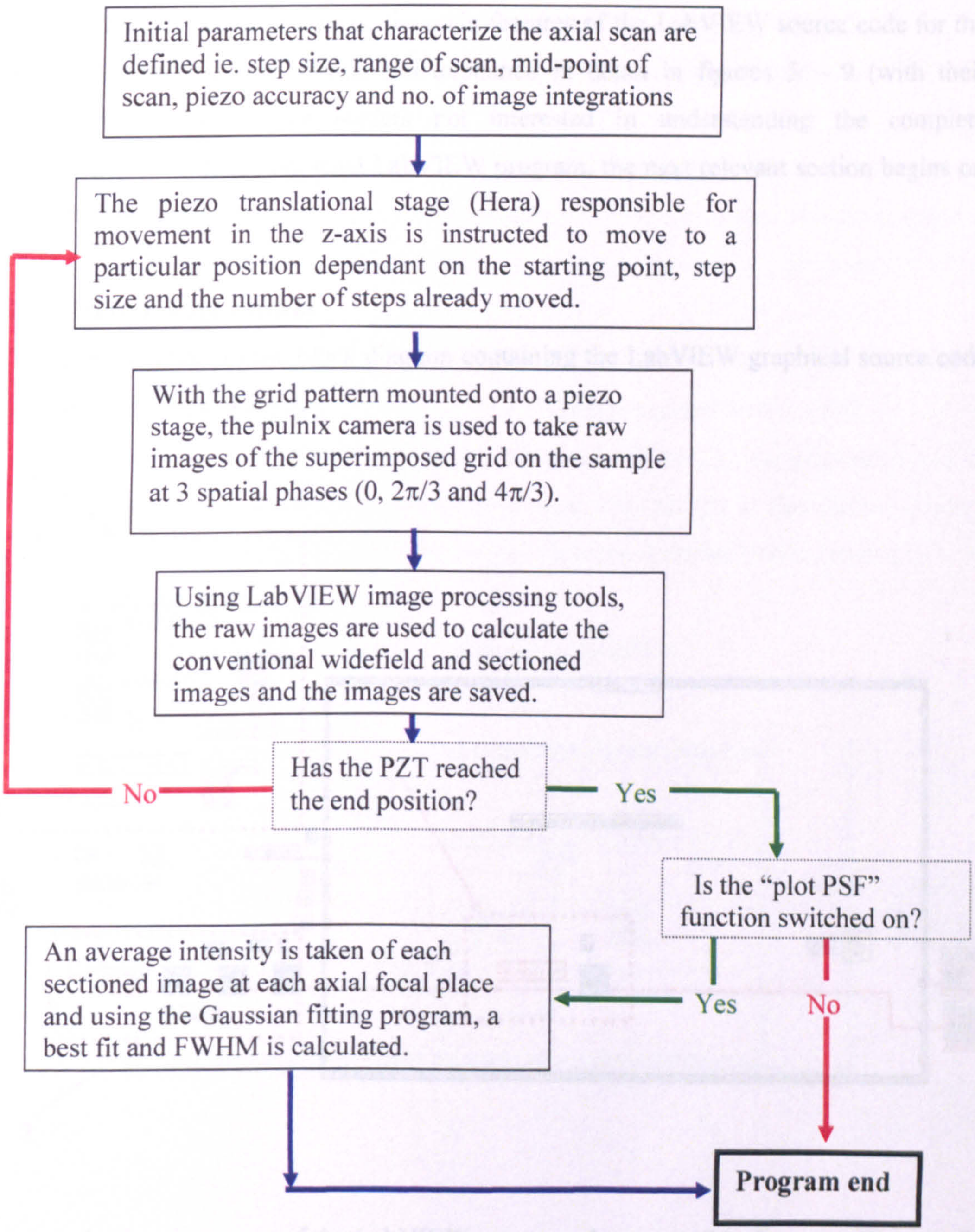

Figure 4: Flow chart diagram explaining the functionality of the structured light program.

In the interests of completeness, the main features of the LabVIEW source code for the structured light VI are shown and explained in detail in figures 5 – 9 (with their corresponding text). For readers not interested in understanding the complete functionality of the constructed LabVIEW program, the next relevant section begins on pg. 263 (section 2.3).

2.2.1 Hera z-stage control

The main features of the block diagram containing the LabVIEW graphical source code are shown in figures 5 – 9.

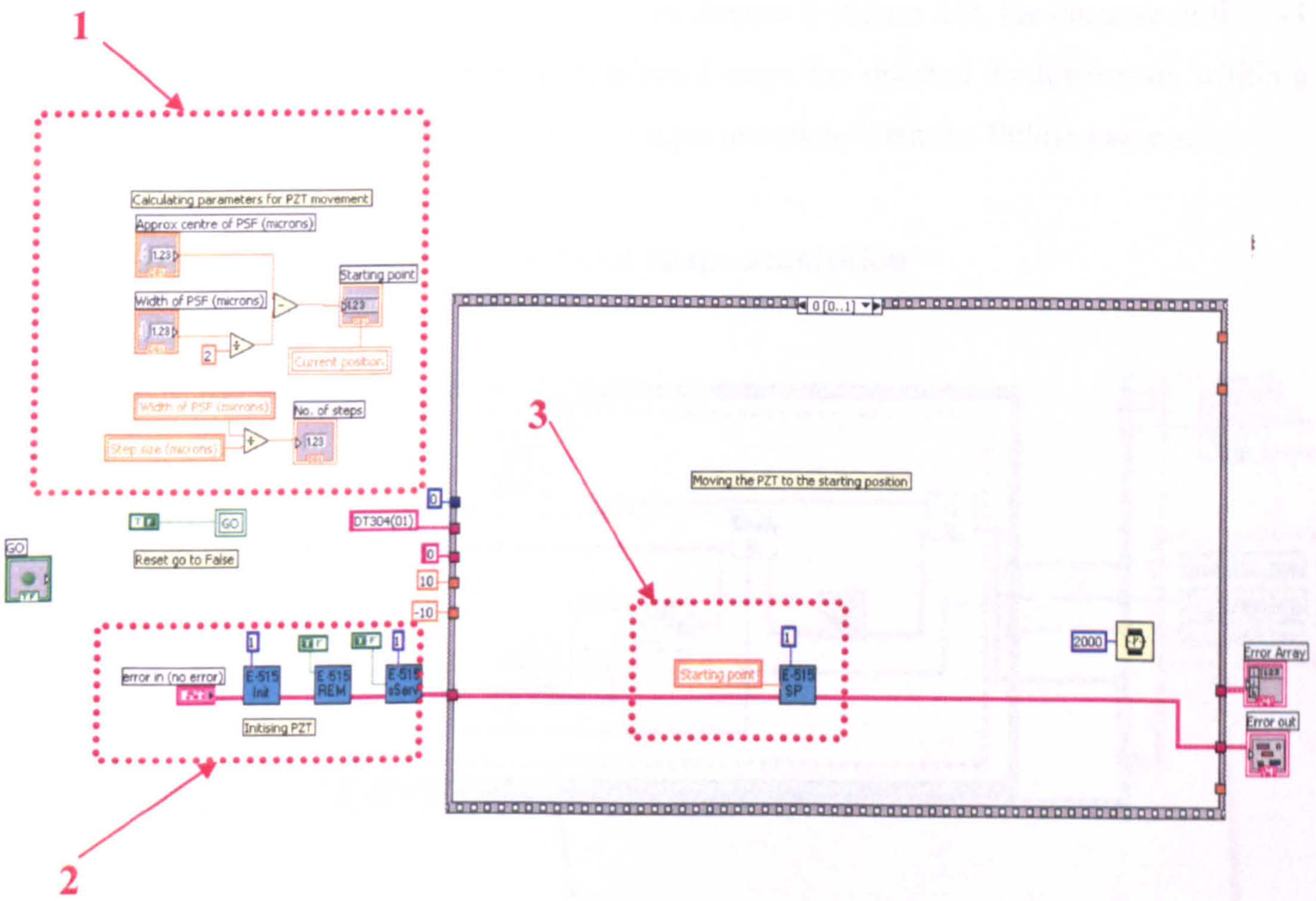

Figure 5: Showing some of the LabVIEW source code responsible for controlling the PI Hera piezo z-translational stage responsible for axial positional movement.

The main features of figure 5 are highlighted in the 4 red-dashed boxes:

1. This section of code is responsible for finding the correct baud-rate and com port to establish remote control of the HERA P625.1 stage through the E-665 control system.
2. Responsible for defining the connected axes and setting the servo mode of the system. In this case, there is only one axis in the z-direction. The servo mode is set to the on position which ensures that the position of the piezo is more accurate.
3. This part of the code commands the piezo stage to move to a particular position defined by the input value. The HERA stage has a range from 0 – 500 μm.
4. Similar to code shown previously in chapter 6 (figure 21), the purpose of this VI is to insure that the piezo translational stage has reached its destination within a set of pre-defined limits, before images are taken from the Pulnix camera.

2.2.2 Grid pattern position control and image acquisition

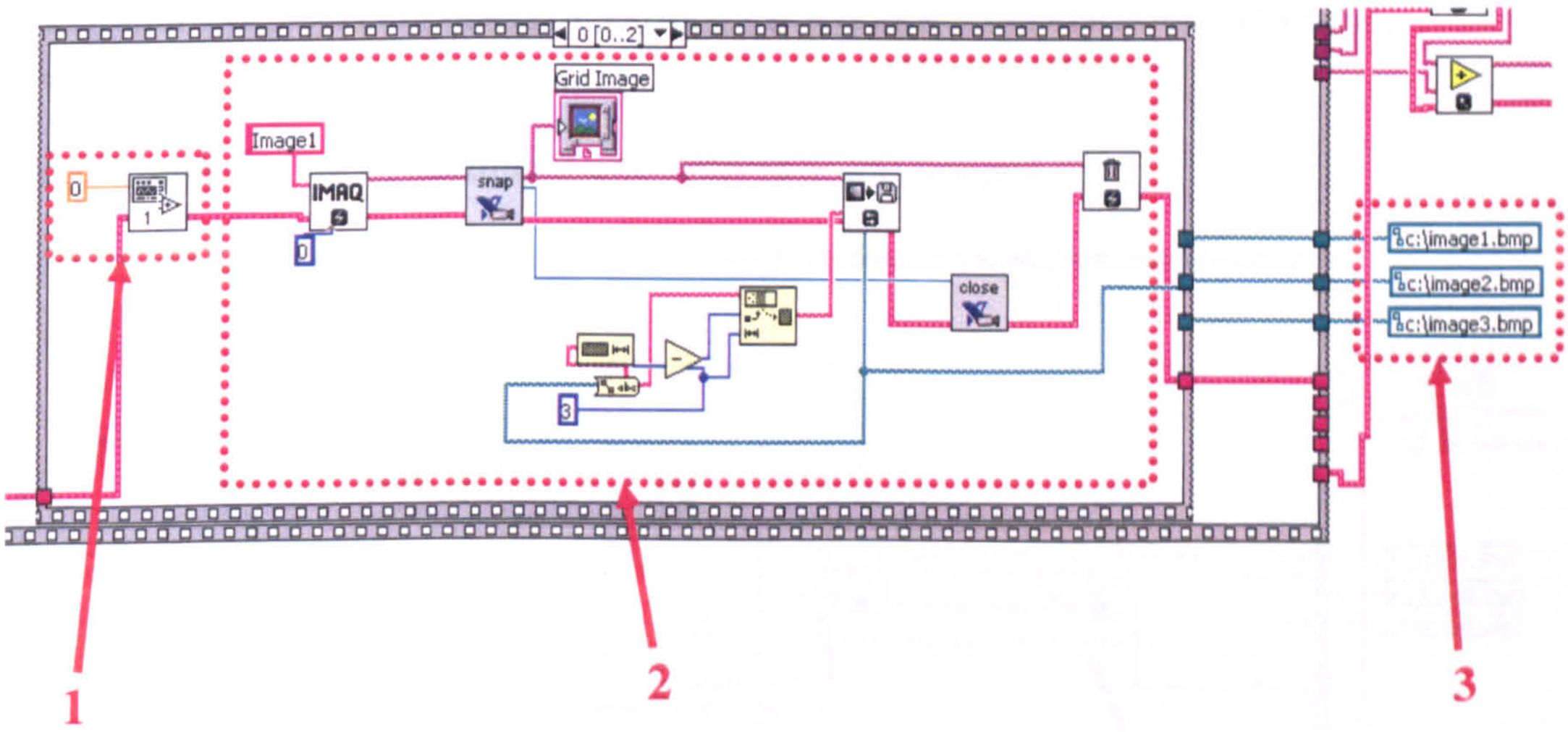

Figure 6: Showing code responsible for moving the grid pattern and taking and saving the subsequent image.

Figure 6 shows a stacked sequence structure which controls grid pattern movement and image capture from the CCD camera. The highlighted boxes in figure 8 are explained below:

1. This sub-VI, explained previously in chapter 6 as "E-515 SP-Mod" is used for controlling the E-515 xyz piezo translation stage. This piezo stage to be controlled is responsible for moving the grid pattern to each of its spatial phases. In the case of the 40lines/mm grid pattern used in this investigation, this translates to a step movement of 8.33μm for each $2\pi/3$ phase change.
2. This portion of code is responsible for initiating the IMAQ (IMage AcQuisition) board and camera, instructing the camera to take an image, and subsequently saving the image onto the computer.
3. For each of the three spatial phases, the images are saved as bitmaps within the c:\ directory as image1, image 2, and image 3.

The sequence of moving the grid pattern and grabbing the subsequent image with the grid pattern at 3 spatial phases to produce the sectioned and conventional image.

2.2.3 Construction of sectioned and conventional images

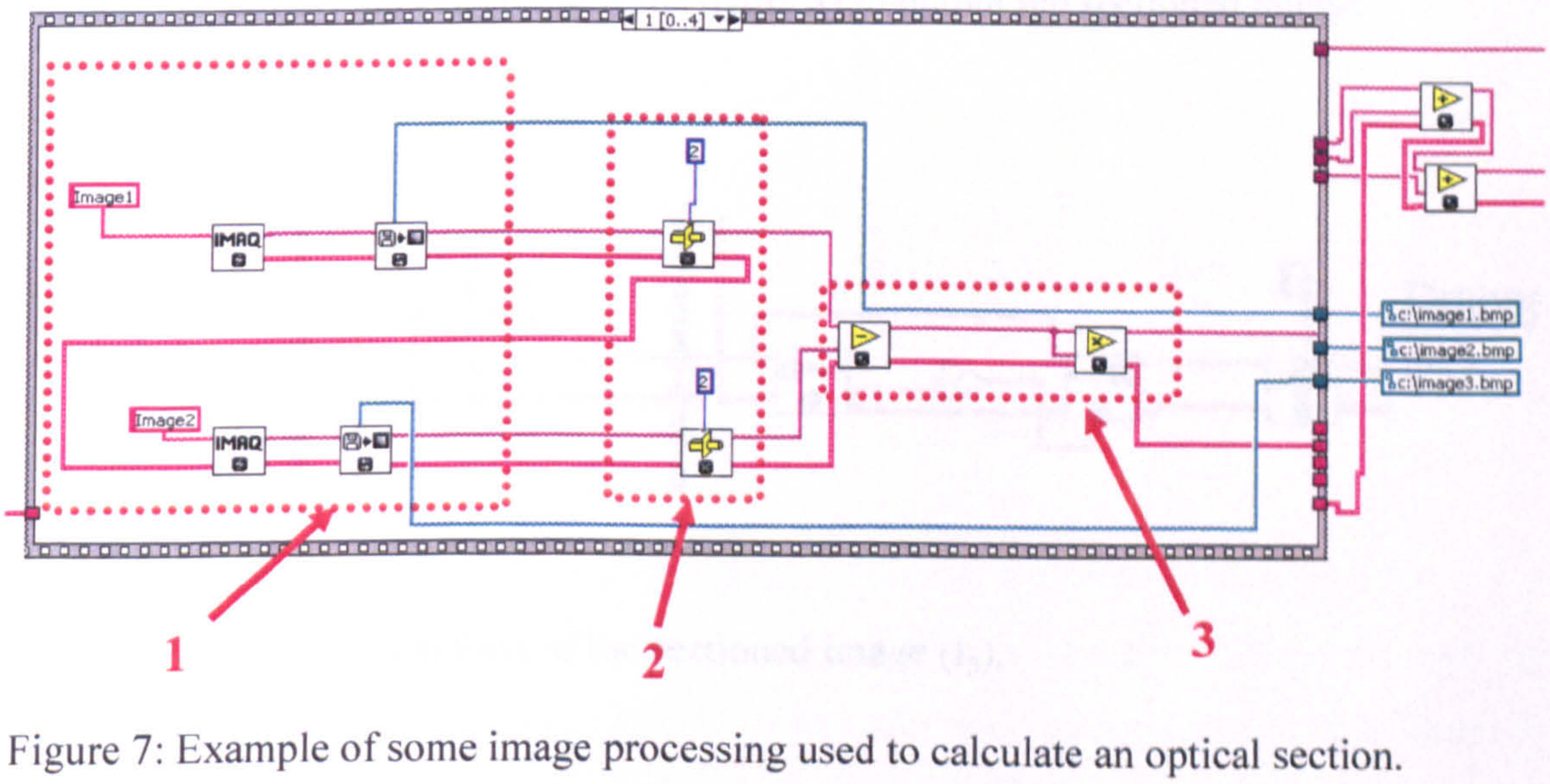

Figure 7: Example of some image processing used to calculate an optical section.

As mentioned previously in chapter 2 (equation 24), the optically sectioned image I_p is calculated by the equation:

$$I_p = \sqrt{\frac{2}{3}}.\left[(I_1 - I_2)^2 + (I_1 - I_3)^2 + (I_2 - I_3)^2\right]^{1/2} \quad (1)$$

Figure 7 shows how $(I_1 - I_3)^2$ is calculated using LabVIEW IMAQ VI image suite. The main features of this section of code are highlighted in the red-dashed boxes:

1. Using "IMAQ create" and "IMAQ readfile" sub VIs, this part of the code is responsible for initiating the IMAQ function and calling image 1 (I_1) and image 3 (I_3) from a previously saved location (c:\ directory).
2. Before any image calculations are performed, they are first converted from 8-bit to 32 bit images using the "IMAQ image cast" function. This is necessary when image multiplication is involved.
3. These sub VIs are responsible for subtracting I_1 from I_3 and squaring the result.

This is then repeated to calculate both $(I_1 - I_2)^2$ and $(I_2 - I_3)^2$ combinations in the next two parts of the stacked sequence (not shown). These 3 combinations are then input into another section of LabVIEW code (see figure 8) to output the sectioned image.

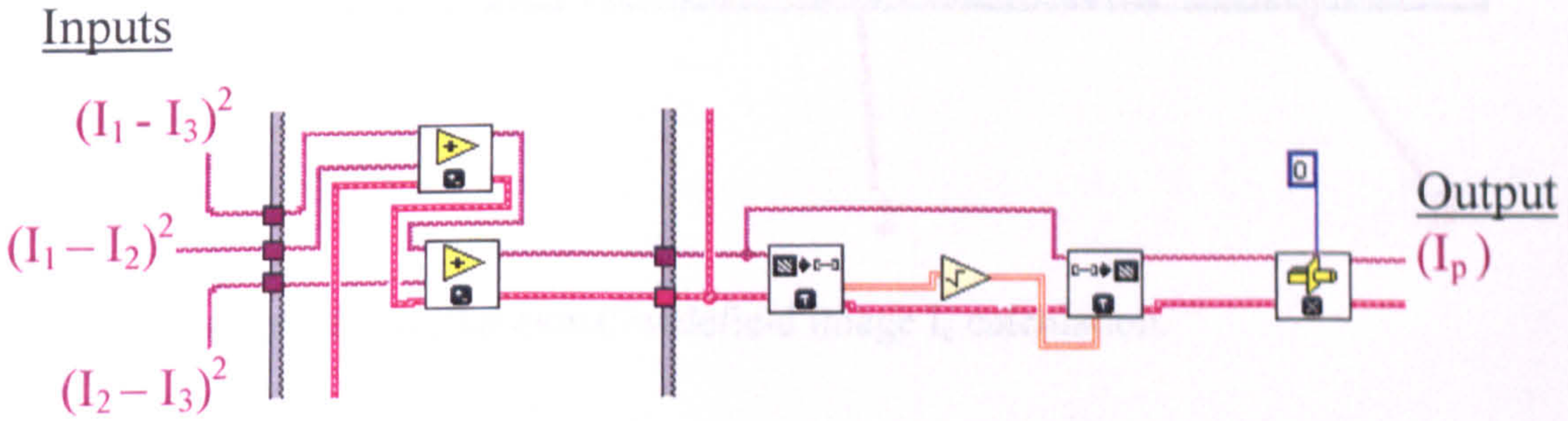

Figure 8: Showing calculation of the sectioned image (I_p).

In figure 8, the results of $(I_1 - I_3)^2$, $(I_1 - I_2)^2$, and $(I_2 - I_3)^2$ are added together. The square root of this resultant image is then calculated using "image to array.vi" and "array to image.vi" functions to produce the optically sectioned image, I_p.

As shown in chapter 2, the conventional widefield image, I_c can be calculated from the images of the grid at three spatial phases using the equation:

$$I_c = \frac{1}{3}(I_1 + I_2 + I_3) \quad (2)$$

The LabVIEW code used to calculate I_c is shown in figure 9.

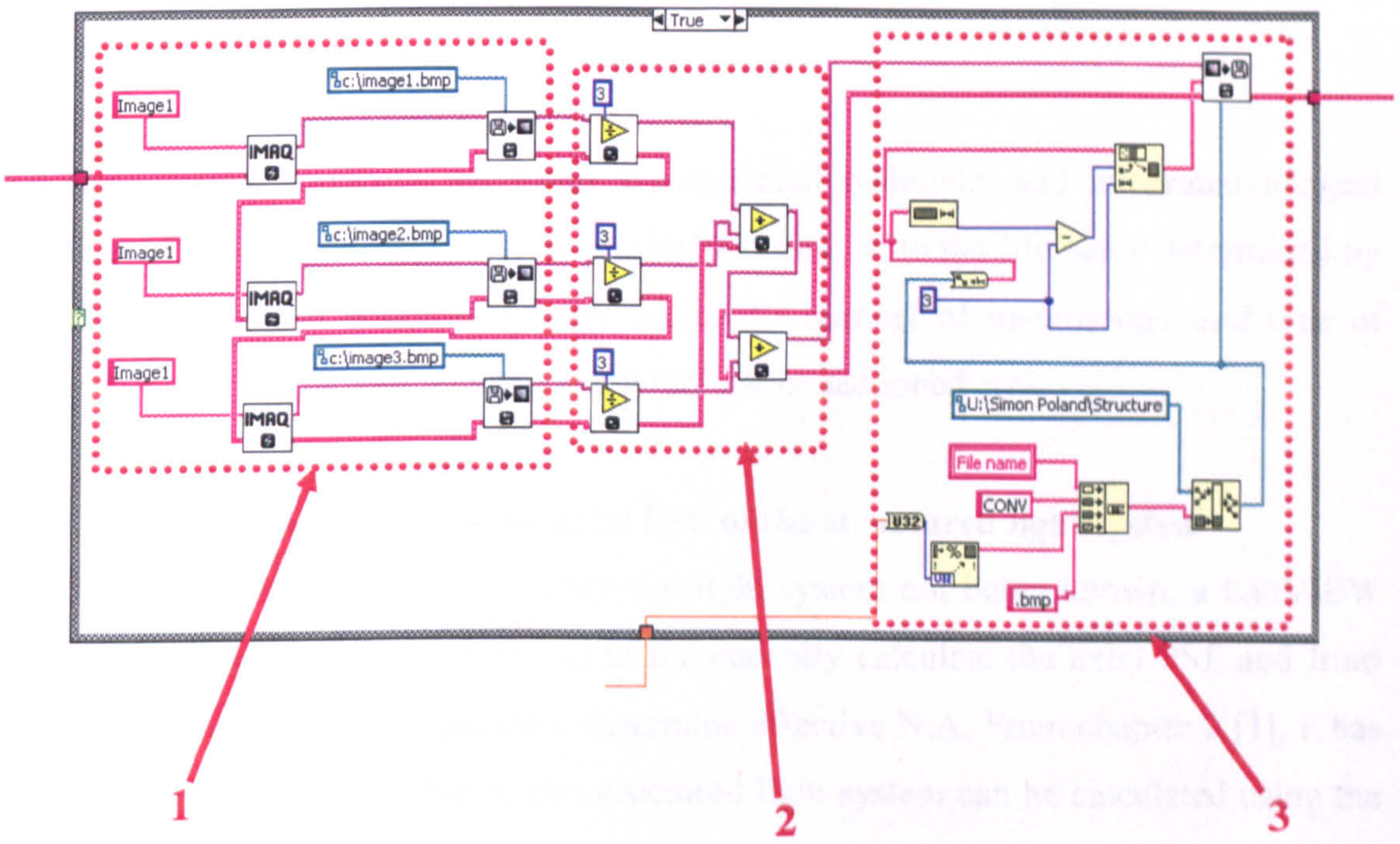

Figure 9: Showing the conventional widefield image I_c calculation.

The main features of this section of code are highlighted in the red-dashed boxes:

1. Using "IMAQ create" and "IMAQ readfile" sub VIs, this part of the code is responsible for initiating the IMAQ function and calling image 1 (I_1), image 2 (I_2) and image 3 (I_3) from a previously saved location (c:\ directory).

2. This section of the code adds each of the three images together to produce the conventional image I_c.
3. This section of the code (seen previously) saves the image as a bitmap at a pre-defined location.

By calculating the average pixel value from an image (using "image to array" and "average array value" VIs) at each axial position, an axial PSF can be plotted. Using the Gaussian fitting program (mentioned previously in this chapter and explained in more detail in chapter 6), the FWHM can be calculated. The moving average, signal differentiation and graph data save functions in the structured light program operate in a similar manner to those explained previously in chapter 6, in figures 14, 15 and 17 respectively.

All images (raw, optically sectioned, conventional widefield, and integrated images) were saved at a pre-defined location on the hard disk, with the file name determined by the axial position at which they were taken, the number of integrations, and type of image (i.e. whether it was conventional widefield or sectioned etc).

2.3 Theoretical calculation of the axial PSF of the structured light system

Due to the effective N.A. of the structured light system not being known, a LabVIEW program was constructed (Figure 10) to theoretically calculate the axial PSF and from comparisons with experimental data, determine effective N.A. From chapter 2 [1], it has been shown that the axial PSF of the structured light system can be calculated using the equation:

$$I_p \approx \left| 2\frac{J_1[2u\bar{\upsilon}(1-\bar{\upsilon}/2)]}{[2u\bar{\upsilon}(1-\bar{\upsilon}/2)]} \right| \tag{4}$$

where J_1 is the Bessel function of the first kind, first order, with

$$\overline{\upsilon} = \frac{\beta\lambda\upsilon}{N.A.} \tag{5}$$

and

$$u = 8\left(\frac{\pi}{\lambda}\right) z \sin^2\left(\alpha/2\right) \tag{6}$$

where β is the magnification between the specimen and the grid plane, λ is the wavelength of the illumination light used, υ is the actual spatial frequency of the grid pattern, $N.A.$ is the numerical aperture, z is the axial distance, and α is the acceptance angle of the objective.

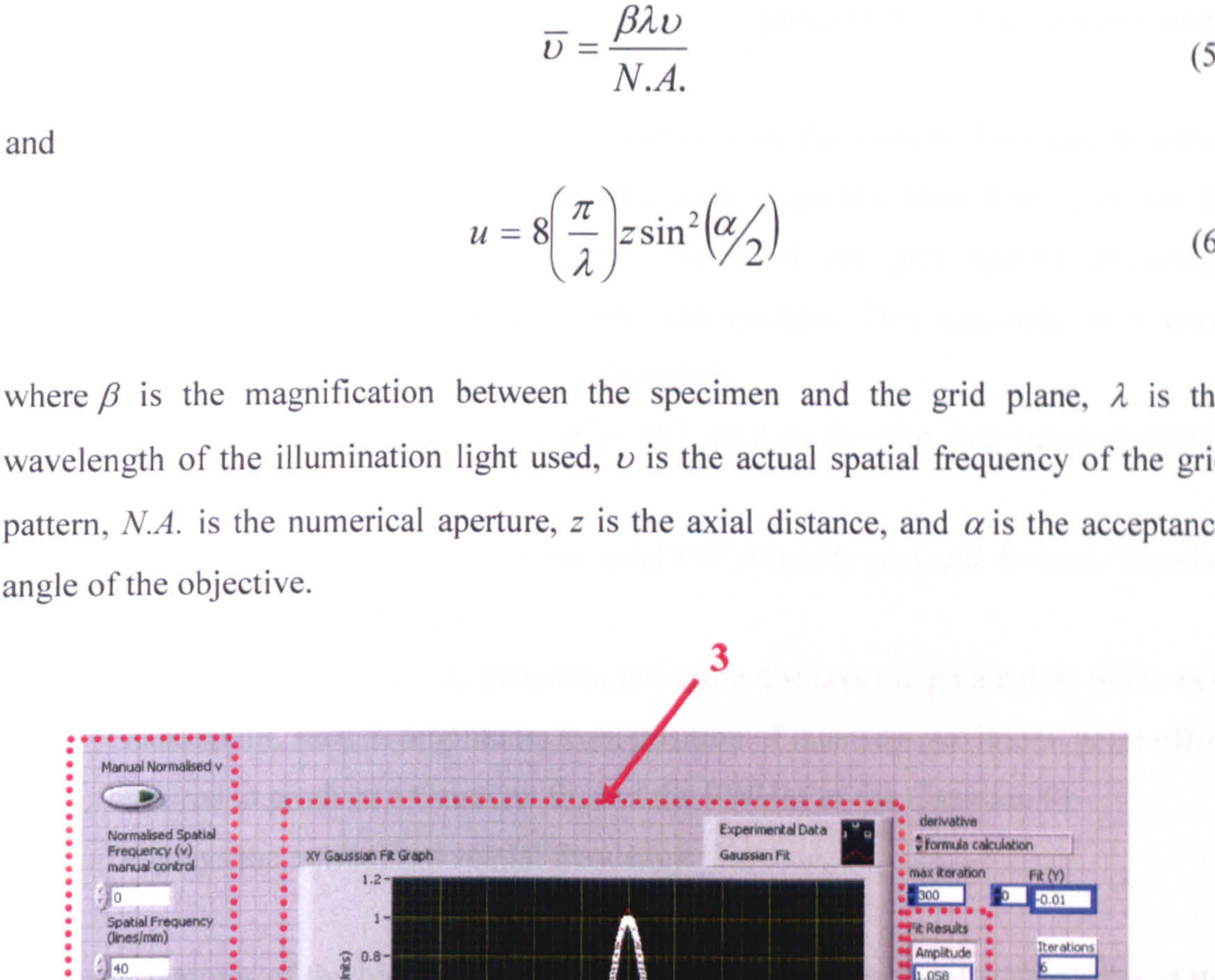

Figure 10: Front panel control written in LabVIEW that calculates the theoretical axial PSF and axial resolution (FWHM) of the structured light system.

Some of the main functions of the PSF program highlighted in the 5 boxes are explained in more detail:

1. Controls the normalised spatial frequency $\overline{\upsilon}$ of the system. This can be either entered manually with a normalised spatial frequency from 0 to 1, or can be calculated from entered parameter values of the grid spatial frequency, magnification, wavelength and numerical aperture. This automatic or manual function is controlled using the toggle switch.
2. Controls the parameters of the axial PSF such as the step size (resolution) and range.
3. This graph displays the theoretical axial PSF intensity plot and the best Gaussian fit to this theorectical data.
4. Using the Gaussian fitting program, this table displays the parameters of the best Gaussian fit, such as amplitude, axial position of intensity maximum, noise offset required to produce a Gaussian fit, and the FWHM of the Gaussian fit.
5. Displays the normalized spatial frequency.

The main features of the block diagram which contains the graphical source code of the LabVIEW program and shows the functionality of the VI are shown in figures 11-13.

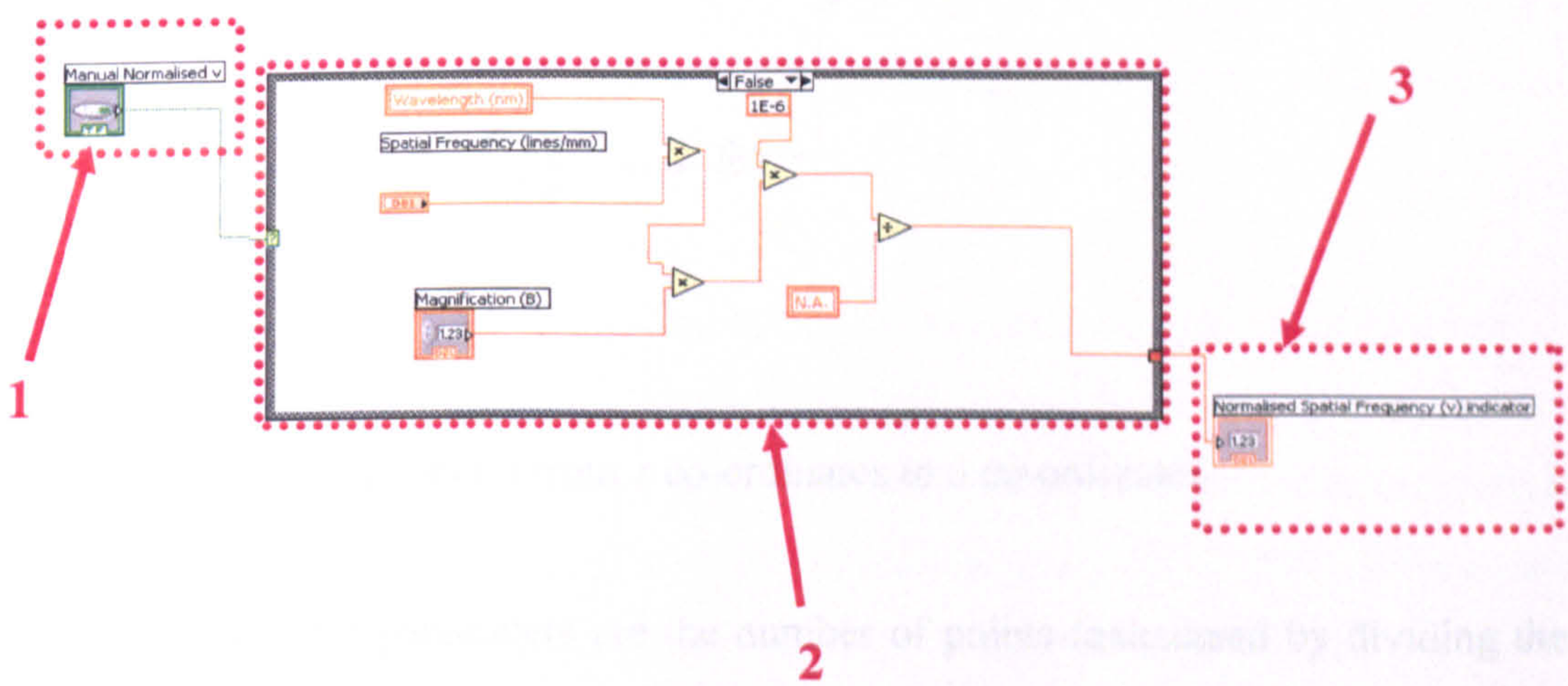

Figure 11: showing a portion of the block diagram of the Axial PSF theoretical calculation VI, responsible for the determination of the normalized spatial frequency.

The main points of interest for figure 11 are highlighted in the red dashed boxes:

1. This toggle controls the case structure which determines whether the normalized spatial frequency is manually entered or automatically calculated by the input parameters. The toggle is switched to off.
2. With the toggle set to the off position, the case structure calculates the normalized spatial frequency. From the input parameters (N.A., λ, u, and magnification), and using arithmetic functions, the normalised spatial frequency, $\overline{\upsilon}$ is calculated.
3. The normalized spatial frequency is presented and saved as a local variable.

Before calculating the axial point spread function, both the step size and the range parameters must be changed from parameters in z to wavelength independent values in u (see equation 3). Figure 12 below shows how this is achieved for the step size.

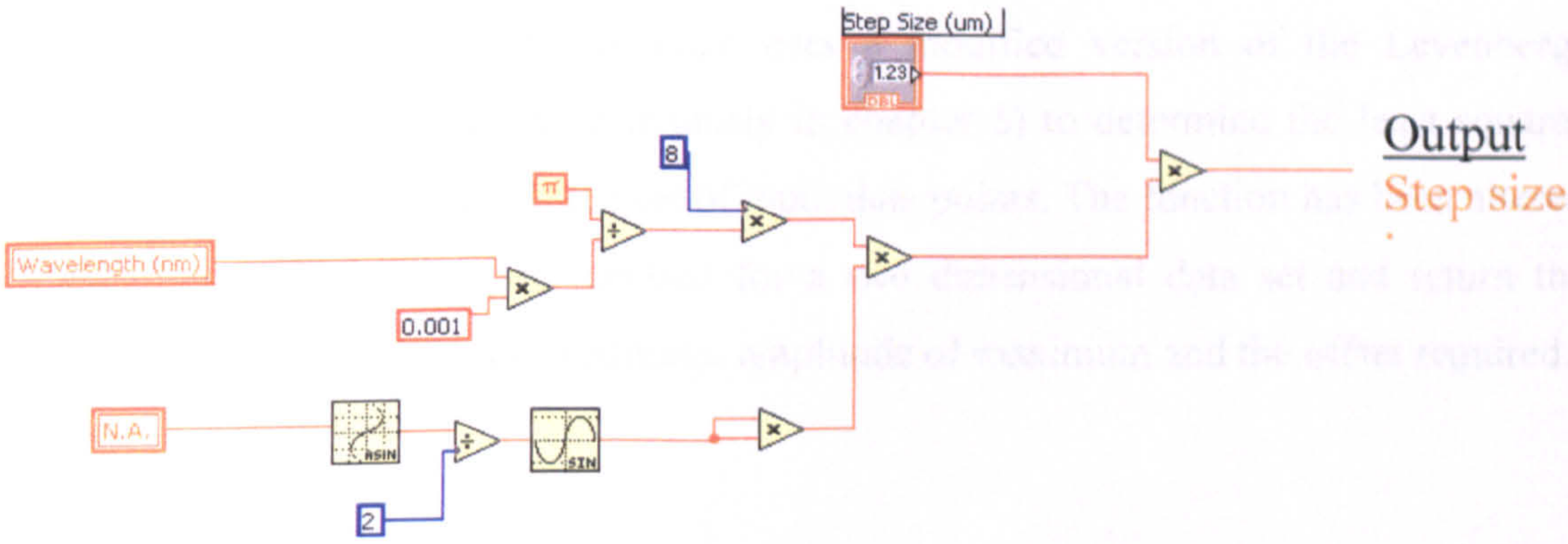

Figure 12: Showing conversion from z co-ordinates to u co-ordinates.

In figure 13, the input parameters are the number of points (calculated by dividing the range by the step size), the starting position (calculated by halving the range and negating it), the step size, as well as the normalized spatial frequency. The step size multiplied by the iteration number, *i*, (located in the blue box) provides the increment

increase for each subsequent iteration. Based on equation 3, this section of the LabVIEW program calculates the intensity value I_p for each u value. Located within the red dashed square box is the Bessel function to the first order J_1, which is required when calculating the I_p value.

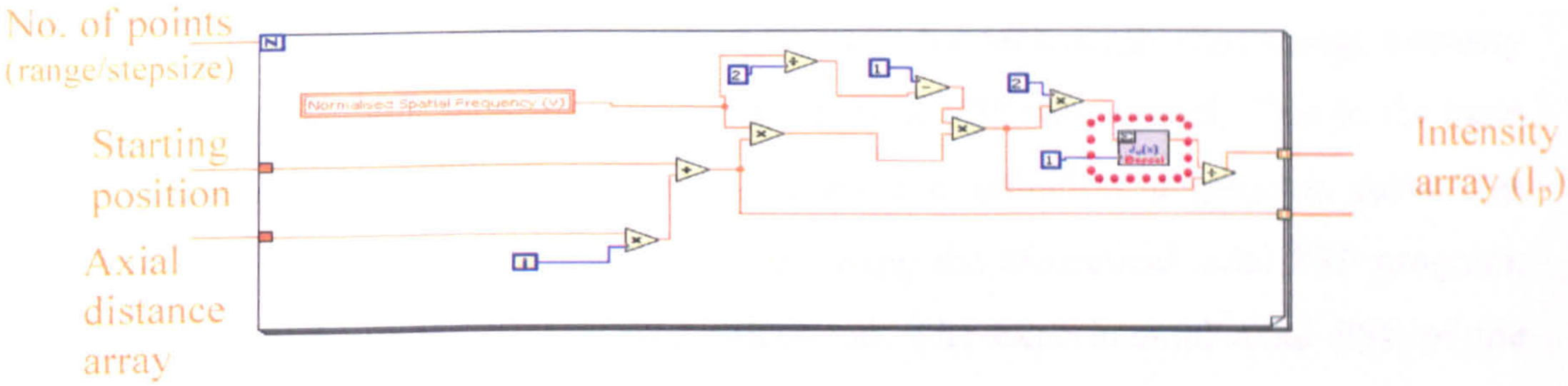

Figure 13: Generation of the axial PSF using a for loop and input parameters.

Using an inverse function to that shown in figure 12, the axial distance in u is converted into z co-ordinates (in μm units). Data is then sent to the Gaussian fitting program which from a set of x-y data (in this case an intensity PSF axial plot), a best fitting Gaussian plot is calculated. The graphical code uses a modified version of the Levenberg-Marquadt algorithm (described previously in chapter 6) to determine the least squares set of co-efficients that best fit the set of input data points. The function has been altered to specifically fit a Gaussian function for a two dimensional data set and return the FWHM, the axial position of maximum, amplitude of maximum and the offset required.

3. Results

3.1 Taking an axial PSF and measuring the axial resolution using the mirror test

Using a test described previously to characterize the axial PSF of the confocal system [2], a single coated aluminium mirror [Comar] was placed into the sample position. Before taking any scan, care was taken to ensure that the super imposed grid pattern and sample where both in focus at the same axial position and that this axial position matched roughly the mid-point of the Hera z-piezo stage (250μm). This was achieved using the manually controlled xyz translational stages to which both the piezo-

translational stages and sample holder are mounted. Care was also taken to ensure that the camera image was not saturated by controlling the internal shutter speed.

Using the structured light LabVIEW program a region of interest was selected and sectioned images where found at successive axial depths (the step size and range of which was pre-defined). From this region of interest for each depth, the average intensity was calculated for each sectioned image and an axial PSF was plotted. Due to the main peak of the axial PSF closely following a normal distribution, a gaussian curve was fitted to the PSF, and the FWHM measured. Using the theoretical axial PSF program, the effective N.A. of the system was calculated. The experimental axial PSF of the structured light system is shown in figure 14.

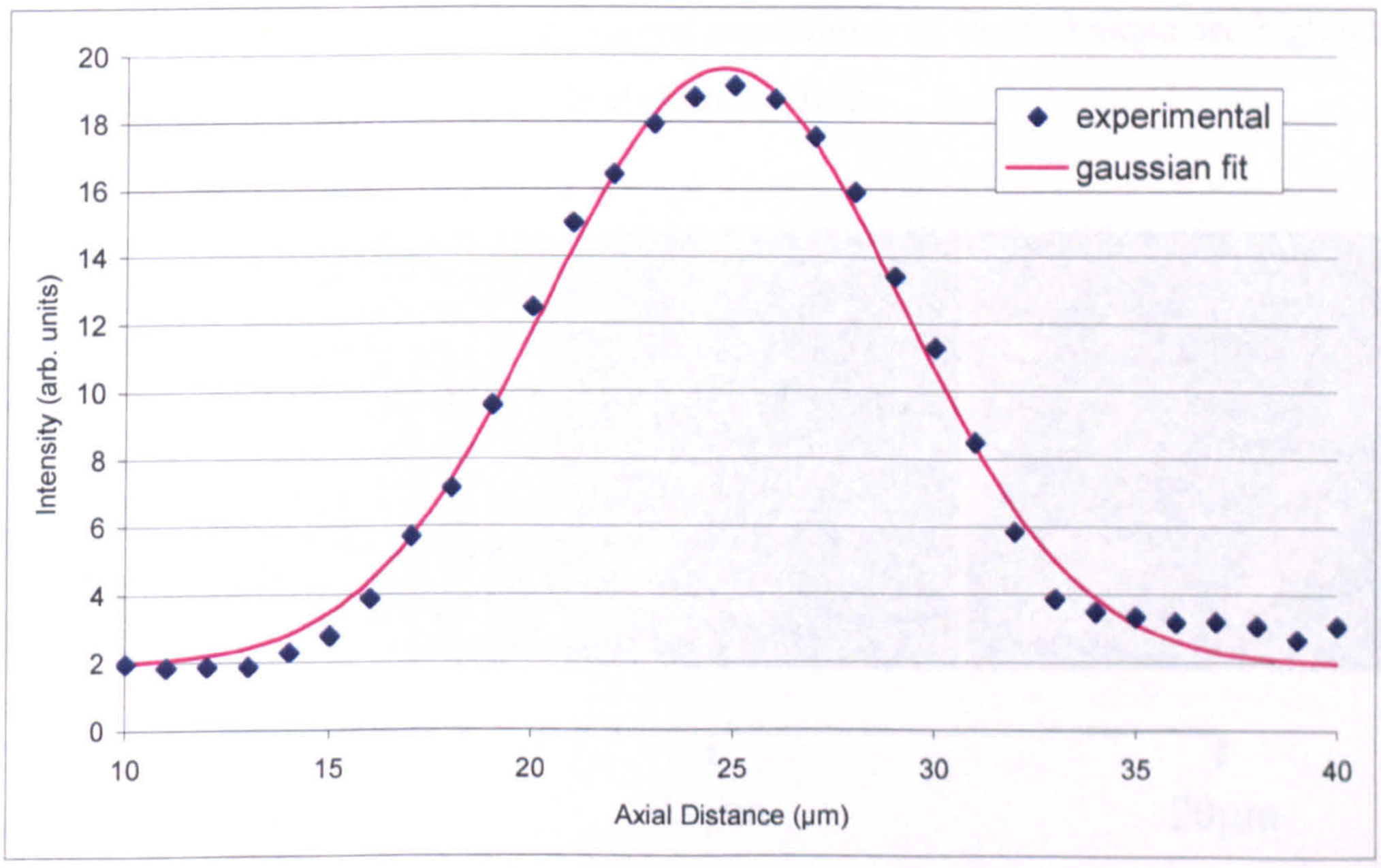

Figure 14: The axial PSF of the structured light system using the mirror test.

From the axial PSF, one can clearly see the optical sectioning capability of the system. The PSF closely follows a Gaussian curve although the slight asymmetry of the curve (seen as the presence of side lobes on only one side) is most likely due to aberrations in the system. From the Gaussian curve fitting routine, the structured light system is found

to have an axial resolution of 10.4 +/- 1.0μm. Knowing the values for grid spatial frequency (40 lines/mm), grid to sample magnification (x5) and illumination wavelength (880nm) and using the LabVIEW program that theoretically calculates the axial PSF, the effective N.A. of the system was deduced to be ~0.25 N.A.

3.2 Surface profiling capabilities of the structured light system

With the optical sectioning capabilities of the structured light system confirmed, a rough highly reflective surface was then used as an example to illustrate the surface profiling properties of the system. In this case, a ten pence piece was used due to both its high reflectivity and highly contoured surface structure features. Using the structured light system, sectioned images where taken at successive axial 4μm steps over a 100μm range. In figure 15, the optical sectioning capabilities of the technique are highlighted with an example of some of the optical sections taken.

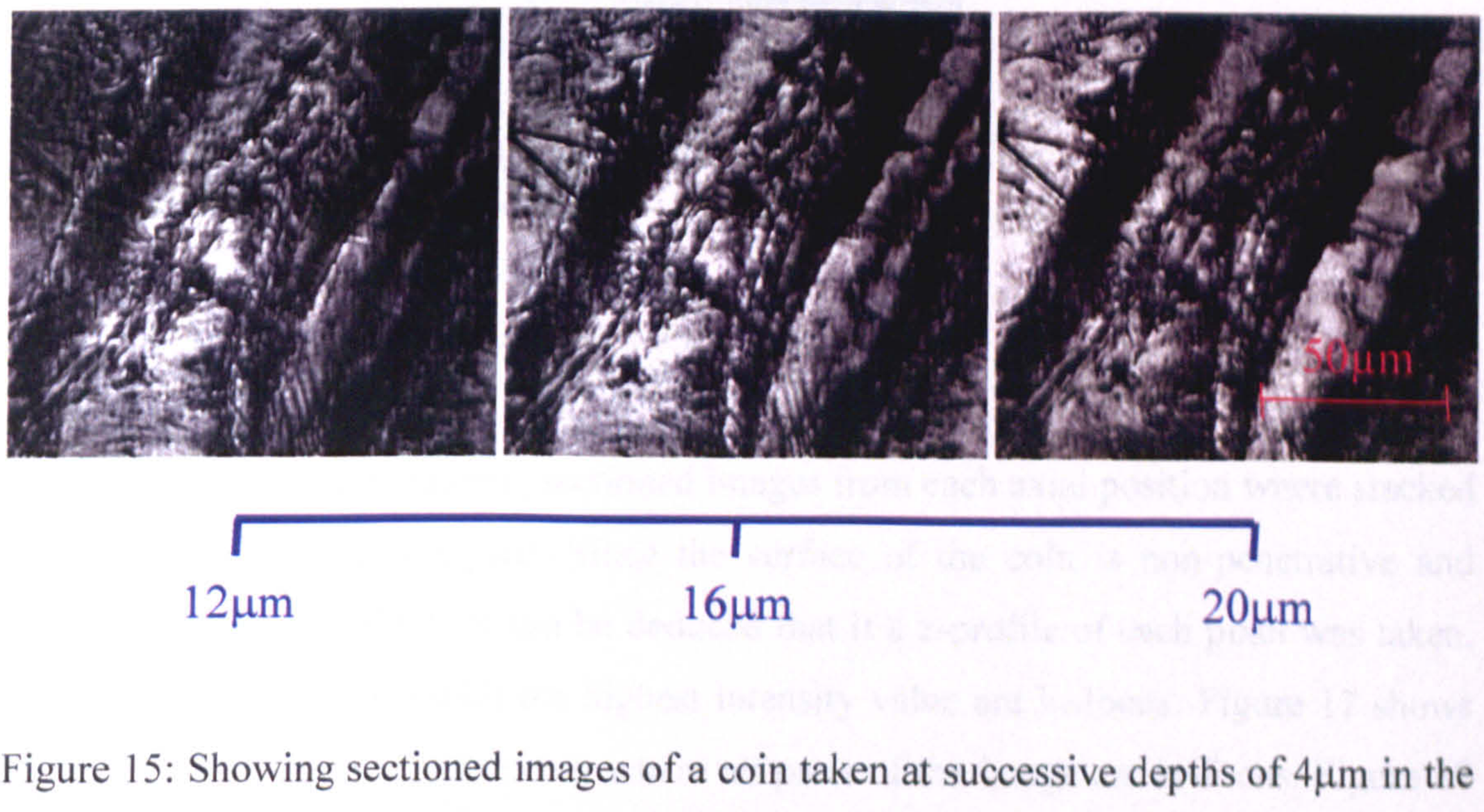

Figure 15: Showing sectioned images of a coin taken at successive depths of 4μm in the optical axis.

The sectioned images where then analysed using the Image J imaging program [3]. Image J is a public domain Java image processing program, freely available on the

internet, which provides the user with a powerful tool for image manipulation, processing, calculation and analysis. Image J allows one to compare and manipulate the corresponding pixels from each section within the stack and can produce three dimensional rendered images from image stack information.

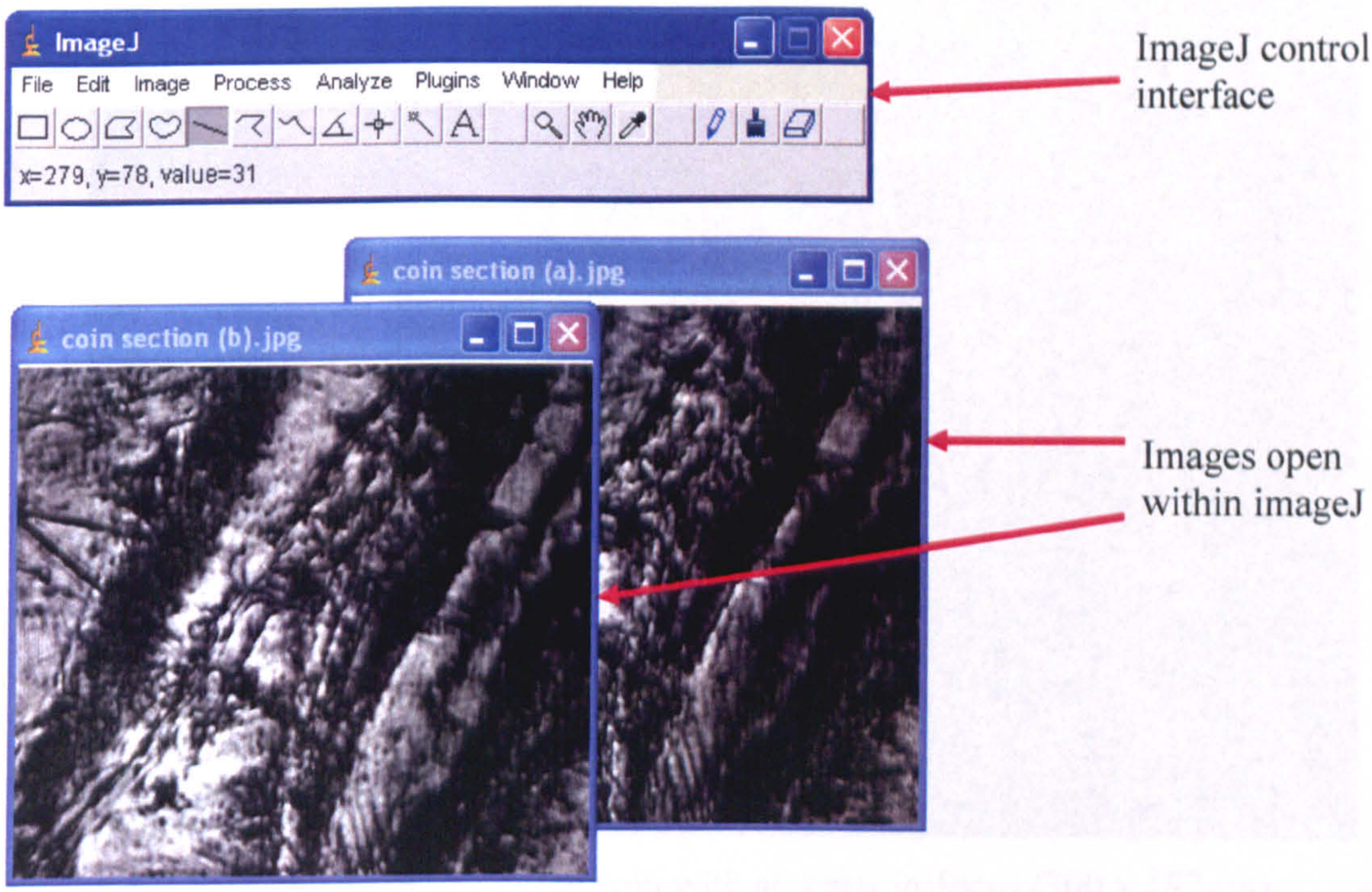

Figure 16: Image J user interface with some images.

Using some of ImageJ features, sectioned images from each axial position where stacked into a single file and analysed. Since the surface of the coin is non-penetrative and highly reflective at 880nm, it can be deduced that if a z-profile of each pixel was taken, the corresponding pixels with the highest intensity value are in-focus. Figure 17 shows an image of the surface of the coin where all parts of the image are in-focus. Figure 18 shows an image of the three dimension reconstruction of the coin surface looking at 65° to the normal axis. The scratched surface structure of the coin, which contains a number of defined gullies, is clearly visible.

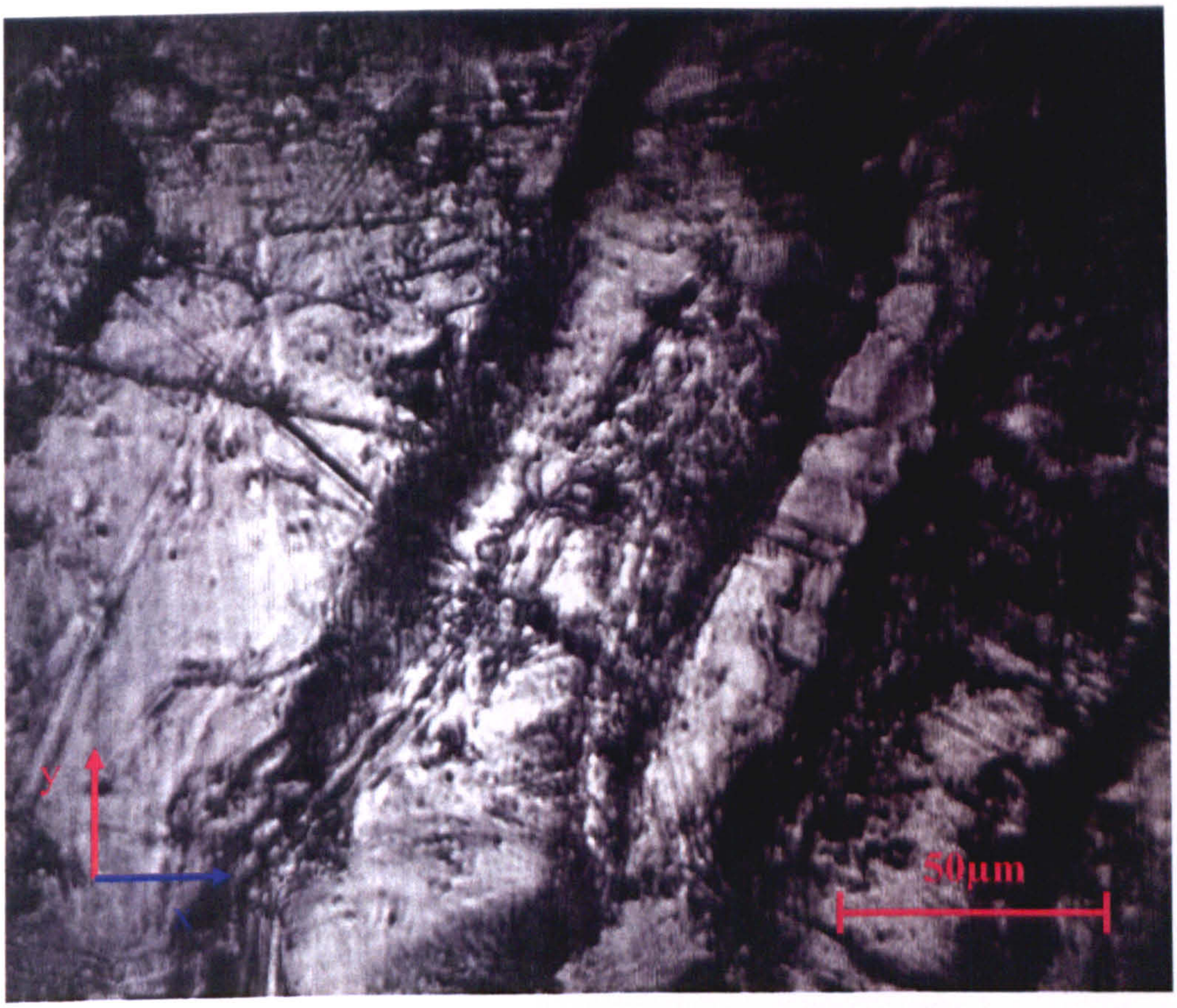

Figure 17: Showing an image of the coin with all parts in-focus (300 x 182µm).

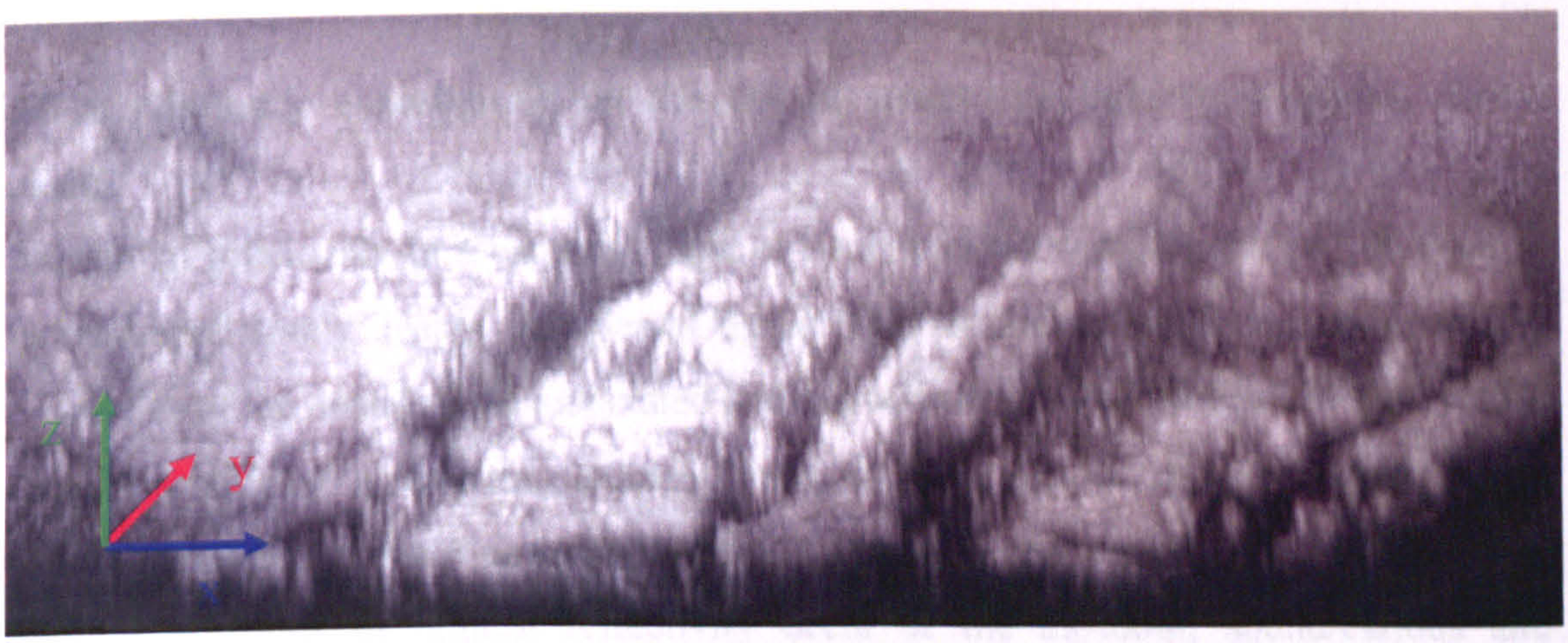

Figure 18: Showing a three dimensional contour plot of the surface of the coin looking at the coin 65° to the normal axis (image size: 300 x 182 x 40µm).

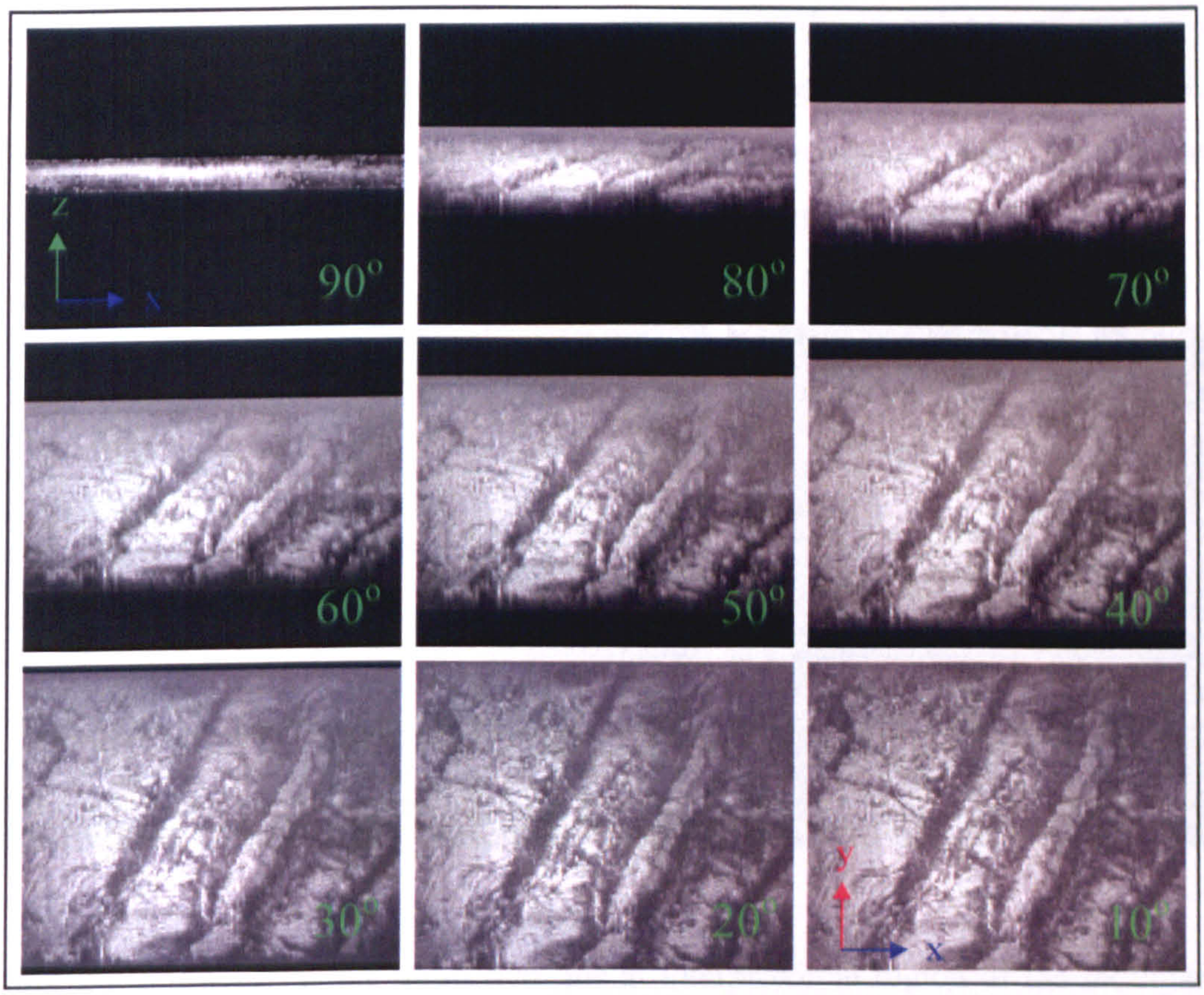

Figure 19: Montage showing a 3-D reconstruction of the surface of the coin sample (image size: 300 x 182 x 40μm).

3.3 Preliminary examination on the use of structured light to diagnosis dental caries

As shown previously in Chapter 4, light at near infrared wavelengths can be used to penetrate relatively deeply into dental tissue. This is due to the decreased scattering properties of the dental tissue associated at these wavelengths which leads to a decreased opacity and hence greater transparency. From previous results (chapter 3), it has been shown that when performing a z-scan from the surface of the tooth using the FOCOM system, positions of highest reflectivity occur at the air/tooth, sound/carious and carious/sound boundaries within the tooth structure. In the structured light system, one would expect to see the same result.

Using the same structured light illumination system, several natural carious areas on a diseased tooth where examined. In this preliminary study, in order to effectively study natural lesions, the tooth containing multiple carious regions, was dissected as shown in figure 20. It should be noted that the tooth was dissected using a wafer slitting saw and the inner surface was smoothed using a conventional lapping procedure.

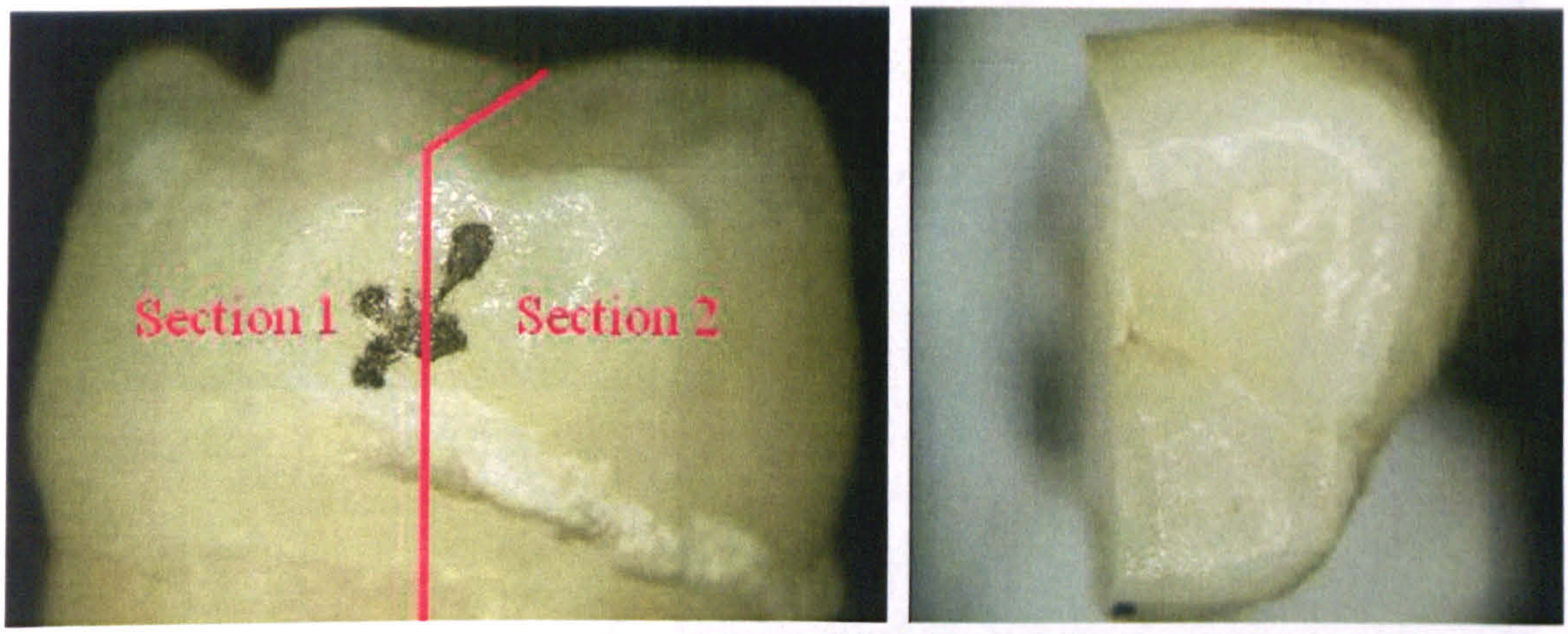

(a) (b)

Figure 20: Showing (a) the dissection line at interproximal region of the tooth and (b) the occlusal surface of tooth section 2 after dissection.

On visual examination of the sectioned tooth surface (see figure 20), the extent to which the carious regions found on the surface permeate through the tooth structure, can be clearly seen. Region 1 (which has been expanded in another window) shows caries at an advanced stage. The diseased portion has in fact extended right through the enamel into dentine structure.

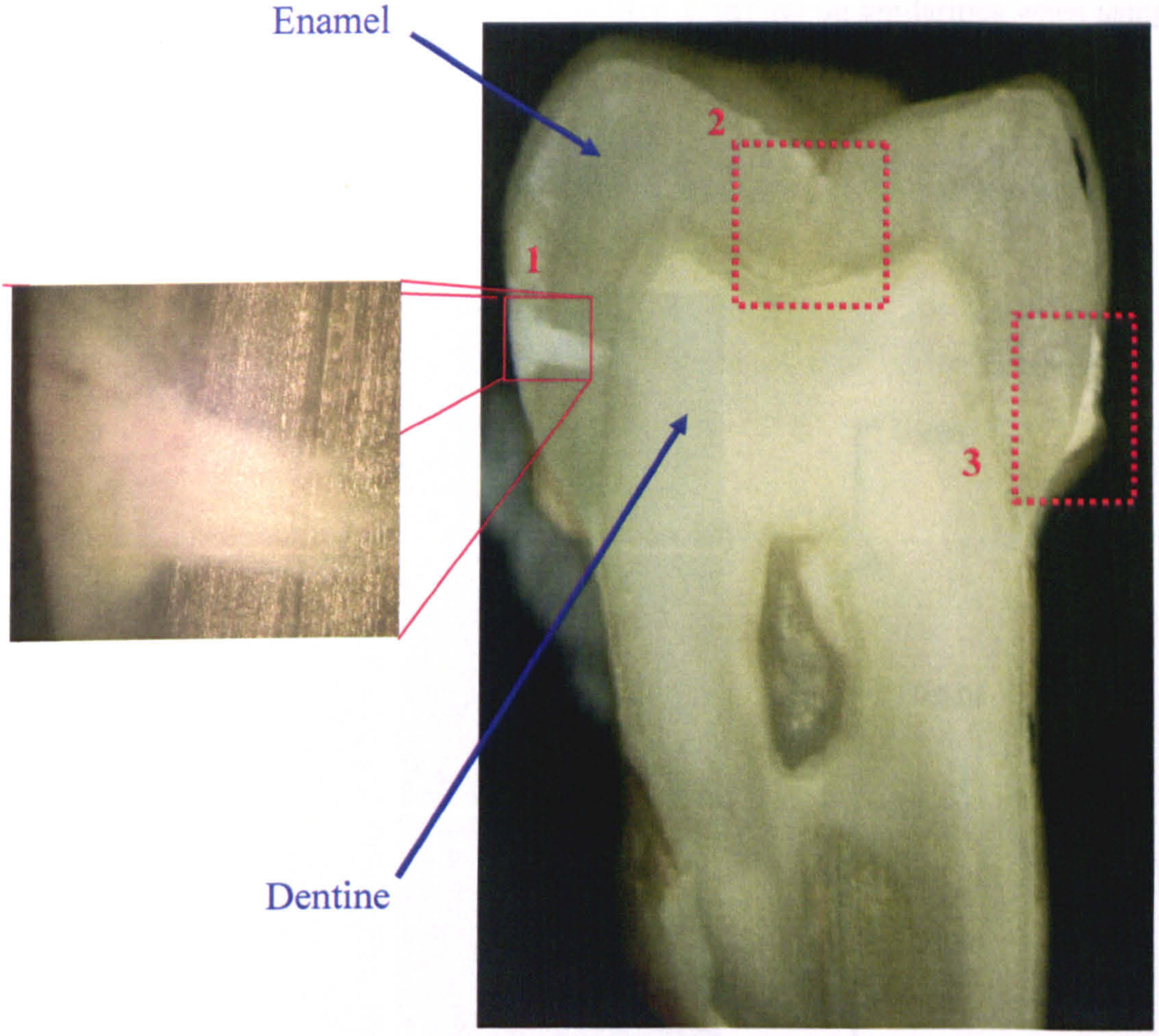

Figure 21: Showing the dissected tooth section 2 with three carious regions highlighted in the red boxes.

Due to problems of associated with getting an objective with a short working distance physically close to occlusal and proximal surfaces surfaces, the flat inner sectioned surface was examined. Using the structured light system, optical sections were taken at a range of axial depths, and three dimensional images constructed.

For each of areas which contain caries, highlighted in figure 21, a region was selected and optical sections taken. For each axial scan, optical sections were taken at 4μm steps over a 100μm axial range. In particular optical sections where chosen that contained

both carious and non-carious areas emphasize their structural dissimilarities when using this imaging technique.

3.3.1 Optical sectioned images of region 1

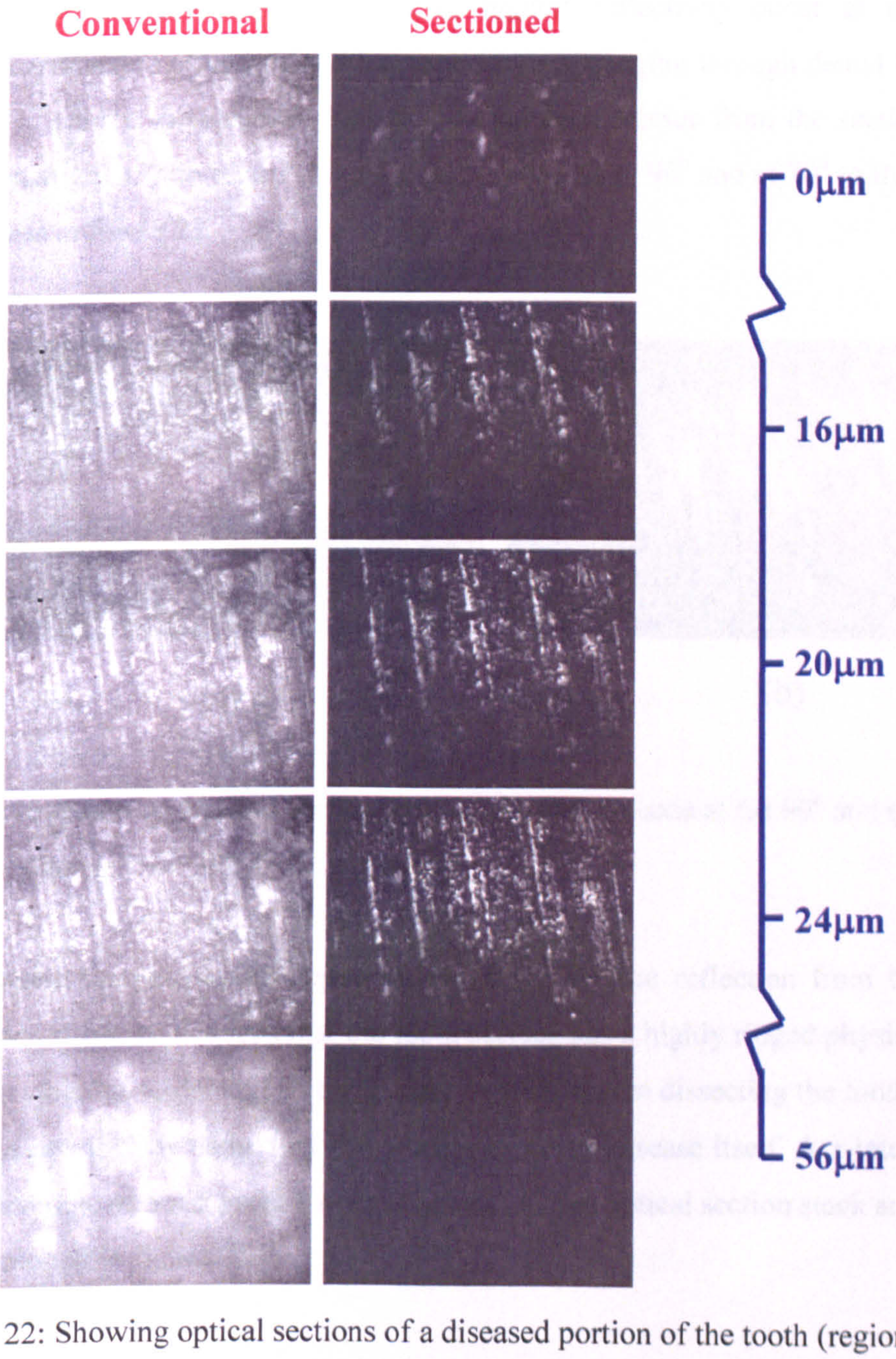

Figure 22: Showing optical sections of a diseased portion of the tooth (region 1). (Image size: 300 x 182µm).

In figure 22, an example of some of the conventional widefield and optically sectioned images taken at different axial positions, are shown. One can see in the conventional case, the images seem quite blurred due to the presence of out of focus light. In the sectioned images, only light that has originated from the focus is present in the image. As mentioned previously, positions of highest reflectivity occur at the air/tooth, sound/carious and carious/sound boundaries when imaging through dental tissue. Using image J, a three dimensional rendering of the dental tissue from the sectioned images was constructed. The render rotated about the x-axis at 90° and at 70° to the normal are displayed in figure 23.

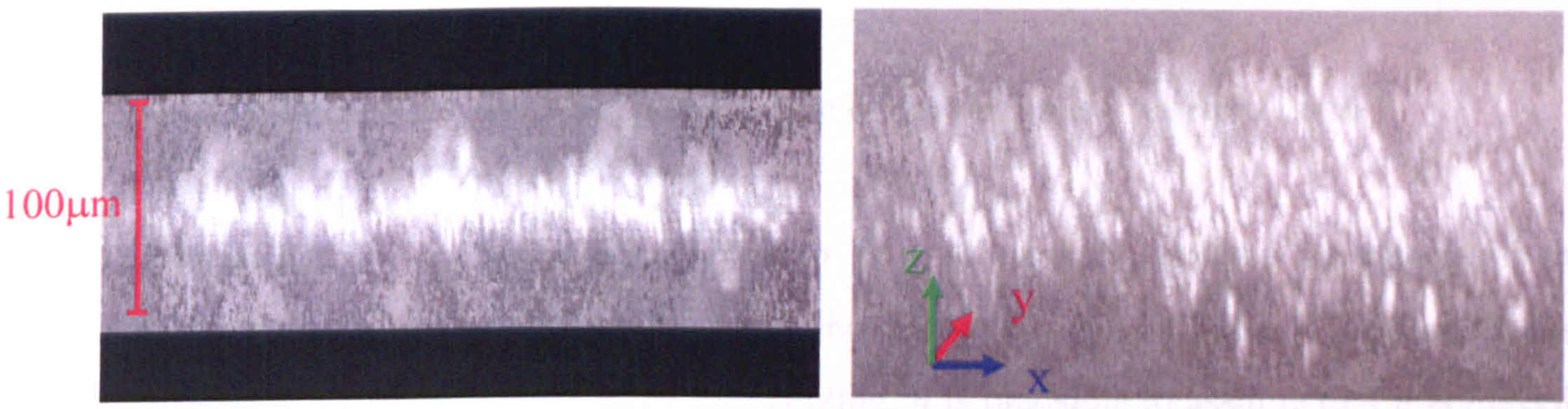

Figure 23: Showing carious surface rotated about the x-axis at (a) 90° and (b) 70° to the normal. (Image size: 300 x 182 x 100µm).

From these images, which appear to show the surface reflection from the air/caries boundary, it can be deduced that the tooth surface has a highly ridged physical structure. This may be due to damage to the surface incurred when dissecting the tooth, or it could be quite possibly by caused by the process of dental disease itself. A z-intensity profile (of an average of 5 x 5 pixels) was taken through the optical section stack and the results where plotted in figure 24.

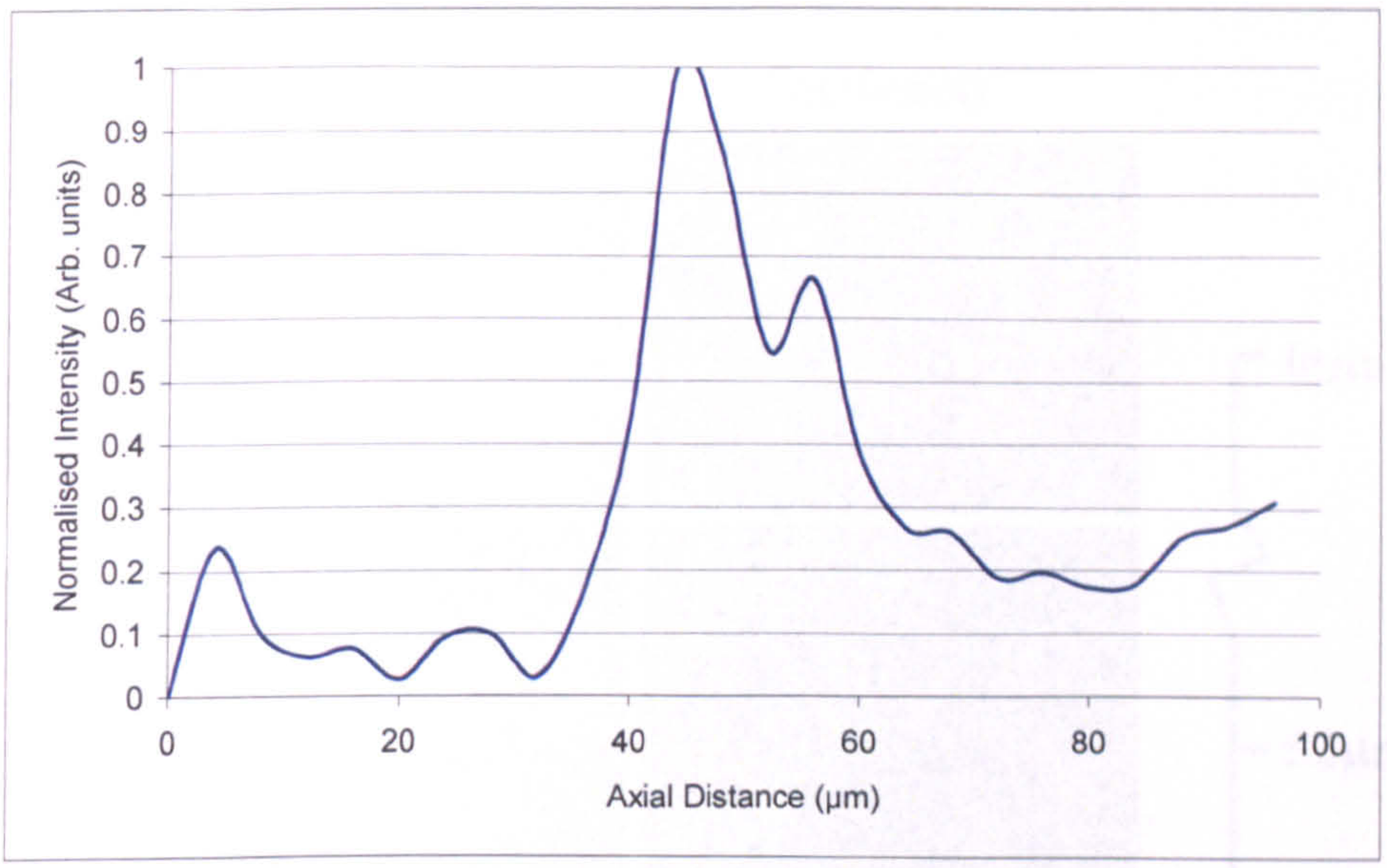

Figure 24: Showing a z-profile intensity plot of the optically sectioned stack.

The intensity plot shown in figure 24 with its multi-peaked structure are analogous to experimental FOCOM axial scans taken through a cavitated region [4]. Since caries examined in region 1 has extended into dentine, it is plausible to assume that it is indeed at an advanced stage of demineralisation. The highly regular structure associated with healthy enamel has broken down and leaving tissue structure with a high porosity containing large refractive index inhomogeneities. This provides a highly scattering medium through which one must image.

3.3.2 An optical section of region 2

In the optical section taken at the central pit of region 2, a small carious enamel region which was surrounded by supposedly healthy dental enamel region was examined. From the images taken of the grid pattern at three different phases, optical sections and conventional images were constructed at 4µm steps over a 100µm axial range. Figure 25 shows examples of some of those constructed conventional widefield and sectioned images.

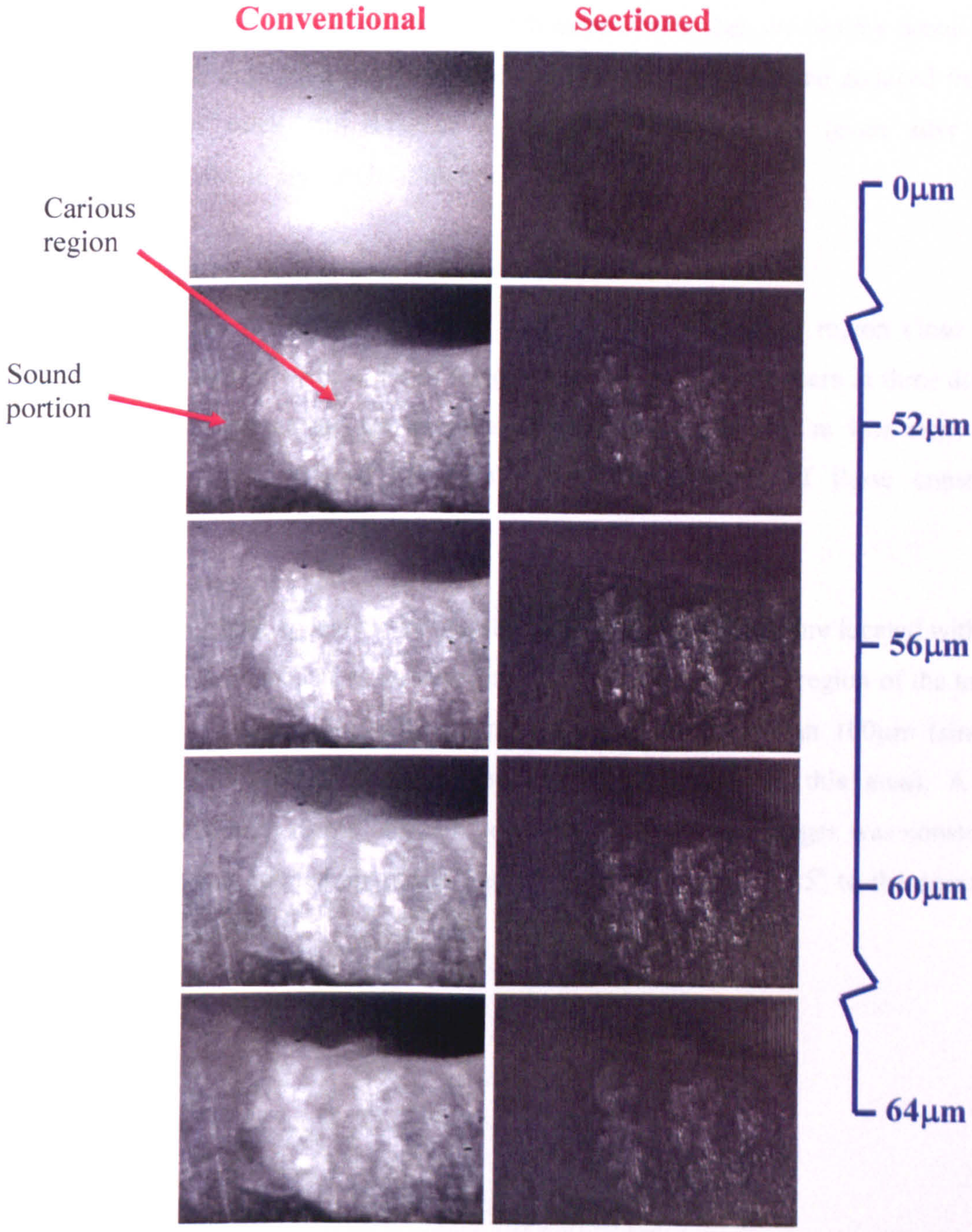

Figure 25: Showing optical sections of a diseased portion of central pit of the tooth (region 2) (Image size: 300 x 182 x 100μm).

Due to the greater back scattering properties associated with carious tissue, the diseased region in the central pit can be clearly much more visible than the healthy dental tissue. Although some indication of the three dimensional structure can be deduced from the optical section stack, the reflected light intensity is too low (even after image integration) to obtain enough information.

3.3.3 An optical section of region 3

For region 3, an optical section stack was taken of the carious region close to the interproximal enamel surface. From images taken with the grid pattern at three different phases, optical sections and conventional images were constructed at 4μm steps over a 100μm axial range. Figure 25 shows examples of some of those constructed conventional and sectioned images.

From figure 26, there appears to be a dark elliptically shaped structure located within the carious region. It is unclear as to whether this is actually a healthy region of the tooth or in fact, a pit (or contusion) with a depth (or height) greater than 100μm (since the 100μm axial scan failed to detect any surface reflection in this area). A three dimensional rendering of the dental tissue from the sectioned images was constructed. The rendering was rotated about the x-axis at 90°, 80°, 60° and 45° to the normal are displayed in figure 27.

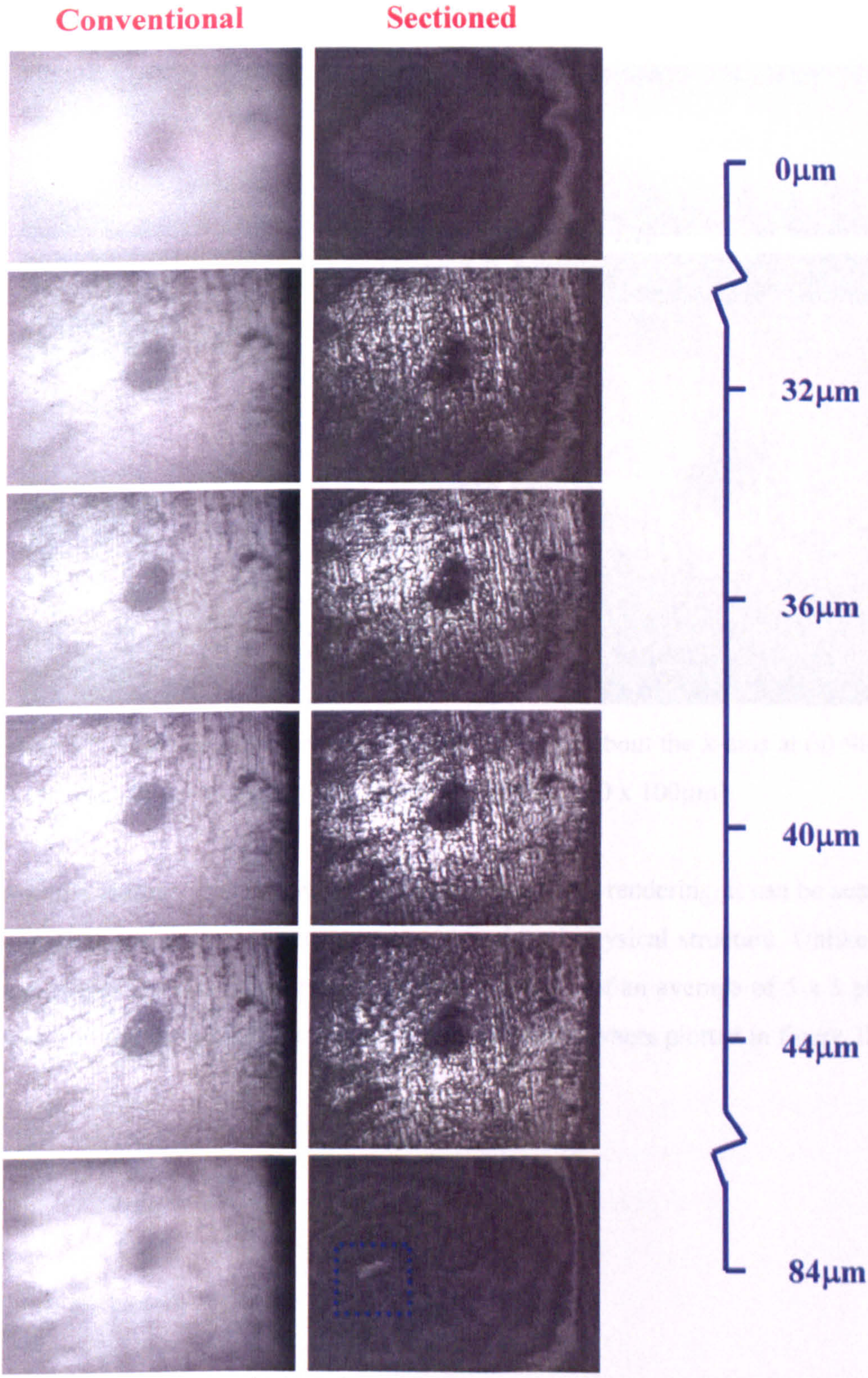

Figure 26: Showing optical sections of a diseased portion of the tooth (region 3). (Image size: 200 x 160μm).

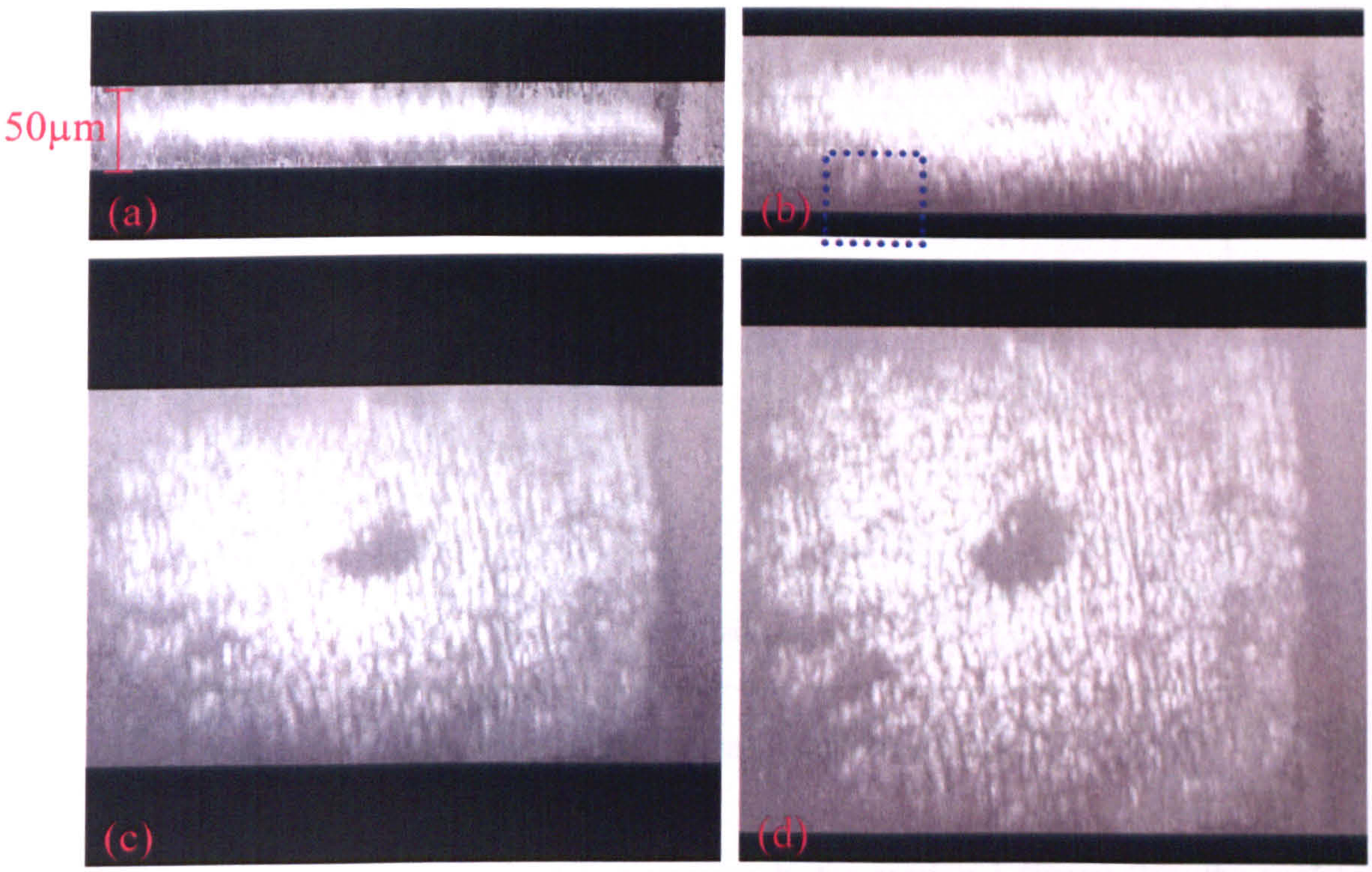

Figure 27: Showing three dimensional render rotated about the x-axis at (a) 90°, (b) 80°, (c) 60° and (d) 45° to the normal. Image size (200 x 160 x 100µm)

From the various orientations of the three dimensional rendering, it can be seen that like the region 1, region 3 contains a somewhat ridged physical structure. Unlike region 1, these ridges are less profound. A z-intensity profile (of an average of 5 x 5 pixels) was taken through the optical section stack and the results where plotted in figure 28.

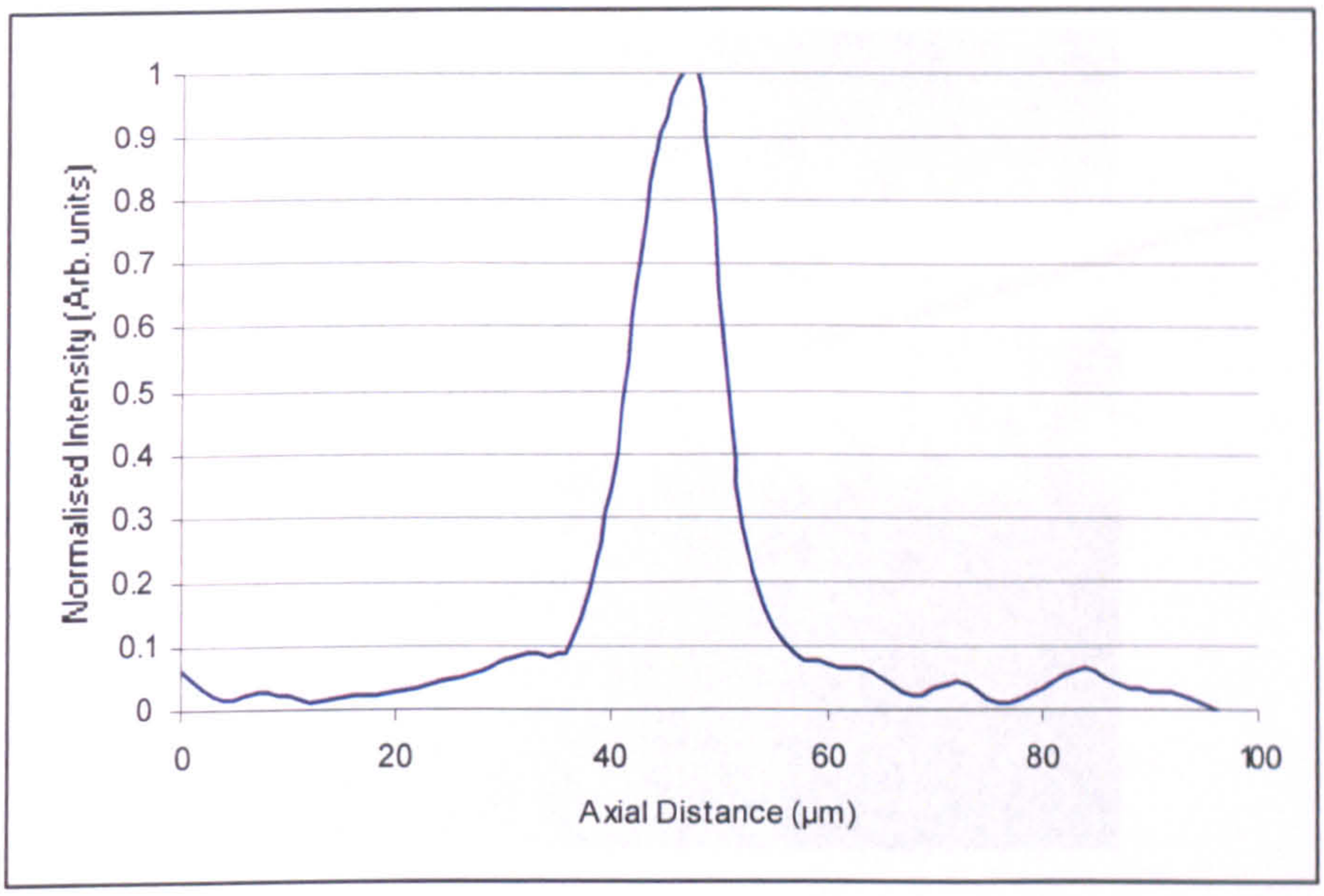

Figure 28: Z-profile intensity plot of the optically sectioned stack.

In comparison with the z-profile taken previously for section 1 (figure 26), the surface reflection from the region 3 (figure 28) appears to display greater uniformity. This could suggest that although carious, some of the regular crystalline structure is intact and contains fewer refractive index inhomogeneities. As a result, the surface is less scattering.

In figure 29, the region highlighted by a blue dashed box in figure 27 (b) is expanded. From this image another structure which is located (a relative) depth of 60µm deeper into the surface reflection can be clearly seen. This is caused by a discontinuity in the enamel structure and is either a boundary reflection from either a region of advanced caries or a region of lower mineral loss than the surrounding region. The actual depth of the carious region can not be determined as the refractive index of the carious enamel is not known exactly (see chapter 7 on the focal shift).

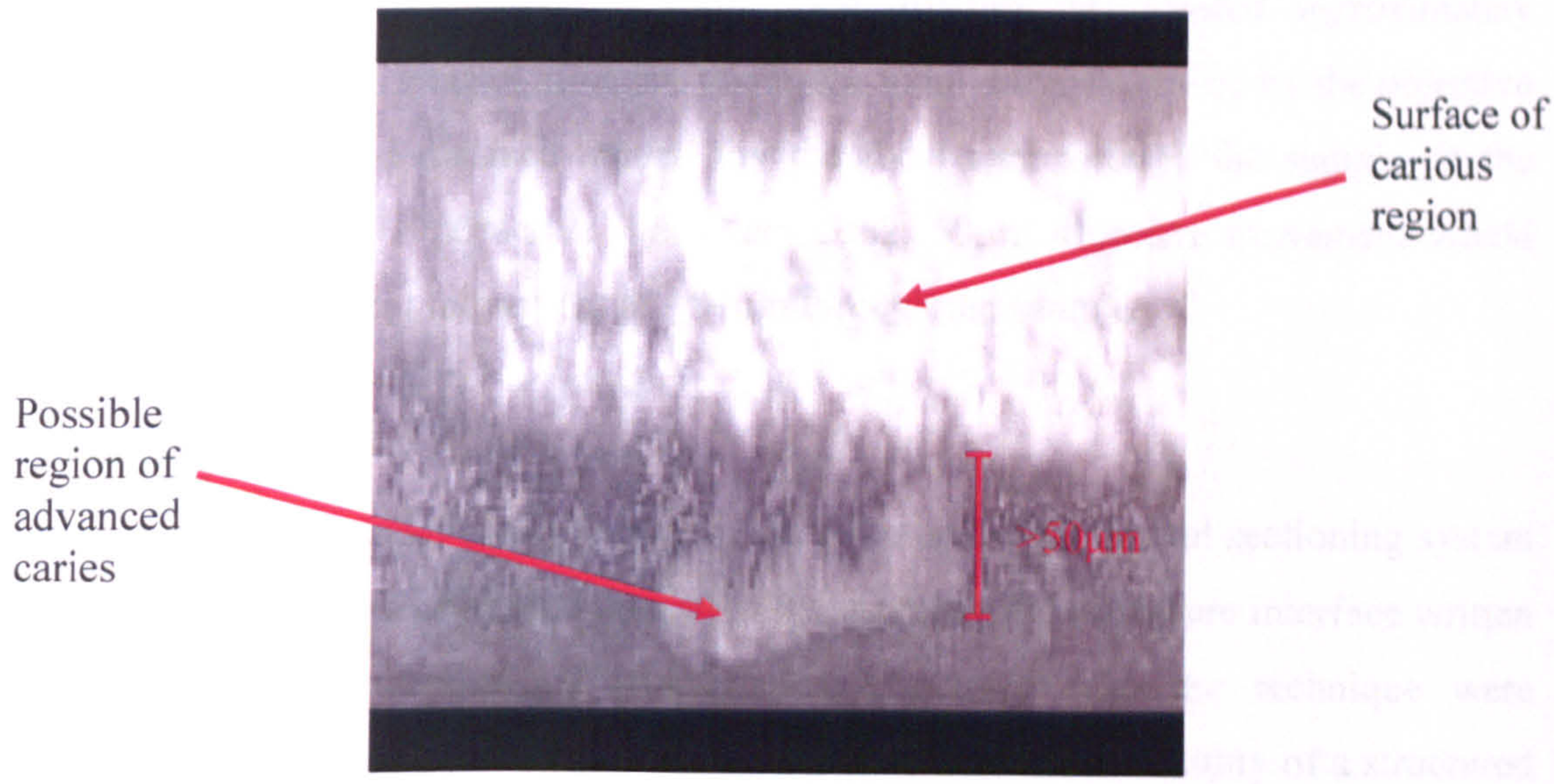

Figure 29: A three-dimensional surface profile of the diseased section of the tooth (Image size: 60 x 60 x 100µm)..

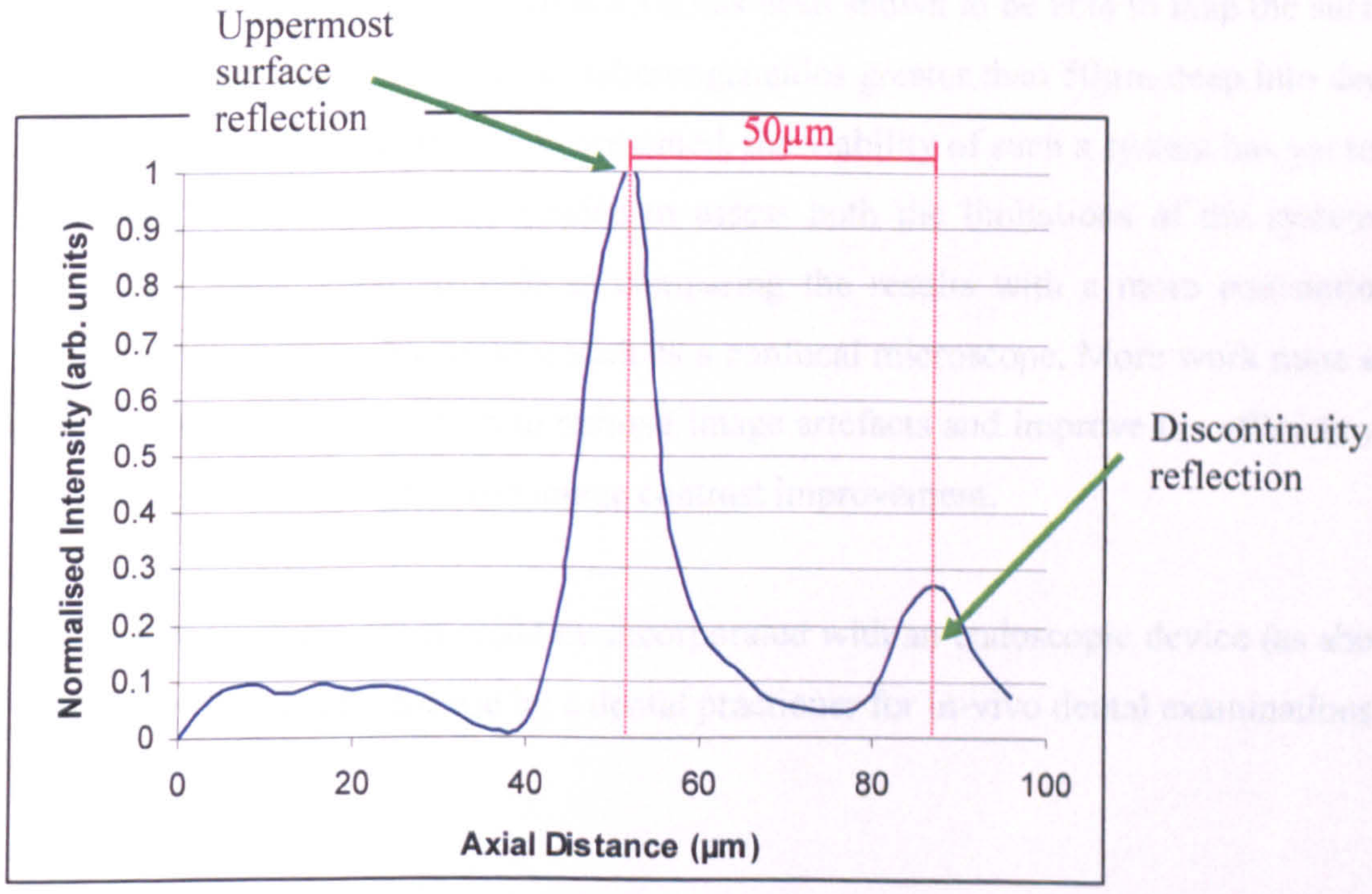

Figure 30: An axial intensity depth profile showing the reflections from the uppermost layer and discontinuity surfaces.

From the axial intensity scan, this sub-surface structure was located approximately 50μm beneath carious enamel structure taking the axial distance moved by the objective to equate to the axial distance moved my the focal spot through the sample. If the enamel structure has a refractive index, n = 1.62, 50μm objective movement would equate to a focused spot movement of ~81μm through the sample.

4. Summary

In this chapter the optical configuration of the structured light optical sectioning system as well as a description of system control with custom written software interface written in LabVIEW was presented. Characteristics associated with the technique were examined and the results from a preliminary study to access the viability of a structured light system as an aid to dentistry were displayed.

Structured light with infrared illumination has been shown to be able to map the surface structure of caries as well as detect inhomogeneities greater than 50μm deep into dental tissue. On the basis of these results presented, the viability of such a system has yet to be determined. More results are needed to assess both the limitations of the system in terms tissue penetration, as well as comparing the results with a more conventional three-dimensional imaging system such as a confocal microscope. More work must also be done with the optical set-up to remove image artefacts and improve the efficiency of the system in terms of speed and image contrast improvement.

In the future, such a system could be incorporated with an endoscopic device (as shown by Karadaglic *et al.* [5]) for use by a dental practioner for in-vivo dental examinations.

References

1. Neil, M.A.A., Juskaitis, R., Wilson, T. (1997) Method of obtaining optical sectioning by using structured light in a conventional microscope. *Optics letters*, 22(24), 1905-1907.
2. Zucker, R.M. (2004) Confocal Microscopy System Performance. Axial Resolution. *Microscopy Today*, 12 (1).
3. ImageJ: Image processing and analysis in Java http://rsb.info.nih.gov/ij/.
4. Rousseau, C., Poland, S., Girkin, J. M., Hall, A. F., Whitters, C. J. (2006) Development of fibre-optic confocal microscopy for detection and diagnosis of dental caries, Accepted by *Car. Res.*
5. Karadaglic, D., Juskaitis, R.,Wilson, T. (2002). Confocal endoscopy via structured illumination. *Scanning*, 24, 301 – 304.

Chapter 9: Conclusions and further developments

1. Introduction

The main aim of this research was to use existing technologies to develop new cost effective techniques that image deeply within biological tissues. The term deep imaging is a relative expression used to describe imaging techniques presented in this investigation. These are concerned respectively with (a) confocal and multiphoton microscopic imaging of tissue cellular structure, where a distance of ~2mm would be considered extremely deep and (b) macroscopic imaging systems concerned with imaging whole tissue structure, where the optical imaging depth is many tens of millimeters.

2. Research to date

2.1 AO Research

1. The development of an adaptive optic feedback system incorporating an optimisation algorithmic feedback loop, for use in confocal and multiphoton biological microscopy, to counteract image degradation and loss of signal intensity due to aberrations, has been demonstrated. The use of various optimisation algorithms with an adaptive element in a confocal system has been shown. The system has displayed significant improvement in the axial and the lateral resolutions, as well as signal intensity when counteracting for simulated aberrations. It has been found that while optimisation algorithms such as GA are more likely to find the global maximum in solution space when compared to MHC, they generally take longer to reach their optimum solution.

2. Using different fitness parameters (associated with the axial PSF) has shown promise in further increasing the effectiveness of algorithms in locating the best mirror shape for various samples. Although, in some biological applications where speed may be required, compromises must be made with resolution. In some cases, the effect of optimising for axial PSF parameters appears in some

cases to have detrimental effects on the lateral PSF and lateral resolution. For situation where the best axial and lateral resolution is required, optimising for signal intensity appears to demonstrate the best all round result.

3. By adapting the axial fitness parameter program, it has been shown that particular desired axial PSF shapes can be reproduced within an aberrated sample using the optimisation procedure. This does appear to have some limitations due to the relative power of the mirror (stroke) and need for some possible specific weighting functions dependant on the shape required. It is expected that this type of system could be useful in the confocal and multiphoton case where the shape of the PSF could be pre-defined and provide an extended depth of focus. One possible use would be to assist with a particular problem presently found when imaging biological fluorescent samples using the multiphoton technique, where by increasing the axial FWHM of the system would allow the operator to locate a possible region of interest.

2.2 Dentistry

1. Using optical techniques, physiological changes associated with the onset of disease in biological tissue can be detected. Taking dental tissue as an example of a highly scattering biological media, its structure and the onset and nature of dental disease (caries) were described. It has been shown that the development of dental diagnosis techniques have been limited due to the complexity of the tooth structure as well as a limited understanding of the nature of optical and scattering variation associated with caries onset.

2. A computer model based upon commercially available software was used to theoretically reproduce experimental results taken using a fibre optical confocal system on dental tissue. The method provides an easy to use technique of simulating tissue scattering and thus a simple route that helps to interpret the complex results frequently obtained in tissue imaging. From simulations, it has

been shown that such a system could be used to measure microscopically the optical properties of a caries lesion within dental enamel non-invasively. Since alterations in the optical and scattering properties of tissue are representative of disease in general, this model can be easily modified for the examination of optical and scattering properties in other biological tissue imaging applications.

3. A system based on the use of structured light to penetrate and quantify early stage dental caries was presented. In a preliminary study involving the examination of a number of naturally formed carious enamel regions on ex–in vivo teeth, the imaging properties of the structured light system were assessed as a possible aid to dentistry. Although the system was able to optically section the carious surface as well as detect inhomogeneities greater than 60μm deep into the tooth sample, more studies must be carried out to assess the limitations of the system in terms of how deep into dental tissue it can penetrate and effectively image.

4. On a macroscopic scale, a cost effective system known as near-infrared Lateral Illumination (L.I.) (which is based on transillumination techniques) was presented. This system makes use of the increased scattering properties associated with carious tooth tissue, when compared with healthy tissue, to effectively diagnose dental disease on the occlusal surface. In a preliminary study involving 15 ex-in vivo adult pre-molars and molars at various stages of dental decay, lateral illumination was found to have a sensitivity and specificity of 0.75 and 0.83 respectively. On comparison with sensitivity and specificity values for other dental caries diagnosis techniques currently available (such as visual examination, X-ray, DiagnoDENT and QLF), L.I. was shown to be the most effective occlusal caries diagnosis system.

3.1 Further Developments

Following this research project, work is expected to progress within the two main research fields of (a) adaptive optical research and (b) dental caries detection and diagnosis.

3.1 AO research

Research is currently underway into increasing the effectiveness of the optimisation algorithms in searching solution space. At present, global search algorithms such as GA, SA and RS take much longer to reach an optimal solution than a local search algorithm (MHC). In live biological imaging applications, where high exposures to light can lead to thermal and phototoxic damage, these problems must be addressed to fully assimilate AO into microscopy. There are currently a number of new of developments to the adaptive optical system as described in the following paragraphs.

3.1.1 The integration of the present AO system into a multiphoton microscope

In a preliminary test carried out at Gray's Cancer Institute, London (GCI), the adaptive optic feedback system incorporating an optimisation algorithmic feedback loop was successfully integrated into their in-house built multiphoton microscope system. Optimising for intensity using the genetic algorithm, the adaptive optical system was used to counteract system aberrations due to the presence of optics and possible inaccuracies in alignment. Figure 1 shows results of the adaptive optical system in action in the multiphoton system.

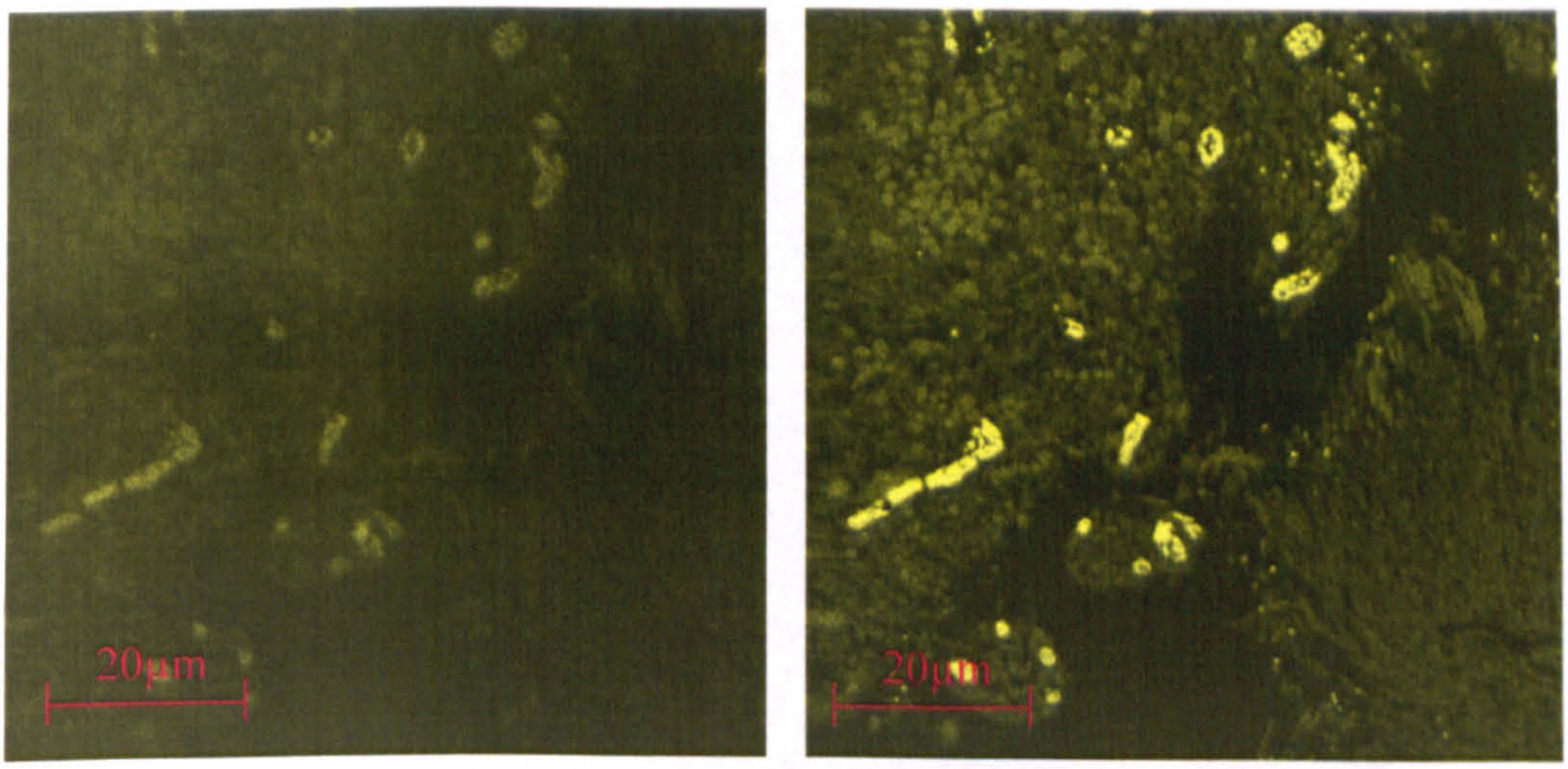

(a) (b)

Figure 1: Histology images of mouse fibrosarcoma (stained with haematoxilin and eosin) taken using the multiphoton system at GCI (a) before system optimisation, and (b) after system optimisation.

Work is currently underway at the Institute of Photonics (IOP) to integrate the adaptive optic system and control into a fully integrated confocal and multiphoton microscope system.

3.1.2 Computer modeling of DMM shape

Work is currently being carried out to develop and calibrate a computer model to calculate from the DMM actuator voltages the actual shape of the Okotech deformable mirror used to compensate for system and sample induced aberrations. The computer model itself incorporates Poisson's equation with boundary conditions to calculate from each actuator voltage, the appropriate electrostatic forces applied to the deformable membrane. Results have already been taken using a Zygo interferometer device (courtesy of Thales, Glasgow) to experimentally measure the AO mirror shape at various actuator voltages, in order to calibrate the theoretical model (see figure 2).

Figure 2: A picture of the Zygo interferometer with wavefront measurement software.

Once calibrated, from a set of optimised actuator voltages, the computer model should be able to accurately calculate the deformable membrane mirror shape and estimate the aberration correction in terms of Zernike polynomials. This computer model (the GUI of which is shown in figure 3) when completed could be used to examine the types of aberrations introduced when imaging within biological samples and could in future be used to predict possible mirror starting shapes for aberration correction to accelerate the optimisation procedure.

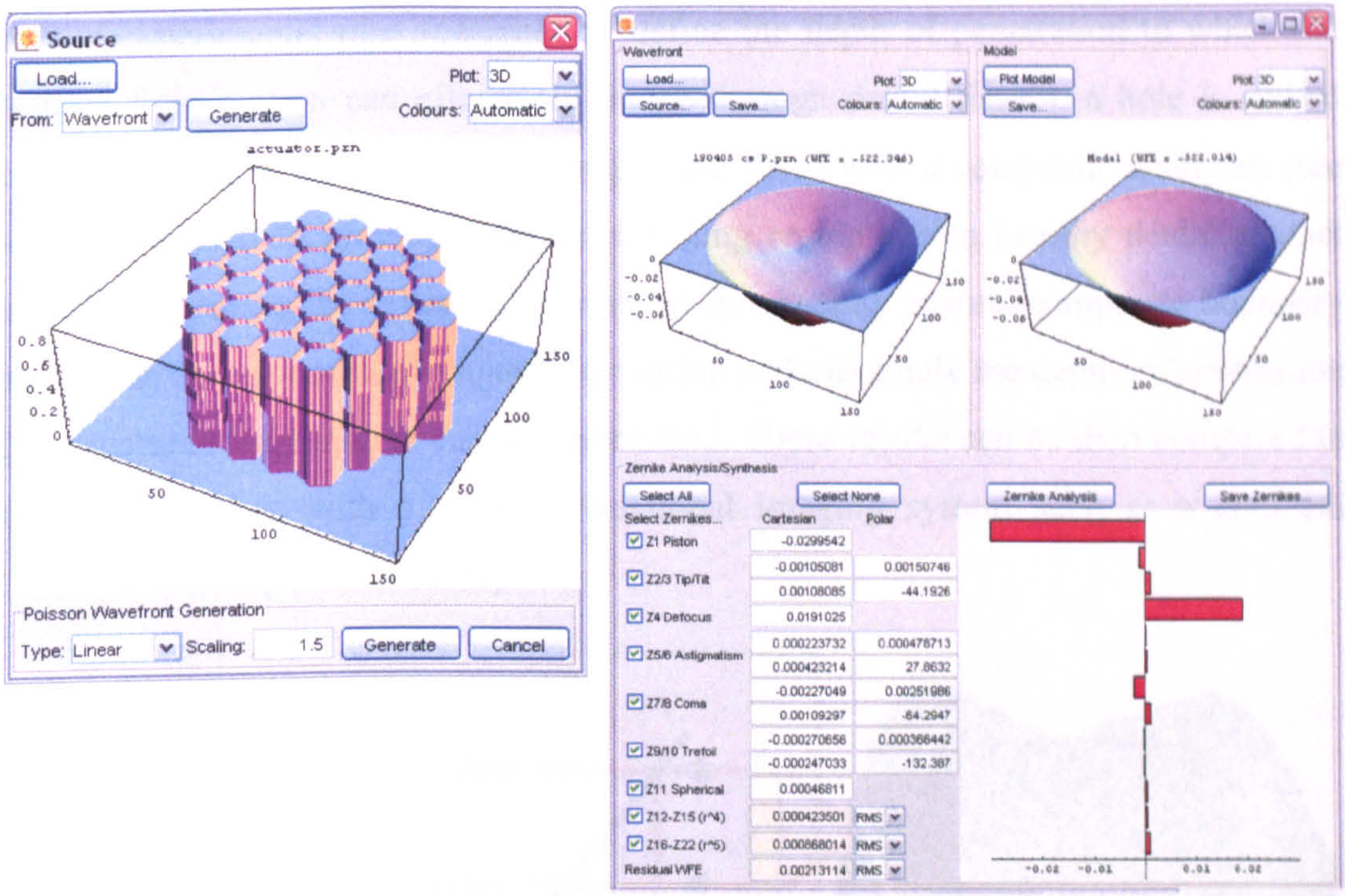

Figure 3: showing computer modeling interface used to determine mirror shape.

3.1.3 Dynamic closed loop focus tracking system

Using both the DMM and a spatial light modulator SLM it has been shown that a dynamic closed-loop method for focus tracking can be developed within a confocal microscope [1]. Although the system was used to provide best-focus, (due to the ease at which defocus could be controlled by the mirror), the system could be modified to simultaneously correct for several aberrations provided they can be reproduced by the DMM.

3.2 Dental caries detection and diagnosis

As well as improving the accuracy of the computer model of the FOCOM dental system to experimental data further research will progress in the following areas.

3.2.1 Structured light system

In a new experimental plan (designed to define the depth of penetration to which the structured light system can effectively image through dental tissue), a hole is drilled through a healthy tooth sample at an angle, and filled with a composite amalgam (see figure 4). This would provide a highly reflecting region within healthy dental enamel tissue. By measuring the reflected intensity at this healthy enamel/composite boundary at increasing tissue depths, the signal attenuation and ultimately the depth of penetration of the structured light system can be determined. These results can be then compared to measurements taken with a more conventional imaging system such as a confocal microscope to verify their accuracy.

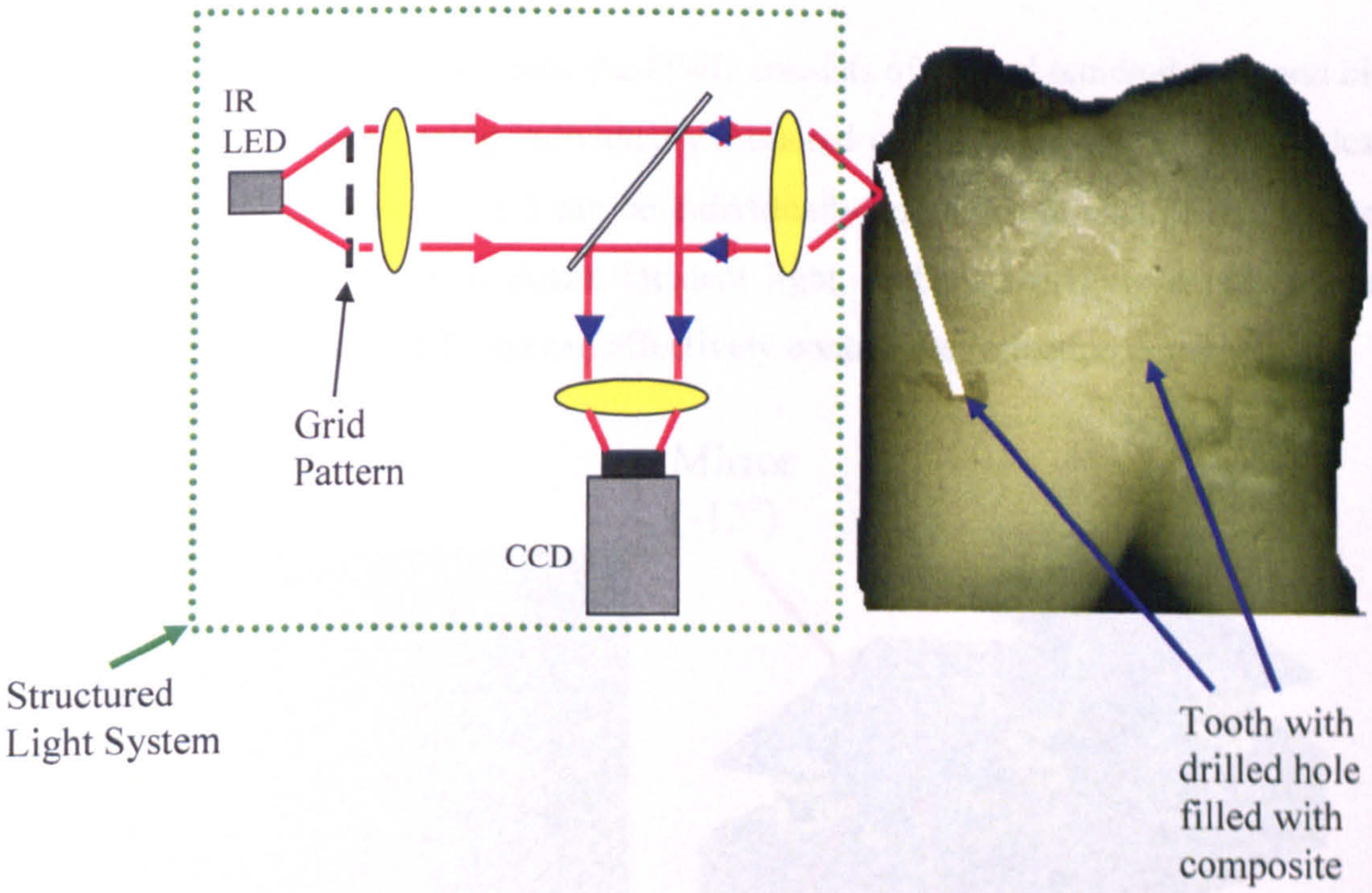

Figure 4: The use of the structured light system to detect the surface reflection from a composite filling, which is at an angle to the surface.

Ultimately, a fibre optical endoscope [2] could be incorporated into the structured light system, and through the use of a high illumination white light source with appropriate

filters, information on tooth surface integrity and degree of dental decay and be quantified quickly. Visible light can be used to monitor surface profile and degree of surface etching, while near infrared light can be used to optically penetrate and detect the degree of tooth decay.

3.2.2 Development of a ballistic photon detection device to monitor caries

Based on previous research by Wist *et al.* [3], a new system is currently being developed at the IOP that incorporates a Digital Mirror Device (DMD) and CCD camera to detect ballistic photons through a highly scattering heterogenous biological media (dental tissue).

First developed by Texas instruments, the DMD consists of several hundred thousand bi-stable micro-mirrors, each being individually mounted onto CMOS control electronics. Each micro-mirror (of area $16\mu m^2$) can be individually addressed to change its position by 12^o which allows one to modulate incident light, and by switching a pre-defined selection of elements on or off, one can effectively control the reflection pattern.

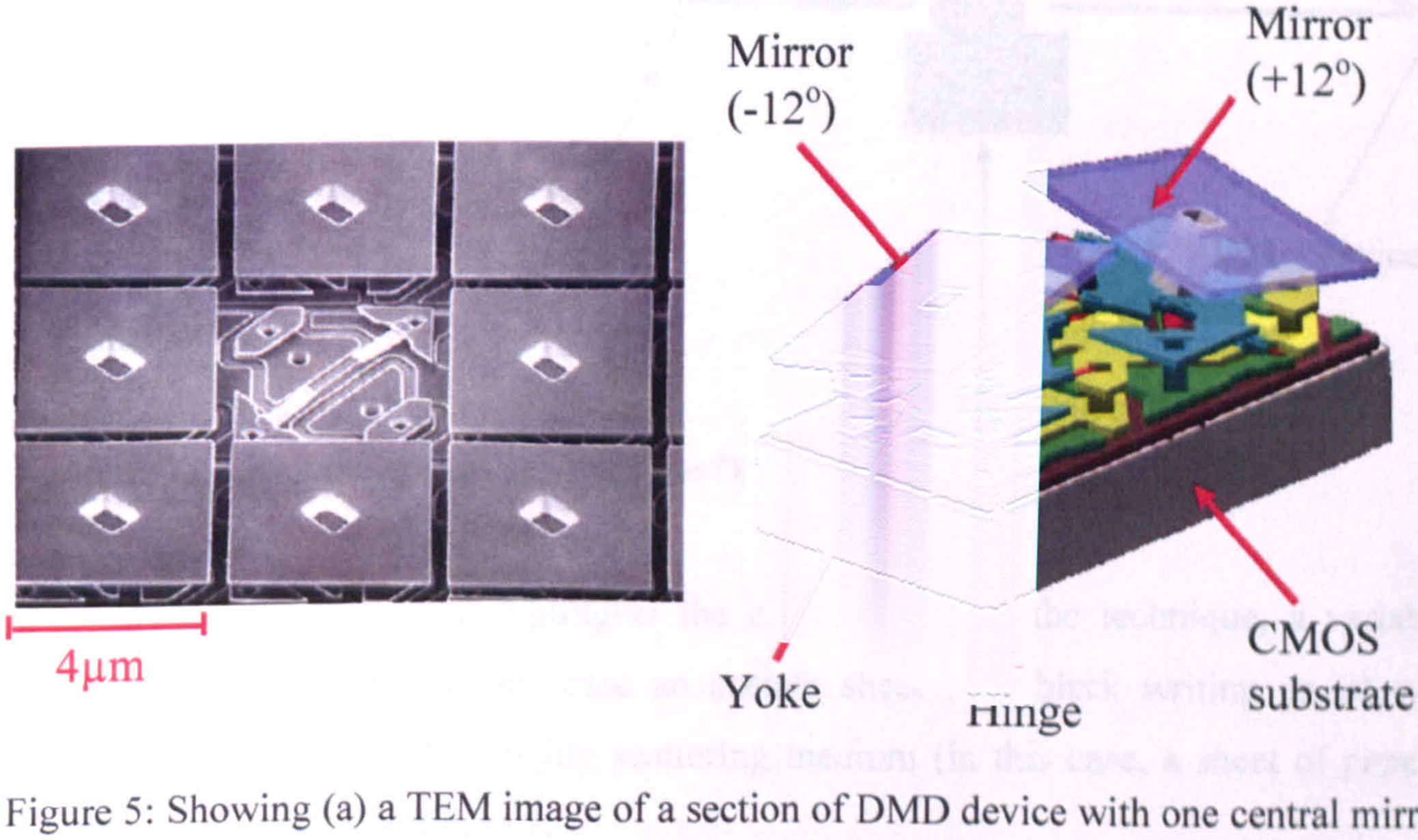

Figure 5: Showing (a) a TEM image of a section of DMD device with one central mirror removed, exposing the underlying hidden-hinge sub-structure responsible for movement and (b) a graphical representation of two adjacent micro-mirrors in operation.

In the present incarnation of the ballistic photon detection device, shown in figure 6, the system works on the premise that by individually addressing and collecting light from each DMD micro-mirror to its corresponding pixel on the CCD camera, only ballistic photons will be detected.

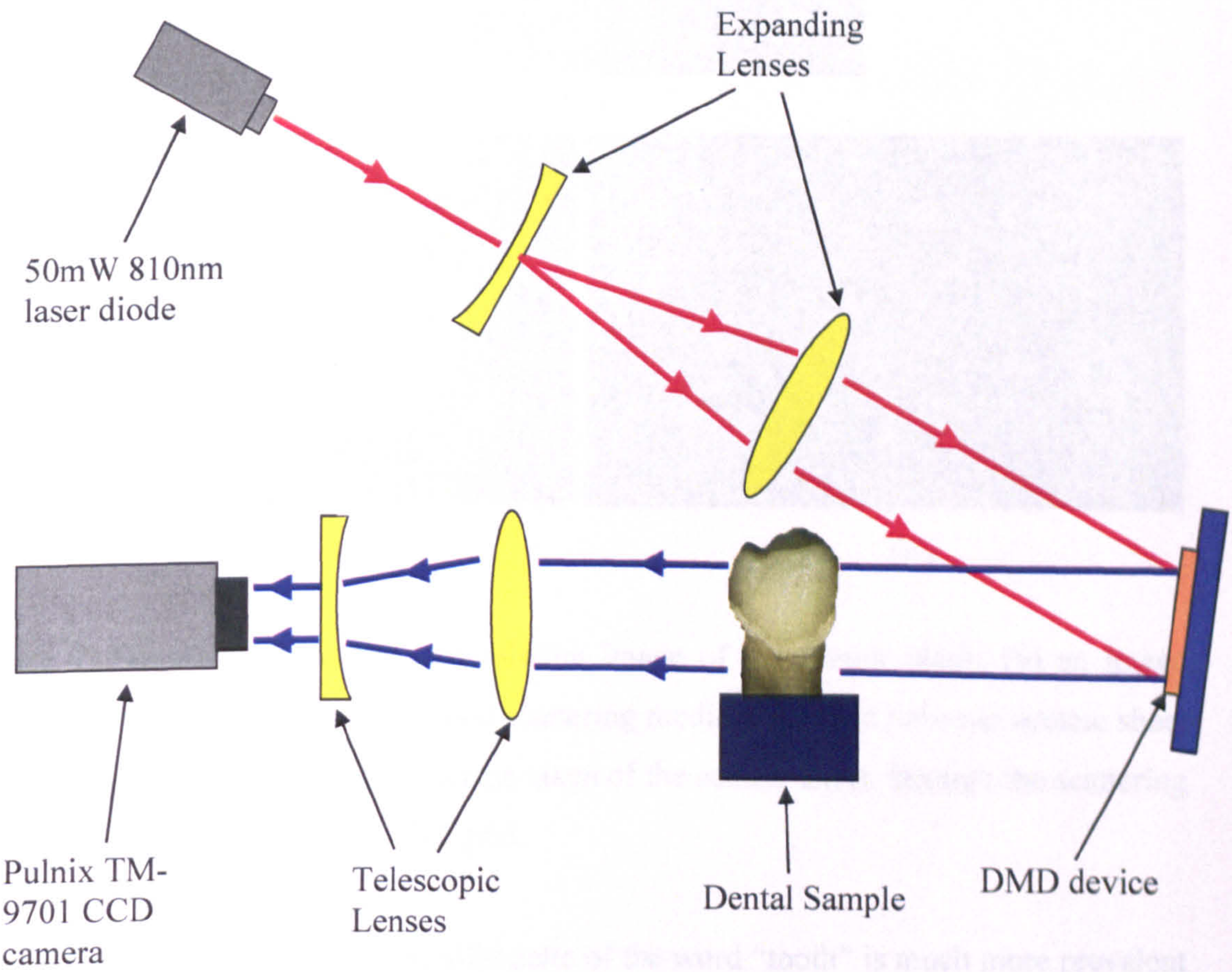

Figure 6: Showing the optical set up of the DMD CCD dental analysis device.

In a preliminary study that highlights the effectiveness of the technique, a variable contrasting test sample (in this case an acetate sheet with black writing on it) was imaged through a through a highly scattering medium (in this case, a sheet of paper). The results are shown in figure 7.

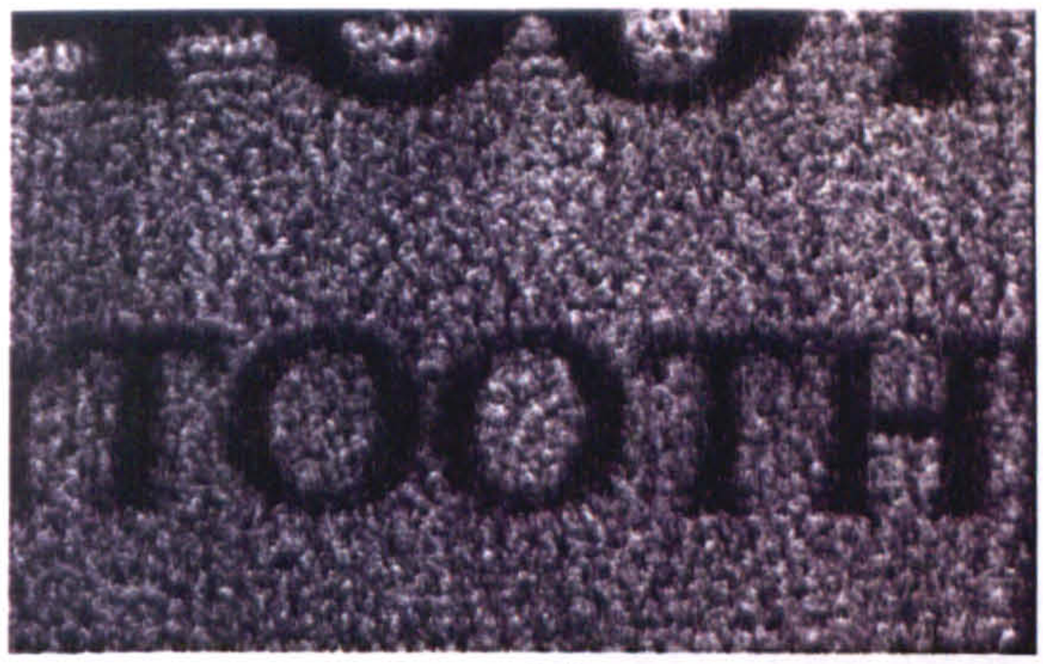

(a)

(b)

(c)

Figure 7: Showing (a) normal transmission image of the acetate sheet, (b) an image taken with the DMD switched off and scattering medium inserted between acetate sheet and the frame grabber, and (c) an image taken of the acetate sheet, through the scattering medium with the DMD set to a 7x5 grid.

As one can see in image 7 (c), the silhouette of the word "tooth" is much more prevalent than the image taken when the DMD system is switched off. The aperture size and hence the degree of ballisticity of the collected photons can be controlled to reproduce the contrast of figure 7 (a) – the only obstacle is the time it would take to produce an image. Current research is underway into developing a dedicated DMD control system (incorporating a CCD camera with a high frame rate) to generate high contrast images to detect variations in scattering properties in dental tissues at high speed. In the future such a system could image through whole teeth and provide an alternative to highly ionizing X-ray scans.

References

1. Wright, A. J., Patterson, B. A., Poland, S. P., Girkin, J. M., Gibson, G. M., Padgett, M. J. (2006) Dynamic closed-loop system for focus tracking using a spatial light modulator and a deformable membrane mirror. *Optics Express* 1 (14), 222-228.
2. Karadaglic, D., Juskaitis, R.,Wilson, T. (2002). Confocal endoscopy via structured illumination. *Scanning*, 24, 301 – 304.
3. Wist, A. O., Faturos, P. P., Herr, S. L. (1993). IEEE Medical Imaging, 12(4), 751-757.

Journal publications and presentations

Publications

Rousseau, C., Poland, S., Girkin, J. M., Hall, A. F., Whitters, J. (2006). Development of fibre-optic confocal microscopy for detection and diagnosis of dental caries. Accepted by *Caries Research.*

Wright AJ, Burns D, Patterson BA, Poland SP, Valentine GJ, Girkin JM. (2005). Exploration of the optimisation algorithms used in the implementation of adaptive optics in confocal and multiphoton microscopy. *Microsc Res Tech.* 67 (1) 36-44.

Poland, S. P., Burns, D., Lubeigt, W., Patterson, B. A., Valentine, G., Wright, A. J., Girkin, J. M. (2006). The use of optimisation algorithmic techniques with active optics for aberration correction in optical sectioning microscopy. *Proc. of SPIE*, 6018, 60181H.

McConnell, G., Poland, S. P., Girkin, J. M. (2006). Fast wavelength multiplexing of a white-light supercontinuum using a digital micromirror device for improved confocal microscopy" , Rev Sci Instrum, 77, 013702 .

Wright, A. J., Patterson, B. A., Poland, S. P., Girkin, J. M., Gibson, G. M., Padgett, M. J. (2006). Dynamic closed-loop system for focus tracking using a spatial light modulator and a deformable membrane mirror. *Optics Express* 1 (14), 222-228.

Poland, S. P., Rousseau, C., Girkin, J. M. (2006). Use of commercially available software to model optical scattering tissue and confocal detection systems. Submitted *to Physics in Medicine and Biology.*

Presentations

Poland, S., Girkin, J., Longbottom, C., Hall, A. *Use of Structured Light In Optical Sectioning of Teeth To Qualitatively And Quantitatively Measure Caries"*, presented at Quantum Electronics and Photonics conference (QEP 16/Photon 04), September 9th 2004, Glasgow, UK.

Poland, S. P., Girkin, J. M. *Photonics technology for dental diagnosis.* Presented at close to market technologies/Medical devices in Scotland, Nexxus meeting, January 20th 2005, Bellshill, UK.

Poland, S. P., Rousseau C., Longbottom, C., Hall, A. F., Girkin, J. M. *Developing imaging systems to detect and diagnose caries in vivo.* Poster presented at SUPA photonics launch event, 31st of May 2005, Glasgow, UK.

Poland, S. P., Burns, D., Lubeigt, W., Patterson, B. A., Valentine, G., Wright, A. J., Girkin, J. M. Adaptive optic techniques for in depth imaging. Presented at the Rank mini-symposium on opto-electronics for use in the diagnosis of cancer, June 21st 2005, Grassmere, UK.

Poland, S. P., Burns, D., Lubeigt, W., Patterson, B. A., Valentine, G., Wright, A. J., Girkin, J. M. *The use of optimisation algorithmic techniques with active optics for aberration correction in microscopy.* Presented at European Optical Society conference (EOS 2004), July 1th 2005, London, UK.

Poland, S. P., Burns, D., Lubeigt, W., Patterson, B. A., Valentine, G., Wright, A. J., Girkin, J. M. *The use of optimisation algorithmic techniques with active optics for aberration correction in optical sectioning microscopy.* Paper presented at the 5th IWAOIM conference, September 1st 2005, Beijing, China.

Poland, S. P., Girkin, J. M. *Photonics to detect dental disease*. Presented at making light work in healthcare and biophotonics, Photonex 05, October 6th 2005, Coventry, UK.